

# Urban climate informatics

**Edited by**

Ariane Middel, Benjamin Bechtel,  
Matthias Demuzere and Negin Nazarian

**Published in**

Frontiers in Environmental Science  
Frontiers in Sustainable Cities



**FRONTIERS EBOOK COPYRIGHT STATEMENT**

The copyright in the text of individual articles in this ebook is the property of their respective authors or their respective institutions or funders. The copyright in graphics and images within each article may be subject to copyright of other parties. In both cases this is subject to a license granted to Frontiers.

The compilation of articles constituting this ebook is the property of Frontiers.

Each article within this ebook, and the ebook itself, are published under the most recent version of the Creative Commons CC-BY licence. The version current at the date of publication of this ebook is CC-BY 4.0. If the CC-BY licence is updated, the licence granted by Frontiers is automatically updated to the new version.

When exercising any right under the CC-BY licence, Frontiers must be attributed as the original publisher of the article or ebook, as applicable.

Authors have the responsibility of ensuring that any graphics or other materials which are the property of others may be included in the CC-BY licence, but this should be checked before relying on the CC-BY licence to reproduce those materials. Any copyright notices relating to those materials must be complied with.

Copyright and source acknowledgement notices may not be removed and must be displayed in any copy, derivative work or partial copy which includes the elements in question.

All copyright, and all rights therein, are protected by national and international copyright laws. The above represents a summary only. For further information please read Frontiers' Conditions for Website Use and Copyright Statement, and the applicable CC-BY licence.

ISSN 1664-8714  
ISBN 978-2-83251-592-1  
DOI 10.3389/978-2-83251-592-1

## About Frontiers

Frontiers is more than just an open access publisher of scholarly articles: it is a pioneering approach to the world of academia, radically improving the way scholarly research is managed. The grand vision of Frontiers is a world where all people have an equal opportunity to seek, share and generate knowledge. Frontiers provides immediate and permanent online open access to all its publications, but this alone is not enough to realize our grand goals.

## Frontiers journal series

The Frontiers journal series is a multi-tier and interdisciplinary set of open-access, online journals, promising a paradigm shift from the current review, selection and dissemination processes in academic publishing. All Frontiers journals are driven by researchers for researchers; therefore, they constitute a service to the scholarly community. At the same time, the *Frontiers journal series* operates on a revolutionary invention, the tiered publishing system, initially addressing specific communities of scholars, and gradually climbing up to broader public understanding, thus serving the interests of the lay society, too.

## Dedication to quality

Each Frontiers article is a landmark of the highest quality, thanks to genuinely collaborative interactions between authors and review editors, who include some of the world's best academicians. Research must be certified by peers before entering a stream of knowledge that may eventually reach the public - and shape society; therefore, Frontiers only applies the most rigorous and unbiased reviews. Frontiers revolutionizes research publishing by freely delivering the most outstanding research, evaluated with no bias from both the academic and social point of view. By applying the most advanced information technologies, Frontiers is catapulting scholarly publishing into a new generation.

## What are Frontiers Research Topics?

Frontiers Research Topics are very popular trademarks of the *Frontiers journals series*: they are collections of at least ten articles, all centered on a particular subject. With their unique mix of varied contributions from Original Research to Review Articles, Frontiers Research Topics unify the most influential researchers, the latest key findings and historical advances in a hot research area.

Find out more on how to host your own Frontiers Research Topic or contribute to one as an author by contacting the Frontiers editorial office: [frontiersin.org/about/contact](http://frontiersin.org/about/contact)

# Urban climate informatics

## Topic editors

Ariane Middel — Arizona State University, United States  
Benjamin Bechtel — Ruhr University Bochum, Germany  
Matthias Demuzere — Ruhr University Bochum, Germany  
Negin Nazarian — University of New South Wales, Australia

## Citation

Middel, A., Bechtel, B., Demuzere, M., Nazarian, N., eds. (2023). *Urban climate informatics*. Lausanne: Frontiers Media SA. doi: 10.3389/978-2-83251-592-1

# Table of contents

- 05 **LCZ Generator: A Web Application to Create Local Climate Zone Maps**  
Matthias Demuzere, Jonas Kittner and Benjamin Bechtel
- 23 **Determining Building Natural Ventilation Potential via IoT-Based Air Quality Sensors**  
Maohui Luo, Yumeng Hong and Jovan Pantelic
- 38 **The Potential of a Smartphone as an Urban Weather Station—An Exploratory Analysis**  
Aly Noyola Cabrera, Arjan Droste, Bert G. Heusinkveld and Gert-Jan Steeneveld
- 54 **Combining High-Resolution Land Use Data With Crowdsourced Air Temperature to Investigate Intra-Urban Microclimate**  
Julia Potgieter, Negin Nazarian, Mathew J. Lipson, Melissa A. Hart, Giulia Ulpiani, William Morrison and Kit Benjamin
- 73 **Towards a Living Lab for Enhanced Thermal Comfort and Air Quality: Analyses of Standard Occupancy, Weather Extremes, and COVID-19 Pandemic**  
Giulia Ulpiani, Negin Nazarian, Fuyu Zhang and Christopher J. Pettit
- 97 **Quantifying Local and Mesoscale Drivers of the Urban Heat Island of Moscow with Reference and Crowdsourced Observations**  
Mikhail Varentsov, Daniel Fenner, Fred Meier, Timofey Samsonov and Matthias Demuzere
- 118 **CrowdQC+—A Quality-Control for Crowdsourced Air-Temperature Observations Enabling World-Wide Urban Climate Applications**  
Daniel Fenner, Benjamin Bechtel, Matthias Demuzere, Jonas Kittner and Fred Meier
- 139 **SmartAirQ: A Big Data Governance Framework for Urban Air Quality Management in Smart Cities**  
Akshara Kaginalkar, Shamita Kumar, Prashant Gargava, Neelesh Kharkar and Dev Niyogi
- 166 **Urban Climate Informatics: An Emerging Research Field**  
Ariane Middel, Negin Nazarian, Matthias Demuzere and Benjamin Bechtel
- 181 **MaRTiny—A Low-Cost Biometeorological Sensing Device With Embedded Computer Vision for Urban Climate Research**  
Karthik K. Kulkarni, Florian A. Schneider, Tejaswi Gowda, Suren Jayasuriya and Ariane Middel

- 196 **A Transformation in City-Descriptive Input Data for Urban Climate Models**  
Mathew J. Lipson, Negin Nazarian, Melissa A. Hart, Kerry A. Nice and Brooke Conroy
- 214 **Resolving Radiant: Combining Spatially Resolved Longwave and Shortwave Measurements to Improve the Understanding of Radiant Heat Flux Reflections and Heterogeneity**  
Coleman Merchant, Forrest Meggers, Miaomiao Hou, Dorit Aviv, Florian Arwed Schneider and Ariane Middel



# LCZ Generator: A Web Application to Create Local Climate Zone Maps

Matthias Demuzere\*, Jonas Kittner and Benjamin Bechtel

Urban Climatology Group, Department of Geography, Ruhr-University Bochum, Bochum, Germany

## OPEN ACCESS

**Edited by:**

Christos H. Haliotis,  
Public Health England,  
United Kingdom

**Reviewed by:**

Ke-Seng Cheng,  
National Taiwan University, Taiwan  
Shuisen Chen,  
Guangzhou Institute of Geography,  
China  
Björn Maronga,  
Leibniz University Hannover, Germany

**\*Correspondence:**

Matthias Demuzere  
matthias.demuzere@rub.de

**Specialty section:**

This article was submitted to  
Environmental Informatics and  
Remote Sensing,  
a section of the journal  
*Frontiers in Environmental Science*

**Received:** 03 December 2020

**Accepted:** 25 March 2021

**Published:** 23 April 2021

**Citation:**

Demuzere M, Kittner J and Bechtel B  
(2021) LCZ Generator: A Web  
Application to Create Local Climate  
Zone Maps.  
*Front. Environ. Sci.* 9:637455.  
doi: 10.3389/fenvs.2021.637455

Since their introduction in 2012, Local Climate Zones (LCZs) emerged as a new standard for characterizing urban landscapes, providing a holistic classification approach that takes into account micro-scale land-cover and associated physical properties. In 2015, as part of the community-based World Urban Database and Access Portal Tools (WUDAPT) project, a protocol was developed that enables the mapping of cities into LCZs, using freely available data and software packages, yet performed on local computing facilities. The LCZ Generator described here further simplifies this process, providing an online platform that maps a city of interest into LCZs, solely expecting a valid training area file and some metadata as input. The web application (available at <https://lcz-generator.rub.de>) integrates the state-of-the-art of LCZ mapping, and simultaneously provides an automated accuracy assessment, training data derivatives, and a novel approach to identify suspicious training areas. As this contribution explains all front- and back-end procedures, databases, and underlying datasets in detail, it serves as the primary "User Guide" for this web application. We anticipate this development will significantly ease the workflow of researchers and practitioners interested in using the LCZ framework for a variety of urban-induced human and environmental impacts. In addition, this development will ease the accessibility and dissemination of maps and their metadata.

**Keywords:** local climate zones, WUDAPT, google earth engine, urban form and function, web application

## 1. INTRODUCTION

Urbanization and climate change may be the two most important trends to shape global development in the decades ahead. On the one hand, cities serve as engines of change, drive economic progress and pull more people out of poverty than at any other time in history. On the other hand, climate change could undercut all of this by exacerbating resource scarcity and putting (vulnerable) communities at risk from a myriad of environmental challenges (e.g., heat waves, droughts, floods, air quality, etc.) (Baklanov et al., 2018). The magnitude of this risk will increase in the coming decades as it is predicted that global urban land will increase significantly (Chen et al., 2020), and by 2050, almost 70% of the world's population will be urban dwellers (UN, 2019). On top, as earth's climate will continue to change over the coming decades, projected global warming and aggravated hydro-climatic extremes will hit urban centers especially hard, being a major threat to the health and well-being of human populations and urban ecosystems (Costello et al., 2009).

Successful mitigation and adaptation to climate change will depend centrally on what happens in cities, as urban areas house the majority of people, assets and infrastructure, and are responsible for about 70% of the world's energy-related CO<sub>2</sub> emissions (Lucon et al., 2014). At the international level, cities are becoming of increasing concern: the new United Nations Agenda and Sustainable

Development Goals have a clear focus on urban resilience, climate, and environment sustainability of smart cities. The Intergovernmental Panel on Climate Change (IPCC) held its first “cities and climate change” conference in 2018, and announced a special report on cities which will be part of the panel’s seventh assessment cycle (Bai et al., 2018). Finally, of the four challenges identified by the World Meteorological Organization (WMO) World Weather Research Program, two are urban related: high-impact weather, including impacts in cities, and urbanization (Creutzig et al., 2016; Masson et al., 2020).

Despite this new focus on cities as a critical scale for climate change management, we know very little about most cities on the planet—being generally ignorant of their extent, how they are constructed and how they are occupied (Demuzere et al., 2020a). First and foremost, climate-relevant urban data consistent in coverage, scale, and content are needed to support risk assessment and its management and to enable effective knowledge transfer between cities. The right data at the right scale are an essential prerequisite for developing fit-for-purpose urban planning policies (Georgescu et al., 2015). A number of projects have mapped the global urban extent at finer and finer detail (e.g., Pesaresi et al., 2013; Corbane et al., 2017; Esch et al., 2017; Gong et al., 2020), but these efforts need to be complemented by a wider range of information-rich intra-urban classes that describe different types of urban land covers and land uses: the Local Climate Zone (LCZ) typology is a good example of such classification scheme (Stewart and Oke, 2012; Demuzere et al., 2020a; Reba and Seto, 2020).

Local Climate Zones refer to a classification system that exists out of 17 classes, 10 of which can be described as urban (**Figure 1**). The system is originally designed to provide a framework for urban heat island studies, allowing the standardized exchange of urban temperature observations (Stewart and Oke, 2012). The LCZ classes are formally defined as “regions of uniform surface cover, structure, material, and human activity that span hundreds of meters to several kilometers in horizontal scale,” exclude “class names and definitions that are culture or region specific,” and are characterized by “a characteristic screen-height temperature regime that is most apparent over dry surfaces, on calm, clear nights, and in areas of simple relief” (Stewart and Oke, 2012). Its universality has important advantages, as it allows a systematic comparability of global intra- and inter-urban heat island studies (e.g., Bechtel et al., 2019a), provides a common platform for knowledge exchange and the description of urban canopy parameters in urban ecosystem processes, and supports model applications, especially for cities with little or insufficient data infrastructure (Stewart and Oke, 2012; Ching et al., 2018; Brousse et al., 2019, 2020b; Demuzere et al., 2020a; Varentsov et al., 2020).

In the early 2010s, Bechtel (2011) and Bechtel and Daneke (2012) first proposed mapping entire cities into Local Climate Zones. This procedure was formalized by Bechtel et al. (2015), relying on an “off-line” workflow that integrates training areas (TAs, a set of LCZ labeled polygons) and Landsat 8 (L8) imagery within the SAGA software package (Conrad et al., 2015) over a limited spatial domain. More specifically, each TA is identified using Google Earth images aided by the visual and numerical

information provided in Stewart and Oke (2012). The TA dataset is then used to extract spectral information from L8 images, which in turn is used in a supervised random forest classifier to categorize the entire region of interest into LCZ types. This procedure was afterwards adopted by the World Urban Database and Access Portal Tools (WUDAPT) community project to create consistent LCZ maps of global cities (Ching et al., 2018).

While this framework is valuable (currently ~150 cities mapped), it will not result in a database that could support urban decision-making globally in a reasonable time frame. Therefore, Demuzere et al. (2019b,c, 2020a) developed a number of strategies to expand LCZ coverage rapidly. The first recognizes that much of the information contained in TA data for one city is transferable to other cities for which no TA data is available. The second employs Google’s Earth Engine (EE)—a cloud-based platform for planetary-scale analysis (Gorelick et al., 2017)—to use its computational power, access to a range of geospatial datasets (Landsat, Sentinel, and others) and a large number of predefined algorithms. Among others, this cloud-based approach resulted in high-resolution Local Climate Zone maps for global cities, Europe and the continental United States of America (Bechtel et al., 2019a,b; Demuzere et al., 2019a,b,c, 2020a,b; Brousse et al., 2020a).

The LCZ Generator web application described here further simplifies this process, as it provides an online platform that maps a city of interest into LCZs, solely expecting a valid TA file and some metadata as input. The application integrates all of the above-mentioned developments and procedures, and simultaneously provides an automated accuracy assessment, TA data derivatives and a novel approach to identify suspicious TAs. As this contribution explains all front- and back-end procedures, databases and underlying datasets in detail, it serves as the primary “User Guide” for this web application.

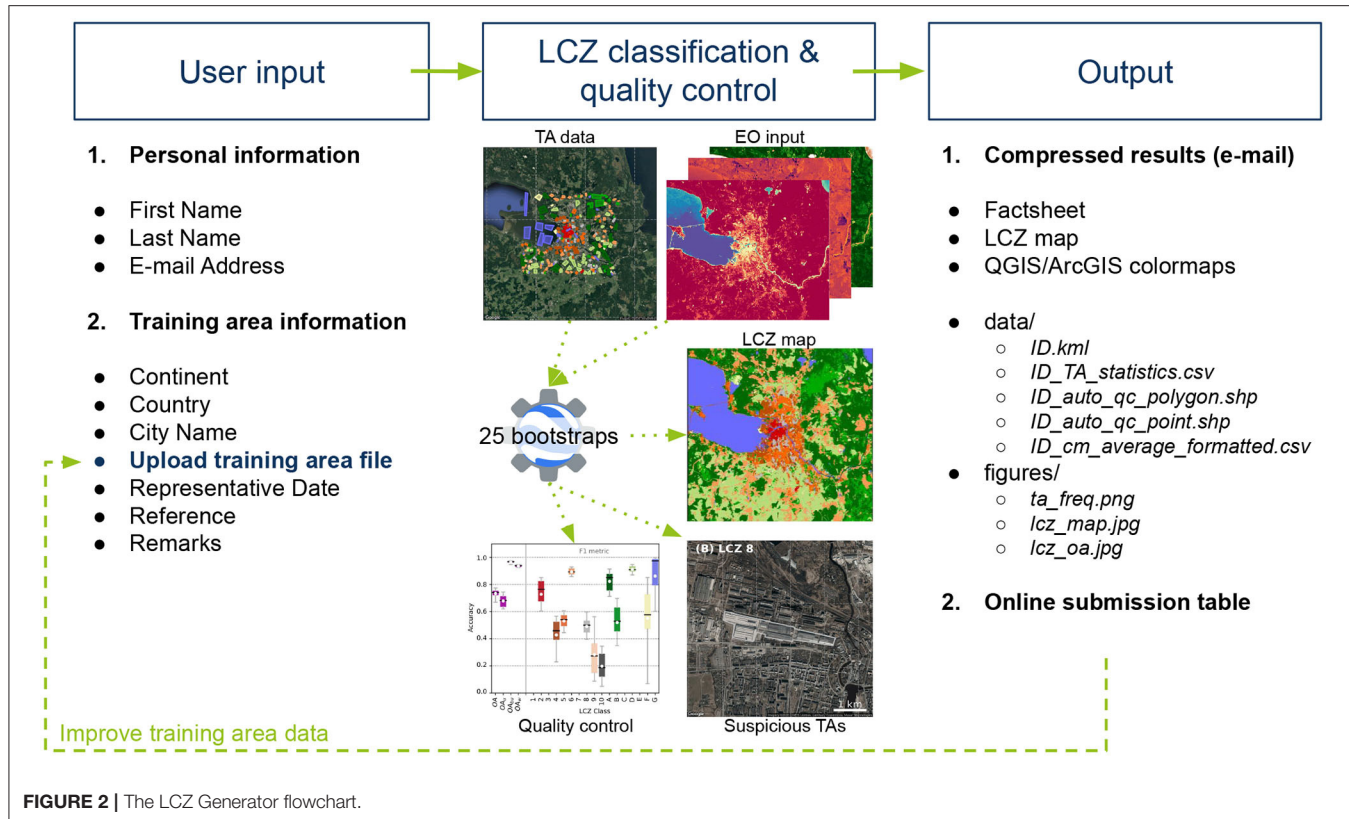
## 2. LCZ GENERATOR DESIGN

The LCZ Generator web application consists out of three major steps (**Figure 2**). In a first step, personal and training information needs to be submitted via the web application (section 2.1). Upon successful submission, the LCZ classification and quality control is launched in the back-end, to produce a quality-controlled LCZ map, metadata statistics, and labels for suspicious polygons (sections 2.2 and 2.3). In a third and final step, compressed results are sent to the user via e-mail, and simultaneously added to the online submission table (section 2.4). Each of these steps are discussed in more detail in the following sections.

### 2.1. User Input

When accessing the LCZ Generator, the user is directed to a submission form that consists out of two sections: personal information and TA information (**Table 1**). The personal information consists out of the author’s first and last name and e-mail address. The name information refers to the primary author of the TA file, which can be acknowledged in case it is used by others. The e-mail is required since the results of the LCZ Generator are sent via e-mail. If the author consents, the



**TABLE 1 |** Overview of the front-end input fields.

	Field	Explanation
Personal information	First Name*	First name of the author of the TA set
	Last Name*	Last name of the author of the TA set
	E-mail Address*	Author e-mail address. Required, since results are send by e-mail.
TA information	Continent*	Drop down menu listing seven continents: Africa, Asia, Europe, North America, Oceania, South America
	Country*	Drop down menu with the world's countries
	City name*	Official name of the city to be mapped.
	Upload file*	Button to upload a Keyhole Markup Language (.kmz) file or its zipped version (.kmz). The back-end expects a file with a format similar to WUDAPT's official TA template <sup>1</sup> .
	Date*	Date for which the TA polygons are representative
	Reference	Reference for TA file: - DOI of published paper if available - if not, full reference including link that points to the online resource - blank in case no reference is available
	Remarks	Additional information on potential co-authors for the TA file ( <i>firstname, lastname</i> ) or any other information that supports the interpretation of the TAs.

Fields denoted with \* are required.

author's first and last name are displayed in the publicly accessible submission table and factsheet (see section 2.4).

The second section of the submission form queries about the TA file. A user can select the continent and country via a drop-down menu, and provide the name of the city of interest. The date field refers to the date for which the training polygons are

representative. This is not necessarily the date on which the TA file is created, but rather the date of the imagery (e.g., in Google Earth, see Bechtel et al., 2015) on which the labeled TAs are developed. The non-required “Reference” and “Remarks” fields allow the user to provide additional metadata about the TA file. The former can be the Digital Object Identifier (DOI) in case the

TA set is published in a (peer-reviewed) paper, a reference to an online resource, or left blank if none of the previous are available. The latter allows free text and can e.g., be used to list additional authors that contributed to the creation of the TA file, or any other information that is relevant to understand the content of the TA file.

Key to the submission is the TA file itself, that can be uploaded via a button and can have any name. Yet upon submission, a file-check is done to make sure it has not been uploaded before and is compatible with the remainder of the LCZ Generator. First of all it is important that the file extension is *.kml* or *.kmz* [Keyhole Markup Language (*.kml*) or its zipped version (*.kmz*) respectively]. In case of *.kmz*, the file is unzipped to *.kml*. Second, it is checked whether the TA file can be read, and contains one or more LCZ folders, as provided in the default WUDAPT LCZ *.kml* template<sup>1</sup>. This strategy is chosen as users can provide any label to a LCZ class (e.g., “LCZ 2a,” “compact midrise 1,” “not sure about this one,” ...), making it difficult for the application to assign an appropriate LCZ label required for the classification. If folders are available, the folder names are used to rename their underlying polygons. Third, if present, empty polygons are removed (e.g., “Style Place Holders” that were not deleted from the *.kml* template). Fourth, each polygon is provided with a unique ID, which is required to perform the automated TA quality control (see section 2.3). Finally, also the size of the region of interest (ROI) is checked. The ROI is defined as the outer extent of the TA polygons, currently with an additional buffer on all sides of 10 km. In order to maintain computational efficiency, the maximum allowed ROI size is currently set to 2.5° x 2.5°.

If any of the above checks fail, a red-framed message is returned to the user upon submission, instructing about ways to solve the issue. If all tests pass, a green-framed message is returned, and the LCZ Generator is launched in the back-end.

## 2.2. LCZ Classification and Quality Control

Before the TAs are used in the classification procedure, they undergo a final pre-processing step: the surface area of large polygons (>1.5 km<sup>2</sup>) is reduced to a radius of approximately 350 m, in line with Demuzere et al. (2019b,c, 2020a) and the minimum allowed surface area described in section 2.3. These large polygons typically represent homogeneous areas such as water bodies and forests, a characteristic that is neither needed nor wanted, as it leads to more imbalanced TA data and computational inefficiency of the classifier.

In addition to the TAs, one needs earth observation data and a supervised classifier (Bechtel et al., 2015). The default WUDAPT workflow relies on Landsat 8 data as input to the random forest classifier, embedded as an “LCZ classification tool” in SAGA GIS (Breiman, 2001; Bechtel et al., 2015; Conrad et al., 2015). Yet here, the LCZ Generator builds further upon the findings of Demuzere et al. (2019b,c, 2020a), Brousse et al. (2020a), in which additional earth observations are used, in combination with the TAs, as input to EE’s implementation of the random forest classifier.

<sup>1</sup>[http://www.wudapt.org/wp-content/uploads/2020/08/WUDAPT\\_L0\\_Training\\_template.kml](http://www.wudapt.org/wp-content/uploads/2020/08/WUDAPT_L0_Training_template.kml)

**TABLE 2 |** Earth observation input features currently available for the LCZ Generator.

Sensor	Band / Ratio / Indicator	Reference
Landsat 8	Median composites for B2 (red), B3 (green), B4 (red), B5 (Near infrared), B6/7 (Shortwave infrared 1/2), B10/11 (Thermal infrared 1/2) Median composites for BCI, NDBal, EBBI, NDWI, NDBI, NDVI 10 and 90th percentile composites for NDVI	See Demuzere et al. (2019b) for details.
Sentinel 1	Single co-polarization (VV), dual-band cross-polarization (VH), and their ratio (VV/VH) Mean and standard deviation of VV and VH combined VH indicator	See Demuzere et al. (2019b) for details. Li et al., 2020
Sentinel 2	Median composite Red edge bands (B5, B6, B7) Median composite NDVI Red Edge 1 and 2 Median composite S2REP, CSI, and SEI	Forkuor et al., 2018 Forkuor et al., 2018 Kaplan and Avdan, 2018; Sun et al., 2019
Other	Global Forest Canopy Height (GFCH) DTM, DEM, DSM	See Demuzere et al. (2019b) for details.

Landsat 8 and Sentinel 1/2 composites are derived over the period 01-01-2017 to 31-12-2019. BCI, Biophysical Composition Index; NDBal, Normalized Difference Bareness Index; EBBI, Enhanced Built-Up and Bareness Index; NDWI, Normalized Difference Wetness Index; NDVI, Normalized Difference Vegetation Index; S2REP, Sentinel-2 Red-Edge Position Index; CSI, Combinational Shadow Index; SEI, Shadow Enhancement Index; DTM, Digital Terrain Model; DEM, Digital Elevation Model; DSM, Digital Surface Model.

Currently, a total of 33 input features are available globally, on a 100 m resolution, and are stored in EE’s online WUDAPT asset folder (3 TB of data) (Table 2). They consist out of 16 features derived from Landsat 8, 5 features from Sentinel-1, 8 features from Sentinel-2, and four additional features reflecting terrain and forest canopy height. Note that the list of input features used in Demuzere et al. (2019b, 2020a) is expanded with Sentinel-2 red edge bands to improve the mapping of wetlands (Forkuor et al., 2018; Kaplan and Avdan, 2018; Brousse et al., 2020a), and a Sentinel-2-based combinational shadow index (CSI) and shadow enhancement index (SEI) median composite (Sun et al., 2019). The system is designed in such a way that, whenever additional, new or improved global earth observation datasets become available, they can easily be added to the asset folder and activated in the classification procedure.

To ensure the quality of the resulting LCZ map, quality control is a vital step (Verdonck et al., 2017). Hence, an automated cross-validation approach using 25 bootstraps is applied (Bechtel et al., 2019a). In each bootstrap, 70% of the TA polygons are used to train and 30% to test; the polygons are selected by stratified (LCZ type) random sampling, maintaining the original LCZ

**TABLE 3 |** File structure and contents of the compressed (.zip) results send to the user via e-mail.

Folder	File(s)	Explanation
	<i>ID_factsheet.html</i>	Webpage containing visual summary of the results (section 2.3)
data/	<i>ID.tif</i>	Geotif with three bands: “lcz,” “lczFilter,” and “classProbability” (section 2.2)
	<i>qgis_lczi_colormap.txt / arcgis_lczi_colormap.lyr</i>	Colormaps to be used in QGIS / ArcGIS
	<i>ID.kml</i>	Original TA file (converted to .kml in case of .kmz) (section 2.1)
	<i>ID_TA_statistics.csv</i>	TA geometry statistics (section 2.3)
	<i>ID_auto_qc_polygon.shp</i>	TA auto quality control (polygons) (section 2.3)
figures/	<i>ID_auto_qc_point.shp</i>	TA auto quality control (points) (section 2.3)
	<i>ID_cm_average_formatted.csv</i>	Average formatted confusion matrix (section 2.2)
factsheet_files/	<i>ta_freq.png</i>	Figure with number of TAs (section 2.3)
	<i>lczi_map.jpg</i>	Figure displaying final filtered LCZ map (section 2.2)
	<i>lczi_oa.jpg</i>	Accuracy boxplot figure (section 2.2)

*ID* refers to the unique identifier given to each submission (section 2.5.1).

class frequency distribution. This procedure is repeated 25 times allowing us to provide confidence intervals around the accuracy metrics. In addition, this approach also allows the creation of a probability map, which indicates how often (in %) the mode was mapped in the iterative procedure.

The resulting LCZ map provided to the user is based on all TAs (100% of the TA polygons) and input features. A filtered version is also provided using the morphological Gaussian filter described in more detail in Demuzere et al. (2020a). This is preferred over the WUDAPT’s traditional majority post-classification, as it accounts for the distance from the center of the kernel and differences in the typical patch size between classes. For example, linear features like rivers are typically removed by the majority filter. The LCZ map, its Gaussian-filtered version and the probability map are provided to the user as a single *.tif* with three bands: “lcz,” “lczFilter,” and “classProbability,” respectively.

The accuracy metrics used follow previous work (see Demuzere et al., 2020a, and references therein): overall accuracy (OA), overall accuracy for the urban LCZ classes only ( $OA_u$ ), overall accuracy of the built vs. natural LCZ classes only ( $OA_{bu}$ ), a weighted accuracy ( $OA_w$ ), and the class-wise metric F1. The overall accuracy denotes the percentage of correctly classified pixels.  $OA_u$  reflects the percentage of classified pixels from the urban LCZ classes only, and  $OA_{bu}$  is the overall accuracy of the built vs. natural LCZ classes only, ignoring their internal differentiation. The weighted accuracy ( $OA_w$ ) is obtained by applying weights to the confusion matrix and accounts for the (dis)similarity between LCZ types (Bechtel et al., 2017, 2020). For example, LCZ 4 is most similar to the other open urban types (LCZs 5 and 6), leaving these pairs with higher weights compared to e.g., an urban and natural LCZ class pair. This results in penalizing confusion between dissimilar types more than confusion between similar classes. Finally, the class-wise accuracy

is evaluated using the F1 metric, which is a harmonic mean of the user’s and producer’s accuracy (Verdonck et al., 2017). Accuracy results are provided to the user in two ways: average confusion matrix over the 25 bootstraps (*\_cm\_average\_formatted.csv*), including Overall, User and Producer Accuracy (in %) and a boxplot figure (*\_cm\_oa\_boxplot.jpg*) depicting the range of all accuracy metrics over all bootstraps.

### 2.3. Automated TA Quality Control

Sections 2.1 and 2.2 are at the core of the LCZ Generator application, explaining how a user’s TA dataset combined with a wealth of earth observation input feeds the random forest classifier, resulting in a quality-controlled LCZ map. Yet an additional automated 3-step TA quality control is added, that aims to facilitate the revision of the original TA submission and resulting LCZ map, since previous work by Bechtel et al. (2017, 2019a) and Verdonck et al. (2019) highlighted that multiple iterations can significantly improve the overall accuracy of the LCZ map, and are thus recommended.

Stewart and Oke (2012) suggested that the typical horizontal scale of a Local Climate Zone—reflecting an area of uniform surface cover, structure, and material—spans hundreds of meters to several kilometers. In addition, the number of TAs selected for each zone can be an indicator for zones which are hard to classify, and the WUDAPT protocol suggests to digitize compact and simple TA sets, characterized by a shape ratio close to one (Bechtel et al., 2019a; Verdonck et al., 2019). Therefore, a summary table (*\_TA\_statistics.csv*) is added to the output, providing, for each available LCZ class, the number of polygons (Count,  $C$ ), the average and total surface area (Avg. / Total area,  $\text{km}^2$ ), the perimeter (km), the shape (-), and number of vertices (-).

Subsequently, a 3-step automated quality control (QC) is applied to label suspicious TA polygons. In a first step (*qc\_step1*),

## LCZ FACTSHEET

**User Information**

---

- Author: Teresa Mansheim

**Submission information**

---

- Continent: Asia
- Country: Russian Federation
- City: Saint Petersburg
- Reference:
- Remarks: Produced as a test sample for the LCZ Generator User Guide paper.
- Representative date: 2020-08-21
- Submission date: 2020-11-26 18:26
- Software version: 0.0.0b4
- ID: 17dc02e450acb7091ccbf7d4ff6fa54249590133

**Training area information**

---

See [this file](#) for more information on:

- Available LCZ classes
- Number of training areas per LCZ class
- Average / Total surface area ( $\text{km}^2$ ) per LCZ class
- Average perimeter (km) per LCZ class
- Average shape per LCZ class
- Average number of vertices per LCZ class

**LCZ map & Accuracy**

---

The final filtered LCZ map is produced using all training areas and input features. Corresponding overall accuracies are:

- OA: 0.73
- OA<sub>u</sub>: 0.67
- OA<sub>bu</sub>: 0.96
- OA<sub>w</sub>: 0.94

Underlying and additional datafiles: [original training areas](#), [geotif](#), [average confusion matrix over all bootstraps](#), [boxplot figure with accuracies](#), and [suspicious training areas \(polygons / points\)](#).

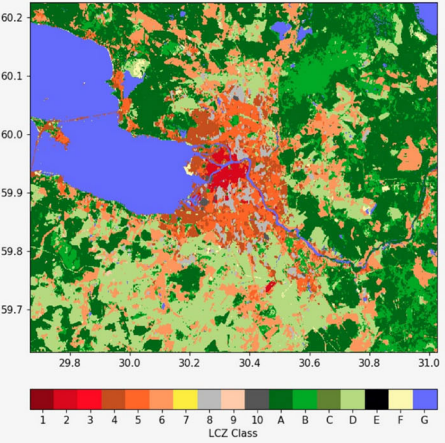


**FIGURE 3 |** Factsheet example for Saint Petersburg. Note that in reality, the factsheet also contains a “Terms of Service” and “Attribution” section (see section 2.5.4). These sections are omitted here for clarity.

Frontiers in Environmental Science | www.frontiersin.org

11

April 2021 | Volume 9 | Article 637455

polygons with a surface area below  $0.04 \text{ km}^2$  (too small) or a shape ratio 3 (too complex shape) are flagged. In a second step (*qc\_step2*), the non-parametric density-based spatial clustering of applications with noise (DBSCAN) (Ester et al., 1996; Schubert et al., 2017) is used to identify whether the average spectral value of a polygon of LCZ class  $i$  is considered as an outlier compared to the average spectral values of all other polygons of that class  $i$ . The method requires two parameters:  $\epsilon$ , which is the maximum distance between two samples for one to be considered as in the neighborhood of the other, and *MinPoints*, the number of minimum samples in a neighborhood for a point to be considered as a core point. Here,  $\epsilon$  is set to 0.3 and *MinPoints* to  $C_i/10$ , based on a number of iterations and expert judgement. Since this method is efficient on large, multi-dimensional datasets, it is applied simultaneously on all earth observation input features discussed in section 2.2.

A third and final QC step (*qc\_step3*) considers all individual pixel values of all polygons in each LCZ class  $i$  compared to the polygon average approach from *qc\_step2*. The same parameter values for  $\epsilon$  and *MinPoints* are used, and the procedure is also applied on all available input features simultaneously. The pixel's latitude and longitude coordinates here serve as an unique identifier to tag suspicious points within polygons.

If polygons are identified as suspicious, the user receives two shapefiles containing the results of the automated quality control procedure. The first shapefile (*ID\_auto\_qc\_polygon.shp*) contains all polygons flagged as suspicious in at least one of the three steps. Since *qc\_step3* returns points, each polygon that intersects with at least one of these flagged points is added. All shapes in this file contain additional metadata fields characterizing their geometry (area, perimeter, shape, vertices) and a boolean value for each of the three QC steps: *True* (1) / *False* (0) in case a TA passed / failed one of the three QC tests. The second shapefile (*ID\_auto\_qc\_point.shp*) contains the individual flagged points, which might provide additional

insights into why certain polygons are flagged as suspicious. In case no polygons or points are labeled as suspicious, the same files are created yet only contain a point with a dummy identifier and a geometry indicating the center pixel of the ROI.

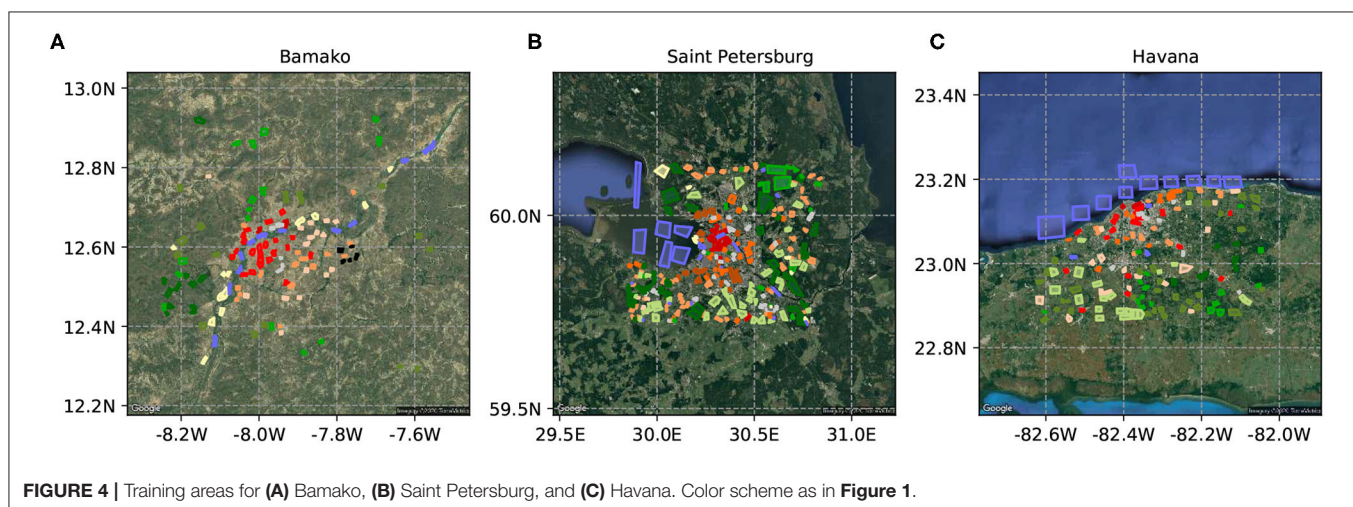
## 2.4. Generated Output

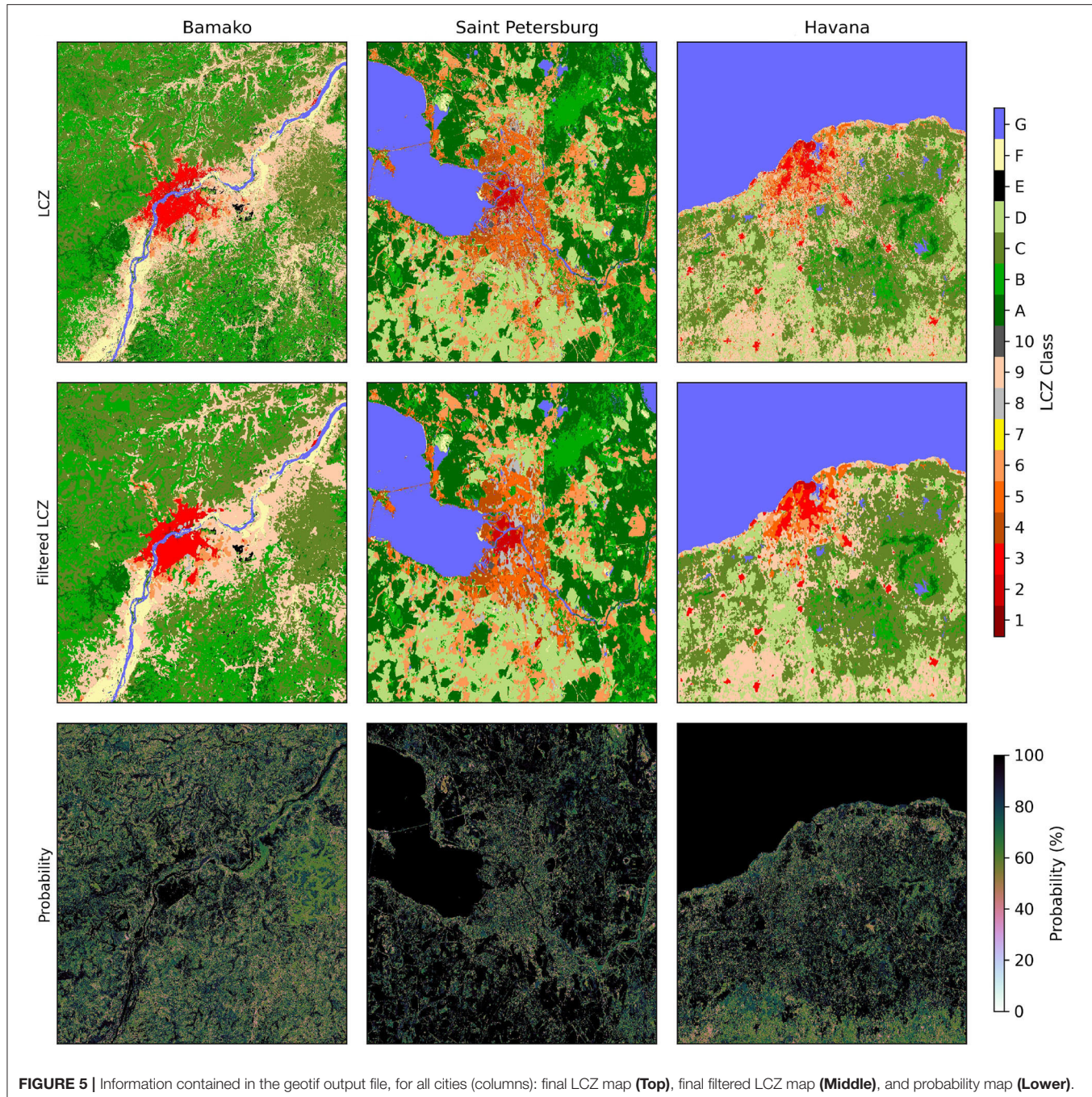
If the LCZ Generator successfully completes all processes, the user is notified via e-mail, that contains a compressed (.zip) archive as attachment. This archive (Table 3) contains the various outputs described in sections 2.2 and 2.3.

The output is listed in an online search- and sortable submission table including information about the city, country, continent, date of the submission, overall accuracy, and a button (*Show Factsheet*) linking to the factsheet that provides a visual summary of all results. In case a user did not agree to display his/her name (see section 2.1), the *Author* field is left blank in both the submission table and factsheet. By checking one or multiple entries using the left-hand side check-boxes of the submission table, one can also download the corresponding .zip archive(s).

The submission table is structured as follows. If a user submitted multiple TAs for one city, only the submission having the best overall accuracy is displayed. In case multiple users submit TAs for the same city, only the best result is displayed, but this time for each individual user. A button (*Show all submissions*) allows the user to view and download all submissions including those where one author submitted multiple versions of TAs for the same city. This structure ensures that only results with the best possible quality are directly available for download, but also that this web application can be used for learning purposes and improving the TA creation technique without adding multiple previous submissions of minor quality to the table.

In the event the LCZ Generator fails after successfully submitting the TAs, the user is notified via e-mail as well. In this





case, the developers automatically receive a message, and can use the log stored in the back-end to solve the issue.

## 2.5. Technical Information, Terms of Service, and Attribution Guidelines

### 2.5.1. Database

All data including the author and submission information, as well as the processing outputs are stored with a unique *ID* in a

*PostgreSQL* database. The TAs are stored in a *PostGIS* table as individual polygons.

### 2.5.2. Versioning

The LCZ-Generator code will be versioned according to semantic versioning<sup>2</sup>: breaking changes to the application programming interface (API)—including changes to the input features (Table 2)—will be indicated by an incremented major

<sup>2</sup><https://semver.org/>

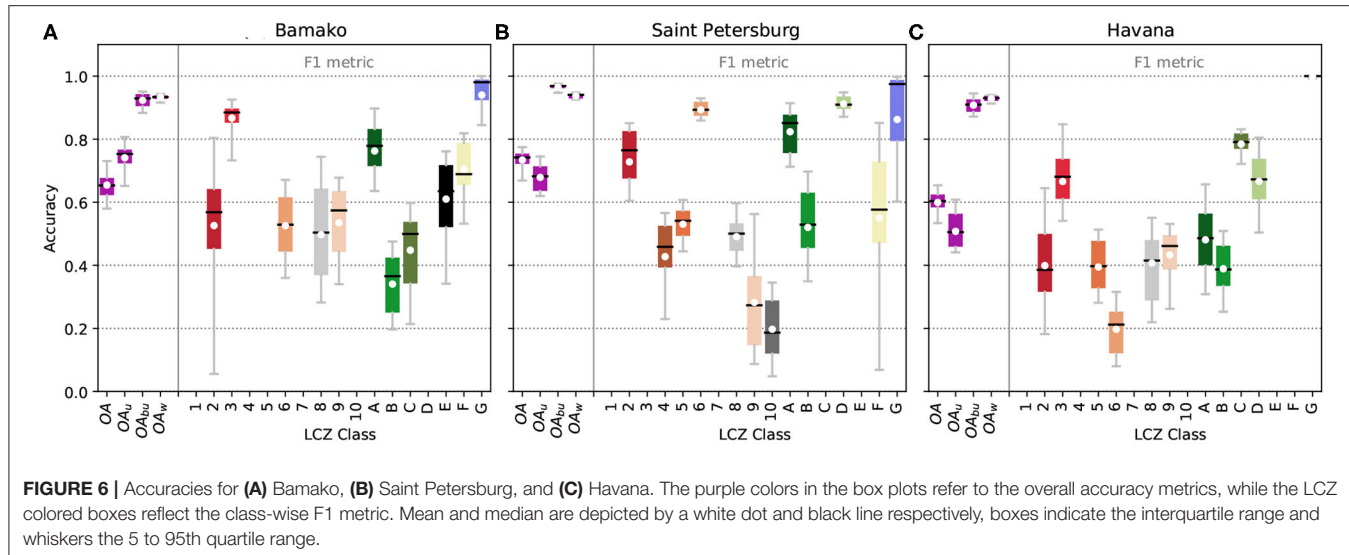


**FIGURE 6 |** Accuracies for (A) Bamako, (B) Saint Petersburg, and (C) Havana. The purple colors in the box plots refer to the overall accuracy metrics, while the LCZ colored boxes reflect the class-wise F1 metric. Mean and median are depicted by a white dot and black line respectively, boxes indicate the interquartile range and whiskers the 5 to 95th quartile range.

version. After the release of version 1.0.0, and for each next release, all changes will be described in a changelog, available on the issue page (section 2.5.3). The version used for creating each LCZ map is stored for each submission and included in the corresponding factsheet.

### 2.5.3. Support

Guidance in how to use the LCZ Generator is provided via the “Getting started” and “Frequently Asked Questions (FAQ)” pages, accessible via the navigation bar of the web application. If users run into issues while using the LCZ Generator, they can open a public issue on the application’s Github issue tracker<sup>3</sup>. In case security bugs are found, we ask the user to not create a public issue but instead reach out to us directly via lcz-generator@rub.de.

### 2.5.4. Terms of Service and Attribution Guidelines

The web application uses the CC BY-SA 4.0 license<sup>4</sup> for all submissions made. The terms of service<sup>5</sup> need to be accepted upon submission. In addition, attribution guidelines<sup>6</sup> are provided on how to acknowledge the materials produced by the LCZ Generator, the authors of the TAs or any of the underlying methods used in the Generator’s classification procedures. This information is also embedded at the end of the factsheet (see also section 3.1).

## 2.6. Test Samples

In this paper, the performance of the LCZ Generator web application is demonstrated via three new TA samples, compiled by three student assistants at the Ruhr University Bochum (Germany). The samples are from different urban ecoregions—which stratify urban areas based on general climate and

vegetation characteristics, regional differences in urban topology, and the level of economic development (Schneider et al., 2010)—and include Saint Petersburg (Russia, “Temperate forest in Asia”), Bamako (Mali, “Tropical, sub-tropical Savannah in Africa”), and Havana (Cuba, “Tropical broadleaf forest in South America”). The TAs are a first version, and did not undergo a manual review by an experienced operator (Bechtel et al., 2019a).

## 3. RESULTS

This section presents and discusses all contents of the resulting .zip archive in more detail. Note that all LCZ results in this paper are displayed with labels 1–10 for the urban classes, and A to G for the natural classes, in line with Stewart and Oke (2012) (Figure 1). However, all underlying files output by the LCZ generator use integers, with labels 11 to 17 for the natural classes.

### 3.1. Submission Table

Figure 3 provides a factsheet example for the city of Saint Petersburg. It summarizes author, submission, TA and LCZ map & accuracy information. In addition to the author’s input discussed in section 2.1, the submission information also contains the submission date, the software version, and the ID. The software version tag is linked to the software’s version in GitHub, so that at any point in time it is clear with which code and parameters each submission is produced (section 2.5.2). The TA information section lists the content of the ID\_TA\_statistics.csv, that is also linked. In addition, a figure is added that displays the number of TAs per available LCZ class. This figure is stored as ta\_freq.png. Finally, the LCZ map & accuracy section provides quick access to all four overall accuracy scores, together with an image of the actual filtered LCZ map (stored as lcz\_map.jpg). Hyperlinks to all underlying data files are provided as well, e.g., by clicking the “boxplot figure with accuracies” link, the author can directly see the full accuracy assessment, including information from all bootstraps and class-wise F1 scores.

<sup>3</sup><https://github.com/RUBclim/LCZ-Generator-Issues>

<sup>4</sup><https://creativecommons.org/licenses/by-sa/4.0/>

<sup>5</sup><https://lcz-generator.rub.de/tos>

<sup>6</sup><https://lcz-generator.rub.de/attribution>

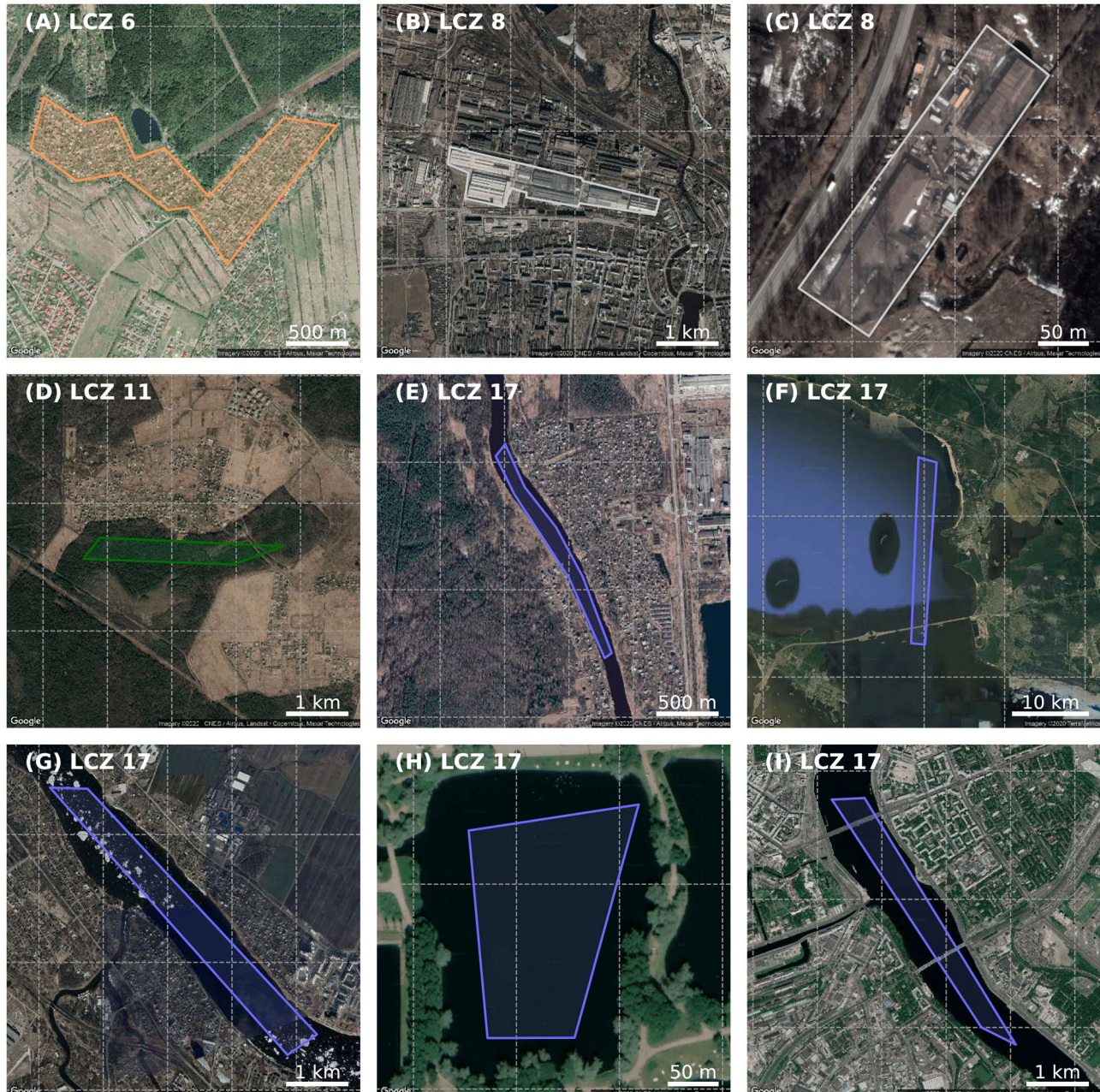


**FIGURE 7 |** All TA polygons tagged as suspicious during the first quality control step, for Saint Petersburg. Color scheme as in **Figure 1**.

### 3.2. LCZ Map and Accuracies

Feeding the random forest in a bootstrapping manner with the submitted TAs (**Figure 4**) and the earth observation input features (**Table 2**) results in a raw and filtered LCZ map, a pixel probability map (**Figure 5**) and overall accuracy metrics (**Figure 6**). Combined with the information from the factsheet (**Figure 3**) and the *ID\_TA\_statistics.csv* file, one can directly assess the amount and distribution of TA polygons. For Saint Petersburg, a total of 310 TA polygons are available, with the highest / lowest frequencies for LCZ 6 (Open

lowrise) and 14 (Low plants) / LCZ 9 (Sparsely built) and 10 (Heavy industry).

The raw and filtered LCZ maps (**Figure 5**) differ mainly in their fine-scale heterogeneity: as single pixels do not constitute an LCZ class, the Gaussian filter procedure is able to remove this granularity. Since the Gaussian parameters (standard deviation and kernel size) are currently derived by experts, and expected to differ between cities and continents (Demuzere et al., 2020a), they deserve further attention and potential adjustments in future versions of the LCZ Generator. The probability maps in **Figure 5**

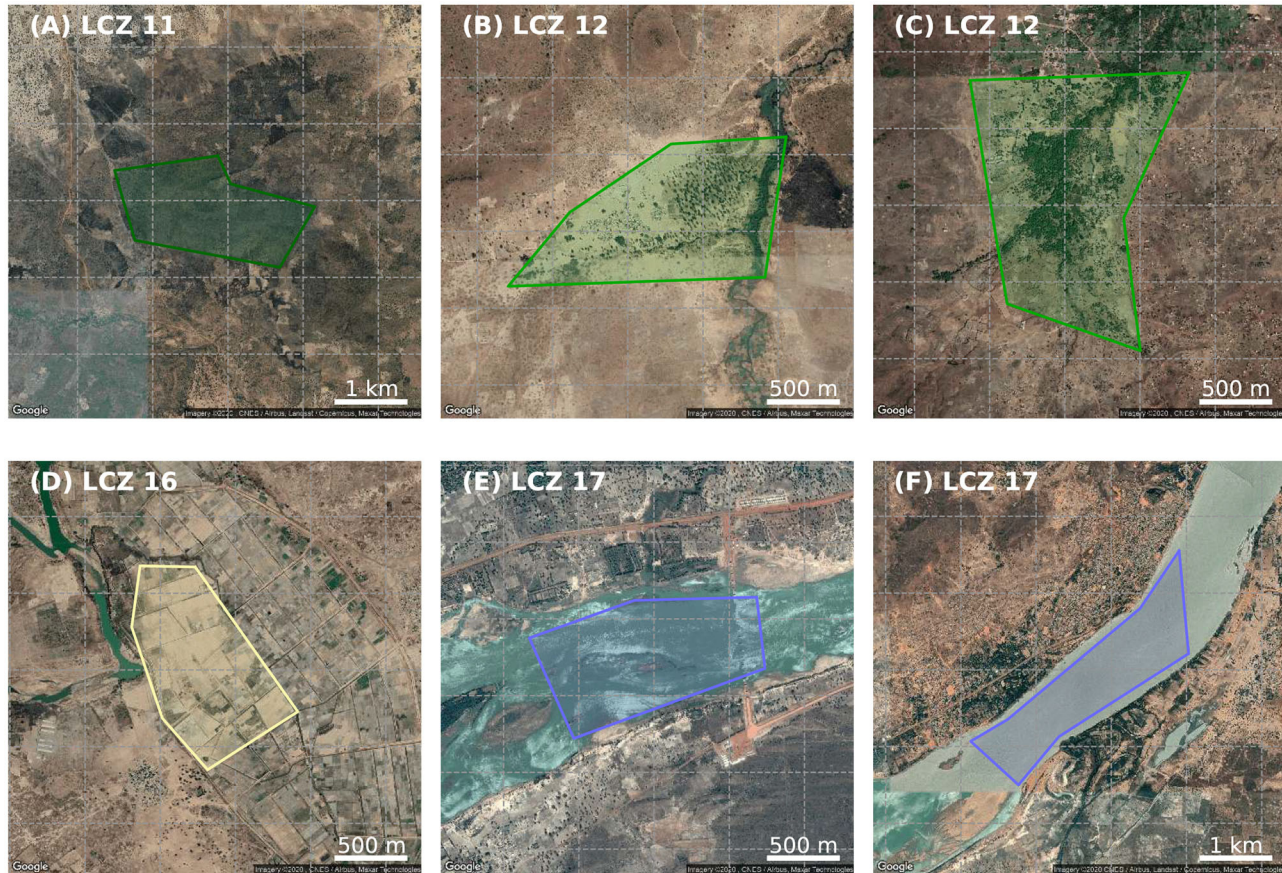


**FIGURE 8 |** A selection of TA polygons tagged as suspicious during the second quality control step, for Bamako. Color scheme as in **Figure 1**.

indicate how often (in %) the mode LCZ class was mapped during the bootstrapping procedure. In general, areas covered by TAs are often mapped as the same LCZ class more than 80% of the time (>20/25 iterations). Areas at the boundaries of the ROI, e.g., southern edge of the Havana domain, or east of Bamako, are often characterized by lower probability scores. Such information helps authors to identify where confusion exists in their ROI.

Finally, the accuracy of the lcz map can be assessed using the accuracy metrics discussed in section 2.2 and displayed in **Figure 6**. For all three cities, the average overall accuracy metrics reach values above 0.5, a minimum accuracy level proposed by Bechtel et al. (2019a) to pass the automated quality control. Lowest class-wise F1 metrics can be seen for LCZs 9 and 10 in Saint Petersburg (corresponding to the LCZs with the lowest TA polygon frequencies), and LCZ 6 in Havana. Note that no F1 metric is available for LCZ 7 in Bamako, even though one TA polygon is available in the TA set (**Figure 4A**). This is because a single polygon does not suffice to perform a quality assessment due to the stratified random sampling of the TAs in training and test data. This is in line with the results of the HUMAN INfluence EXperiment (HUMINEX, Bechtel et al., 2017; Verdonck et al., 2019) indicating that, when the number of TAs for a specific zone is low, the representativeness of this TA

might be low, leading to lower accuracies. This is often caused by (inexperienced) authors spending a lot of time searching for TAs for all seventeen LCZs, even though some of the zones are not large enough or occur too sparsely in the city to constitute a LCZ.

### 3.3. Automated TA Quality Control

In total, 36 (25%), 80 (25%), and 27 (16%) polygons are flagged as suspicious in at least one of the quality control steps, for Bamako, Saint Petersburg, and Havana, respectively. Some examples from all cities and for each quality control step are described in more detail below.

**Figure 7** displays all polygons from Saint Petersburg flagged as suspicious during the first quality control step. Two polygons are flagged because they have a surface area below the  $0.04 \text{ km}^2$  threshold (**Figures 7C,H**), the remainder because of their shape exceeding the maximum allowed value of 3. The latter polygons typically correspond to linear (narrow and very long) shapes, often pointing to rivers (LCZ 17, **Figures 7E,G,I**) or complex shapes not adhering to the guidelines of digitizing simple block shapes (**Figures 7A,B**). While these are not necessarily wrong, complex shapes may lead to a suboptimal sampling of the satellite input features, or may lead to a mixed spectral signature in

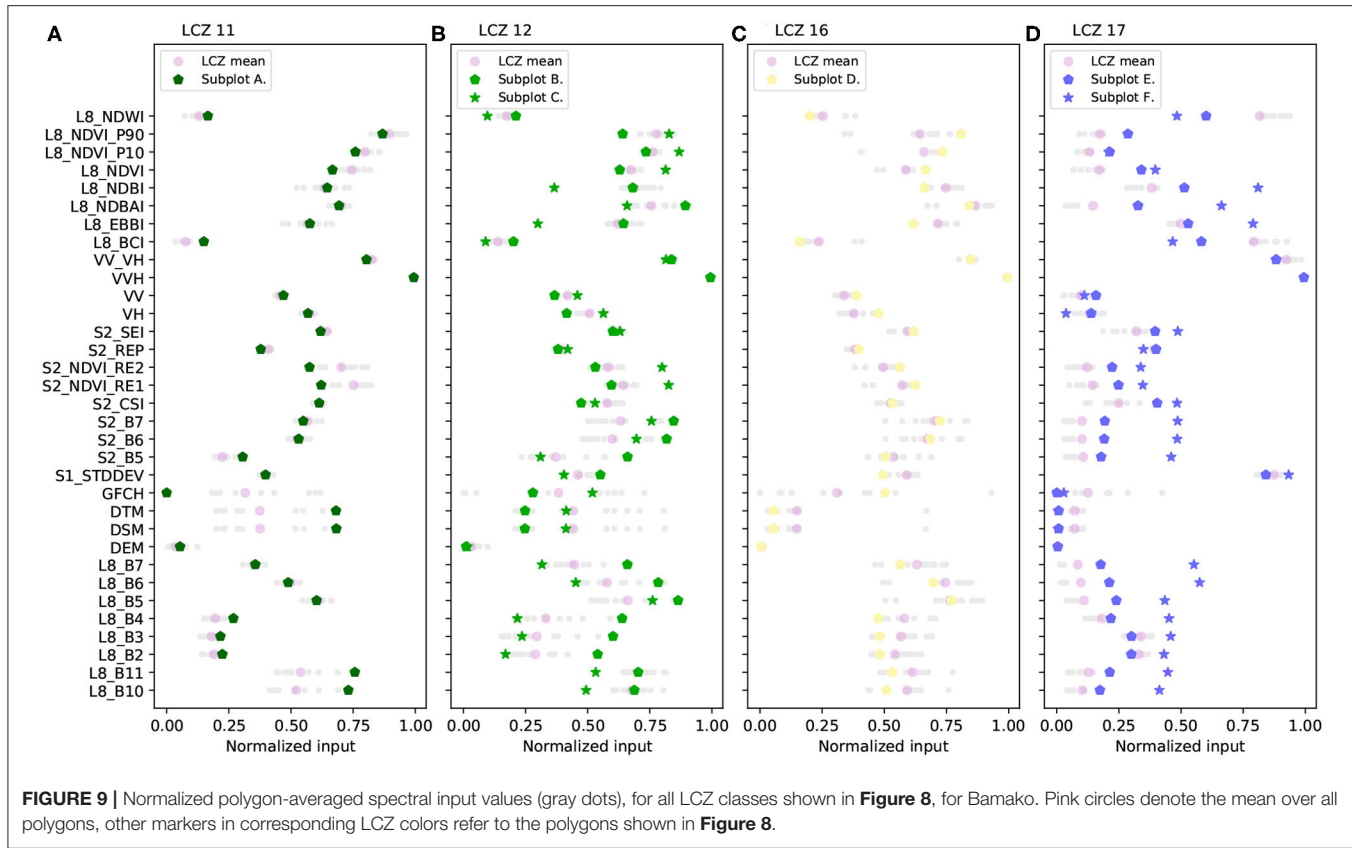


**FIGURE 9 |** Normalized polygon-averaged spectral input values (gray dots), for all LCZ classes shown in **Figure 8**, for Bamako. Pink circles denote the mean over all polygons, other markers in corresponding LCZ colors refer to the polygons shown in **Figure 8**.

case polygons are too narrow and/or are close to other land covers/uses (Verdonck et al., 2019). More information on best practices for digitizing TAs is available in Verdonck et al. (2019) and on the WUDAPT webpage<sup>7</sup>.

Some examples for the second quality control step are shown in **Figure 8**. They are all natural LCZ classes consisting out of LCZ 11 (or A, Dense trees), 12 (or B, Scattered trees), 16 (or F, Bare soil or sand) and 17 (or G, Water). The true color RGB satellite information reveals that the dense tree polygon (**Figure 8A**) might be closer to LCZ B (Scattered trees). This is supported by the spectral profiles in **Figure 9A**, with e.g., lower values for the forest canopy height (GFCH), and higher values for Landsat's red (L8\_B4) and thermal infrared (L8\_B10/B11) bands, when compared to the expected spectral value space for all LCZ 11 polygons. For the LCZ 12 polygons (**Figures 8B,C**), the true color satellite imagery reveals a rather heterogeneous landscape, covered by patches of dense and scattered trees, agricultural fields, bare soils, small settlements or sparsely built areas, and a small (seasonal) river. The latter two are captured by the higher than expected value for Landsat's NDWI (L8\_NDWI) and a lower than expected enhanced built up and bare soil index (L8\_EBBI), where lower EBBI values refer to built-up areas (Assyakur et al., 2012) (**Figure 9B**). The polygon in **Figure 8D** is labeled as bare soil or sand, even though the man-made land use pattern suggest this area to be farm land, which should thus be labeled as LCZ 14 (or D, Low plants). This is also

visible from Landsat's median, 10 and 90th percentile normalized difference vegetation index values (L8\_NDVI(\_P10/\_P90) being higher than the expected LCZ 16 values (**Figure 9C**). Lastly, the LCZ 17 polygons in **Figures 9E,F** represent two sections of the Niger river, characterized by strong fluctuations in water levels according to the rainy and dry seasons. Using the Global Surface Water Explorer<sup>8</sup> (Pekel et al., 2016) or Google's timelapse tool<sup>9</sup>, one can infer that these polygons are mapped in sections of the river that are seasonal and thus only have water for some time of the year. This is supported by the Landsat's NDVI and NDWI values for the LCZ 17 polygons (**Figures 9D, 10**): while all LCZ 17 polygons are sampling from the Niger river (**Figure 4A**), the NDWI values for the polygons in **Figures 8E,F** are significantly lower than those from the other polygons. The same but opposite observation can be made for the NDVI values.

The third quality control step performs a similar analysis as the second step, yet this time on the pixel level. **Figure 11** displays a selected number of polygons over Havana, together with the pixels flagged as suspicious. The first polygon (**Figure 11A**) is labeled as LCZ 9 (Sparsely built), reflecting the small or medium-sized buildings widely spaced across a landscape with abundant vegetation. Yet the polygon also includes a water body large enough to be detected by the 100 m input feature pixels. Visualizing the NDWI values of these pixels against e.g., the combined shadow index derived from Sentinel-2 (S2\_CSI)

<sup>7</sup><http://www.wudapt.org/create-lcz-training-areas/>

<sup>8</sup><https://global-surface-water.appspot.com/map>

<sup>9</sup><https://earthengine.google.com/timelapse/>

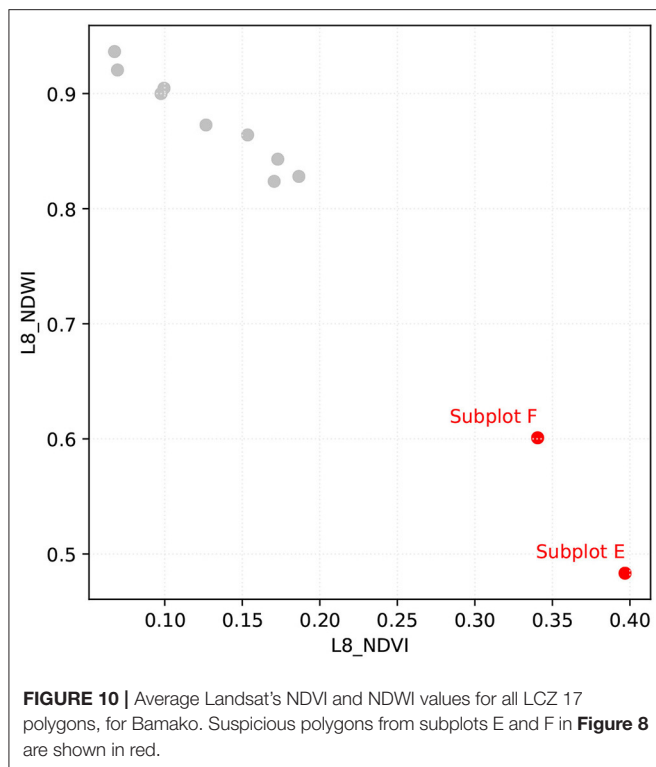


**FIGURE 10 |** Average Landsat's NDVI and NDWI values for all LCZ 17 polygons, for Bamako. Suspicious polygons from subplots E and F in **Figure 8** are shown in red.

reveals the outlier position of these pixels (**Figure 12A**). A similar analysis can be done for the other selected polygons: the LCZ 14 polygon in **Figure 11B** mostly constitutes agricultural land, yet also contains a farm flagged as suspicious. The compact lowrise LCZ 3 polygon in **Figure 11C** contains a park in the middle surrounded by trees, being flagged as suspicious. **Figure 11D** is labeled as LCZ 13 (Bush and scrub) even though it should probably be LCZ D (Low plants). The flagged dots in this case refer to areas with seasonal waters, which can again be visualized using Google Earth's historical imagery tool. Finally, **Figures 11E,F** are two additional examples of compact lowrise polygons. And even though some of the spectral signatures tend to be outliers compared to all other pixel values for this LCZ class (**Figures 12E,F**), it is not self-evident to pin-point the exact reasons for the polygons to be flagged. In **Figure 11E**, a pixel is flagged with abundant vegetation, yet elsewhere in the polygon similar areas can be found that are not flagged. The polygon in **Figure 11F** represents a homogeneous neighborhood in terms of urban form, yet here the flagged pixel is on top of a large-scale warehouse, potentially large enough to influence the pixel's spectral values with its different radiative characteristics.

## 4. DISCUSSION AND CONCLUSIONS

Since their introduction in 2012 (Stewart and Oke, 2012), Local Climate Zones (LCZs) emerged as a new standard for characterizing urban landscapes, providing a holistic classification approach that takes into account micro-scale land-cover and associated physical properties (Demuzere et al., 2020a).

This is reflected by the growing number of scientific publications having "LCZ" or "Local Climate Zones" listed as keywords: according to Web of Science, as of February 4 2021, a total of 139 papers were published, 38 of them in 2020 alone. The default LCZ mapping procedure, adopted as Level 0 (lowest level of detail) by the WUDAPT grass-root effort, and relying only on open-source data (Landsat 8) and software (SAGA GIS, Conrad et al., 2015), was certainly instrumental to this success (Bechtel et al., 2015; Ching et al., 2018). However, some features of this default procedure inhibit global up-scaling in a reasonable time, e.g., the need to download and pre-process Landsat 8 data from the United States Geological Survey (USGS) Earth Explorer, the processing of the LCZ classifier embedded in SAGA GIS on your local computer, the unavailability of an automated cross-validation, and the manual review by an experienced operator before the data is made publicly available (Bechtel et al., 2015, 2019a).

The LCZ Generator addresses these shortcomings, by adopting well-tested and -documented cloud-based LCZ mapping strategies using Google's earth engine (Gorelick et al., 2017; Brousse et al., 2019, 2020a,b; Demuzere et al., 2019b,c, 2020a,c; Varentsov et al., 2020). The result of this is an online platform, that maps a city of interest into LCZs, solely expecting a valid TA file and some metadata as input. The web application simultaneously provides an automated accuracy assessment, in line with the cross-validation procedure detailed in Bechtel et al. (2019a). To date, this bootstrap-based accuracy assessment was not available in the SAGA GIS context, often leading to insufficiently robust accuracy assessments during the production of LCZ maps (Verdonck et al., 2017). In addition, the novel 3-step TA quality control facilitates the revision of the original TAs, allowing the user to revise the initial submission, and re-submit to the LCZ Generator, as previous work highlighted the importance of additional iterations (Bechtel et al., 2017, 2019a; Verdonck et al., 2019). Results in this study reveal for example that users should be more careful when digitizing TAs (e.g., compact shapes, scales, and borders), and should take into account seasonal properties of the underlying land cover/use. Note however that this TA quality control implementation is still experimental, and was successfully tested on a limited number of TA samples only. The LCZ Generator can assist in this respect to gather more TA samples in order to populate a spectral LCZ library across urban (eco)regions (Jackson et al., 2010; Schneider et al., 2010; Demuzere et al., 2019c), enabling a better assessment of spectral outliers.

The LCZ Generator should be considered as a dynamic application, that will be updated whenever new scalable mapping techniques and globally-available input features become available. In case updates occur in the future, they will be tracked via the software version number and described in the changelog available on the Github Issue page. For example, some successfully tested the use of object-based image analysis (Collins and Dronova, 2019; Simanjuntak et al., 2019), others obtained promising results using (residual) convolutional neural networks (Qiu et al., 2019, 2020; Yoo et al., 2019; Liu and Shi, 2020; Rosentreter et al., 2020; Zhu et al., 2020). Yet to date, the feasibility of such procedures for large-scale LCZ mapping has

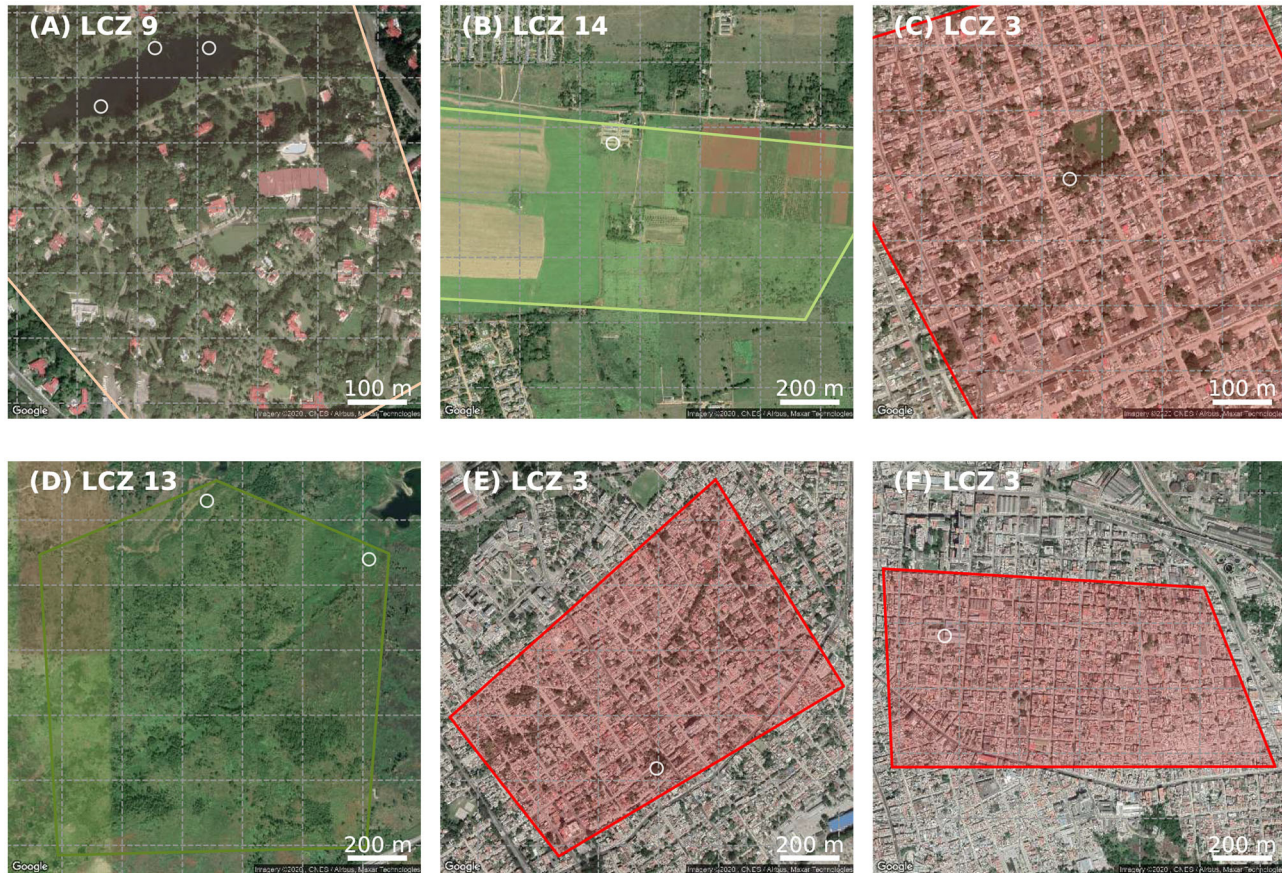


**FIGURE 11 |** As **Figure 8**, but for the third quality control step, for Havana. White circles refer to the centroids of the actual pixels flagged in this quality control step.

not yet been demonstrated (Demuzere et al., 2020a). Many others have developed GIS-based approaches using datasets from e.g., city administrations or derived from crowd-sourced cartographic services such as OpenStreetMap (Lelovics et al., 2014; Quan et al., 2017; Samsonov and Trigub, 2017; Wang et al., 2018; Hidalgo et al., 2019; Quan, 2019; Oliveira et al., 2020; Zhou et al., 2020). The latter study also proposes an extension to the default WUDAPT accuracy assessment, by integrating GIS data (e.g., building footprints and heights, and pervious surface fraction). While all these efforts are considered valuable, they have one thing in common limiting their implementation into the LCZ Generator: the underlying datasets are to date not globally available.

We anticipate that the LCZ Generator will ease the production, quality assessment and dissemination of LCZ maps and related products. This easy-to-use and accessible online platform should therefore continue to support researchers and practitioners in using the LCZ framework for a variety of applications, such as urban heat (risk) assessment studies (Demuzere et al., 2020a, and references therein), climate sensitive design and urban planning (policies) (Perera and Emmanuel, 2016; Vandamme et al., 2019; Maharoof et al., 2020), anthropogenic heat and building carbon emissions (Wu et al.,

2018; Santos et al., 2020), quality of life (Sapena et al., 2021), multi-temporal urban land change (Vandamme et al., 2019; Wang et al., 2019), and urban health issues (Brousse et al., 2019, 2020a). This development will in addition accelerate the key aim of WUDAPT, that is “to capture consistent information on urban form and function for cities worldwide that can support urban weather, climate, hydrology and air quality modeling” (Ching et al., 2018, 2019). Examples of modeling systems currently using LCZ information are the Surface Urban Energy and Water Balance Scheme (SUEWS, Alexander et al., 2016), ENVI-met (Bande et al., 2020), the urban multi-scale environmental predictor (UMEP, Lindberg et al., 2018), MUKLIMO\_3 (Bokwa et al., 2019; Gál et al., 2021), COSMO-CLM and the WUDAPT-TO-COSMO tool (Wouters et al., 2016; Brousse et al., 2019, 2020b; Varentsov et al., 2020), and the Weather Research and Forecasting model (WRF, Brousse et al., 2016; Hammerberg et al., 2018; Wong et al., 2019; Patel et al., 2020; Zonato et al., 2020). While WRF currently uses the WUDAPT-to-WRF tool to ingest LCZ information (Brousse et al., 2016), its next release expected in spring 2021 should offer this compatibility by default (A. Zonato, personal communication).

To conclude, and in line with the assessment of Creutzig et al. (2019), we firmly believe that this LCZ Generator

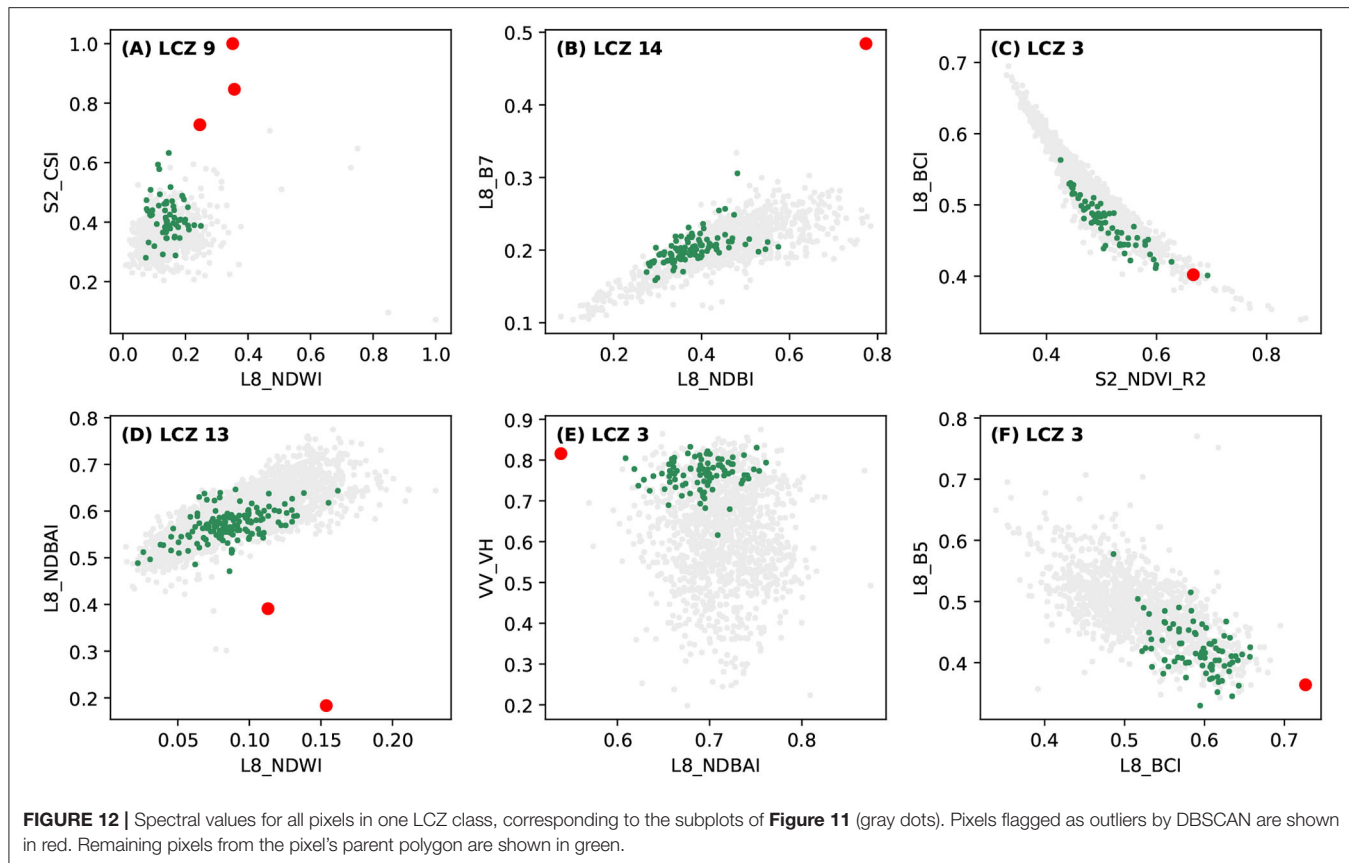


**FIGURE 12 |** Spectral values for all pixels in one LCZ class, corresponding to the subplots of **Figure 11** (gray dots). Pixels flagged as outliers by DBSCAN are shown in red. Remaining pixels from the pixel's parent polygon are shown in green.

has the potential to become a key part in mainstreaming and harmonizing urban data collection, upscale urban climate solutions and effect change at the global scale.

## DATA AVAILABILITY STATEMENT

Publicly available datasets were analyzed in this study. This data can be found at: <https://lcz-generator.rub.de>.

## AUTHOR CONTRIBUTIONS

The authors jointly devised the concept of the LCZ Generator. MD developed the LCZ-related codes. JK developed the database and front- and back-end. MD developed all visualizations. MD led the writing with contributions from JK and BB.

## REFERENCES

- Alexander, P., Bechtel, B., Chow, W., Fealy, R., and Mills, G. (2016). Linking urban climate classification with an urban energy and water budget model: multi-site and multi-seasonal evaluation. *Urban Clim.* 17, 196–215. doi: 10.1016/j.uclim.2016.08.003
- As-syakur, A. R., Adnyana, I. W. S., Arthana, I. W., and Nuarsa, I. W. (2012). Enhanced built-UP and bareness index (EBBI) for mapping built-UP and bare land in an urban area. *Remote Sens.* 4, 2957–2970. doi: 10.3390/rs4102957
- Bai, X., Dawson, R. J., Ürge-Vorsatz, D., Delgado, G. C., Barau, A. S., Dhakal, S., et al. (2018). Six research priorities for cities. *Nature* 555, 23–25. doi: 10.1038/d41586-018-02409-z
- Baklanov, A., Grimmond, C., Carlson, D., Terblanche, D., Tang, X., Bouchet, V., et al. (2018). From urban meteorology, climate and environment research to integrated city services. *Urban Clim.* 23, 330–341. doi: 10.1016/j.uclim.2017.05.004
- Bande, L., Manandhar, P., Ghazal, R., and Marpu, P. (2020). Characterization of local climate zones using ENVI-met and site data in the city of Al-Ain, UAE. *Int. J. Sustain. Dev. Plann.* 15, 751–760. doi: 10.18280/ijsdp.150517
- Bechtel, B. (2011). “Multitemporal Landsat data for urban heat island assessment and classification of local climate zones,” in *2011 Joint Urban Remote Sensing Event* (Munich: IEEE), 129–132.
- Bechtel, B., Alexander, P., Böhner, J., Ching, J., Conrad, O., Feddema, J., et al. (2015). Mapping local climate zones for a worldwide database of the form and function of cities. *ISPRS Int. J. Geo Inform.* 4, 199–219. doi: 10.3390/ijgi4010199
- Bechtel, B., Alexander, P. J., Beck, C., Böhner, J., Brousse, O., Ching, J., et al. (2019a). Generating WUDAPT Level 0 data – Current status of production and evaluation. *Urban Clim.* 27, 24–45. doi: 10.1016/j.uclim.2018.10.001

## FUNDING

This work was conducted in the context of project ENLIGHT, funded by the German Research Foundation (DFG) under grant No. 437467569.

## ACKNOWLEDGMENTS

We thank USGS and NASA for the free Landsat data, and the Copernicus programme of ESA for the Sentinel data, all acquired and processed via Google's earth engine. We acknowledge support by the Open Access Publication Funds of the Ruhr-Universität Bochum (RUB, Germany). Moreover, we thank RUB's student assistants Christian Moede, Lara van der Linden, and Teresa Mansheim for the training areas used in this study.

- Bechtel, B., and Daneke, C. (2012). Classification of local climate zones based on multiple earth observation data. *IEEE J. Sel. Top. Appl. Earth Observ. Remote Sens.* 5, 1191–1202. doi: 10.1109/JSTARS.2012.2189873
- Bechtel, B., Demuzere, M., Mills, G., Zhan, W., Sismanidis, P., Small, C., et al. (2019b). SUHI analysis using Local Climate Zones—A comparison of 50 cities. *Urban Clim.* 28:100451. doi: 10.1016/j.ulclim.2019.01.005
- Bechtel, B., Demuzere, M., Sismanidis, P., Fenner, D., Brousse, O., Beck, C., et al. (2017). Quality of crowdsourced data on urban morphology—The Human Influence Experiment (HUMINEX). *Urban Sci.* 1:15. doi: 10.3390/urbansci1020015
- Bechtel, B., Demuzere, M., and Stewart, I. D. (2020). A weighted accuracy measure for land cover mapping: comment on Johnson et al. Local Climate Zone (LCZ) map accuracy assessments should account for land cover physical characteristics that affect the local thermal environment. *Remote Sens.* 2019, 11, 2420. *Remote Sens.* 12:1769. doi: 10.3390/rs12111769
- Bokwa, A., Geletić, J., Lehnhert, M., Žuvela-Aloise, M., Hollósi, B., Gál, T., et al. (2019). Heat load assessment in Central European cities using an urban climate model and observational monitoring data. *Energy Build.* 201, 53–69. doi: 10.1016/j.enbuild.2019.07.023
- Breiman, L. (2001). Random forests. *Mach. Learn.* 45, 5–32. doi: 10.1023/A:1010933404324
- Brousse, O., Georganos, S., Demuzere, M., Dujardin, S., Lennert, M., Linard, C., et al. (2020a). Can we use Local Climate Zones for predicting malaria prevalence across sub-Saharan African cities? *Environ. Res. Lett.* 15:124051. doi: 10.1088/1748-9326/abc996
- Brousse, O., Georganos, S., Demuzere, M., Vanhuyse, S., Wouters, H., Wolff, E., et al. (2019). Urban Climate Using Local Climate Zones in Sub-Saharan Africa to tackle urban health issues. *Urban Clim.* 27, 227–242. doi: 10.1016/j.ulclim.2018.12.004
- Brousse, O., Martilli, A., Foley, M., Mills, G., and Bechtel, B. (2016). WUDAPT, an efficient land use producing data tool for mesoscale models? Integration of urban LCZ in WRF over Madrid. *Urban Clim.* 17, 116–134. doi: 10.1016/j.ulclim.2016.04.001
- Brousse, O., Wouters, H., Demuzere, M., Thiery, W., Van de Walle, J., and Lipzig, N. P. M. (2020b). The local climate impact of an African city during clear-sky conditions—Implications of the recent urbanization in Kampala (Uganda). *Int. J. Climatol.* 40, 4586–4608. doi: 10.1002/joc.6477
- Chen, G., Li, X., Liu, X., Chen, Y., Liang, X., Leng, J., et al. (2020). Global projections of future urban land expansion under shared socioeconomic pathways. *Nat. Commun.* 11, 1–12. doi: 10.1038/s41467-020-14386-x
- Ching, J., Aliaga, D., Mills, G., Masson, V., See, L., Neophytou, M., et al. (2019). Pathway using WUDAPT's Digital Synthetic City tool towards generating urban canopy parameters for multi-scale urban atmospheric modeling. *Urban Clim.* 28:100459. doi: 10.1016/j.ulclim.2019.100459
- Ching, J., Mills, G., Bechtel, B., See, L., Feddema, J., Wang, X., et al. (2018). WUDAPT: an urban weather, climate, and environmental modeling infrastructure for the anthropocene. *Bull. Am. Meteorol. Soc.* 99, 1907–1924. doi: 10.1175/BAMS-D-16-0236.1
- Collins, J., and Dronova, I. (2019). Urban landscape change analysis using local climate zones and object-based classification in the Salt Lake Metro Region, Utah, USA. *Remote Sens.* 11:1615. doi: 10.3390/rs1113165
- Conrad, O., Bechtel, B., Bock, M., Dietrich, H., Fischer, E., Gerlitz, L., et al. (2015). System for Automated Geoscientific Analyses (SAGA) v. 2.1.4. *Geosci. Model Dev.* 8, 1991–2007. doi: 10.5194/gmdd-8-2271-2015
- Corbane, C., Pesaresi, M., Politis, P., Syrris, V., Florczyk, A. J., Soille, P., et al. (2017). Big earth data analytics on Sentinel-1 and Landsat imagery in support to global human settlements mapping. *Big Earth Data* 1, 118–144. doi: 10.1080/20964471.2017.1397899
- Costello, A., Abbas, M., Allen, A., Ball, S., Bell, S., Bellamy, R., et al. (2009). Managing the health effects of climate change. *Lancet* 373, 1693–1733. doi: 10.1016/S0140-6736(09)60935-1
- Creutzig, F., Agoston, P., Minx, J. C., Canadell, J. G., Andrew, R. M., Quéré, C. L., et al. (2016). Urban infrastructure choices structure climate solutions. *Nat. Clim. Change* 6:1054. doi: 10.1038/nclimate3169
- Creutzig, F., Lohrey, S., Bai, X., Baklanov, A., Dawson, R., Dhakal, S., et al. (2019). Upscaling urban data science for global climate solutions. *Global Sustain.* 2:e2. doi: 10.1017/sus.2018.16
- Demuzere, M., Bechtel, B., Middel, A., and Mills, G. (2019a). European LCZ map. *Figshare*.
- Demuzere, M., Bechtel, B., Middel, A., and Mills, G. (2019b). Mapping Europe into local climate zones. *PLOS ONE* 14:e0214474. doi: 10.1371/journal.pone.0214474
- Demuzere, M., Bechtel, B., and Mills, G. (2019c). Global transferability of local climate zone models. *Urban Clim.* 27, 46–63. doi: 10.1016/j.ulclim.2018.11.001
- Demuzere, M., Hankey, S., Mills, G., Zhang, W., Lu, T., and Bechtel, B. (2020a). Combining expert and crowd-sourced training data to map urban form and functions for the continental US. *Sci. Data* 7:264. doi: 10.1038/s41597-020-00605-z
- Demuzere, M., Hankey, S., Mills, G., Zhang, W., Lu, T., and Bechtel, B. (2020b). CONUS-WIDE LCZ map and Training Areas. *Figshare*.
- Demuzere, M., Mihara, T., Redivo, C. P., Feddema, J., and Setton, E. (2020c). Multi-temporal LCZ maps for Canadian functional urban areas.
- Esch, T., Heldens, W., Hirne, A., Keil, M., Marconcini, M., Roth, A., et al. (2017). Breaking new ground in mapping human settlements from space - The Global Urban Footprint-. *ISPRS J. Photogrammetr. Remote Sens.* 134, 30–42. doi: 10.1016/j.isprsjprs.2017.10.012
- Ester, M., Kriegel, H. P., Sander, J., and Xu, X. (1996). “A density-based algorithm for discovering clusters in large spatial databases with noise,” in *Proceedings of the 2nd International Conference on Knowledge Discovery and Data Mining* (Portland, OR), 226–231.
- Forkuor, G., Dimobe, K., Serme, I., and Tondoh, J. E. (2018). Landsat-8 vs. Sentinel-2: examining the added value of sentinel-2's red-edge bands to land-use and land-cover mapping in Burkina Faso. *GIScience Remote Sens.* 55, 331–354. doi: 10.1080/15481603.2017.1370169
- Gál, T., Mahó, S. I., Skarbit, N., and Unger, J. (2021). Numerical modelling for analysis of the effect of different urban green spaces on urban heat load patterns in the present and in the future. *Comput. Environ. Urban Syst.* 87:101600. doi: 10.1016/j.compenvurbsys.2021.101600
- Georgescu, M., Chow, W. T. L., Wang, Z. H., Brazel, A., Trapido-Lurie, B., Roth, M., et al. (2015). Prioritizing urban sustainability solutions: coordinated approaches must incorporate scale-dependent built environment induced effects. *Environ. Res. Lett.* 10:061001. doi: 10.1088/1748-9326/10/6/061001
- Gong, P., Li, X., Wang, J., Bai, Y., Chen, B., Hu, T., et al. (2020). Annual maps of global artificial impervious area (GAIA) between 1985 and 2018. *Remote Sens. Environ.* 236:111510. doi: 10.1016/j.rse.2019.111510
- Gorelick, N., Hancher, M., Dixon, M., Ilyushchenko, S., Thau, D., and Moore, R. (2017). Google Earth Engine: planetary-scale geospatial analysis for everyone. *Remote Sens. Environ.* 202, 18–27. doi: 10.1016/j.rse.2017.06.031
- Hammerberg, K., Brousse, O., Martilli, A., and Mahdavi, A. (2018). Implications of employing detailed urban canopy parameters for mesoscale climate modelling: a comparison between WUDAPT and GIS databases over Vienna, Austria. *Int. J. Climatol.* 38, e1241–e1257. doi: 10.1002/joc.5447
- Hidalgo, J., Dumas, G., Masson, V., Petit, G., Bechtel, B., Bocher, E., et al. (2019). Comparison between local climate zones maps derived from administrative datasets and satellite observations. *Urban Clim.* 27, 64–89. doi: 10.1016/j.ulclim.2018.10.004
- Jackson, T. L., Feddema, J. J., Oleson, K. W., Bonan, G. B., and Bauer, J. T. (2010). Parameterization of urban characteristics for global climate modeling. *Ann. Assoc. Am. Geogr.* 100, 848–865. doi: 10.1080/00045608.2010.497328
- Kaplan, G., and Avdan, U. (2018). Sentinel-1 and Sentinel-2 data fusion for wetlands mapping: Balıkesir, Turkey. *Int. Arch. Photogramm. Remote Sens. Spatial Inform. Sci. ISPRS Arch.* 42, 729–734. doi: 10.5194/isprs-archives-XLII-3-729-2018
- Lelovics, E., Unger, J., Gál, T., and Gál, C. V. (2014). Design of an urban monitoring network based on Local Climate Zone mapping and temperature pattern modelling. *Clim. Res.* 60, 51–62. doi: 10.3354/cr01220
- Li, X., Zhou, Y., Gong, P., Seto, K. C., and Clinton, N. (2020). Developing a method to estimate building height from Sentinel-1 data. *Remote Sens. Environ.* 240:111705. doi: 10.1016/j.rse.2020.111705
- Lindberg, F., Grimmond, C., Gabey, A., Huang, B., Kent, C. W., Sun, T., et al. (2018). Urban Multi-scale Environmental Predictor (UMEPI): an integrated tool for city-based climate services. *Environ. Model. Softw.* 99, 70–87. doi: 10.1016/j.envsoft.2017.09.020
- Liu, S., and Shi, Q. (2020). Local climate zone mapping as remote sensing scene classification using deep learning: a case study of metropolitan China. *ISPRS J. Photogrammetr. Remote Sens.* 164, 229–242. doi: 10.1016/j.isprsjprs.2020.04.008
- Lucon, O., Ürge-Vorsatz, D., Ahmed, A. Z., Akbari, H., Bertoldi, P., Cabeza, L.F., et al. (2014). “Chapter 9 – Buildings,” in *Climate Change 2014: Mitigation of*

- Climate Change. IPCC Working Group III Contribution to AR5* (Cambridge: Cambridge University Press).
- Mahroof, N., Emmanuel, R., and Thomson, C. (2020). Compatibility of local climate zone parameters for climate sensitive street design: influence of openness and surface properties on local climate. *Urban Clim.* 33:100642. doi: 10.1016/j.ulim.2020.100642
- Masson, V., Heldens, W., Bocher, E., Bonhomme, M., Bucher, B., Burmeister, C., et al. (2020). City-descriptive input data for urban climate models: model requirements, data sources and challenges. *Urban Clim.* 31:100536. doi: 10.1016/j.ulim.2019.100536
- Oliveira, A., Lopes, A., and Niza, S. (2020). Local Climate Zones in five Southern European cities: an improved GIS-based classification method based on free data from the Copernicus Land Monitoring Service. *Urban Clim.* 33:100631. doi: 10.1016/j.ulim.2020.100631
- Patel, P., Karmakar, S., Ghosh, S., and Niyogi, D. (2020). Improved simulation of very heavy rainfall events by incorporating WUDAPT urban land use/land cover in WRF. *Urban Clim.* 32:100616. doi: 10.1016/j.ulim.2020.100616
- Pekel, J.-F., Cottam, A., Gorelick, N., and Belward, A. S. (2016). High-resolution mapping of global surface water and its long-term changes. *Nature* 540, 418–422. doi: 10.1038/nature20584
- Perera, N., and Emmanuel, R. (2016). A “Local Climate Zone” based approach to urban planning in Colombo, Sri Lanka. *Urban Clim.* 23, 188–203. doi: 10.1016/j.ulim.2016.11.006
- Pesaresi, M., Huadong, G., Blaes, X., Ehrlich, D., Ferri, S., Gueguen, L., et al. (2013). A global human settlement layer from optical HR/VHR RS data: concept and first results. *IEEE J. Sel. Top. Appl. Earth Observ. Remote Sens.* 6, 2102–2131. doi: 10.1109/JSTARS.2013.2271445
- Qiu, C., Mou, L., Schmitt, M., and Zhu, X. X. (2019). Local climate zone-based urban land cover classification from multi-seasonal Sentinel-2 images with a recurrent residual network. *ISPRS J. Photogramm. Remote Sens.* 154, 151–162. doi: 10.1016/j.isprsjprs.2019.05.004
- Qiu, C., Tong, X., Schmitt, M., Bechtel, B., and Zhu, X. X. (2020). Multilevel feature fusion-based CNN for local climate zone classification from sentinel-2 images: benchmark results on the So2Sat LCZ42 dataset. *IEEE J. Sel. Top. Appl. Earth Observ. Remote Sens.* 13, 2793–2806. doi: 10.1109/JSTARS.2020.295711
- Quan, J. (2019). Enhanced geographic information system-based mapping of local climate zones in Beijing, China. *Sci. China Technol. Sci.* 62, 2243–2260. doi: 10.1007/s11431-018-9417-6
- Quan, S. J., Dutt, F., Woodworth, E., Yamagata, Y., and Yang, P. P. J. (2017). Local climate zone mapping for energy resilience: a fine-grained and 3D approach. *Energy Proc.* 105, 3777–3783. doi: 10.1016/j.egypro.2017.03.883
- Reba, M., and Seto, K. C. (2020). A systematic review and assessment of algorithms to detect, characterize, and monitor urban land change. *Remote Sens. Environ.* 242:111739. doi: 10.1016/j.rse.2020.111739
- Rosentreter, J., Hagensieker, R., and Waske, B. (2020). Towards large-scale mapping of local climate zones using multitemporal Sentinel 2 data and convolutional neural networks. *Remote Sens. Environ.* 237:111472. doi: 10.1016/j.rse.2019.111472
- Samsonov, T., and Trigub, K. (2017). “Towards computation of urban local climate zones (LCZ) from openstreetmap data” in *Proceedings of the 14th International Conference on GeoComputation* (Leeds), 1–9.
- Santos, L. G. R., Singh, V. K., Mughal, M. O., Nevat, I., Norford, L. K., and Fonseca, J. A. (2020). “Estimating building’s anthropogenic heat: a joint local climate zone and land use classification method,” in *eSIM 2021 Conference* (Vancouver, BC), 12–19.
- Sapena, M., Wurm, M., Taubenböck, H., Tuia, D., and Ruiz, L. A. (2021). Estimating quality of life dimensions from urban spatial pattern metrics. *Comput. Environ. Urban Syst.* 85:101549. doi: 10.1016/j.compenvurbsys.2020.101549
- Schneider, A., Friedl, M. A., and Potere, D. (2010). Mapping global urban areas using MODIS 500-m data: new methods and datasets based on ‘urban ecoregions’. *Remote Sens. Environ.* 114, 1733–1746. doi: 10.1016/j.rse.2010.03.003
- Schubert, E., Sander, J., Ester, M., Kriegel, H. P., and Xu, X. (2017). DBSCAN revisited, revisited: why and how you should (still) use DBSCAN. *ACM Trans. Database Syst.* 42:19. doi: 10.1145/3068335
- Simanjuntak, R. M., Kuffer, M., and Reckien, D. (2019). Object-based image analysis to map local climate zones: the case of Bandung, Indonesia. *Appl. Geogr.* 106, 108–121. doi: 10.1016/j.apgeog.2019.04.001
- Stewart, I. D., and Oke, T. R. (2012). Local climate zones for urban temperature studies. *Bull. Am. Meteorol. Soc.* 93, 1879–1900. doi: 10.1175/BAMS-D-11-00019.1
- Sun, G., Huang, H., Weng, Q., Zhang, A., Jia, X., Ren, J., et al. (2019). Combinational shadow index for building shadow extraction in urban areas from Sentinel-2A MSI imagery. *Int. J. Appl. Earth Observ. Geoinform.* 78, 53–65. doi: 10.1016/j.jag.2019.01.012
- UN (2019). *World Urbanization Prospects: The 2018 Revision*. Population Division of the United Nations Department of Economic and Social Affairs.
- Vandamme, S., Demuzere, M., Verdonck, M.-L., Zhang, Z., and Coillie, F. V. (2019). Revealing Kunming’s (China) historical urban planning policies through local climate zones. *Remote Sens.* 11:1731. doi: 10.3390/rs11141731
- Varentsov, M., Samsonov, T., and Demuzere, M. (2020). Impact of urban canopy parameters on a Megacity’s modelled thermal environment. *Atmosphere* 11:1349. doi: 10.3390/atmos11121349
- Verdonck, M.-L., Demuzere, M., Bechtel, B., Beck, C., Brousse, O., Droste, A., et al. (2019). The Human Influence Experiment (Part 2): guidelines for improved mapping of local climate zones using a supervised classification. *Urban Sci.* 3:27. doi: 10.3390/urbansci3010027
- Verdonck, M.-L., Okujeni, A., van der Linden, S., Demuzere, M., De Wulf, R., and Van Coillie, F. (2017). Influence of neighborhood information on ‘Local Climate Zone’ mapping in heterogeneous cities. *Int. J. Appl. Earth Observ. Geoinform.* 62, 102–113. doi: 10.1016/j.jag.2017.05.017
- Wang, R., Cai, M., Ren, C., Bechtel, B., Xu, Y., and Ng, E. (2019). Detecting multi-temporal land cover change and land surface temperature in Pearl River Delta by adopting local climate zone. *Urban Clim.* 28:100455. doi: 10.1016/j.ulim.2019.100455
- Wang, R., Ren, C., Xu, Y., Lau, K. K.-L., and Shi, Y. (2018). Mapping the local climate zones of urban areas by GIS-based and WUDAPT methods: a case study of Hong Kong. *Urban Clim.* 24, 567–576. doi: 10.1016/j.ulim.2017.10.001
- Wong, M. M. F., Fung, J. C. H., Ching, J., Yeung, P. P. S., Tse, J. W. P., Ren, C., et al. (2019). Evaluation of uWRF performance and modeling guidance based on WUDAPT and NUDAPT UCP datasets for Hong Kong. *Urban Clim.* 28:100460. doi: 10.1016/j.ulim.2019.100460
- Wouters, H., Demuzere, M., Blahak, U., Fortuniak, K., Maiheu, B., Camps, J., et al. (2016). Efficient urban canopy parametrization for atmospheric modelling: description and application with the COSMO-CLM model (version 5.0\_clm6) for a Belgian Summer. *Geosci. Model Dev.* 9, 3027–3054. doi: 10.5194/gmd-2016-58-supplement
- Wu, Y., Sharifi, A., Yang, P., Borjigin, H., Murakami, D., and Yamagata, Y. (2018). Mapping building carbon emissions within local climate zones in Shanghai. *Energy Proc.* 152, 815–822. doi: 10.1016/j.egypro.2018.09.195
- Yoo, C., Han, D., Im, J., and Bechtel, B. (2019). Comparison between convolutional neural networks and random forest for local climate zone classification in mega urban areas using [Landsat] images. *ISPRS J. Photogramm. Remote Sens.* 157, 155–170. doi: 10.1016/j.isprsjprs.2019.09.009
- Zhou, X., Okaze, T., Ren, C., Cai, M., Ishida, Y., and Mochida, A. (2020). Mapping local climate zones for a Japanese large city by an extended workflow of WUDAPT Level 0 method. *Urban Clim.* 33:100660. doi: 10.1016/j.ulim.2020.100660
- Zhu, X. X., Hu, J., Qiu, C., Shi, Y., Kang, J., Mou, L., et al. (2020). So2Sat LCZ42: a benchmark data set for the classification of global local climate zones [Software and Data Sets]. *IEEE Geosci. Remote Sens. Magaz.* 8, 76–89. doi: 10.1109/MGRS.2020.2964708
- Zonato, A., Martilli, A., Di Sabatino, S., Zardi, D., and Giovannini, L. (2020). Evaluating the performance of a novel WUDAPT averaging technique to define urban morphology with mesoscale models. *Urban Clim.* 31:100584. doi: 10.1016/j.ulim.2020.100584

**Conflict of Interest:** The authors declare that the research was conducted in the absence of any commercial or financial relationships that could be construed as a potential conflict of interest.

Copyright © 2021 Demuzere, Kittner and Bechtel. This is an open-access article distributed under the terms of the Creative Commons Attribution License (CC BY). The use, distribution or reproduction in other forums is permitted, provided the original author(s) and the copyright owner(s) are credited and that the original publication in this journal is cited, in accordance with accepted academic practice. No use, distribution or reproduction is permitted which does not comply with these terms.



# Determining Building Natural Ventilation Potential via IoT-Based Air Quality Sensors

**Maohui Luo<sup>1</sup>, Yumeng Hong<sup>2</sup> and Jovan Pantelic<sup>3,4\*</sup>**

<sup>1</sup>School of Mechanical Engineering, Tongji University, Shanghai, China, <sup>2</sup>China Academy of Art, Hangzhou, China, <sup>3</sup>Centre for the Built Environment, University of California, Berkeley, Berkeley, CA, United States, <sup>4</sup>Department of Biosystems, KU Leuven, Leuven, Belgium

## OPEN ACCESS

### Edited by:

Negin Nazarian,  
University of New South Wales,  
Australia

### Reviewed by:

Francesco Salamone,  
Consiglio Nazionale delle Ricerche  
(CNR), Italy  
Kai Zhang,  
University of Texas Health Science  
Center at Houston, United States  
Bin Yang,  
Xi'an University of Architecture and  
Technology, China

### \*Correspondence:

Jovan Pantelic  
*Jovan.pantelic@kuleuven.edu.be*

### Specialty section:

This article was submitted to  
Environmental Informatics  
and Remote Sensing,  
a section of the journal  
*Frontiers in Environmental Science*

**Received:** 28 November 2020

**Accepted:** 20 April 2021

**Published:** 18 August 2021

### Citation:

Luo M, Hong Y and Pantelic J (2021)  
Determining Building Natural  
Ventilation Potential via IoT-Based Air  
Quality Sensors.  
*Front. Environ. Sci.* 9:634570.  
doi: 10.3389/fenvs.2021.634570

Natural ventilation (NV) represents the most energy-efficient way to operate buildings and, in an attempt to reduce the built environment's global carbon footprint, represents a resource, the usage of which has to be maximized. This study demonstrated how a combination of an IoT environmental sensing network implemented locally outdoors and indoors can help to determine the NV potential and actual utilization throughout the year with the consideration of outdoor climate variance, air pollution levels, and window open/closed status. An NV potential index was developed by analyzing indoor and outdoor PM<sub>2.5</sub>, and outdoor air temperature and air speed throughout the year at different spatial (from room scale to building level and local weather stations) and temporal (instantaneous, season, and annual) scales. The index was applied on a case building located in Berkeley, California, during the period of August 2018 to the end of 2019. Compared to the potential NV availability, the actual window opening time in typical rooms was less than 35%. These results point out that the actual window usage behavior was the key limiting factor in NV potential utilization. Even during periods when climate- and pollution-wise outdoor conditions allowed use of the NV, many occupants kept their windows closed. Keeping windows open or closed was significantly affected by outdoor climate condition and air pollution levels, especially during the wild-fire period.

**Keywords:** natural ventilation, IoT-Internet of things, indoor-outdoor Pollution, thermal comfort, occupant activities, occupant actions

## INTRODUCTION

People spend nearly 90% of their daily lives indoors and rely on mechanical heating, ventilation, and air-conditioning (HVAC) systems to maintain indoor environments comfortable. The building sector accounts for 40% of total energy use and around one-third of CO<sub>2</sub> emission in major economies such as Europe (Commission, 2010), the United States (EIA, 2021), and China (Xiong et al., 2015). A large proportion of this energy was consumed by HVAC systems, which is particularly true in cold and tropical climate zones where the outdoor climate intensifies the HVAC usage. In response to the high energy consumption of mechanical HVAC systems, there has been an increase in research on natural ventilation (NV), and alternative indoor environment conditioning strategies for residential (Oropeza-Perez and Østergaard, 2014) and commercial buildings (da Graça et al., 2004).

## Natural Ventilation

NV refers to the process of supplying air to and removing air from an indoor space without using mechanical systems. Taking advantage of pressure differences arising from natural forces, for example, wind-driven force and buoyancy-driven force, the external air flows into an indoor space, while the internal air flows out (Asfour, 2015). With a proper design, NV can replace cooling systems in the milder months of the year, reducing ventilation- and cooling-related energy demand (Dutton et al., 2013). The NV strategy can also be integrated with the mechanical HVAC system, forming a mixed-mode strategy that allows alternatives between the HVAC and NV throughout the day or the year depending on weather conditions (Luo et al., 2015). The advantages of applying the NV strategy in buildings include but are not limited to 1) reducing operation costs, 2) increasing occupants' thermal comfort, and 3) improving air quality due to more fresh air.

While many studies emphasize the advantages of NV, the actual NV use can be affected by many external factors such as the outdoor climate and pollutant levels (Zhou et al., 2015; Costanzo et al., 2019). The results of the study by Martins and Carrilho da Graça (2017) showed that using NV in moments when the outside weather is favorable can result in HVAC energy savings of 25–80%. However, limiting NV use to moments with outdoor particle levels below  $12 \mu\text{g}/\text{m}^3$  decreases this energy-saving potential to 20–60%. In the majority of the cities analyzed in the study by Martins and Carrilho da Graça (2017), the use of NV led to an increase in indoor exposure to  $\text{PM}_{2.5}$  of outdoor origin of 400–500%. Additionally, building occupants' habits and altitudes in interacting with building openings like the windows will also affect the NV performance by a large margin. Therefore, understanding how these factors would limit the NV usage and how to consider these factors in real-building NV operation are of great value.

On the one hand, many studies have investigated the correlations between window status and the outdoor climate conditions. Raja et al. (Raja et al., 2001) studied the relationship of windows, doors, blinds, fans, etc. with indoor and outdoor temperatures in 15 naturally ventilated office buildings in Oxford and Aberdeen, in the UK, during a summer period. It is found that proportion of open windows increases with an increase in indoor and outdoor temperature. Only few windows are open when the outdoor temperature is below  $15^\circ\text{C}$ , whereas most windows are open when the temperature exceeds about  $25^\circ\text{C}$ . Nicol and Humphrey (2001) surveyed the window usage in naturally ventilated buildings in the UK, Sweden, France, Portugal, Greece, and Pakistan. They found that occupants started to open windows at a temperature above  $10^\circ\text{C}$ , and as the temperature rises, there is an increased probability that a window will be open. Based on the observations in the literature, the percentage of open windows, opening hours, and the frequency of opening or closing windows depend on seasons, outdoor temperature, indoor temperature, time of the day, and the presence of the occupants. For a well-designed building with low internal gains, user-controlled windows may be opened for outdoor temperatures for as low as  $10^\circ\text{C}$  (Raja et al., 2001). The typical maximum outdoor temperature for NV use in

an office is  $28^\circ\text{C}$  (de Dear and Brager, 2002); above this temperature, the indoor environment tends to become uncomfortably warm.

On the other hand, few studies have considered outdoor particle levels as limiting factors of NV use. When the building operates in the NV mode, windows will be opened to promote the large outdoor airflows that are required for ventilated cooling so that indoor exposure to outdoor particulate matter (PM) can be significant, with I/O ratios that are close to one (Martins and Carrilho da Graça, 2017). To avoid this problem, a building connected to an outdoor  $\text{PM}_{2.5}$  sensor network must close the NV openings and revert to conventional HVAC during periods of high  $\text{PM}_{2.5}$ . This requirement reduces the number of hours when NV can be used and requires HVAC energy consumption during these periods. It is likely that the magnitude of this impact will depend on the local weather condition and particle source patterns, as particles suspended in the outdoor air are in an unstable state and their concentration can be changed by meteorological conditions, such as precipitation and wind sweeping. In the majority of urban environments, outdoor air is a source of pollutants that have a detrimental impact on indoor air quality (IAQ). There is strong evidence of adverse health effects from exposure to airborne particles that are small enough to be inhaled (diameter below  $10 \mu\text{m}$  (Fenger, 2009; Talbott et al., 2015)). Limiting airborne particle exposure has long been a priority of the World Health Organization (WHO), leading to continuously updated guidelines for maximum short-term and annual mean exposures to airborne particles (WHO Regional Office for Europe, 2013). Continued exposure to  $\text{PM}_{2.5}$  in amounts that are just above the natural background concentration of  $3–5 \mu\text{g}/\text{m}^3$  can cause adverse health effects (Nicol and Humphrey, 2001). The combination of a mostly anthropogenic origin and an increased exposure risk makes  $\text{PM}_{2.5}$  the preferred indicator for assessing health impacts from outdoor particles.

## The Emergence of IoT Sensing Technology

Internet of Things (IoT) environmental sensing platforms for the measurement of various environmental parameters are deployed on the urban and building scale. Low-cost sensing platforms provide higher measurement granularity than the government-owned and operated air quality station on an urban scale (Morawska et al., 2018). On a building scale, a number of different environmental sensing platforms are deployed to enable visibility of indoor conditions to building managers and potentially occupants (Parkinson et al., 2019). These two fields of science and engineering are currently kept entirely separate, with a single publication showing the potential of integrating indoor and outdoor data for effective building operations during wildfire (Pantelic et al., 2019). There is a clear gap in understanding of how to use available information to better operate buildings or to understand key aspects of how buildings work, especially naturally ventilated buildings that are dependent on outdoor conditions, indoor conditions, and the behavior of occupants.

**TABLE 1** | Available data amount for different variables.

Room no	Room function	Room area (m <sup>2</sup> )	CO <sub>2</sub> h (%)	PM2.5 h (%)	Window opening h (%)	Window closed h (%)	Outdoor temperature (%)	Beginning and ending dates
170 <sup>a</sup>	Classroom	108	1,171 (51.9%)	NA	NA	NA	100	7/19/2018–10/20/2018
172	Classroom	105	2,061 (97.6%)	NA (NA)	NA (NA)	NA (NA)		7/19/2018–10/15/2018
232	Office	69	6,064 (71.8%)	NA (NA)	NA (NA)	NA (NA)		10/20/2018–7/10/2019
250a	Office	10	5,239 (95.7%)	NA (NA)	NA (NA)	NA (NA)		10/22/2018–6/7/2019
270	Classroom	31	246 (85.4%)	5,136 (93.9%)	810 (14.8%)	543 (9.9%)		10/20/2018–11/1/2018
272b	Office	18	2,793 (94.6%)	NA (NA)	NA (NA)	NA (NA)		2/4/2019–6/7/2019
348	Office	16	5,003 (91.4%)	2,601 (88.1%)	474 (16.1%)	2,376 (80.5%)		10/22/2018–6/7/2019
353	Office	12	4,949 (47.4%)	5,004 (91.4%)	45 (0.8%)	1,323 (24.2%)		10/22/2018–12/31/2019
373a	Office	15	5,989 (94.9%)	5,109 (48.9%)	225 (2.2%)	817 (7.8%)		10/21/2018–7/11/2019
373b	Office	13	2,240 (95.2%)	NA (NA)	385 (6.1%)	818 (13.0%)		3/1/2019–6/7/2019
373c	Office	39	5,054 (91.6%)	2,236 (95.1%)	3 (0.1%)	2,219 (94.3%)		10/20/2018–6/7/2019
382b	Office	15	2,997 (92.5%)	4,873 (88.3%)	241 (4.4%)	888 (16.1%)		1/23/2019–6/7/2019
388	Office	15	3,918 (71.6%)	3,006 (92.8%)	76 (2.3%)	2,990 (92.3%)		10/23/2018–6/8/2019
390a	Office	15	3,134 (29.9%)	3,961 (72.4%)	855 (15.6%)	3,152 (57.6%)		10/20/2018–12/31/2019
390d	Meeting room	15	5,574 (53.3%)	3,135 (29.9%)	72 (0.7%)	861 (8.2%)		10/21/2018–12/31/2019

<sup>a</sup>The first number refers to the floor. For example, room 170 and room 270 are on the first floor and the second floor, respectively.

## Objectives of This Study

This study aimed to demonstrate how a combination of an IoT environmental sensing network implemented locally outdoors and indoors can help to determine NV potential and actual utilization in the building throughout the year. NV potential is evaluated by considering outdoor climate variance and air pollution levels, and the actual NV use was evaluated using environmental data and occupant behavior with respect to the use of windows. In doing this, we analyzed indoor and outdoor PM<sub>2.5</sub>, indoor CO<sub>2</sub>, and outdoor air temperature throughout the year at different spatial (from room scale to building level and local weather stations) and temporal scales (instantaneous and long-term) to demonstrate the application of NV assessment tools. We used an NV case building located in Berkeley (California) during the period of August 2018 to the end of 2019. By reliance on an NV potential index considering outdoor PM<sub>2.5</sub>, temperature, and wind speed, the study sought to quantify the NV availability throughout the year.

## MATERIALS AND METHODS

### Experimental Design

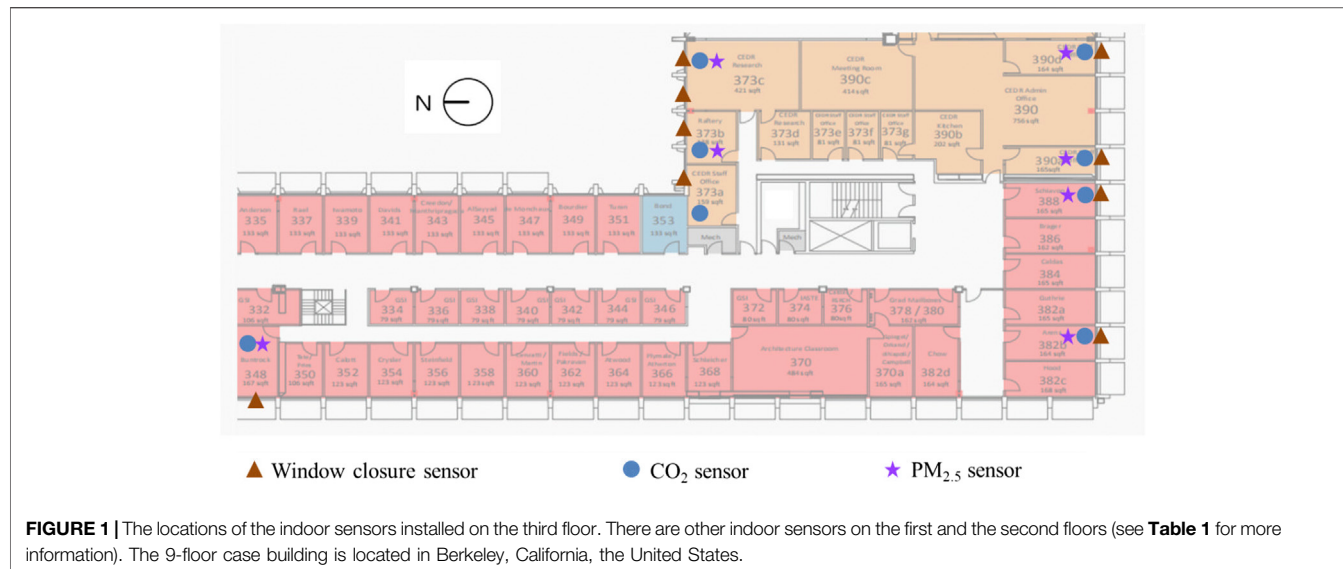
The IoT sensing network was deployed in Wurster Hall, a 9-floor mixed-mode operated building in Berkeley, CA. During the spring, summer, and autumn, the building is operated in the natural ventilation mode, while in winter there is mechanical heating. When the building operates in the NV mode, it relies on operable windows for ventilation and cooling. The building has a high level of infiltration, as shown by typical CO<sub>2</sub> levels below 550 ppm during normal operation. The building has multiple function rooms, such as a classroom, conference room, private, and open offices, with approximately 300 full-time occupants.

The IoT sensing network was deployed on July 19, 2018, and the study ended in December 2019. During this time period, the town of Berkeley was affected by the Chico Camp wildfire from November 18, 2018 to November 25, 2018. This offered a great opportunity to investigate how high outdoor particulate pollutants would affect the NV use and how building occupants would respond to these episodes. When doing the test, the building level of outdoor temperature and PM<sub>2.5</sub> concentration, room level of indoor CO<sub>2</sub> and PM<sub>2.5</sub> concentrations, and window status were monitored. The indoor sensors were installed in 15 rooms (the room number and room functions are listed in Table 1), including classrooms, meeting rooms, and office rooms. Figure 1 shows the locations of installed sensors on the third floor. The window closure sensors were installed at the bottom or on the side of the frame of openable windows. The CO<sub>2</sub> and PM<sub>2.5</sub> sensors were installed on the walls ~1.2 m from the floor.

The study also contained surveys of building occupants about their motivations or reasons for open windows. Detailed survey questions can be found in the Appendix. Questions could be classified into several categories of which there are three main aspects related to thermal comfort, air quality, and psychological motivations.

### Experimental Apparatus

The study utilized two types of indoor PM<sub>2.5</sub> sensors (Clarity Inc., and Senseware) and outdoor PM<sub>2.5</sub> sensor (Clarity Inc.). The outdoor sensors were installed at the top of Wurster Hall, a 9-floor building. Indoor sensors were placed in different spaces in Wurster Hall (see Figure 1 as examples). Both Clarity and Senseware PM<sub>2.5</sub> nodes count the particle number using the principle of light scattering. The accuracy of all the sensors was the same—within ± 10 µg/m<sup>3</sup> in the range of 0–100 µg/m<sup>3</sup> and ±10% in the range of 100–1,000 µg/m<sup>3</sup>. Data were collected at



15 min intervals for Clarity nodes and 1 min intervals for Senseware nodes. Clarity and Senseware PM<sub>2.5</sub> nodes are factory-calibrated with Arizona Test Dust (ATD). To accurately measure PM<sub>2.5</sub> concentrations, the Clarity nodes apply colocation of nodes and post-processing correction factors based on referencing government air quality stations. We colocated all sensors and adjusted readings. Indoor CO<sub>2</sub> levels were measured by Senseware CO<sub>2</sub> sensors with an accuracy of  $\pm 50$  ppm from 400 ppm to 2000 ppm. The CO<sub>2</sub> sensors were paired with PM<sub>2.5</sub> measurements.

Window status was monitored with Senseware contact sensors (Model COZIR-LP) placed on the windows. The detection was binary (i.e., open/closed) and did not provide information on the opening area or window angle. The on/off signals from the sensors enable us to know generally if the window was open or closed, but not to which extent the window was open. All the windows in the buildings were awning type, opening outward for up to 45°. Friction hinges on the windows were able to maintain the angle after they were open. The contact sensors sensed status information through Senseware IoT platform every 5 min.

Weather conditions including outdoor temperature and wind speed were collected from the Weather Underground webpage from the Oakland-9925 International Boulevard, which is 16 km from Wurster Hall. Outdoor PM<sub>2.5</sub> concentrations were collected from California Air Quality Board webpage from the Oakland-9925 International Boulevard (station 1), Berkeley Aquatic Park (station 2), and Oakland-Laney College stations (station 3), which are 10, 16, and 9 km away from Wurster Hall, respectively. PM<sub>2.5</sub> and CO<sub>2</sub> concentrations were also measured at the edge of the roof of Wurster Hall.

## Data Analysis

### Missing Data and Quality Control

All the data collected were averaged by hour, and then, the number of hours in each room was counted. The sum of the total hours for each room equals the length of effective time of

each room. Therefore, the interval between recording data can be ignored (data are recorded in different intervals by two nodes of sensors). The starting and ending dates of each room are different, and in some rooms, data were recorded only partially. This means that the period with valid data is often less than the whole monitoring period. The total duration of the data is 12,744 h. The median percentage of valid data for CO<sub>2</sub>, PM<sub>2.5</sub>, and window closure is 31, 35, and 69%, respectively. The amount of data recorded when the window is closed is significantly higher than that of data recorded when the window is open, and their medians are 55.6 and 12.9%, respectively. Data on outdoor temperature are available throughout the study period.

The percentage of valid data varied between rooms. For example, the room with the largest amount of valid data of CO<sub>2</sub> is room 172, while the room with the smallest amount of CO<sub>2</sub> is room 390a. The percentage of valid data of PM<sub>2.5</sub> in each room is similar to that of valid data of CO<sub>2</sub>. For room 170, room 172, room 232, and room 373a, the PM<sub>2.5</sub> and window closure data were not recorded. With these data, we developed and evaluated tools to quantify and assess the building's NV potential throughout the year.

### Evaluation Method

**Indoor PM<sub>2.5</sub> concentration threshold.** The World Health Organization (WHO) guidelines for PM<sub>2.5</sub> of 25 µg/m<sup>3</sup> for 24 h mean exposure were chosen to evaluate building operation. WHO guidelines have the strictest concentration limit and the best health outcome for the exposed occupants. Alternative guidelines such as those of the Environmental Protection Agency (EPA) may be used in other local regions of the world. When doing the comparison, the median hourly indoor PM<sub>2.5</sub> concentration (i.e., median value from all indoor sensors) was compared to WHO 24 h mean exposure guideline using the Exceedance index (E-index), as shown in **Eq. 1**. The E-index is a unitless value that is informed by how much hourly

$\text{PM}_{2.5}$  concentration exceeds the recommended level. Using this index, percentage of hours that indoor  $\text{PM}_{2.5}$  concentration exceeds specified levels during the air pollution episode can be calculated so that it can evaluate occupant exposure to extreme air pollution events across buildings or on a space-by-space basis within the same building.

$$E = \frac{C_{\text{measured PM}_{2.5}}}{25 \mu\text{g}/\text{m}^3}. \quad (1)$$

In addition to indoor  $\text{PM}_{2.5}$  exposure evaluation, it is also important to know how outdoor pollution levels would affect indoor pollutions. The I/O ratios, shown in Eq. 2, were applied to quantify building resilience to penetration and infiltration of outdoor  $\text{PM}_{2.5}$ .

$$I/O = \frac{C_{\text{in}}(t)}{C_{\text{out}}(t)}. \quad (2)$$

The I/O ratio was calculated for each indoor sensor location using hourly mean indoor and outdoor  $\text{PM}_{2.5}$  concentration (Eq 2, where  $C_{\text{in}(t)}$  and  $C_{\text{out}(t)}$  are the hourly means). To calculate the whole building instantaneous I/O ratio, the median hourly mean  $\text{PM}_{2.5}$  from the indoor sensors was compared to the hourly mean outdoor  $\text{PM}_{2.5}$  concentrations. The median values were used instead of the mean values because they were robust to outlier instances.

Indoor  $\text{CO}_2$  levels were compared with the 700 ppm thresholds for sedentary activities plus the typical outdoor value that is 400 ppm for Berkeley, CA.

When doing the analysis, working hours were from 8:00 am to 18:00 pm, while other hours were nonworking hours. Weekdays include Monday, Tuesday, Wednesday, Thursday, and Friday, while Saturday and Sunday were weekends. The time periods from 2018-8-15 to 2018-8-28 and from 2018-11-08 to 2018-11-25 were marked as “wildfire,” and other periods were noted as “non-wildfire.”

## NV Potential Index

The NV potential was defined as a measure to check if the outdoor weather and air quality condition were favorable for NV. It can be derived from outdoor meteorological data and air pollution level. Detailed methodologies regarding NV availability calculation can be seen in previous studies (Yin et al., 2010; Chen et al., 2017).

Regarding the outdoor temperature, two common methods were employed to determine whether it is favorable for NV. The first approach is to set fixed upper and lower limits throughout the year. As shown in Eq. 3, 12.8°C and 26°C were set as the lower limit and the upper limit, respectively, which means that NV is assumed to be available when outdoor temperature is between 12.8°C and 26°C (Herkel et al., 2008; ASHRAE Standard 55-2013 Thermal Environmental Conditions for Human Occupancy (ANSI Approved), 2013). Another approach is to take advantage of the adaptive comfort model proposed by de Dear and Brager (de Dear and Brager, 2002), which allows the upper limit ( $T_{\text{up}}$ ) to vary by month. Eq. 4 shows the calculation of the upper temperature limit, where  $T_{\text{out}}$  is the monthly average

outdoor temperature determined from weather data.  $\Delta T_{80\%}$  is the 80% acceptability comfort zone band, which is equal to 7°C, while the 90% acceptability comfort zone band should be 5°C. Favorable temperature thresholds are when the outdoor temperature is below the upper limit ( $T_{\text{up}}$ ) but greater than lower limit ( $T_{\text{low}}$ ) of 12.8°C.

$$12.8^\circ\text{C} \leq T_{\text{out}} \leq 26^\circ\text{C}, \quad (3)$$

$$T_{\text{up}} = 0.31T_{\text{out}} + 17.8 + \frac{1}{2}\Delta T_{80\%}. \quad (4)$$

The maximum outdoor wind speed ( $u_{\text{out,max}}$ ) was derived by Eq. 5 that was developed by Phaff et al. (1980), whereas the maximum allowable indoor air velocity  $u_{\text{in,max}}$  is 0.8 m/s (ASHRAE Standard 55-2013 Thermal Environmental Conditions for Human Occupancy (ANSI Approved), 2013).  $\Delta T_{\text{max}}$  is the hourly maximum temperature difference between the outdoor temperature and indoor temperature during NV hours. Here,  $\Delta T_{\text{max}}$  was approximated as the difference between the upper temperature limit ( $T_{\text{up}}$ ) and the lower temperature limit ( $T_{\text{low}}$ ). C1 is the wind speed coefficient, C2 is the buoyancy coefficient, and C3 is the turbulence coefficient. Their values are  $C_1 = 0.001$ ,  $C_2 = 0.0035 (\text{ms}^{-2} \text{K}^{-1})$ , and  $C_3 = 0.01 (\text{m}^2 \cdot \text{s}^{-2})$  (Phaff et al., 1980).

$$u_{\text{in,max}} = \sqrt{C_1 u_{\text{out,max}}^2 + C_2 h \Delta T_{\text{max}} + C_3}. \quad (5)$$

As for the outdoor particle pollution level,  $\text{PM}_{2.5}$  concentration was selected to reflect the outdoor air quality. It is assumed that when the outdoor  $\text{PM}_{2.5}$  is below or equal to 25  $\mu\text{g}/\text{m}^3$ , that is, the limit set by both the WHO and EPA, the outdoor air quality is favorable for NV.

## Statistical Tools Used

The IoT sensing and occupant survey data were analyzed using R version 3.6.1 software (The R Foundation, 2021). Statistical analysis was performed on the measured sensor data to compare between sensor locations (i.e., among different rooms and different regional weather stations) and to compare survey responses between typical pollutant conditions (i.e., wildfire and non-wildfire periods). The data under consideration were not normally distributed, so the nonparametric tests were adopted. To assess statistical significance between the measured  $\text{PM}_{2.5}$  concentrations or outdoor temperatures at different locations, a two-sided Wilcoxon rank-sum test, also known as the Mann–Whitney test, was used.

## RESULTS

### Indoor/Outdoor $\text{PM}_{2.5}$ , $\text{CO}_2$ , and Temperature

Figure 2 shows the overall distribution of hourly average indoor and outdoor  $\text{PM}_{2.5}$ , indoor  $\text{CO}_2$ , and outdoor temperature during the period from July 19, 2018 to the end of 2019. During this period, the median outdoor  $\text{PM}_{2.5}$  concentration was 3.5  $\mu\text{g}/\text{m}^3$ , slightly higher than the 1.4  $\mu\text{g}/\text{m}^3$  of

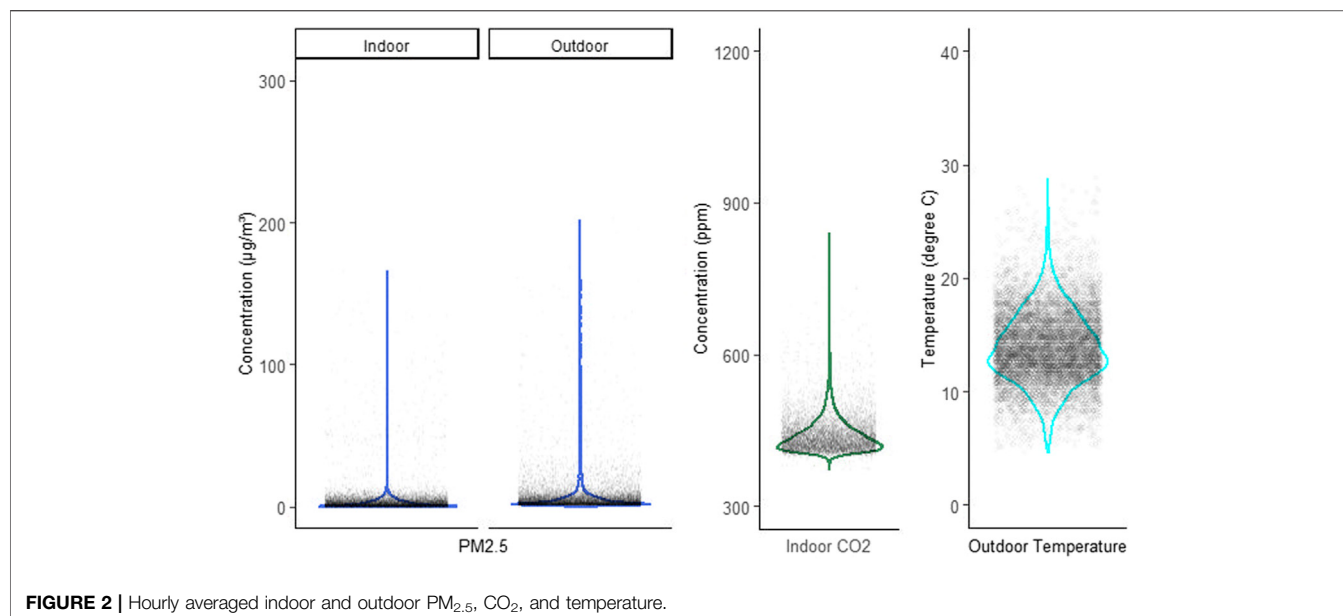


**FIGURE 2 |** Hourly averaged indoor and outdoor PM<sub>2.5</sub>, CO<sub>2</sub>, and temperature.

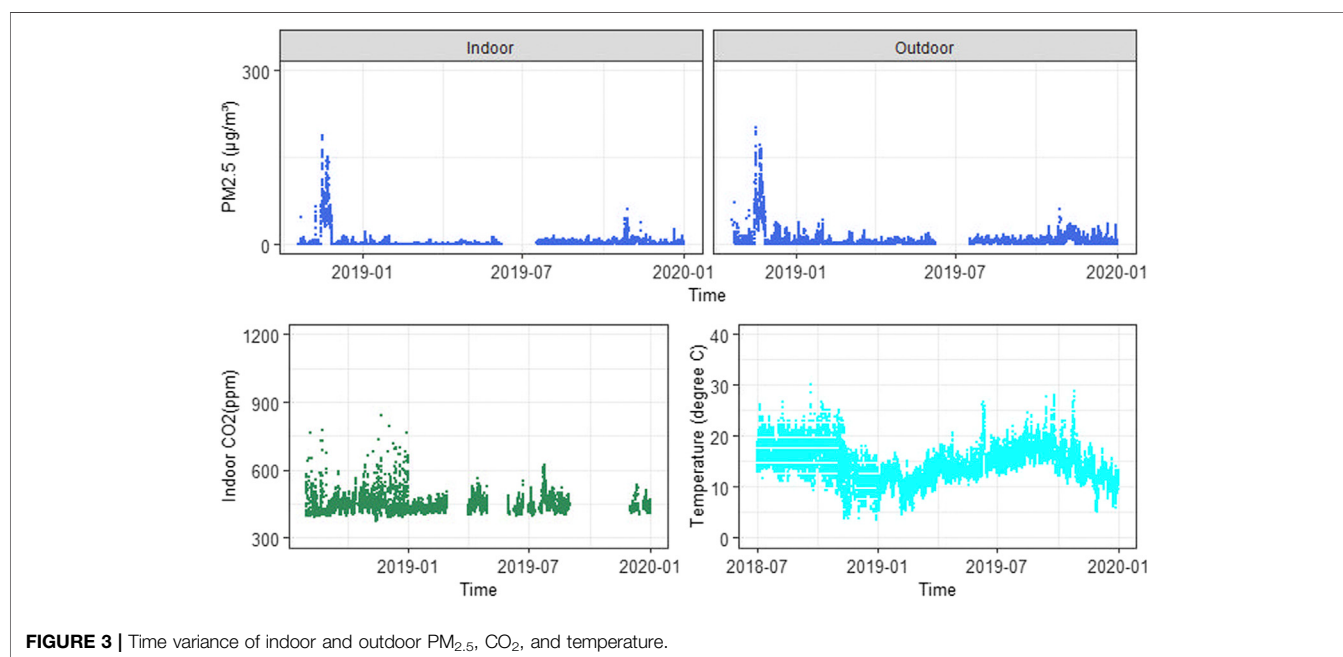


**FIGURE 3 |** Time variance of indoor and outdoor PM<sub>2.5</sub>, CO<sub>2</sub>, and temperature.

indoor PM<sub>2.5</sub>. A majority of the PM<sub>2.5</sub> concentration values, 97.3% for outdoor and 95.5% for indoor, were lower than the recommended value of 25 µg/m<sup>3</sup>. With a median value of 437.2 ppm, the measured indoor CO<sub>2</sub> concentration was low, 94.0% of the time was lower than 500 ppm and 72.3% of the time was lower than 450 ppm. The outdoor temperature ranged from 11.5°C (lower quartile) to 17.4°C (upper quartile), with a median value of 14.0°C. But there were also few extreme weather conditions with outdoor temperatures lower than 10°C or higher than 30°C.

To see how these parameters varied with time, Figure 3 presents them in the time series view. Most of the time, both indoor and outdoor PM<sub>2.5</sub> maintained at a level lower than 25 µg/m<sup>3</sup>. But there were some short periods, for example, August 15 to August 28 and November 8 to November 25 in 2018, and the PM<sub>2.5</sub> concentrations climbed up to as high as over 200 µg/m<sup>3</sup>. This sudden change in the pollutant level was caused by wildfire, which will be discussed in the later analysis. Different from the PM<sub>2.5</sub>, the CO<sub>2</sub> concentration fluctuated over the study period, while the temperature was mainly affected by the season.

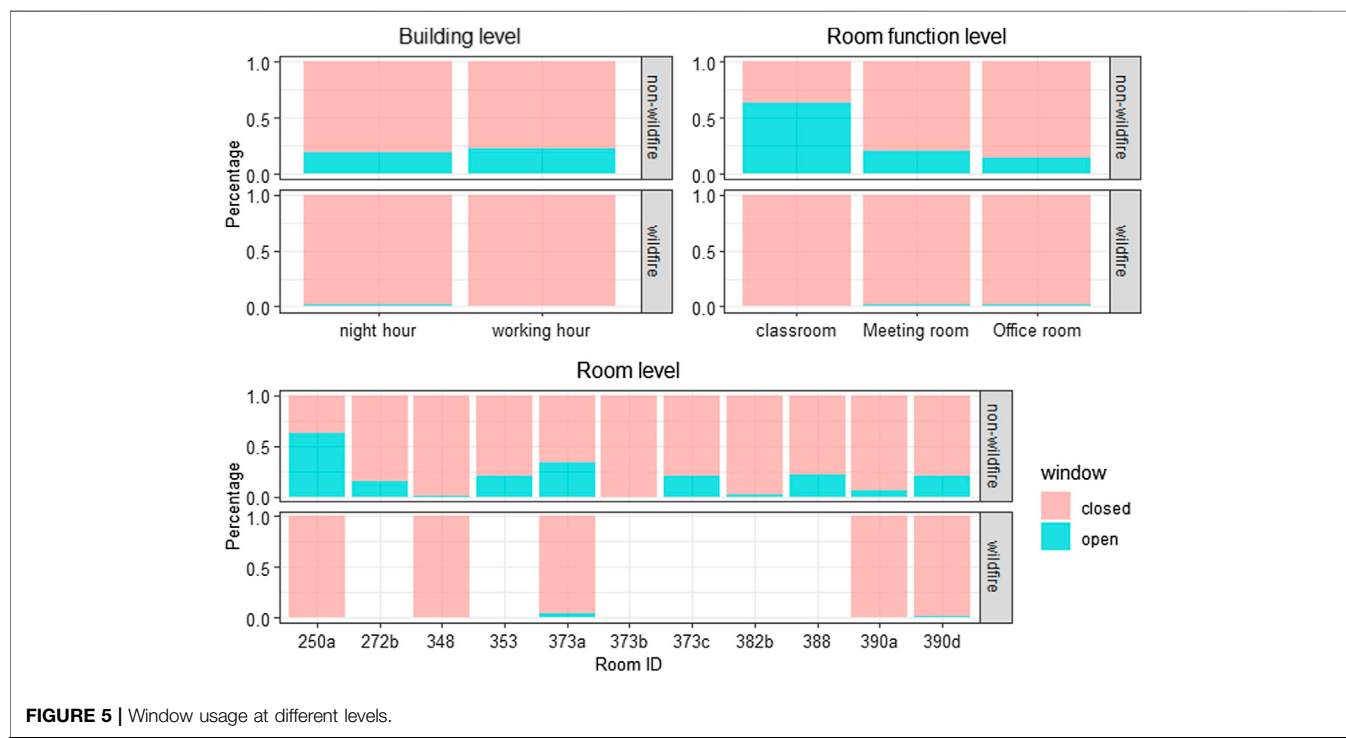
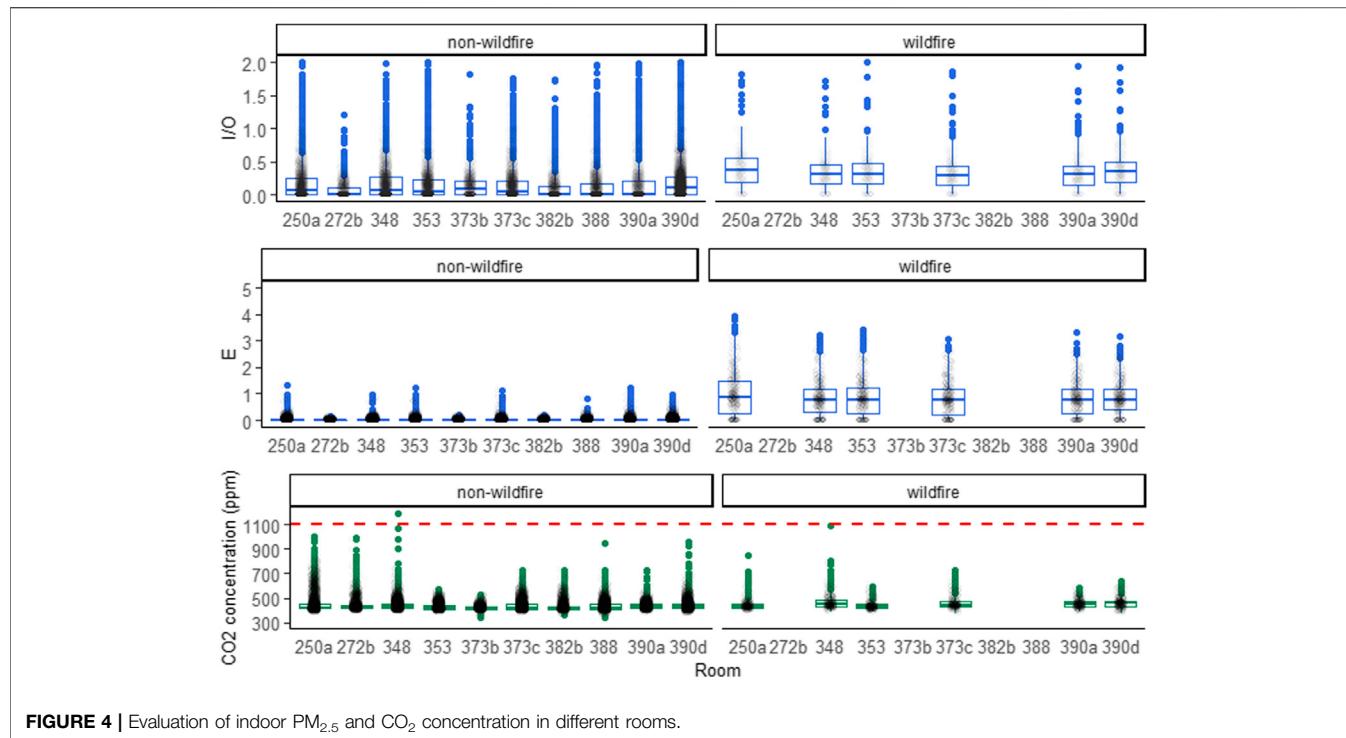


**Figure 4** shows the E index and I/O ratio of the PM<sub>2.5</sub> and CO<sub>2</sub> concentrations, respectively, for each room. When there was no wildfire, the indoor PM<sub>2.5</sub> concentrations were usually lower than 25 µg/m<sup>3</sup> so that the E indexes were smaller than 1, and only 1.9% of E indexes were larger than 1. When there was a wildfire, the indoor PM<sub>2.5</sub> increased significantly, resulting in higher E indexes, and 93% of those are larger than 1. The observation

can be validated by the I/O ratio which compares the indoor and outdoor PM<sub>2.5</sub> concentrations. For non-wildfire periods, the room level I/O ratios were usually below 0.5, with only 0.6% of spikes higher than 0.5. During the wildfire period, the I/O ratios climbed to 0.5–1 range. Different from PM<sub>2.5</sub>, the indoor CO<sub>2</sub> concentration in different rooms was not significantly affected by extreme events like the wildfire.

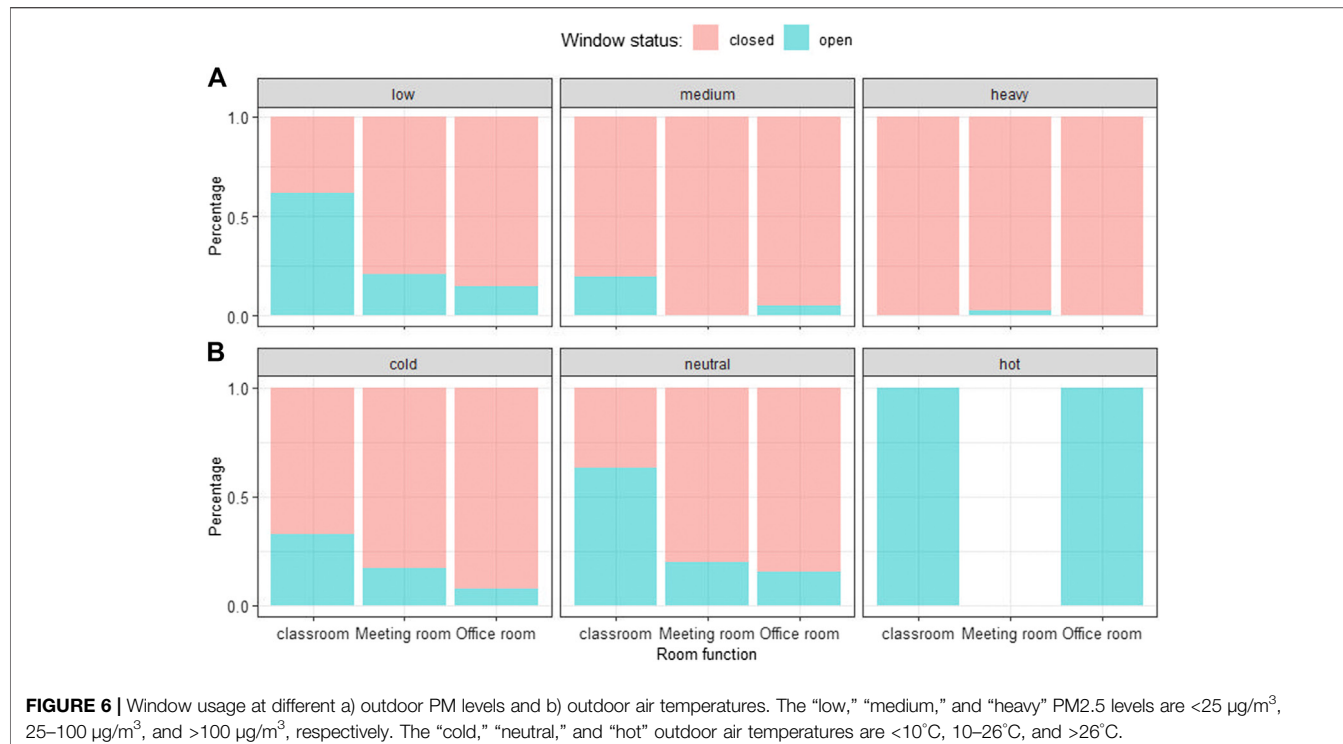


**FIGURE 6 |** Window usage at different a) outdoor PM levels and b) outdoor air temperatures. The “low,” “medium,” and “heavy” PM<sub>2.5</sub> levels are <25 µg/m<sup>3</sup>, 25–100 µg/m<sup>3</sup>, and >100 µg/m<sup>3</sup>, respectively. The “cold,” “neutral,” and “hot” outdoor air temperatures are <10°C, 10–26°C, and >26°C.



**FIGURE 7 |** Analysis of the reasons why occupants open windows.

## Use of Windows

To investigate how the building occupants interacted with the windows, **Figure 5** shows the use of windows at three levels. First, the building-level chart compares the night-time and working-time window usage during the wildfire period and that in the non-fire period. 21% of windows were open during the non-fire period, while all of the windows were closed if there was a wildfire. The window usage were similar in nighttime and working time. 24.3% windows were open during working hours, close to the 21.5% of night hours. Second, different room functions may have different window usage rates. The classroom with 63.1% of window open time used the windows more frequently than the meeting room and office room. Third, the window usages for each room varied significantly during the non-wildfire period. Some rooms opened the windows for over 50% of the time, while some others kept the window closed all the time. This observation suggests that usage pattern of the windows depends on the occupants’ behavior and also on the number of occupants in

the room. Some occupants opened and closed the window actively, some did not.

**Figure 6** shows window usage during different outdoor conditions. The visible outdoor pollutants like the PM<sub>2.5</sub> significantly affect the window usage. Occupants tended to close windows when the outdoor pollutant level was “heavy” (PM<sub>2.5</sub> > 100 µg/m<sup>3</sup>) and open windows more when the outdoor pollutant level was “low” (PM<sub>2.5</sub> < 25 µg/m<sup>3</sup>). At the same time, the outdoor temperature can also affect the window usage. As the outdoor temperature increased from “cold” (<10°C) to “hot” (>26°C), there was an increasing percentage of opening windows.

The survey depicted in **Figure 7**, asked occupants about their motivations and reasons for opening windows and shows that the primary reason was to improve their thermal comfort and indoor air quality. A significant body of knowledge already exists on the use of NV for thermal comfort and indoor air quality. These reasons are intuitive, and often adopt the perspective of occupants. People open windows if they want

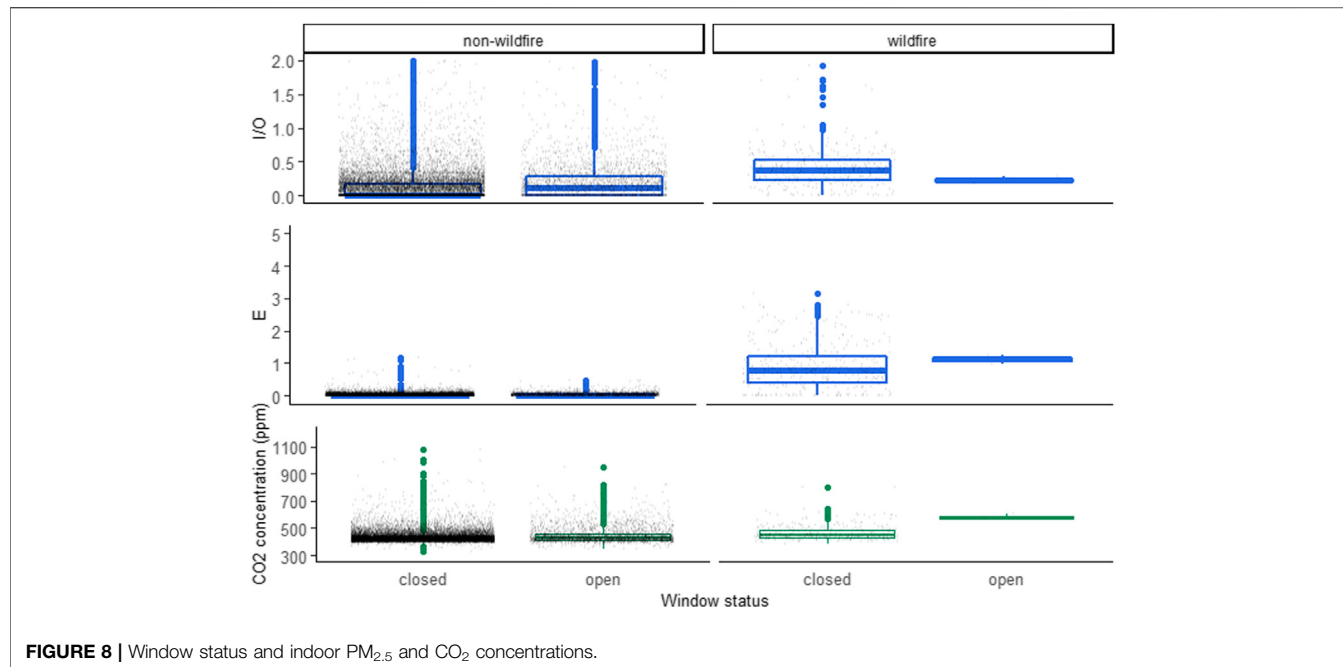


**FIGURE 8 |** Window status and indoor PM<sub>2.5</sub> and CO<sub>2</sub> concentrations.

to feel cooler or they feel that air is stuffy and needs to be refreshed. Psychological reasons like feeling connected to the outdoors ranked third in this survey. This is a very important finding that points out the third most important group of drivers that cause people to use windows. These groups of reasons are responsible for the significant amount of time windows are actually used when compared to the total amount of hours windows are open.

The results depicted in **Figure 7** also show that energy conservation or energy savings ranked as fourth in this survey with 5% responses. This suggests that energy saving does not play a very important role in the occupant's decision-making process when it comes to keeping windows open or closed. Details of the survey can be found in the Appendix.

## Effects of Window Status on Indoor Air Quality

**Figure 8** shows the effects of window status on indoor PM<sub>2.5</sub> and CO<sub>2</sub> concentrations. When outdoor air was polluted, the median of I/O and E-index were much higher. Although the I/O ratio is higher due to equilibrium between indoor and outdoor conditions, E-index is important to show if those levels have impact on occupant's health. Desired building operation would be to have the I/O ratio ~1, indicating that windows are open and outdoor air is entering indoor environment but keeping E-index < 1 suggesting that air is clean. During the wildfire period, although the windows were kept closed, the median I/O (about 0.48) and median E-index (about 1.1) were much higher than those of non-wildfire periods with open and closed windows. The median I/O ratio and E-index were both

close to 0.1 during the non-wildfire period. CO<sub>2</sub> concentration varied with the occupancy of the rooms but did not change significantly with the window status. During the non-wildfire period, CO<sub>2</sub> was 424 and 428 ppm when windows were closed and open, while it grew slightly to 453 ppm when there were wildfires outside the building. During the wildfires, although the windows were closed, only partial occupancy was in the building. To this end, the CO<sub>2</sub> concentrations were similar to those during the open-window periods.

**Figure 9** shows the hourly deviation between the room-level PM<sub>2.5</sub> and CO<sub>2</sub> and the building-level median values. Both during the wildfire period and the non-fire period, the PM<sub>2.5</sub> and CO<sub>2</sub> deviations were around 0, and they all have very small quartile numbers, indicating that the difference between the median of each room and the median of the whole building was very small. Given this, every room can be used as a partial study of the whole.

## Comparison Between Building-Scale and Urban-Scale Environmental Measurements Over a Year

**Figure 10** shows the comparison of outdoor temperature, wind speed, and PM<sub>2.5</sub> concentration at different weather stations from January 2019 to January 2020. For outdoor temperature, the variation and the distribution are similar from three weather stations. For wind speed, the violin plot shows that the three weather stations had approximately the same temperature distribution with similar medians. The *p* values from Wilcoxon tests show no significant difference among weather stations. For outdoor PM<sub>2.5</sub> concentration, data from three

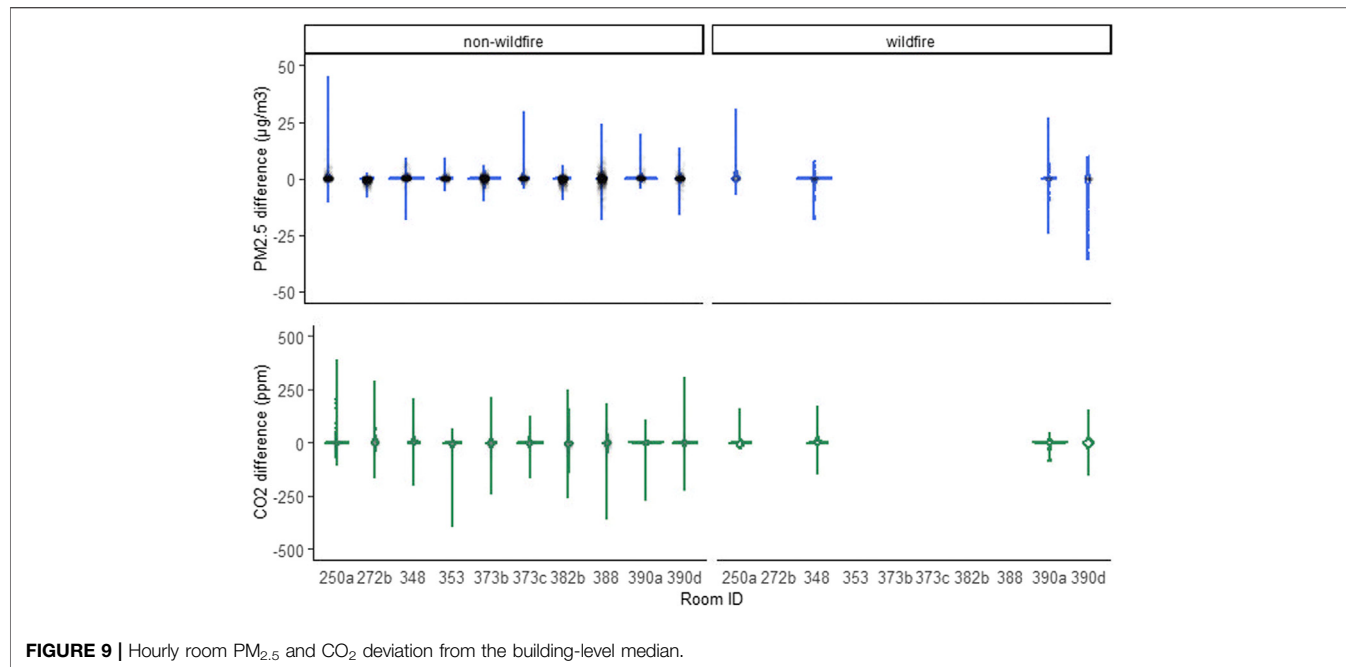


**FIGURE 9** | Hourly room PM<sub>2.5</sub> and CO<sub>2</sub> deviation from the building-level median.

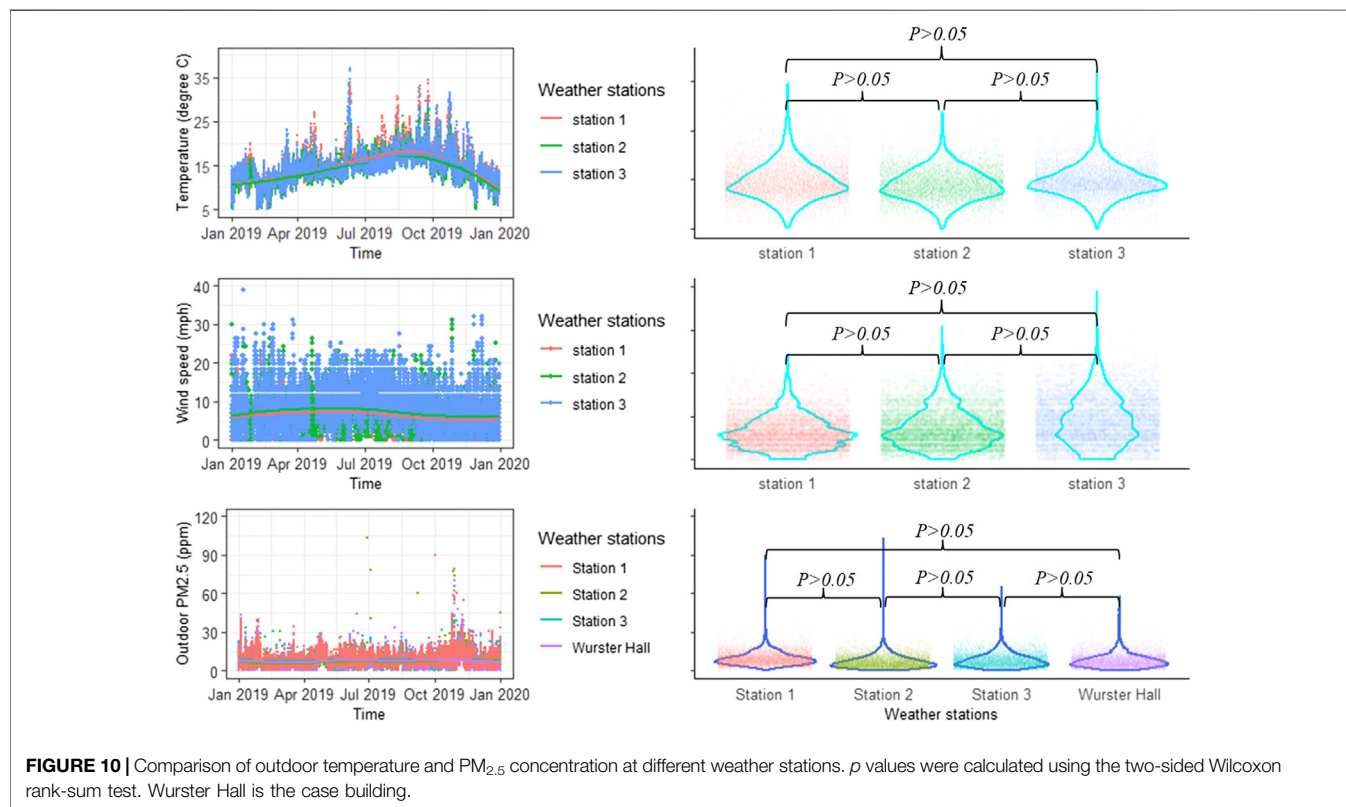


**FIGURE 10** | Comparison of outdoor temperature and PM<sub>2.5</sub> concentration at different weather stations. *p* values were calculated using the two-sided Wilcoxon rank-sum test. Wurster Hall is the case building.

weather stations are close to each other, and the outdoor PM<sub>2.5</sub> concentration measured at the top of Wurster Hall (the case building) was almost the same as those from the three weather

stations, all in a very low level. Overall, it can be seen that outdoor temperature, wind speed, and PM<sub>2.5</sub> concentration from different weather stations show little difference.

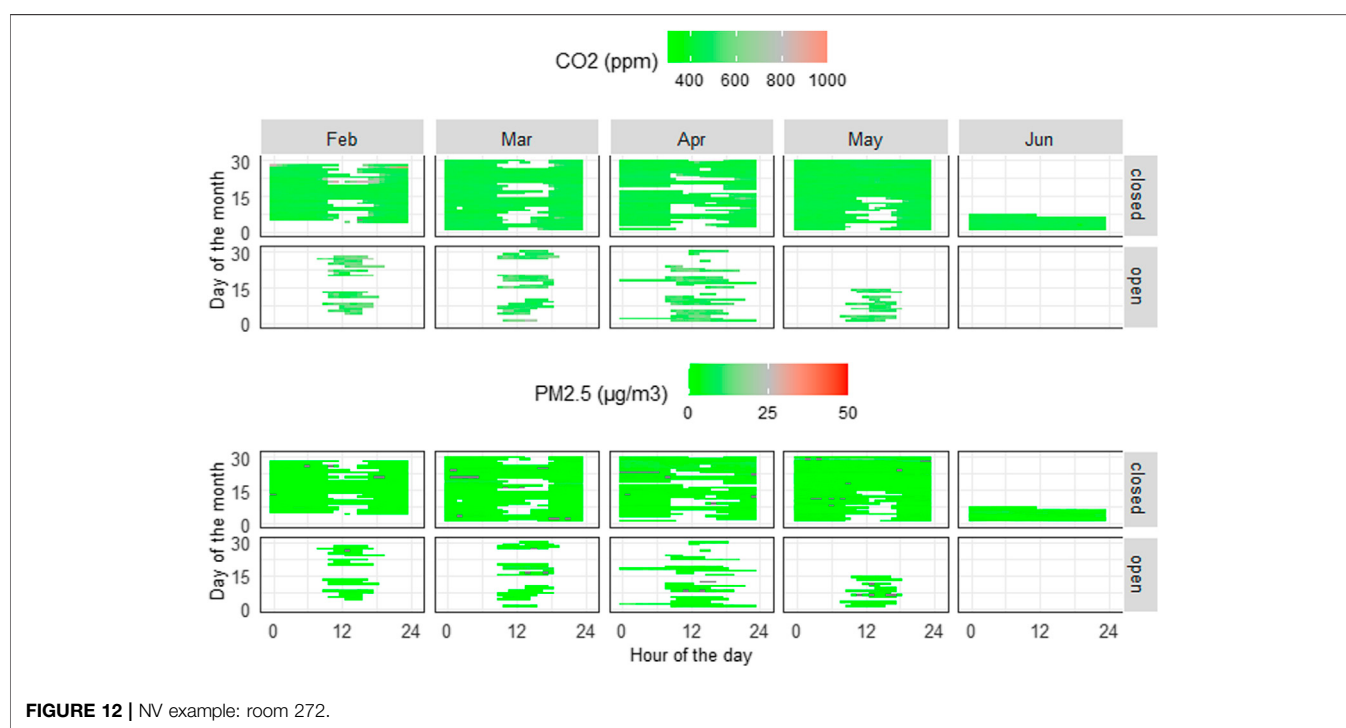
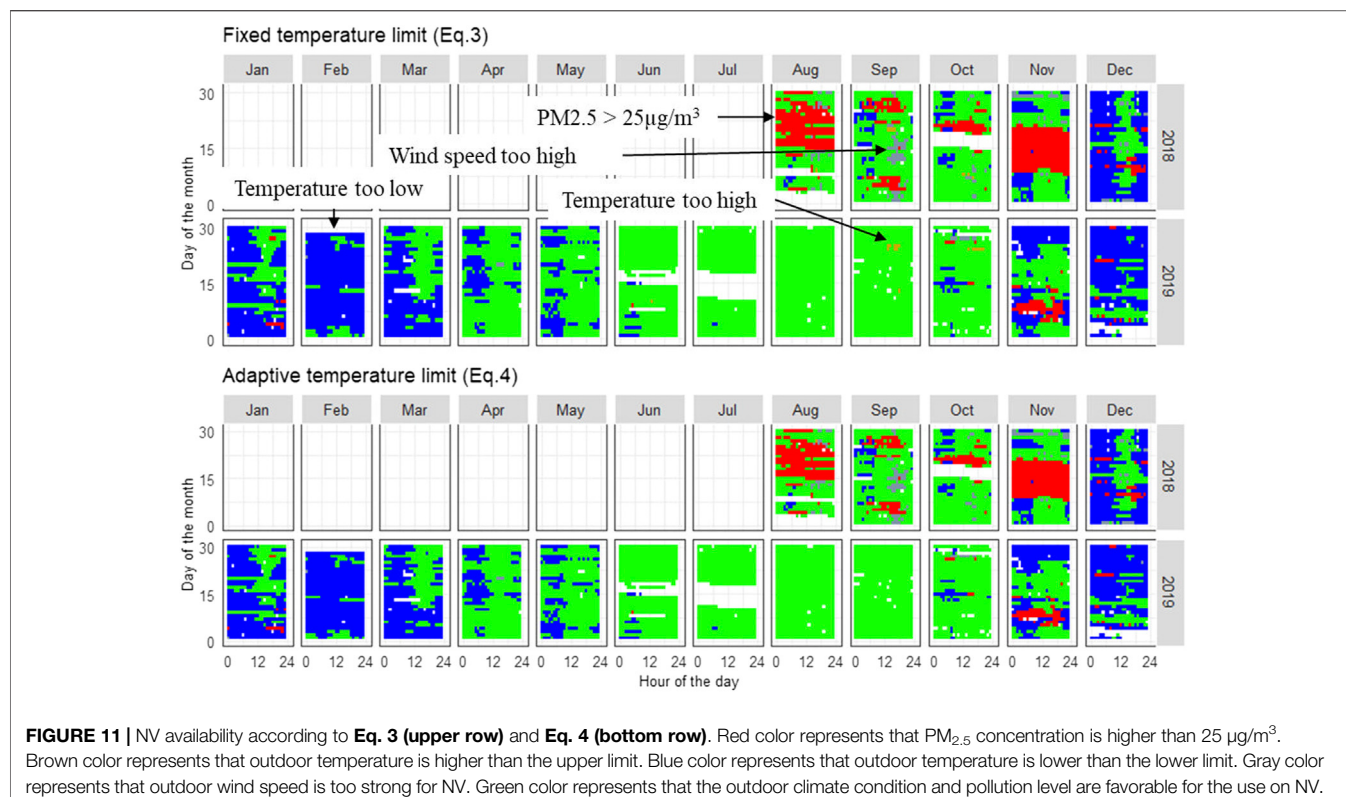


**TABLE 2** | Potential NV availability and actual window opening hours in typical rooms<sup>a</sup>.

Rooms	Data available period	Actual window opening hours (h)	Potential NV available hours (h)	
			Fixed temperature limit (Eq. 3)	Adaptive temperature limit (Eq. 4)
272b	2/4/2019–6/7/2019	474	1,372	1,434
373b	3/1/2019–6/7/2019	3	1,349	1,461
382b	1/23/2019–6/7/2019	76	1,464	1,489
388	10/23/2018–6/8/2019	85	2,251	2,343

<sup>a</sup>The rooms in this table were selected because their window usage data availability was higher than 80% during the monitored period.

## DISCUSSION

### NV Evaluation

Figure 11 shows the NV potential index throughout the study period. The red color represents periods when outdoor PM<sub>2.5</sub> pollution was above 25  $\mu\text{g}/\text{m}^3$ , periods caused by episodic events like the wildfire. The blue and brown colors represent cold and hot outdoor conditions, respectively. The gray color marks periods when mean outdoor wind speed is higher than the upper limit calculated using Eq. 5. The green color depicts periods when outdoor conditions are favorable and NV potential is available. Results show that the high outdoor PM<sub>2.5</sub> concentrations mostly occurred during the hot and dry seasons, usually from August to November. The hot outdoor temperatures mainly occurred from August to October, while the cold outdoor conditions mostly happened from November to March of the next calendar year. Throughout the year of 2019, 5,075 h out of 8,287 h (with valid data), resulting in 61.2% of time, were favorable for the use on NV.

Table 2 compares the potential NV availability and the actual window opening hours in typical rooms. There is a huge gap between the actual NV usage and the potential availability. Even using the more conservative method (Eq. 3), the actual usage rate was less than 34.5%. This significant gap can be attributed to the occupant's behavior. In an earlier study, Gao et al. (2014) showed that indoor conditions are better when manually opening windows is replaced with automatic window opening. A breakdown of the multiple motives for opening the windows is shown in Figure 7. Opening the windows or keeping them closed was always based on the occupant's perception of conditions and without knowing if conditions outside are suitable for utilization of NV or if indoor conditions can be improved with the use of NV. Informing occupants that NV is available and should be used can potentially reduce the gap between actual NV use and available potential. A previous work that focused on CO<sub>2</sub> and classroom pointed out that visual signals were effective means of increasing NV use (Wargocki, 2015).

Figure 12 takes room 272 (a classroom) as an example to show the actual NV usage. It can be seen that occupants in that room frequently interacted (open/close) with the windows. From February to May, the windows were frequently opened to take advantage of the NV when the room was occupied. The indoor CO<sub>2</sub> and PM<sub>2.5</sub> were very low during the measured

period. CO<sub>2</sub> was typically below 600 ppm, while the PM<sub>2.5</sub> was below 25  $\mu\text{g}/\text{m}^3$ .

### Limitations of This Study

This study shows how to integrate indoor and outdoor information to better describe building operation. Previously, the study by Pantelic et al. (2019) demonstrated how IoT sensing can be used to describe building resilience to episodical pollution events. The current study builds on that knowledge and extends it to demonstrate how environmental and occupant behavioral data can be combined and quantify available natural potential and level of utilization of the potential. Results in this study indicate that IoT sensing information needs to be communicated with the building occupants to improve their use of NV. This is a new and largely unexplored field. When doing this, there are some limitations that could be noteworthy for future studies. First, the percentage of missing data in this study (Table 1) is relatively high for quantifying the window usage and indoor air quality throughout the year. Second, if the outdoor weather conditions, including outdoor temperature, relative humidity, wind speed, and direction can be monitored, they could provide useful information when comparing with nearby weather stations. The current study used information from the weather station 5 km away from the buildings and omitted the microclimate effects which may induce errors. Third, there are other important factors that can influence the NV availability. For example, humidity can affect the building occupant's perception, changing their sense of a comfortable temperature range (Zhang et al., 2014). In addition to PM<sub>2.5</sub>, nitrogen dioxide (NO<sub>2</sub>) can be a major air pollution source that affects the NV usage, particularly in areas that are close to major roads (Zhang and Batterman, 2013).

## CONCLUSION

Previous studies have shown that air temperature or air pollution level are limiting factors, reducing available NV potential compared to the theoretical level. This study employed a combination of an IoT environmental sensing network monitoring indoor and outdoor climate (temperature and wind speed), air pollution level (PM<sub>2.5</sub> and CO<sub>2</sub> concentrations), and window use behaviors (open and

closed status) throughout the year. Indexes have been applied to evaluate the indoor air quality and NV usage potential of the buildings on different temporal and spatial scales and during episodic pollution events. The following findings are noteworthy:

- 1) With the help of an IoT sensor network, an NV availability tool with consideration of outdoor temperature, wind speed, and outdoor PM<sub>2.5</sub> concentrations was applied in the case building located in Berkeley, California. The tool can identify when the conditions are favorable for NV use and visualize the unfavorable factors *via* color variance.
- 2) By applying the NV potential index to the case building, 61.2% of time throughout the year of 2019 was determined to be favorable for NV usage. However, its actual NV usage was much less (<35%) than the potential availability. This suggests that human behavior is responsible for the gap and represents additional factors that should be considered when the NV strategy is planned and designed.
- 3) The actual window usage behavior (open/closed status) was significantly affected by outdoor climate condition and air pollution levels. Occupants tend to open windows when outdoor temperature is comfortable (neutral to warm) and air pollution is low.

## REFERENCES

- Asfour, O. (2015). *Natural Ventilation in Buildings: An Overview*. New York, NY: NOVA Publication, 1–25.
- ASHRAE Standard 55-2013 Thermal Environmental Conditions for Human Occupancy (ANSI Approved) (2013). MADCAD.Com, (n.d.). Available at: <http://www.madcad.com/store/subscription/ASHRAE-Standard-55-2013?landing=1> (Accessed September 12, 2017).
- Chen, Y., Tong, Z., and Malkawi, A. (2017). Investigating Natural Ventilation Potentials across the Globe: Regional and Climatic Variations. *Building Environ.* 122, 386–396. doi:10.1016/j.buildenv.2017.06.026
- Commission, E. (2010). Directive 2010/31/EU of the European Parliament and of the Council of 19 May 2010 on the Energy Performance of Buildings. *Off. J. Eur. Union*, 13–35. doi:10.2833/281509
- Costanzo, V., Yao, R., Xu, T., Xiong, J., Zhang, Q., and Li, B. (2019). Natural Ventilation Potential for Residential Buildings in a Densely Built-Up and Highly Polluted Environment. A Case Study. *Renew. Energ.* 138, 340–353. doi:10.1016/j.renene.2019.01.111
- da Graça, G. C., Linden, P., and Haves, P. (2004). Design and Testing of a Control Strategy for a Large, Naturally Ventilated Office Building. *Building Serv. Eng. Res. Tech.* 25, 223–239. doi:10.1191/0143624404bt107oa
- de Dear, R. J., and Brager, G. S. (2002). Thermal Comfort in Naturally Ventilated Buildings: Revisions to ASHRAE Standard 55. *Energy and Buildings* 34, 549–561. doi:10.1016/s0378-7788(02)00005-1
- Dutton, S. M., Banks, D., Brunswick, S. L., and Fisk, W. J. (2013). Health and Economic Implications of Natural Ventilation in California Offices. *Building Environ.* 67, 34–45. doi:10.1016/j.buildenv.2013.05.002
- EIA (2021). Annual Energy Outlook 2017. Available at: <https://www.eia.gov/outlooks/aeo/> (Accessed September 12, 2017).
- Fenger, J. (2009). Air Pollution in the Last 50 Years - from Local to Global. *Atmos. Environ.* 43, 13–22. doi:10.1016/j.atmosenv.2008.09.061
- Gao, J., Wargocki, P., and Wang, Y. (2014). Ventilation System Type, Classroom Environmental Quality and Pupils' Perceptions and Symptoms. *Building Environ.* 75, 46–57. doi:10.1016/j.buildenv.2014.01.015
- Herkel, S., Knapp, U., and Pfafferott, J. (2008). Towards a Model of User Behaviour Regarding the Manual Control of Windows in Office Buildings. *Building Environ.* 43, 588–600. doi:10.1016/j.buildenv.2006.06.031
- Luo, M., Cao, B., Damiens, J., Lin, B., and Zhu, Y. (2015). Evaluating Thermal Comfort in Mixed-Mode Buildings: A Field Study in a Subtropical Climate. *Building Environ.* 88, 46–54. doi:10.1016/j.buildenv.2014.06.019
- Martins, N. R., and Carriño da Graça, G. (2017). Impact of Outdoor PM<sub>2.5</sub> on Natural Ventilation Usability in California's Nondomestic Buildings. *Appl. Energ.* 189, 711–724. doi:10.1016/j.apenergy.2016.12.103
- Morawska, L., Thai, P. K., Liu, X., Asumadu-Sakyi, A., Ayoko, G., Bartonova, A., et al. (2018). Applications of Low-Cost Sensing Technologies for Air Quality Monitoring and Exposure Assessment: How Far Have They Gone?. *Environ. Int.* 116, 286–299. doi:10.1016/j.envint.2018.04.018
- Nicol, J. F., and Humphreys, M. A. (2001). A Stochastic Approach to Thermal Comfort-Occupant Behavior and Energy Use in Buildings/DISCUSSION - ProQuest, (n.d.). Available at: <https://search.proquest.com/docview/192502303?pq-origsite=gscholar&fromopenview=true> (Accessed July 25, 2020).
- Oropeza-Perez, I., and Østergaard, P. A. (2014). Potential of Natural Ventilation in Temperate Countries - A Case Study of Denmark. *Appl. Energ.* 114, 520–530. doi:10.1016/j.apenergy.2013.10.008
- Pantelic, J., Dawe, M., and Licina, D. (2019). Use of IoT Sensing and Occupant Surveys for Determining the Resilience of Buildings to Forest Fire Generated PM<sub>2.5</sub>. *PLOS ONE* 14, e0223136. doi:10.1371/journal.pone.0223136
- Parkinson, T., Parkinson, A., and de Dear, R. (2019). Continuous IEQ Monitoring System: Context and Development. *Building Environ.* 149, 15–25. doi:10.1016/j.buildenv.2018.12.010
- Phaff, J., de Gids, W., Ton, J., van der Ree, D., and Schijndel, L. (1980). *The Ventilation of Buildings: Investigation of the Consequences of Opening One Window on the Internal Climate of a Room*. Delft, Netherlands: TNO Institute for Environmental Hygiene and Health Technology (IMG-TNO).
- The R Foundation (2021). R: The R Project for Statistical Computing. Available at: <https://www.r-project.org/> (Accessed July 24, 2020).
- Raja, I. A., Nicol, J. F., McCartney, K. J., and Humphreys, M. A. (2001). Thermal Comfort: Use of Controls in Naturally Ventilated Buildings. *Energy Buildings* 33, 235–244. doi:10.1016/s0378-7788(00)00087-6

## DATA AVAILABILITY STATEMENT

The raw data supporting the conclusions of this article will be made available by the authors, without undue reservation.

## ETHICS STATEMENT

The studies involving human participants were reviewed and approved by UC Berkeley. The patients/participants provided their written informed consent to participate in this study.

## AUTHOR CONTRIBUTIONS

ML: data analysis, writing, and revising the manuscript; YH: data analysis and writing the manuscript; JP: conceptualizing the study, data collection, and reviewing the manuscript.

## ACKNOWLEDGMENTS

This study was funded by CITRIS and Banatao Institute under 2018 CITRIS Seed Funding Program Award. We would also like to thank Sean Wihera from Clarity.io and Julien Stamatakis from Sensware Inc. for their valuable inputs on IoT sensing.

- Talbott, E. O., Arena, V. C., Rager, J. R., Clougherty, J. E., Michanowicz, D. R., Sharma, R. K., et al. (2015). Fine Particulate Matter and the Risk of Autism Spectrum Disorder. *Environ. Res.* 140, 414–420. doi:10.1016/j.envres.2015.04.021
- Wargozi, P., and Da Silva, N. A. F. (2015). Use of Visual CO<sub>2</sub> Feedback as a Retrofit Solution for Improving Classroom Air Quality. *Indoor Air* 25, 105–114. doi:10.1111/ina.12119
- WHO Regional Office for Europe (2013). *Review of Evidence on Health Aspects of Air Pollution – REVIHAAP Project: Technical Report*. Copenhagen, Denmark: WHO Regional Office for Europe. Available at: <http://www.ncbi.nlm.nih.gov/books/NBK361805/> (Accessed July 21, 2020).
- Xiong, W., Wang, Y., Mathiesen, B. V., Lund, H., and Zhang, X. (2015). Heat Roadmap China: New Heat Strategy to Reduce Energy Consumption towards 2030. *Energy* 81, 274–285. doi:10.1016/j.energy.2014.12.039
- Yin, W., Zhang, G., Yang, W., and Wang, X. (2010). Natural Ventilation Potential Model Considering Solution Multiplicity, Window Opening Percentage, Air Velocity and Humidity in China. *Building Environ.* 45, 338–344. doi:10.1016/j.buildenv.2009.06.012
- Zhang, K., and Batterman, S. (2013). Air Pollution and Health Risks Due to Vehicle Traffic. *Sci. Total Environ.* 450–451, 307–316. doi:10.1016/j.scitotenv.2013.01.074
- Zhang, K., Li, Y., Schwartz, J. D., and O'Neill, M. S. (2014). What Weather Variables Are Important in Predicting Heat-Related Mortality? A New Application of Statistical Learning Methods. *Environ. Res.* 132, 350–359. doi:10.1016/j.envres.2014.04.004
- Zhou, J., Chen, A., Cao, Q., Yang, B., Chang, V. W.-C., and Nazaroff, W. W. (2015). Particle Exposure during the 2013 Haze in Singapore: Importance of the Built EnvironmentParticle Exposure during the 2013 Haze in Singapore: Importance of the Built Environment. *Building Environ.* 93, 14–23. doi:10.1016/j.buildenv.2015.04.029

**Conflict of Interest:** The authors declare that the research was conducted in the absence of any commercial or financial relationships that could be construed as a potential conflict of interest.

**Publisher's Note:** All claims expressed in this article are solely those of the authors and do not necessarily represent those of their affiliated organizations, or those of the publisher, the editors and the reviewers. Any product that may be evaluated in this article, or claim that may be made by its manufacturer, is not guaranteed or endorsed by the publisher.

Copyright © 2021 Luo, Hong and Pantelic. This is an open-access article distributed under the terms of the Creative Commons Attribution License (CC BY). The use, distribution or reproduction in other forums is permitted, provided the original author(s) and the copyright owner(s) are credited and that the original publication in this journal is cited, in accordance with accepted academic practice. No use, distribution or reproduction is permitted which does not comply with these terms.

## GLOSSARY

**ATD** Arizona Test Dust

**CO<sub>2</sub>** Carbon dioxide

**IAQ** Indoor air quality

**IoT** Internet of Thing

**HVAC** Heating, ventilation, and air-conditioning

**NO<sub>2</sub>** Nitrogen dioxide

**NV** Naturally ventilated buildings

**WHO** the World Health Organization

**EPA** Environmental Protection Agency

**I/O** Indoor/outdoor ratio

**E index** Exceedance index

**PM<sub>2.5</sub>** Particulate matter that have a diameter <2.5 μm

**C<sub>measured PM<sub>2.5</sub></sub>** Measured PM<sub>2.5</sub> concentration (μg/m<sup>3</sup>)

**C<sub>in(t)</sub>** Hourly mean indoor PM<sub>2.5</sub> concentration (μg/m<sup>3</sup>)

**C<sub>out(t)</sub>** Hourly mean outdoor PM<sub>2.5</sub> concentration (μg/m<sup>3</sup>)

**u<sub>in,max</sub>** The maximum allowable indoor air speed (m/s)

**u<sub>out,max</sub>** The maximum allowable outdoor air speed (m/s)

**C<sub>1</sub>** Wind speed coefficient

**C<sub>2</sub>** Buoyancy coefficient (m·s<sup>-2</sup>·K<sup>-1</sup>)

**C<sub>3</sub>** Turbulence coefficient (m<sup>2</sup>·s<sup>-2</sup>)

**T<sub>up</sub>** Upper temperature limit (°C)

**T<sub>low</sub>** Lower temperature limit (°C)

**ΔT<sub>max</sub>** Maximum difference between indoor and outdoor temperatures (°C)



# The Potential of a Smartphone as an Urban Weather Station—An Exploratory Analysis

Aly Noyola Cabrera<sup>1</sup>, Arjan Droste<sup>1,2\*</sup>, Bert G. Heusinkveld<sup>1</sup> and Gert-Jan Steeneveld<sup>1</sup>

<sup>1</sup>Meteorology and Air Quality Section, Wageningen University, Wageningen, Netherlands, <sup>2</sup>Hydrology and Quantitative Water Management Group, Wageningen University, Wageningen, Netherlands

## OPEN ACCESS

**Edited by:**

Benjamin Bechtel,  
Ruhr University Bochum, Germany

**Reviewed by:**

Shuisen Chen,  
Guangzhou Institute of Geography,

China

Konstantinos Demertzis,  
International Hellenic University,  
Greece

**\*Correspondence:**

Arjan Droste  
[arjan.droste@wur.nl](mailto:arjan.droste@wur.nl)

**Specialty section:**

This article was submitted to  
Environmental Informatics and Remote  
Sensing,  
a section of the journal  
*Frontiers in Environmental Science*

**Received:** 28 February 2021

**Accepted:** 03 August 2021

**Published:** 20 August 2021

**Citation:**

Cabrera AN, Droste A, Heusinkveld BG  
and Steeneveld G-J (2021) The  
Potential of a Smartphone as an Urban  
Weather Station—An  
Exploratory Analysis.

*Front. Environ. Sci.* 9:673937.  
doi: 10.3389/fenvs.2021.673937

The ongoing urbanization requires enhanced understanding of the local meteorological and climatological conditions within the urban environment for multiple applications, concerning energy demand, human health, and spatial planning. Identifying areas with harmful meteorological conditions enables citizens and local authorities to take actions to optimize quality of life for urban dwellers. At the moment cities have (in general) limited networks of meteorological monitoring stations. To overcome this lack of observations, the use of non-traditional data sources is rapidly increasing. However, the use of such data sources without enough prior verification has become a controversial topic in the scientific community. This study aims to verify and assess one of the main non-traditional data sources, i.e. smartphones. The goal is to research the potential of smartphones (using the Samsung Galaxy S4 as an example phone model) to correctly sense air temperature, relative humidity, and solar radiation, and to determine to what extent environmental conditions negatively affect their performance. The smartphone readings were evaluated against observations from reference instrumentation at a weather station and a mobile measurement platform. We test the response time of the smartphone thermometer and hygrometer, and the light sensor's cosine response. In a lab setting, we find that a smartphone can provide reliable temperature information when it is not exposed to direct solar radiation. The smartphone's hygrometer performs better at low relative humidity levels while it can over-saturate at higher levels. The light sensor records show substantial correlation with global radiation observations, and short response times. Measurements along an urban transect of 10 km show the smartphone's ability to react to fast changes of temperature in the field, both in time and space. However, a bias correction (dependent on wind speed and radiation) is required to represent the reference temperature. Finally we show that after such a bias correction, a smartphone record can successfully capture spatial variability over a transect as well.

**Keywords:** smartphone, urban heat island, urban meteorology, crowdsourcing, citizen science, opportunistic sensing, weather station, urban climate

## 1 INTRODUCTION

Urban meteorology has been studied for nearly 200 years, including the “Urban Effects” on temperature (Oke, 1982; Arnfield, 2003) and humidity (Hage, 1975). Howard (1833) was the first to show that air temperature is generally higher within a city (~ 2°C higher) compared to its surroundings, known as the urban heat island (UHI). The intensity of the UHI and other “Urban Effects” depend largely on local climate, surrounding geography, extent of urban environment, urban geometry, type and quantity of anthropogenic emissions (Rydin et al., 2012; Oke et al., 2017) and population density (e.g., Steeneveld et al. (2011); Shi et al. (2019); Li et al. (2020)). Anthropogenic heat production is another key concept in urban meteorology, defined as the heat flux generated by vehicular emissions, heating and cooling of buildings, industrial processing Sailor (2011) and metabolic heat release by people (Santamouris and Kolokotsa, 2016).

The impacts of the UHI on society are diverse and interdependent, ranging from negative effects on human health to increased energy consumption. During warm spells the UHI can intensify health problems like heat strokes, and dehydration: especially to those with diabetes (Kovats and Bickler, 2012). Increased exposure to high temperatures shows an increment in morbidity and mortality rates (Höppe, 2002; Laaidi et al., 2006; Tertre et al., 2006; Baccini et al., 2008; Gasparrini et al., 2015). The IPCC (2014) states that by the end of the 21<sup>st</sup> century, heat-waves might double their frequency (in the worst case scenario RCP8.5), which will strongly impact the urban environment.

The urban microclimate also influences energy demand related to heating and cooling of buildings (Allegri et al., 2012). This rising energy demand potentially increases both anthropogenic heat production and greenhouse gas emissions, creating a positive feedback loop. Several studies have found high correlations between temperature and energy demand (Keirstead and Sivakumar, 2012; Fazeli et al., 2016). These findings are already being considered by the urban design community (Svensson and Eliasson, 2002; Pijpers-van Esch, 2015; Klemm et al., 2017) whilst some governmental agencies are working on ways to minimize the negative effects of the UHI. All the mentioned problems can be reduced or even mitigated by early warning systems together with the identification of the most susceptible areas within a city.

The understanding of urban meteorology is of paramount importance as illustrated above. Gaining a better understanding of urban meteorological phenomena will allow meteorological institutes to develop better and faster weather forecasting systems, which consequently will facilitate timely and precise warning mechanisms to prevent adverse health problems and casualties. Many countries already implemented Heat Health Warning Systems, which have been promoted by the World Health Organization and the World Meteorological Organization. However, these warning systems are commonly based on simplified thermal assessment procedures. More detailed forecasting methods could offer more precise warnings in the near future (MacLeod et al., 2016; Di Napoli et al., 2020). A higher

spatial density of these forecasting systems is necessary to determine local effects of urban meteorology phenomena including the UHI (Rydin et al., 2012; Ronda et al., 2017). Even though there are some networks of professional *in-situ* meteorological stations in several cities around the world, this is still not enough to research UHI at a finer scale.

To overcome the lack of spatiotemporal availability of meteorological observations in cities, crowdsourcing and citizen science projects might offer an alternative data source Meier et al. (2017); Chapman et al. (2017); Nipen et al. (2019); Masson et al. (2020); Cheval et al. (2020); Bárdossy et al. (2020). Muller et al. (2015) define crowdsourcing as: “*obtaining data or information by enlisting the services of a potentially large number of people and/or sensors, generally transmitted via Internet*”. Chapman et al. (2017) discuss whether using crowdsourcing weather observations is part of a paradigm shift in observational techniques in the atmospheric sciences. They conclude crowdsourcing has potentially far-reaching consequences for the way in which measurements are collected and used in the field. A large amount of data is now being obtained from such sources, and the quantity is substantially increasing Krennert et al. (2018); Uteuv et al. (2019). Zhu et al. (2020) summarized the crowdsourcing efforts at meteorological and hydrological services and categorized the use of crowdsourced data in relationship discovery, knowledge generalization and systemized service. Nazarian et al. (2021) provide a thorough showcase of the use of wearable devices (smartphones, smartwatches etc.,) to study biometeorology and (urban) heat exposure. Such devices are typically worn close to the skin, making them excellent choices for heat stress studies. The potential of using cars and other vehicles as sensor platforms has been acknowledged for a time now (Mahoney and O’Sullivan, 2013; Abdelhamid et al., 2014), and though the techniques are still being developed, recent results seem promising for e.g., improving precipitation forecasts based on windshield wiper data from cars (Siems-Anderson et al., 2020).

Nowadays, many people around the world carry smartphones, which are potential data acquisition devices. Several projects have been developed to take advantage of many smartphone features and sensors: among others, Madaus and Mass (2017) used smartphone pressure records harvested via crowdsourcing to assimilate in numerical weather prediction models to enhance the forecast of severe weather events. Overeem et al. (2013) used smartphone battery temperature records taken in eight different metropoles across the globe to estimate the air temperatures on a daily-mean and city-wide scale. Thereto they developed a linear heat-transfer model that accounts for heat conduction between the smartphone to the human body on one hand and to the atmosphere on the other hand. With about 800 smartphones records per day, they were able to successfully estimate air temperatures. Using São Paulo as testbed, Droste et al. (2017) refined this method towards smaller (hourly) scales and showed that this method also allows for estimating differences in the UHI effect between neighborhoods. A lab-test to refine this technique was performed by He et al. (2020), which reduced the temperature bias to around 1°C. In addition, de Vos et al.

(2020) show the potential of the combined crowdsourcing of temperature, humidity, rainfall and radiation illustrated for Amsterdam (the Netherlands), using among others 3.14 million smartphone records collected over just 1 month. Also, Mandement and Caumont (2020) successfully applied low cost personal weather stations to monitor the evolution of deep convection.

Data from such unorthodox sources require a stringent quality-control to ensure its usefulness, since the devices are typically not built to measure the environment at high accuracy. Hamdi et al. (2020) mention the need to identify the signal-to-noise ratio in crowdsourced observations. Machine learning is often applied as a way to reduce this noise; e.g., Trivedi et al. (2021) successfully use machine learning to use smartphone records for estimating indoor temperatures, and Li et al. (2021) devised a bias-correction method for smartphone pressure data based on a machine learning approach. Napoly et al. (2018) and Meier et al. (2017) have developed a quality-control procedure for personal weather stations measuring temperature, and similar procedures have been developed for rainfall (de Vos et al., 2019) and wind observations (Droste et al., 2020).

Despite these research efforts, the accuracy and response times of smartphone sensors are poorly known. Some disadvantages of using smartphones as measurement equipment have been brought to light, but those mostly relate to the phone and its usage as a whole, not the sensors themselves. Examples are uncertain GPS location (indoors vs outdoors); unknown elevation; or the influence of human behavior on the readings. Knowledge about the performance of the most useful sensors for urban meteorology inside smartphones and identifying the variables that affect accuracy and reliability will enhance the potential of this crowdsourcing data. This study aims to investigate the accuracy and response times of smartphone temperature, humidity and light sensors, during different usage conditions. The goal of this work is to establish what the potential of the smartphone as a measurement platform is, in terms of response times and accuracy. To that end, we specifically focus on direct smartphone sensor measurements, and not of derived quantities using the battery temperature, for instance. We also aim to identify potential error sources that influence smartphone sensor readings. We make use of a specific type of smartphone: the Samsung Galaxy S4, a relatively older model which contains several environmental sensors, to answer the following research questions:

1. How do smartphone readings of air temperature, relative humidity and solar radiation compare (in accuracy and response time) to reference sensors specifically designed for meteorological observation? In particular, under weather conditions that are favorable for high UHI, as well as for different usage conditions (battery charging, intensive CPU usage etc.)
2. Which variables and environmental conditions affect smartphone readings of ambient temperature and relative humidity, and to what effect?

While we do use a specific type of smartphone, we expect the type of error sources and typical response times to be illustrative

for not just the specific sensor types in the S4, but rather for any smartphone used as a measurement platform. While values of response times might change between sensor brands, the errors and typical responses are expected to be more universal, related to how a smartphone is built and used. This paper is organized as follows: **Section 2** presents our methodology and utilized observations, and **section 3** presents the results for the temperature, humidity and light sensor. **Section 4** discusses our findings and conclusions are drawn in **section 5**.

## 2 METHODOLOGY AND DATA

### 2.1 Smartphone Records

Air temperature, relative humidity and light intensity readings are obtained with a Samsung Galaxy S4 GT-I9515 smartphone (running Android 5.0.1). This smartphone has been selected for its wide global distribution, since more than 40 million devices were sold. This device incorporates the SHTC1<sup>1</sup> digital humidity and temperature sensor developed and manufactured by Sensirion. Furthermore, the smartphone contains a CM3323E light sensor, which is primarily used to sense RGB and white light to automatically adjust brightness and color temperature of the device screen. All sensor data is retrieved from the phone using the Android application “AndroSensor v1.9.6.3”. The main set of experiments was performed during September 2017 through to March 2018. A second field experiment under summer conditions was executed during a hot spell in June 2021.

### 2.2 Mobile Reference Observations

Smartphone temperature ( $T_s$ ), relative humidity ( $RH_s$ ), and light ( $L_s$ ) are compared against *in-situ* measurements and (over a trajectory) against instrumentation mounted on a custom measurement-tricycle developed by Heusinkveld et al. (2010). The micrometeorological observations on the tricycle consist of a shielded thermometer-hygrometer (model CS215L, Campbell Scientific, United States), an ultrasonic 2-D anemometer (Gill WindSonic, Gill Instruments, United Kingdom) six pyranometers (Hukseflux) and six pyrheliometers, and a GPS system (**Figure 1**). In addition the wheel speed is recorded to estimate the true wind speed by correcting the sonic anemometer record with the wheel speed. Further details about the tricycle and its use in urban climate research are available in Heusinkveld et al. (2014) and Koopmans et al. (2020).

### 2.3 Reference Weather Station

The experiments took place in and around Wageningen (the Netherlands) which is a mid-size town of about  $3 \times 3$  km, and with  $\sim 39,000$  inhabitants. The site is located in a temperate climate [Cfb in the Köppen climate classification, Kottek et al. (2006)]. The urban morphology of Wageningen consists of typically two to three stories tall residential buildings. Observations from the Veenkampen weather station<sup>2</sup>, run

<sup>1</sup>[https://wikidevi.wi-cat.ru/Samsung\\_Galaxy\\_S4\\_\(SHV-E300S\)](https://wikidevi.wi-cat.ru/Samsung_Galaxy_S4_(SHV-E300S))

<sup>2</sup><https://ruisdael-observatory.nl/veenkampen/>

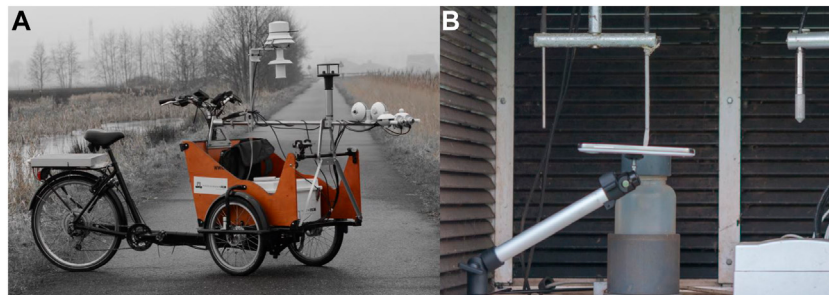


**FIGURE 1 |** The measurement cargo tricycle (**A**) and the smartphone setup in the Stevenson screen at the Veenkampen weather field (**B**). The smartphone is positioned horizontally with minimum contact points to prevent conduction.

**TABLE 1 |** Overview of the different experiments performed for this study.

Measuring variable	Type of experiment	Number of repetitions
1) Temperature response time from cold to warm	Lab experiment	12
2) Temperature response time from warm to cold	Lab experiment	12
3) Temperature response time from cold to warm with wind influence	Lab experiment	6
4) Temperature response time from warm to cold with wind influence	Lab experiment	4
5) Relative humidity response time from humid to dry	Lab experiment	12
6) Relative humidity response time from dry to humid	Lab experiment	12
7) Light response time from light to dark	Lab experiment	2
8) Light response time from dark to light	Lab experiment	2
9) Cosine response analysis of smartphone light sensor	Lab experiment	12
10) Temperature comparison against reference instrumentation at meteorological station	Field experiment	. 5 sets during winter 2017–2018 . 2 sets during summer 2021
11) Relative humidity comparison against reference instrumentation at meteorological station	Field experiment	. 5 sets during winter 2017–2018 . 2 sets during summer 2021
12) Temperature, relative humidity, and light	Urban transect experiment	12 routes at different times of the day during autumn 2017

by the Meteorology and Air Quality section of Wageningen University, are used to evaluate the accuracy of  $T_s$ , RH and  $L_s$  readings under diverse meteorological conditions. The weather station is located to the west of Wageningen (51.981°N, 5.622°E), and consists of a flat well-watered and regularly mowed grass field over a 0.5 m clay soil on top of a 1.5 m peat soil layer. The site has a Stevenson screen to measure temperature and humidity at 1.5 m level by a Väisälä-HMP155 sensor, containing a heated humidity sensor, and a PT100 temperature sensor. The measurement accuracy amounts to 0.2 K for temperature and 2% for RH (for  $10 < \text{RH} < 100\%$ ).

## 2.4 Time Response Analysis

The first step in the research quantifies the response time of  $T_s$ , RH<sub>s</sub> and L<sub>s</sub>. Time response is defined as the amount of time it takes to a sensor to respond to a rapid change of a variable, and reach the new value. To quantify this response the calculation of a time constant ( $\tau$ ) is needed.  $\tau$  is the time for the system (sensor) needed to reach 63.2% or  $1 - (1/e)$  of its final asymptotic value (the expected value). To determine  $\tau$  of the sensors, they have to reach an equilibrium state and then get exposed to a step change. The following series of experiments are designed to obtain ( $\tau$ ) for

$T_s$  and RH<sub>s</sub> (Table 1 contains the overview of the different experimental setups of this study):

1. To quantify the response time of  $T_s$  and RH<sub>s</sub>, the smartphone records data in a room at a constant temperature and constant relative humidity.
2. After reaching equilibrium the device is situated in a new place with different but also stable levels.
3. The experiments to calculate the response time have been designed in both directions (from warm to cold, from dry to humid, and vice versa) and starting from different steady states. The experiment has been repeated 12 times in each direction.

For instance, the device is placed at room temperature/humidity (~18°C and 60% RH), and then the smartphone is quickly placed into a freezer, which has a lower temperature and higher RH (~ -8°C and 75% respectively) until equilibrium is reached. Precise details of starting and environmental temperature and RH are provided in the **Supplementary Material**. At all times the device is positioned on top of a platform which only has 3 contact points to minimize heat transfer. After some time, the equilibrium is reached, and the

device is put outside the freezer until a new steady state is attained. In order to include more step-changes from different temperature levels, the device in some cases is also positioned below an incandescent light, which generates stable high temperatures (around 40°C). The selected sampling rate for these tests is 1 s with a resolution of 0.01°C and 0.01% RH. Furthermore, it is also important to understand the effect of wind on  $T_s$  and  $RH_s$  response times. Hence, the previously explained experiment has been repeated while varying the wind speed. For these cases, a fan is used to generate wind, measured by a cup anemometer. This experiment variation has been repeated 10 times.

The response time of the light sensor is not specified by the manufacturer, but usually this type of sensor responds fast to a step change. To quantify  $\tau$  of  $L_s$ :

1. The device is located in a dark room.
2. The light sensor is suddenly exposed to an intense concentrated light source, using a lamp.
3. The procedure is performed in the opposite way (from light to darkness).

Considering that a light sensor tends to have a relatively small  $\tau$ , 10 milliseconds is the selected sample rate, which is the fastest rate available by the AndroSensor application.

## 2.5 Measurement Accuracy

Measurement accuracy of the smartphone is tested using the Veenkamp weather field reference instruments. Four different experiments are designed and executed to test the sensor accuracy under various conditions:

1. The smartphone is placed at the weather field, inside a Stevenson screen (**Figure 1**) next to the reference hygrometer and thermometer, at 1.5 m height. Data is recorded for 5 blocks of 12 daytime hours.
2. The smartphone is placed outside the Stevenson screen, around 0.5 m away at 1.3 m height.
3. The smartphone battery is being charged and smartphone's CPU is under heavy workload. The experiment runs for 60 min and is executed under stable and constant room temperature.
4.  $T_s$  and  $RH_s$  are compared against instrumentation installed in the tricycle (described in **section 2** and **Figure 1**). The objective of this comparison is to analyze the accuracy of the smartphone readings across an urban transect, and to evaluate the characteristics and understand the general features of the data.

Data from the experiment outside the Stevenson screen, and the experiments mounting the smartphone on the tricycle are used to assess the accuracy of  $L_s$ . In addition, we test the response of the light sensor to radiation incident at an angle with respect to the surface. The sensor's response to radiation incident at different angles is a parameter widely used to understand its capacity and overall quality. The response of such sensors to radiation incident at an angle  $\theta$ , with respect to the horizontal

plane is called cosine response. We calculate the cosine response by directing a light beam towards the sensor from different angles, always maintaining the same distance and light intensity. The ideal cosine response is proportional to  $\theta$ , and any deviation from this ideal value causes underestimations (Martínez et al., 2009).

## 3 RESULTS

This section presents the results of the analyses for the sensor response time, accuracy and bias identification of the temperature, relative humidity and light sensors in a lab environment (in **sections 3.1–3.3**, respectively). Subsequently, the spatial/temporal performance of the smartphone sensors will be compared against reference instruments, as well as a bias-correction procedure following this verification (**section 3.4**).

### 3.1 Temperature Sensor

#### 3.1.1 Response Time Analysis

As previously described,  $\tau$  equals the time required by the thermometer to register 63.2% of a step change in air temperature (WMO, 2014). According to the manufacturer<sup>3</sup>, the SHTC1 sensor installed in the Samsung S4 has a  $\tau$  between 5 and 30 s. However, as shown in **Supplementary Table S1** and **Supplementary Table S2**, such values are difficult to achieve because the sensor is enclosed inside the device, and the ventilation is poor. The average  $\tau$  estimated for the negative step-change in temperature amounts to 188.25 and 161.76 s for a positive step-change, with a standard deviation of 27.13 and 56.68 s, respectively (**Supplementary Table S1** and **Figure 2**). The WMO states that for routine meteorological observations there is no advantage in using thermometers with very small  $\tau$ . Instead, they recommend the use of thermometers with a  $\tau$  of approximately 20 s (WMO, 2008; Burt and de Podesta, 2020). However, thermometers with large time constants can introduce errors in cases where air temperature changes at a fast rate (e.g., during urban transect measurements). Since  $\tau$  is the time required for the sensor to reach 63.2% of a step change, five times  $\tau$  is the time required to get a near full reading (99.3%). Therefore, during an abrupt change in temperature the smartphone might take around 15 min to get a correct reading compared, where 1.6 min is recommended for conventional meteorological observations with a thermometer.

The difference between the time responses can be explained since a relatively warm smartphone in a cold environment will induce turbulent convection which is an efficient transport mechanism for heat. On the contrary, when a relatively small cold smartphone is located in a warm environment, a stable layer will form over the smartphone, and turbulent transport in stable conditions is suppressed, which inhibits the heat exchange and as such results in a longer response time. The temperature response curve appears to behave like a second order system, with an

<sup>3</sup>[https://www.mouser.com/datasheet/2/682/Sensirion\\_Humidity\\_Sensors\\_SHTC1\\_Datasheet-1511754.pdf](https://www.mouser.com/datasheet/2/682/Sensirion_Humidity_Sensors_SHTC1_Datasheet-1511754.pdf)

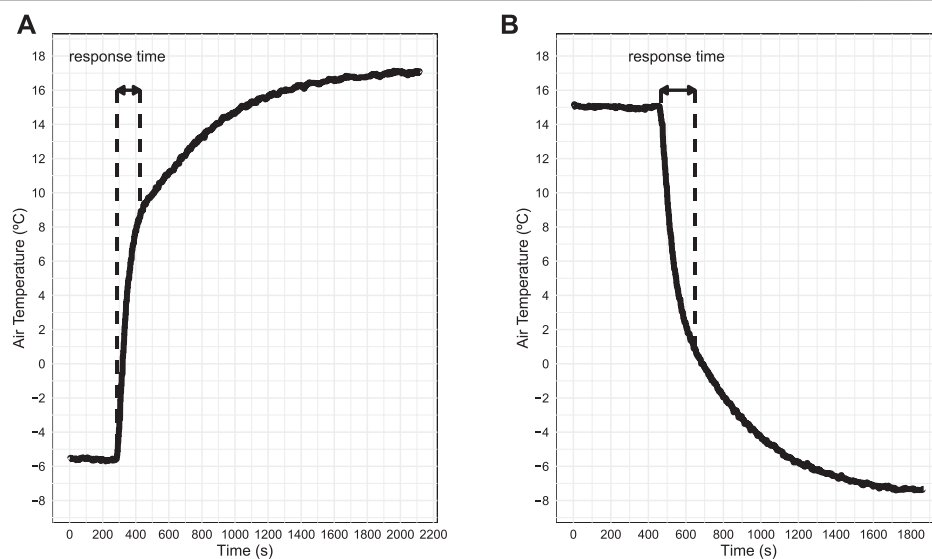


**FIGURE 2 |** Observed temperature response for a positive (A) and negative (B) temperature exposure for one of the 12 experiments performed (see text). The time axis represents time since start of the measurements (s). Dashed lines indicate the estimated response time ( $\tau$ ).

overshoot (peak) in the temperature measured as consequence of the step change. However, after the overshoot, the response time appears to return to equilibrium as a first order system instead of having an oscillation effect.

The origin of the behavior previously described is difficult to identify, the measurements were taken alongside a calibrated Digital thermometer (GTH 175/Pt), and such behavior was not present in the thermometer readings. It seems that Sensirion (the sensor manufacturer) put in place a software algorithm which calibrates the air temperature readings by using “information from other areas of the device”, presumably battery temperature readings. This is called “The Sensirion Compensation Engine”, and according to them, the algorithm is specially calibrated for the Samsung S4 smartphone<sup>4</sup>. The same posts suggests that the post-processing algorithm helps to improve temperature response time. So, perhaps this compensation algorithm generates the measurement errors previously described. The latter might happen since ambient air is also supplied to the battery temperature sensor (due to wind exposure) warming it up at a faster rate than the assumed by the compensation-algorithm, therefore, generating the observed sudden increase in the sensed air temperature. Without further details on the functioning of the algorithm it is impossible to confirm this hypothesis. Such a “black box” algorithm is likely present in most mobile devices, where the manufacturers do not always detail how these algorithms are set up. As such, they could be considered inherent to such mobile devices which needs to be taken into account when using these devices to gather environmental data.

All the lab experiments described above were executed with airflow close to  $0 \text{ ms}^{-1}$ . However, as stated by the WMO (2008),  $\tau$

depends on the airflow over the sensor, which required some experiments to assess how wind affects  $\tau$ . In theory, wind might help to reduce response time, since it helps to refresh the sensor with ambient air temperature and more efficiently dissipate heat. A separate set of experiments (not shown here) simulated the effect of low wind speeds (between  $0.5$  and  $4 \text{ ms}^{-1}$  generated by an electric fan) on  $\tau$ . The  $\tau$  for the experiments with wind was consistently higher than a wind-less environment. This could be caused by condensation of water vapor on the smartphone when moving into a warmer environment: this moisture requires energy to be evaporated again (a latent heat flux). Since this energy needs to be provided by the smartphone, this prolongs the time before temperature equilibrium is reached. All the ten experiments performed under these conditions exhibit the same behavior.

### 3.1.2 Sensor Accuracy

The air temperature measurements from the smartphone  $T_s$  are compared and validated against the air temperature readings from the Veenkampen meteorological station ( $T_{ref}$ ). One set of experiments was performed under relatively cold autumn and winter conditions (afternoon temperatures around  $10^\circ\text{C}$ ; **Figure 3**) and another during a warm spell in summer (afternoon  $T$  above  $25^\circ\text{C}$ ; **Figure 4**). The smartphone was placed inside the same Stevenson screen for 5 days, at the same height (1.5 m) as the calibrated thermometer, as described in **section 2**. The results show a cold bias for the smartphone both for the autumn and summer experiments (**Figures 3,4**, respectively). The mean error including day and night measurements amounts to  $-2.0^\circ\text{C}$ . The timeseries is very similar to the reference, with the smartphone exhibiting a cold bias, even during much hot conditions. Part of the summer experiment also included a duplicate measurement with

<sup>4</sup><https://www.sensirion.com/en/markets/sensor-solutions-for-smart-home-applications/>

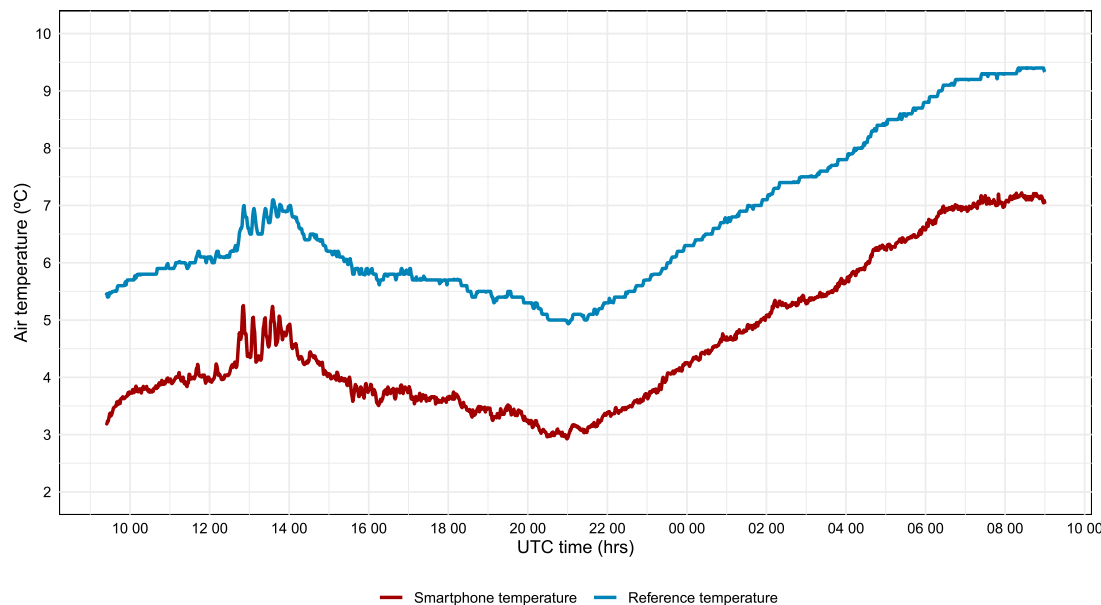


**FIGURE 3 |** Time series of observed air temperature from the smartphone and reference weather station Veenkampen. During this experiment the smartphone is located inside the Stevenson screen. The experiment was executed from January 27<sup>th</sup> 2018 10:00 UTC till January 28<sup>th</sup> 2018 10:00 UTC.

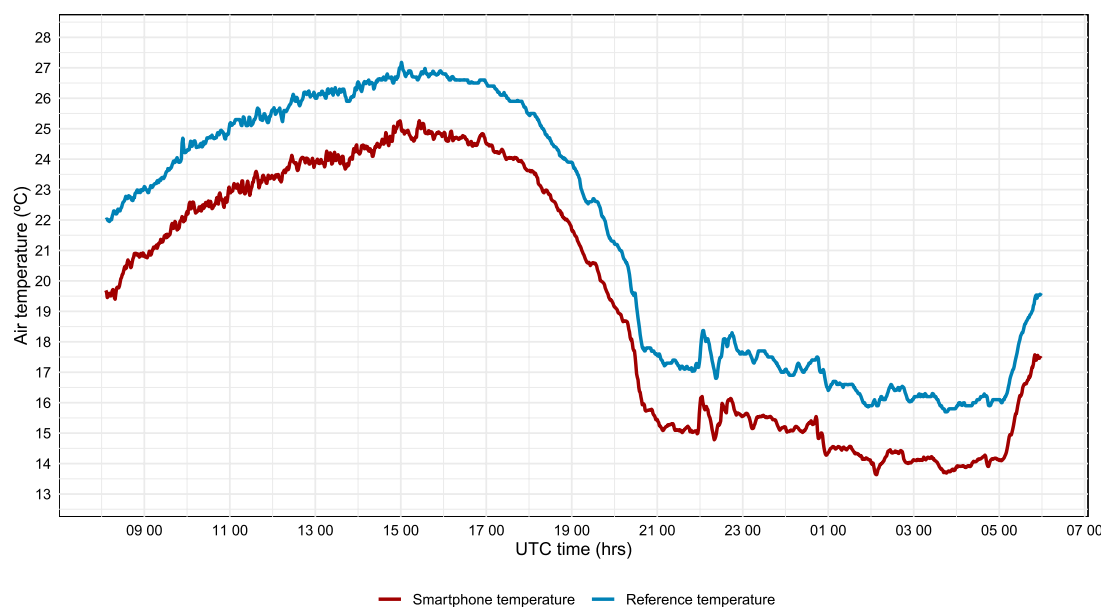


**FIGURE 4 |** Time series of observed air temperature from the smartphone and reference weather station Veenkampen during a follow-up experiment in June 2021. During this experiment the smartphone is located inside the Stevenson screen. The experiment was executed from June 3<sup>rd</sup> 2021 08:00 UTC till June 4<sup>th</sup> 2021 06:00 UTC.

another smartphone of the same model, measuring at the same location. Differences between these duplicate measurements were not statistically significant (MAE of 0.1°C and RMSE of 0.13°C; results not shown), which indicates that this bias is systematic and

not due to a single faulty sensor. Additionally, since the autumn and summer experiments were 3.5 years apart yet find a nearly identical bias, it suggests the sensors have not been subject to degradation due to aging. We find that the distribution of the

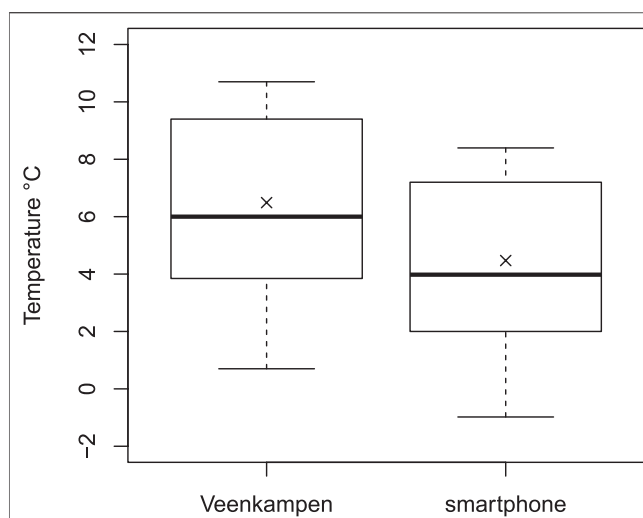


**FIGURE 5 |** Box-plot comparing 1.5 m height air temperature observations from the smartphone and Veenkampen meteorology station thermometer (for the autumn and winter experiments). Smartphone is placed in the same Stevenson screen. Each box ranges from 25<sup>th</sup> to 75<sup>th</sup> percentile (interquartile range IQR), median is denoted as the horizontal line inside the box, arithmetic mean is represented by the cross, whiskers have a maximum length of 1.5 \* IQR.

observed temperature between the smartphone and the temperature sensor at Veenkampen meteorological station is very similar (**Figure 5**).  $T_s$  and  $T_{ref}$  correlate very well: results show a strong positive linear relation with a Pearson correlation coefficient of 0.99 with a  $p$ -value  $< 0.05$ . The mean error was similar for the temperature range during the observations from inside the Stevenson screen, pointing at a good performance for sensitivity.

### 3.1.3 Temperature Readings Error Sources

Heat generated by the smartphone battery and electronics when it is under heavy CPU/GPU workload has proven to be a major source of error for temperature measurements, and it is a source that is not directly related to external weather conditions.  $T_s$  can easily give readings twice as warm as the actual air temperature: one experiment resulted in  $T_s$  reading 35°C when the actual room temperature was 15°C. For this particular experiment the smartphone was placed directly over a textile padding for 60 min, it was covered by a cotton cloth (simulating being inside a pocket), thus, hindering the heat exchange between the smartphone and the atmosphere. Such conditions would portray a common usage of the phone.

Even providing the best possible conditions for the smartphone to dissipate the heat by itself (smartphone placed over a platform with a negligible contact area),  $T_s$  was 20°C in contrast with the 15°C room temperature, with a temperature increase rate of 1°C per minute after the workload simulation started (results not shown). In **section 3.1.1** the mean response time was calculated for both positive and negative step changes (under lab conditions), but these values are not valid when  $T_s$  increases due to internal heat generation since the temperature

changes are not fast enough to be considered step changes. For comparison a pseudo response time is calculated. The pseudo response time for the smartphone to cool down after heavy CPU/GPU workload amounts to 27 min, which might be a relatively long period for many meteorological applications, and is nearly double the  $\tau$  previously found. This experiment was performed under conditions without wind, and thus with limited turbulent exchange of heat between the smartphone and the air, which explains the relatively long response time. In real-world applications the phone might be subject to air flows, which would make heat transfer much more efficient, as shown in **section 3.1.1**.

For the case when the smartphone battery is charging, the error proved difficult to characterize. During the charging,  $T_s$  decreases in sudden jumps. The most viable explanation for this behavior resides in the post-processing algorithm, which apparently tries to compensate for the increase in temperature caused by the battery being charged.

One of the main external sources of temperature measurement errors (for conventional thermometers) is the incoming solar radiation. Its effects become more prominent in cases where a sensor is directly exposed to solar radiation without proper ventilation. An effective ventilation system supplies a constant flow of ambient air to the sensor, thus preventing overheating issues. As shown in **section 3.1.2**, when the smartphone measures temperature inside a properly built Stevenson screen, measurement errors as consequence of global radiation (direct + diffuse solar radiation) are not relevant. However, during active outdoor use, the smartphone will likely be exposed to direct sunlight, hence it is necessary to quantify the relation between solar radiation and temperature error. This research took place mostly in winter; therefore, higher radiation values were artificially created using a heat lamp. **Figure 6** shows the smartphone mean temperature bias as a combined function of wind speed and global radiation. The values are obtained from the experiments performed outside the Stevenson screen. The higher the radiation levels are at low wind speed, the more the device overheats, and the lack of ventilation prevents the ambient air from outside to quickly reach the sensor, thereby, increasing  $T_s$ .

Note that when the smartphone is exposed to more than 600 Wm<sup>-2</sup> the wind speed appears to play a relatively larger role. Lack of ventilation appears to worsen temperature measurement errors at relatively high values of global radiation, whereas at low levels of radiation it is less dominant. During nighttime (global radiation  $\leq 0$  Wm<sup>-2</sup>) the smartphone showed readings with an average of 4.2°C lower than the reference value, this is a net difference of 2.1°C colder in comparison with the smartphone inside the temperature screen. This difference suggests that the smartphone outside the Stevenson screen emits net more long-wave radiation which is not corrected for. The glass of which a smartphone has been composed of has a surface emissivity typically between 0.92 and 0.94, which is substantially smaller than the emissivity of the atmosphere. This process of rapid cooling is similar to the relatively rapid cooling of a car's windshield on a clear calm night.

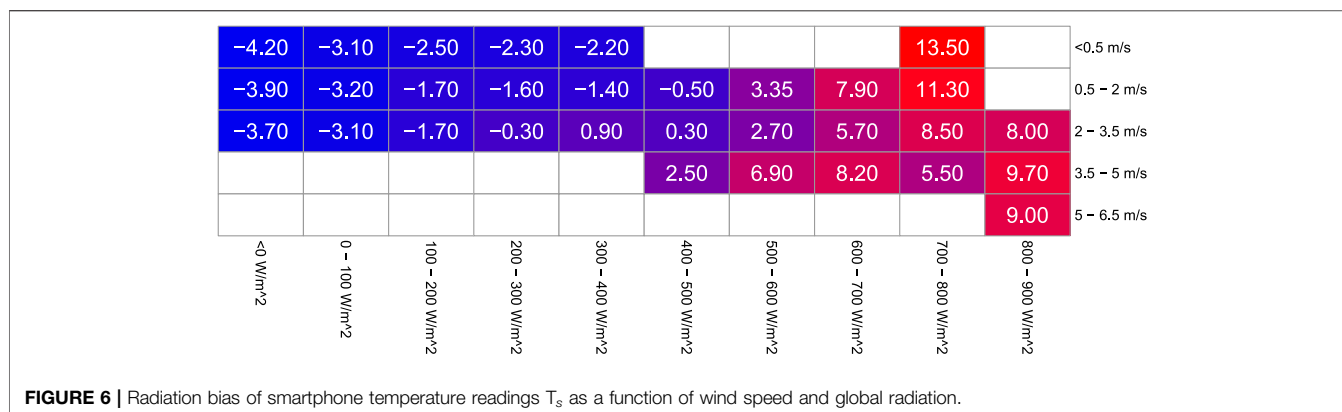


**FIGURE 6 |** Radiation bias of smartphone temperature readings  $T_s$  as a function of wind speed and global radiation.

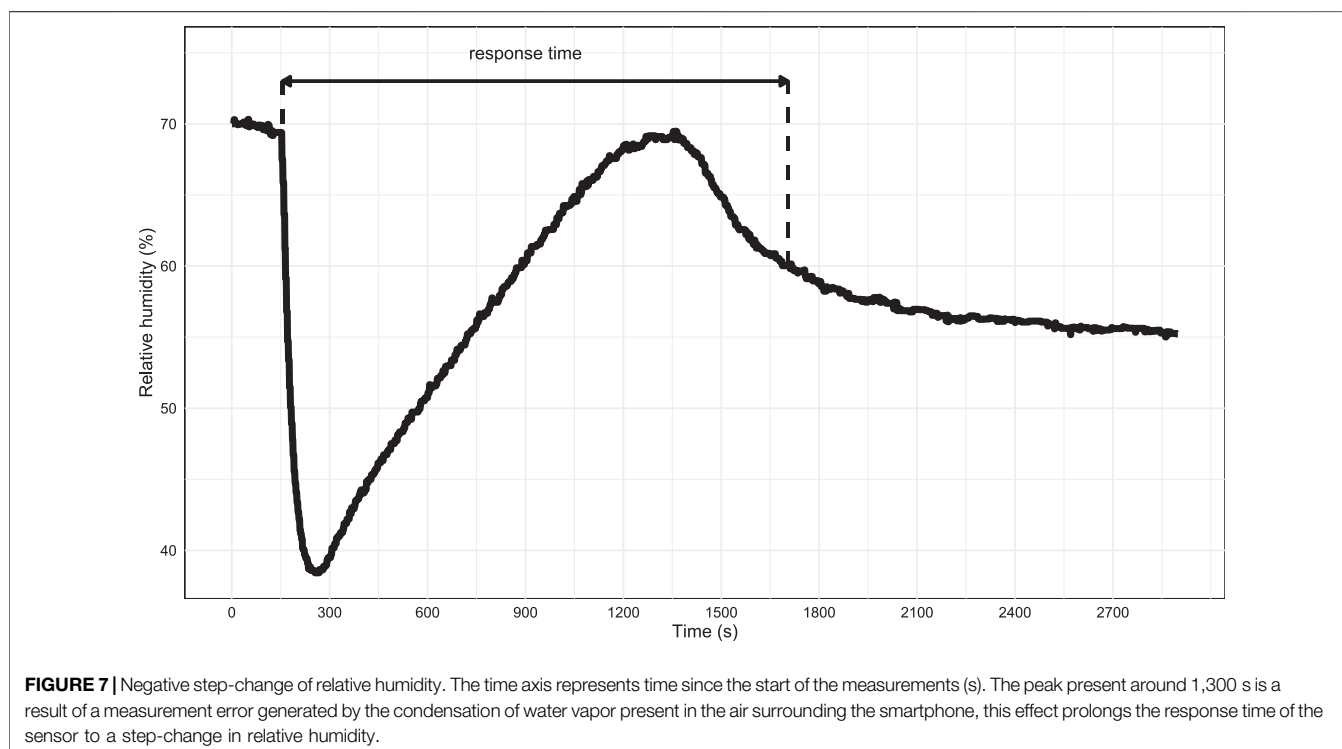


**FIGURE 7 |** Negative step-change of relative humidity. The time axis represents time since the start of the measurements (s). The peak present around 1,300 s is a result of a measurement error generated by the condensation of water vapor present in the air surrounding the smartphone, this effect prolongs the response time of the sensor to a step-change in relative humidity.

## 3.2 Relative Humidity Sensor

### 3.2.1 Response Time Analysis

For the capacitive relative humidity sensor found in the Samsung S4, Sensirion specifies that  $\tau = 8\text{ s}^5$ , though this value corresponds to a stand-alone sensor at 25°C and an airflow of 1 ms<sup>-1</sup>. Twelve experiments were performed: the first ten experiments to calculate  $\tau$  for a positive step-change involved an actual change of humidity in the air, while the last two, represent  $\tau$  where the humidity remains constant but temperature decreases. The experiments show a much slower response time compared to manufacturer specification. When a change in humidity occurs,

the average  $\tau$  amounts to 13.4 min and when a change in relative humidity is only driven by a temperature change,  $\tau$  is faster, with 4.7 min (details in **Supplementary Table S3** and **Supplementary Table S4**). In the case of the negative step-change experiments (**Figure 7**), the results show an interesting phenomenon. When the smartphone is exposed from a cold and humid environment (inside the freezer) to a warmer and drier one (room temperature), the water vapor present in the surrounding air condenses outside and inside the smartphone. The condensation generates an abrupt increase in relative humidity, producing measurement errors and delaying the real response time of the sensor (see peak in **Figure 7**). Note that the abrupt initial decrease in  $RH_s$  is an expected behavior: the hygrometer is reacting to the sudden change in temperature. In two cases,  $\tau$  of  $RH_s$  surpassed

<sup>5</sup>[https://www.mouser.com/datasheet/2/682/Sensirion\\_Humidity\\_Sensors\\_SHTC1\\_Datasheet-1511754.pdf](https://www.mouser.com/datasheet/2/682/Sensirion_Humidity_Sensors_SHTC1_Datasheet-1511754.pdf)

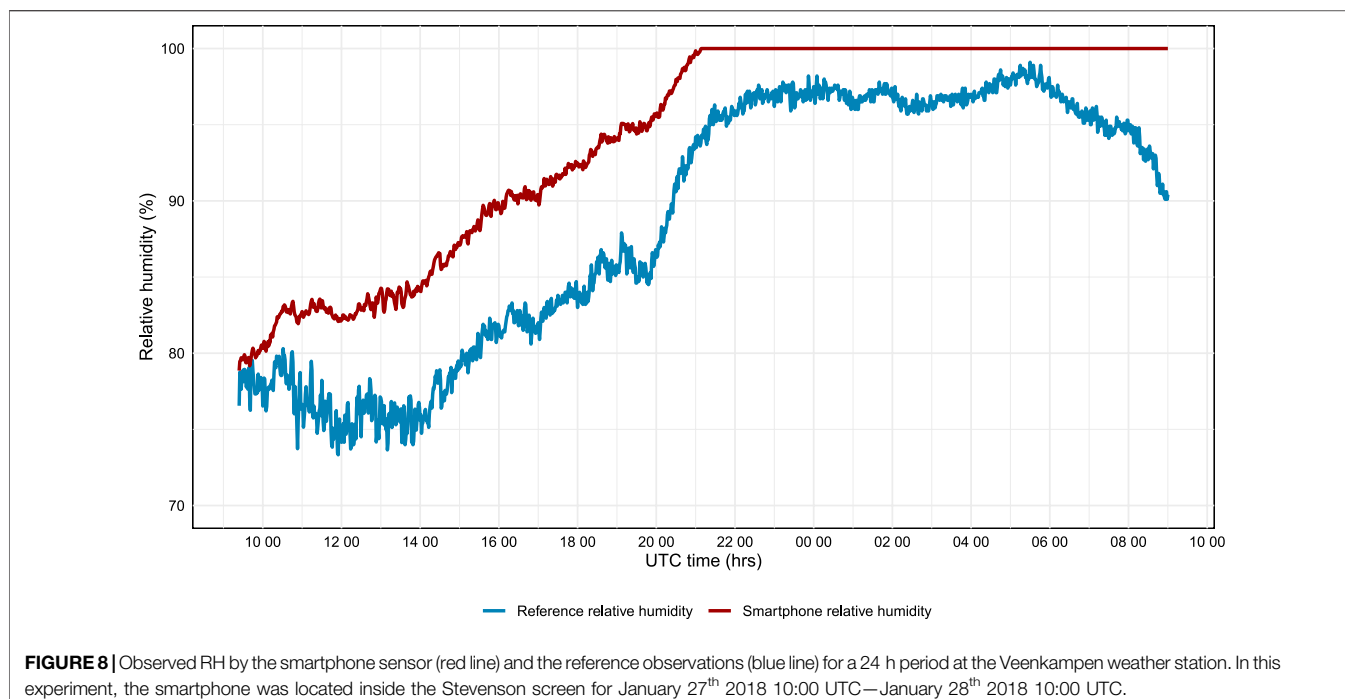


**FIGURE 8 |** Observed RH by the smartphone sensor (red line) and the reference observations (blue line) for a 24 h period at the Veenkampen weather station. In this experiment, the smartphone was located inside the Stevenson screen for January 27<sup>th</sup> 2018 10:00 UTC—January 28<sup>th</sup> 2018 10:00 UTC.

30 min. However, without condensation occurring in the experiment, the average response time amounts to 2.04 min (**Supplementary Table 3**). WMO (2008) states that ideal  $\tau$  for relative humidity sensors is between 1 and 50 s.

### 3.2.2 Measurement Accuracy

Relative humidity measurements from the smartphone ( $RH_s$ ) are compared against reference observations from the Veenkampen meteorological station ( $RH_{ref}$ ). The results show a mean positive bias of 7.42% RH when taking all the measurements into account. However, as shown in **Figure 8**, generally when  $RH_{ref}$  is greater than 90%,  $RH_s$  reaches 100% RH, suggesting an oversaturation of the sensor. For this reason, a more accurate bias is calculated where  $RH_s$  values of 100% are excluded, resulting in a mean bias of +8.16% RH. The Pearson correlation coefficient between  $RH_s$  and  $RH_{ref}$  is 0.69, suggesting a moderate positive linear relation ( $p < 0.05$ ). Possible causes of the errors are discussed in the following section.

### 3.2.3 Relative Humidity Error Sources

To assess relative humidity measurements and quantify biases is a challenging task for many reasons. First, the sensor in the smartphone is a relatively inexpensive electrical capacitive hygrometer, which is not individually calibrated (the phones are mass-produced). Thus, the calibration process is not perfect, and the sensor might have significant systematic biases. For the case of the SHTC1 smartphone sensor, the accuracy is within  $\pm 4.5\%$  RH (where the % unit is in RH units and not a percentage of the measurement) for RH between 20 and 80% at 25°C, and the accuracy might decrease to  $\pm 7.5\%$  with  $RH < 20\%$  and  $RH > 80\%$ . Since the accuracy of relative humidity also depends on air temperature, typical RH

accuracy values are evaluated at different temperatures and RH levels (note that the maximal tolerance accuracy values can still be  $\pm 3\%$  RH). Sensirion<sup>6</sup> explicitly states that the long-time exposure to conditions >80% may offset the RH signal, causing the sensor to recalibrate itself. Given the long duration of the experiments at fairly high humidity values, it is possible that this happened during the oversaturation periods, which offset the sensor. Given the errors present in the air temperature readings (**section 3.1.3**), the smartphone RH readings will have an additional level of uncertainty caused by the smartphone temperature sensor.

### 3.3 Light Sensor

The light sensor in the smartphone is designed to measure light intensity (lux), rather than radiation. Nevertheless, obtained lux values correlate well with the pyranometer recording global radiation at the weather field (Pearson correlation values above 0.9 for all the field experiments).

The time response analysis gave a near-instant response to the change in light level: as fast or faster than the measurement frequency (10 ms). This fast response can be useful in certain weather conditions, e.g. rapid change in cloud cover. This might occur in the reported observations (**Figure 9**) just after 900 s, though cloud-cover observations are not available at the weather station. In addition, the fast response is also useful for traverse observations in streets in order to accurately trace sunlit shaded locations in street canyons.

<sup>6</sup>[https://www.mouser.com/datasheet/2/682/Sensirion\\_Humidity\\_Sensors\\_SHTC1\\_Datasheet-1511754.pdf](https://www.mouser.com/datasheet/2/682/Sensirion_Humidity_Sensors_SHTC1_Datasheet-1511754.pdf)

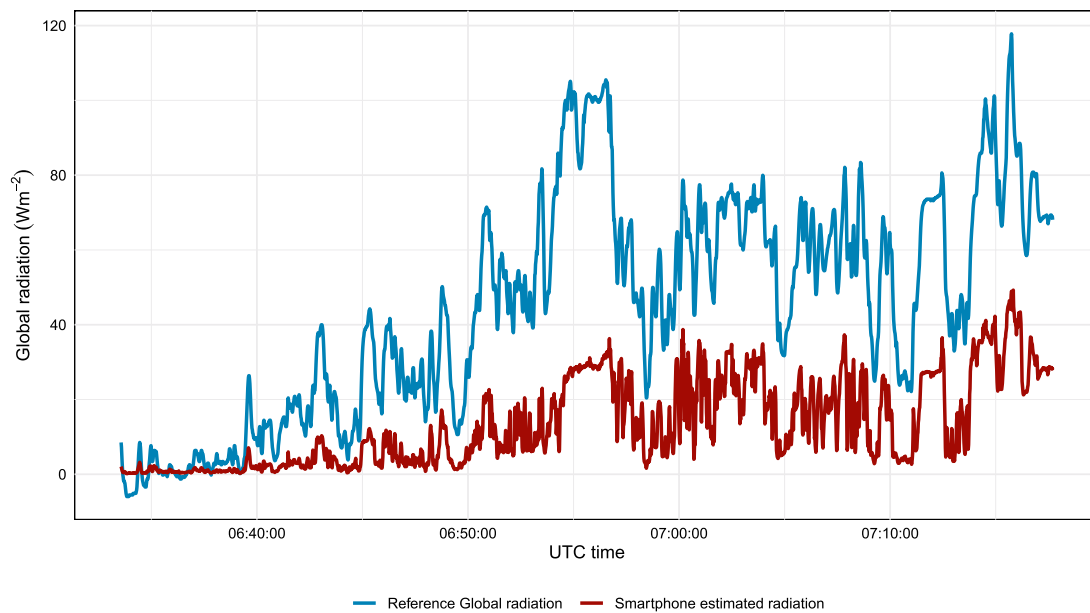


**FIGURE 9** | Observed light sensor signal from Samsung S4 (red line) and observed global radiation at the surface at the Veenkampen reference station (blue line) for a period of nearly three quarters of an hour. Measurements taken on October 19<sup>th</sup> 2017.

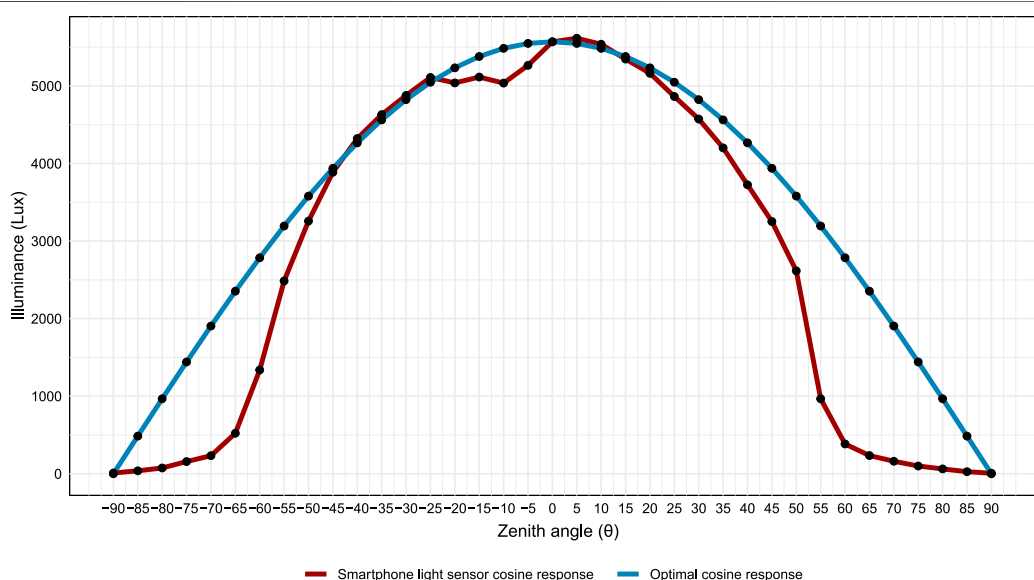
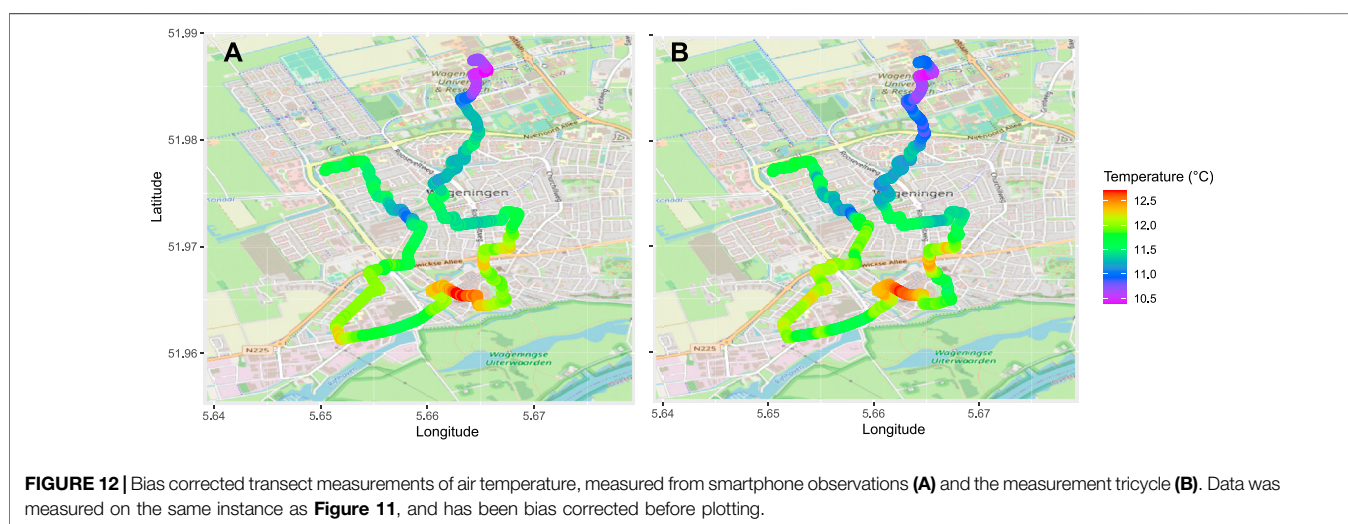
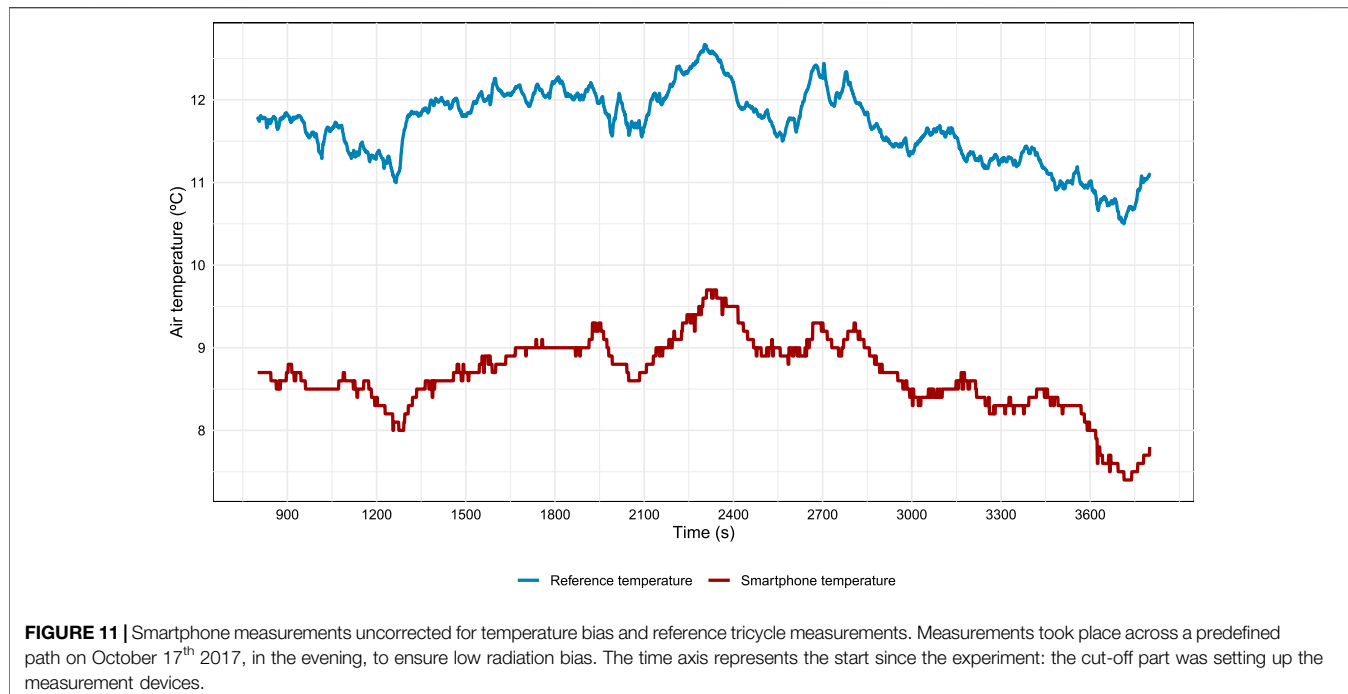


**FIGURE 10** | Observed cosine response of the light sensor in the smartphone Samsung S4 as function of zenith angle (red line) and ideal cosine response (blue line).

**Figure 10** shows the sensor cosine response to the incident light from angles  $-90^\circ$  to  $90^\circ$ . The experiment to calculate the cosine response of the light sensor was replicated more than 10 times, with similar results. For comparison, a second class pyranometer (like the Hukseflux LP02 installed on the tricycle) has a mean  $\pm 2\%$  deviation from the optimal cosine response for all zenith angles from  $-90$  to  $90^\circ$ , while the

smartphone light sensor mean deviation is  $-33.87\%$ . Only between  $-45$  and  $45^\circ$  the smartphone light sensor performs within the accepted range of  $\pm 5\%$  deviation of the ideal cosine response of standard pyranometers. This has consequences for use of actual smartphone data, since those will likely not be angled towards the Sun, which will reduce their accuracy at estimating direct incoming radiation.



### 3.4 Spatial Analysis

In this section air temperature from the smartphone is compared against the instrumentation on the tricycle. One-hour data of temperature, relative humidity, wind speed and global radiation retrieved by instrumentation installed on the tricycle was compared against the one retrieved by Veenkampen meteorological station at the same day as the transect measurements from **Figures 11,12** (calibration results not shown). The comparison was made to double-check the data quality retrieved by the bicycle instrumentation and thus, being able to further use it for assessment and comparison against the smartphone data. Data from the

tricycle shows a mean temperature bias of  $0.02^{\circ}\text{C}$  with respect to the Veenkampen weather station. However, for cases when global radiation is greater than  $300 \text{ W m}^{-2}$ , temperature shows a stronger positive bias of  $0.43^{\circ}\text{C}$ . All measurements were recorded with  $1.4 \text{ ms}^{-1}$  average wind speed at  $2 \text{ m}$  height. For relative humidity, the results (not shown) display a mean error of  $-3.4 \% \text{RH}$ . For wind speed, no fully direct comparison is possible since the wind at the Veenkampen weather station and on the tricycle are measured at different heights,  $1.5$  and  $2 \text{ m}$  respectively. Nonetheless, the observations are between the expected values for a  $0.5 \text{ m}$  height difference between them, with the

sonic anemometer averaging a mean error of  $-0.3 \text{ ms}^{-1}$ . Finally, when comparing global radiation, the pyranometer on the tricycle showed a mean error of  $-3.8 \text{ Wm}^{-2}$ , which meets the manufacturer specifications. This confirms that the tricycle instrumentation serves as a proper reference to compare the smartphone data against over a transect.

For transect measurements made during the day (results not shown), the downwelling solar radiation impacts the device directly, causing large occasional errors when the phone is exposed to the Sun. Spikes in  $T_s$  are preceded by higher levels of downwelling radiation, resulting in an overall correlation coefficient of 0.69. On the other hand, when the experiment is executed during the evening (**Figure 11**, the air temperature readings from smartphone and the ones from the tricycle instrumentation correlate better with one another, with a total correlation coefficient of 0.86, though the absolute difference is substantial still (3 K).

In scenarios with low levels of solar radiation, the bias correction to the smartphone temperature readings is a straightforward process, using linear regression analysis. However, the preconditions are the following:

1. Smartphone is not close to an external heat source.
2. The phone is not being charged.
3. The phone is not under heavy CPU/GPU workload (app usage).

The time series in **Figure 11** has also been detrended, assuming an overall linear change in temperature between start and finish, to identify solely spatial differences in air temperature. When this data is plotted across the map (**Figure 12**), it is possible to see similar temperature patterns with both instruments (smartphone and calibrated thermometer on tricycle). This shows that the smartphone, even with its delayed reaction time, is capable of making meteorological measurements that vary on the urban scale. The various open and sunlit areas around the center of Wageningen that receive more solar radiation are well-represented by the smartphone data, as are some of the more shaded cooler locations. While a detrending and correction procedure are necessary, this does show that smartphone temperature data has the potential to represent even small-scale variability in time and space, even though the fairly large  $\tau$  values for  $T_s$  would have initially suggested otherwise (**section 3.1.1**).

## 4 DISCUSSION

This section addresses the significance of this research within the context of urban meteorology, and approaches the opportunities crowdsourcing from smartphones may offer for urban meteorology.

The results of this exploratory research topic show the capabilities of a smartphone (illustrated by use of a Samsung S4) as a meteorological data acquisition device, although smartphones have not been designed nor manufactured to be accurate at measuring meteorological variables. Nonetheless,

many smartphone types able to sense air temperature, light intensity and some devices even measure ambient humidity. Even though a single smartphone cannot record accurate measurements under all environmental conditions, the true potential is the large amount of data already available, together with the wide spatial and temporal distribution of the measurements. The two keys to fully take advantage of the amount of data already available is: firstly, to understand under which scenarios/circumstances the measurements are useful, and secondly, to identify, develop and test procedures to improve the data quality as in Meier et al. (2017), and Droste et al. (2020).

We find the outdoor smartphone temperature and relative humidity readings relate very well during periods of relatively small levels of downwelling solar radiation. This might be particularly useful to detect the UHI, which normally peaks several hours after sunset. Still, the device usage has to meet the right conditions to be useful and reliable for meteorological data acquisition. For instance, the device battery should not be charging, the smartphone CPU is not heavily used, and the device should not be influenced by the human body temperature. With information from about the battery status, light and/or proximity sensor, the right conditions can be selected for our analysis. Computing power increases rapidly and it might already be enough to evaluate big datasets and to identify reliable data in them. Since the thermometer and hygrometer sensor are encapsulated inside the smartphone, the response times exceed the WMO recommendations. WMO requires 20 s while our analysis finds a response time of around 120 s (though the RH sensor can oversaturate and take >20 minutes to get to equilibrium). In addition we would like to remark that we tested only the responses of a single smartphone. Of course, repeated experiments with multiple phones of the same brand and type would have resulted in more robust statistics, though the general source of errors and time responses will likely be the same.

Moreover, it is illustrative to compare the estimated time constants for our experiment with the earlier estimates as in Droste et al. (2017). They estimated the cooling rate of a smartphone with power  $P$  which is surrounded with clothing of heat conductivity  $\kappa$  and heat capacity  $mc$ . In their approach the typical time scale at which the temperature responds to a temperature change is estimated by  $\kappa/(mc)$ , and amounts to  $0.8 \text{ W/m/K}/(0.13 \text{ kg} * 600 \text{ J/kg/K}) = 98 \text{ s}$ . This value is slightly smaller, though still relatively close to our value of 170 s as reported in **Supplementary Table 1**, despite their estimate is an *a priori* estimate based on material properties. For comparison we report that Cao et al. (2020) found a time constant of 9.7 s for a basic temperature sensor built on IoT technology. Their study calculated this time constant during their transect measurements: we see in our **Figures 11,12** that the time constant over the urban transect appears lower than in the lab, and more similar to Cao et al. (2020)'s findings.

Considering that our research found a typical temperature bias of about 2 K, Niforatos et al. (2017) studied the potential of participatory sensing for weather estimation, by developing

the crowdsourcing weather app Atmos that periodically samples smartphones' weather-related sensors. Their approach also allows users to enter their own estimates of both current weather conditions. Using 32 months of observations they found a temperature bias of  $2.7^{\circ}\text{C}$  based on the pure sensor data, which is close to our findings. Their bias dropped to  $1.9^{\circ}\text{C}$  when manual user input was allowed as well. Trivedi et al. (2021) show that this bias could be reduced by using machine learning and multiple phone records (they report  $0.5^{\circ}\text{F}$ ).

Also, it is interesting to address the temperature differences in smartphones in case different sensors are employed. Gavin and Sidhu (2015) report on a lab study that compares two temperature sensor types to measure ambient temperatures with a smartphone. Both sensors were placed in a sheltered location and were left to take a series of readings at regular intervals. No significant difference between the readings taken from a smartphone temperature sensor and a established sensor. Their histogram shows that differences between the two sensors do not exceed  $0.04\text{ K}$ , which is accurate for our application.

We have been positively surprised about the performance of the light sensor, which illustrates its enormous potential for smartphones to be used as "economic pyranometers". Initially, more work is needed to be able to distinguish the light source detected by the light sensor (detect if solar light or artificial light). However, for specific, well defined experiments (during fast changes in cloud cover, or for fog observation/detection) the light sensor from smartphones is a good choice for research.

However, despite all the experiments performed and the data analyzed, the results represent the behavior of a single smartphone model. The duplicate measurement confirmed that other devices of the same brand and model behave in similar manner, but the use of other smartphones is recommended to check and increase the confidence of the findings presented in this research. The Samsung Galaxy S4 is used in this research, since there are already available datasets containing data from this smartphone, however it may be necessary to also work on more updated models. An earlier study by Breda et al. (2019) estimates indoor air temperatures by smartphones and found an error of  $1.4\%$ . They also estimate the time responses for the smartphone in modes of screen, CPU, network and charging activities. Most interesting for our application is their observed response time of about  $1,000\text{ s}$  in a phase when the smartphone is cooling. Although this is slightly higher than in our case, and this may depend on the particular phone type (Google Pixel phone in their case), the order of magnitude is rather similar.

It is important to mention that despite this study provides a verification of the accuracy of smartphone records for UHI studies with respect to a professional weather station, in many of our applications in urban meteorological research, the human behavior remains a substantial player in the records that are obtained. Droste et al. (2017) and Overeem et al. (2013) utilize massive amounts of smartphone records, filter a substantial amount based on the proximity sensor and the charging status of the battery, though full control of the smartphone

environment (in a hand, in a pocket, in a hand bag) remains unknown.

A particular problem with the use of smartphones is the gradual reduction of sensors in popular smartphones. In order to e.g., the recently released Samsung A50 does not have a temperature, humidity, or pressure sensor. On the other hand, the Covid-19 pandemic initiated the introduction of a temperature sensor again in the Honor Play4. Additionally, smartphones will maintain to be employed by battery temperature sensors for monitoring the health of the phone. To overcome the limited presence of air temperature sensors, Chau (2019) developed an approach in which air temperature data are estimated based on the recorded smartphone battery sensor, either from in pocket or out pocket readings. However their method was based on lab tests with a limited number of smartphone copies and models, and therefore an experiment to prove the wider and outdoor applicability needs to be developed.

## 5 CONCLUSION

Crowdsourcing, i.e., the harvesting of a large number of sensor data *via* internet has increased interest as data source for weather and climate studies, in particular in cities where traditional observation techniques are difficult to implement. Earlier studies showed that massive amounts of pressure, temperature, humidity and light observations by smartphones can offer successfully information of local weather conditions, provided a proper data quality assessment and selection is performed. To enhance our understanding of the value of these smartphones records, here we evaluate the quality of weather observations by smartphones (using a Samsung S4 in this case) with respect to automated weather station observations and traverse observation on a cargo bike. Under lab conditions, we find the smartphone observations have a time constant of about  $180\text{ s}$  for temperature and between  $120$  and  $650\text{ s}$  for relative humidity (depending on the direction of change and provided no condensation occurs). We show that smartphone temperature observations are subject to a bias that depends on wind speed and solar radiation, but this bias can be corrected for. After applying this bias correction during traverse observations, smartphone temperature observations can successfully replicate temperature observations by a professional weather station. The smartphone light sensor appears to have a cosine response with substantial data loss for angles  $>45^{\circ}$ , though after a scaling correction the light sensor shows high potential for atmospheric research due to its immediate response.

## DATA AVAILABILITY STATEMENT

The raw data supporting the conclusion of this article will be made available by the authors, without undue reservation.

## AUTHOR CONTRIBUTIONS

AC contributed to the research design, execution, analysis, and manuscript writing. BGH contributed with research design and execution. AD, G-JS, and BGH supervised the research, and contributed to manuscript writing, and editing.

## FUNDING

G-JS and AD acknowledge funding from NWO VIDI project 864.14.007.

## REFERENCES

- Abdelhamid, S., Hassanein, H. S., and Takahara, G. (2014). "Vehicle as a mobile Sensor," in The 9th International Conference on Future Networks and Communications (FNC'14)/The 11th International Conference on Mobile Systems and Pervasive Computing (MobiSPC'14)/Affiliated Workshops, Niagara Falls, ON, August 17–20, 2014, 286–295. doi:10.1016/j.procs.2014.07.025
- Allegri, J., Dorer, V., and Carmeliet, J. (2012). Influence of the Urban Microclimate in Street Canyons on the Energy Demand for Space Cooling and Heating of Buildings. *Energy Build.* 55, 823–832. doi:10.1016/j.enbuild.2012.10.013
- Arnfield, A. J. (2003). Two Decades of Urban Climate Research: a Review of Turbulence, Exchanges of Energy and Water, and the Urban Heat Island. *Int. J. Climatol.* 23, 1–26. doi:10.1002/joc.859
- Bárdossy, A., Seidel, J., and El Hachem, A. (2020). The Use of Personal Weather Station Observation for Improving Precipitation Estimation and Interpolation. *Hydrol. Earth Syst. Sci. Discuss.* 2020, 1–23. doi:10.5194/hess-2020-42
- Baccini, M., Biggeri, A., Accetta, G., Kosatsky, T., Katsouyanni, K., Analitis, A., et al. (2008). Heat Effects on Mortality in 15 European Cities. *Int. J. Biometeorol.* 19, 711–719. doi:10.1097/EDE.0b013e318176bfcd
- Breda, J., Trivedi, A., Chulabhaya Wijesundara, P. B., Irwin, D., Shenoy, P., and Taneja, J. (2019). "Hot or Not: Leveraging mobile Devices for Ubiquitous Temperature Sensing," in Proceedings of the 6th ACM International Conference on Systems for Energy-Efficient Buildings, Cities, and Transportation (BuildSys 2019), New York, November 13–14, 2019 (New York, NY: Association for Computing Machinery), 41–50.
- Burt, S., and Podesta, M. (2020). Response Times of Meteorological Air Temperature Sensors. *Q. J. R. Meteorol. Soc.* 146, 2789–2800. doi:10.1002/qj.3817
- Cao, C., Yang, Y., Lu, Y., Schultze, N., Gu, P., Zhou, Q., et al. (2020). Performance Evaluation of a Smart Mobile Air Temperature and Humidity Sensor for Characterizing Intracity Thermal Environment. *J. Atmos. Oceanic Technol.* 37, 1891–1905. doi:10.1175/jtech-d-20-0012.1
- Chapman, L., Bell, C., and Bell, S. (2017). Can the Crowdsourcing Data Paradigm Take Atmospheric Science to a New Level? a Case Study of the Urban Heat Island of London Quantified Using Netatmo Weather Stations. *Int. J. Climatol.* 37, 3597–3605. doi:10.1002/joc.4940
- Chau, N. H. (2019). Estimation of Air Temperature Using Smartphones in Different Contexts. *J. Inf. Telecommun.* 3, 494–507. doi:10.1080/24751839.2019.1634869
- Cheval, S., Micu, D., Dumitrescu, A., Irimescu, A., Frighenciu, M., Ioja, C., et al. (2020). Meteorological and Ancillary Data Resources for Climate Research in Urban Areas. *Climate* 8, 37. doi:10.3390/cli8030037
- Vos, L. W., Leijnse, H., Overeem, A., and Uijlenhoet, R. (2019). Quality Control for Crowdsourced Personal Weather Stations to Enable Operational Rainfall Monitoring. *Geophys. Res. Lett.* 46, 8820–8829. doi:10.1029/2019GL083731
- de Vos, L. W., Droste, A. M., Zander, M. J., Overeem, A., Leijnse, H., Heusinkveld, B. G., et al. (2020). Hydrometeorological Monitoring Using Opportunistic Sensing Networks in the Amsterdam Metropolitan Area. *Bull. Am. Meteorol. Soc.* 101, E167–E185. doi:10.1175/BAMS-D-19-0091.1
- Di Napoli, C., Barnard, C., Prudhomme, C., Cloke, H. L., and Pappenberger, F. (2020). ERA5-HEAT: A Global Gridded Historical Dataset of Human thermal comfort Indices from Climate Reanalysis. *Geosci. Data J.* 8, 2–10. doi:10.1002/gdj3.102
- Droste, A. M., Pape, J. J., Overeem, A., Leijnse, H., Steeneveld, G. J., Van Delden, A. J., et al. (2017). Crowdsourcing Urban Air Temperatures through Smartphone Battery Temperatures in São Paulo, Brazil. *J. Atmos. Oceanic Technol.* 34, 1853–1866. doi:10.1175/JTECH-D-16-0150.1
- Droste, A. M., Heusinkveld, B. G., Fenner, D., and Steeneveld, G. J. (2020). Assessing the Potential and Application of Crowdsourced Urban Wind Data. *Q. J. R. Meteorol. Soc.* 146, 2671–2688. doi:10.1002/qj.38110.1002/qj.3811
- Fazeli, R., Ruth, M., and Davidsdottir, B. (2016). Temperature Response Functions for Residential Energy Demand - A Review of Models. *Urban Clim.* 15, 45–59. doi:10.1016/j.uclim.2016.01.001
- Gasparrini, A., Guo, Y., Hashizume, M., Lavigne, E., Zanobetti, A., Schwartz, J., et al. (2015). Mortality Risk Attributable to High and Low Ambient Temperature: a Multicountry Observational Study. *Lancet* 386, 369–375. doi:10.1016/s0140-6736(14)62114-0
- Gavin, S., and Sidhu, B. (2015). The Effectiveness of Smartphone Temperature Sensors for Ambient Temperature Monitoring. *BCIT Environ. Publ. Health J.* doi:10.47339/ephj.2015.121
- Hage, K. D. (1975). Urban-Rural Humidity Differences. *J. Appl. Meteorol.* 14, 1277–1283. doi:10.1175/1520-0450(1975)014<1277:urhd>2.0.co;2
- Hamdi, R., Kusaka, H., Doan, Q.-V., Cai, P., He, H., Luo, G., et al. (2020). The State-Of-The-Art of Urban Climate Change Modeling and Observations. *Earth Syst. Environ.* 4, 631–646. doi:10.1007/s41748-020-00193-3
- He, L., Lee, Y., and Shin, K. G. (2020). Mobile Device Batteries as Thermometers. *Proc. ACM Interact. Mob. Wearable Ubiquitous Technol.* 4, 1–21. doi:10.1145/3381015
- Heusinkveld, B., van Hove, L., Jacobs, C., Steeneveld, G., Elbers, J., Moors, E., et al. (2010). "Use of a mobile Platform for Assessing Urban Heat Stress in Rotterdam," in Proceedings of the 7th Conference on Biometeorology, Berichte des Meteorologischen Instituts der Albert-Ludwigs-Universität Freiburg, Freiburg, April 12–14, 2010 Freiburg: Albert-Ludwigs-Universität Freiburg, 433–438.
- Heusinkveld, B. G., Steeneveld, G. J., van Hove, L. W. A., Jacobs, C. M. J., and Holtslag, A. M. (2014). Spatial Variability of the Rotterdam Urban Heat Island as Influenced by Urban Land Use. *J. Geophys. Res. Atmos.* 119, 677–692. doi:10.1002/2012JD019399
- Höppe, P. (2002). Different Aspects of Assessing Indoor and Outdoor thermal comfort. *Energy Build.* 34, 661–665. Special Issue on Thermal Comfort Standards. doi:10.1016/s0378-7788(02)00017-8
- Howard, L. (1833). *The Climate of London*. London: Harvey and Darton, 221.
- IPCC (2014). *Impacts, Adaptation, and Vulnerability. Summaries, Frequently Asked Questions, and Cross-Chapter Boxes* (NA: IPCC).
- Keirstead, J., and Sivakumar, A. (2012). Using Activity-Based Modeling to Simulate Urban Resource Demands at High Spatial and Temporal Resolutions. *J. Ind. Ecol.* 16, 889–900. doi:10.1111/j.1530-9290.2012.00486.x
- Klemm, W., Lenzholzer, S., and van den Brink, A. (2017). Developing green Infrastructure Design Guidelines for Urban Climate Adaptation. *J. Landscape Architect.* 12, 60–71. doi:10.1080/18626033.2017.1425320
- Koopmans, S., Heusinkveld, B. G., and Steeneveld, G. J. (2020). A Standardized Physical Equivalent Temperature Urban Heat Map at 1-m Spatial Resolution to Facilitate Climate Stress Tests in the Netherlands. *Build. Environ.* 181, 106984. doi:10.1016/j.buildenv.2020.106984

## ACKNOWLEDGMENTS

We thank our colleagues Aristofanis Tsiringakis, Bert Holtslag, Iris Manola, Sytse Koopmans, and former MSc student Fitria Sari for feedback on our results.

## SUPPLEMENTARY MATERIAL

The Supplementary Material for this article can be found online at: <https://www.frontiersin.org/articles/10.3389/fenvs.2021.673937/full#supplementary-material>

- Kottek, M., Grieser, J., Beck, C., Rudolf, B., and Rubel, F. (2006). World Map of the Köppen-Geiger Climate Classification Updated. *Meteorol. Z.* 15, 259–263. doi:10.1127/0941-2948/2006/0130
- Kovats, S., and Bickler, G. (2012). Health protection and Heatwaves: The Need for Systematic Reviews. *Cochrane Database Syst. Rev.* 11, ED000044. doi:10.1002/14651858.ED000044
- Krennert, T., Pistotnik, G., Kaltenberger, R., and Csekits, C. (2018). Crowdsourcing of Weather Observations at National Meteorological and Hydrological Services in Europe. *Adv. Sci. Res.* 15, 71–76. doi:10.5194/asr-15-71-2018
- Laaidi, M., Laaidi, K., and Besancenot, J.-P. (2006). Temperature-related Mortality in France, a Comparison between Regions with Different Climates from the Perspective of Global Warming. *Int. J. Biometeorol.* 51, 145–153. doi:10.1007/s00484-006-0045-8
- Li, Y., Schubert, S., Kropp, J. P., and Rybski, D. (2020). On the Influence of Density and Morphology on the Urban Heat Island Intensity. *Nat. Commun.* 11, 2647. doi:10.1038/s41467-020-16461-9
- Li, R., Zhang, Q., Sun, J., Chen, Y., Ding, L., and Wang, T. (2021). Smartphone Pressure Data: Quality Control and Impact on Atmospheric Analysis. *Atmos. Meas. Tech.* 14, 785–801. doi:10.5194/amt-14-785-2021
- MacLeod, D. A., Cloke, H. L., Pappenberger, F., and Weisheimer, A. (2016). Improved Seasonal Prediction of the Hot Summer of 2003 over Europe through Better Representation of Uncertainty in the Land Surface. *Q.J.R. Meteorol. Soc.* 142, 79–90. doi:10.1002/qj.2631
- Madaus, L. E., and Mass, C. F. (2017). Evaluating Smartphone Pressure Observations for Mesoscale Analyses and Forecasts. *Weather Forecast.* 32, 511–531. doi:10.1175/WAF-D-16-0135.1
- Mahoney, W. P., and O’Sullivan, J. M. (2013). Realizing the Potential of Vehicle-Based Observations. *Bull. Am. Meteorol. Soc.* 94, 1007–1018. doi:10.1175/BAMS-D-12-00044.1
- Mandement, M., and Caumont, O. (2020). Contribution of Personal Weather Stations to the Observation of Deep-Convection Features Near the Ground. *Nat. Hazards Earth Syst. Sci.* 20, 299–322. doi:10.5194/nhess-20-299-2020
- Martínez, M., Andújar, J., and Enrique, J. (2009). A New and Inexpensive Pyranometer for the Visible Spectral Range. *Sensors* 9, 4615–4634. doi:10.3390/s90604615
- Masson, V., Lemonsu, A., Hidalgo, J., and Voogt, J. (2020). Urban Climates and Climate Change. *Annu. Rev. Environ. Resour.* 45, 411–444. doi:10.1146/annurev-environ-012320-083623
- Meier, F., Fenner, D., Grassmann, T., Otto, M., and Scherer, D. (2017). Crowdsourcing Air Temperature from Citizen Weather Stations for Urban Climate Research. *Urban Clim.* 19, 170–191. doi:10.1016/j.ulclim.2017.01.006
- Muller, C. L., Chapman, L., Johnston, S., Kidd, C., Illingworth, S., Foody, G., et al. (2015). Crowdsourcing for Climate and Atmospheric Sciences: Current Status and Future Potential. *Int. J. Climatol.* 35, 3185–3203. doi:10.1002/joc.4210
- Napoly, A., Grassmann, T., Meier, F., and Fenner, D. (2018). Development and Application of a Statistically-Based Quality Control for Crowdsourced Air Temperature Data. *Front. Earth Sci.* 6, 118. doi:10.3389/feart.2018.00118
- Nazarian, N., Liu, S., Kohler, M., Lee, J. K. W., Miller, C., and Chow, W. T. L. (2021). Project Coolbit: Can your Watch Predict Heat Stress and Thermal Comfort Sensation? *Environ. Res. Lett.* 16 (3), 034031. doi:10.1088/1748-9326/abd130
- Niforatos, E., Vourvopoulos, A., and Langheinrich, M. (2017). Understanding the Potential of Human-Machine Crowdsourcing for Weather Data. *Int. J. Human-Computer Stud.* 102, 54–68. Special Issue on Mobile and Situated Crowdsourcing. doi:10.1016/j.ijhcs.2016.10.002
- Nipen, T. N., Seierstad, I. A., Lussana, C., Kristiansen, J., and Hov, Ø. (2020). Adopting Citizen Observations in Operational Weather Prediction. *Bull. Am. Meteorol. Soc.* 101, E43–E57. doi:10.1175/BAMS-D-18-0237.1
- Oke, T. R., Mills, G., Christen, A., and Voogt, J. A. (2017). *Urban Climates*. Cambridge: Cambridge University Press. doi:10.1017/9781139016476
- Oke, T. (1982). The Energetic Basis of the Urban Heat Island. *Q. J. R. Meteorol. Soc.* 108, 1–24. doi:10.1002/qj.4971084550210.1256/smssqj.45501
- Overeem, A., Robinson, J. C. R., Leijnse, G. J., Steeneveld, G. J., Horn, B. K. P., Uijlenhoet, R., et al. (2013). Crowdsourcing Urban Air Temperatures from Smartphone Battery Temperatures. *Geophys. Res. Lett.* 40, 4081–4085. doi:10.1002/grl.5078610.1002/grl.50786
- Pijpers-van Esch, M. (2015). *Designing the Urban Microclimate*. Delft: Delft University of Technology. doi:10.7480/abe.2015.6
- Ronda, R. J., Steeneveld, G. J., Heusinkveld, B. G., Attema, J. J., and Holtslag, A. A. M. (2017). Urban Finescale Forecasting Reveals Weather Conditions with Unprecedented Detail. *Bull. Am. Meteorol. Soc.* 98, 2675–2688. doi:10.1175/BAMS-D-16-0297.1
- Rydin, Y., Bleahu, A., Davies, M., Dávila, J. D., Friel, S., De Grandis, G., et al. (2012). Shaping Cities for Health: Complexity and the Planning of Urban Environments in the 21st century. *Lancet* 379, 2079–2108. doi:10.1016/s0140-6736(12)60435-8
- Sailor, D. J. (2011). A Review of Methods for Estimating Anthropogenic Heat and Moisture Emissions in the Urban Environment. *Int. J. Climatol.* 31, 189–199. doi:10.1002/joc.2106
- Santamouris, M., and Kolokotsa, D. (2016). *Urban Climate Mitigation Techniques*. 1st Edn. London: Routledge.
- Shi, Y., Xiang, Y., and Zhang, Y. (2019). Urban Design Factors Influencing Surface Urban Heat Island in the High-Density City of Guangzhou Based on the Local Climate Zone. *Sensors* 19, 3459. doi:10.3390/s19163459
- Siems-Anderson, A., Lee, J. A., Brown, B., Wiener, G., and Linden, S. (2020). Impacts of Assimilating Observations from Connected Vehicles into a Numerical Weather Prediction Model. *Transportation Res. Interdiscip. Perspect.* 8, 100253. doi:10.1016/j.trip.2020.100253
- Steeneveld, G. J., Koopmans, S., Heusinkveld, B. G., van Hove, L. W. A., and Holtslag, A. A. M. (2011). Quantifying Urban Heat Island Effects and Human comfort for Cities of Variable Size and Urban Morphology in the Netherlands. *J. Geophys. Res.* 116, D20129. doi:10.1029/2011JD015988
- Svensson, M. K., and Eliasson, I. (2002). Diurnal Air Temperatures in Built-Up Areas in Relation to Urban Planning. *Landscape Urban Plann.* 61, 37–54. doi:10.1016/S0169-2046(02)00076-2
- Le Tertre, A., Lefranc, A. s., Eilstein, D., Declercq, C., Medina, S., Blanchard, M., et al. (2006). Impact of the 2003 Heatwave on All-Cause Mortality in 9 French Cities. *Epidemiology* 17, 75–79. doi:10.1097/01.ede.0000187650.36636.1f
- Trivedi, A., Bovornkeeratiroj, P., Breda, J., Shenoy, P., Taneja, J., and Irwin, D. (2021). Phone-based Ambient Temperature Sensing Using Opportunistic Crowdsensing and Machine Learning. *Sustainable Comput. Inform. Syst.* 29, 100479. doi:10.1016/j.suscom.2020.100479
- Uteuov, A., Kalyuzhnaya, A., and Boukhanovsky, A. (2019). “The Cities Weather Forecasting by Crowdsourced Atmospheric Data,” in 8th International Young Scientists Conference on Computational Science, YSC2019, 24–28 June 2019, Heraklion, Greece, Heraklion, June 24–28, 2019, 347–356. doi:10.1016/j.procs.2019.08.211
- WMO (2008). *Guide to Instruments and Methods of Observation*. Geneva: World Meteorological Organization.
- Zhu, Y., Zhang, S., Li, Y., Lu, H., Shi, K., and Niu, Z. (2020). Social Weather: A Review of Crowdsourcing-assisted Meteorological Knowledge Services through Social Cyberspace. *Geosci. Data J.* 7, 61–79. doi:10.1002/gdj3.85

**Conflict of Interest:** The authors declare that the research was conducted in the absence of any commercial or financial relationships that could be construed as a potential conflict of interest.

**Publisher’s Note:** All claims expressed in this article are solely those of the authors and do not necessarily represent those of their affiliated organizations, or those of the publisher, the editors and the reviewers. Any product that may be evaluated in this article, or claim that may be made by its manufacturer, is not guaranteed or endorsed by the publisher.

Copyright © 2021 Cabrera, Droste, Heusinkveld and Steeneveld. This is an open-access article distributed under the terms of the Creative Commons Attribution License (CC BY). The use, distribution or reproduction in other forums is permitted, provided the original author(s) and the copyright owner(s) are credited and that the original publication in this journal is cited, in accordance with accepted academic practice. No use, distribution or reproduction is permitted which does not comply with these terms.



# Combining High-Resolution Land Use Data With Crowdsourced Air Temperature to Investigate Intra-Urban Microclimate

Julia Potgieter<sup>1</sup>, Negin Nazarian<sup>1,2,3\*</sup>, Mathew J. Lipson<sup>4</sup>, Melissa A. Hart<sup>1</sup>, Giulia Ulpiani<sup>2,5</sup>, William Morrison<sup>6</sup> and Kit Benjamin<sup>6</sup>

<sup>1</sup>ARC Centre of Excellence for Climate Extremes, University of New South Wales, Sydney, NSW, Australia, <sup>2</sup>School of Built Environment, University of New South Wales, Sydney, NSW, Australia, <sup>3</sup>City Futures Research Centre, University of New South Wales, Sydney, NSW, Australia, <sup>4</sup>ARC Centre of Excellence for Climate System Science, University of New South Wales, Sydney, NSW, Australia, <sup>5</sup>Climate Change Research Centre, UNSW, Sydney, NSW, Australia, <sup>6</sup>Department of Meteorology, University of Reading, Reading, United Kingdom

## OPEN ACCESS

### Edited by:

Christos H. Halios,  
Public Health England,  
United Kingdom

### Reviewed by:

Saumitra Mukherjee,  
Jawaharlal Nehru University, India  
Costica Nitu,  
Politehnica University of Bucharest,  
Romania

### \*Correspondence:

Negin Nazarian  
n.nazarian@unsw.edu.au

### Specialty section:

This article was submitted to  
Environmental Informatics  
and Remote Sensing,  
a section of the journal  
*Frontiers in Environmental Science*

Received: 04 June 2021

Accepted: 24 August 2021

Published: 13 September 2021

### Citation:

Potgieter J, Nazarian N, Lipson MJ, Hart MA, Ulpiani G, Morrison W and Benjamin K (2021) Combining High-Resolution Land Use Data With Crowdsourced Air Temperature to Investigate Intra-Urban Microclimate. *Front. Environ. Sci.* 9:720323.  
doi: 10.3389/fenvs.2021.720323

The spatial variability of land cover in cities results in a heterogeneous urban microclimate, which is often not represented with regulatory meteorological sensor networks. Crowdsourced sensor networks have the potential to address this shortcoming with real-time and fine-grained temperature measurements across cities. We use crowdsourced data from over 500 citizen weather stations during summer in Sydney, Australia, combined with 100-m land use and Local Climate Zone (LCZ) maps to explore intra-urban variabilities in air temperature. Sydney presents unique drivers for spatio-temporal variability, with its climate influenced by the ocean, mountainous topography, and diverse urban land use. Here, we explore the interplay of geography with urban form and fabric on spatial variability in urban temperatures. The crowdsourced data consists of 2.3 million data points that were quality controlled and compared with reference data from five synoptic weather stations. Crowdsourced stations measured higher night-time temperatures, higher maximum temperatures on warm days, and cooler maximum temperatures on cool days compared to the reference stations. These differences are likely due to siting, with crowdsourced weather stations closer to anthropogenic heat emissions, urban materials with high thermal inertia, and in areas of reduced sky view factor. Distance from the coast was found to be the dominant factor impacting the spatial variability in urban temperatures, with diurnal temperature range greater for sensors located inland. Further differences in urban temperature could be explained by spatial variability in urban land-use and land-cover. Temperature varied both within and between LCZs across the city. Crowdsourced nocturnal temperatures were particularly sensitive to surrounding land cover, with lower temperatures in regions with higher vegetation cover, and higher temperatures in regions with more impervious surfaces. Crowdsourced weather stations provide highly relevant data for health monitoring and urban planning, however, there are several challenges to overcome to interpret this data including a lack of metadata and an uneven distribution of stations with a possible socio-economic bias. The sheer number of crowdsourced weather stations available can provide a high-resolution

understanding of the variability of urban heat that is not possible to obtain via traditional networks.

**Keywords:** crowdsourcing, air temperature, urban microclimate, coastal cities, land use data, Sydney (Australia), local climate zones

## INTRODUCTION

With more than half of the world's population living in urban areas, future development and planning rely on a complete understanding of the relationship between built environment characteristics and local climate. Air temperature, one of the key parameters of urban microclimate, is significantly influenced by the radiative and thermal properties of built materials, as well as anthropogenic heat released due to human activities (Masson et al., 2020). This temperature increase is further exacerbated by global climate change, leading to negative impacts on urban energy loads, local emissions, and citizen health and wellbeing (Masson et al., 2020).

The elevated temperature in cities exhibits a high spatial variability due to differences in urban form and fabric. Similarly, urban microclimate is temporally variable and is affected by meso- and synoptic-scale processes, as well as extreme and high-impact weather events. Such variabilities motivate fine-grained and continuous monitoring of microclimate across a range of urban characteristics, particularly to understand the role of urban design and planning. Furthermore, expansive and real-time monitoring of urban climate is critical during extreme weather events such as heatwaves, which have been increasing in intensity, frequency, and duration (Perkins et al., 2012). Thus, datasets with fine spatial and temporal resolutions are required to understand a city's local climate, assess the effectiveness of heat mitigation strategies, and most effective plans for future development. However, scientific meteorological stations used for climate monitoring are traditionally installed for the purpose of assessing synoptic-scale weather conditions and as such, the siting aims to minimise the impact of urbanisation. In response, urban monitoring stations have been established to better understand microclimate characteristics in different cities (Rotach et al., 2005; Schroeder et al., 2005; Poutiainen et al., 2006; Basara et al., 2011; Christen et al., 2013; Warren et al., 2016). These weather stations, although pivotal for gaining a fundamental understanding of urban climate, are expensive to set up and maintain by experts, leading to sparse coverage and insufficient detail to fully analyse the intra-urban variability in climate (Muller et al., 2013).

Over the last decade, the emergence of internet-enabled, wireless, and lay person-friendly solutions have enabled a range of environmental sensor networks that can address the need for real-time and fine-grained temperature measurements, covering a wide range of spatial and temporal distributions in cities (Pantelic et al., 2021). The "Internet of things" (IoT) has enabled crowdsourcing and ubiquitous sensing of urban data, where data is gathered from and by the public using citizen-science solutions as opposed to centrally-managed measurement campaigns. Several studies have used crowdsourced data collected

through consumer-grade weather monitors, or citizen weather stations, to assess the urban thermal climate of large cities such as London (Chapman et al., 2017; Benjamin 2019), Berlin (Fenner et al., 2017), Oslo (Venter et al., 2020) and Moscow (Varentsov et al., 2020). Crowdsourced data from over 50,000 citizen weather stations across Europe has also been compared to satellite data for measurement of urban heat island (UHI) indicating that satellite data overestimated UHI measurements by six times compared to crowdsourced data, which is more relevant for public health (Venter et al., 2021). These studies indicate that crowdsourced data achieves a higher spatial resolution than otherwise possible with regulatory monitoring networks, while highlighting the importance of data filtering and quality control to overcome accuracy concerns of low-cost sensing. Thorough quality control is required to remove any data that may be unrepresentative of local external conditions or caused by human interferences. Accordingly, several quality control procedures have been proposed, such as Meier et al. (2017) that removes outliers based on a comparison to reference data and Napoly et al. (2018) which removes readings based on the possible errors in data collection.

In addition to spatial microclimate data, clear metadata on urban characteristics is key to identifying the drivers of intra-urban variability. Using crowdsourced data, the location of each citizen weather station is known but, quite often, there is no specific information regarding the characteristics of the local environment (such as urban density, built materials, vegetation cover). One way to address this is to combine crowdsourced data with Local climate zone (LCZ) classifications that provide a landscape classification system for urban surface structure and cover, consistent across global cities (Stewart and Oke 2012). This classification in combination with crowdsourced temperature data can provide a thorough understanding of how local climate is impacted by different urban land-use and land surface characteristics. A study in Berlin assessed the intra- and inter-LCZ variability in urban temperature during the day and overnight (Fenner et al., 2017) and observed that within each LCZ, the temperature variance during the day was generally smaller than at night, and higher in summer than in winter. Inter-LCZ variability showed significant differences between not only urban and rural sites, but also between most common LCZs found within the city. Additionally, crowdsourced data used to assess the urban heat island (UHI) and identify intra-urban temperature variability in London observed cool anomalies near greenspaces (Chapman et al., 2017). This cool anomaly near urban parks was also reported in Moscow, while the areas still exhibited warmer temperatures than rural areas (Varentsov et al., 2020). These findings indicate that in addition to LCZ classifications, there is a need for a higher-resolution dataset on urban form and fabric (such as detailed vegetation cover and

street canopy characteristics) that can assist with interpreting the inter- and intra-LCZ variability in urban temperature.

The current study is motivated by these emerging crowdsensing efforts addressing the need for high-resolution data monitoring in cities, while exploring overlaying datasets and urban classifications (such as LCZs and building-level urban data) that can identify key drivers for intra-urban temperature variability. Additionally, we focus on Sydney, Australia, which extends previous analyses to a coastal city with unique mesoscale processes and synoptic scale circulations that dominate urban ventilation throughout the city (Hirsch et al., 2021). When analysing the urban heat island (UHI) in Sydney, Santamouris et al. (2017) found that a strong UHI effect was observed to the west of the central business district, beyond the reach of sea breezes from the east. The reference station used to quantify the UHI at other stations was adjacent to the central business district and Sydney Harbour, and close to the coast. Therein lies one of the difficulties in quantifying an urban heat island for Sydney. The complex nature of the city, with its substantial geographical differences between coastal and inland suburbs, and the lack of non-urbanised sites reflective of these differences, make it difficult to calculate an accurate UHI intensity across the city. Further, a calculated UHI intensity may not always provide data that is of relevance for urban heat mitigation (Martilli et al., 2020). Therefore, in the current study, we leverage the crowdsourced monitoring stations to focus on how urban heat varies in Sydney both geographically-taking into account distance from the coast and topography- and in different local climate zones.

A variety of other studies have assessed Sydney's climate. A link has been identified between synoptic conditions, in particular those associated with heat waves, and air pollution, leading to increased adverse health impacts at higher temperatures (Dean and Green 2018; Vaneckova et al., 2008; Jiang et al., 2017). The relationship between land surface temperature and green infrastructure has also been investigated and the temperature differences between green infrastructure classes were found to be more evident during summer and daytime, although the effect of impervious surfaces was found to dominate over the cooling effect of vegetation and water (Bartesaghi-Koc et al., 2019). Sydney temperatures are generally increasing over time (Livada et al., 2019), and an analysis of heat waves and urban overheating found that the urban overheating magnitude increased with the distance from the coast despite a reduced population density and increase in nonurban surfaces further inland (Khan et al., 2021).

These studies demonstrate the high spatial variability in urban temperature across the Greater Sydney region that is brought about through a combination of urban design and local climate factors, and in turn, the importance of urban climate monitoring. In this paper, we use crowdsourced data to obtain temperature observations of higher spatial resolution in Sydney. We then investigate the impact of both geography, via distance from coast and elevation, and urban fabric and form, via LCZs and other urban characteristics (such as eave height and surface cover), on temperature. By using high-resolution temperature observations combined with urban datasets, we aim to understand the

interplay of geography and land use on urban heat in a complex coastal city, and further assess the validity of crowdsourced measurements as a method for analyses of urban heat.

Details of the collection and quality control of the crowdsourced data, urban data sets used, and analyses undertaken are explained in *Data and Methods*. *Results and Discussion* compares the crowdsourced data to the reference data from scientific meteorological stations, analyses the impact of geography, land use and land cover on the data, and explores the benefits and challenges of using such data in urban climate studies. Future directions for the use of crowdsourced urban temperature are discussed in *The Applicability of Crowdsourced Data and High-Resolution Land Use Data*.

## DATA AND METHODS

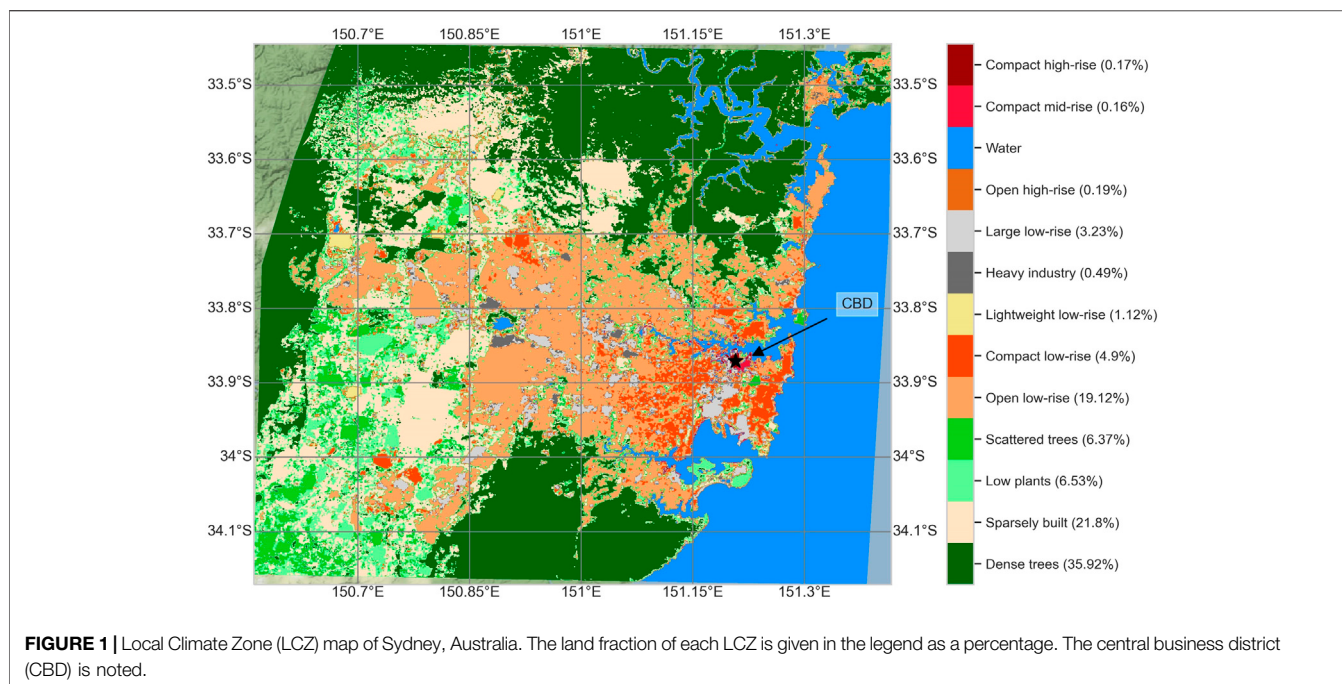
### Study Area and Time Period

This study focuses on the city of Sydney, Australia, which has a population of approximately 4.8 million. Sydney sits mostly within a basin between mountains and the coast, resulting in a complex interaction between mesoscale land and sea breezes. The metropolitan area is more densely populated in the east near the coast, with Greater Sydney extending almost 100 km west into the Blue Mountains. Beyond the mountains further west of Sydney lies grassland and arid shrubland. According to the modified Köppen classification system developed by the Bureau of Meteorology (BoM) based on a standard 30-years climatology, Sydney's climate classification is temperate with a warm summer and no dry season. The study area includes most of the Greater Sydney region (**Figure 1**).

The sea breeze has a significant impact on cooling the coastal regions of the metropolitan area, while being deficient in reaching the western regions particularly at the base of the mountains, leading to extremely high temperatures. The western regions of Sydney are those most impacted by increasing urban development and therefore it is critical that detailed and high-resolution observations are available to assess the impact of urban heat in order to plan subsequent measures to ensure liveability in the future.

The time period assessed in this study is the 2020–2021 summer, from December to February. During this period, Sydney experienced slightly above average rainfall due to La Niña, and temperatures much cooler than recent summers. The daytime temperatures across Greater Sydney were 1–2°C below the average of recent decades. However, this time period also included several heatwaves with the highest temperature recording of 41.6°C recorded at Sydney Airport on Jan 26, 2021 (Bureau of Meteorology 2021).

To fully represent urban structure and land use across Sydney, we used two datasets. A map of local climate zones (LCZ), at 100 m resolution obtained by World Urban Database and Access Portal Tools [WUDAPT] (Ching et al., 2018; Bechtel et al., 2015) is used to provide a standardised landscape classification system to consistently compare different regions in urban areas across Sydney (**Figure 1**). There are thirteen LCZs in Sydney with three



dominating categories: dense trees, sparsely built, and open low-rise (**Figure 3A**).

Since LCZ maps are determined through supervised machine learning applied to satellite imagery (Demuzere et al., 2021), there is no direct spatial or building height data informing their creation. Therefore, characteristics for these locally derived LCZ areas can differ from “typical” values presented in Stewart and Oke 2012. To provide additional information on the urban landscape not given by LCZ, an independent dataset of landcover and building characteristics (Geoscape) was used to categorise impervious fraction and vegetation as well as ground elevation and building height at a 100 m resolution (PSMA Australia, 2020). **Figure 2** shows the processed Geoscape data at a 500 m resolution for Sydney while **Table 1** summarizes the characteristic values for locally derived LCZs. Eave height refers to the height from the ground to where the wall and roof intersect. Sydney eave height is for the most part below 20 m, with small CBD areas having mean eave heights up to 50 m. Sydney elevation varies between 0 and 500 m (**Figure 2B**). Surface cover fraction data was available as bare earth, roads and paths, grass, trees, other vegetation, built area, buildings, and water. To simplify analysis, here an aggregate vegetation category has been used, defined by the sum of the grass, trees and other vegetation fractions (**Figure 2C**). Similarly, an impervious category has been defined by the sum of the roads and paths, built areas and buildings fractions (**Figure 2D**).

## Measurements: Crowd-Sourced Atmospheric Data

Crowdsourced air temperature and humidity data were collected from 551 Netatmo “Smart Home Weather Stations” across

Sydney. The Netatmo stations consist of an indoor and outdoor module. The outdoor module collects real-time weather data including temperature, humidity, and barometric pressure which, should the user agree, is displayed on the Netatmo Weathermap web portal. Historical data is not available; data for this study has been collected *via* quarterly scraping of the Weathermap over the 2020–2021 summer (Dec 2020–Feb 2021), leading to over two million air temperature readings collected.

The outdoor temperature and humidity sensors have accuracy of  $\pm 0.3^{\circ}\text{C}$  (over a range of  $-40^{\circ}\text{C}$ – $65^{\circ}\text{C}$ ) and 3%, respectively. The temperature accuracy has been validated and confirmed by Meier et al. (2017) using a climate chamber over the temperature range  $0^{\circ}\text{C}$ – $30^{\circ}\text{C}$ . However, the placement conditions of the outdoor module can have a significant impact on the temperature readings (*Quality Control*) (Varentsov et al., 2020).

Ideally, sensors would be distributed across built LCZs corresponding to the distribution found in the city. However, more than half of the locations at which data is collected represent the open and compact low-rise zones, with only a small number representing dense trees and sparsely built zones (**Figure 3B**).

## Quality Control

While stations placed correctly in shaded areas have reasonable accuracy, those kept in direct sunlight or even indoors or other inappropriate locations can report a range of inaccurate readings (Varentsov et al., 2020). The quality of each reading has therefore been checked and the data filtered according to the four main steps (M1 to M4) defined in the framework by Napoly et al. (2018).

The first main step, M1, removes stations with identical latitude and longitude as this indicates incorrect set up of the

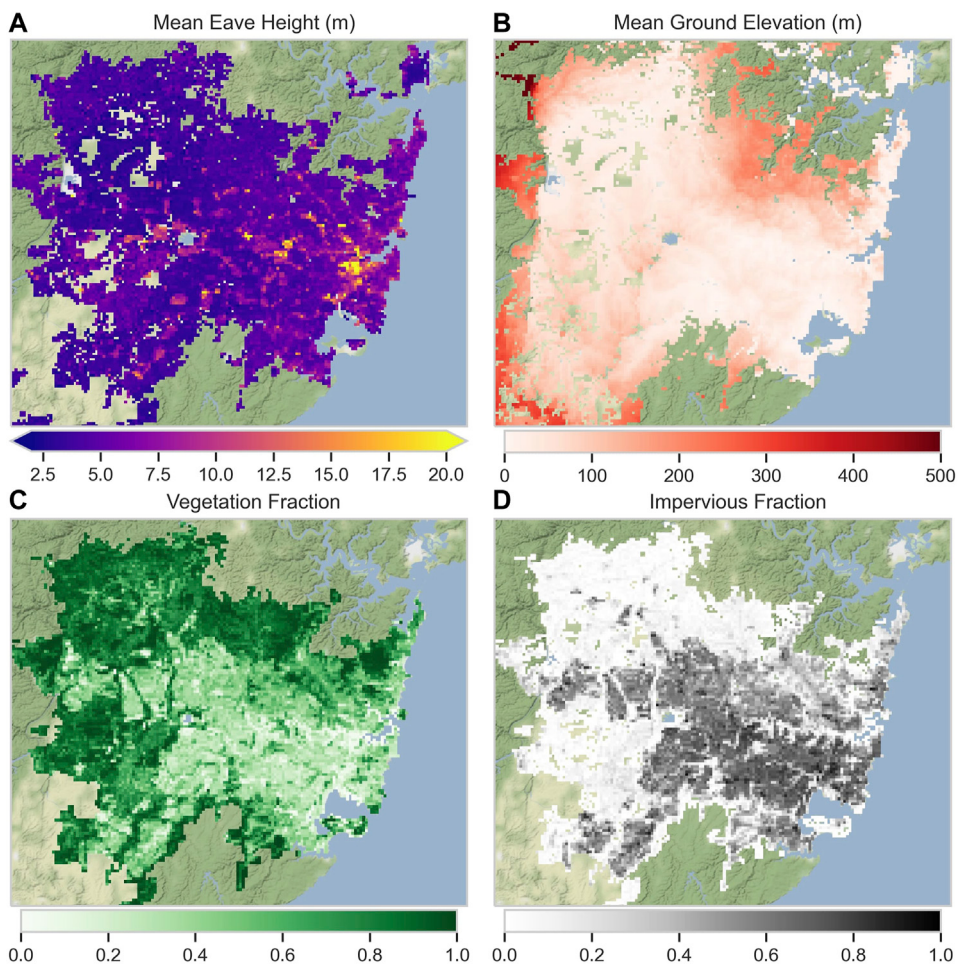


**FIGURE 2 | (A)** Mean eave height (m) and **(B)** ground elevation (m), and **(C)** vegetation and **(D)** impervious fractions across Sydney.

station. Based on unique ID numbers for each station, no stations in Sydney had repeated coordinates. Rather, in some cases a request had been made to the server before the next readings had been recorded and updated on the Weathermap, leading to duplicate recordings. As such, identical readings from each station with the same timestamp have been removed.

Step M2 of this framework finds and removes outliers based on each hourly distribution. The main purpose of this step is to remove significantly high readings likely from stations in direct sunlight. The data was separated into hours, and a “Z-score” for each reading was defined as:

$$Z = \frac{T - \text{median}(T)}{Q_n(T)} \quad (1)$$

where  $T$  is air temperature ( $^{\circ}\text{C}$ ) and  $Q_n$  is a robust estimator for variance given by the 0.25 quantile of the distances  $\{|x_i - x_j|; i < j\}$  (Rousseeuw and Croux 1993). Following Napoly et al. (2018), readings with a Z-score outside the range  $-2.32$  to  $1.64$  were removed, leaving 92.45% of data remaining.

In step M3, at each station if step M2 removed more than 20% of readings during 1 month, then the entire month is removed. This reduced the data to 85.58%.

The final step M4 targets indoor stations by comparing the Pearson correlation between each station and the median of all stations in each month. If the correlation was less than 0.9, all readings from the station were removed for said month. This left a remaining 81.74% of data for analysis after step M4, similar to values reported in Napoly et al., 2018 (82.21 and 81.45%).

Between steps three and four the data was reorganised into 30-min intervals (using mean values wherever a station had multiple readings in a half-hour period), which simplified finding the Pearson correlation and mean temperatures, and all later processing. This was completed after steps M1 to M3 so that specific outliers could be removed prior to averaging. Quality control reduced the number of stations from 551 to 492.

### Site Decomposition and Data Aggregation

Warm and cool days were defined based on daily maximum of mean half-hourly temperatures of all stations. The median of daily maximum of  $25.7^{\circ}\text{C}$  then set the threshold, evenly dividing days

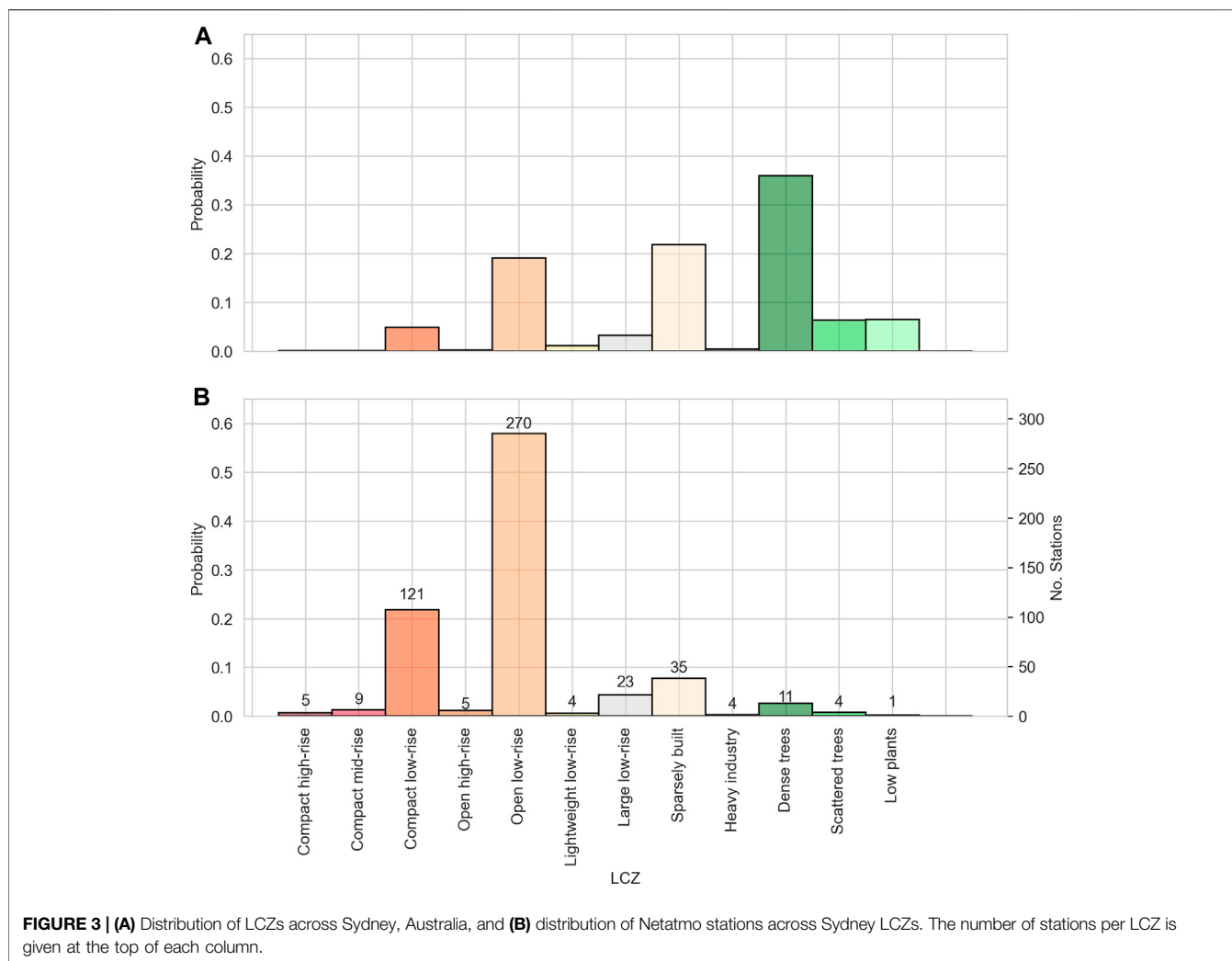


**TABLE 1** | The characteristic values for locally derived LCZs for grids containing Netatmo stations, formatted for comparison with values presented in Stewart and Oke, 2012 (S&O: where impervious surface fraction does not include building fraction). Here the 25<sup>th</sup>–75<sup>th</sup> percentile ranges are shown, with mean values bracketed.

		Building surface fraction (%)	S&O impervious surface fraction (%)	Pervious surface fraction (%)	Eave height (m)
LCZ1	Compact high-rise	17–54 (36)	8–15 (12)	30–72 (52)	7–10 (9)
LCZ2	Compact midrise	44–51 (45)	19–29 (27)	23–32 (28)	7–20 (17)
LCZ3	Compact low-rise	34–45 (38)	21–34 (28)	24–41 (33)	4–7 (6)
LCZ4	Open high-rise	30–40 (35)	26–40 (32)	29–43 (33)	20–22 (20)
LCZ5	Open midrise	na	na	na	na
LCZ6	Open Low-rise	21–35 (27)	16–27 (22)	39–61 (51)	4–5 (5)
LCZ7	Lightweight low-rise	42–57 (46)	33–38 (34)	6–22 (19)	3–3 (3)
LCZ8	Large low-rise	35–44 (38)	27–40 (38)	18–29 (24)	6–12 (10)
LCZ9	Sparingly built	5–25 (16)	5–29 (17)	45–87 (66)	3–5 (4)
LCZ10	Heavy industry	44–48 (44)	25–40 (33)	12–32 (23)	8–12 (10)

between warm and cool days. The timeseries of warm and cool days can be seen in **Figure 4**. Compared with 30-years climate averages for Sydney, 2020–2021 was a slightly cooler summer with

above average rainfall. Additionally, data from BoM meteorological stations indicate that cool days mostly occurred under rainy or overcast conditions (Bureau of Meteorology, 2021).

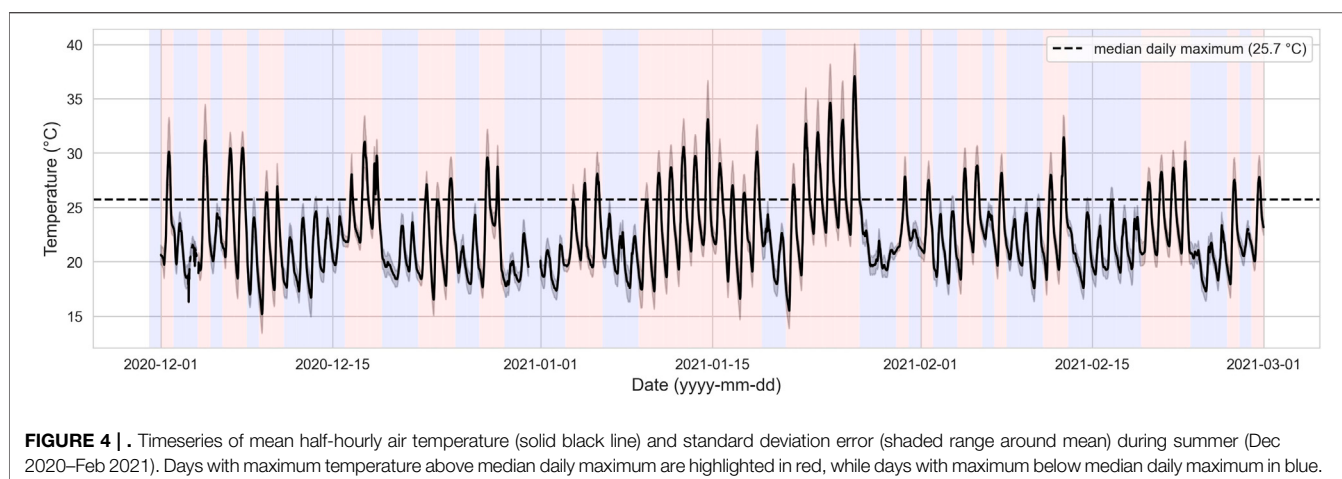


**FIGURE 4 |** Timeseries of mean half-hourly air temperature (solid black line) and standard deviation error (shaded range around mean) during summer (Dec 2020–Feb 2021). Days with maximum temperature above median daily maximum are highlighted in red, while days with maximum below median daily maximum in blue.

To understand the crowdsourced data in the context of urban climate monitoring and how it may be interpreted, a comparison has been made with weather station data from the BoM. To help explore the impacts of both geography and urbanisation on urban heat the metropolitan area has been divided into three regions (inland, central, and coastal) running approximately parallel to the coast (Figure 7, detailed in *Geographical Influences on Urban Temperature*). The warm and cool aggregate day representations of these regions are shown in Figure 8.

## RESULTS AND DISCUSSION

In this section, we use crowdsourced data to detail the impacts of urban form and fabric (indicated by LCZs as well as surface cover and building height data) as well as local geography on intra-urban temperature variability in Sydney.

### Difference Between Crowdsourced Data and Reference Stations

Crowdsourced temperature data across Sydney, Australia, is first compared with reference weather stations established by BoM. There are approximately 600 BoM weather stations across Australia, sited according to the World Meteorological Organization guidelines to measure synoptic scale conditions rather than the local or micro scales (Bureau of Meteorology 1997). The key differences in siting are that BoM weather stations are installed within approved shelters at a height of 1.1 m above ground level, within a 30 by 30 m buffer of low natural vegetation (e.g., grass), and taller obstructions outside the buffer being at a distance of up to 10 times their height. These requirements make the placement difficult in highly urbanised areas. Netatmo sensors, however, are placed where people live (e.g., in backyards or on balconies).

The location of BoM sites compared to Netatmo stations is shown in Figure 5. A total of 10 BoM weather observation stations were identified within the study area (Greater Sydney Region) marked as black triangles in Figure 5 and their readings

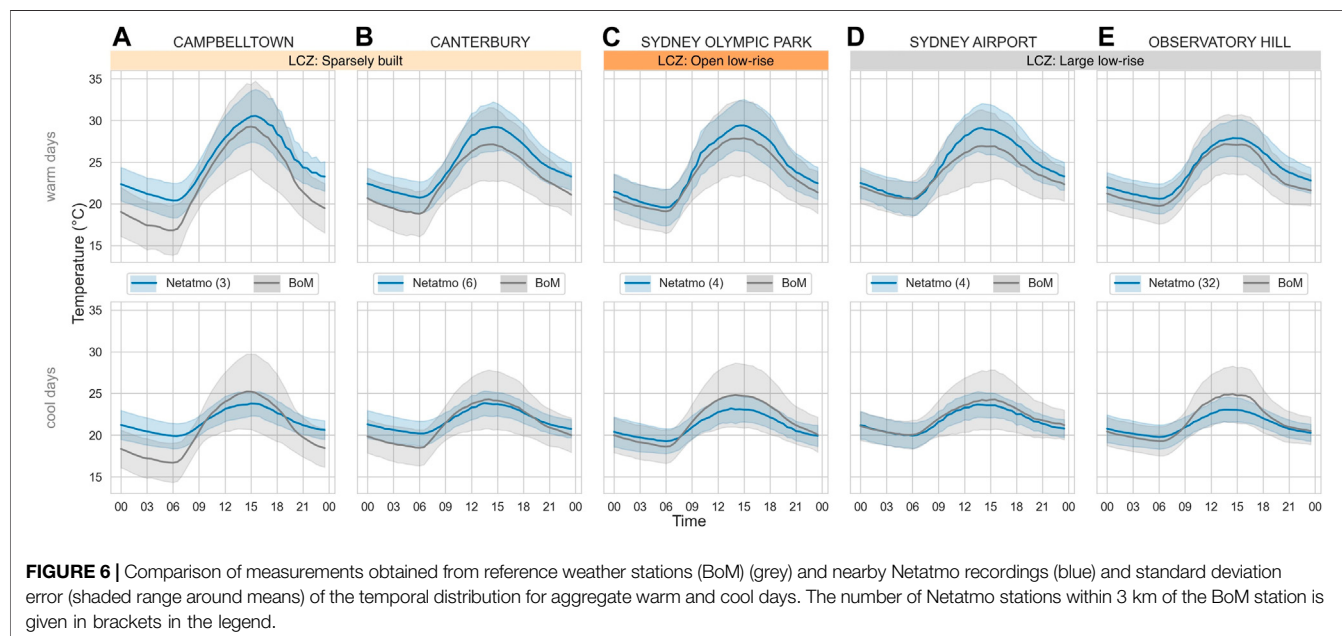
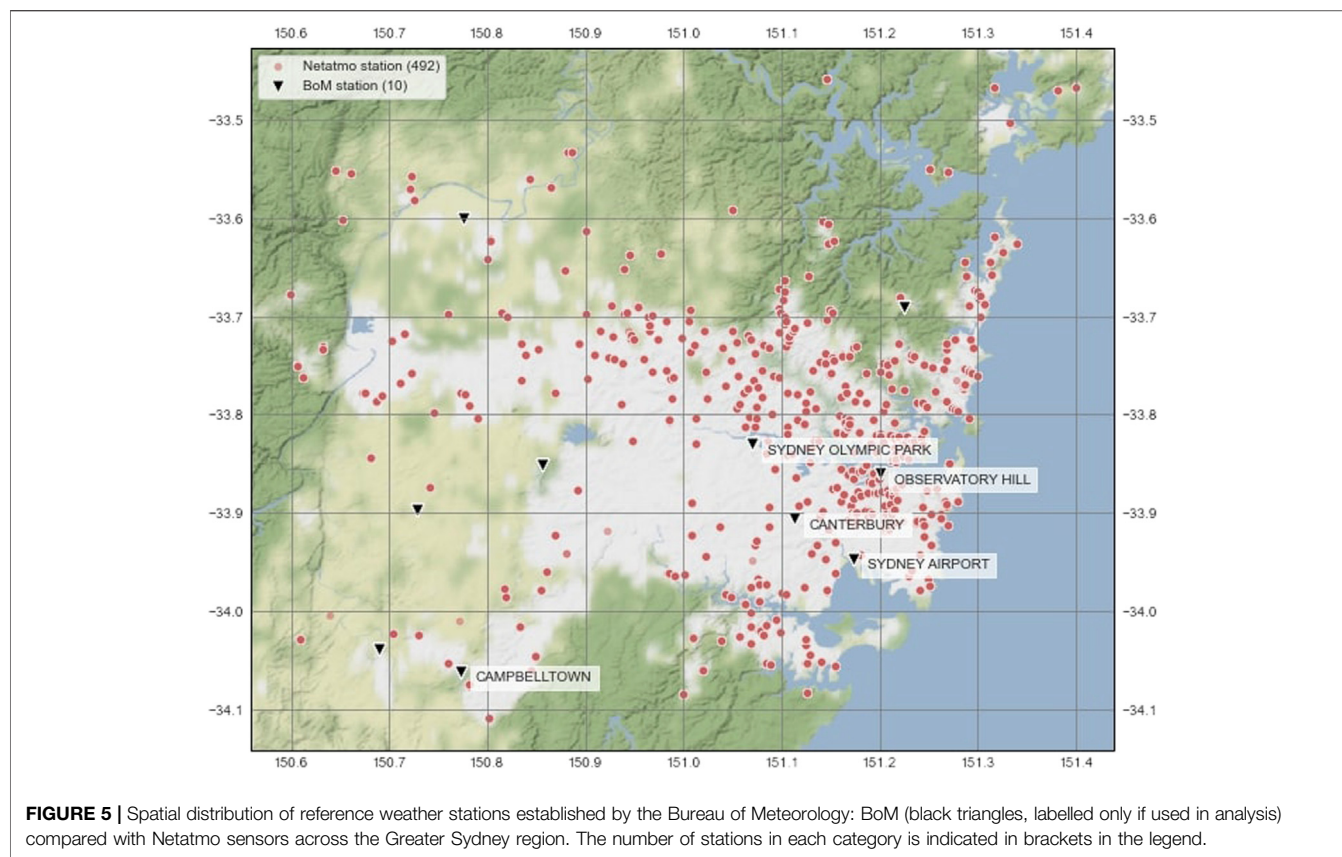
were compared with Netatmo stations identified within the 3 km radius. A threshold of at least three Netatmo stations was implemented for this comparison, which reduced the number of BoM stations to five (named in Figure 5). The comparison is further divided into aggregate warm and cool days detailed in *Site Decomposition and Data Aggregation*.

A comparison of Netatmo measurements with neighbouring reference stations (not shown) showed a high correlation between crowdsourced and reference station observations (Pearson regression correlation ranging between 0.75–0.99), with no clear pattern of change observed between day- and night-time or cool/warm days. Therefore, we focus our analyses on comparing the diurnal evolution of air temperature recorded by both monitoring networks (Figure 6).

When compared with reference measurements during the day, the citizen weather stations consistently observed higher daytime temperatures on warm days and cooler daytime temperatures on cool days. For both warm and cool days and across all stations, Netatmo readings were higher at night. The consistency of results across locations, and persistent elevated temperatures at night (i.e., without direct sunlight confounders) indicate a robust difference in typical microclimate conditions between BoM and Netatmo sites.

Elevated urban temperatures can be caused by a range of factors, including greater absorption and retention of solar and thermal radiation by urban materials and geometries, lower levels of evapotranspiration, and greater release of heat from anthropogenic sources (Stewart and Oke, 2012). Additionally, the high heat capacity and increased surface area of urban structures can reduce the amplitude of diurnal temperature variation (Wang et al., 2018). Netatmo measurements have both elevated temperatures (particularly during warm days) and reduced amplitude diurnal patterns (particularly on cooler days) compared with BoM measurements.

Other studies have observed similar patterns. For example, in London a similar comparison found that the reference stations measured slightly lower mean daily maxima and minima on warm days, and a slightly increased or similar diurnal temperature range as compared to Netatmo stations



(Benjamin 2019). In Berlin, reference stations observed increased daytime and decreased overnight temperatures as compared to crowdsourced data (Fenner et al., 2017), indicating a relationship more similar to that seen on cool days in the current study.

The sites located at Campbelltown, a sparsely built suburban location approximately 50 km west of the CBD, showed the largest warm day overnight difference of 3.6°C at 3am, whereas Sydney Olympic Park and Sydney Airport, both

located close to water bodies, showed the smallest differences at 3am of  $\sim 0.5^{\circ}\text{C}$ . A large overnight difference is also observed at Campbelltown on cool days.

At Campbelltown, large consistent differences between BoM and Netatmo stations may be due to the impact of local siting (i.e., direct interaction with nearby built form) and of more regional interactions (i.e., lack of sea breeze in Western Sydney leading to less local mixing, compounding microclimate differences). The other stations are located in open low-rise and large low-rise zones, and closer to the ocean. These areas are more densely built than Campbelltown, which means the BoM stations are likely more affected by larger-scale urban warming effects from more densely built areas, and more vigorous mixing of air by sea breezes, reducing differences with Netatmo stations.

During the day on warm days, Sydney Airport showed the largest difference in maximum temperature, where crowdsourced air temperature at 2pm was approximately  $2.5^{\circ}\text{C}$  higher than reference measurements. The specific attributes of this site are likely the cause of this increased discrepancy. The reference station is located very near the airport grounds and the coast, thus is exposed to increased ventilation and higher sky view factor due to the openness, affecting convective and radiative heat transfer. The Netatmo stations, however, are located within the suburb around the airport, where cooling mechanisms associated with wind and radiation are weaker.

On cool days, a wider diurnal range is recorded by the reference sensors compared to the citizen weather stations. Our investigation of the BoM dataset indicates that cool days during this period occurred on overcast sky conditions or received light-moderate rainfall. With lower shortwave radiation during the day, the convection and conduction from surrounding surfaces dominate heat transfer balance, and consequently air temperature, in the urban canopy. Accordingly, it is likely that the lack of built materials with high thermal inertia near the BoM stations has led to a wider range in temperatures.

Similar to warm days, Campbelltown had the largest overnight discrepancy of  $3.2^{\circ}\text{C}$  between 4:30 to 5:30 am. During the day, Observatory Hill, located in the Sydney central business district and adjacent to Sydney Harbour, had the largest discrepancy of  $1.9^{\circ}\text{C}$  at 2:30pm.

This comparison has identified differences between stations due to their location, including the LCZ and the distance from the coast. It is clear that the local climate near the coast is strongly influenced by the sea breeze and as such, stations near and far from the coast cannot be directly compared. Assessing stations within regions of increasing distance from the coast allows each region to be analysed individually, as well as comparison between regions.

## Geographical Influences on Urban Temperature

For analysing intra-urban temperature variability in a coastal city, it is critical to account for the intertwined nature of urban topography and the distance from the coast combined with

urban design characteristics (such as urban density and sprawl). The distance from the ocean has a strong impact on temperature in Sydney (Hirsch et al., 2021) as also observed in other coastal metropolises like Los Angeles (Vahmani and Ban-Weiss 2016). Accordingly, we divide the crowdsourced datasets based on regions (inland, central, and coastal shown in **Figure 7**) before assessing the impact of urban design and land cover on temperature variabilities (*Land Use and Land Cover Influence on Urban Temperature*). The regions are divided using an approximately uniform width, slightly shifted to maintain a sufficiently large number of Netatmo stations per region (particularly inland).

As anticipated, temperature distribution (particularly on a warm day), is highly influenced by the geographic region (**Figure 8**), which is in turn affected by the distance from the coast as well as elevation due to proximity to mountain ranges in the south and west. We observe that the inland region experienced the largest diurnal range with an average of  $11.7^{\circ}\text{C}$  and  $4.6^{\circ}\text{C}$  on warm (**Figure 8A**) and cool days (**Figure 8C**), respectively, compared to  $7.8^{\circ}\text{C}$  and  $3.3^{\circ}\text{C}$  in the coastal region.

Accordingly, in order to focus on intra-urban variabilities brought about by urban design characteristics, the impact of elevation was removed using the lapse rate, defined as

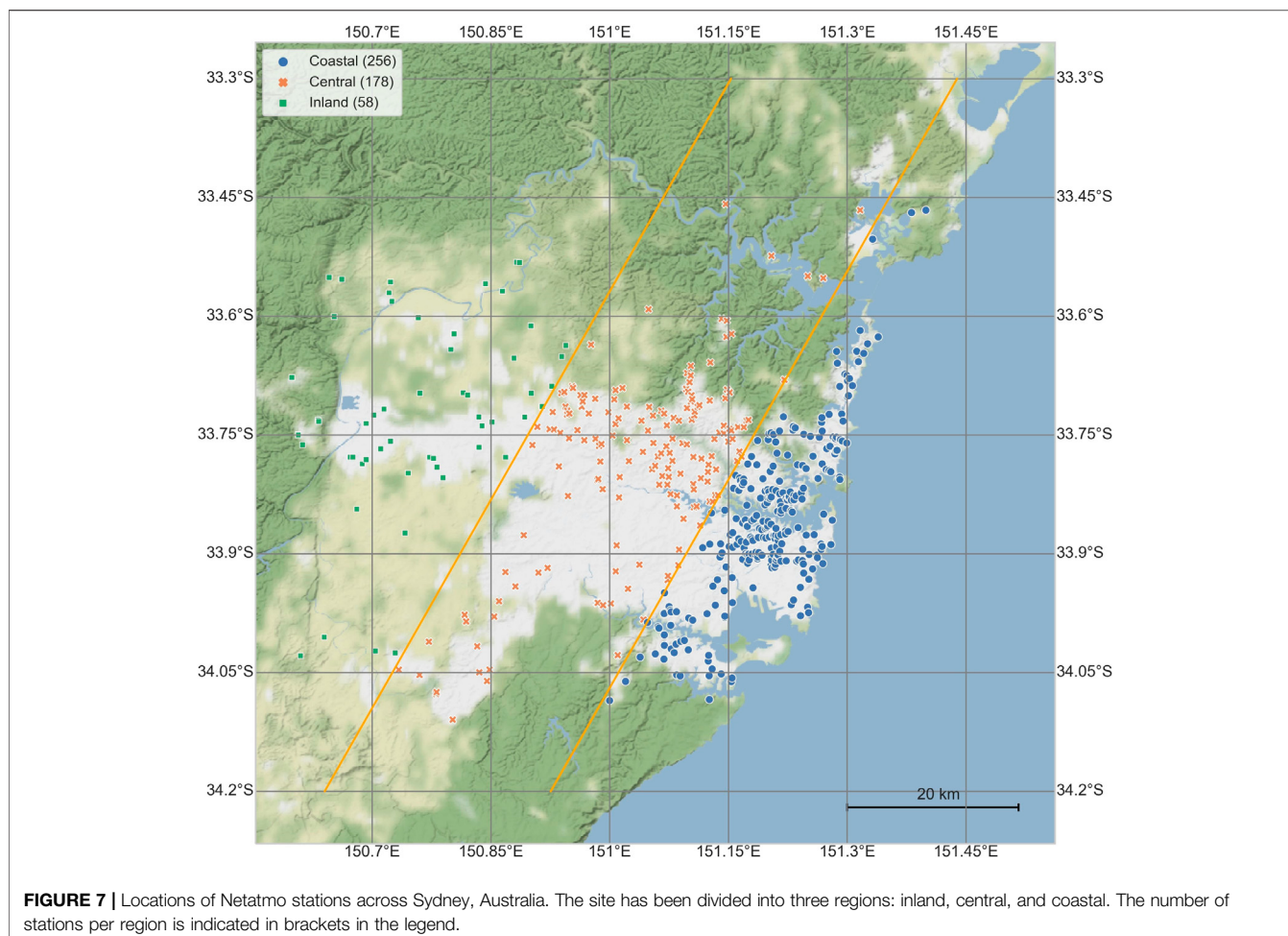
$$T' = T + 0.0065(z - \text{mean}(z)) \quad (2)$$

where  $z$  is the elevation of each station in metres (Napoly et al., 2018). Temperatures were adjusted to an equivalent temperature at a constant elevation of 63.3 m (the mean elevation of the stations). The impact of this elevation adjustment is more evident on cool days than warm, showing a clearer increase in diurnal range with distance from the coast (**Figure 8**).

With higher elevations generally found further from the coast, elevation and coastal impacts are correlated. After adjusting for the elevation, the remaining differences between regions are primarily land cover differences and distance from the coast. To ascertain how the impact of land use and cover differs across the city, maximum and minimum temperatures have been compared between classes of the urban design characteristics, and between regions in the following analyses (**Figures 9–12**). Dividing the area into regions aims to separate out the impact of the coast, however interpretation of data from the coastal region still remains a challenge due to the varying impact of the ocean in this region. The moderating influence of the ocean and the cooling effect of the sea breeze may be more impactful nearer to the coast. Whereas for the central and inland regions the influence of the distance from the coast is fairly consistent which allows for individual comparison of other urban design characteristics.

## Land Use and Land Cover Influence on Urban Temperature

To investigate the impact of urban design and land cover on intra-urban variability of air temperature, we compare crowdsourced measurements with LCZ and Geoscape data for



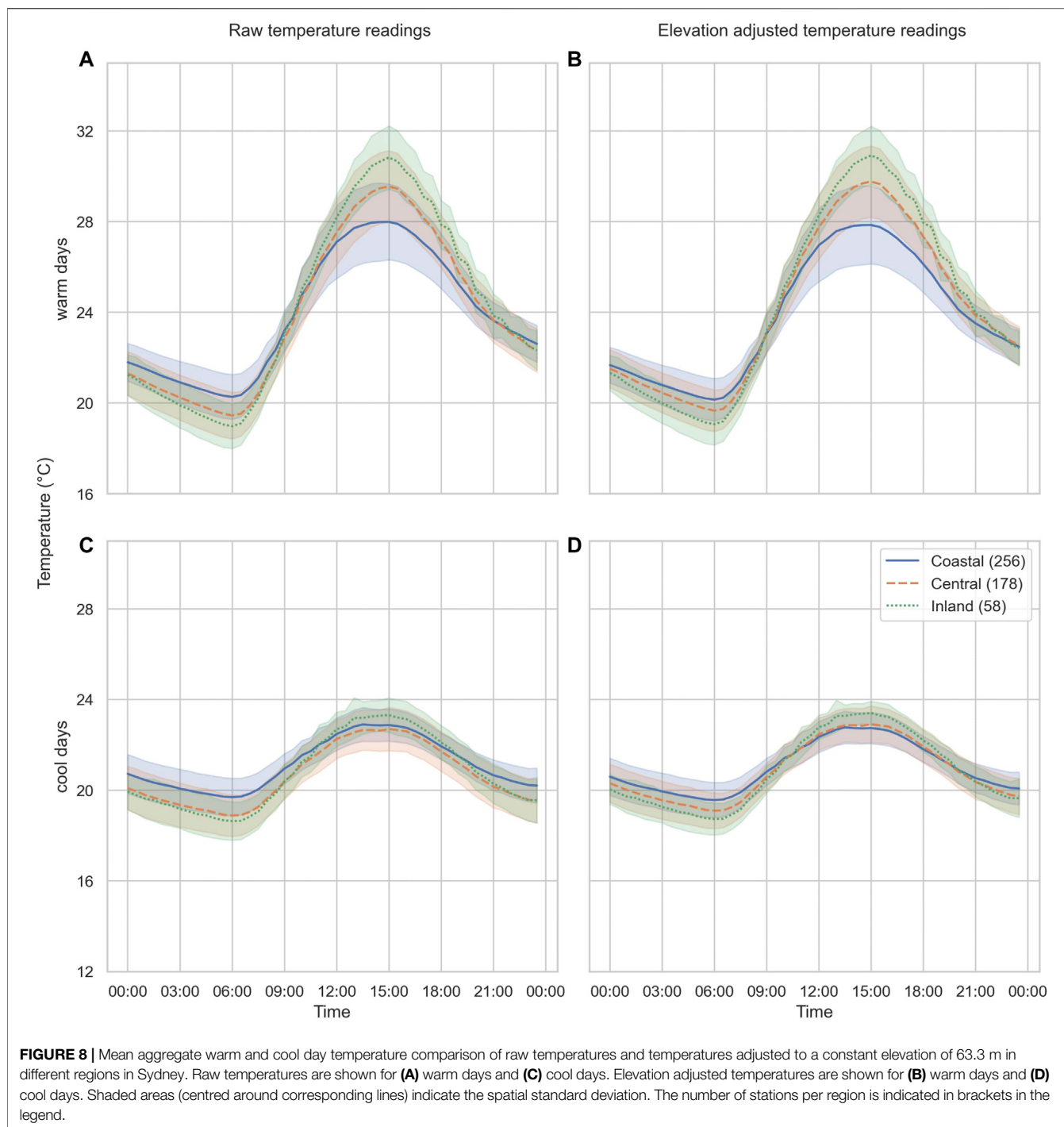
Sydney (*Study Area and Time Period*). For this analysis, the station mean maximum and minimum temperatures in warm and cool days have been assessed. Between regions, these values have the largest differences (**Figure 8**) and thus will give an indication of the significance of the impact of each urban design characteristic. The maximum temperature of the mean warm day has been calculated by finding the maximum temperature for each warm day for each station, and then taking the mean over days. Similarly, the maximum and minimum of mean cool or warm days were found. Accordingly, the datapoints in **Figures 9–12** represent the distribution of maximum/minimum temperature across different stations.

**Figure 9** shows the boxplot distribution of air temperature in each region categorised by LCZ. In this analysis, we focus on urbanised LCZs which also include the highest number of Netatmo stations (**Figure 3B**): open and compact low-rise, lightweight and large low-rise, compact midrise, and open and compact high-rise. Only LCZs with at least three stations in a region were assessed. As shown in **Figure 1**, fewer urban LCZs are represented in the inland and central regions compared to coastal areas. In general, compact LCZs recorded a smaller diurnal range than open LCZs, with lower maxima and higher minima, except for the compact high-rise LCZ. Increasing minima and

decreasing maxima were observed with increasing height, again excluding the compact high-rise LCZ. In general, we expect to see smaller temperature diurnal ranges in more densely built areas because of increased thermal inertia (Wang et al., 2018).

Considering the low-rise LCZs, open low-rise recorded higher maxima and lower minima than compact low-rise. In the open LCZ, a higher sky view factor (SVF) leads to higher solar radiation penetration, increasing the maximum temperature. Overnight, on the other hand, more ventilation and higher SVF in the open LCZ result in a lower minimum (Oke, 1981; Skarbit et al., 2017).

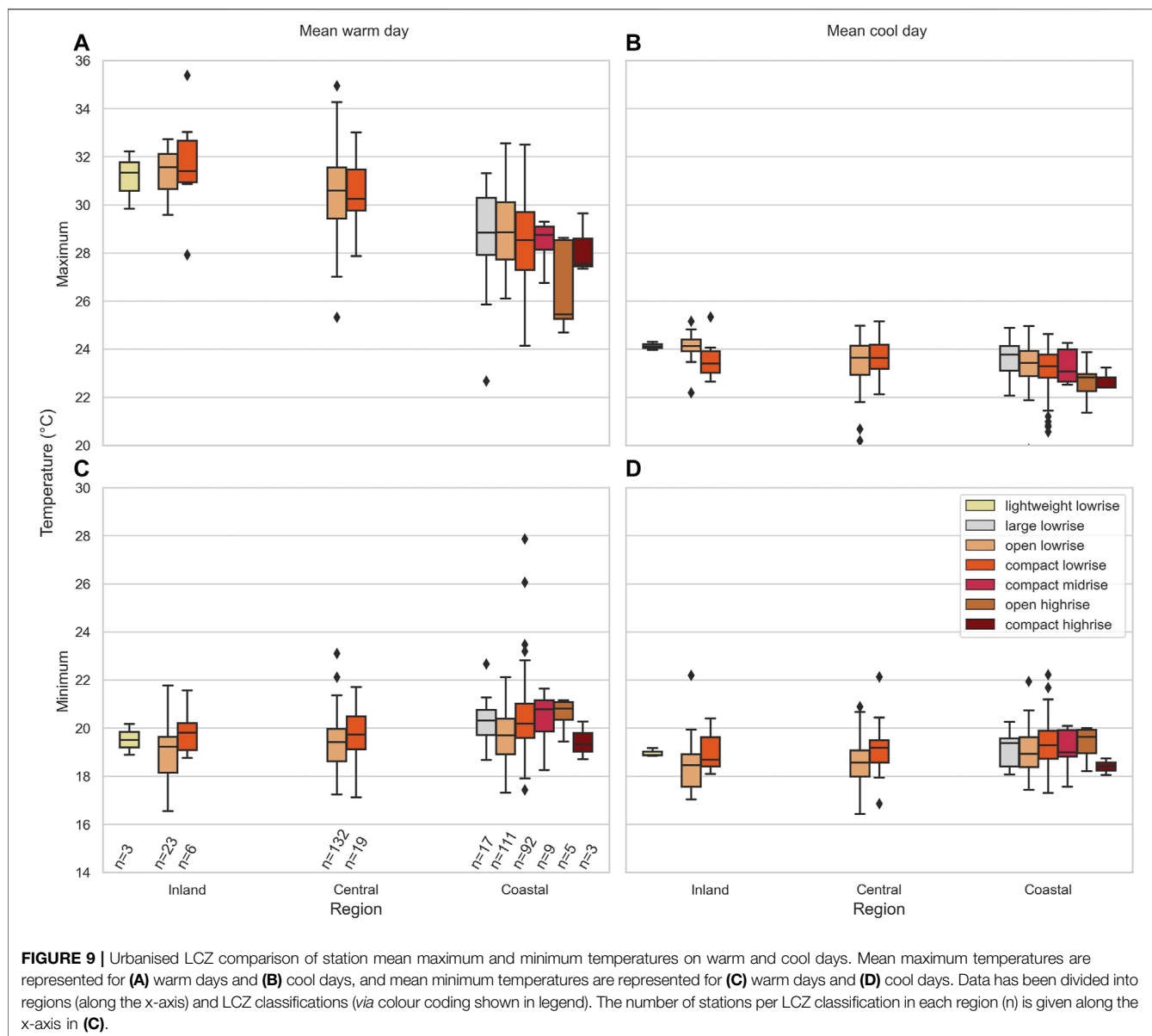
On the contrary, the high-rise LCZs observed a wider diurnal range in the compact zone compared to the open zone. The high-rise LCZs are only present near the coast, and recorded the lowest maxima. However, when comparing the minima, open high-rise recorded the highest minima while compact high-rise recorded the lowest minima across all urbanised LCZs. Since the main difference between these LCZs is the density, the impact on temperature is likely due to the interaction between convective, conductive, and radiative heat fluxes affected by density. In the compact zone, higher density results in increased shading due to the deeper canyons (Johansson, 2006; Masson et al., 2020), whereas in the open zone, a higher SVF



allows more solar radiation to be absorbed during the day. However, it is expected that during the night, radiative cooling and sensible heat flux increase with decreasing density (Nazarian and Klessil, 2015), resulting in lower surface and air temperatures, which is not observed with crowdsourced data. As for maxima, compact subzones recorded the worst overheating episodes rather than open subzones. In this case, the shadowing effect in canyons is countervailed by reduced wind speeds and ventilation as well as by additional heating mechanisms that typify dense clusters of tall

buildings, such as multiple solar inter-reflections bouncing between overlooking facades (Battista et al., 2021). The compound effect may be the cause of the increased maximum temperatures.

Across all land use and land cover comparisons, there was reduced variability in the cool day maxima as compared to the warm day maxima. This indicates that local conditions and micro/mesoscale phenomena have a reduced influence on the maximum temperatures over cool periods, governed by



larger-scale dynamics. This is likely due to the increased cloud cover on cool days which reduced both the incoming solar radiation and the transparency in the atmospheric window, which enables radiative cooling. As such, the effect of optical properties (e.g., albedo, emissivity) and thermal inertia of materials is mitigated and moderated across LCZs, thus reducing the range in temperatures otherwise observed.

Another important result of this analysis is the range of temperatures observed within a single LCZ, namely the intra-LCZ range shown by each box. For warm days, a wider range of temperatures within each LCZ is observed for the maximum temperatures than the minimum temperatures, whereas for cool days a similar range is observed between maximum and minimum temperatures. These observations are contrary to those seen in Berlin and Szeged, where intra-LCZ daytime temperatures in general varied less than overnight, and LCZs

with a larger number of stations had the widest temperature ranges (Fenner et al., 2017; Skarbit et al., 2017). This variability was attributed to microscale differences in exposure, surface cover, and anthropogenic heat sources near the measurement sites, as well as due to the grouping of LCZ classifications regardless of location, neglecting meso-scale effects. In this study however, some meso-scale effects have been included by the division of regions.

Despite covering a relatively small area with few stations, the open high-rise LCZ had the widest interquartile range for warm day maximum temperatures of approximately 3.3°C. For minimum temperatures however, this LCZ had one of the smallest temperature ranges of 0.7°C. This may be due to variable shading in the canyon during the day causing highly varying recordings, while overnight heat release from materials affects all stations and moderates temperatures.

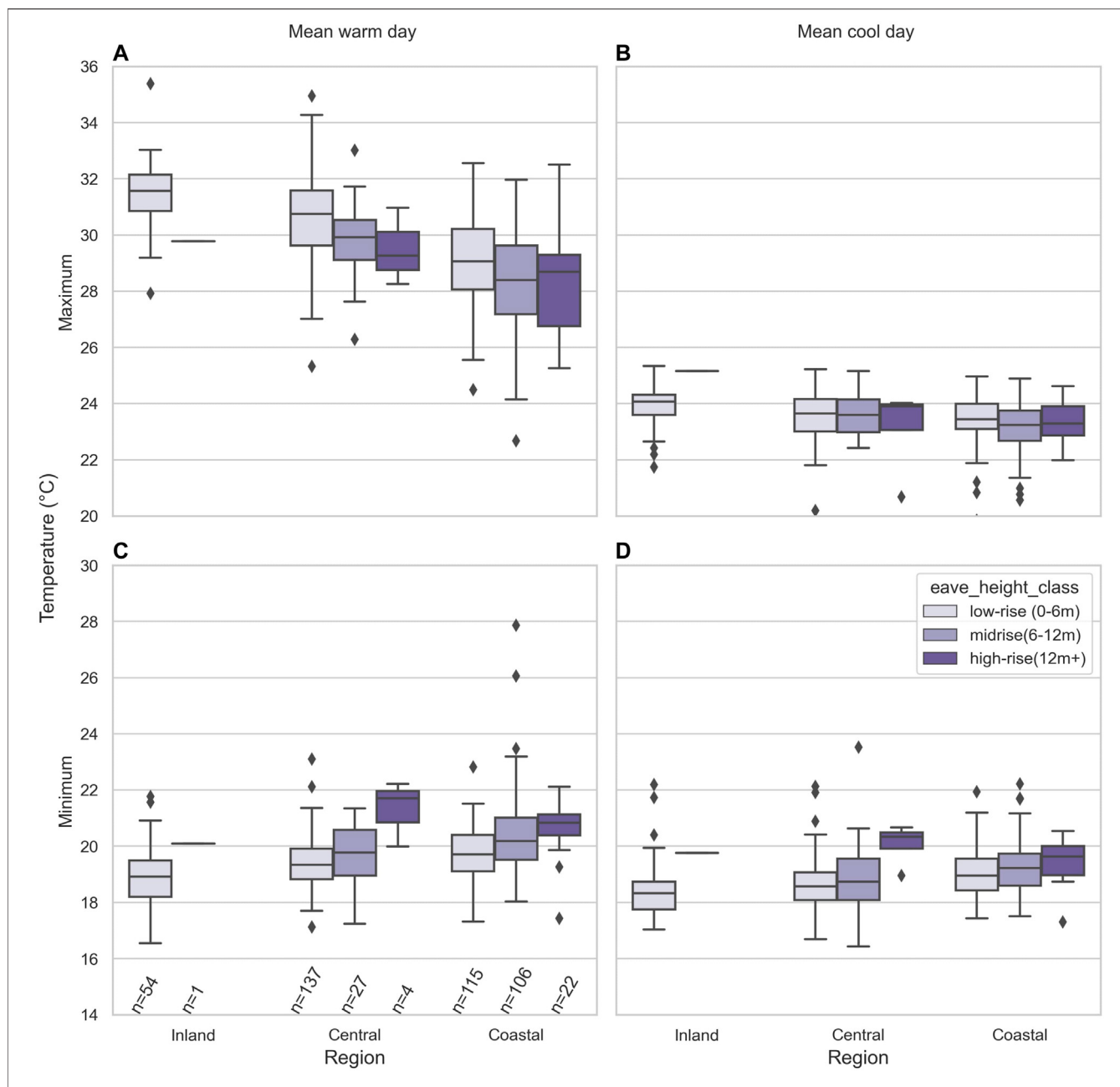


**FIGURE 10 |** Eave height comparison of mean maximum and minimum temperatures on warm and cool days. Mean maximum temperatures are represented for (A) warm days and (B) cool days, and mean minimum temperatures are represented for (C) warm days and (D) cool days. Data has been divided into regions (along the x-axis) and eave height classifications (via colour coding shown in legend). The number of stations per LCZ classification in each region (n) is given along the x-axis in (C).

The open and compact low-rise LCZs have fairly consistent temperature ranges across the regions. The coastal and inland maximum temperatures in the open low-rise zones have the largest difference in temperature ranges with a range of  $1.5^{\circ}\text{C}$  inland and  $2.4^{\circ}\text{C}$  near the coast. This indicates that within these LCZs there is some variability in local climate, however this variability is consistent across the regions and thus is likely not due to the influence of the coast.

The intra-LCZ ranges indicate that there are other urban factors at play which influence the local temperature

distribution. Further comparison with more specific urban design characteristics has been made in order to identify their individual impacts.

As noted in *Study Area and Time Period*, LCZ maps are determined through supervised machine learning applied to satellite imagery (Demuzere et al., 2021) and their characteristics can differ from “typical” values presented in Stewart and Oke 2012 (locally derived values presented in Table 1). We therefore complement the above results using an independent spatial dataset which includes direct spatial and

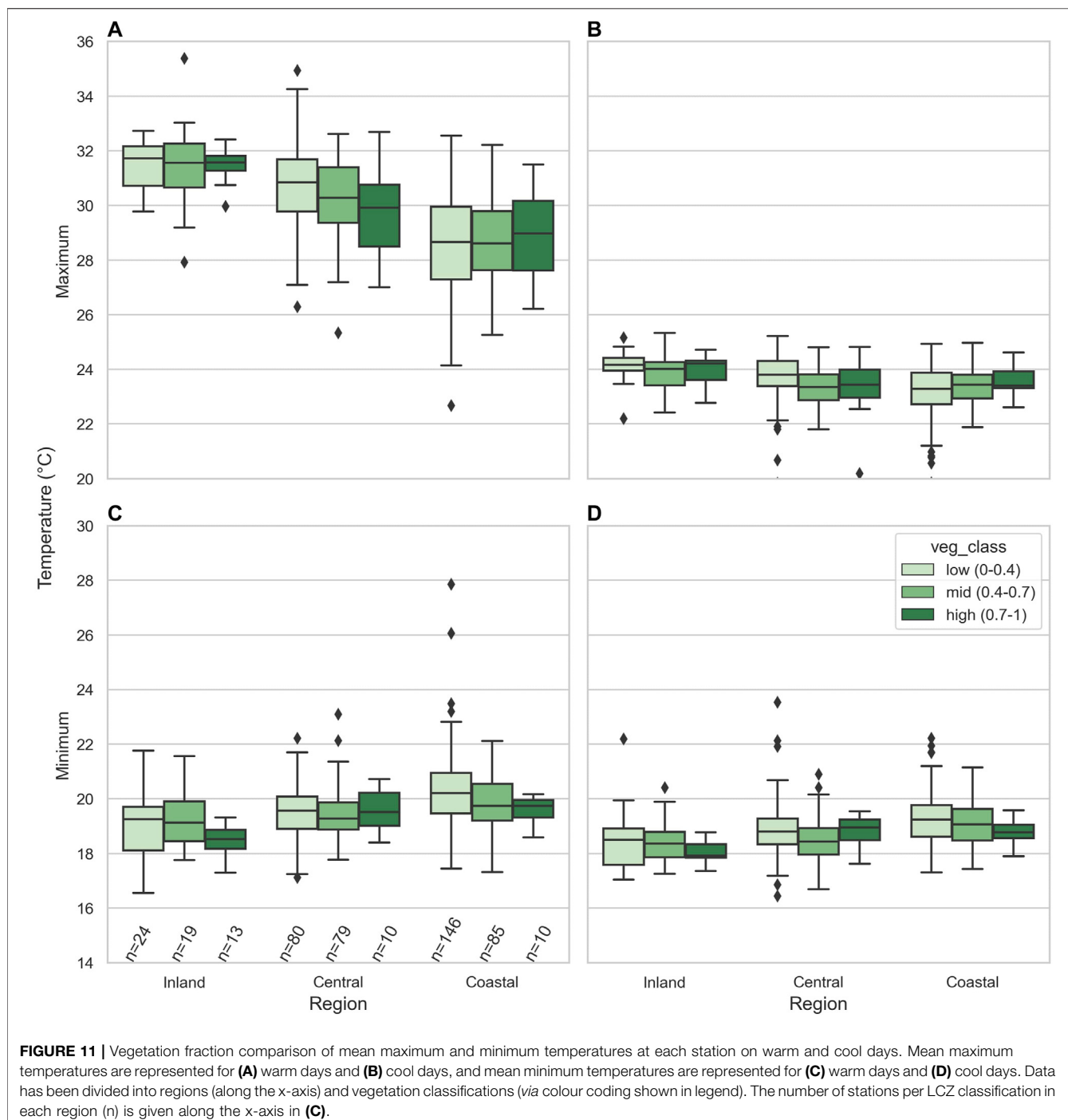


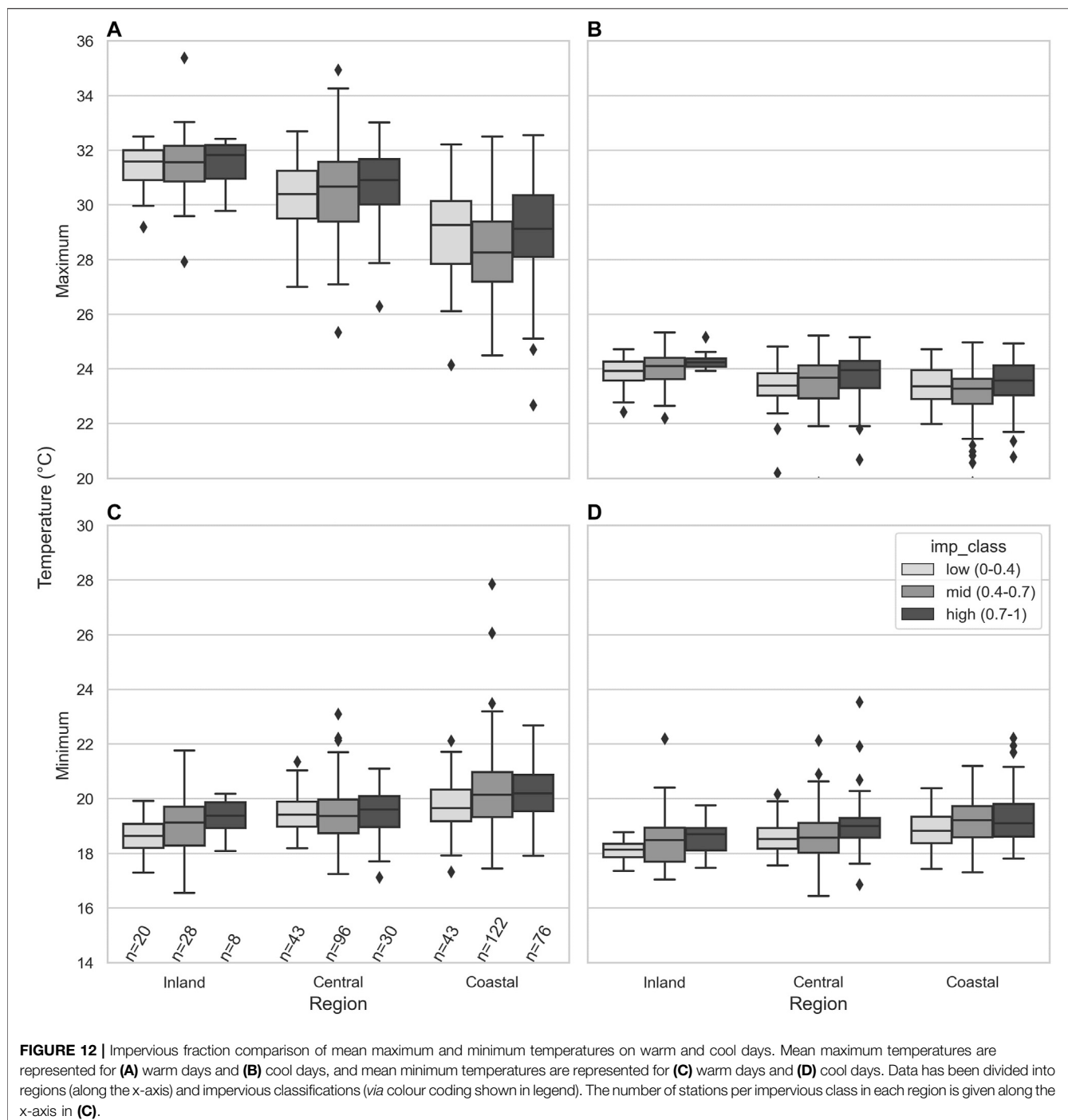
**FIGURE 11 |** Vegetation fraction comparison of mean maximum and minimum temperatures at each station on warm and cool days. Mean maximum temperatures are represented for **(A)** warm days and **(B)** cool days, and mean minimum temperatures are represented for **(C)** warm days and **(D)** cool days. Data has been divided into regions (along the x-axis) and vegetation classifications (via colour coding shown in legend). The number of stations per LCZ classification in each region (*n*) is given along the x-axis in **(C)**.

building height information for Sydney (PSMA Australia, 2020).

The LCZ building height classifications are low-rise (2–10 m), midrise (10–25 m) and high-rise (25 m+). Across Sydney, stations are mostly categorised by LCZ low-rise, with very few in midrise and high-rise areas which does not allow for clear comparison between height categories. As such, when using the independent dataset, the classification thresholds of low-, mid- and high-rise have been adjusted to better suit the Sydney urban

landscape. Mean eave height has been broken down into the following three categories: low-rise (0–6 m), mid-rise (6–12 m), and high-rise (12 m+). Low-rise defines housing of 1–2 storeys, and high-rise defines buildings of four storeys or higher in which an elevator is required.

**Figure 10** shows the boxplot comparison of crowdsourced temperature in different eave height classes per region. The high-rise category (12 m+) was not present inland, and midrise (6–12 m) was only represented by one station in this region.



In both the central and coastal regions, the number of stations representing high-rise areas was significantly lower than those representing low- and mid-rise.

The eave height comparison is consistent with the LCZ height comparisons, and shows these trends more clearly. In general, the diurnal range decreased with increasing eave height. The minimum temperatures increased with increasing eave height, with ranges in median temperature of 1.4°C and 1.1°C in the central region, and 1.1°C and 0.6°C in the coastal region, on warm

and cool days, respectively. Conversely, the warm day maximum decreased with increasing eave height, with a range in median temperature of 2.0°C in the central region and 1.6°C near the coast.

Here, we extend the analyses to evaluate the impact of surface cover determined by impervious and vegetated surface covers. The fraction of land covered by vegetation and impervious surfaces (*Study Area and Time Period*) is found using 100 m gridded data to represent neighbourhood scales. Vegetation and

**TABLE 2** | Advantages and disadvantages of crowdsourced data.

Advantages	Disadvantages
Crowdsourced datasets often achieve a higher spatial resolution across a city	Distribution of stations is skewed towards more densely populated regions. Additionally, it is likely that more sensors are located in affluent areas, contributing to urban climate injustice in analyses and interpretation
Citizen weather stations are located in and around where people occupy, live, and work, providing relevant data for assessing thermal exposure in the immediate environment of residents	Siting of stations is uncontrolled. Stations are often placed close to buildings, walls or other heat-emitting materials causing a bias in the readings
Driven by the low cost, crowdsourced sensor networks are established through decentralised effort and are maintained by the public	Decentralized effort and reduced maintenance also often translate to the lack of metadata regarding the sensor location and quality assurance. Additionally, the low cost of sensors suggests lower accuracy and more likeliness for sensor drift
Citizen weather stations enables more citizen involvement and enablement	Citizen engagement presents challenges with regards to data ownership, privacy, and access. In the case of Netatmo sensors, for instance, data access is limited to the live web portal and therefore prior planning is needed for data collection. Historical data not publicly available

impervious classes were compared per region (**Figures 11, 12**). These classes were defined by the ranges 0–0.4, 0.4–0.7 and 0.7–1 of the aggregate vegetation and impervious fractions. All vegetation and impervious classes were represented in all regions. Note that the impervious fraction is not simply the opposite of the vegetation fraction; there are other surface cover fractions which are not included in either of these categories. These include water bodies and swimming pools.

No clear trend was observed in the maximum temperatures, although in the central region areas with increased impervious fraction and reduced vegetation fraction recorded higher temperatures for both warm and cool day maxima. In general, minimum temperatures are higher in areas of high impervious fraction, on both warm and cool days. This is likely due to increased heat absorption and thermal inertia of impervious materials and increased surface temperatures (Masson et al., 2020). Thermal inertia has been observed to have a stronger influence on UHI than anthropogenic heat and population, causing increased overnight temperatures as observed here on both warm and cool days (Varquez and Kanda 2018).

This is expected to lead to reduced minimum temperatures in areas of high vegetation fraction, consistent with observations by Sharifi and Lehmann (2014) and Varquez and Kanda (2018), however this is not as clearly observed. There is a slight disruption in this trend in the coastal and central regions on warm days, and the central region on cool days. This may be due to the high impervious fraction in this region; the presence of impervious surfaces can significantly reduce the cooling effect of vegetation which may be causing the anomaly (Myint et al., 2010; Bartesaghi-Koc et al., 2019). However, the high variability near the coast and the reduced representation of the highly vegetated areas may have introduced a bias.

Across all urban design characteristic comparisons, a clear trend is observed between regions. Maximum temperatures increase with distance from the coast, and minimum temperatures decrease with distance from the coast, indicating an increased diurnal range inland compared to the coastal region, as observed in **Figure 8**. This is clear regardless of which urban design characteristic is being assessed, which indicates that the distance from the coast has the largest impact on air temperature across the city. The distance from the coast is the

key factor affecting the impact of the sea breeze, however there is also interplay of topography and land use. Los Angeles has a similar geography to Sydney with both coastal and mountainous boundaries and similar effects have been observed in terms of UHI dynamics, including a dominating role played by sea breeze, vegetation having a positive effect on overnight UHI and urban fraction having a negative effect on UHI (Vahmani and Ban-Weiss 2016).

## THE APPLICABILITY OF CROWDSOURCED DATA AND HIGH-RESOLUTION LAND USE DATA

The crowdsourced data used in this study has provided a novel understanding of the complexity of Sydney's urban climate, presenting a unique opportunity for infilling the measurements gaps across the city. However, crowdsourced data also presents certain shortcomings that require careful attention in data analysis.

**Table 2** lists a combination of conditions in crowdsourced data collection that can be considered as a source of error, or indeed a "feature" where thermal environment is assessed in the immediate environment of city dwellers, focusing on exposure where people reside and occupy. The high spatial resolution is the key driver for the use of crowdsourcing, but often comes at the cost of uneven distribution of stations in cities, leading to spatial and socio-economic bias in the data. To avoid this, crowdsourced campaigns may be complemented with centralized efforts to place additional stations in areas of low representation, or a threshold of sensors may be required in each region to remove statistical outliers. Furthermore, collecting data in the proximity of where people live and occupy is key to understanding thermal exposure, which is more helpful for estimating health impacts and planning for future infrastructure. However, this also influences data collection due to the proximity of other heat-emitting materials such as nearby walls or buildings. Each of these difficulties must be addressed when assessing the data quality and interpreting the data as discussed in *Quality Control*.

The low cost of the sensors, which leads to higher number of measurement sites as well as citizen engagements, can further result

in a lack of quality assurance, calibration, or testing, and since sensors are set up by the public, there is a lack of metadata. An understanding of how these stations may be sited is required to interpret the data. Additionally, more controlled-environment and long-term experiments can be planned, such that we fully quantify the uncertainties associated with low-cost weather stations.

Another key part of interpreting the crowdsourced data is understanding the local environment at each site. Various datasets describing urban characteristics can be overlayed with crowdsourced measurements, including the LCZ classifications that aim to represent urban form and fabric in a universal way. LCZ maps give an indication of the context of city in relation to other built environments worldwide, however, are not sufficient for identifying individual urban design characteristics that modify urban microclimate. Each LCZ represents a range in height, vegetation cover, sky view factor, and so forth, which provide limited comparison with regards to microclimate variabilities when evaluating one city with only a few dominant LCZ types. To address this, emerging high-resolution urban datasets can be used to describe surface cover and urban morphology. Overlaying such datasets with LCZ maps and crowdsourced measures assist in providing a better characterisation of each area more specific to a city and provide further insight into the influences on the urban microclimate.

## CONCLUSION

In this study, we used quality controlled crowdsourced data from over 500 citizen weather stations to explore intra-urban variabilities in air temperature during a Sydney summer, totalling 2.3 million data points. Crowdsourcing has provided a higher spatial resolution climate dataset for Sydney which has allowed a clearer understanding of the local climate at a finer scale. Overlaying datasets and urban classifications (such as LCZs and building-level urban data) have been explored to identify the key drivers of intra-urban variability.

The key findings from this paper are:

- Crowdsourced air temperature data and the combination of land use and land cover data layers have provided novel insight into the air temperature distribution across a complex coastal city, by investigating the contribution of both geographic and urbanised influences on intra-urban variability in air temperature.
- The strongest impact on air temperature was distance from the coast causing an increase in diurnal temperature range at locations further inland.
- Intra-urban variability was observed both within LCZs and between different LCZs.
- Increasing building density and height resulted in a reduced diurnal temperature range, and increasing impervious fraction resulted in increased temperatures.

A comparison of crowdsourced data with reference data indicated that on warm days citizen weather stations continuously observed increased temperatures throughout the day, whereas on cool days the diurnal range of crowdsourced temperatures was smaller than that of

reference stations. The crowdsourced overnight temperatures were higher for all stations across both warm and cool days. These differences are likely due to the siting of citizen weather stations closer to materials with high thermal inertia, solar radiation exposure, and in areas with decreased ventilation.

The impact of the sea breeze and moderating influence of the ocean has been identified by the difference in air temperature between the inland, central and coastal regions. This coastal effect dominated over all other impacts on local climate, and as such other possible influences on air temperature were compared considering distance from the coast. There was very little variability in the cool day maxima across all urban characteristics due to the increased cloud cover and precipitation on cool days. The significant impact of distance from the coast has been assessed by splitting the city into regions, however analysis of the coastal region still remains a challenge due to the varying effect of the sea breeze across this region. Further investigation into sea breeze flow is necessary to fully understand the urban climate in this area.

Crowdsourced data typically come with some limitations which require critical evaluation of the information collected. Despite the higher spatial resolution, not all regions are represented equally; the inner-city areas have a significantly higher number of stations than the outer areas due to a combination of cost and population density. To ensure the entire population is equally represented when using data such as this, it may be necessary to supplement with additional sensors in some areas.

## DATA AVAILABILITY STATEMENT

Publicly available datasets were analyzed in this study. This data can be found here: Crowdsourced air temperature and humidity data were obtained from Netatmo “Smart Home Weather Stations” across Sydney. The sensors collect and display real-time weather data including temperature, humidity, and barometric pressure which, should the user agree, is displayed on the Netatmo Weathermap web portal (<https://weathermap.netatmo.com>). Historical data is not available; data for this study has been collected *via* quarter-hourly scraping of the Weathermap over Dec 2020–Feb 2021, leading to over two million air temperature readings collected.

## AUTHOR CONTRIBUTIONS

NN and MH conceived of the presented idea. ML obtained the crowdsourced data through web scraping and provided processed land-use data with help from WM and KB. JP analysed the data and wrote the manuscript with support from NN, MH, ML, and GU.

## FUNDING

This project is supported through funding from the Australian research council (arc) Centre of excellence for climate extremes (clex) (CE170100023). JP was funded on a CLEX undergraduate scholarship.

## REFERENCES

- Bartesaghi-Koc, C., Osmond, P., and Peters, A. (2019). Spatio-temporal Patterns in green Infrastructure as Driver of Land Surface Temperature Variability: The Case of Sydney. *Int. J. Appl. Earth Observation Geoinformation* 83, 101903. doi:10.1016/j.jag.2019.101903
- Basara, J. B., Illston, B. G., Fiebrich, C. A., Browder, P. D., Morgan, C. R., McCombs, A., Bostic, J. P., McPherson, R. A., Schroeder, A. J., and Crawford, K. C. (2011). The Oklahoma City Micronet. *Meteorol. Appl.* 18 (3), 252–261. doi:10.1002/met.189
- Battista, G., de Lieto Vollaro, E., Ocioñ, P., and Vallati, A. (2021). Effect of Mutual Radiative Exchange between the Surfaces of a Street canyon on the Building thermal Energy Demand. *Energy* 226, 120346. doi:10.1016/j.energy.2021.120346
- Bechtel, B., Alexander, P., Böhner, J., Ching, J., Conrad, O., Feddema, J., Mills, G., See, L., and Stewart, I. (2015). Mapping Local Climate Zones for a Worldwide Database of the Form and Function of Cities. *Ijgi* 4 (1), 199–219. doi:10.3390/ijgi4010199
- Benjamin, K. (2019). *Crowdsourcing Urban Temperature Data for Building Energy and Human Health Estimation*. Reading, UK: Masters thesis, University of Reading.
- Bureau of Meteorology (2021). Greater Sydney in Summer 2020-21: Cooler Than Recent Years' Bureau of Meteorology, viewed 11/05/21, Available at: <http://www.bom.gov.au/climate/current/season/nsw/sydney.shtml>.
- Bureau of Meteorology (1997). *Observation Specification No. 2013.1: Guidelines for the Siting and Exposure of Meteorological Instruments and Observing Facilities*. Available at: [http://www.bom.gov.au/climate/cdo/about/observation\\_specification\\_2013.pdf](http://www.bom.gov.au/climate/cdo/about/observation_specification_2013.pdf) Accessed August 20, 2021.
- Chapman, L., Bell, C., and Bell, S. (2017). Can the Crowdsourcing Data Paradigm Take Atmospheric Science to a New Level? A Case Study of the Urban Heat Island of London Quantified Using Netatmo Weather Stations. *Int. J. Climatol.* 37 (9), 3597–3605. doi:10.1002/joc.4940
- Ching, J., Mills, G., Bechtel, B., See, L., Feddema, J., Wang, X., Ren, C., Brousse, O., Martilli, A., Neophytou, M., Mouzourides, P., Stewart, I., Hanna, A., Ng, E., Foley, M., Alexander, P., Aliaga, D., Niyogi, D., Shreevastava, A., Bhalachandran, P., Masson, V., Hidalgo, J., Fung, J., Andrade, M., Baklanov, A., Dai, W., Milcinski, G., Demuzere, M., Brunsell, N., Pesaresi, M., Miao, S., Mu, Q., Chen, F., and Theeuwes, N. (2018). WUDAPT: An Urban Weather, Climate, and Environmental Modeling Infrastructure for the Anthropocene. *Bull. Am. Meteorol. Soc.* 99 (9), 1907–1924. doi:10.1175/bams-d-16-0236.1
- Christen, A., Oke, T., Grimmond, S., Steyn, D., and Roth, M. (2013). 35 Years of Urban Climate Research at the 'Vancouver-Sunset' Flux tower. *FluxLetter*. doi:10.14288/1.0103588
- Dean, A., and Green, D. (2018). Climate Change, Air Pollution and Human Health in Sydney, Australia: A Review of the Literature. *Environ. Res. Lett.* 13 (5), 053003. doi:10.1088/1748-9326/aac02a
- Demuzere, M., Kittner, J., and Bechtel, B. (2021). LCZ Generator: A Web Application to Create Local Climate Zone Maps. *Front. Environ. Sci.* 9. doi:10.3389/fenvs.2021.637455
- Fenner, D., Meier, F., Bechtel, B., Otto, M., and Scherer, D. (2017). *Intra and Inter-local Climate Zone'variability of Air Temperature as Observed by Crowdsourced Citizen Weather Stations*. Berlin, Germany: Technische Universität Berlin. doi:10.14279/depositonce-10378
- Hirsch, A. L., Evans, J. P., Thomas, C., Conroy, B., Hart, M. A., Lipson, M., and Ertler, W. (2021). Resolving the Influence of Local Flows on Urban Heat Amplification during Heatwaves. *Environ. Res. Lett.* 16, 064066. doi:10.1088/1748-9326/ac0377
- Jiang, N., Scorgie, Y., Hart, M., Riley, M. L., Crawford, J., Beggs, P. J., Edwards, G. C., Chang, L., Salter, D., and Virgilio, G. D. (2017). Visualising the Relationships between Synoptic Circulation Type and Air Quality in Sydney, a Subtropical Coastal-basin Environment. *Int. J. Climatol.* 37 (3), 1211–1228. doi:10.1002/joc.4770
- Johansson, E. (2006). Influence of Urban Geometry on Outdoor thermal comfort in a Hot Dry Climate: A Study in Fez, Morocco. *Building Environ.* 41 (10), 1326–1338. doi:10.1016/j.buildenv.2005.05.022
- Khan, H. S., Santamouris, M., Paolini, R., Caccetta, P., and Kassomenos, P. (2021). Analyzing the Local and Climatic Conditions Affecting the Urban Overheating Magnitude during the Heatwaves (HWs) in a Coastal City: A Case Study of the Greater Sydney Region. *Sci. Total Environ.* 755, 142515. doi:10.1016/j.scitotenv.2020.142515
- Livada, I., Synnefa, A., Haddad, S., Paolini, R., Garshasbi, S., Ulpiani, G., Fiorito, F., Vassilakopoulou, K., Osmond, P., and Santamouris, M. (2019). Time Series Analysis of Ambient Air-Temperature during the Period 1970–2016 over Sydney, Australia. *Sci. Total Environ.* 648, 1627–1638. doi:10.1016/j.scitotenv.2018.08.144
- Martilli, A., Krayenhoff, E. S., and Nazarian, N. (2020). Is the Urban Heat Island Intensity Relevant for Heat Mitigation Studies? *Urban Clim.* 31, 100541. doi:10.1016/j.uclim.2019.100541
- Masson, V., Lemonsu, A., Hidalgo, J., and Voogt, J. (2020). Urban Climates and Climate Change. *Annu. Rev. Environ. Resour.* 45, 411–444. doi:10.1146/annurev-environ-012320-083623
- Meier, F., Fenner, D., Grassmann, T., Otto, M., and Scherer, D. (2017). Crowdsourcing Air Temperature from Citizen Weather Stations for Urban Climate Research. *Urban Clim.* 19, 170–191. doi:10.1016/j.uclim.2017.01.006
- Muller, C. L., Chapman, L., Grimmond, C. S. B., Young, D. T., and Cai, X. (2013). Sensors and the City: a Review of Urban Meteorological Networks. *Int. J. Climatol.* 33 (7), 1585–1600. doi:10.1002/joc.3678
- Myint, S. W., Brazel, A., Okin, G., and Buyantuyev, A. (2010). Combined Effects of Impervious Surface and Vegetation Cover on Air Temperature Variations in a Rapidly Expanding Desert City. *GIScience & Remote Sensing* 47 (3), 301–320. doi:10.2747/1548-1603.47.3.301
- Nopoly, A., Grassmann, T., Meier, F., and Fenner, D. (2018). Development and Application of a Statistically-Based Quality Control for Crowdsourced Air Temperature Data. *Front. Earth Sci.* 6, 118. doi:10.3389/feart.2018.00118
- Nazarian, N., and Kleissl, J. (2015). CFD Simulation of an Idealized Urban Environment: Thermal Effects of Geometrical Characteristics and Surface Materials. *Urban Clim.* 12 (June), 141–159. doi:10.1016/j.uclim.2015.03.002
- Oke, T. R., Mills, G., Christen, A., and Voogt, J. A. (2017). *Urban Climates*. Cambridge University Press.
- Oke, T. R. (1981). Canyon Geometry and the Nocturnal Urban Heat Island: Comparison of Scale Model and Field Observations. Cambridge, UK. *J. Climatol.* 1 (3), 237–254. doi:10.1002/joc.3370010304
- Pantelic, J., Nazarian, N., Meggers, F., Lee, J. K. W., Miller, C., and Licinia, D. D. (2021). *Transformational IoT Technologies for Air Quality and Thermal Comfort at the Urban, Building, and Human Scales*. Berkeley, California, USA. Submitted to Sustainable Cities and Society.
- Perkins, S. E., Alexander, L. V., and Nairn, J. R. (2012). Increasing Frequency, Intensity and Duration of Observed Global Heatwaves and Warm Spells. *Geophys. Res. Lett.* 39, 20. doi:10.1029/2012gl053361
- Poutiainen, J., Saltikoff, E., Dabberdt, W. F., Koistinen, J., and Turtiainen, H. (2006). "December Helsinki Testbed: A New Open Facility to Test Instrumentation Technology for Atmospheric Measurements," in *Extended Abstracts, WMO Technical Conf. On Meteorological and Environmental Instruments and Methods of Observation* (P. 13 (Geneva, Switzerland: World Meteorological Society, Instruments and Observing Methods RepWMO/TD-1354).
- PSMA Australia (2020). Geoscape Surface Cover (v1.6) and Buildings (v2.0) Datasets. Available at: <https://geoscape.com.au>.
- Rotach, M. W., Vogt, R., Bernhofer, C., Batchvarova, E., Christen, A., Clappier, A., Feddersen, B., Gryning, S. E., Martucci, G., Mayer, H., and Mitev, V. (2005). BUBBLE—an Urban Boundary Layer Meteorology Project. *Theor. Appl. Climatology* 81 (3), 231–261. doi:10.1007/s00704-004-0117-9
- Rousseeuw, P. J., and Croux, C. (1993). Alternatives to the Median Absolute Deviation. *J. Am. Stat. Assoc.* 88 (424), 1273–1283. doi:10.1080/01621459.1993.10476408
- Santamouris, M., Haddad, S., Fiorito, F., Osmond, P., Ding, L., Prasad, D., Zhai, X., and Wang, R. (2017). Urban Heat Island and Overheating Characteristics in Sydney, Australia. An Analysis of Multiyear Measurements. *Sustainability* 9 (5), 712. doi:10.3390/su9050712
- Schroeder, J. L., Burgett, W. S., Haynie, K. B., Sonmez, I., Skwira, G. D., Doggett, A. L., and Lipe, J. W. (2005). The West Texas Mesonet: a Technical Overview. *J. Atmos. Oceanic Techn.* 22 (2), 211–222. doi:10.1175/jtech-1690.1
- Sharifi, E., and Lehmann, S. (2014). *Comparative Analysis of Surface Urban Heat Island Effect in central Sydney*. Canadian Center of Science and Education. Journal of Sustainable Development, 2014; 7 (3), 23–34.
- Skarbit, N., Stewart, I. D., Unger, J., and Gál, T. (2017). Employing an Urban Meteorological Network to Monitor Air Temperature Conditions in the 'local

- Climate Zones' of Szeged, Hungary. *Int. J. Climatol.* 37, 582–596. doi:10.1002/joc.5023
- Stewart, I. D., and Oke, T. R. (2012). Local Climate Zones for Urban Temperature Studies. *Bull. Am. Meteorol. Soc.* 93 (12), 1879–1900. doi:10.1175/bams-d-11-00019.1
- Vahmani, P., and Ban-Weiss, G. A. (2016). Impact of Remotely Sensed Albedo and Vegetation Fraction on Simulation of Urban Climate in WRF-Urban Canopy Model: A Case Study of the Urban Heat Island in Los Angeles. *J. Geophys. Res. Atmos.* 121 (4), 1511–1531. doi:10.1002/2015jd023718
- Vaneckova, P., Hart, M. A., Beggs, P. J., and De Dear, R. J. (2008). Synoptic Analysis of Heat-Related Mortality in Sydney, Australia, 1993–2001. *Int. J. Biometeorol.* 52 (6), 439–451. doi:10.1007/s00484-007-0138-z
- Varentsov, M. I., Konstantinov, P. I., Shartova, N. V., Samsonov, T. E., Kargashin, P. E., Varentsov, A. I., Fenner, D., and Meier, F. (2020). Urban Heat Island of the Moscow Megacity: The Long-Term Trends and New Approaches for Monitoring and Research Based on Crowdsourcing Data. *IOP Conf. Ser. Earth Environ. Sci.* 606, 1012063. doi:10.1088/1755-1315/606/1/012063
- Varquez, A. C., and Kanda, M. (2018). Global Urban Climatology: a Meta-Analysis of Air Temperature Trends (1960–2009). *npj Clim. Atmos. Sci.* 1 (1), 1–8. doi:10.1038/s41612-018-0042-8
- Venter, Z. S., Chakraborty, T., and Lee, X. (2021). Crowdourced Air Temperatures Contrast Satellite Measures of the Urban Heat Island and its Mechanisms. *Sci. Adv.* 7 (22), eabb9569. doi:10.1126/sciadv.eabb9569
- Venter, Z. S., Brousse, O., Esau, I., and Meier, F. (2020). Hyperlocal Mapping of Urban Air Temperature Using Remote Sensing and Crowdsource Weather Data. *Remote Sensing Environ.* 242, 111791. doi:10.1016/j.rse.2020.111791
- Wang, K., Li, Y., Luo, Z., Yin, S., and Chan, P. W. (2018). Harmonic Analysis of 130-Year Hourly Air Temperature in Hong Kong: Detecting Urban Warming from the Perspective of Annual and Daily Cycles. *Clim. Dyn.* 51 (1–2 July 1), 613–625. doi:10.1007/s00382-017-3944-y
- Warren, E. L., Young, D. T., Chapman, L., Muller, C., Grimmond, C. S., and Cai, X. M. (2016). The Birmingham Urban Climate Laboratory-A High Density, Urban Meteorological Dataset, from 2012–2014. *Sci. Data* 3 (1), 160038–8. doi:10.1038/sdata.2016.38
- Conflict of Interest:** The authors declare that the research was conducted in the absence of any commercial or financial relationships that could be construed as a potential conflict of interest.
- Publisher's Note:** All claims expressed in this article are solely those of the authors and do not necessarily represent those of their affiliated organizations, or those of the publisher, the editors and the reviewers. Any product that may be evaluated in this article, or claim that may be made by its manufacturer, is not guaranteed or endorsed by the publisher.

Copyright © 2021 Potgieter, Nazarian, Lipson, Hart, Ulpiani, Morrison and Benjamin. This is an open-access article distributed under the terms of the Creative Commons Attribution License (CC BY). The use, distribution or reproduction in other forums is permitted, provided the original author(s) and the copyright owner(s) are credited and that the original publication in this journal is cited, in accordance with accepted academic practice. No use, distribution or reproduction is permitted which does not comply with these terms.



# Towards a Living Lab for Enhanced Thermal Comfort and Air Quality: Analyses of Standard Occupancy, Weather Extremes, and COVID-19 Pandemic

**Giulia Ulpiani<sup>1,2</sup>, Negin Nazarian<sup>1,3,4\*</sup>, Fuyu Zhang<sup>1</sup> and Christopher J. Pettit<sup>1,4</sup>**

<sup>1</sup>School of Built Environment, University of New South Wales, Sydney, NSW, Australia, <sup>2</sup>Climate Change Research Centre, UNSW, Sydney, NSW, Australia, <sup>3</sup>ARC Centre of Excellence for Climate Extremes, Sydney, NSW, Australia, <sup>4</sup>City Futures Research Centre, University of New South Wales, Sydney, NSW, Australia

## OPEN ACCESS

### Edited by:

Marco Casazza,  
University of Naples Parthenope, Italy

### Reviewed by:

Asniza Hamimi Abdul Tharim,  
MARA University of Technology,  
Malaysia  
Pontip Nimlyat,  
University of Jos, Nigeria

### \*Correspondence:

Negin Nazarian  
[n.nazarian@unsw.edu.au](mailto:n.nazarian@unsw.edu.au)

### Specialty section:

This article was submitted to  
Environmental Informatics and Remote  
Sensing,  
a section of the journal  
*Frontiers in Environmental Science*

**Received:** 16 June 2021

**Accepted:** 02 November 2021

**Published:** 25 November 2021

### Citation:

Ulpiani G, Nazarian N, Zhang F and  
Pettit CJ (2021) Towards a Living Lab for  
Enhanced Thermal Comfort and Air  
Quality: Analyses of Standard  
Occupancy, Weather Extremes, and  
COVID-19 Pandemic.

*Front. Environ. Sci.* 9:725974.  
doi: 10.3389/fenvs.2021.725974

Maintaining indoor environmental (IEQ) quality is a key priority in educational buildings. However, most studies rely on outdoor measurements or evaluate limited spatial coverage and time periods that focus on standard occupancy and environmental conditions which makes it hard to establish causality and resilience limits. To address this, a fine-grained, low-cost, multi-parameter IoT sensor network was deployed to fully depict the spatial heterogeneity and temporal variability of environmental quality in an educational building in Sydney. The building was particularly selected as it represents a multi-use university facility that relies on passive ventilation strategies, and therefore suitable for establishing a living lab for integrating innovative IoT sensing technologies. IEQ analyses focused on 15 months of measurements, spanning standard occupancy of the building as well as the Black Summer bushfires in 2019, and the COVID-19 lockdown. The role of room characteristics, room use, season, weather extremes, and occupancy levels were disclosed via statistical analysis including mutual information analysis of linear and non-linear correlations and used to generate site-specific re-design guidelines. Overall, we found that 1) passive ventilation systems based on manual interventions are most likely associated with sub-optimum environmental quality and extreme variability linked to occupancy patterns, 2) normally closed environments tend to get very unhealthy under periods of extreme pollution and intermittent/protracted disuse, 3) the elevation and floor level in addition to room use were found to be significant conditional variables in determining heat and pollutants accumulation, presumably due to the synergy between local sources and vertical transport mechanisms. Most IEQ inefficiencies and health threats could be likely mitigated by implementing automated controls and smart logics to maintain adequate cross ventilation, prioritizing building airtightness improvement, and appropriate filtration techniques. This study supports the need for continuous and capillary monitoring of different occupied spaces in educational buildings to compensate for less perceivable threats, identify the room for improvement, and move towards healthy and future-proof learning environments.

**Keywords:** environmental sensing and monitoring, thermal comfort, indoor air quality, Internet of Things, living lab, COVID-19, bushfire, educational buildings

## INTRODUCTION

It is widely acknowledged that, in developed countries, people spend the majority of their time indoors. In the United States, it is estimated that 87% of the time is allocated to indoor activities (Klepeis et al., 2001), while in Australia, the percentage reaches 90% (Australian Government, 2020). These figures are expected to soar in the next decades as a consequence of the progressive dispossession of outdoor public spaces caused by 1) deterioration of urban liveability, 2) escalation of overheating episodes, and 3) intensification of weather extremes (IPCC Fifth Assessment Report (AR5), 2013; Santamouris, 2020). This poses an urgent need for providing adequate indoor environmental quality (IEQ), specifically in buildings that host vulnerable populations and a high density of users, or those whose occupants require long-lasting preservation of attention, productivity, and health. Educational buildings feature all these criteria and thus represent a priority target for IEQ assessments (Eide et al., 2010; Simons et al., 2010; Mendell et al., 2013).

In educational facilities, such as schools and universities, maximizing students' and staff's performance while preventing absenteeism is a basic, yet challenging requirement particularly due to the wide range of possible metabolic rates, clothing levels, and activities that typify the user category (Havenith, 2007; Kim et al., 2009). These variables arbitrate whether a defined indoor air quality and thermal condition can negatively impact the occupants' cognitive performance by altering the decision-making ability (Satish et al., 2012) or productivity (Wyon, 2004; Ebenstein et al., 2016). Beyond comfort and efficiency, multiple studies on educational facilities indicate that failure to manage indoor air quality could increase the risk of acute and chronic effects on students' physical and mental health (Loh and Andaman; Annesi-Maesano et al., 2013; Andualem et al., 2019). Indoor air pollution impairs cognitive functions, damages the nervous system, increases ischaemic stroke risk, depression, and mood disorders in adult populations (Calderón-Garcidueñas et al., 2015; Taylor et al., 2015) and even more in infants and youngsters (Gent et al., 2003). Further, extensive evidence demonstrates the negative health impacts of different pollutants indoors, such as ozone ( $O_3$ ) and fine particles (Mi et al., 2006; Zhao et al., 2015), as well as nitrogen dioxide ( $NO_2$ ), carbon monoxide (CO), volatile organic compounds (VOCs) and benzene, toluene, ethylbenzene, xylenes (BTEX) (Chen et al., 2000; Evrard et al., 2006). An overview of challenges and impacts can be found in (Chatzidiakou et al., 2012).

Comparatively underexplored are the damaging effects of extreme ambient environmental stressors, such as heatwaves or wildfires. These further exacerbate the range and severity of health deterioration (Saggu et al., 2018; Reid et al., 2019), but the topic-specific literature is sparse. The risk assessment of human exposure to health-threatening indoor environmental conditions, and consequently the choice of containment measures and risk prevention, are critical tasks that need to be adequately informed (Rocca et al., 2020). This further motivates a fine-grained, site-specific monitoring of exposure to environmental stressors (Nazarian and Lee, 2021) as well as smart control of rooms,

such that we compensate for less perceivable threats, passive ventilation inefficiencies, and excessive energy consumption.

A variety of studies reveals that occupants are rather insensitive to most Sick Building Syndrome (SBS) drivers. For instance, in Haverinen-Shaughnessy et al. (2015), ventilation rate, temperature, and hygiene of high contact surfaces manifested as health- and performance-threatening IEQ parameters in classrooms. A 70-school district in the United States was monitored during two academic years in terms of ambient air temperature (T), relative humidity (RH) and carbon dioxide ( $CO_2$ ). Settled dust and cleaning effectiveness, as well as student data (socioeconomic background, absenteeism, performance, and number of visits to school nurse) was recorded. Significant associations were stricken between high academic grades and levels of T and  $CO_2$  as well as between  $CO_2$ /culturable bacteria and medical visits due to respiratory or gastrointestinal symptoms. Furthermore, IEQ measurements and perception analyses in nine naturally ventilated schools in Athens, Greece (Dorizas et al., 2015) revealed that PM and  $CO_2$  levels were significantly and positively correlated with SBS symptoms, scholastic performance, and health symptoms. However, the personal perception of IAQ degradation was rather insensitive to increased levels of particulate matter, while being strongly correlated with temperature variations. This is in line with (Stazi et al., 2017), according to which temperature was the key driver for students' control actions on ventilation, while  $CO_2$  increments went unnoticed.

Other studies highlight that passive buildings, even those built upon sustainability principles, are prone to inadequate ventilation. Almeida and de Freitas (2014) verified the IEQ impacts of the rehabilitation of school buildings via retrofitting in Portugal. They monitored annual T, RH,  $CO_2$ , and ventilation rates in 24 classrooms across nine school buildings, out of which seven were retrofitted. Non-retrofitted buildings were compared against retrofitted schools with HVAC or natural/mechanical ventilation systems. Statistical analyses and simulations confirmed that 1) the ventilated schools were the best-performing, 2) non-retrofitted schools provided inadequate IEQ throughout the year, and 3) retrofitted classrooms were affected by the limited use of mechanical ventilation, thus experiencing serious overheating episodes. Further IEQ analyses in a secondary school Germany (Ortiz Perez et al., 2018) demonstrate the complexity of maintaining adequate IEQ levels in passively ventilated classrooms even in case of high frequency of ventilation, pointing towards the need for capillary monitoring and control of rooms, also for energy minimisation. The same inefficiency was found in passively ventilated school buildings in Italy (Schibuola and Tambani, 2020). An experimental campaign was carried out in wintertime in four classrooms having similar shape, size, occupancy pattern, windows type, and dimensions and the interlink between IAQ, ventilation rate, Hazard Index, and Cancer Risk was investigated. It was found that 1) in absence of appreciable internal pollution sources, the indoor concentrations of chemical pollutants were correlated to the corresponding outdoor concentrations and 2) manual operation of ventilation controls was insufficient to guarantee

acceptable IAQ levels over 24 h. To tackle such a need for smart ventilation in schools, a sense-and-act approach in a secondary school is proposed in (Stazi et al., 2017) where an automatic system opens and closes the hopper windows based on Humphreys' adaptive algorithm (Humphreys et al., 2013) with coefficients adjusted to the specific climate and CO<sub>2</sub> levels. The research was carried out in two similar and adjacent classrooms, one equipped with the automatic system, one left to manual operation. Results proved that CO<sub>2</sub> and T comfort levels easily surpassed the acceptable range in both classrooms, however, the automated system promptly restored acceptable levels, while control actions in the manually-operated classroom (particularly associated with CO<sub>2</sub> levels) were typically untimely. A similar approach was proposed in Sydney, Australia (Haddad et al., 2021), where two adjacent classrooms were characterized in terms of infiltration and ventilation rate, and were monitored to measure thermal comfort and air quality during the school year. One room only was equipped with a cloud-connected, demand-controlled mechanical ventilation system. Under automatic control of air extraction, CO<sub>2</sub> levels were largely maintained within comfortable and attention-preserving levels. Peak values were shaved by nearly 70% as compared to the free-running twin classroom.

Previous studies support the need for high spatial and temporal resolution monitoring of IEQ in educational buildings to track its distinctive variability, which can then feed into human-centric and automated control actions for enhanced air quality and thermal comfort. So far, however, limited studies have deployed expansive sensor networks that also provide a long-term assessment of educational buildings for different environmental conditions and occupancy patterns. The emergence of low-cost, internet-enabled environmental sensors aims to address this shortcoming, establishing educational buildings as living labs for integrating innovative sensing, data analytics, and automated control methods that enhance IEQ. An example of such large-scale Internet-of-Things (IoT) sensor deployment in schools is seen in (Palacios Temprano et al., 2020), where 280 classrooms hosting nearly 10,000 children are continuously monitored for 5 years. Preliminary results reveal how indoor climate conditions differ considerably across classrooms and throughout the academic year, indicating that sensors need to be installed in each individual classroom and for at least one academic year to build up accurate, longitudinal IEQ assessments and capture causal links. The heterogeneity of IEQ is further exacerbated in university buildings - where occupants are more diverse (encompassing students, academic, professional, and management staff, and visitors) and follow a less-regulated occupancy schedule compared to primary and secondary schools. IoT environmental sensing can be used to detect this distinctive variability and transform it into tailor-made local control actions. An example is described in (Luo et al., 2021), where the authors demonstrate that IoT networks implemented locally can help determine the natural ventilation potential and its optimal utilization throughout the year.

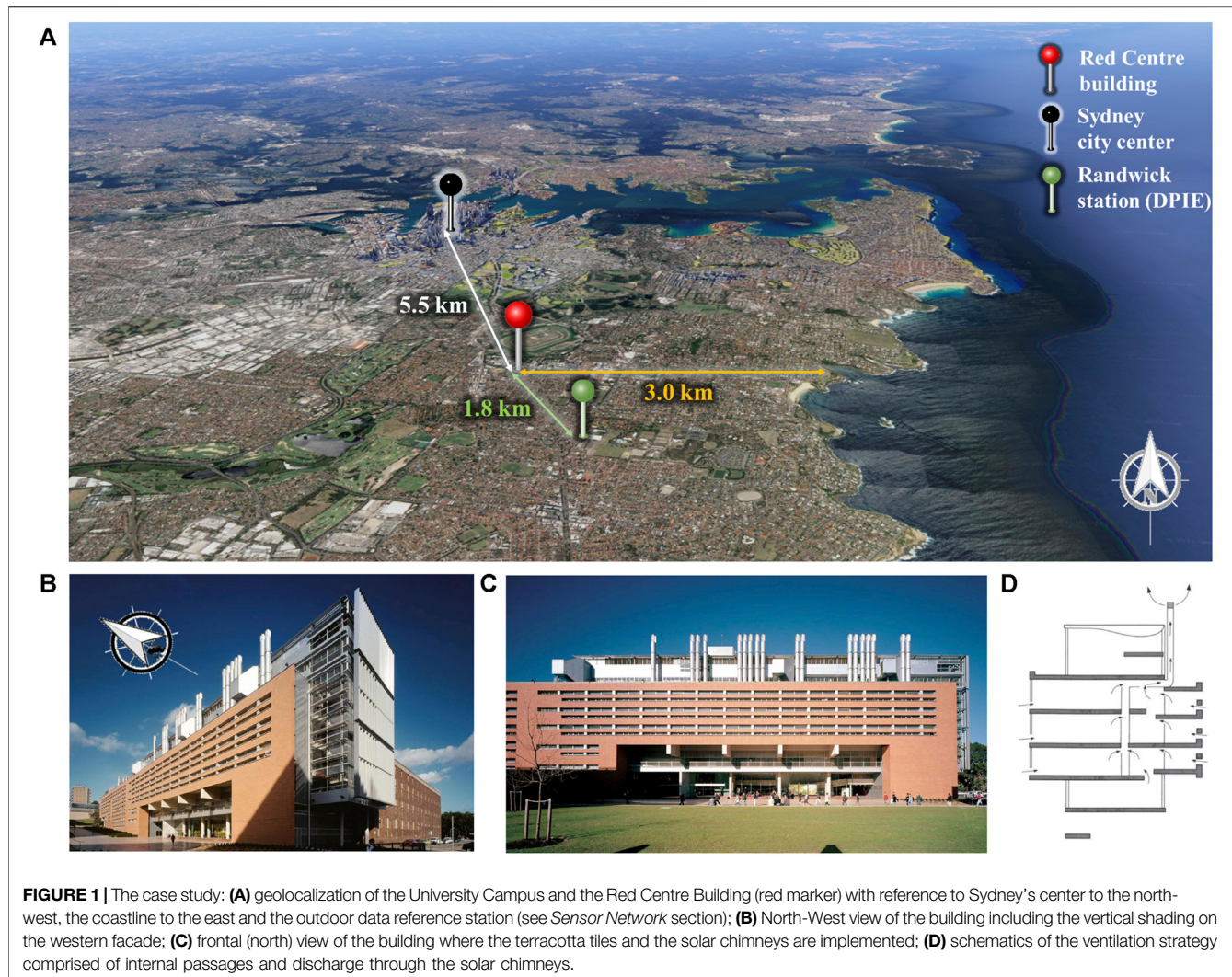
The present study aims to address the need for comprehensive and continuous monitoring of IEQ, and is novel in three main aspects. First, it applies a fine-grained IoT monitoring approach by setting up a capillary indoor sensor network in a designated

university building, looking not just at classrooms and offices but at all occupied spaces including labs, meeting rooms, and print rooms. By profiling the IEQ behaviour of different room types on account of orientation, floor level, A/C provisions, and access to environmental controls, this approach makes it possible to strike associations between microenvironmental characteristics and IEQ preservation, thus eradicating the misconception of one-fits-all IEQ solutions for highly variegated educational environments. Second, it investigates not only seasonal variabilities, but also behavioural and weather extremes by comparing the statistical behaviour of the monitored building under standard occupancy against that under the 2019/2020 catastrophic bushfire season in Australia as well as the COVID-19 lockdown period. Lastly, this study targets an IEQ-sensitive subclass of educational buildings: low-tech university buildings, designed based on natural ventilation and novel design practices committed to sustainability principles. Despite these intentions, a post-occupancy user satisfaction survey revealed that the building (the Red Centre, University of New South Wales, Sydney) ranked third from the bottom amongst 30 institutional and commercial buildings throughout 11 countries (Baird, 2013). Understanding the reasons behind its poor IEQ performance is key to delivering good practices and strategies for other buildings alike. Furthermore, COVID-19 pandemic has prompted renewed interest in the assessment of deficient indoor air quality conditions, especially in educational buildings. Notably, recent studies point to the need for indoor air quality monitoring and prediction solutions based on IoT and machine learning capabilities (Mumtaz et al., 2021) as well as reassessing ventilation protocols (Alonso et al., 2021; Meiss et al., 2021). Accordingly, we further discuss the insight gathered from the data collected during the COVID-19 pandemic.

In the following section (*Materials and Methods* section), the case study is presented and critically analysed, followed by a detailed description of the experimental method, the sensor network and the research framework in light of relevant international and Australian standards. The outcomes are presented in the *Results* section, broken down into general time trends, site characterization, and distinct patterns under non-nominal conditions (bushfires, lockdown). By means of statistical analysis, including mutual information analysis of correlation, we investigate the site-specific IEQ performance across different seasons and quantify the proclivity to extreme events. We use the Heat Index to merge the effects of temperature and humidity and delineate heat safe conditions. We further perform mutual information analysis to look into linear and nonlinear correlations and to interrogate the role of indoor and outdoor parameters in establishing heterogeneous IEQ conditions. *Discussion and Design Guidelines* and *Conclusion* sections discuss and summarize the main findings.

## MATERIALS AND METHODS

This section introduces the case study characteristics and the Internet-of-Things (IoT) strategy adopted to investigate its



spatio-temporal variability of indoor thermal comfort and air quality. IEQ metrics adopted for determining the performance of monitored spaces are also detailed.

## Case Study and Background Climate

This study is focused on establishing a living lab in the *Red Centre* building located in the Kensington campus of the University of New South Wales, Sydney, Australia (**Figure 1A**). The climatic subtype of Sydney is classified as temperate with warm summer and cold winter, according to the modified Köppen-Geiger classification system used by the Australian Bureau of Meteorology and based on a standard 30-years climatology (1961–1990) (BOM, 2021a, Australian Government). The campus area is largely influenced by moist, maritime airflows from subtropical anticyclonic cells to the west. Located in the Southern Hemisphere, the coldest month is July, with a mild average temperature (mean maximum temperature around 16°C and mean minimum temperature of 8°C) and sporadic frosts. The hottest month is January (mean maximum temperature around 26°C and mean minimum temperature just below 20°C), with

generally high daytime temperatures, quite distinctive diurnal oscillations ( $>7^{\circ}\text{C}$ ) and frequent warm, oppressive nights (BOM, 2021). Winter rainfall is derived primarily from frontal cyclones along the polar front, whereas summer precipitation is driven by convectional thunderstorm activity and enhanced by tropical cyclones. Statistically significant increasing tendency of average temperatures and extreme heat events have further been reported in recent years as compared to the beginning of the XXI century (Livada et al., 2019; Yun et al., 2020).

The Red Centre building is particularly selected as it was constructed considering a variety of natural ventilation strategies - including cross ventilation and air updraft by solar chimneys - that aim to integrate passive environmental control and energy efficiency principles during the design stage (**Figure 1D**). Air-conditioning (A/C) was restricted, except for high internal load areas like computer labs, meeting rooms, studios and for occupied areas in the basement (Baird and Marriage; Baird, 2003) where A/C was provided by single-split air conditioners. In absence of A/C provisions, a number of ceiling fans was installed, proportional to the floor area. The building stretches across 6

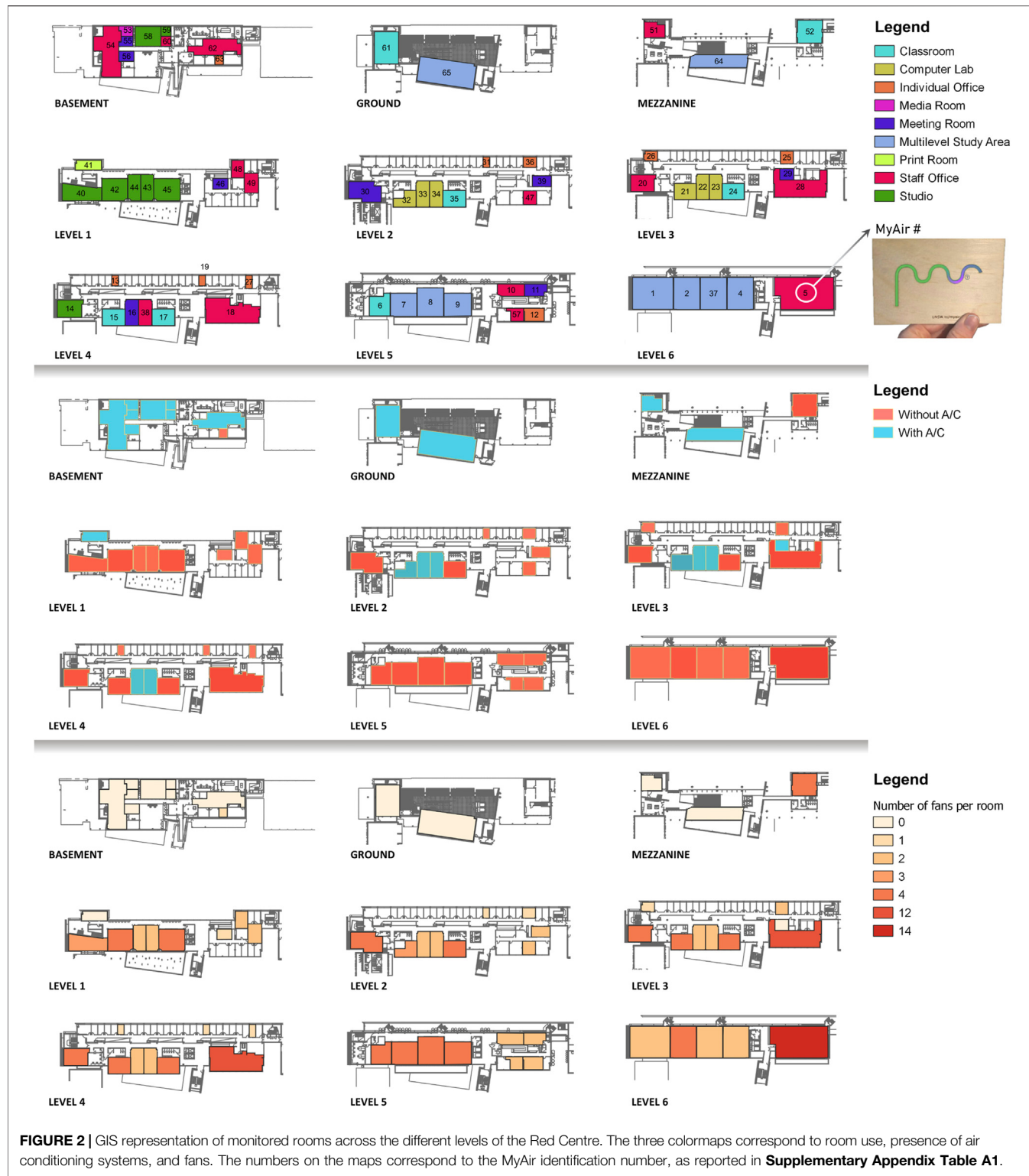


**FIGURE 2 |** GIS representation of monitored rooms across the different levels of the Red Centre. The three colormaps correspond to room use, presence of air conditioning systems, and fans. The numbers on the maps correspond to the MyAir identification number, as reported in **Supplementary Appendix Table A1**.

levels, on top of basement, ground level and mezzanine, each connected to the lower levels by complex architectures of air passages aimed at verticalized exhaust air expulsion. The building is 150 m long and 15.7–19.3 m wide, with a total internal area of about 16,000 m<sup>2</sup> (Baird, 2003) and an almost perfect alignment

with cardinal directions (<10° mismatch). Its strategic exposure to the north/south axis, and its limited depth along the east-west axis allows for a high proportion of natural lighting. Other passive sustainability principles include the protection of the west glazed facade with operational vertical shading devices (**Figure 1B**), and

the localized increase in thermal mass by making use of terracotta tiles on the northern facade (**Figure 1C**). The southern side is typically characterized by glazed facades with louvres, while the northern side typically features twin glazing “slots” to avoid glare and sunlight overexposure.

Despite the technical adroitness and the number of awards received for sustainable design, the Red Centre building largely fails at preserving IEQ. In 2015, a post-occupancy user satisfaction survey was conducted on 30 highly sustainable institutional and commercial buildings across 11 countries (Baird, 2013). Respondents were asked to rate 45 factors on a 7-point scale, including 1) operational aspects (e.g., space use, furniture, facilities), 2) environmental aspects (e.g., temperature and gradients, humidity, air quality), 3) lighting (e.g., natural/artificial light, glare), 4) noise (e.g., source and magnitude, frequency of undesired interruptions), 5) personal control (e.g., access to HVACs controls, to windows operation, to noise source switches), and 6) user satisfaction (e.g., comfort, health, productivity). The Red Centre building ranked 27th overall, 27th in terms of comfort, 23rd in terms of health preservation, and 25th in terms of perceived productivity and was noted as being excessively cold in winter, hot in summer and noisy. Most penalties were associated with excessively intense ventilation and wind whistling across the building. The survey emphasized that, with exception of image and lighting which scored well, most other IEQ aspects were poorly addressed and ventilation was substantially misapplied.

## Sensor Network

To investigate the reasons behind poor IEQ performance, a fine-grained IoT sensor network was established across the building from the basement to level 6, distributed in offices, classrooms, computer labs, studios, meeting rooms, print rooms, media rooms, and multilevel study areas. **Figure 2** shows a GIS representation of room locations on different floors and sensor locations within each surveyed room. **Supplementary Appendix Table A1** provides additional quantitative and qualitative information used to characterize the different rooms, including HVAC provisions (e.g., A/C units, fans), and window characteristics (e.g., facade coverage, shadings, operability). Sensor numbering in **Figure 2** corresponds to that in **Supplementary Appendix Table A1**.

The MyAir sensors deployed in this study represent an in-house, low-cost multi-parameter detector that includes an Arduino board with twin full-colour LEDs and three onboard sensors developed based on IoT paradigms. The sensors monitor four parameters: CO<sub>2</sub> (Non Dispersive Infrared sensor, T6713 Amphenol), TVOCs (metal oxide semiconductor sensor, CCS811 AMS), and T/RH (thermistor, BME280 Adafruit). All components are open source, including hardware schematics, firmware, server back-end, front-end and sensor data. The sensors were calibrated against the LST Heat Shield (ELR610M) and Aeroqual (Series 500) Portable Indoor Monitor, which are scientific grade sensor solutions for microclimate and air quality analysis. During calibration, the MyAirs returned reliable and stable measurements under a variety of thermodynamic conditions with recorded accuracy of  $\pm 0.9^{\circ}\text{C}$  for T,  $\pm 3.5\%$  for RH,  $\pm 3\%$  for CO<sub>2</sub> and  $\pm 30\text{ ppm}$

for TVOCs. Additionally, to inform the occupants' activities and decision making in real time, a LED-coloured indicator was added on the front side to reflect the indoor CO<sub>2</sub> level. The readings are sent to the real-time visualisation dashboard and stored in the cloud-based storage server (UNSW, 2021). 65 MyAir devices were originally installed in the Red Centre building in December 2018, at 1.5 m above the floor, away from doors, windows and A/C units. The sampling time was set to 15 s.

The monitoring campaign discussed in this paper represents the period between February 18th, 2019 and May 31st, 2020. This window is selected to analyse IEQ not only in a period with standard occupancy, but also the Black Summer bushfire season (peaking between November 2019 and January 2020) and the COVID lockdown period (March 31 - May 30, 2020). This extended analysis offers a unique opportunity for comparison and identification of IEQ anomalies associated with extreme natural hazards and occupancy patterns.

Within the first 2 weeks of monitoring, several sensors were deemed faulty (with regards to connection to the cloud server), vandalized, or stolen in public locations. Accordingly, compared to 65 sensors initially set up, a smaller number is used in each analysis presented, based on either having >75% readings across the whole monitoring campaign (38 sensors) or having >90% readings within comparative periods (23–42 sensors). The comparative periods last 1 month each and are hereinafter referred as 1) Term 1 (1–30 April 2019), Term 2 (1–31 July 2019), Bushfire (1–30 November 2019), and COVID-19 (1–31 May 2020). Term 1 and Term 2 indicate the academic terms with hottest and coldest outdoor conditions and are representative of standard occupancy levels. Bushfire is representative of late spring conditions exacerbated by catastrophic bushfires all around the city of Sydney. “Safer-at-home” orders were issued during this period. COVID-19 is representative of the pandemic “stay-at-home” period in autumn 2020. **Supplementary Appendix Table A2** collects the list of sensors used for the analysis of each considered time period.

Over the same period, outdoor data was taken at a NATA-accredited meteorological and air quality monitoring station less than 2 km away from the Red Centre building, established by the New South Wales (NSW) Department of Planning, Industry and Environment (DPIE) network. The outdoor measurements are included to 1) investigate the indoor-outdoor inter-parameter correlations, and 2) identify which rooms were more responsive to outdoor variations.

## IEQ Metrics

Here, we focus on indoor thermal comfort and air quality as metrics for IEQ. Thermal comfort is one of the most common metrics in IEQ analyses and found to be strongly correlated with occupants' working performance and productivity (Abdul Rahman et al., 2014), health and morbidity (Quinn et al., 2014) as well as perception of indoor air quality (Fang et al., 1998).

Comfort indices customarily account for six parameters affecting human thermoregulation (air temperature, air velocity, humidity, mean radiant temperature, metabolic rate and thermo-physical properties of clothing) and are

commonly calculated based on the heat balance of the human body (Potchter et al., 2018). In indoor environments, however, low wind speed and solar radiation is assumed, leading to the estimations of thermal comfort based on temperature and humidity measurements. Several temperature-humidity indices are well established internationally for indoor environments or in shade and have been extensively used in literature: the Heat Index (HI), the Thom's Discomfort Index (DI), and the Humidex (HD). Thom's DI fails under cold conditions, and climate-specific variants are better used when available (Moran et al., 1998; Chernev et al., 2012). HI is used operationally by the US National Weather Service (NOAA, 2021), while HD is the standard Canadian index (Government of Canada, 2021). Previous research proved that HD very often leads to the underestimation of workplace heat-related dangerousness and a poor reliability of comfort prediction when it is used in indoor situations (Alfano et al., 2011). Accordingly, in this study, we applied HI analysis for the summer (Rothfusz and Headquarters, 1990) and referred to existing thermal comfort Standards for the winter given the available microclimate data and information.

Beyond microclimatic parameters, CO<sub>2</sub> and VOCs are two common indoor air pollutants associated with indoor ventilation rates, SBS symptoms and health risks (Apte et al., 2000; Apte and Erdmann, 2002; Norbäck and Nordström, 2008; Gallego et al., 2011). CO<sub>2</sub> is a typical indirect metric of occupancy levels, amount of ventilation, and electronic appliances use, whereas VOC emissions are in the form of gases released from common furniture materials and appliances, such as wood products, photocopiers, printers and cleaning products. These compounds are extremely sensitive to both occupancy and pollution episodes, which makes them especially meaningful in comparing the control period of standard occupancy (Term 1) with natural (Bushfire) and anthropogenic (COVID-19) extremes. Besides, the locally dominating arboreal genus, Eucalyptus, is a major natural polluter of biogenic volatile organic compounds (BVOCs) such as isoprene and monoterpenes, whose normal emission rate gets amplified during bushfire events (Bolan, 2020).

In this study, we adopted standardized thresholds to identify different health risk levels for each of the considered IEQ indexes. The United States National Weather Service classifies HI into four categories including *Caution*, *Extreme Caution*, *Danger* and *Extreme Danger*, associated with a range of potential health effects under prolonged exposure (Nws, 2021). Indoor CO<sub>2</sub> is classified based on commonly-used international guidelines, into 6 categories ranging from *Good* to *Hazardous*, (Saad et al., 2017). The impacts on cognitive performance and health (e.g., headaches, dizziness, vomit) soars when CO<sub>2</sub> reaches 1,000 ppm (Loh and Andamon; Satish et al., 2012), which is the commonly accepted threshold for indoor CO<sub>2</sub> concentration in literature and regulations (Daisey et al., 2003; ANSI/ASHRAE, 2016; Abcb, 2018). Finally, the German Federal Environmental Agency has expanded the World Health Organization (WHO) guidelines for TVOCs classification (World Health Organization, 2000) to incorporate 5 classes of increasing health impact from *Excellent* to *Unhealthy* (*Umweltbundesamt*, 2007). The different

classes and their corresponding class limits are listed in **Table 1** below.

## RESULTS

### General Descriptive Analysis

**Figure 3** depicts all measured variables across the 15-months monitoring period, based on available MyAir sensors (coloured dots in the background). The daily means of all sensors in the occupied hours (9am–6pm) are overlapped as black lines with the yellow shade indicating the standard deviation range. The grey vertical blocks in the background identify weekends, while the arrow-like annotations on top of the figure locate the comparison periods across the timeline. For pollutants, the health classification is displayed as well in the form of dashed horizontal lines and is labelled according to **Table 1**. For T and RH, the blue lines with diamond-shaped markers denote outdoor measurements. **Table 2** complements the trends in **Figure 3** by reporting general statistics on minima, means and maxima among the whole set of MyAir sensors, considering the 15-min time-averaged data.

On average, the hottest and coldest months in the indoor spaces were March (average of 30.2°C) and August (average of 13.6°C), yet extreme hot days also occurred in April. The most humid time of the year was January, February, and November (average of ~85%), while the driest occurred between June and August (average of ~37%). CO<sub>2</sub> and TVOCs typically hit higher concentrations in summertime (November–December) and October–November, and reached lower concentrations in October and April, respectively. Over the period of analysis, the hourly mean outdoor T was 18.1°C, hitting a maximum of 41.7°C in the middle of the bushfire season (late January 2020) at peak hours, and a minimum of 4.2°C in mid-winter (August 24, 2019) in the early morning. The corresponding values in terms of relative humidity were 70.3%, 100% and 7.3% with both maximum and minimum occurring between November and December 2019, in the morning and afternoon respectively. These trends impacted on different rooms in the building in a distinct way.

The absolute maxima of indoor T, RH, CO<sub>2</sub>, and TVOCs observed in sensor measurements were 38.0°C, 100%, 4,688 ppm, and 1,156 ppb, respectively, and were recorded over occupied hours on workdays. Notably, the T maximum was observed in the morning during summer term, while the CO<sub>2</sub> maximum was seen in March 2020 right before the beginning of COVID-19 lockdown at about 3pm. Both RH and TVOCs maxima were measured on the same day (Aug 12, 2019) between 5 and 6 pm. T, RH and TVOCs maxima were all measured in individual offices, located on Level 2 (T) or Level 4 (RH and TVOCs). In sharp contrast, the CO<sub>2</sub> absolute maximum was recorded in a classroom located on the mezzanine. All maxima occurred in north-oriented rooms featuring no A/C. The maximum averages were 27.8°C, 76.3%, 675 ppm and 109 ppb, with all values (but RH's) higher than measurements averaged for the entire week (including weekends and nights). The maximum of average T (for all sensors) was measured in an individual office on Level 2, facing north, whereas the maximum RH mean was measured

**TABLE 1 |** IEQ Classification based on Heat Index and measured pollutants.

HI [°C]		CO <sub>2</sub> [ppm]		TVOCs [ppb]
Caution	26.7–32.2	Good	<380	Excellent <65
Extreme Caution	32.2–39.4	Moderate	380–450	Good 65–220
Danger	39.4–51.1	Unhealthy for Sensitive	450–1,000	Moderate 220–660
Extreme Danger	>51.1	Unhealthy	1,000–5,000	Poor 660–2,200
		Very Unhealthy	5,000–30,000	Unhealthy 2,200–5,500
		Hazardous	30,000–40,000	

in a studio on Level 1, facing south. In both cases, no A/C was in use. Conversely, air-conditioned rooms were conducive to higher average pollutant concentrations: the maximum CO<sub>2</sub> mean was recorded in the print room on Level 1, while the maximum TVOCs mean was recorded in a staff office in the basement.

Interestingly, the room use associated with most absolute maxima (individual offices) was also associated with most absolute minima, at 10.3°C, 17.3%, 232 ppm and 0 ppb. Indeed, RH, CO<sub>2</sub> and TVOCs minima were all measured in individual offices on different levels (2 north-side, 4 north-side and 5 south-side respectively), with no A/C. The absolute T minimum was reached in a classroom located on the ground floor, western-oriented and air-conditioned, and not in colder months. Minima in T and CO<sub>2</sub> were aligned in time as both occurred in March 2020 early afternoon, but even more aligned were the minima in RH and TVOCs both recorded on June 24, 2019 at around 5:30 pm. The minimum averages were 19.3°C, 43.6%, 432 ppm and 23 ppb, with all values (but RH's) higher than those measured for the entire week. The minimum T and RH averages were measured in non-air-conditioned rooms on Level 2, the former in a south-exposed classroom, and the latter in a north-exposed individual office. Conversely, both CO<sub>2</sub> and TVOC minimum averages occurred in meeting rooms, located in the basement and Level 2 and featuring A/C and ceiling fans respectively.

Overall, the absence of an air-conditioning system was conducive to greater indoor extremes. North-exposure was associated with both T maxima and maximum means. In the southern hemisphere, north-facing windows receive twice the winter Sun than east and west facing windows, allowing light and warmth into the building. Relative humidity peaks are associated with the availability of moisture and latent heat which depends on people and their activities, construction materials, and presence of cold surfaces, water sources (e.g., kitchens), and rain penetration. Windows, walls, and doors that lack proper insulation and tightness and have limited exposure to Sun radiation are common cool surfaces. This explains why maximum RH mean levels were measured in high-occupancy rooms potentially featuring a variety of moisture sources (studios), located close to the ground and facing south, where shading from neighbouring elements (e.g., building, trees) is most effective and sunlight penetration is weakest. In terms of room use, individual offices exhibit a distinctive behaviour. Indeed, they represent the smallest rooms on average and thus accumulate heat, moisture, and pollutants more easily and more promptly. Having a small air volume with one longitudinal, highly

transmitting windowed side, these rooms respond very quickly to outdoor variations too. On the other side, as one single person is typically the greatest source of all measured parameters and controls all ventilation adjustment actions, these rooms are extremely susceptible to occupancy patterns and comfort-restoring actions, which explains the variability range. Maximum means in pollutants concentration are associated with the room use and ventilation rates, which justifies the poor air quality in print rooms and the accumulation in the basement. Cleaning and renovation activities also occurred during the monitoring period which are mostly associated with TVOCs peaks.

## Site Characterization

Room use, level, orientation, HVAC provisions, and window extent and operability are key actors in arbitrating IEQ levels across an educational building. As such, the following analysis is focused on spotting spatial heterogeneity and inter-parameter associations conditioned over room characteristics. The analysis is performed using the hourly dataset over occupied hours, focusing on workdays only.

## Role of Room Use Under Standard Occupancy

To get an understanding of how room use is associated with higher or lower IEQ levels, we focused on the time period with standard occupancy and warm-to-hot outdoor conditions (Term 1). **Figure 4** shows a combined box and swarmplot of hourly and daily averages respectively, grouped by room use. Only sensors with more than 90% data over the studied time interval are considered (**Supplementary Appendix Table A2**). All room types are represented here except for the print room, which was monitored by only one sensor and will be discussed later. The average is further displayed as a green horizontal line and used to order the boxplots (decreasing mean).

During Term 1, rooms exhibited distinct behaviors, summarized in **Table 3**. Computer labs and individual offices exhibited the highest T mean (24.6°C). High local production of heat from local appliances, typical elevation, exposure, presence of partially glazed facade and absence of solar shadings are major triggers and further explain why computer labs, together with classrooms, exhibit the highest mean CO<sub>2</sub> (527.0 ppm) and TVOCs (82.0 ppb) concentrations with significant extreme episodes. As observed in *General Descriptive Analysis* section, individual offices tend to experience high variability and the most extreme high-temperature events. This is demonstrated by the wide interquartile (IQR) range (4.6°C) and the dense cloud of

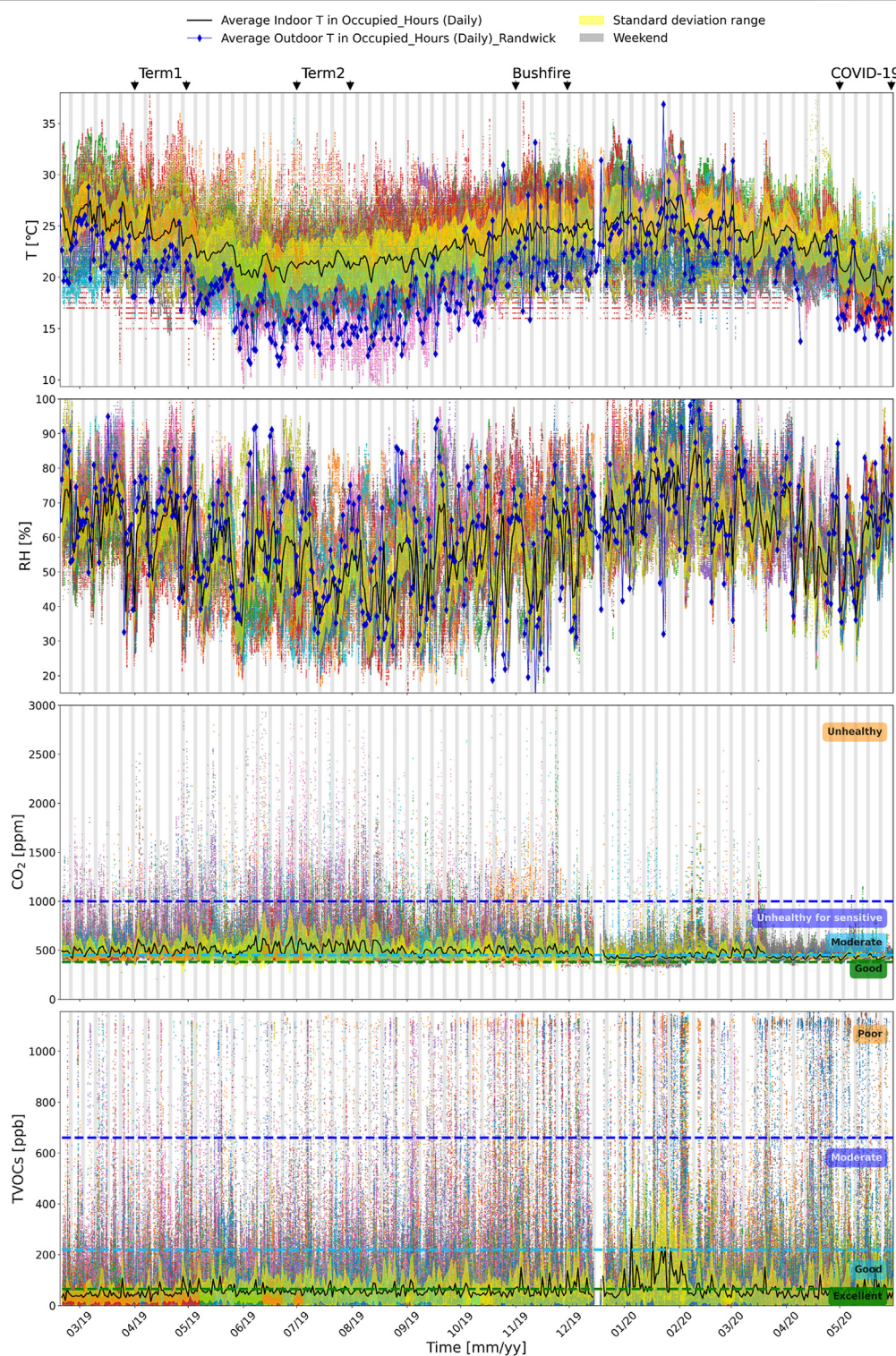


**FIGURE 3 |** Time trends of temperature, relative humidity, CO<sub>2</sub> and TVOCs between February 2019 and June/May 2020. Outdoor measurements are taken from the DPIE station located in Randwick. A blackout period occurred between the 14th and the December 21, 2019, causing all MyAirs to stop recording.

recordings above 26.7°C. Reasons include the low air volume and the presence of portable heating devices which also result in drier air (mean of 55.0%, typical range = 46.6–64.0%). In terms of

pollutants, individual offices had the lowest CO<sub>2</sub> and TVOCs means (470.5 ppm and 51.7 ppb), mainly due to lower internal gains. While heat cannot be efficiently controlled due to the

**TABLE 2** | Statistical analysis across all MyAir sensors and over the entire observation period (Feb 2019–Jun 2020).

	Minima				Mean values				Maxima			
	T	RH	CO <sub>2</sub>	TVOCs	T	RH	CO <sub>2</sub>	TVOCs	T	RH	CO <sub>2</sub>	TVOCs
mean	16.0	25.6	328.9	0.4	23.1	60.6	464.7	66.9	31.3	93.5	1589.2	1091.4
Std	2.5	7.3	34.5	0.9	1.7	6.1	29.3	28.4	2.6	6.3	692.9	135.7
Min	9.3	15.0	204.0	0.0	19.5	46.1	432.1	21.5	24.5	74.0	514.5	301.0
25%	14.6	21.4	320.0	0.0	21.9	57.2	445.3	46.9	29.7	89.5	975.1	1109.8
50%	16.0	24.0	329.5	0.0	23.4	59.4	452.9	59.8	31.2	95.0	1416.8	1129.5
75%	17.4	28.0	344.3	0.5	24.5	63.1	481.8	90.3	32.6	100.0	2008.3	1148.8
max	23.5	59.0	391.0	4.0	26.4	82.2	588.3	129.7	38.0	100.0	2950.0	1156.0

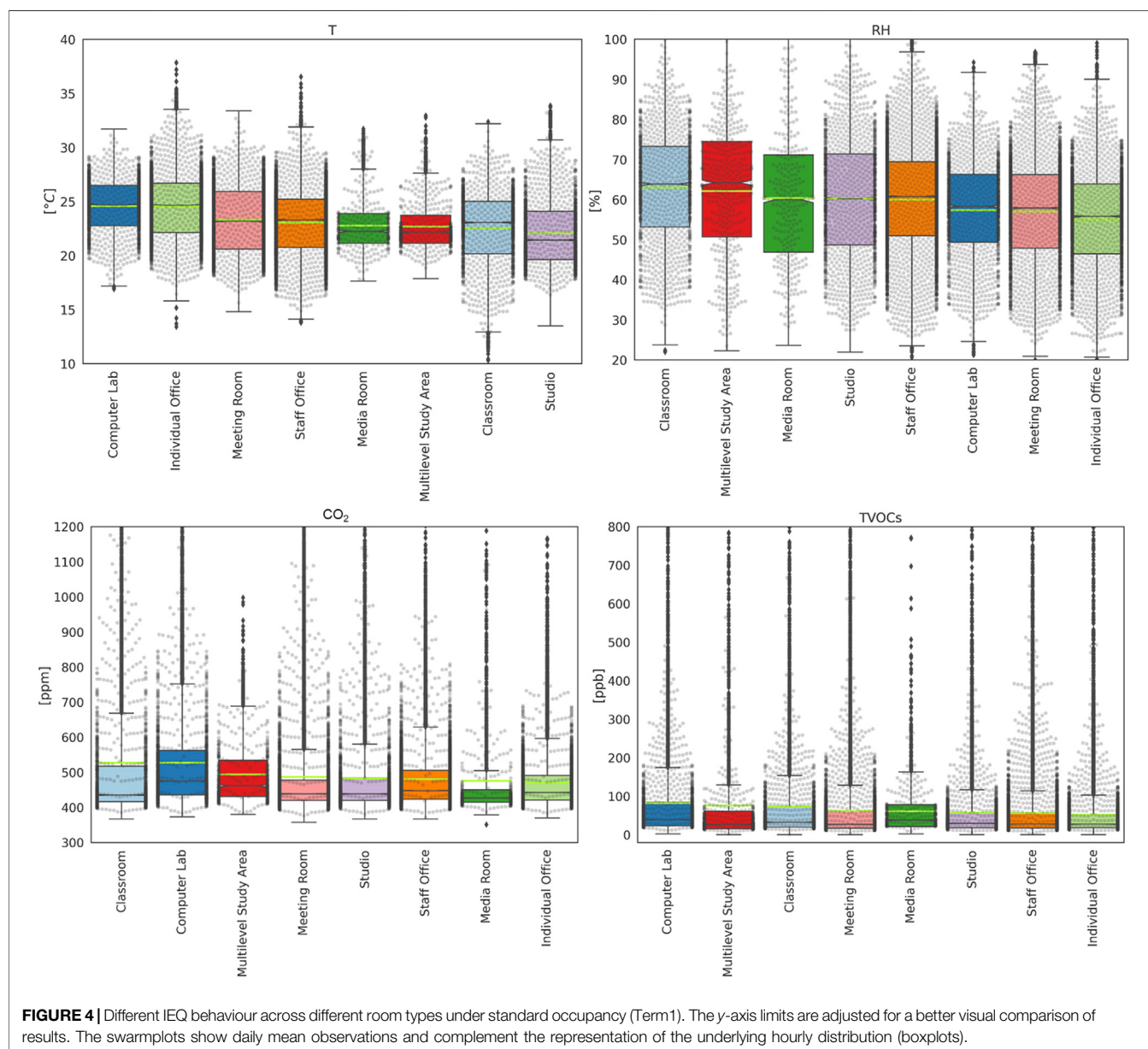
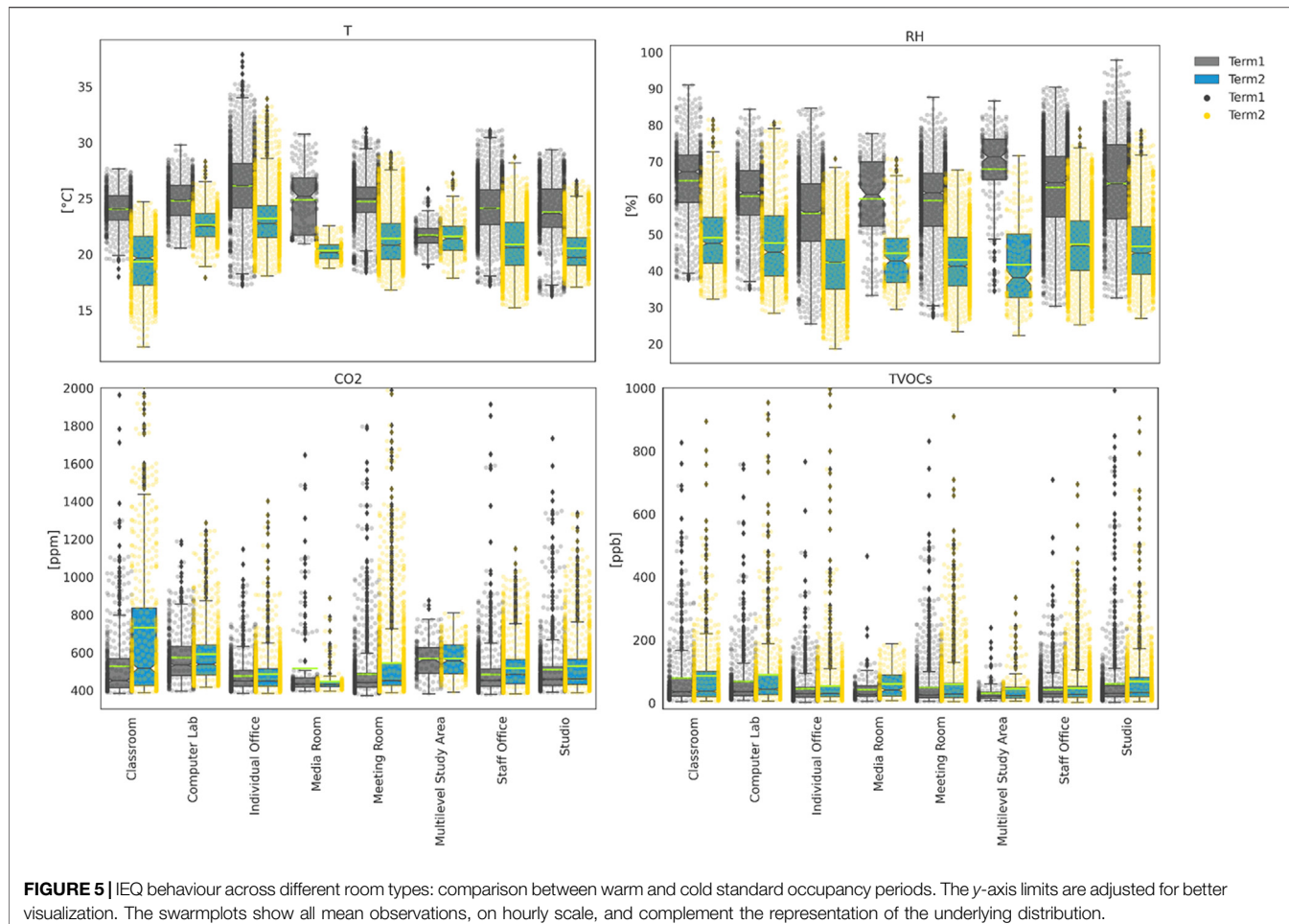


**TABLE 3 |** Typical IEQ pattern per room use under standard occupancy.

Room use	Main observations	Causes
Computer lab	- highest mean temperature - highest mean CO <sub>2</sub> and TVOCs - relative humidity typically maintained between 50 and 66%	- located between the 2nd and the 3rd floor, south-exposed, with a partially glazed facade having no solar shadings - under standard occupancy, these rooms are densely occupied (exceeding 1.5 people/m <sup>2</sup> ) and affected by a considerable production of sensible heat and pollutants from local appliances such as computers and personal electronic devices - usually locked and used for lectures and tutorials which typically prevent or delay occupants' comfort-restoring actions not to interrupt the lesson (Stazi et al., 2017)
Individual office	- highest mean temperature - lowest mean relative humidity - lowest CO <sub>2</sub> and TVOCs means	- low air volume which increases the sensitivity to both outdoor- and indoor-generated heat - north-facing rooms that tend to easily accumulate heat due to the higher thermal mass of terracotta tiles on the outside - no A/C in place - partial shading provisions - likely presence of portable heating devices, such as radiant units and extra emitting equipment (multiple computers) - low internal production of pollutants, ceiling fans combined with operable windows
Meeting room	- generally comfortable thermo-hygrometric and pollution levels - pollution and heat peaks during closed-door meetings	- irregular occupancy pattern, scattered in time and short-lasting - mostly located centrally and in the basement, with no windows and direct outdoor air inlet. Those exposed to the outdoors are completely shaded or mostly shaded. Half of them are equipped with split systems, the other half with ceiling fans - noise and privacy concerns are likely the key factors promoting closed-door meetings resulting in adverse thermal comfort and air quality
Staff office	- generally comfortable thermo-hygrometric and CO <sub>2</sub> levels - frequent extreme TVOCs episodes	- partially glazed facades, complete shading available, low occupancy density - major renovations, re-painting and cleaning activities performed between 2019/2020 throughout the admin sector in the Red Centre
Media room	- limited variability in T, CO <sub>2</sub> , and TVOCs	- irregular occupancy pattern, scattered in time and short-lasting - local humidity sources and reduced ventilation
Multi-level study areas	- medium-low T levels, high RH, CO <sub>2</sub> and TVOCs	- efficient heat removal by horizontal and vertical cross ventilation - humidity and pollutants accumulation at user level - non-openable fully glazed facades, limiting the intake of outdoor air
Classrooms	- high humidity and CO <sub>2</sub> levels - low T and TVOCs	- south-exposed with shaded and operable partially glazed facades - high latent heat and carbon dioxide release from people - no A/C in place
Studio	- low T, but significant extremes - comfortable RH and TVOCs levels - moderate-high CO <sub>2</sub> levels	- south-exposed - fully glazed facades - almost all located on Level 1 - no A/C in place

considerable solar gains (due to exposure, insufficient shading provisions), the combination of operable windows and ceiling fans proved sufficient in limiting the accumulation of pollutants. Meeting rooms experienced fairly comfortable thermo-hygrometric and pollution levels, likely caused by the irregular occupancy pattern, scattered in time and short-lasting. Temperatures were lower compared to individual offices and computer labs, yet higher than rooms having even higher occupancy density (e.g., classrooms) but better ventilated. This also explains the amount of outliers in CO<sub>2</sub> and TVOCs charts, with both reaching unhealthy levels during closed-door meetings. In staff offices (encompassing shared and open-plan areas), the mean T is at 23.1°C, and the mean RH around 60.0% due to the local presence of latent heat sources. While very limited health-threatening events were recorded in terms of CO<sub>2</sub>, frequent extreme TVOCs episodes occurred which can be imputed to major renovations, re-painting and cleaning activities. The media room (a multipurpose space outfitted for video-making and media releases) exhibited limited temperature variability (within ±1.5°C of the mean 22.8°C) but comparatively high

RH (46.9–71.1%). TVOCs never crossed unhealthy levels and CO<sub>2</sub> very rarely. The CO<sub>2</sub> mean (475.6 ppm) was the second-to-last across all room uses. This pattern is mostly related to its sporadic and time-framed use. Multi-level study areas, located across Level 5 and 6, exhibited medium-low T levels (mean of 22.7°C), yet high RH, CO<sub>2</sub> and TVOCs (means of 62.1%, 493.8 ppm and 75.4 ppb). Despite benefitting from both horizontal and vertical cross ventilation, this proved sufficient only at removing heat, but not moisture and pollutants which tended to accumulate on lower levels, gathering the contributions of multiple floors. Further, these rooms are typified by non-openable fully glazed facades, thus limiting the intake of outdoor air. Classrooms were fresher (with T typically in the 20–25°C range) and experienced limited TVOCs accumulation (levels below 73.2 ppb) thanks to their south-exposure and operable shading provisions, however mean CO<sub>2</sub> was the highest (527.3 ppm) and frequently crossed the unhealthy threshold and high humidity levels (mean of 63.0%) occurred, both likely caused by the high internal gains. Studios exhibited the lowest T levels (mean of 22.1°C), and a relatively comfortable RH



range (50–71%). However, temperature levels were skewed towards the upper quartile with extremes over 30°C, likely caused by the presence of fully glazed facades, although south-exposed. CO<sub>2</sub> could surpass the unhealthy threshold, while TVOCs stayed within moderate levels. Because CO<sub>2</sub> is heavier than air, it sinks to the lower floors across the building. Almost all studios are located on Level 1 and feature no A/C that could extract the excess CO<sub>2</sub> or facilitate its removal.

The effect of seasonality is explored in **Figure 5**, where the warmest (Term1) and coldest (Term2) periods of standard occupancy are compared, based on sensors having more than 90% of data in both the time windows (**Supplementary Appendix Table A2**). During Term 1, the outdoor temperature was  $18.9 \pm 3.3^\circ\text{C}$  with a maximum of  $27.8^\circ\text{C}$  and a minimum of  $9.8^\circ\text{C}$ . Relative humidity ranged within  $75.9 \pm 14.9\%$ , reaching a maximum and minimum of 98.6 and 23.4%, respectively. During Term 2, the outdoor temperature was 6° lower ( $13.0 \pm 3.3^\circ\text{C}$ ) while relative humidity was nearly 13% lower on average ( $62.5 \pm 18.1\%$ ). The outdoor temperature is consistently lower than indoor throughout the whole year. This is attributed to the weather station location (green, open area, closer to the coastline) and the internal gains.

In both Terms, the indoor temperature was 1–2°C warmer and <5% more humid as compared to outdoor conditions, due to high thermal transmittances, extensive glazed surfaces and emission of latent heat from occupants. Some exceptions occurred. The indoor temperature difference was much more limited in computer labs and multilevel study areas, where the internally-generated heat outweighed the heat loss through the building envelope and to unconditioned indoors. Classrooms could reach significantly lower temperatures having extensive shaded windowed sides on the north facade. The relative humidity difference was close to 15% on average, with multilevel study areas touching a major gap of more than 20%. Generally speaking, the humidity levels tended to equalize across different rooms in the colder Term with medians within a 5% range, compared to more than 10% in Term1. The reasons are to be found in the extensive use of portable heaters that efficiently dried the air down to a RH of about 45% on average. As for CO<sub>2</sub>, mild discrepancies are observed between Term 1 and Term 2, which entails that CO<sub>2</sub> levels are not governed by seasonal cycles. A standalone behaviour is that of classrooms where considerably higher CO<sub>2</sub> levels are recorded. The reason is likely behavioural: while classes tend to start and go on with open windows during

**TABLE 4 |** Statistical analysis for the print room over Term 1 and Term 2.

	Term 1				Term 2			
	T	RH	CO <sub>2</sub>	TVOCs	T	RH	CO <sub>2</sub>	TVOCs
mean	23.3	61.7	937.8	43.1	23.2	43.9	898.2	54.9
Std	0.5	10	338.4	45.7	0.7	7	303.6	65.6
min	21.9	38	354.4	7	20.6	32.2	414.8	7.3
25%	22.9	51.4	654.1	17.1	22.6	39.3	620.5	15.8
50%	23.3	66.2	906.2	27.5	23.2	42.8	904.6	25.3
75%	23.6	69.2	1136.5	47.2	23.7	46.7	1097	60.6
max	24.8	74	2296.3	396.6	24.5	58.7	1782.3	346.5

the warm Term, this is hardly the case during wintertime, when windows and doors are kept closed to maintain the warmth inside. As such, people's respiratory emissions were not dispersed as efficiently as in Term 1 and accumulated over unhealthy levels, with the mean being nearly 200 ppm higher. Finally, the offset in terms of TVOCs was negligible regardless of the room use.

The print room on Level 1 lacked enough data in Term 1, however its IEQ pattern is of special interest due to a combination of aggravating factors. Beyond the presence of printing devices, the room is exposed to the outdoors on three sides, with the northern being the longest. A single unshaded window of about 1 m<sup>2</sup> stretches along the western side. No cross ventilation occurs given that the door is spring-loaded to automatically close and even though air conditioning is in place, ventilation is very limited. The sensor continuously recorded from the April 14, 2019 on, as such a month period up to the May 15, 2019 was used to characterize its behaviour in Term 1. The results over occupied hours and workdays only are summarized in **Table 4**. Temperature and TVOCs stayed very low, at levels comparable to those of multilevel study spaces in **Figure 4**, while relative humidity stayed high at levels comparable to those of the media room. The most critical observation is made in CO<sub>2</sub> concentration: the average exceeded 937.8 ppm which is 410 ppm higher than the highest level recorded by any other room type during the same period, with an IQR of 482.4 ppm which is 10-fold that of other rooms. This suggests that the average conditions inside the print room are unhealthy for the sensitives and cross the health-risk threshold of 1,000 ppm more than 25% of the time. Only a negligible improvement is recorded in Term 2. This calls for major redesign measures in order to meet minimum liveability levels.

### Proclivity to IEQ Deterioration

In this section, statistical analysis is performed to identify which rooms were more prone to seasonal IEQ extremes and criticalities. Only sensors having more than 90% recordings over each season were included (**Supplementary Appendix Table A2**). Upper and lower outliers are those exceeding the 75th percentile or falling below the 25th percentile by 1.5 times the interquartile range. For each sensor and each parameter, the percent occurrence of upper and lower outliers was computed. **Figure 6** is a summary GIS representation of the 4 most critical extremes in terms of IEQ deterioration: summer upper outliers for T and TVOCs, winter lower outliers for RH, and winter upper

outliers for CO<sub>2</sub>. It allows immediate visualization of the locations most prone to extreme conditions.

Most high extreme temperature events occurred in summertime, with 22% of the sensors recording outliers. The maximum percent occurrence was 4.5% in the north-oriented meeting room at Level 5. Comparatively, 16.7, 7.9, and 12.1% of the sensors recorded outliers in autumn, winter, and spring with a maximum of 3.6% of the time. Lower outliers mostly occurred in springtime with 36.4% of the sensors measuring up to 28% of the time below the threshold. Most extreme dry events took place in winter, with 78.9% of the sensors measuring outliers. In an individual office on Level 2, extreme dry events occurred for 41% of the time, likely caused by an overuse of portable heaters. Dry events were recorded at almost all locations also in other seasons but rarely surpassed 10% of time. Conversely, extreme humid episodes concentrated in summertime but over limited time periods (<1%). CO<sub>2</sub> extreme events exacerbated in wintertime, with 84.2% of the sensors recording poor air quality, typically for more than 20% of the time. As mentioned in *Role of Room Use Under Standard Occupancy* section, the print room recorded the worst conditions with an astonishing 74.1% of the time under extreme CO<sub>2</sub> levels. Further a computer lab on Level 2 and a studio on Level 1, both south exposed, recorded outliers for more than 50% of the time. Almost all sensors recorded extreme CO<sub>2</sub> levels in any other season, however the time coverage was typically lower than 20%. In terms of TVOCs, summer was by far the worst season: all sensors recorded outliers and most for more than 10% of the time. The greatest time coverage was 38.3% and occurred in a centrally located staff office in the basement.

The above analysis suggests that the most critical conditions to moderate not to pose a risk on occupants' health and productivity are wintertime CO<sub>2</sub> levels.

### Heat Index

Heat stress occurs out of the boundaries of the zone of homeothermy, namely the range of environmental conditions in which humans maintain heat balance and thereby a steady core temperature by minimal thermal adjustments (comfort zone) or mild thermoregulating reactions like shivering and sweating (Lacetera et al., 2003). Here, the hottest average indoor temperatures were recorded in March 2019, while the highest extremes were recorded in April 2019. Consequently, the heat index analysis was performed contemplating both months. **Figure 7A** shows the result, based on sensors having more than 90% of data only (coloured dots in the background). The daily means in the occupied hours (9 am–6pm) are overlapped as salmon-shaded, red lines with the shade indicating the one standard deviation span. The health classification thresholds are displayed in the form of dashed horizontal lines and labelled according to **Table 1**.

The mean HI ranged between 24.2 and 32.2°C, with the lower limit measured in a north-oriented studio in the basement and the upper limit in a north-oriented individual office on Level 2. The maximum HI ranged between 26.4 and 41.7°C with the absolute peak recorded in a centrally located studio in the basement. Conversely, the minimum ranged between 14.3 and

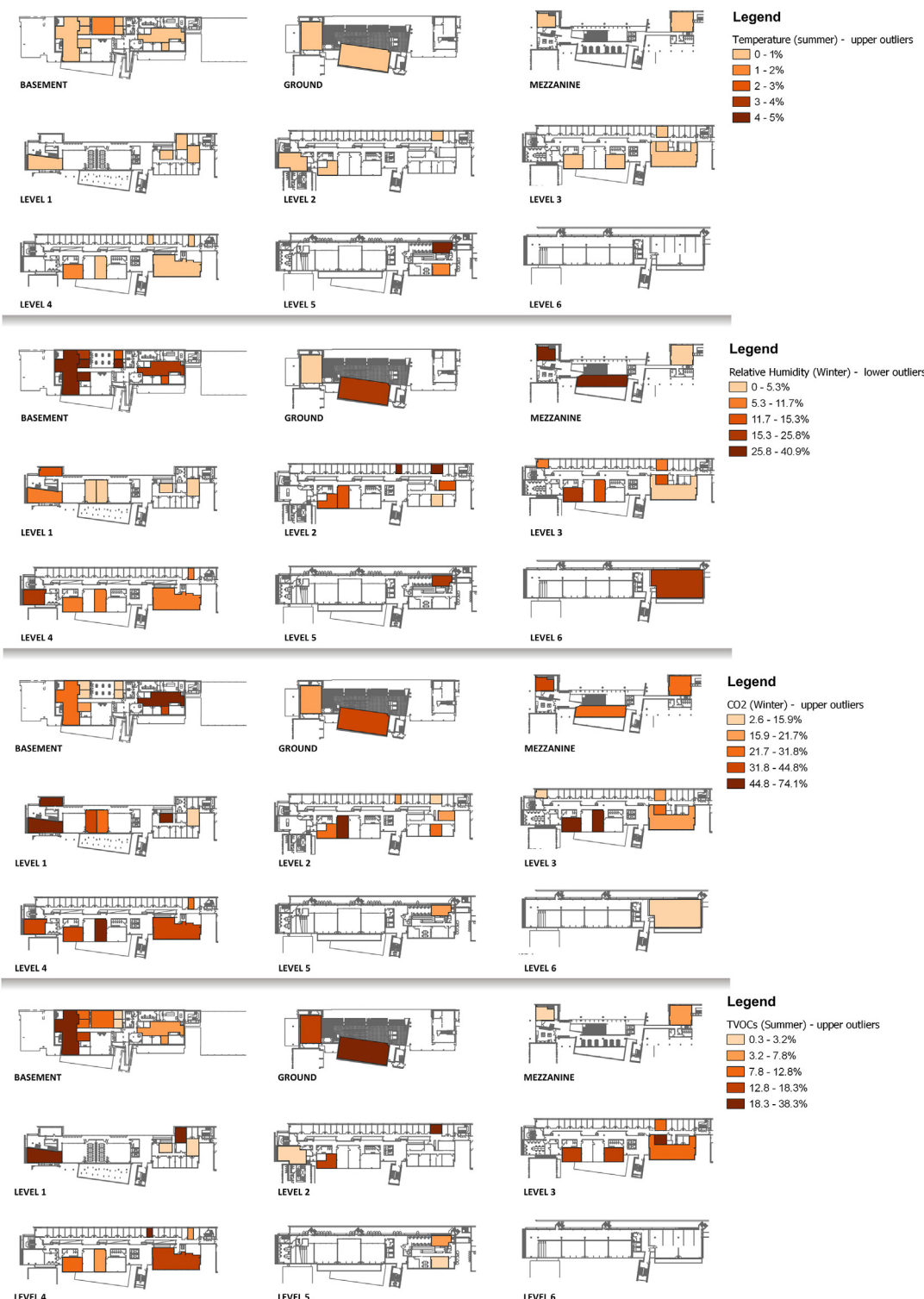


**FIGURE 6 |** GIS localization and categorization of rooms according to their proclivity to extreme events. From top to bottom: occurrence of summer upper T outliers, winter lower RH outliers, winter upper CO<sub>2</sub> outliers, and summer upper TVOCs outliers (percent time). Upper and lower outliers are those exceeding the 75th percentile or falling below the 25th percentile by 1.5 times the interquartile range.

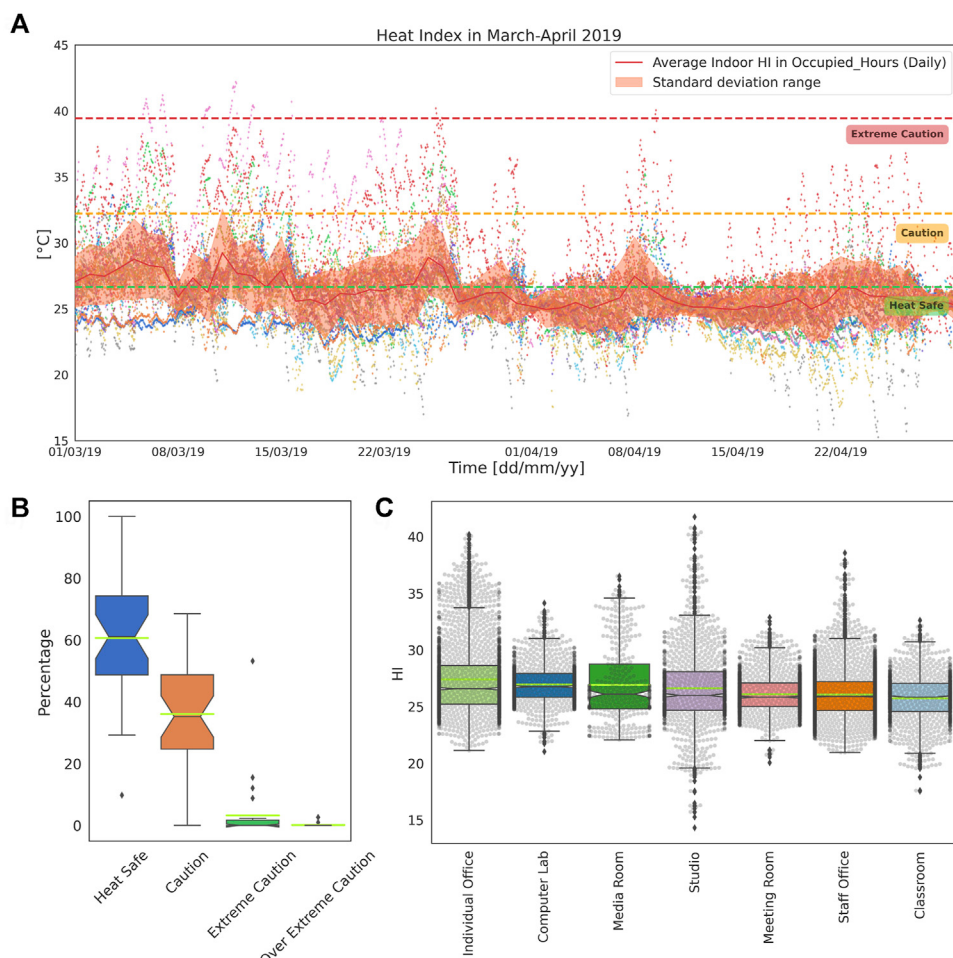
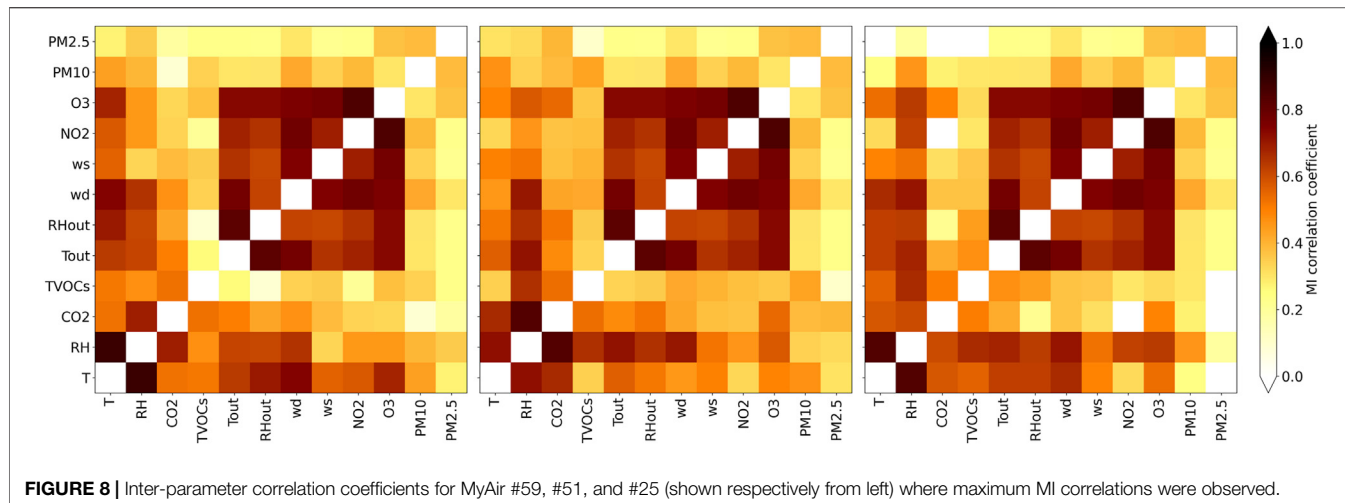


**FIGURE 7 |** Heat index analysis: **(A)** time trends between March and April 2019; **(B)** boxplot of occurrences under different health risk levels and **(C)** box and swarmplots of HI level broken down by room type, both showing mean observations, on hourly basis.

24.5°C with the absolute low observed again in the north-oriented studio in the basement. Maxima typically occurred in the 12–1 pm and 3–4 pm windows. In contrast, minima mostly occurred in the morning. **Figure 7B** shows the percent time spent into increasing levels of health risk in the form of a boxplot. Heat safe conditions were largely dominant, with two offices in the basement never experiencing any sort of risk (possibly due to A/C access). The lowest percent time in heat safe conditions (9.8%) pertains to the individual office on Level 2 typified by extremely dry air (which also scored the maximum percent time in the Extreme Caution zone, 53.2%), followed by 29.2% in a west-oriented studio on Level 4 (that also scored the maximum percent time in the Caution zone, 68.5%). All rooms having significant percentages (9–16%) in the Extreme Caution zone and even above it are located in the basement. We observe that rooms located in the basement may experience the best and worst HI conditions depending on the efficiency of air conditioning and on the ability to dissipate excess humidity. In terms of room use (**Figure 7C**), individual offices hit the worst HI conditions, having mean above the heat-safe upper threshold (27.4°C *versus* 26.7°C)

and 75th percentile close to the Caution threshold. Computer labs follow closely with mean HI at 27°C, but much lower variability (IQR equal to 2.1°C *versus* 3.4°C) and much less frequent extremes. The media room in the basement and studios also exists on the borderline of heat safe conditions (mean of 26.9 and 26.6°C) with HI distribution significantly skewed towards upper values. As for the print room whose IEQ was deteriorated by CO<sub>2</sub> levels, this analysis reveals how major redesign measures are required for individual offices, computer labs, studios, and media rooms in order to maintain heat safe conditions, on average. Health-preserving strategies should target both temperature and humidity as both contribute to establishing heat stress conditions in the warm season (compare **Figure 4**). Meeting rooms, staff offices and classrooms behave very similarly with mean levels in the 25.9 ± 0.2°C range. Meeting rooms exhibit the least IQR (2.1°C), comparable to that of computer labs. Maxima reach or slightly exceed 40°C, thus trespassing the Extreme Caution threshold. Minima typically stay around 20°C. Studios show the widest variability by far, ranging between the absolute minimum (14.3°C) and the absolute maximum (41.7°C). Much



safer conditions pertain to classrooms, whose variability range is completely contained within the Heat Safe bounds, to the benefit of students' productivity and comfort.

### Inter-parameter Correlations and Key Variables

In this section, the correlation among indoor and outdoor parameters is investigated by means of Mutual Information (MI) analysis. MI is a statistical metric that measures the degree of "shared information" between time series  $x, y$  by quantifying the difference between marginal and joint entropies (Fraser and Swinney, 1986; Cellucci et al., 2005; Frenzel and Pompe, 2007). It is typically normalized to range between 0 and 1, where 0 connotes mutual independence, and expressed as:

$$MI(X; Y) = \sqrt{1 - \exp(-2 \cdot I(X; Y))} \quad (1)$$

where  $I$  is calculated based on the probability density  $p$  as follows:

$$I(X; Y) = \int_{R^2} p(x, y) \log\left(\frac{p(x, y)}{p(x)p(y)}\right) d(x, y) \quad (2)$$

MI is a powerful correlation measure for exploratory analysis of variable pairs for three main reasons: 1) it captures both linear and non-linear relationships, being equivalent to Pearson correlation in the linear case, 2) it can be conditioned on a third, possibly multidimensional, variable, being analogous to partial correlation, and 3) it is invariant under monotonic transformations of variables, including linearization. Conditioned MI returns the degree of association with the effect of a given controlling variable removed. For instance, conditioning over the day of the year removes the effect of seasonal cycles. MI has been applied in atmospheric science (Zaidan et al., 2018, 2019) and urban analysis (Li et al., 2014; Ryu et al., 2018; Ulpiani et al., 2021), revealing strong non-linear associations especially when wind-related and air quality parameters are concerned. In this study, we applied MI correlation to look for the inter-parameter associativity under

standard occupancy (Term 1) via k-nearest neighbour search. The correlation matrices for the rooms where maxima MI were computed are shown in **Figure 8**. We also investigated if and which site-specific parameters (e.g., altitude, orientation, A/C provisions, window types and shadings) govern the strength of correlation by applying conditional MI (Laarne et al., 2021). We included outdoor parameters measured at the DPIE station in Randwick, which comprised wind speed (ws), wind direction (wd) and four outdoor pollutants ( $\text{NO}_2$ ,  $\text{O}_3$ ,  $\text{PM}_{10}$  and  $\text{PM}_{2.5}$ ), outdoor temperature ( $T_{\text{out}}$ ) and relative humidity ( $RH_{\text{out}}$ ). **Supplementary Appendix A3** collects the list of parameters that were significantly correlated to the four MyAir measurements. The significance threshold was set to 0.5, namely midway between mutual independence and full correlation.

Relative humidity was, by far, the most correlated parameter, followed by temperature,  $\text{CO}_2$  and TVOCs. The absolute maximum correlation coefficient for  $T$  was with  $RH$  and reached 0.88. It was recorded in a studio in the basement. Temperature tended to be most correlated to  $RH$  (86.0% of cases),  $T_{\text{out}}$  (7.0%) and  $\text{CO}_2$  (7.0%) while it exhibited mild correlation with all other outdoor parameters and with TVOCs. In terms of  $RH$ , the absolute maximum correlation coefficient was the same as for  $T$ , measured in the basement studio. Relative humidity was typically correlated with  $T$  (79.1% of cases), equally followed by  $\text{CO}_2$  and  $wd$  (9.3%) and then by  $RH_{\text{out}}$  (2.3%). Indeed, in Sydney, the wind direction dictates whether humid fresh air is entrained by the sea breeze from the east or dry warm air is advected by desert winds coming from the western fringe. This dualism has been largely investigated and governs the magnitude and spatial heterogeneity of urban heat island and outdoor heat stress (Santamouris et al., 2017; Yun et al., 2020). As for  $\text{CO}_2$ , the absolute maximum correlation coefficient was with  $RH$  and reached 0.83. It was recorded in an air-conditioned, west-exposed staff office on the mezzanine.  $\text{CO}_2$  tended to be most correlated to  $RH$  (74.4% of cases),  $T$  (20.9%) and both  $T_{\text{out}}$  and TVOCs equally (2.3%). A strong linear and positive correlation between carbon dioxide and relative humidity was also found in other naturally ventilated school

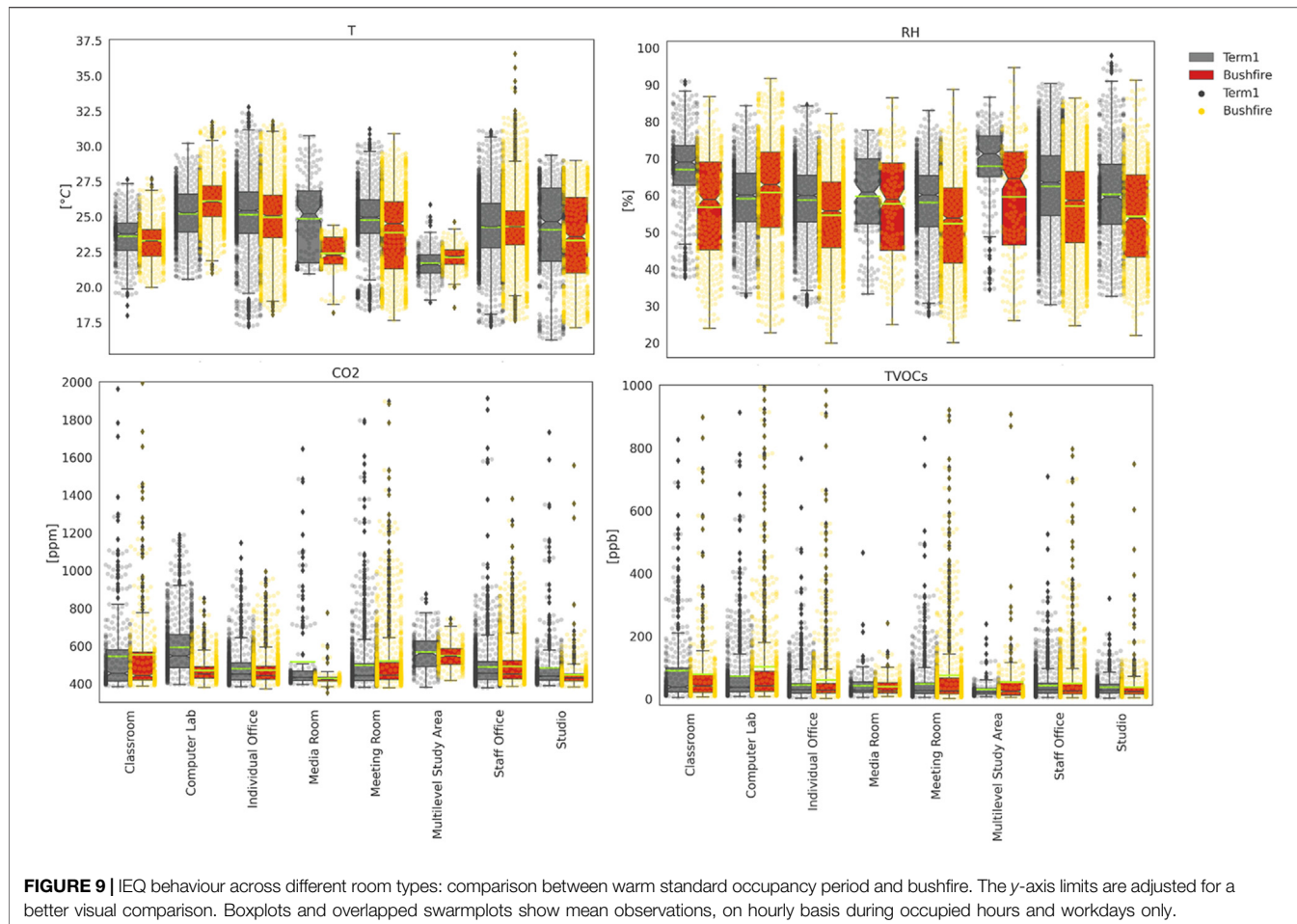


**FIGURE 9 |** IEQ behaviour across different room types: comparison between warm standard occupancy period and bushfire. The y-axis limits are adjusted for a better visual comparison. Boxplots and overlapped swarmplots show mean observations, on hourly basis during occupied hours and workdays only.

buildings elsewhere in the world (Lazović et al., 2016). Finally, the absolute maximum correlation coefficient for TVOCs was with RH and reached 0.67. It was recorded in a non-conditioned, north-oriented individual office on Level 3 that underwent extensive cleaning during the time of observation (MyAir #25). TVOCs were most typically correlated with CO<sub>2</sub> levels (34.9% of cases) and RH (32.6%), but in some cases significant correlation was found with T (16.3%), wd (7.0%) and outdoor T, ws, NO<sub>2</sub>, O<sub>3</sub> parimerito (2.3%).

Floor level, orientation, room use, air volume, A/C and ceiling fan provisions, cross ventilation, type of windows, level of shadings and windows operability (refer to **Supplementary Appendix Table A1**) were codified and included in the dataset to verify whether knowing the room characteristics could lead to stronger associations and thus better predictability. We iterated across the different conditional parameters and calculated the difference in correlation coefficients between conditional and unconditional matrices. Interestingly, only the floor level was associated with higher correlation coefficients. The average increase was 0.09. Above average increments are those in the mutual correlation between T-CO<sub>2</sub> (+0.17), RH-CO<sub>2</sub> (+0.15), RH-TVOCs (+0.15), T-RH (+0.14), T-wd (+0.14), T-ws (+0.11), T-T<sub>out</sub> (+0.11), and T-NO<sub>2</sub> (+0.10). Hence floor level is a major trigger for inter-

parameter associations, especially in terms of pollutants. Since CO<sub>2</sub> and TVOCs are heavier than air, they travel all the way down from the upper levels to the ground. At the same time warmer, drier air tends to move upwards convectively, especially in naturally ventilated buildings provided with vertical air communication. This explains why the strength of correlation between thermo-hygrometric and air quality parameters significantly depends on the elevation.

## Weather Extremes and Occupancy Anomalies

This section is dedicated to the impacts of microclimatological and occupancy anomalies on IEQ preservation by comparing the control period of standard occupancy (Term 1) with the Bushfire and COVID-19 subsets, respectively. The analysis is conducted by considering the records of sensors having more than 90% data in the paired time windows (**Supplementary Appendix Table A2**).

**Figure 9** shows the impact of 2019/2020 Black Summer, during which hundreds of bushfires ravaged the urban fringe causing extreme pollution, heat waves and droughts. The multiple microclimatic impacts in the city of Sydney have been analysed elsewhere and include 1) health-threatening PMs accumulation due to long-transport mechanisms and complex interactions

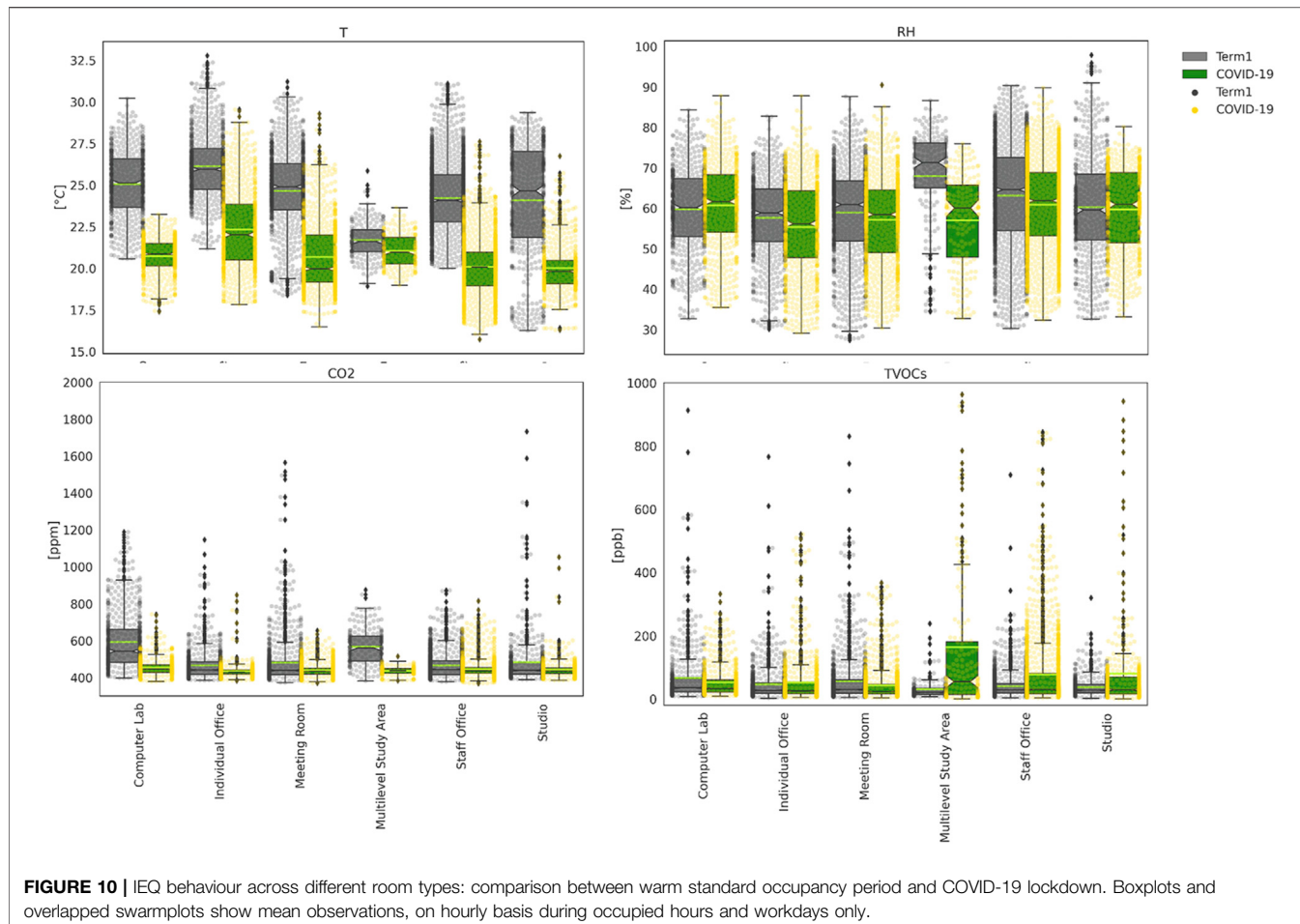
between prevailing and local winds, 2) strongly attenuated UV radiation and radiative forcing impairment, and 3) exacerbated urban heat island intensity and absence of cool island events (Ulpiani et al., 2020). In November 2019, a dense plume of smoke blanketed the city and safer-at-home orders were put in place, thus altering standard occupancy patterns. The outdoor temperature was  $19.7 \pm 4.0^\circ\text{C}$  (higher than Term 1 by less than  $1^\circ\text{C}$ ) with a maximum of  $35.5^\circ\text{C}$  and a minimum of  $10.3^\circ\text{C}$ . Relative humidity ranged within  $63.9 \pm 21.7\%$  (lower than during Term 1 by more than 10% and much more fluctuating), hitting a high of 96.1% and an extreme low of 7.3%. These trends were closely reflected indoors, although extreme events were all strongly exacerbated. The following exemptions stood out. Computer labs are electronically locked thus acting as hermetically sealed sinks for heat, moisture and pollutants under periods of unoccupancy. Furthermore, extra heat may have also been released by remotely controlled computers as coarse dust from the bushfires amassed. Computer overheating is most commonly caused by the heat sink and fans being clogged with dust and debris. Indeed, the mean T was  $4.0^\circ\text{C}$  above the mean of most other rooms and was  $1.0^\circ\text{C}$  above the mean in Term 1. Meetings, conferences, and gathering stopped during the bushfires critical phase, thus causing a significant decrease in internal heat gains in meeting rooms as mirrored both in terms of sensible (T) and latent (RH) heat balance. The T mean was  $0.5^\circ\text{C}$  lower than in Term 1, and the 25th percentile was  $21.3^\circ\text{C}$ ,  $2.5^\circ\text{C}$  less than in Term 1. A standalone behaviour is that of the media room in the basement, where humidity equalled Term 1 levels while temperature dropped, suggesting intense evaporative cooling. The T mean and maximum,  $22.4$  and  $24.4^\circ\text{C}$  respectively, were nearly  $2.4$  and  $6^\circ\text{C}$  less than in Term 1. The reasons for this specific trend require further investigation and might have been caused by A/C failures and water leakages.

In terms of pollutants, very interesting and distinctive patterns emerge in the comparison with Term 1. CO<sub>2</sub> levels dropped everywhere caused by the altered occupancy pattern. The maximum offset was again recorded in computer labs and amounted to  $-122.1$ ,  $-115.9$ , and  $-336.4$  ppm in terms of mean, IQR, and maximum, respectively. The following largest mean decrease pertained to the media room and the multilevel study areas, hitting  $-87.8$  and  $-18.5$  ppm respectively, with multilevel study areas showing also a significant drop in IQR and absolute maximum ( $-51.3$  and  $-130.9$  ppm). The reduction in means was around 5–20 ppm also in the other room types, but milder in terms of IQR and maxima. The greatest drops were recorded in rooms with high standard occupancy density (e.g., computer labs, classrooms) or receiving the contributions from multiple floors (multilevel study areas), as those were most impacted by the reduced flow of people. In sharp contrast, TVOCs increased everywhere because of biogenic emissions from biomass burning. The offset with respect to Term 1 was greatest in computer labs, multilevel study areas, and meeting rooms, reaching a maximum of  $30.0$ ,  $14.5$ , and  $58.9$  ppb (mean, IQR and maximum) in computer labs. The increase in meeting rooms was comparable ( $26.7$ ,  $17.1$ , and  $263.3$  ppb), followed by  $23.1$ ,  $23.5$ , and  $668.7$  ppb recorded in multilevel study areas.

These rooms remained locked with no A/C during the safer-at-home orders and thus could not disperse air pollutants as efficiently as during standard occupancy. Smart logics should be put in place to control the A/C and door opening/closing cycles in electronically operated rooms of these types to avoid generating highly health-threatening indoor environments during bushfire events. Such results suggest an urgent need to prioritize building air tightness improvement, appropriate filtration techniques, and emergency strategies to expel excess dust towards future-proof buildings in Sydney and similar regions in the world, as also stressed elsewhere (Rajagopalan and Goodman, 2021).

The role of occupancy levels and patterns emerges even more vividly when comparing Term 1 with COVID-19 lockdown period, as displayed in **Figure 10**. In May 2020, the outdoor temperature was  $14.9 \pm 3.3^\circ\text{C}$  (exactly  $4^\circ\text{C}$  lower than during Term 1) with a maximum of  $25.5^\circ\text{C}$  and a minimum of  $7.6^\circ\text{C}$ . Relative humidity ranged within  $69.1 \pm 17.1\%$  (less than 10% lower than during Term 1), hitting a high of 96.2% and an extreme low of 29.1%. While during Term 2 the outdoor T offset with respect to Term 1 was mitigated by  $1$ – $2^\circ\text{C}$  indoors, during the lockdown it got amplified in most room types by about  $0.5^\circ\text{C}$ . Statistically significant gaps were recorded everywhere, with reductions in the 75th percentile reaching  $7^\circ\text{C}$  under the lockdown, given the concerted fall in heat gains from both people and equipment. The only exception to this pattern is represented by multilevel study areas whose temperature stayed low in Term 1 too. Interestingly, the absence of people flattened out the differences across room types with all T means lying within a  $1^\circ\text{C}$  range across  $20^\circ\text{C}$ . This indicates that occupants and their actions (including central A/C or portable devices activation, windows/doors opening and closing) are pivotal in driving room-specific average temperature levels. In sharp contrast, the humidity levels in Term 1 and during the lockdown show marginal differences (<5% for almost all room types) as the loss of latent heat was largely compensated by higher relative humidity under lower temperatures. This also explains why the gap was especially narrow in studios and especially wide in multilevel study areas.

Similar to the bushfire period, CO<sub>2</sub> levels dropped everywhere. The maximum offset was again recorded in computer labs and reached  $-138.7$ ,  $-136.8$ , and  $-445.3$  ppm in terms of mean, IQR and maximum, respectively, which closely resemble the values recorded during the bushfire when the labs were closed as well. The following largest decrease pertained to multilevel study areas, whose corresponding drops amounted to  $-130.8$ ,  $-69.2$ , and  $-359.8$  ppm larger than during the bushfire as a result of the complete absence of people. The reduction in means was around 30–40 ppm also in the other room types, but milder in terms of IQR and maxima. It is thus confirmed that greatest drops occur where the occupancy density is typically higher or where multiple floors are interconnected. Looking at TVOCs, the pattern is less clear, with most room uses showing negligible changes. The only rooms that experienced significantly higher TVOCs were multilevel study areas, staff offices and studios. Notably, the offset with respect to Term 1 reaches a maximum of  $133.0$ ,  $147.5$  and  $858.0$  ppb (mean, IQR, and maximum) in multilevel study areas, again due to the vertical contribution from



interconnected floors and the greatest air volume. All multilevel study areas and staff offices on Level 5/6 underwent major renovations and cleaning during the lockdown period which explains the increase in TVOCs associated with the use of cleaning products, paints and varnishes.

To further investigate the perturbing actions of bushfires and COVID lockdown on the inter-parameter equilibria, we performed mutual information analysis on the subset of sensors having more than 90% of reading over Term 1, Bushfire and COVID-19 periods. Then we calculated the difference in correlation coefficients with respect to Term 1, to determine which associations got stronger or weaker under extreme events. We focused the analysis on 4 locations per each period, where the absolute maximum, maximum average, absolute minimum and minimum average difference was recorded. The results are displayed in Figure 11. During the bushfires, the absolute maximum difference (0.60) occurred in a non-conditioned, north-oriented individual office on Level 4 and affected the relationship between indoor CO<sub>2</sub> and outdoor PM<sub>10</sub>. The maximum mean difference (0.09) was recorded at the same location, where the temperature was more correlated with O<sub>3</sub>, RH with both PMs and TVOCs with wd. This suggests that, under bushfire conditions, temperature-triggered photochemistry as well as wet deposition phenomena are critical in defining the

IEQ conditions with a major role played by temperature, humidity, and wind-related parameters. The absolute minimum difference (-0.46) was detected in a north-oriented individual office on Level 3 and affected the TVOCs-PM<sub>2.5</sub> relationship, again induced by cleaning works. The minimum mean difference (0.003) was recorded in a south-oriented individual office on Level 5, where T was much less correlated with NO<sub>2</sub>, RH with TVOCs and NO<sub>2</sub>, CO<sub>2</sub> with TVOCs and O<sub>3</sub>, and TVOCs with RH, CO<sub>2</sub> and PM<sub>2.5</sub>. Such a wide decrease in associativity is likely caused by the transient effects of pollutants intake from the outdoors and the tendency to accumulate towards lower floors. All major differences occurred in individual offices, as their limited air volume was more responsive to short-lived variations.

During COVID-19 lockdown, the correlations tended to get stronger as more stable conditions were established across the building. The absolute maximum difference (0.73) occurred in a non-conditioned, south-oriented staff office on Level 4 and affected the relationship between indoor CO<sub>2</sub> and wind speed. As people's contribution to CO<sub>2</sub> emissions disappeared, the relative weight of outdoor carbon dioxide transported by the wind increased. The maximum mean difference (0.17) was recorded in a computer lab on level 3, where almost all correlations increased by more than 0.5. This suggests that

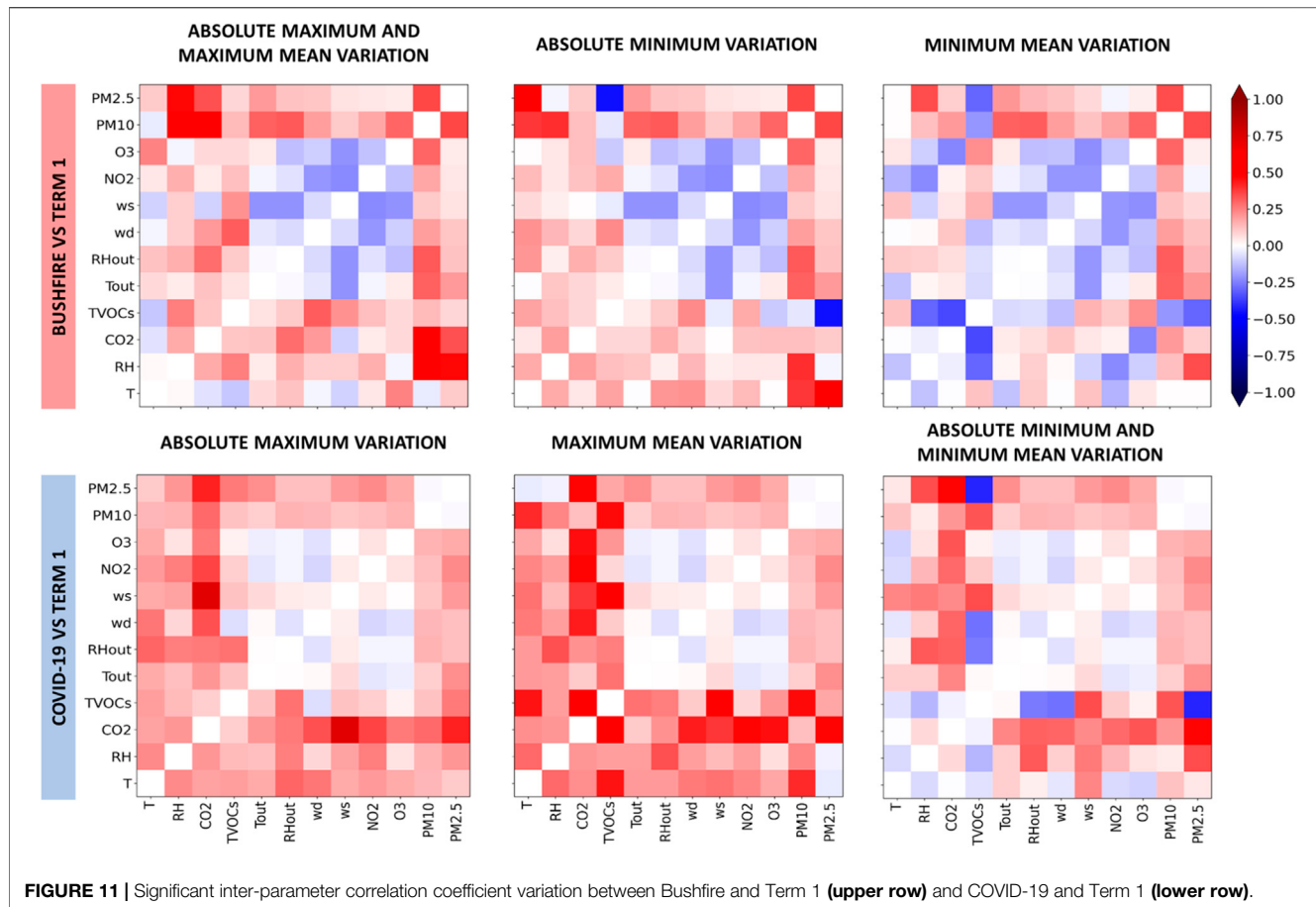


**FIGURE 11 |** Significant inter-parameter correlation coefficient variation between Bushfire and Term 1 (**upper row**) and COVID-19 and Term 1 (**lower row**).

occupancy dictates the IEQ level in spaces of standard high-density, on all counts. The absolute minimum difference ( $-0.42$ ) was detected in the centrally located studio in the basement and affected the TVOCs-PM<sub>2.5</sub> relationship. This location experienced also the minimum mean difference ( $0.08$ ), since the correlations across indoor parameters were strongly attenuated. This decrease in associativity is partly compensated by the increase in associativity with outdoor parameters, which, in the end, is the overarching effect of the lockdown.

## DISCUSSION AND DESIGN GUIDELINES

A public health imperative exists for educational buildings to be heat- and pollution-safe, particularly on account of escalating heatwaves and tropical nights events that impair night flush cooling (Gershunov et al., 2009; Dengel and Swainson, 2012). To achieve these objectives, results from fine-grained and long-term measurements can be used in identifying priority areas and emerging patterns, which can inform re-design strategies for IEQ preservation. These insights can be further useful for other buildings with similar building types, usage, and characteristics.

Focusing on room characteristics, we find that:

- the absence of an air-conditioning system was conducive to greater heat stress, while its presence triggered higher average pollutant concentrations. This is particularly due to the fact that passive ventilation systems - such as louvres that are embedded to assist with air circulation in the building - entirely rely on manual interventions that are not commonly used. Accordingly, the optimum natural ventilation of the building envisioned in the design is hardly achieved. This results in significantly higher CO<sub>2</sub> levels in rooms with high occupancy, as users tend to be less sensitive to CO<sub>2</sub> levels, further supporting the need for automated demand-driven controls that can be actioned informed by real-time data;
- north-exposure was associated with the hottest conditions, suggesting a non-efficient use of thermally massive materials, ineffectiveness of solar shading devices, and limited natural ventilation;
- insufficient thermal insulation and air tightness result in excessively humid episodes in high-occupancy rooms close to the ground and facing south, where shading was most effective;
- rooms located in the basement, which lack windows and mostly rely on air conditioning, experienced the best and worst heat stress conditions depending on manual interventions to condition the air and dissipate excess humidity.

Focusing on room use, we find that:

- individual offices (mostly north-facing) exhibited most absolute maxima and minima, owing to the small air volume, the highly transmitting windowed side, and the extreme variability associated with occupancy patterns. These rooms also represent the highest user autonomy and, therefore, likelihood for implementing manual interventions. The use of portable A/C devices and the amount of electronic equipment should clearly be considered in individual offices to enhance heat index and IEQ levels;
- computer labs exhibited the highest mean temperature, CO<sub>2</sub>, and TVOCs, with significant extreme episodes. Being densely occupied, electronically closed, and prone to untimely comfort-restoring actions, these rooms, on average, act as sinks for heat and pollutants and fail at maintaining heat safe conditions. Particularly during extreme events such as bushfires, these rooms should be closely monitored and intensively ventilated to avoid unhealthy conditions for occupants. This further extend the service life of the electronic equipment from dust clogging;
- studios exhibited HI conditions requiring caution and significant pollution episodes, with CO<sub>2</sub> crossing the unhealthy thresholds. These rooms were mostly located on lower floors, likely leading to the accumulation of pollutants from upper levels in addition to local emissions from typical equipment used on site. Relocation of studio-like environments with higher occupancy to upper floors should be considered;
- multi-level study areas benefited from better air circulation, but were prone to extreme pollutant accumulation due to the presence of fully glazed facades that cannot be opened;
- meeting rooms succeeded in maintaining the comfort zones on average, but exhibited very high-risk events during closed-door meetings. Both CO<sub>2</sub> and TVOCs could reach unhealthy levels in short periods of use. Due to concerns regarding noise levels, doors are often kept shut which leads to extremely unhealthy conditions particularly during extreme weather events. Large, acoustically-insulated grids or automated controls could be implemented to maintain adequate cross ventilation while addressing concerns regarding noise;
- staff offices were typically heat-safe, thanks to extensive shading, very low occupancy, and AC provisions. Similar to individual offices, these spaces are also more likely to be subject to manual interventions. However, the presence of TVOC-emitting equipment and major renovations exacerbated TVOCs levels;
- classrooms outperformed all other environments in terms of thermo-hygrometric conditions with no A/C in place, particularly due to their south exposure, the extensive provision of shadings and operable windows, and the efficient cross ventilation. The temperature typically lied in the 20–25°C range, the HI stayed within the heat-safe zone, and TVOCs never crossed the unhealthy threshold in warm

periods. However, mean CO<sub>2</sub> levels could put sensitive people at risk and frequently crossed the unhealthy threshold, with further accumulation in wintertime when windows and doors were typically closed, thus stressing the need for year-round ventilation strategies;

- Utility rooms (such as the print and media rooms) further exhibited unique characteristics. The print room reached CO<sub>2</sub> levels so high that health-threatening levels (even for short exposure) were the norm. Major redesign measures are imperative in order to meet minimum advised levels. On the other hand, the media room in the basement, which is sporadically used for media content production, frequently experienced extreme HI episodes due to unusually high humidity levels and equipment in use. This further suggests that utility rooms, even if not regularly occupied, require active control actions or redesign to avoid adverse IEQ conditions.

On top of this, the mutual information analysis revealed that 1) relative humidity is especially correlated with carbon dioxide levels, hence a better control over RH is expected to be extremely impactful on IAQ preservation; 2) during bushfire events, a major role is played by temperature and wind-related parameters, whereas during lockdown periods (i.e., in the absence of occupants) the influence of outdoor parameters becomes dominant; 3) elevation arbitrates the strength of correlation between thermo-hygrometric and air quality parameters. Future-proof re-design strategies should be built upon these associations.

Pertaining to the application of fine-grained IoT networks for assessing environmental quality, we note that in addition to insights gathered in this analysis, certain challenges and limitations should be considered. First, not only the spatial and temporal distribution of data collection but also the parameters monitored have a big impact on drawing insights from results. For instance, behavioural parameters - such as occupancy and manual interventions - are not commonly recorded in the environmental networks, but have a significant impact on IEQ particularly in educational buildings on university campuses. Here, room types are used as a proxy for determining occupancy patterns, but future measurement campaigns should consider collecting detailed behavioural data that focus the analyses solely on occupied hours. Similarly, detailed metadata on room characteristics are extremely hard to obtain and rarely incorporated in the IoT environmental data platforms. Here, exhaustive and manual surveys of rooms were conducted to determine room characteristics in the studied research (summarized in **Supplementary Appendix A1**). Future research should focus on automated integration of fine-grained building information with real-time sensor data, establishing a digital twin of buildings to effectively integrate, communicate, and analyze environmental quality. More importantly, such integration with building data can inform automated control actions that enhance IEQ. Lastly, larger deployment of sensors often dictates that sensors are lower cost which can have an impact on sensor accuracy and

lifetime. Quality controls are applied in these analyses (before sensor installation and after data collection), but longer-term data collection likely requires recalibrations to account for sensor drifts and faulty devices. This is in addition to maintenance challenges regarding theft and vandalism that have been experienced in this project.

On a conclusive note, the proposed monitoring design departs from conventional data collection methods, relying on controlled-environment testing or short-term monitoring. It captures the IEQ nuances in a realistic and unbiased fashion. Accordingly, we did not intend, nor had the ability, to control for environmental/occupancy conditions that the building was going to be subject to in the long term. This non-invasive approach makes it harder to disclose clear patterns and run comparative assessments, yet it gives us the chance to appreciate the complexity of a living environment without data degradation or alteration.

## CONCLUSION

In this study, we targeted an educational building in Sydney, whose proclivity to IEQ deterioration is aggravated by design inefficiencies and local weather extremes. A novel, low-cost, multi-parameter IoT sensor network was deployed to fully depict the spatial heterogeneity and temporal variability in terms of thermal comfort and air quality. The data has been analysed through a variety of statistical methods including unconditioned and conditioned mutual information analysis and through established comfort metrics on account of room characteristics, room use, season, weather extremes and standard *versus* atypical occupancy patterns as those recorded during the bushfire season and the COVID-19 pandemic. By merging the results presented in *Results* section, a variety of redesign strategies could be delineated (*Discussion and Design Guidelines* section) thanks to the fine-grained, site-specific monitoring of each room type across

different floors and orientations. Such a detailed analysis compensates for less perceivable threats, pinpoints passive ventilation inefficiencies, identifies the room for improvement, and suggests an urgent need to prioritize building air tightness improvement, appropriate filtration techniques and smart logics. This study offers a roadmap for other campaigns alike in order to verify climate dependencies and general patterns and move towards more resilient and healthy educational buildings. However, future directions in IoT environmental sensor networks should focus on not only covering spatial heterogeneity of IEQ, but also consider comprehensive data collection (encompassing environmental and behavioural factors), integration of building metadata, and dynamic quality controls to provide most comprehensive insights.

## DATA AVAILABILITY STATEMENT

The raw data supporting the conclusion of this article will be made available by the authors, without undue reservation.

## AUTHOR CONTRIBUTIONS

NN and CP conceived the presented idea, established and maintained the IoT sensor network, and supervised the project. FZ obtained the data and performed quality controls. GU analysed the data and wrote the manuscript with support from NN, CP, and FZ.

## SUPPLEMENTARY MATERIAL

The Supplementary Material for this article can be found online at: <https://www.frontiersin.org/articles/10.3389/fenvs.2021.725974/full#supplementary-material>

## REFERENCES

- Abc (2018). *Indoor Air Quality Handbook*. CANBERRA ACT.
- Abdul Rahman, I., Putra, J. C. P., and Nagapan, S. (2014). Correlation of Indoor Air Quality with Working Performance in Office Building. *Mod. Appl. Sci.* 8, 153–160. doi:10.5539/mas.v8n6p153
- Alfano, F. R. A., Palella, B. I., and Riccio, G. (2011). Thermal Environment Assessment Reliability Using Temperature -Humidity Indices. *Ind. Health* 49, 95–106. doi:10.2486/indhealth.ms1097
- Almeida, R. M. S. F., and de Freitas, V. P. (2014). Indoor Environmental Quality of Classrooms in Southern European Climate. *Energy and Buildings* 81, 127–140. doi:10.1016/j.enbuild.2014.06.020
- Alonso, A., Llanos, J., Escandón, R., and Sendra, J. J. (2021). Effects of the COVID-19 Pandemic on Indoor Air Quality and Thermal Comfort of Primary Schools in Winter in a Mediterranean Climate. *Sustainability* 13, 2699. doi:10.3390/su13052699
- Andualem, Z., Gizaw, Z., Bogale, L., and Dagne, H. (2019). Indoor Bacterial Load and its Correlation to Physical Indoor Air Quality Parameters in Public Primary Schools. *Multidiscip. Respir. Med.* 14, 2. doi:10.1186/s40248-018-0167-y
- Annesi-Maesano, I., Baiz, N., Banerjee, S., Rudnai, P., and Rive, S. The SINPHONIE Group (2013). Indoor Air Quality and Sources in Schools and Related Health Effects. *J. Toxicol. Environ. Health B* 16, 491–550. doi:10.1080/10937404.2013.853609
- ANSI/ASHRAE (2016). *ANSI/ASHRAE 62-1 Ventilation for Acceptable Indoor Air Quality*.
- Apte, M. G., and Erdmann, C. A. (2002). *Associations of Indoor Carbon Dioxide Concentrations, VOCs, Environmental Susceptibilities with Mucous Membrane and Lower Respiratory Sick Building Syndrome Symptoms in the BASE Study: Analyses of the 100 Building Dataset*. Berkeley, CA: Lawrence Berkeley National Lab. doi:10.2172/806126
- Apte, M. G., Fisk, W. J., and Daisey, J. M. (2000). Associations between Indoor CO<sub>2</sub> Concentrations and Sick Building Syndrome Symptoms in U.S. Office Buildings: an Analysis of the 1994–1996 BASE Study Data. *Indoor Air* 10, 246–257. doi:10.1034/j.1600-0668.2000.010004246.x
- Australian Government (2020). Air Quality – Indoor Air. Department of Agriculture, Water and the Environment. Available at: <https://www.environment.gov.au/protection/air-quality/indoor-air> (Accessed October 3, 2021).
- Baird, G., and Marriage, G. (2015). User Satisfaction with Academic Buildings-FFindings from post Occupancy Evaluations. Available at: [http://anzasca.net/wp-content/uploads/2015/12/059\\_Baird\\_Marriage\\_ASA2015.pdf](http://anzasca.net/wp-content/uploads/2015/12/059_Baird_Marriage_ASA2015.pdf).
- Baird, G. (2013). Sustainable Buildings-Best and Worst Performers in Terms of Comfort, Health and Productivity. Smart and Sustainable Built Environments. Available at: [https://www.researchgate.net/profile/Nurul\\_Sakina\\_Mokhtar-Azizi2/publication/283479398\\_Proceedings\\_of\\_Smart\\_and\\_Sustainable\\_Built\\_Environments/links/5639c01108aecf1d92a9fa63/Proceedings-of-Smart-and-Sustainable-Built-Environments.pdf#page=365](https://www.researchgate.net/profile/Nurul_Sakina_Mokhtar-Azizi2/publication/283479398_Proceedings_of_Smart_and_Sustainable_Built_Environments/links/5639c01108aecf1d92a9fa63/Proceedings-of-Smart-and-Sustainable-Built-Environments.pdf#page=365).

- Baird, G. (2003). *The Architectural Expression of Environmental Control Systems*. Taylor & Francis. doi:10.4324/9780203362488
- Bolan, N. (2020). A Burning Issue: Volatile Organic Compounds from Bushfire. *Chem. Aust.*, 21–23.
- BOM (2021a). Australian Government Climate Classification Maps. Available at: [http://www.bom.gov.au/jsp/ncc/climate\\_averages/climate-classifications/index.jsp?maptype=kpn#maps](http://www.bom.gov.au/jsp/ncc/climate_averages/climate-classifications/index.jsp?maptype=kpn#maps) (Accessed April 29, 2021).
- BOM (2021). Climate Statistics for Australian Locations - Summary Statistics SYDNEY. Available at: [http://www.bom.gov.au/climate/averages/tables/cw\\_066062.shtml](http://www.bom.gov.au/climate/averages/tables/cw_066062.shtml) (Accessed March 23, 2021).
- Calderón-Garcidueñas, L., Calderón-Garcidueñas, A., Torres-Jardón, R., Avila-Ramírez, J., Kulesza, R. J., and Anguilli, A. D. (2015). Air Pollution and Your Brain: what Do You Need to Know Right Now. *Prim. Health Care Res. Dev.* 16, 329–345. doi:10.1017/s146342361400036x
- Cellucci, C. J., Albano, A. M., and Rapp, P. E. (2005). Statistical Validation of Mutual Information Calculations: Comparison of Alternative Numerical Algorithms. *Phys. Rev. E Stat. Nonlin. Soft Matter Phys.* 71, 066208. doi:10.1103/PhysRevE.71.066208
- Chatzidiakou, L., Mumovic, D., and Summerfield, A. J. (2012). What Do We Know about Indoor Air Quality in School Classrooms? A Critical Review of the Literature. *Intell. Buildings Int.* 4, 228–259. doi:10.1080/17508975.2012.725530
- Chernev, L., Targino, A. C., Coraiola, G. C., and Krecl, P. (2012). “Outdoor thermal comfort Indices and Their Relation to Land Use over an Urban Area during winter Time,” in *XI Congresso Argentino de Meteorología* (Mendoza, Argentina). Available at: <http://www.congremet.prmarg.org/upload/chernevluca.pdf>.
- Daisey, J. M., Angell, W. J., and Apté, M. G. (2003). Indoor Air Quality, Ventilation and Health Symptoms in Schools: an Analysis of Existing Information. *Indoor Air* 13, 53–64. doi:10.1034/j.1600-0668.2003.00153.x
- Dengel, A., and Swainson, M. (2012). *Overheating in New Homes: A Review of the Evidence*. Milton Keynes: Building Research Establishment.
- Dorizas, P. V., Assimakopoulos, M.-N., and Santamouris, M. (2015). A Holistic Approach for the Assessment of the Indoor Environmental Quality, Student Productivity, and Energy Consumption in Primary Schools. *Environ. Monit. Assess.* 187, 259. doi:10.1007/s10661-015-4503-9
- Ebenstein, A., Levy, V., and Roth, S. (2016). The Long-Run Economic Consequences of High-Stakes Examinations: Evidence from Transitory Variation in Pollution. *Am. Econ. J. Appl. Econ.* 8, 36–65. doi:10.1257/app.20150213
- Eide, E. R., Showalter, M. H., and Goldhaber, D. D. (2010). The Relation between Children’s Health and Academic Achievement. *Child. Youth Serv. Rev.* 32, 231–238. doi:10.1016/j.childyouth.2009.08.019
- Evrard, A.-S., Hmon, D., Billon, S., Laurier, D., Jougl, E., Tirmarche, M., et al. (2006). Childhood Leukemia Incidence and Exposure to Indoor Radon, Terrestrial and Cosmic Gamma Radiation. *Health Phys.* 90, 569–579. doi:10.1097/01.hp.0000198787.93305.35
- Fang, L., Clausen, G., and Fanger, P. O. (1998). Impact of Temperature and Humidity on the Perception of Indoor Air Quality. *Indoor Air* 8, 80–90. doi:10.1111/j.1600-0668.1998.t01-2-00003.x
- Fraser, A. M., and Swinney, H. L. (1986). Independent Coordinates for Strange Attractors from Mutual Information. *Phys. Rev. A* 33, 1134–1140. doi:10.1103/physreva.33.1134
- Frenzel, S., and Pompe, B. (2007). Partial Mutual Information for Coupling Analysis of Multivariate Time Series. *Phys. Rev. Lett.* 99, 204101. doi:10.1103/physrevlett.99.204101
- Gallego, E., Roca, F. J., Perales, J. F., and Guardino, X. (2011). “Assessment of Chemical Hazards in Sick Building Syndrome Situations: Determination of Concentrations and Origin of VOCs in Indoor Air Environments by Dynamic Sampling and TD-GC/MS Analysis,” in *Sick Building Syndrome in Public Buildings and Workplaces* (Springer), 289–333. doi:10.1007/978-3-642-17919-8\_16
- Gent, J. F., Triche, E. W., Holford, T. R., Belanger, K., Bracken, M. B., Beckett, W. S., et al. (2003). Association of Low-Level Ozone and fine Particles with Respiratory Symptoms in Children with Asthma. *JAMA* 290, 1859–1867. doi:10.1001/jama.290.14.1859
- Gershunov, A., Cayan, D. R., and Jacobellis, S. F. (2009). The Great 2006 Heat Wave over California and Nevada: Signal of an Increasing Trend. *J. Clim.* 22, 6181–6203. doi:10.1175/2009jcli2465.1
- Government of Canada (2021). Wind Chill and Humidex Calculators. Available at: [https://weather.gc.ca/windchill/wind\\_chill\\_e.html](https://weather.gc.ca/windchill/wind_chill_e.html) (Accessed March 24, 2021).
- Haddad, S., Synnefa, A., Ángel Padilla Marcos, M., Paolini, R., Delrue, S., Prasad, D., et al. (2021). On the Potential of Demand-Controlled Ventilation System to Enhance Indoor Air Quality and thermal Condition in Australian School Classrooms. *Energy and Buildings* 238, 110838. doi:10.1016/j.enbuild.2021.110838
- Havenith, G. (2007). Metabolic Rate and Clothing Insulation Data of Children and Adolescents during Various School Activities. *Ergonomics* 50, 1689–1701. doi:10.1080/00140130701587574
- Haverinen-Shaughnessy, U., Shaughnessy, R. J., Cole, E. C., Toyinbo, O., and Moschandreas, D. J. (2015). An Assessment of Indoor Environmental Quality in Schools and its Association with Health and Performance. *Building Environ.* 93, 35–40. doi:10.1016/j.buildenv.2015.03.006
- Humphreys, M. A., Rijal, H. B., and Nicol, J. F. (2013). Updating the Adaptive Relation between Climate and comfort Indoors; New Insights and an Extended Database. *Building Environ.* 63, 40–55. doi:10.1016/j.buildenv.2013.01.024
- IPCC Fifth Assessment Report (AR5) (2013). *WMO, IPCC Secretariat*.
- Kim, E.-K., Kim, G.-S., and Park, J.-S. (2009). Comparison of Activity Factor, Predicted Resting Metabolic Rate, and Intakes of Energy and Nutrients between Athletic and Non-athletic High School Students. *J. Korean Diet. Assoc.* 15, 52–68.
- Klepeis, N. E., Nelson, W. C., Ott, W. R., Robinson, J. P., Tsang, A. M., Switzer, P., et al. (2001). The National Human Activity Pattern Survey (NHAPS): a Resource for Assessing Exposure to Environmental Pollutants. *J. Expo. Sci. Environ. Epidemiol.* 11, 231–252. doi:10.1038/sj.jea.7500165
- Laarne, P., Zaidan, M. A., and Nieminen, T. (2021). Ennemi: Non-linear Correlation Detection with Mutual Information. *SoftwareX* 14, 100686. doi:10.1016/j.softx.2021.100686
- Lacetera, N., Bernabucci, U., Khalifa, H. H., Ronchi, B., and Nardone, A. (2003). *Interaction between Climate and Animal Production*. Wageningen Academic Publishers.
- Lazović, I., Stevanović, Ž. M., Jovašević-Stojanović, M., Živković, M. M., and Banjac, M. J. (2016). Impact of CO<sub>2</sub> Concentration on Indoor Air Quality and Correlation with Relative Humidity and Indoor Air Temperature in School Buildings in Serbia. *Therm. Sci.* 20, S297–S307. doi:10.2298/tsci150831173l
- Chen, L., Jennison, B. L., Yang, W., and Omaye, S. T. (2000). Elementary School Absenteeism and Air Pollution. *Inhalation Toxicol.* 12, 997–1016. doi:10.1080/08958370050164626
- Li, C., Wang, W., Xiong, J., and Chen, P. (2014). Sensitivity Analysis for Urban Drainage Modeling Using Mutual Information. *Entropy* 16, 5738–5752. doi:10.3390/e16115738
- Livada, I., Synnefa, A., Haddad, S., Paolini, R., Garshasbi, S., Ulpiani, G., et al. (2019). Time Series Analysis of Ambient Air-Temperature during the Period 1970–2016 over Sydney, Australia. *Sci. Total Environ.* 648, 1627–1638. doi:10.1016/j.scitotenv.2018.08.144
- Loh, J. Y. S., and Andaman, M. M. A Review of IAQ Standards and Guidelines for Australian and New Zealand School Classrooms. *anzasca.Net*. Available at: [http://anzasca.net/wp-content/uploads/2017/11/ASA\\_2017\\_Loh\\_Andaman.pdf](http://anzasca.net/wp-content/uploads/2017/11/ASA_2017_Loh_Andaman.pdf).
- Luo, M., Hong, Y., and Pantelic, J. (2021). Determining Building Natural Ventilation Potential via IoT-Based Air Quality Sensors. *Front. Environ. Sci.* 9. doi:10.3389/fenvs.2021.634570
- Meiss, A., Jimeno-Merino, H., and Poza-Casado, I. (2021). Indoor Air Quality in Naturally Ventilated Classrooms. Lessons Learned from a Case Study in a COVID-19 Scenario. *Sustain. Sci. Pract. Pol.* 13 (15), 8446. doi:10.3390/su13158446
- Mendell, M. J., Eliseeva, E. A., Davies, M. M., Spears, M., Lobscheid, A., Fisk, W. J., et al. (2013). Association of Classroom Ventilation with Reduced Illness Absence: a Prospective Study in California Elementary Schools. *Indoor Air* 23, 515–528. doi:10.1111/ina.12042
- Mi, Y.-H., Norbäck, D., Tao, J., Mi, Y.-L., and Ferm, M. (2006). Current Asthma and Respiratory Symptoms Among Pupils in Shanghai, China: Influence of Building Ventilation, Nitrogen Dioxide, Ozone, and Formaldehyde in Classrooms. *Indoor Air* 16, 454–464. doi:10.1111/j.1600-0668.2006.00439.x
- Moran, D. S., Shapiro, Y., Epstein, Y., Matthew, W., and Pandolf, K. B. (1998). “A Modified Discomfort index (MDI) as an Alternative to the Wet Bulb globe Temperature (WBGT),” in *Environmental Ergonomics VIII*. Editors J. A. Hodgdon, J. H. Heaney, and M. J. Buono, 77–80.
- Mumtaz, R., Zaidi, S. M. H., Shakir, M. Z., Shafiq, U., Malik, M. M., Haque, A., et al. (2021). Internet of Things (IoT) Based Indoor Air Quality Sensing and

- Predictive Analytic-A COVID-19 Perspective. *Electronics* 10, 184. doi:10.3390/electronics10020184
- Nazarian, N., and Lee, J. K. (2021). Personal Assessment of Urban Heat Exposure: a Systematic Review. *Environ. Res. Lett.* 16, 033005. doi:10.1088/1748-9326/abd350
- NOAA (2021). Summer Weather Safety and Survival: the Heat Index. Available at: <https://www.weather.gov/oun/safety-summer-heatindex> (Accessed March 24, 2021).
- Norbäck, D., and Nordström, K. (2008). Sick Building Syndrome in Relation to Air Exchange Rate, CO<sub>2</sub>, Room Temperature and Relative Air Humidity in university Computer Classrooms: an Experimental Study. *Int. Arch. Occup. Environ. Health* 82, 21–30. doi:10.1007/s00420-008-0301-9
- Nws, U. (2021). What Is the Heat index. Available at: <https://www.weather.gov/ama/heatindex> (Accessed March 24, 2021).
- Ortiz Perez, A., Bierer, B., Scholz, L., Wöllensteijn, J., and Palzer, S. (2018). A Wireless Gas Sensor Network to Monitor Indoor Environmental Quality in Schools. *Sensors* 18, 4345. doi:10.3390/s18124345
- Palacios Temprano, J., Eichholz, P., Willeboordse, M., and Kok, N. (2020). Indoor Environmental Quality and Learning Outcomes: Protocol on Large-Scale Sensor Deployment in Schools. *BMJ Open* 10, e031233. doi:10.1136/bmjopen-2019-031233
- Potchter, O., Cohen, P., Lin, T.-P., and Matzarakis, A. (2018). Outdoor Human thermal Perception in Various Climates: A Comprehensive Review of Approaches, Methods and Quantification. *Sci. Total Environ.* 631–632, 390–406. doi:10.1016/j.scitotenv.2018.02.276
- Quinn, A., Tamerius, J. D., Perzanowski, M., Jacobson, J. S., Goldstein, I., Acosta, L., et al. (2014). Predicting Indoor Heat Exposure Risk during Extreme Heat Events. *Sci. Total Environ.* 490, 686–693. doi:10.1016/j.scitotenv.2014.05.039
- Rajagopalan, P., and Goodman, N. (2021). Improving the Indoor Air Quality of Residential Buildings during Bushfire Smoke Events. *Climate* 9, 32. doi:10.3390/cli9020032
- Reid, C. E., Considine, E. M., Watson, G. L., Telesca, D., Pfister, G. G., and Jerrett, M. (2019). Associations between Respiratory Health and Ozone and fine Particulate Matter during a Wildfire Event. *Environ. Int.* 129, 291–298. doi:10.1016/j.envint.2019.04.033
- Rocca, M., Leccese, F., and Salvadori, G. (2020). "Health and Well-Being in Indoor Work Environments: Features of an Expert Assessment Campaign in an Italian University Hospital," in 2020 IEEE International Conference on Environment and Electrical Engineering and 2020 IEEE Industrial and Commercial Power Systems Europe (EEEIC/I CPS Europe), Madrid, Spain, 9–12 June 2020 (IEEE), 1–6. doi:10.1109/ieeeiccpseurope49358.2020.9160493
- Rothfusz, L. P., and Headquarters, N. S. R. (1990). *The Heat index Equation (Or, More than You Ever Wanted to Know about Heat index)*. Fort Worth, Texas: National Oceanic and Atmospheric Administration, National Weather Service, Office of Meteorology, 9023. Available at: [http://wonder.cdc.gov/wonder/help/Climate/ta\\_htindx.PDF](http://wonder.cdc.gov/wonder/help/Climate/ta_htindx.PDF).
- Ryu, U., Wang, J., Kim, T., Kwak, S., and UJuhyo, J. (2018). Construction of Traffic State Vector Using Mutual Information for Short-Term Traffic Flow Prediction. *Transportation Res. C: Emerging Tech.* 96, 55–71. doi:10.1016/j.trc.2018.09.015
- Saad, S. M., Shakaff, A. Y. M., Saad, A. R. M., Yusof, A. M., Andrew, A. M., Zakaria, A., et al. (2017). Development of Indoor Environmental index: Air Quality index and thermal comfort index. *AIP Conf. Proc.* 1808, 020043. doi:10.1063/1.4975276
- Sagguru, G. S., Mittal, S. K., Agarwal, R., and Beig, G. (2018). Epidemiological Study on Respiratory Health of School Children of Rural Sites of Malwa Region (India) during Post-harvest Stubble Burning Events. *MAPAN* 33, 281–295. doi:10.1007/s12647-018-0259-3
- Santamouris, M., Haddad, S., Fiorito, F., Osmond, P., Ding, L., Prasad, D., et al. (2017). Urban Heat Island and Overheating Characteristics in Sydney, Australia. An Analysis of Multiyear Measurements. *Sustainability* 9, 712. doi:10.3390/su9050712
- Santamouris, M. (2020). Recent Progress on Urban Overheating and Heat Island Research. Integrated Assessment of the Energy, Environmental, Vulnerability and Health Impact. Synergies with the Global Climate Change. *Energy and Buildings* 207, 109482. doi:10.1016/j.enbuild.2019.109482
- Satish, U., Mendell, M. J., Shekhar, K., Hotchi, T., Sullivan, D., Streufert, S., et al. (2012). Is CO<sub>2</sub>an Indoor Pollutant? Direct Effects of Low-To-Moderate CO<sub>2</sub>Concentrations on Human Decision-Making Performance. *Environ. Health Perspect.* 120, 1671–1677. doi:10.1289/ehp.1104789
- Schibuela, L., and Tambani, C. (2020). Indoor Environmental Quality Classification of School Environments by Monitoring PM and CO<sub>2</sub> Concentration Levels. *Atmos. Pollut. Res.* 11, 332–342. doi:10.1016/j.apr.2019.11.006
- Simons, E., Hwang, S.-A., Fitzgerald, E. F., Kielb, C., and Lin, S. (2010). The Impact of School Building Conditions on Student Absenteeism in Upstate New York. *Am. J. Public Health* 100, 1679–1686. doi:10.2105/ajph.2009.165324
- Stazi, F., Naspi, F., Ulpiani, G., and Di Perna, C. (2017). Indoor Air Quality and thermal comfort Optimization in Classrooms Developing an Automatic System for Windows Opening and Closing. *Energy and Buildings* 139, 732–746. doi:10.1016/j.enbuild.2017.01.017
- Taylor, L., Watkins, S. L., Marshall, H., Dascombe, B. J., and Foster, J. (2015). The Impact of Different Environmental Conditions on Cognitive Function: A Focused Review. *Front. Physiol.* 6, 372. doi:10.3389/fphys.2015.00372
- Ulpiani, G., Ranzi, G., and Santamouris, M. (2020). Experimental Evidence of the Multiple Microclimatic Impacts of Bushfires in Affected Urban Areas: The Case of Sydney during the 2019/2020 Australian Season. *Environ. Res.* 2, 065005. doi:10.1088/2515-7620/ab9e1a
- Ulpiani, G., Ranzi, G., and Santamouris, M. (2021). Local Synergies and Antagonisms between Meteorological Factors and Air Pollution: A 15-year Comprehensive Study in the Sydney Region. *Sci. Total Environ.* 788, 147783. doi:10.1016/j.scitotenv.2021.147783
- Umweltbundesamt (2007). Evaluation of Indoor Air Contaminants by Means of Reference and Guideline Values. *Bundesgesundheitsblatt Gesundheitsforschung Gesundheitsschutz* 50, 990–1005. doi:10.1007/s00103-007-0290-y
- UNSW (2021). Myair Air Quality Sensors. City Futures Research Centre. Available at: <https://citydata.be.unsw.edu.au/layers/geonode%3Amyair#more> (Accessed March 23, 2021).
- World Health Organization (2000). *Air Quality Guidelines for Europe*. Copenhagen: WHO Reg Publ Eur Ser, V–273.
- Wyon, D. P. (2004). The Effects of Indoor Air Quality on Performance and Productivity. *Indoor Air* 14 (7), 92–101. doi:10.1111/j.1600-0668.2004.00278.x
- Yun, G. Y., Ngarambe, J., Duhirwe, P. N., Ulpiani, G., Paolini, R., Haddad, S., et al. (2020). Predicting the Magnitude and the Characteristics of the Urban Heat Island in Coastal Cities in the Proximity of Desert Landforms. The Case of Sydney. *Sci. Total Environ.* 709, 136068. doi:10.1016/j.scitotenv.2019.136068
- Zaidan, M. A., Dada, L., Alghamdi, M. A., Al-Jeelani, H., Lihavainen, H., Hyvärinen, A., et al. (2019). Mutual Information Input Selector and Probabilistic Machine Learning Utilisation for Air Pollution Proxies. *Appl. Sci.* 9, 4475. doi:10.3390/app9204475
- Zaidan, M. A., Haapasila, V., Relan, R., Paasonen, P., Kerminen, V.-M., Junninen, H., et al. (2018). Exploring Non-linear Associations between Atmospheric New-Particle Formation and Ambient Variables: a Mutual Information Approach. *Atmos. Chem. Phys.* 18, 12699–12714. doi:10.5194/acp-18-12699-2018
- Zhao, D., Azimi, P., and Stephens, B. (2015). Evaluating the Long-Term Health and Economic Impacts of Central Residential Air Filtration for Reducing Premature Mortality Associated with Indoor Fine Particulate Matter (PM<sub>2.5</sub>) of Outdoor Origin. *Ijerph* 12, 8448–8479. doi:10.3390/ijerph120708448

**Conflict of Interest:** The authors declare that the research was conducted in the absence of any commercial or financial relationships that could be construed as a potential conflict of interest.

**Publisher's Note:** All claims expressed in this article are solely those of the authors and do not necessarily represent those of their affiliated organizations, or those of the publisher, the editors and the reviewers. Any product that may be evaluated in this article, or claim that may be made by its manufacturer, is not guaranteed or endorsed by the publisher.

Copyright © 2021 Ulpiani, Nazarian, Zhang and Pettit. This is an open-access article distributed under the terms of the Creative Commons Attribution License (CC BY). The use, distribution or reproduction in other forums is permitted, provided the original author(s) and the copyright owner(s) are credited and that the original publication in this journal is cited, in accordance with accepted academic practice. No use, distribution or reproduction is permitted which does not comply with these terms.



# Quantifying Local and Mesoscale Drivers of the Urban Heat Island of Moscow with Reference and Crowdsourced Observations

Mikhail Varentsov<sup>1,2,3\*</sup>, Daniel Fenner<sup>4,5</sup>, Fred Meier<sup>6\*</sup>, Timofey Samsonov<sup>1,2</sup> and Matthias Demuzere<sup>4</sup>

<sup>1</sup>Research Computing Center/Faculty of Geography, Lomonosov Moscow State University, Moscow, Russia, <sup>2</sup>Moscow Center for Fundamental and Applied Mathematics, Moscow, Russia, <sup>3</sup>Smart Urban Nature Laboratory, Agrarian Technological Institute, Peoples Friendship University of Russia (RUDN University), Moscow, Russia, <sup>4</sup>Urban Climatology Group, Department of Geography, Ruhr University Bochum, Bochum, Germany, <sup>5</sup>Chair of Environmental Meteorology, Institute of Earth and Environmental Sciences, Faculty of Environment and Natural Resources, University of Freiburg, Freiburg, Germany, <sup>6</sup>Chair of Climatology, Institute of Ecology, Technische Universität Berlin, Berlin, Germany

## OPEN ACCESS

### Edited by:

Tomas Halenka,  
Charles University, Czechia

### Reviewed by:

Valéry Masson,  
Météo-France, France  
Marcus Thatcher,  
Oceans and Atmosphere (CSIRO),  
Australia

### \*Correspondence:

Mikhail Varentsov  
[mikhail.varentsov@srcc.msu.ru](mailto:mikhail.varentsov@srcc.msu.ru)  
Fred Meier  
[fred.meier@tu-berlin.de](mailto:fred.meier@tu-berlin.de)

### Specialty section:

This article was submitted to  
Interdisciplinary Climate Studies,  
a section of the journal  
Frontiers in Environmental Science

Received: 29 May 2021

Accepted: 28 October 2021

Published: 25 November 2021

### Citation:

Varentsov M, Fenner D, Meier F, Samsonov T and Demuzere M (2021) Quantifying Local and Mesoscale Drivers of the Urban Heat Island of Moscow with Reference and Crowdsourced Observations. *Front. Environ. Sci.* 9:716968.  
doi: 10.3389/fenvs.2021.716968

Urban climate features, such as the urban heat island (UHI), are determined by various factors characterizing the modifications of the surface by the built environment and human activity. These factors are often attributed to the local spatial scale (hundreds of meters up to several kilometers). Nowadays, more and more urban climate studies utilize the concept of the local climate zones (LCZs) as a proxy for urban climate heterogeneity. However, for modern megacities that extend to dozens of kilometers, it is reasonable to suggest a significant contribution of the larger-scale factors to the temperature and UHI climatology. In this study, we investigate the contribution of local-scale and mesoscale driving factors of the nocturnal canopy layer UHI of the Moscow megacity in Russia. The study is based on air temperature observations from a dense network consisting of around 80 reference and more than 1,500 crowdsourced citizen weather stations for a summer and a winter season. For the crowdsourcing data, an advanced quality control algorithm is proposed. Based on both types of data, we show that the spatial patterns of the UHI are shaped both by local-scale and mesoscale driving factors. The local drivers represent the surface features in the vicinity of a few hundred meters and can be described by the LCZ concept. The mesoscale drivers represent the influence of the surrounding urban areas in the vicinity of 2–20 km around a station, transformed by diffusion, and advection in the atmospheric boundary layer. The contribution of the mesoscale drivers is reflected in air temperature differences between similar LCZs in different parts of the megacity and in a dependence between the UHI intensity and the distance from the city center. Using high-resolution city-descriptive parameters and different statistical analysis, we quantified the contributions of the local- and mesoscale driving factors. For selected cases with a pronounced nocturnal UHI, their respective contributions are of similar magnitude. Our findings highlight the importance of taking both local- and mesoscale effects in urban climate studies for megacities into account. Furthermore, they underscore a need for an extension of the LCZ concept to take mesoscale settings of the urban environment into account.

**Keywords:** urban heat island, crowdsourcing, local climate zone, mesoscale, local scale, Moscow, citizen weather station, Netatmo

## INTRODUCTION

The urban heat island (UHI) is one of the most studied examples of inadvertent climate modification due to humans and refers to the fact that cities are almost always warmer than their natural surroundings (Oke et al., 2017; Stewart, 2019). UHIs affect urban dwellers in various (in)direct ways, e.g., by increased levels of heat risk/stress and heat-related mortality (Tan et al., 2010; Gabriel and Endlicher, 2011; Zemtsov et al., 2020), and are, thus, important to include in weather forecasts (Barlage et al., 2016; Baklanov et al., 2018; Rivin et al., 2020), climate-responsive urban planning (Svensson and Eliasson, 2002; Fernandez Milan and Creutzig, 2015; Emmanuel, 2021), and ecological and epidemiological applications (Gregg et al., 2003; Mironova et al., 2019; Brousse et al., 2020). UHIs are expressed at different vertical levels from subsurface soil temperatures to atmospheric boundary layer (ABL), yet the most studied and relevant for many applied tasks is a so-called canopy layer UHI, defined as the difference between the near-surface air temperatures below roof level (Oke et al., 2017). It is typically studied based on the screen level (1.5–2 m) temperature observations. Further in this paper, by UHI, we mean exactly the canopy layer UHI.

A distinctive feature of urban climates is their high spatial heterogeneity, determined by a variety of urban forms, land cover types, and anthropogenic activity on different spatial scales, and the complexity of the surface–atmosphere interaction in cities. The question of spatial scale is acknowledged as central in urban climate studies (Oke et al., 2017). It is important for observational data analysis and numerical modeling, for resolving the climatic heterogeneity in applied tasks, and for developing physically based urban climate models. However, while its importance has been recognized over decades of urban climate research (Stewart, 2019), specific contributions of processes at different spatial scales to certain urban climate phenomena remain vague.

Heterogeneity of urban forms and land cover types can be expressed on a wide range of spatial scales from micro- to mesoscale, each corresponding to typical horizontal length scales from meters to kilometers (Oke et al., 2017), and leading to scale-dependent urban climate phenomena (Pacifici et al., 2019). Among this range of scales, the so-called local scale (i.e., hundreds of meters to several kilometers) is considered to be especially relevant for UHI studies. At such scale, canopy layer air temperatures are directly influenced by their underlying surface properties (Stewart and Oke, 2012). In order to make urban climate studies more comparable and to facilitate metadata collection and description of measurement sites, Stewart and Oke (2012) developed the concept of local climate zones (LCZs), where LCZs are defined as regions of uniform surface cover, structure, material, and human activity that span hundreds of meters to several kilometers in horizontal scale. This concept classifies urban and rural environments according to local-scale surface cover, morphology, and human activities into 10 “built”

and 7 “natural” classes, where each class has a set of characteristic parameter values (e.g., sky view factor, built-up surface fraction, and vegetation surface fraction). The body of literature using the LCZ concept is fast growing (Demuzere et al., 2021), highlighting the applicability of the concept in UHI studies and showing that different LCZs possess different air temperature regimes (see, e.g., Alexander and Mills, 2014; Fenner et al., 2014; Stewart et al., 2014; Skarbit et al., 2017; Beck et al., 2018a; Verdonck et al., 2018; Milošević et al., 2021). Despite the fact that a microscale temperature heterogeneity can still be observed within the same LCZs or neighborhoods (Ellis et al., 2015; Leconte et al., 2015; Quanz et al., 2018; Shi et al., 2018; Pacifici et al., 2019), the LCZ system is widely acknowledged as a global standard for urban temperature studies (Stewart and Oke, 2012; Jiang et al., 2021).

Beyond the LCZ framework, several studies attempted to explain UHI spatial structures through local-scale variability of land cover and morphology properties. Several studies revealed dependencies between the UHI intensity and land cover parameters such as green area fraction, artificial cover fraction, and building area fraction (Bottyán et al., 2005; van Hove et al., 2015; Scott et al., 2017). More advanced statistical models were developed to predict UHI intensity, e.g., for Portland, United States (Hart and Sailor, 2009), Wroclaw, Poland (Szymański and Kryza, 2009), Rotterdam, Netherlands (Heusinkveld et al., 2014), and 35 European cities (Sangiorgio et al., 2020), using several local-scale parameters as predictors, e.g., building and road density, surface roughness, albedo, greenery, and anthropogenic heat flux.

Local-scale variations in surface cover and morphology determine modifications of the surface–atmosphere interaction regime within the surface layer of the atmosphere with a depth of a few tens of meters (Oke et al., 2017). However, for medium-sized cities and even more so for megacities, the influence of the various neighborhoods on the atmosphere is accumulated and further transformed over tens of kilometers, resulting in modifications of the whole ABL and the development of the phenomena induced by the city as a whole. According to the classification of atmospheric processes by scale (Orlanski, 1975), such phenomena can be considered as mesoscale processes. The examples of urban-induced mesoscale atmospheric phenomena include the ABL heat island with a vertical extent of hundreds of meters (Bornstein, 1968; Oke, 1995; Wouters et al., 2013; Lokoshchenko et al., 2016; Varentsov et al., 2018), urban plumes (Clarke, 1969; Wang et al., 2020), urban-induced modifications of regional circulation (Lemonsu and Masson, 2002; Varentsov et al., 2018), and deep convection systems, precipitation, and cloudiness (Bornstein and Lin, 2000; Dixon and Mote, 2003; Han et al., 2014).

The urban-caused mesoscale phenomena not only involve the “bottom-up” urban forcing affecting the ABL and lower troposphere but also provide “top-down” impacts on the canopy layer climate and spatial patterns of the UHI. The

latter is clearly expressed, e.g., in the UHI advection to the leeward side of the city and its neighboring rural areas, as reported both by modeling (Zhang et al., 2011; Heaviside et al., 2015) and observation-based (Bassett et al., 2016; Bassett et al., 2017) studies. On a quasi-climatic approximation, heat advection from varied wind directions, together with diffusion, and mixing by mesoscale circulations, are expected to smooth the local-scale thermal heterogeneity of the urban environment, and to make the climate of the given site sensitive to surface parameters outside its local-scale neighborhood. Mesoscale smoothing is expected to be among the factors establishing the known logarithmic relation between UHI intensity and city size or population (Oke, 1973; Zhou et al., 2017; Li et al., 2020).

Despite the obvious contribution of mesoscale processes to the development of urban climates, they are often ignored in spatially resolving UHI studies, including those ones aimed to predict urban temperature heterogeneity based on land cover parameters (Hart and Sailor, 2009; Szymanowski and Kryza, 2009; Heusinkveld et al., 2014). A few counterexamples include the studies for Leipzig, Germany (Franck et al., 2013), Detroit, United States, (Oswald et al., 2012), and several French (Gardes et al., 2020) and Dutch (Theeuwes et al., 2017) cities, where the authors attempted to account for both local-scale parameters and the meso-climatic features of the area through the distance from the city center and large water bodies. On the other hand, local-scale factors may be also ignored. For example, the recent work by Manoli et al. (2019) continues to explore the varying UHI intensity with population size, yet others believe this coarse-grained approach is insufficient and inappropriate, even as a first-order guidance approach (Martilli et al., 2020).

The abovementioned contradictions about the scale-dependent drivers of the UHI may, in part, be attributed to the lack of detailed observational data. To resolve urban climate phenomena with observations, high-density observational networks with stations installed in various settings are required. Such networks are deployed in different cities, e.g., in Birmingham, United Kingdom (Chapman et al., 2015); Dijon, France (Richard et al., 2018); Szeged, Hungary (Lelovics et al., 2014); and Novi Sad, Serbia (Milošević et al., 2021); see review in Muller et al. (2013) for further examples. However, the large majority of global cities do not possess such networks, as they are costly to install and maintain over longer periods of time (Muller et al., 2013).

In recent years, the use of nontraditional and opportunistic-sensing technologies in meteorological and climatological research, such as smartphones (Overeem et al., 2013b; Mass and Madaus, 2014; Droste et al., 2017), cars (Haberlandt and Sester, 2010; Mahoney and O'Sullivan, 2013; Bartos et al., 2019), commercial microwave links (Messer et al., 2006; Zinevich et al., 2009; Overeem et al., 2013a; Chwala and Kunstmann, 2019), wrist-mounted wearables (Nazarian et al., 2020), and privately owned citizen weather stations (CWSs), e.g., Wolters and Brandsma (2012), Bell et al. (2015), de Vos et al. (2017), Meier et al. (2017), Fenner et al. (2019), Droste et al. (2020), and Mandement and Caumont (2020), have shown to provide additional and reliable information, thus, highlighting a multitude of possible applications in research and beyond (de

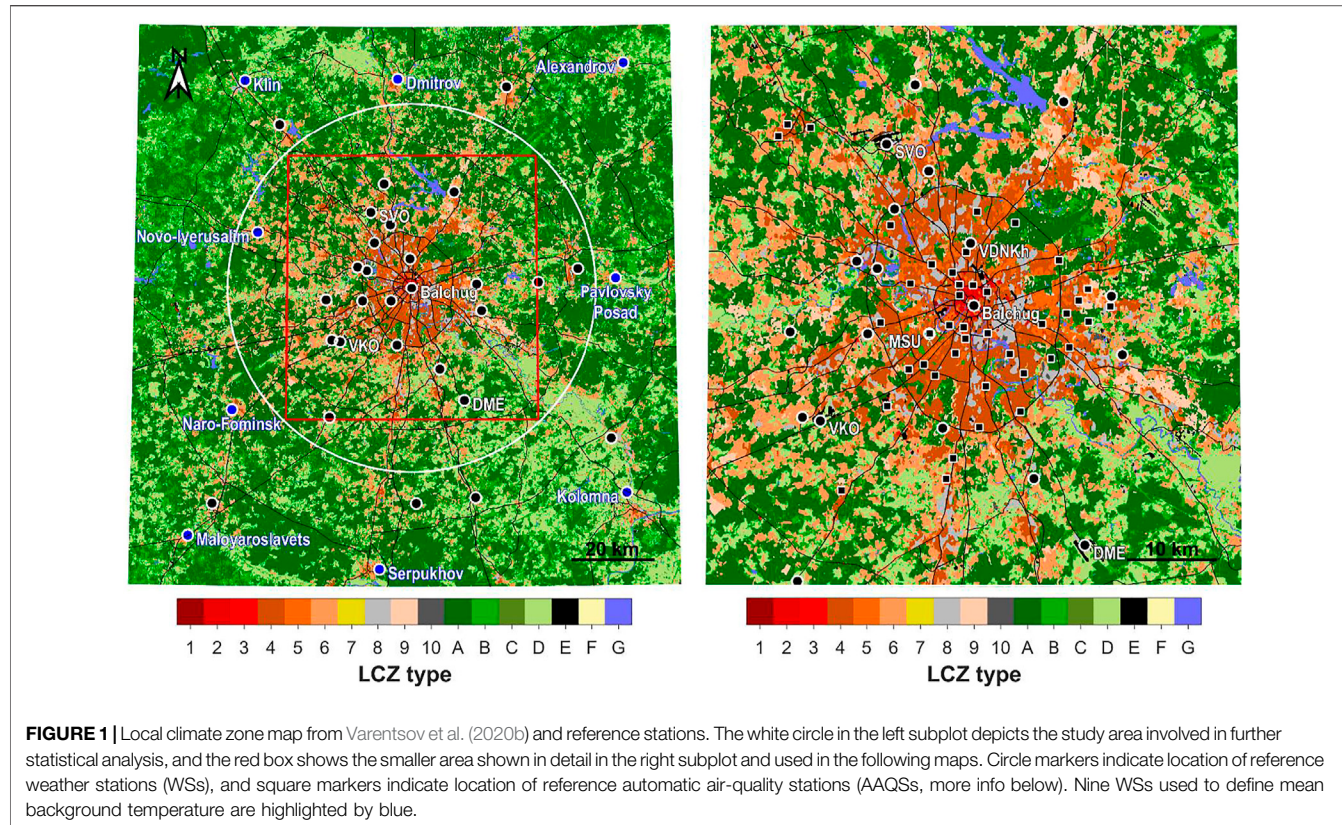
Vos et al., 2019; Nipen et al., 2020). To study urban air temperatures and the UHI effect, data from CWSs have been used in a variety of studies (Steeneveld et al., 2011; Chapman et al., 2017; Fenner et al., 2017; de Vos et al., 2020; Feichtinger et al., 2020; Venter et al., 2020; Vulova et al., 2020), focusing on different cities. One major advantage of CWSs over traditional meteorological stations is their large number within a single city (Meier et al., 2017). Further, CWSs are located in a large variety of micro- and local-scale settings, distributed all over a city region (Fenner et al., 2017), thus, detecting the spatial heterogeneity of urban air temperatures.

Decades of research provide evidence that local- and mesoscale processes are important drivers shaping urban thermal environment. This is relevant both for specific atmospheric processes as well as the scales of the surface heterogeneity influencing the climate of specific site, which are referred to as drivers in this study. However, it remains largely unknown to what extent both scales determine the spatial heterogeneity of urban air temperatures. To disentangle these two influencing spatial scales, this study focuses on the megacity of Moscow, Russia. The city is a perfect testbed for this question since it is located far away from the sea and has no significant topography, ruling out these geographic controls on the formation of its UHI. Furthermore, a large set of near-surface observations is available from both professionally maintained stations and amateur CWSs in a large variety of meso- and local-scale settings. The overall aim of the study is to investigate the respective contributions of meso- and local-scale heterogeneity of urban surface to the nighttime canopy layer UHI in Moscow.

## DATA AND ITS PREPROCESSING

### Study area

Moscow is the most populous Russian and European megacity ( $55.75^{\circ}\text{N}$ ,  $37.62^{\circ}\text{E}$ ) with a population of approximately 17 million people (considering the whole urban agglomeration) (Cox, 2017). The actual area of the city (excluding the suburbs and satellite cities) is about  $1,000 \text{ km}^2$ . Moscow has a temperate humid and moderately continental climate (Dfb in the Köppen–Geiger climate classification, Beck et al., 2018b) with an annual mean air temperature of  $5.8^{\circ}\text{C}$ , and mean June and January temperatures of  $19.2^{\circ}\text{C}$  and  $-6.5^{\circ}\text{C}$ , respectively (values are given for VDNKh weather station, Figure 1, for the period 1981–2010). Due to the cold winters, Moscow is known as one of the coldest megacities of the world. The intense urban-induced meteorological effects of Moscow are easy to detect against the homogeneous rural surroundings. The city experienced an increasing UHI intensity over the last decades (Kislov et al., 2017), with a present-day annual mean UHI intensity of  $2^{\circ}\text{C}$ , peaking to more than  $10^{\circ}\text{C}$  during calm and clear nights (Lokoshchenko, 2014; Lokoshchenko, 2017). Recently, Moscow served as a testbed for a series of high-resolution urban climate modeling studies with the COSMO model (Varentsov et al., 2017; Varentsov et al., 2019; Garbero et al., 2021), revealing persistent urban-induced mesoscale effects in the lower atmosphere (Varentsov et al., 2018) and high



sensitivity of the simulated UHI to the spatial patterns of the urban canopy parameters (Varentsov et al., 2020b). Nonetheless, despite the numerous previous studies, the spatial patterns of the Moscow UHI and their physical drivers have not been systematically analyzed yet.

This study focuses on an area centered around the city center of Moscow with a 60-km radius, thereby including Moscow itself, its suburbs, and satellite cities, yet not including the medium-sized cities around Moscow that are separated from the megacity by wide countryside areas (**Figure 1**).

## Reference meteorological observations

We use regular observations from a dense reference network (hereafter referred to as REF) consisting of weather stations (WSs) of the Russian hydrometeorological service (Roshydromet) and automatic air-quality stations (AAQS) of Mosecomonitoring, the official environmental monitoring service of Moscow. The WSs provide the most reliable screen-level (1.5–2 m above the ground) air temperature observations according to the standards of the World Meteorological Organization (WMO). Yet, only a few WSs are available in urbanized areas: the Balchug WS in the city center, the meteorological observatory of the Lomonosov Moscow State University (MSU), VDNKh WS in an urban park, and several WSs in the suburbs. AAQSs cover the city with a denser network (**Figure 1**) but provide less accurate meteorological data. Meteorological observations by AAQSs do not comply with the WMO standards, e.g., the sensors are located at a height

of 2 m above roofs of metal containers and 4 m above the ground. Previous studies showed that AAQS air temperature measurements may be biased during daytime. However, daily mean and nighttime temperatures are accurate enough for spatially explicit UHI studies (Varentsov et al., 2019).

We use REF air temperature data on a one-hourly temporal resolution with instantaneous values at the full hour to be consistent with the temporal resolution of the CWS data (see next subsection *Citizen weather stations*). The data were downsampled from the original 10- and 20-min resolutions of WSs and AAQSs, respectively. For a few WSs where only three-hourly observations are available, missing one-hourly temperature values were gap filled based on existing three-hourly values and one-hourly values for the nearest WSs, where they are available. In total, we use data from up to 42 WSs and up to 40 AAQSs (the actual number of stations varies due to data availability for the considered periods).

## Citizen weather stations

Crowdsourced air temperature data from CWSs of the “Netatmo” company (<https://www.netatmo.com/en-us/weather>) were acquired using the application programming interface (API) provided by the company (<https://dev.netatmo.com/apidocumentation/weather>). A full description of the device itself and the data acquisition, i.e., crowdsourcing, is given in Meier et al. (2017); a brief summary is given in the following. The device consists of an indoor and an outdoor module. From the latter, air temperature and relative humidity data can be acquired

via the API. The specified accuracy for the air temperature sensor is  $\pm 0.3$  K in the range  $-40^{\circ}\text{C}$ – $65^{\circ}\text{C}$ . Each CWS takes measurements approximately every 5 min, data are then automatically uploaded to the server of the company via WiFi connection. Netatmo data for the study area was collected at an hourly resolution (instantaneous values) using the workflow as described in Meier et al. (2017).

Netatmo CWSs provide uncertified observations, which can be misrepresentative for many reasons. For example, outdoor modules may be installed directly at walls or even inside buildings (Meier et al., 2017). Beyond these extreme cases, other typical ways of CWS installation could, nonetheless, be different from standards of meteorological observations, such as observations on balconies or below trees.

Previous studies have already shown the opportunity to filter out misrepresentative and faulty data using quality-control (QC) algorithms. Here, we developed a QC algorithm based on ideas from previous studies (Meier et al., 2017; Napoly et al., 2018) with some modifications, which allows to exploit the high number of reference observations in the Moscow region (**Figure 1**).

The preprocessing step, *L0*, removes CWSs with the same location (assuming that the location was wrongly defined by using the IP address; Meier et al., 2017). The following three steps, *L1*–*L3*, depend on statistics calculated over a period  $\Delta t = 14$  days before the *i*-th moment for which the QC is applied. *L1* is passed if the missing data ratio for the *j*-th CWS over the  $\Delta t$  period is lower than a threshold ( $R_{\text{gaps}} = 0.5$ ). *L2* is passed when the temperature mean value  $\overline{T_j^{\text{CWS}}}$  and the standard deviation  $\sigma(T_j^{\text{CWS}})$  for the *j*-th CWS for the  $\Delta t$  period are within an acceptable range, determined by min/max values within a set of *n* reference stations in the study area, with an additional *k<sub>1</sub>* sigma tolerance (*k<sub>1</sub>* is set to 1.5):

$$\left\{ \begin{array}{l} \min(\overline{T_{1..n}^{\text{ref}}}) - k_1 \cdot \sigma(\overline{T_{1..n}^{\text{ref}}}) \leq \overline{T_j^{\text{CWS}}} \leq \max(\overline{T_{1..n}^{\text{ref}}}) + k_1 \cdot \sigma(\overline{T_{1..n}^{\text{ref}}}) \\ \min(\sigma(\overline{T_{1..n}^{\text{ref}}})) - k_1 \cdot \sigma(\sigma(\overline{T_{1..n}^{\text{ref}}})) \leq \sigma(T_j^{\text{CWS}}) \leq \max(\sigma(\overline{T_{1..n}^{\text{ref}}})) + k_1 \cdot \sigma(\sigma(\overline{T_{1..n}^{\text{ref}}})) \end{array} \right.$$

This approach rejects CWSs if the outdoor module is located indoors and partially eliminates cases when the outdoor module is not shaded properly. The *L3* step checks the Pearson correlation coefficient *R* between the data for the *j*-th CWS and the mean temperature over the five nearest reference stations over the  $\Delta t$  period. The level is passed if  $R > 0.9$ . Levels *L4* and *L5* depend on the data for the *i*-th time moment only. The *L4* step checks whether the CWS temperature value for individual hours is within an acceptable range determined by min/max values within a set of reference stations with an additional *k<sub>2</sub>* sigma tolerance (*k<sub>2</sub>* is also set to 1.5):

$$\min(\overline{T_{1..n}^{\text{ref}}}) - k_2 \cdot \sigma(\overline{T_{1..n}^{\text{ref}}}) \leq \overline{T_j^{\text{CWS}}} \leq \max(\overline{T_{1..n}^{\text{ref}}}) + k_2 \cdot \sigma(\overline{T_{1..n}^{\text{ref}}}).$$

Finally, a fifth step (*L5*) is added to remove too high spatial variability among closely located CWSs within a 3-km distance, following the idea of a “buddy check” from Båserud et al. (2020) and Nipen et al. (2020). The criteria for the *L5* step for the temperature value for *j*-th CWS at *i*-th

moment is based on its deviation from the mean value over the neighboring CWS:

$$\left| T_j^{\text{CWS}} - \overline{T_{k_1..k_m}^{\text{CWS}}} \right| \leq 3 \cdot \sigma(T_{k_1..k_m}^{\text{CWS}})$$

where  $T_{k_1..k_m}^{\text{CWS}}$  are temperature values of *m* other CWSs within a 3-km distance. This condition is applied only if  $m \geq 4$ , and the temperature deviation  $|T_j^{\text{CWS}} - \overline{T_{k_1..k_m}^{\text{CWS}}}|$  is higher than twice the declared accuracy of Netatmo CWS air temperature measurements ( $0.6^{\circ}\text{C}$ ).

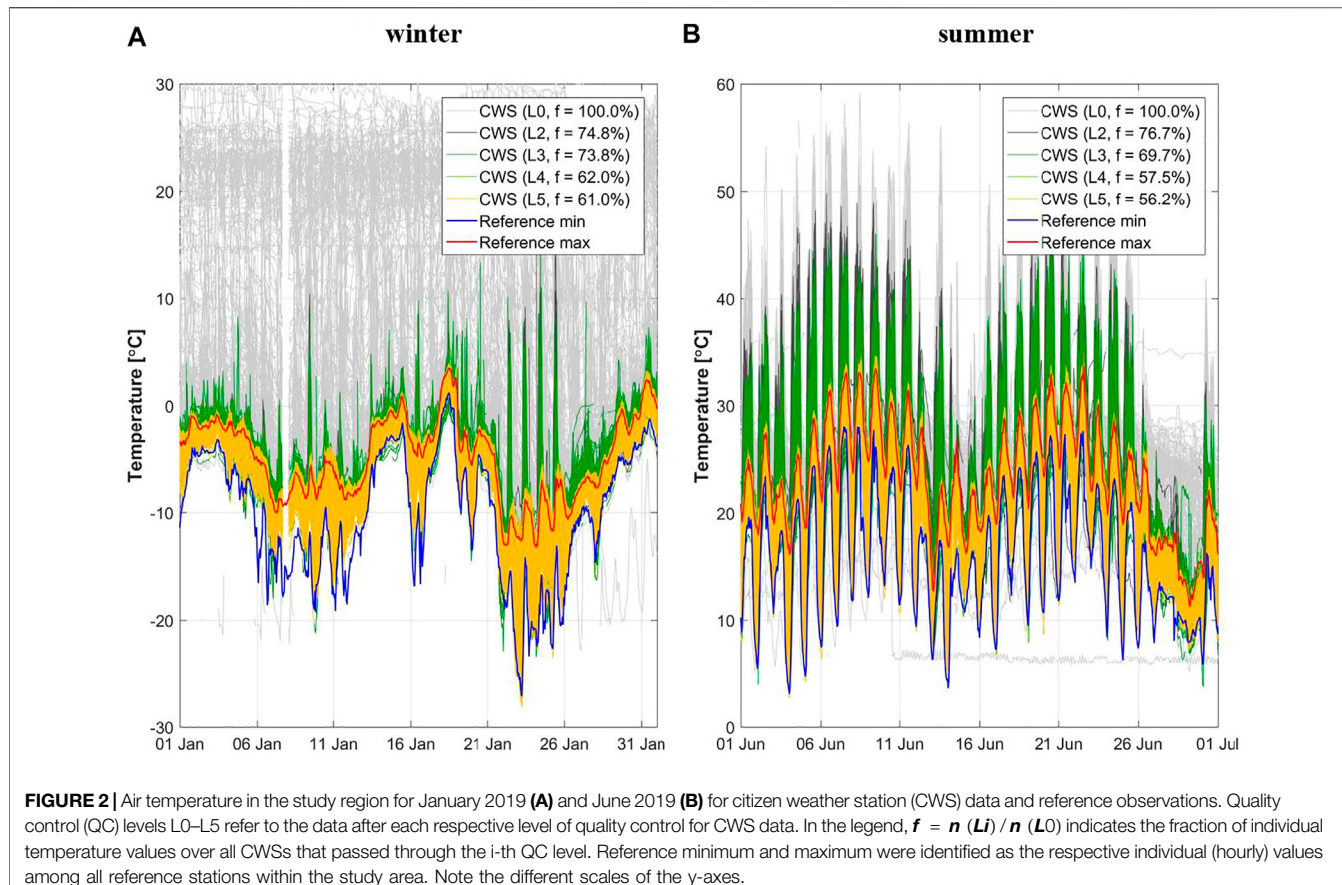
For comparison with this new QC scheme, the raw CWS data were also filtered according to the “CrowdQC” procedures until level O1 (Grassmann et al., 2018; Napoly et al., 2018). Based on evaluation of the quality-controlled CWS data against closely located REF sites, we found that the proposed algorithm noticeably decreases the CWS errors with respect to unfiltered data and performs even better than CrowdQC, but passes slightly less data (see **Supplementary S2** for details).

The quality-controlled CWS data is still not free from uncertainties, associated with the height of a CWS installation above the ground. CWSs may be installed at different heights, including the upper floors of high-rise buildings, which is far away from the standards of the WMO. Unfortunately, no methods of identification for the installation height of the CWS have been proposed so far. However, we assume that CWSs are typically installed below roof level and characterize the temperature of typically well-mixed air within the urban canopy and, hence, could be used to study the canopy layer UHI studies as already shown, e.g., in Fenner et al. (2017), Meier et al. (2017), Napoly et al. (2018), and Feichtinger et al. (2020).

## Sampling and preprocessing the observations

Based on availability of REF and CWS data, as well as on weather conditions, we selected the periods of winter 2018/2019 (December and January) and summer 2019 (May and June) for our study. During the two winter months Moscow experienced low temperatures with a strong cold wave at the end of January 2019 (**Figure 2A**). May and June 2019 experienced warm weather that was favorable for UHI development, while July and August 2019 were cold, rainy, and unfavorable for UHI appearance. Therefore, we did not include July and August 2019 in the analyzed summer period.

In the selected winter and summer periods, CWS data were collected from, respectively, 1,646 and 1,673 unique CWSs. Raw CWS data included numerous artifacts, which are typical for Netatmo temperature readings according to previous studies: unrealistically high daytime temperatures due to overheating of the unshaded outdoor modules by direct sunlight and unrealistic temperatures without expected diurnal variations for the CWSs placed somewhere indoors instead of outdoors (Meier et al., 2017; Napoly et al., 2018). The proposed QC algorithm successfully filters out such artifacts, which decreases the amount of individual temperature readings by 39% in winter and 44% in summer (**Figure 2**).



To analyze the spatial structure of the UHI and the factors of its formation in a quasi-climatological approximation, we sampled a selection of summer and winter cases characterized by intense UHIs. UHI intensity ( $\Delta T$ ) is defined in line with several previous studies for Moscow (Varentsov et al., 2018, 2019; Varentsov et al., 2020a) as the air temperature deviation from the mean background air temperature. The latter is averaged over nine weather stations surrounding the city at a distance from 53 to 110 km from its center (see Figure 1; Supplementary Table S1). Only one among them, Novo-Ierusalim, is inside the selected study area. Some of these stations are not purely “rural” due to their location close to smaller towns or within rural/suburban settlements, typically in LCZ 6 (Supplementary Table S1). We note that the calculated UHI values might, hence, be underestimated, as even villages are shown to have UHI effects (Dienst et al., 2018; Dienst et al., 2019). Nevertheless, such an approach to use several stations surrounding the city allows eliminating the influence of a potentially existing large-scale horizontal temperature gradient on  $\Delta T$ . For any given site and at each hour,  $\Delta T$  is defined as follows:

$$\Delta T = T - \frac{1}{N} \sum_{k=1 \dots N} T_{b,k} \quad (1)$$

where  $N = 9$  is the number of selected background stations, and  $T_{b,k}$  is the air temperature at the  $k$ -th background station.

We used  $\Delta T$  of the city center (Balchug WS)  $> 4$  K as a criterion for sampling the cases for further analyses. Such a criterium corresponds to the 50th percentile of the daily maximum  $\Delta T$  in summer and the 90th percentile in winter. In summer, such UHI intensities are common for Moscow during nocturnal hours, while in winter, they may be observed during the whole day under frosty weather conditions (Yushkov et al., 2019; Varentsov et al., 2020b). Nonetheless, to exclude the effects of direct solar heating on the UHI spatial patterns and possible uncertainties of the CWSs and AAQSSs, we considered only the nocturnal and early morning hours, i.e., 21–2 UTC (0–5 local time) for summer and 18–6 UTC (21–9 local time) for winter. Based on this criterion, we sampled 196 individual cases (one-hourly values) for summer and 62 cases for winter. Further analyses were performed for the mean air temperature and  $\Delta T$ , averaged over these sampled summer or winter cases.

As expected for cases with pronounced UHI, the sampled cases are characterized by generally calm weather conditions with a near-surface wind speed lower than 3 m/s and generally low low-level cloudiness (see Supplementary Figure S3 for details). Wind direction during the sampled cases is not homogeneous but is still quite diverse (Supplementary Figure S3.1), so we deem it acceptable for a coarse quasi-climatic approximation.

For the final analyses, we considered only reference stations and CWSs with a ratio of missed or QC-filtered values over all cases  $< 25\%$ , resulting in a total of 477 and 500 CWSs, and 67 and

61 REF sites within the study area, for winter and summer, respectively. The remaining stations were gap filled using a regression-based algorithm adopted after Tardivo and Berti (2012) to obtain continuous and homogeneous time series. Each individual gap for a specific station was filled based on a multiple linear regression using air temperature observations at neighboring stations as predictors (for each station, three to five neighboring stations were used that provided the best regression result). Regression coefficients were derived based on the data before and after each individual gap, separately for each hour of the day. When applying gap filling for CWS data, we only used REF data as predictors.

For each station, we calculated the mean air temperature over the selected summer or winter cases. To exclude a larger-scale spatial temperature gradient from our analysis, a two-dimensional latitude-longitude mean temperature trend was identified based on the observations at rural WSs for a larger area (within 300 km around Moscow) and subtracted from the mean temperatures. Finally, we calculated the mean  $\Delta T$  based on Eq. 1 and detrended temperatures. Since the topography of the Moscow region is relatively flat, altitude differences between the stations are small (123–212 m within the study area), and no height correction of the air temperature was carried out.

## Local climate zones and city-descriptive parameters

To characterize the heterogeneity of the underlying surface properties, our study combined two popular approaches, namely, the LCZ classification (Stewart and Oke, 2012) and independent quantitative estimation of city-descriptive parameters. The LCZ map for the Moscow region (Figure 1) is available from Varentsov et al. (2020b) at a 100-m spatial resolution. It was created based on training areas selected by Samsonov and Trigub (2018) and post-processed using a Gaussian kernel majority filter (Demuzere et al., 2020).

Each observation site (WS, AAQS, or CWS) was assigned to an LCZ class based on a majority filter applied for a circle with a 250-m radius around each site as suggested in Fenner et al. (2017). An important but nontrivial component of the LCZ assignment procedure is to detect the measurement sites surrounded by heterogeneous LCZ coverage and to exclude them from further analyses. Fenner et al. (2017) proposed to consider sites only if the LCZ for the central pixel of the kernel is equal to the major LCZ of the kernel and that this LCZ covers  $\geq 80\%$  of the area of the kernel. However, applying the same criteria for Moscow resulted in losing a high number of stations from both REF and CWS networks. We found that a lot of sites were excluded in cases where they are surrounded by two or more relatively similar LCZs. For example, a site may be surrounded by mixed open mid- and high-rise buildings, classified into LCZs 4 (open high-rise) and 5 (open mid-rise), or by low-rise private houses surrounded by vegetation classified as LCZs 6 (open low-rise) and 9 (sparsely built). To avoid such data loss, we proposed a procedure of LCZ assignment that accounts for the similarity between surrounding LCZs. For a kernel where the  $i$ -th LCZ

occupies the largest area fraction  $\lambda_{LCZ_i}$ , the similarity-weighted fraction  $\lambda_{LCZi, sim}$  is calculated as follows:

$$\lambda_{LCZi, sim} = \sum_{j=1 \dots 17} w_{i,j} \cdot \lambda_{LCZ_j}$$

where  $\lambda_{LCZ_j}$  are the area fractions of each LCZ in the kernel, and  $w_{i,j}$  are similarity coefficients between the  $i$ -th and  $j$ -th LCZs. These coefficients refer to the similarity of LCZ classes in terms of openness, height of roughness elements, land cover, and thermal inertia (Bechtel et al., 2017; Bechtel et al., 2020). They were originally designed for assessing the accuracy of LCZ maps, as confusion between dissimilar types (e.g., LCZs 1 and A) should be penalized more than confusion between similar classes (e.g., LCZs 1 and 2). For greater rigor, we use only  $w_{i,j} > 0.5$ ; otherwise, we treat it as zero.

Based on the proposed approach, we considered a site to be in quasi-homogenous local-scale surroundings if the area fraction of the modal LCZ of the kernel is  $> 0.5$ , and the similarity-weighted area fraction is  $> 0.75$ . Otherwise, the station was excluded from the LCZ-dependent analyses. Additionally, and in contrast to the LCZ assignment procedure from Fenner et al. (2017), we do not use a condition that the LCZ for the nearest pixel of a station has to correspond to the modal LCZ, since the location of the stations are not always known with enough precision.

On top of the LCZ-based approach, several city-descriptive parameters were sourced from OpenStreetMap data, Sentinel-2 images, and Copernicus Global Land Cover (CGLC) data, following Samsonov and Varentsov (2020). Based on the literature review, we selected the following parameters that are commonly used as predictors for  $\Delta T$ : urban (built up) land cover class area fraction according to CGLC ( $\lambda_{urb}$ ), impervious area fraction ( $\lambda_{ISA}$ ), and building area fraction ( $\lambda_{bld}$ ). Additionally, we consider building volume, derived as  $V_{bld} = H \cdot \lambda_{bld}$ , where  $H$  is the mean building height. These parameters were defined on a 250-m grid. On the smallest scale, the surroundings of the measurement sites were characterized by the values of these parameters specified as a weighted-mean within four nearest grid cells of a 250 m by 250 m grid, with weights equal to inverted distances between the location of the sites and grid cell centers. To characterize the urban surroundings of a specific site on larger scales, a set of smoothed 2D fields of all listed parameters was prepared using a running square kernel filter with size of  $m \times m$  grid cells, where  $m = 2 * r / 0.25 + 1$ , and  $r$  is what we further call a smoothing radius. We prepared smoothed fields with  $r$  equal to 0.25, 0.5, 1, 2, 3, 5, 7, 10, 15, and 20 km. Figure 3 shows the spatial distribution of  $\lambda_{urb}$ ,  $\lambda_{ISA}$ , and  $\lambda_{bld}$  parameters on the original 250-m grid and after applying a smoothing kernel with radii of 3 and 10 km.

## ANALYSIS STRATEGY

The central hypothesis of our study is that the  $\Delta T$  at a given site is determined by the surface properties in the local neighborhood of this point and a larger area with a size corresponding to mesoscale. The local-scale heterogeneity may be characterized by the LCZ map and selected city-descriptive parameters. To

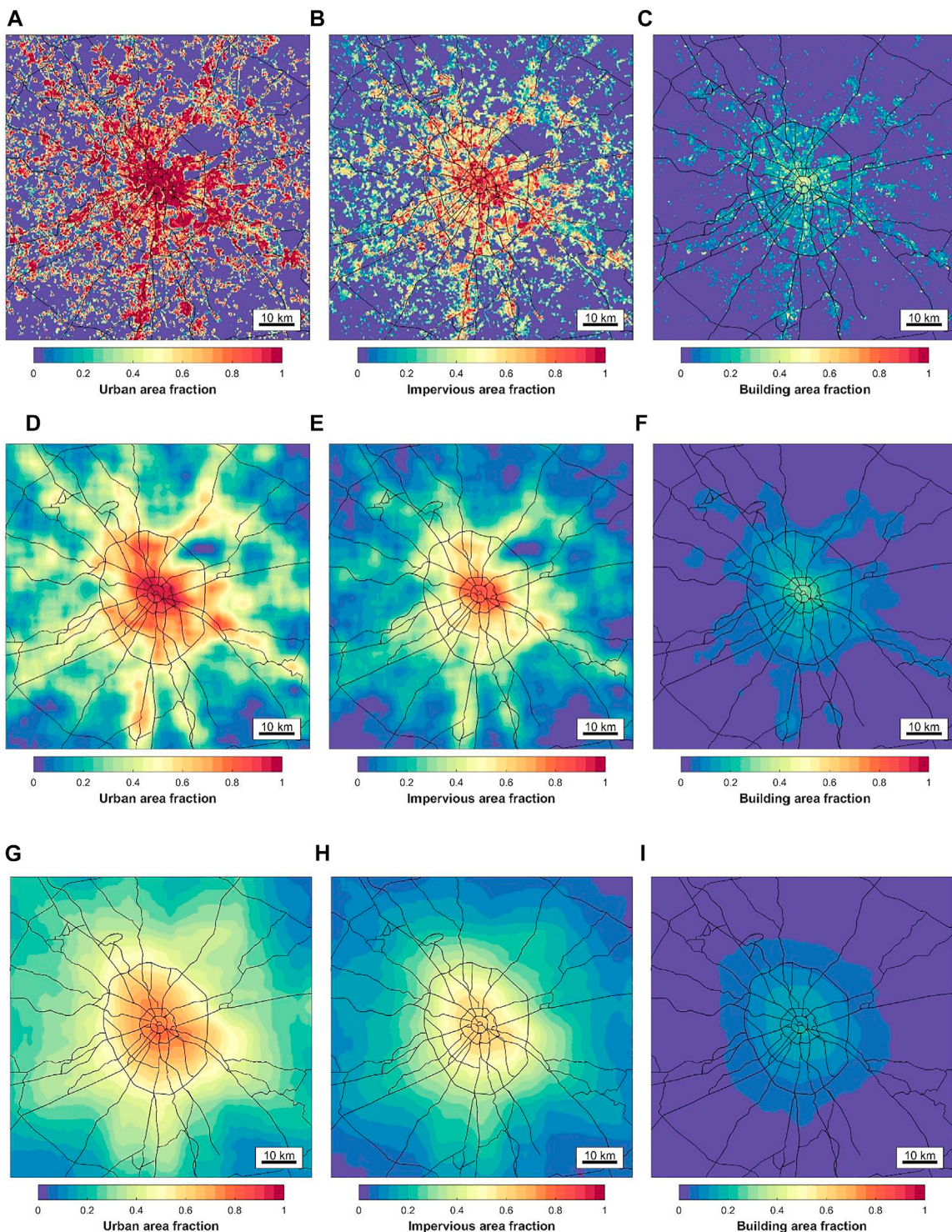


**FIGURE 3 |** Spatial distribution of city-descriptive parameters  $\lambda_{urb}$  (A, D, G),  $\lambda_{ISA}$  (B, E, H), and  $\lambda_{bld}$  (C, F, I) on the original 250-m grid and after smoothing within a radii of 3 km (A–D) and 10 km (G–I).

characterize the mesoscale heterogeneity, we use again the city-descriptive parameters, smoothed with different radii,  $r$ . Additionally, the concentric structure of Moscow (Figure 3)

allows considering the distance to the city center as a simplified proxy for mesoscale heterogeneity. To disentangle the contribution of the local-scale and mesoscale heterogeneity

of the urban land cover to the observed UHI spatial patterns, we perform several types of statistical analyses, described below:

- LCZ-dependent analysis. This analysis focuses on the intra- and inter-LCZ variability of  $\Delta T$  in order make our results comparable with other LCZ-based UHI studies.
- Simple correlation analysis. This analysis focuses on the relationships between  $\Delta T$  and selected city-descriptive parameters, smoothed with different radii,  $r$ . We analyze the Spearman correlation between  $\Delta T$  and these parameters to estimate at what scale it is maximal.
- Regression analysis with local-scale and mesoscale predictors. Based on the central hypothesis of our study, we propose to predict the observed  $\Delta T$  using a multiple linear regression (MLR) with two predictors, where the first one represents the local-scale surroundings ( $x_{loc}$ ), and the second one represents the mesoscale surroundings ( $x_{meso}$ ):

$$\Delta T_{reg} = k_0 + k_{loc} \cdot x_{loc} + k_{meso} \cdot x_{meso} \quad (2)$$

- As local-scale predictors  $x_{loc}$ , we consider  $\lambda_{urb}$ ,  $\lambda_{ISA}$ ,  $\lambda_{bld}$ , and  $V_{bld}$  values on the original 250-m grid ( $r = 0$ ) or smoothed with  $r$  of 250 and 500 m, i.e., with a square kernel with a size of 750 and 1,250 m. As mesoscale predictors  $x_{meso}$ , we consider the same parameters smoothed with  $r$  of 1, 2, 3, 7, 10, 15, and 20 km. We do not pretend to establish prognostic relationships between  $\Delta T$  and specific parameters. Instead, we consider all possible pairs of  $x_{loc}$  and  $x_{meso}$  (384 combinations in total). For each pair, we further estimate unknown regression coefficients  $k_0$ ,  $k_{loc}$ , and  $k_{meso}$  using the *regress* function of Matlab and then calculate several statistical parameters. First, we calculate the regression coefficient  $R_{reg} = R_{\Delta T, \Delta T_{reg}}$  (correlation coefficient between observed and predicted  $\Delta T$ ) and correlation coefficients between  $\Delta T$  and each of the predictors,  $R_{loc} = R_{x_{loc}, \Delta T}$  and  $R_{meso} = R_{x_{meso}, \Delta T}$ . To exclude correlations between the local-scale and mesoscale predictors, we use partial correlation coefficients  $R_{xy/z}$  that allow to estimate the correlation between  $x$  and  $y$  variables excluding their correlation with variable  $z$ . In this way, we calculate partial correlation coefficients  $P_{loc} = R_{\Delta T, x_{loc}/x_{meso}}$ ,  $P_{meso} = R_{\Delta T, x_{meso}/x_{loc}}$  using the *pcorr* function of Matlab.
- Regression analysis with multi-scale predictors. Assuming that an MLR model with predictors of only two scales may be oversimplified and, therefore, skew the results, additional analyses are performed using an MLR model simultaneously involving predictors  $x_r$  smoothed with all  $n_r = 11$  considered radii  $r$  from 0 to 20 km:

$$\Delta T_{reg} = k_0 + \sum_{i=1 \dots n_r} k_i \cdot x_{r_i} \quad (3)$$

- To avoid appearance of meaningless negative values of  $k_i$ , we build the MLR models with an additional constraint  $k_i > 0$  using the *lsqlin* function of Matlab. In order to obtain more robust results, we processed 1,000 randomly generated

combinations of predictors (independently changing  $\lambda_{urb}$ ,  $\lambda_{ISA}$ ,  $\lambda_{bld}$ , and  $V_{bld}$  for each  $x_{r_i}$ ) and select the best 25% for further analysis according to regression coefficient  $R_{reg}$ , defined in the same way as before as  $R_{\Delta T, \Delta T_{reg}}$ . All parameters  $x_{r_i}$  were preliminary normalized to fit the range from 0 to 1, which allows to compare and analyze their relative weights  $w_i = k_i / \sum_{i=1 \dots n_r} k_i$ .

## RESULTS

### Spatial patterns of the nocturnal urban heat island in Moscow

**Figure 4** shows the spatial distribution of the  $\Delta T$  in the central part of the study area. Both for winter and summer, the highest  $\Delta T$  is observed in the central parts of the city, with a general decrease in  $\Delta T$  with increasing distance away from the city center. This pattern is visible in both the REF and CWS data. To further illustrate this, **Figure 5** displays the relation between the distance to the city center of Moscow (defined here as the Balchug WS, 55.74556°N, 37.63°E) and the mean  $\Delta T$  of each station. For both networks and both seasons, we find significant ( $p < 0.05$ ) strong negative correlations. The strength of the correlation is similar between winter and summer for CWSs and lower for reference stations during summer compared with winter (**Figure 5**). Both networks are similar in terms of their regression slope, with an approximate decrease in  $\Delta T$  of 1 K per 5 km away from the city center. At the same time, such regressions clearly show that the CWS data are generally biased with respect to the reference  $\Delta T$  for the whole range of distances. The mean difference between the trend lines is approximately 1 K. This is not surprising, since the CWSs are typically installed on the buildings themselves or in their immediate vicinity. Even after passing QC, they exhibit warm biases against the reference network (see **Supplementary S2** for more details).

### Intra- and inter-LCZ variability of air temperature

**Figure 6** displays  $\Delta T$  for each station, grouped by LCZ type. Intra-LCZ variability of air temperature and thus also  $\Delta T$  is large for most LCZs, both for REF (**Figures 6A, C**) and CWS data (**Figures 6B, D**). Generally, more stations per LCZ lead to higher intra-LCZ variability. Yet, LCZs 6 and 9 display the largest intra-LCZ variability among all LCZ types for CWS data, even though they are not the LCZs with the highest number of stations. Furthermore, even though the number of CWSs in LCZ 6 is three to four times the number of CWS in LCZ 9, interquartile ranges (IQR) in  $\Delta T$  are much alike between these LCZ types. Both these LCZs display the largest IQR for “built” LCZ types (1–10), being approximately double the IQR of the other built LCZ types. Especially, LCZ 4 stands out, containing the maximum number of CWS, yet showing a narrow IQR compared with LCZ 6 with almost the same number of CWS (**Figures 6B, D**). Intra-LCZ variability of  $\Delta T$  for LCZ 4, calculated from REF data, shows a similar absolute range and larger IQR compared with CWS data, even though the number of stations is much smaller.

Comparing mean  $\Delta T$  across LCZ types, the highest values are observed for LCZ 1, 2, 4, 5, and 8. LCZ 2 displays the highest  $\Delta T$

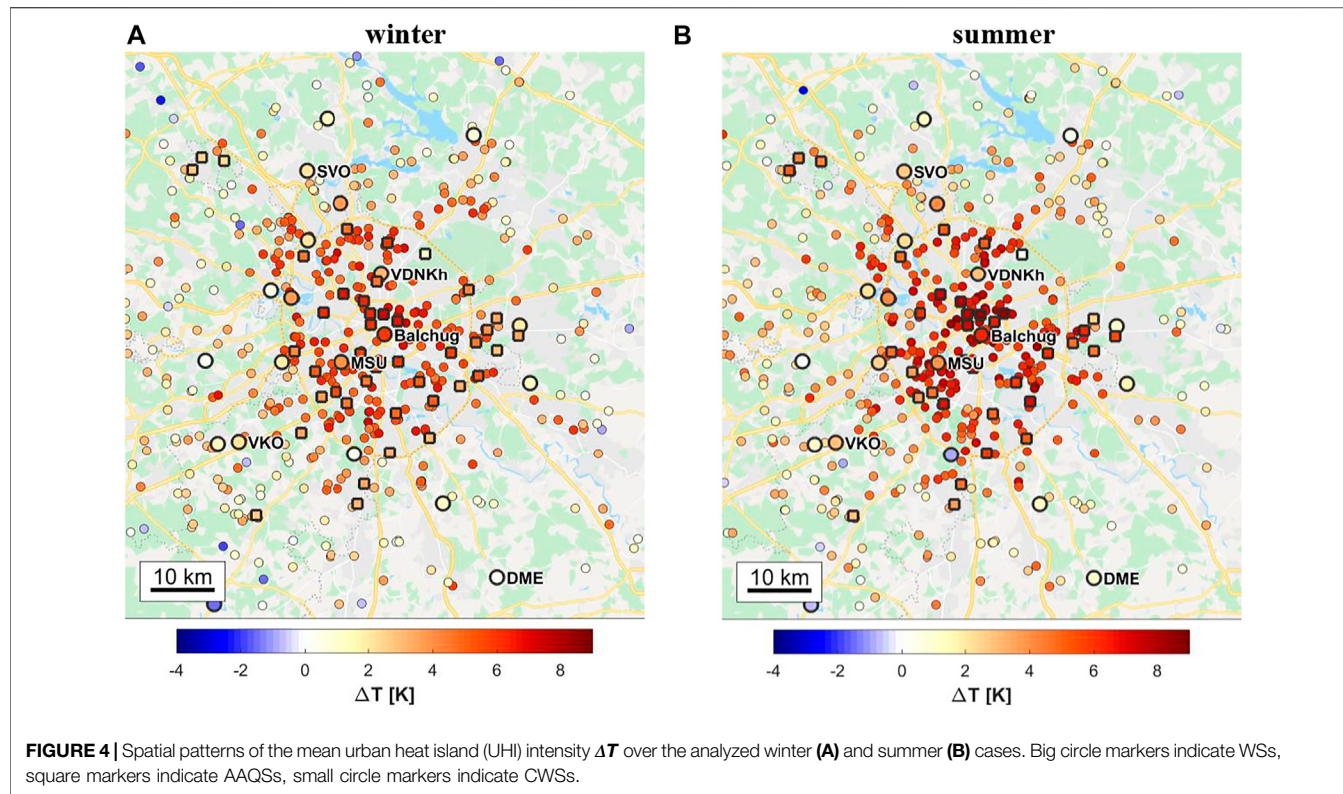


**FIGURE 4** | Spatial patterns of the mean urban heat island (UHI) intensity  $\Delta T$  over the analyzed winter (**A**) and summer (**B**) cases. Big circle markers indicate WSs, square markers indicate AAQSSs, small circle markers indicate CWSs.

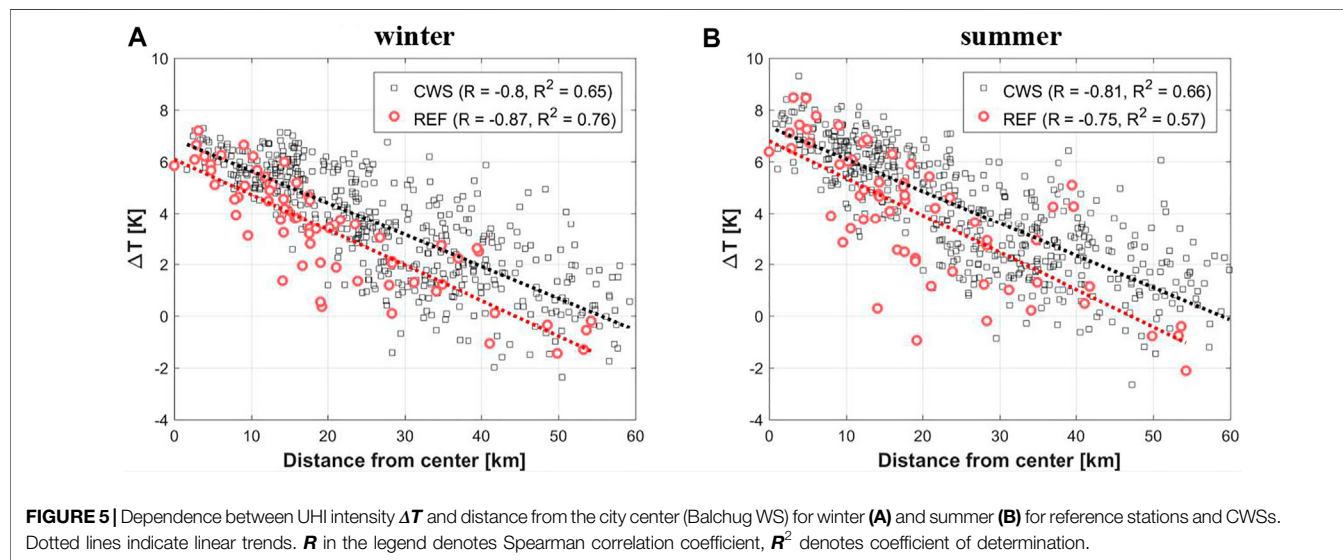


**FIGURE 5** | Dependence between UHI intensity  $\Delta T$  and distance from the city center (Balchug WS) for winter (**A**) and summer (**B**) for reference stations and CWSs. Dotted lines indicate linear trends. **R** in the legend denotes Spearman correlation coefficient, **R**<sup>2</sup> denotes coefficient of determination.

for winter and summer, and for REF and CWS data. Mean  $\Delta T$  for LCZs 6 and 9 are alike when compared within the same network. These two “built” classes are also the only ones with stations exhibiting lower values than the background REF stations, i.e.,  $\Delta T < 0$  K. When comparing  $\Delta T$  per LCZ type between the two networks, CWS data generally display higher values than REF data. This is particularly prominent in mean  $\Delta T$  and less so in absolute maximum values per LCZ type (Figure 6).

To further investigate the intra-LCZ variability of  $\Delta T$  seen in Figure 6, mean  $\Delta T$  values per station for summer and winter are displayed in Figure 7 in relation to the distance to the city center of Moscow. Despite the overall higher UHI intensities in the CWS data compared with the REF data (as seen in Figure 5), a dependence between distance from city center and mean  $\Delta T$  is observable in both networks and for both seasons. Mean  $\Delta T$  decreases with increasing distance from the center. The

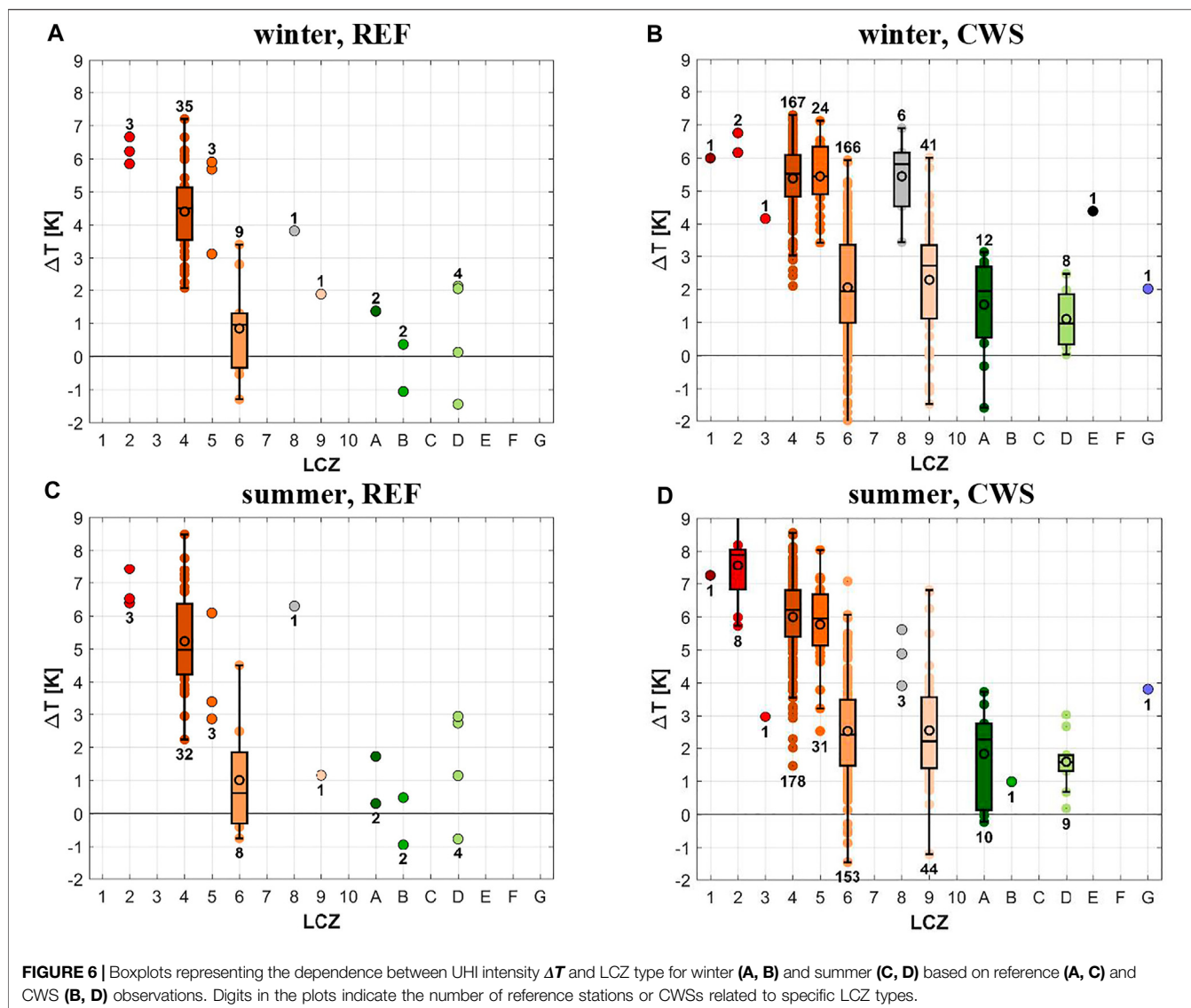


**FIGURE 6 |** Boxplots representing the dependence between UHI intensity  $\Delta T$  and LCZ type for winter (A, B) and summer (C, D) based on reference (A, C) and CWS (B, D) observations. Digits in the plots indicate the number of reference stations or CWSs related to specific LCZ types.

dependence is similar for the different LCZ groups, and for the reference and CWS data (Figure 7). Yet, despite this general decreasing dependence, large variability is also present for the same distance to the center, both in the REF and CWS data. This can especially be seen for LCZs 6 and 9 in winter between 40 and 50 km away from the center for CWS (Figure 7B), or for LCZs 4 and 5 in summer around 10 km away from the center for the REF data (Figure 7C). Meanwhile, coefficient of determination  $R^2$ , i.e., the proportion of the temperature variation that is predictable by analyzed dependence, exceeds 0.5 for several LCZ groups in Figure 7 (LCZs 4 and 5, 6 and 9 for REF data in winter, 8 and 10 for CWS data in winter, 6 and 9 for REF data in summer), as well as for several individual LCZs (see Supplementary S4). Hence, distance to city center may explain up to 50% and even more of intra-LCZ temperature variability.

These LCZ-dependent results are, to some extent, sensitive to the thresholds used in the procedure of LCZ assignment for REF and CWS sites (see the *Local climate zones and city-descriptive*

parameters section). Nevertheless, the key results and conclusions do not change (not shown).

## Quantifying the local-scale and mesoscale drivers

Within a framework of simple correlation analysis, we analyzed correlations between  $\Delta T$  and selected city-descriptive parameters,  $\lambda_{urb}$ ,  $\lambda_{ISA}$ ,  $\lambda_{bld}$ , and  $V_{bld}$ , defined on a 250-m grid and further smoothed with several radii  $r$  from 250 m to 20 km. Corresponding Spearman correlation coefficients ( $R$ ) are presented in Figure 8, separately for different seasons and networks. Despite the differences in correlation strength between REF and CWS data, both networks demonstrate the following. First, there is only a small difference in  $R$  values between selected city-descriptive parameters, which is not surprising since they are highly correlated (all pairwise correlation coefficients on 250 m grid exceeds 0.7). Only  $\lambda_{urb}$ ,

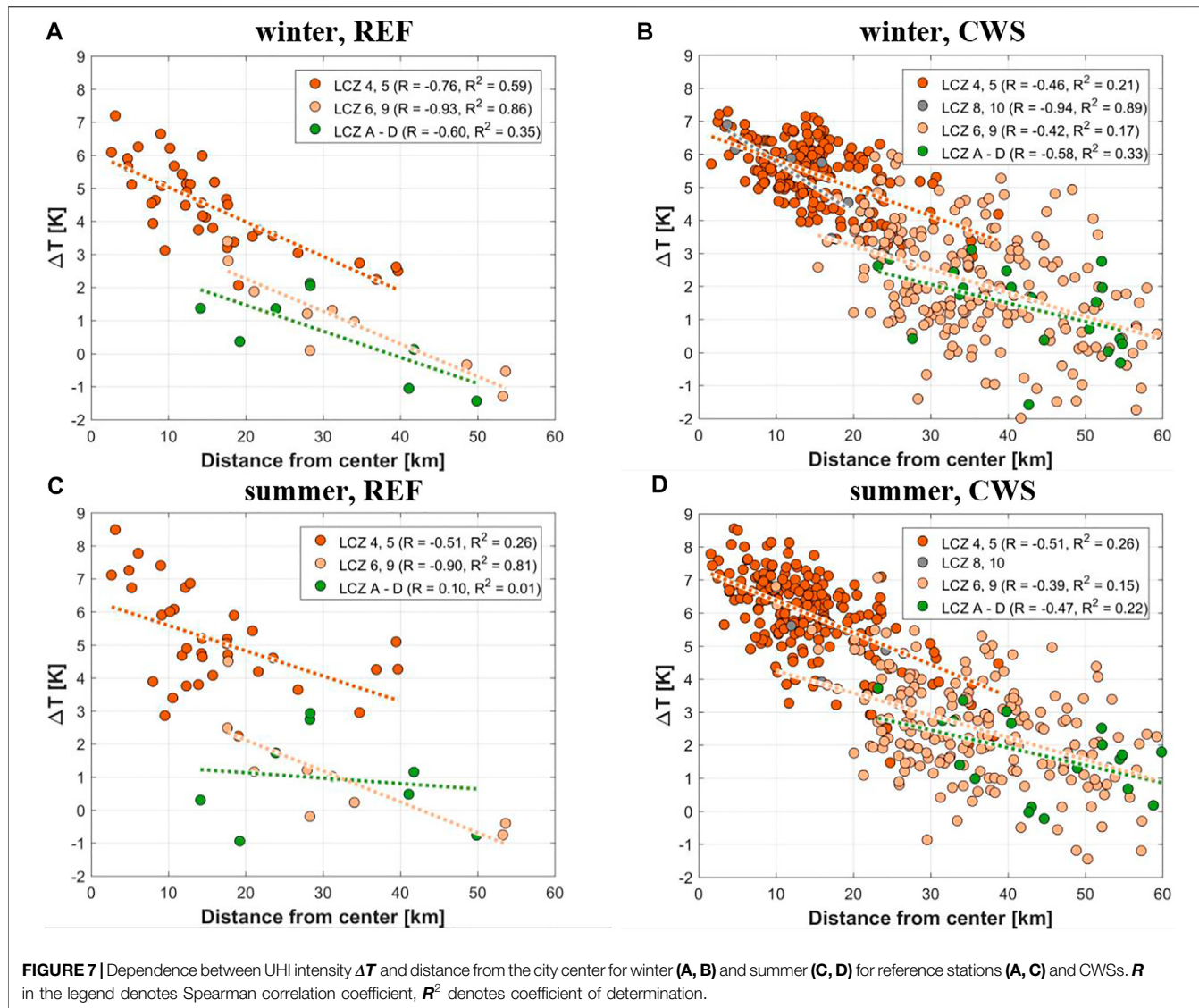


**FIGURE 7 |** Dependence between UHI intensity  $\Delta T$  and distance from the city center for winter (A, B) and summer (C, D) for reference stations (A, C) and CWSs (B, D).  $R$  in the legend denotes Spearman correlation coefficient,  $R^2$  denotes coefficient of determination.

the CGLC built up area fraction, slightly stands out from the rest and provides lower  $R$  values for smaller smoothing scales. This is likely because  $\lambda_{urb}$  includes urban vegetation and weakly differentiates more or less built-up urban areas (Varentsov et al., 2020b; Samsonov and Varentsov, 2020). Second, there is a tendency for the strength of the correlation to increase with increasing  $r$ , especially for  $r < 2$  km. For the REF data,  $R$  increases until maxima are found for  $r$  in a range 1–2 km in summer and 2–10 km in winter. For the CWS data,  $R$  increases until the end of the considered  $r$  range for summer, even though differences for  $r > 2$  km are small. For winter, the CWS data show  $R$  maxima at similar radii as for the REF data (Figures 8A, B).

Results of the simple correlation analysis may be misinformative due to cross-correlation between city-descriptive parameters, smoothed with different radii. For example, the correlation coefficient between  $\lambda_{ISA}$  on the 250-m grid and smoothed with a 10-km radius is 0.58. To avoid this, we built MLR models with one local-scale and one mesoscale

predictors, as described by Eq. 2 in the *Analysis strategy* section, and further analyzed partial correlation coefficients,  $P_{meso}$  and  $P_{loc}$ , for the best pairs of predictors.

**Table 1** presents the results for the five combinations of predictors with the highest  $R_{reg}$ , separately for different seasons and CWS/REF data. Despite the variety of predictors in these combinations, their common feature is the prevalence of  $P_{meso}$  over  $P_{loc}$ . A second common feature is that almost all best combinations include one of the fields smoothed with  $r = 10$  km or higher as mesoscale predictor, except REF data for summer, where best regressions are obtained with  $r = 2$  or 3 km (Table 1). For a more robust view, we consider  $R_{reg}$  values and  $P_{meso}/P_{loc}$  ratio, averaged over the top 25% of predictor combinations for each pair of  $r_{meso}$  and  $r_{loc}$  (four best combinations among 16 for each pair). From Figure 9 it can be seen that the best results are typically obtained when combining local-scale predictors with 500-m smoothing and mesoscale predictors with 10–15 km smoothing. An exception is again the REF data for summer,

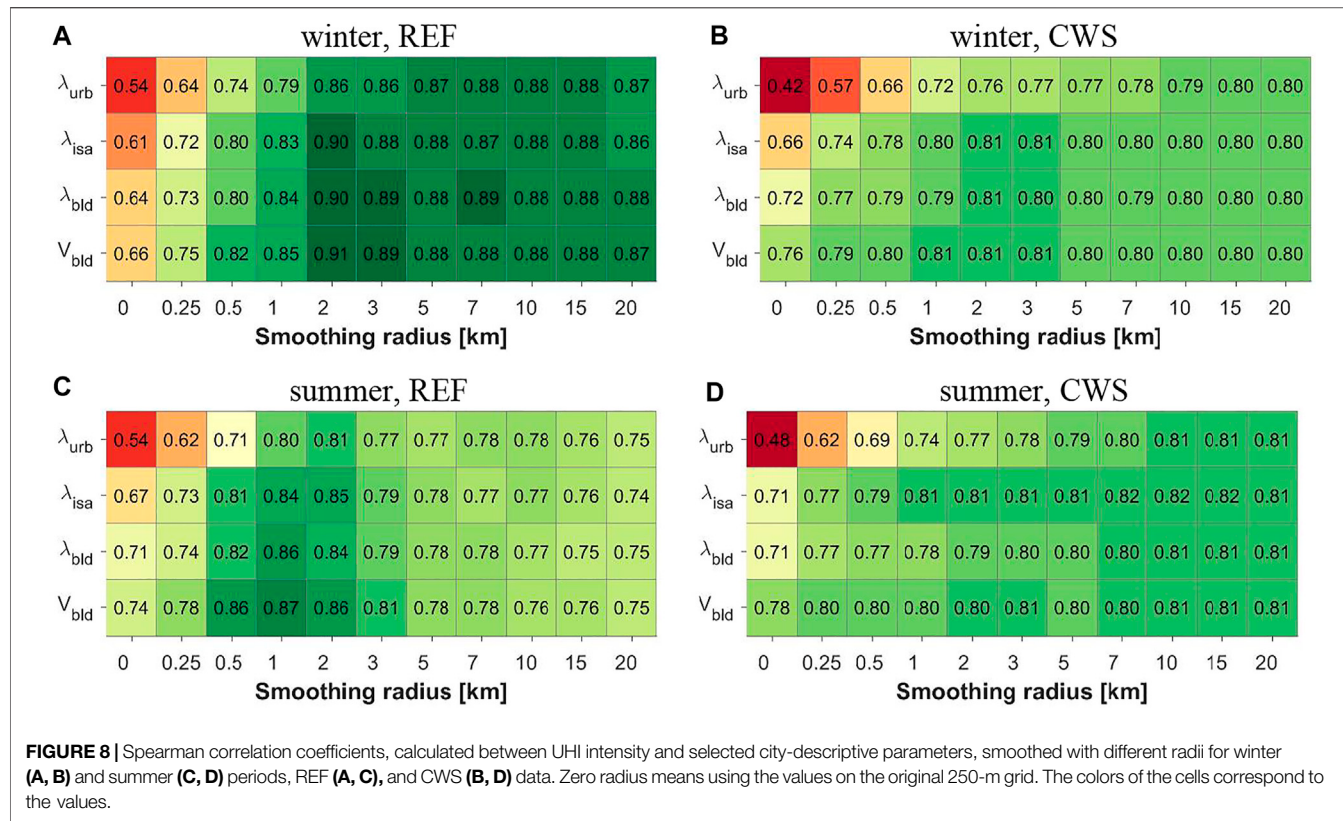


**FIGURE 8 |** Spearman correlation coefficients, calculated between UHI intensity and selected city-descriptive parameters, smoothed with different radii for winter (**A, B**) and summer (**C, D**) periods, REF (**A, C**), and CWS (**B, D**) data. Zero radius means using the values on the original 250-m grid. The colors of the cells correspond to the values.

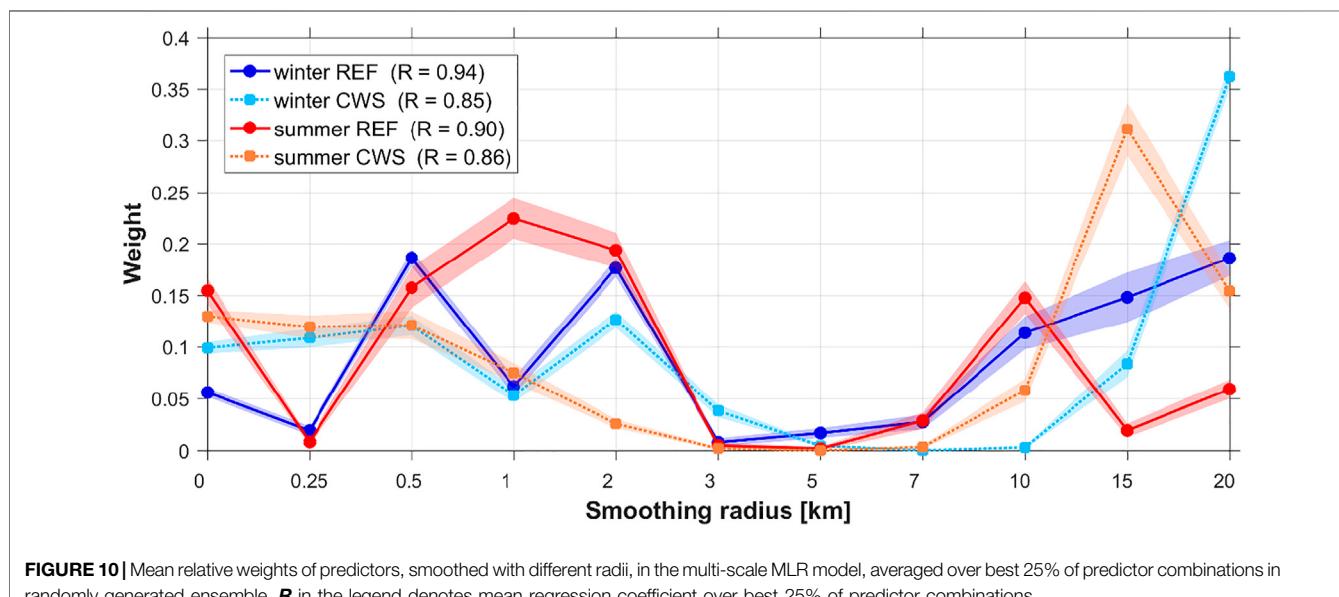
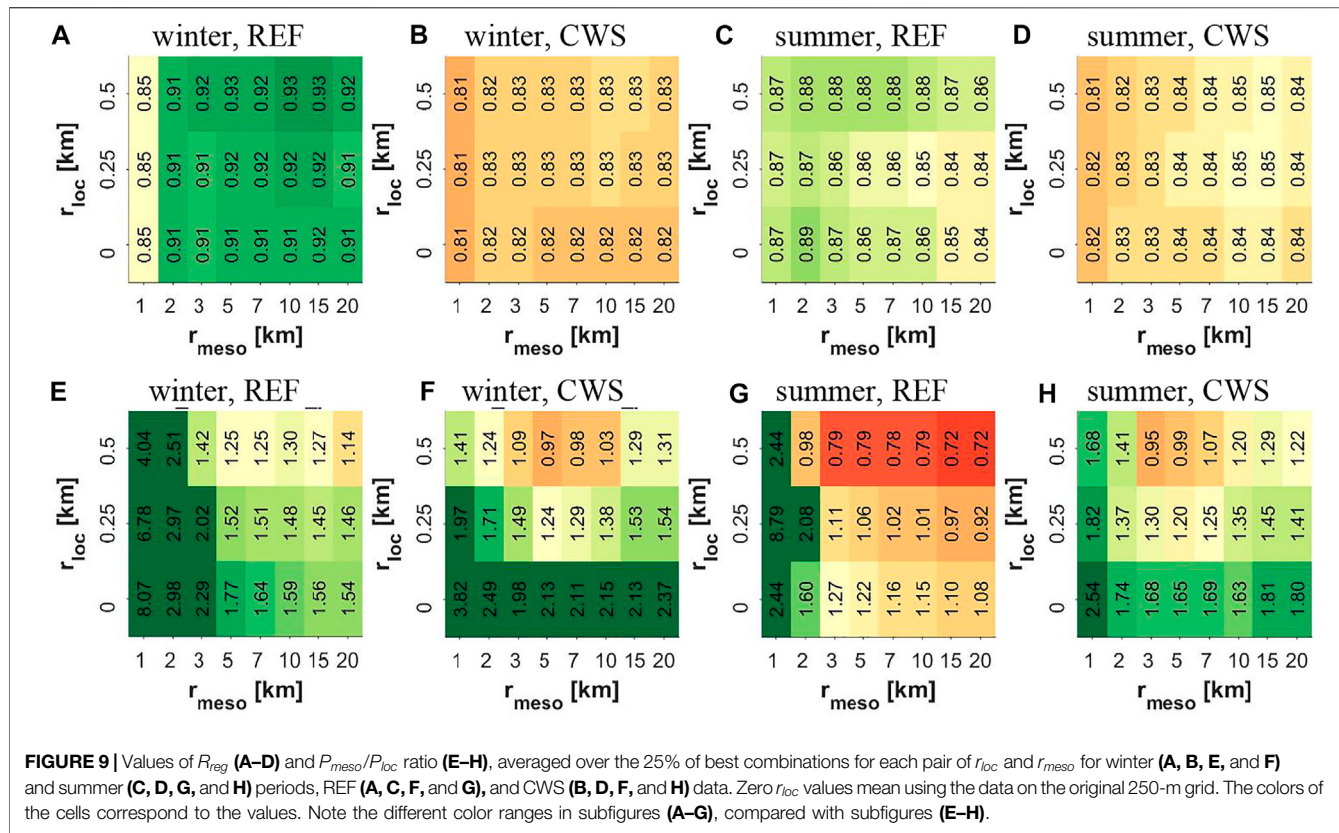
**TABLE 1 |** Results of the multiple linear regression predicting of the summer and winter urban heat island (UHI) intensity based on reference network (REF) and citizen weather station (CWS) data.

Data type and season	$x_{loc}$	$r_{loc}, \text{km}$	$x_{meso}$	$r_{meso}, \text{km}$	$R_{reg}$	$P_{loc}$	$P_{meso}$	$R_{loc}$	$R_{meso}$
REF winter	$\lambda_{urb}$	0.5	$\lambda_{urb}$	15	0.93	0.61	0.84	0.74	0.88
	$V_{bld}$	0.5	$\lambda_{isa}$	10	0.93	0.61	0.75	0.82	0.88
	$V_{bld}$	0.5	$\lambda_{urb}$	10	0.93	0.62	0.77	0.82	0.88
	$V_{bld}$	0.5	$\lambda_{bld}$	5	0.93	0.54	0.64	0.82	0.88
	$V_{bld}$	0.5	$\lambda_{urb}$	15	0.93	0.65	0.76	0.82	0.88
CWS winter	$\lambda_{isa}$	0.5	$\lambda_{isa}$	10	0.83	0.39	0.48	0.77	0.79
	$\lambda_{isa}$	0.5	$\lambda_{urb}$	10	0.83	0.40	0.48	0.77	0.79
	$\lambda_{isa}$	0.25	$\lambda_{isa}$	10	0.83	0.38	0.55	0.74	0.79
	$\lambda_{isa}$	0.25	$\lambda_{urb}$	10	0.83	0.39	0.55	0.74	0.79
	$V_{bld}$	0.5	$\lambda_{urb}$	10	0.83	0.39	0.44	0.78	0.79
REF summer	$V_{bld}$	0	$\lambda_{isa}$	2	0.90	0.47	0.75	0.74	0.85
	$V_{bld}$	0.5	$\lambda_{isa}$	2	0.89	0.44	0.55	0.86	0.85
	$V_{bld}$	0	$V_{bld}$	2	0.89	0.42	0.70	0.74	0.86
	$V_{bld}$	0.5	$\lambda_{isa}$	3	0.89	0.56	0.51	0.86	0.79
	$V_{bld}$	0	$\lambda_{bld}$	2	0.89	0.50	0.65	0.74	0.84
CWS summer	$V_{bld}$	0.25	$\lambda_{isa}$	10	0.85	0.37	0.53	0.80	0.82
	$\lambda_{isa}$	0.25	$\lambda_{isa}$	10	0.85	0.40	0.56	0.77	0.82
	$\lambda_{isa}$	0.5	$\lambda_{isa}$	15	0.85	0.39	0.52	0.79	0.82
	$\lambda_{isa}$	0.25	$\lambda_{isa}$	15	0.85	0.39	0.58	0.77	0.82
	$V_{bld}$	0.25	$\lambda_{isa}$	15	0.85	0.35	0.55	0.80	0.82

Note: For each period and data type, results are shown for the top five predictor combinations with highest  $R_{reg}$ .

where optimal  $r_{meso}$  is shifted to lower values, and additional  $R_{reg}$  maximum exists at  $r_{meso} = 2 \text{ km}$  and  $r_{loc} = 0$ . The  $P_{meso}/P_{loc}$  ratio generally decreases with increasing  $r_{meso}$  and increasing  $r_{loc}$ , but

typically remains  $>1$ , indicating a larger contribution of the mesoscale heterogeneity. For the REF data in summer, values are  $<1$  when using the local-scale predictor with highest



smoothing ( $r_{\text{loc}} = 0.5 \text{ km}$ ). In summer, the  $P_{\text{meso}}/P_{\text{loc}}$  ratio is generally lower than in winter, which is especially clear for REF data and still noticeable for CWS data.

MLR models with multi-scale predictors, constructed as described by Eq. 3 in the *Analysis strategy* section, allow to compare the contribution of the specific scales of the surface

heterogeneity to the observed UHI. **Figure 10** shows the relative weights of predictors with different smoothing radius, averaged over the top 25% of predictor combinations among the randomly generated ensemble of 1,000 members. Despite the differences between plots for REF and CWS data, both networks demonstrate consistent patterns indicating the major

contribution of the scales corresponding to  $r$  between 0 and 2 km, and  $>10$  km, and near-zero contribution from  $r$  between 3 and 7 km (these radii are almost not presented in the top 25% of predictor combinations). Differences between plots for summer and winter again suggest larger contribution of the smaller scales in summer. Thus, both types of regression analyses confirm the contribution of the mesoscale variation of the city-descriptive parameters (on a scale of about 10 km and higher) is comparable or even higher than the local-scale variation of these parameters.

## DISCUSSION

The UHI has been studied for decades, and it is one of the clearest examples of inadvertent climate modification due to humans (Oke et al., 2017). Land cover properties are known to play a crucial role in its development, yet the role of their spatial heterogeneity at various spatial scales remains unclear. The current study addresses this issue by linking the latter to the observed nocturnal canopy layer UHI of Moscow. Our results thereby provide a systematic understanding of the spatial scales affecting the UHI of a megacity.

The identified spatial patterns of the canopy layer UHI of Moscow are consistent with studies for other cities. As found by other studies focusing on LCZs and their thermal regimes (Stewart et al., 2014; Fenner et al., 2017; Skarbit et al., 2017; Beck et al., 2018a; Verdonck et al., 2018; Kwok et al., 2019; Milošević et al., 2021), we revealed a dependence between  $\Delta T$  and LCZ type (**Figure 6**). The highest temperatures are found for densely built compact LCZs (1–3), which are warmer than open high-/mid-rise LCZs (4, 5), which again are warmer than low-rise residential areas (LCZ 6, 9) and natural LCZs. At the same time, intra-LCZ variability is comparable or even higher than inter-LCZ differences, especially for the most frequent LCZs in the study area (4, 6, and 9), which is consistent with previous studies (Leconte et al., 2015; Fenner et al., 2017; Skarbit et al., 2017; Quanz et al., 2018; Shi et al., 2018; Kwok et al., 2019).

Meanwhile, we obtained a strong negative correlation ( $R < -0.75$ ) between  $\Delta T$  and distance to the city center (**Figure 5**), which is also visible within specific LCZ classes (**Figure 7**). The dependence of  $\Delta T$  to this distance may explain more than 50% of the intra-LCZ variability that is obtained for the whole city region (**Figure 7, Supplementary Table S4**). In other words, a specific LCZ in the city center is warmer than the same LCZ at the edge of the city. Such dependency has, to date, gained little attention, reporting ambiguous results. As strong correlation as for Moscow ( $R < -0.7$ ) was previously only reported for the medium-sized city of Szeged, Hungary (Bottány et al., 2005). Weaker dependencies ( $R = -0.41$ ) were found by Oswald et al. (2012) for the nocturnal UHI in Detroit, United States. Kwok et al. (2019) showed higher air temperature per LCZ class in regions close to the city center of Toulouse, France, and lower values for the same classes in regions farther away. Similarly, Gardes et al. (2020) reported an impact of the distance to the city center on the

intra-LCZ variability for 42 French cities, yet with large scatter around the average. In contrast, only a weak impact of the distance to city center on the urban temperatures was found for Augsburg, Germany (Straub et al., 2019), and Leipzig, Germany (Franck et al., 2013).

In order to explore the impacts of the land cover heterogeneity of different scales on the UHI spatial patterns, we suggest a novel approach based on a set of the city-descriptive parameters, defined on a 250-m grid, and further smoothed with several radii ( $r$ ) from 250 m to 20 km. Based on several types of statistical analysis, our results indicate that the observed UHI is shaped by both local and mesoscale land cover heterogeneity, with comparable, or even dominant, contributions of the mesoscale features. The local scale, which is considered as highly relevant for urban climate studies, is defined as “hundreds of meters to several kilometers” (Stewart and Oke, 2012), but is often associated with only scales of a few hundred meters (Fenner et al., 2017; Skarbit et al., 2017; Beck et al., 2018a), while the mesoscale is typically associated with scales  $>2$  km (Orlanski, 1975). Our correlation analysis revealed that the local-scale (a few hundred meters) urban land cover description is less correlated with nocturnal  $\Delta T$  compared with a smoothed  $r \geq 2$  km (**Figure 8**). Furthermore, using MLR analyses with two predictors, representing heterogeneity of the urban land cover on local ( $r_{loc} \leq 500$  m) and meso ( $r_{meso} > 1$  km) scales, we found the best results of  $r_{meso} \approx 10$  km and have shown a typically larger importance of the mesoscale predictor (**Table 1, Figure 9**). Our final, more comprehensive MRL analysis with predictors representing the wide range of scales allowed to separate two dominant ranges of contributing scales,  $r \leq 2$  km, and a second with  $r > 7$  km (**Figure 10**).

The presence of two dominant ranges of spatial scales suggests their connection with different physical processes. The contribution of scales with  $r > 7$  km, which represents the mesoscale UHI variability, is likely related to the horizontal and vertical advection of warmer urban air by the larger-scale airflow. UHI advection to the leeward side of the city was reported by observation-based (Bassett et al., 2016; Bassett et al., 2017) and modeling studies (Zhang et al., 2011; Heaviside et al., 2015). At this scale, UHI advection takes place across the whole urban boundary layer, and can extend to the countryside via heat plumes (Clarke, 1969; Varentsov et al., 2018; Wang et al., 2020). Available observations allow to demonstrate this phenomenon for Moscow as well, which is shown by comparing two cases with southwesterly and southeasterly wind directions (**Figure 11**). In these examples, differences in wind direction resulted in a shift of the UHI hotspot by more than 10 km. Of course, UHI advection depends on the wind speed, atmospheric stability, and other factors, which require accurate quantification in further studies. Nonetheless, since the wind direction during the sampled cases largely varies (see **Supplementary S3**), one can expect that UHI advection in different directions resulted in smoothing of the mean  $\Delta T$  fields on a scale of several kilometers and more. Adverted air is additionally mixed by boundary-layer turbulence. Moreover, city-wide UHI smoothing may be forced by other atmospheric phenomena, e.g., urban-induced circulations (urban breeze) in

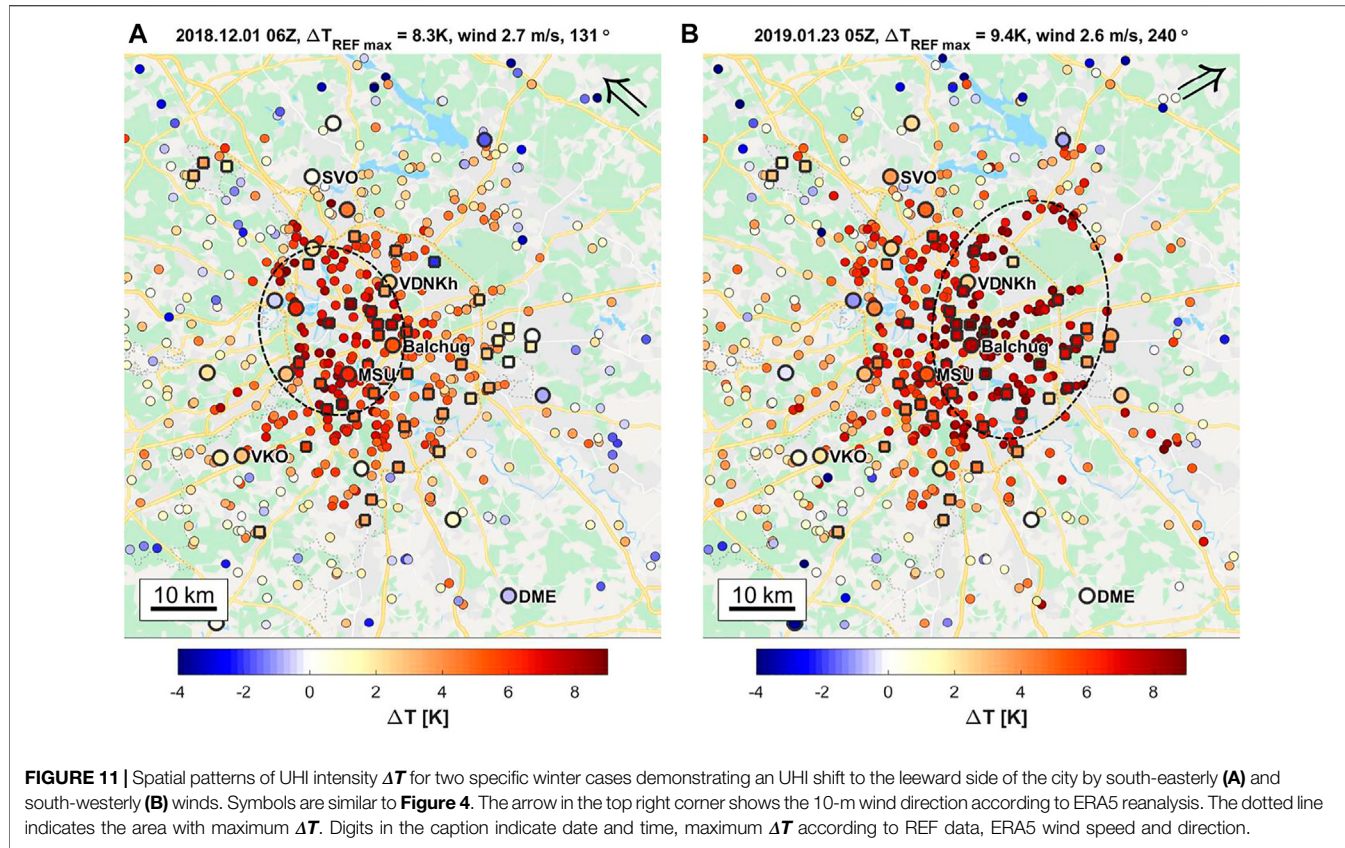


**FIGURE 11 |** Spatial patterns of UHI intensity  $\Delta T$  for two specific winter cases demonstrating an UHI shift to the leeward side of the city by south-easterly (**A**) and south-westerly (**B**) winds. Symbols are similar to **Figure 4**. The arrow in the top right corner shows the 10-m wind direction according to ERA5 reanalysis. The dotted line indicates the area with maximum  $\Delta T$ . Digits in the caption indicate date and time, maximum  $\Delta T$  according to REF data, ERA5 wind speed and direction.

the urban dome (Lemonsu and Masson, 2002; Varentsov et al., 2018). In the case of Moscow, smoothing with  $r \geq 10$  km turns the observed heterogeneity of urban land cover to almost concentric spatial structures (**Figure 3**), resulting in the observed dependence of  $\Delta T$  and distance to city center. Mesoscale UHI smoothing also explains the dependence between maximum UHI intensity and city size, which is known from observational (Oke, 1973; Zhou et al., 2017) and modeling (Varentsov et al., 2017; Li et al., 2020) studies.

The range of contributing scales with  $r \leq 2$  km is more difficult to interpret. On the local scale, the thermal environment is expected to be uniform due to the homogeneity of the land cover and building morphology, and the surface-layer turbulent mixing, which can remain quite intensive in urban canopy layer even at night (Oke et al., 2017). However, in our case, the contributing scales extend to a “gray zone” between local and mesoscales. For example,  $r = 2$  km corresponds to an area width of 4 km, which still fits the “several km” from the local scale definition but is generally larger than the definition typically used in many urban climate studies. In Moscow, urban areas of such size are typically highly heterogeneous and include parks, building blocks, and industrial zones.

In order to relate the contributing spatial scales revealed in our analysis to the heterogeneity of the LCZ classes in Moscow, we estimated the typical surface area size of homogenous LCZ

patches. For this, we applied the “circle-based region width estimation” method (Samsonov et al., 2019) that assigns—to each pixel inside an LCZ patch—a characteristic radius. That radius corresponds to the largest circle covering the pixel without intersecting other LCZ classes (**Supplementary Figure S5.1**). Analyzing these radii grouped by LCZ class within the study area indicates that the typical LCZ class radius (mean or median) does not exceed 500 m for all LCZs, and is <300 m for all urban LCZs except 2 and 4 (**Supplementary Figure S5.2**). Such values are noticeably smaller than the range of 1–2 km, which provide significant contribution to the spatial UHI patterns (**Figure 10**). Hence, the range of contributing scales with  $r$  between 1 and 2 km cannot only be explained by the alteration of different LCZs. Possible explanations for its contribution include two options. The first one is the similarity of LCZ classes, e.g., 4 and 5, 6 and 9, A and B, etc. (Bechtel et al., 2017; Bechtel et al., 2020), as discussed in the *Local climate zones and city-descriptive parameters* section. The second option is atmospheric mixing, forced by specific processes with typical scales of a few kilometers, e.g., by advection between neighboring LCZs (Quanz et al., 2018), and by coherent structures in the atmospheric boundary layer, including local circulations, induced by urban blocks or green areas. This could be addressed in future studies using high-resolution modeling approaches.

## CONCLUSION AND OUTLOOK

Based on dense reference and crowdsourced air temperature observations, we analyzed linkages between the nocturnal canopy layer UHI of Moscow and the land cover heterogeneity on different spatial scales, ranging from a few hundred meters to tens of kilometers. Land cover properties were described using the local climate zone (LCZ) classification and specific city-descriptive parameters, derived on a 250-m grid and smoothed with different radii ( $r$ ) to represent their variations on different scales.

Our results underscore that the thermal environment in Moscow is influenced by the heterogeneity of land cover properties on different scales, including local scale (a few hundred meters,  $r < 1$  km) and mesoscale (from the first km to the first tens of kilometers, with typical  $r \approx 10$  km). The mesoscale contribution to the observed UHI spatial patterns is established by smoothing the smaller-scale thermal heterogeneity by atmospheric processes, including advection and diffusion. For Moscow, with its symmetric planning pattern, this mesoscale contribution is reflected in a dependence between UHI intensity and distance to city center, which is also visible for specific LCZ classes. This mesoscale contribution is comparable to, or even exceeds, the contribution of the local scale to observed UHI intensity. Finally, we show a significant contribution from the scale within a “gray zone” between local and mesoscales ( $r = 1 \div 2$  km). This is likely associated with the similarities between different LCZ types and again with atmospheric mixing at that scale, yet requires further studies.

Our results recommend considering the mesoscale heterogeneity of land cover properties alongside the local-scale heterogeneity in urban climate studies and practical applications, especially for large cities. Our findings are especially relevant for statistical modeling of the urban thermal environment. It can be expected that the use of predictors reflecting mesoscale heterogeneity of land cover properties will improve the accuracy of temperature mapping for urban areas. Our results are also relevant for urban planning, since they underline the impact of local changes in specific areas (e.g., new urban developments) to its neighborhood on a mesoscale.

In order to assess the robustness of our findings, we propose the following research directions for follow-up studies:

- The proposed hypothesis should be tested for other cities, including more complex geographic controls, and for longer periods, since the sampling size in our study is relatively small, especially for winter. Moreover, the presented results are valid only for nocturnal cases with a pronounced UHI signature. Different patterns of air temperature may be expected during daytime and should be further investigated.
- Further studies are needed for deeper understanding of the physical processes beyond the revealed local-scale and mesoscale drivers. Yet, our study is based on a coarse-grained approach that analyzes the influencing scales of land cover heterogeneity through spatial smoothing of the

city-descriptive parameters. Our results allow only suggesting about the physical processes responsible for such smoothing. More detailed and reliable knowledge may be gained based on high-resolution numerical simulations with mesoscale models, coupled to urban canopy schemes. Such modeling seems to be the only way to comprehensively analyze the interaction between UHI and atmospheric processes at different scales and different vertical levels from the surface up to the ABL.

- Despite the overall consistent results from the CWS and REF data, further research is needed to understand differences between the two types of stations, particularly regarding their spatial representativeness. Differences in the setup of the stations likely affect results regarding the contribution of scales; yet to what extent is not understood.
- Follow-up studies could explore the use of machine learning (ML) techniques that are already used to study and predict UHI spatial patterns (Straub et al., 2019; Gardes et al., 2020; Vulova et al., 2020). Simultaneously, existing ML-based techniques could be improved by considering the mesoscale heterogeneity of the urban environment.
- Additional attention should be paid to the scale smaller than the local scale, i.e., the microscale, which is ignored in our study. Yet, studies have shown that there is microscale variability within LCZs or neighborhoods, even of similar local-scale characteristic (see, e.g., Heusinkveld et al., 2014; Ellis et al., 2015; Leconte et al., 2015; Quanz et al., 2018; Shi et al., 2018; and Pacifici et al., 2019). Such an intra-LCZ variability is expected due to microscale variations in surface cover and morphology, exposure of the sensors, and anthropogenic heat sources. In the case of CWS, one can argue that due to their non-standard setup, the microscale influence is more pronounced than for reference observations (Fenner et al., 2017). This may explain the higher correlation coefficient for the CWS data without smoothing ( $r = 0$ ), compared with the REF data (Figure 8). In order to further delineate micro-, local-, and mesoscale influences on  $T$  and  $\Delta T$ , datasets with higher spatial resolution are needed to resolve features down to few tens of meters. Such datasets should not only include parameters representing the building spatial extent as in the current study, but should also reflect their morphology, thermal, and radiative characteristics, e.g., sky view factor or albedo.
- In the end, our study highlights that further research is needed to systematically understand the contribution of spatial scales in urban thermal climate investigations across geographic and climatic regions, and cultures. This could lead to a possible extension of the LCZ concept to take mesoscale settings of the urban environment into account, further enhancing communication and reporting on the UHI effect throughout the scientific literature.

## DATA AVAILABILITY STATEMENT

The raw data supporting the conclusion of this article will be made available by the authors, without undue reservation.

## AUTHOR CONTRIBUTIONS

MV, DF, and FM proposed the concept of the study. DF and FM collected the CWS data. MD developed the LCZ map. TS developed the dataset with city-descriptive parameters and performed addition calculations with the LCZ map. MV collected the reference data, performed the bulk of the data analysis, and prepared the figures. MV, DF, and MD wrote the paper. All authors participated in the discussions and editing.

## FUNDING

Processing and analysis of the observational data performed by MV was supported by the Russian Ministry of Education and Science, agreement no. 075-15-2021-574. The development of the city-descriptive datasets performed by TS and MV was supported by the Russian Ministry of Education and Science as part of the program of the Moscow Center for Fundamental and Applied Mathematics under agreement no. 075-15-2019-1621. Development of QC algorithm for CWS data was partially supported by the Interdisciplinary Scientific and Educational School of Moscow University «Brain, Cognitive Systems, Artificial Intelligence». Regression analysis of the linkages between UHI intensity and spatial predictors performed by MV was supported by the Russian Science Foundation, project no. 19-77-30012. Development of the impervious surface area

fraction dataset and paper preparation was supported by the RUDN University Strategic Academic Leadership Program. The contributions of MD and DF were conducted in the context of project ENLIGHT, funded by the German Research Foundation (DFG) under grant no. 437467569. We acknowledge support by the German Research Foundation and the Open Access Publication Fund of TU Berlin for APC payment.

## ACKNOWLEDGMENTS

We thank all the citizens who make their Netatmo weather data publicly available. The authors are especially grateful to administration and staff of Hydrometeorological Research Center of Russian Federation, meteorological observatory of the Lomonosov Moscow State University and Budgetary Environmental Protection Institute "Mosecomonitoring" for providing the data of reference meteorological observations used in the study.

## SUPPLEMENTARY MATERIAL

The Supplementary Material for this article can be found online at: <https://www.frontiersin.org/articles/10.3389/fenvs.2021.716968/full#supplementary-material>

## REFERENCES

- Alexander, P., and Mills, G. (2014). Local Climate Classification and Dublin's Urban Heat Island. *Atmosphere* 5, 755–774. doi:10.3390/atmos5040755
- Baklanov, A., Grimmond, C. S. B., Carlson, D., Terblanche, D., Tang, X., Bouchet, V., et al. (2018). From Urban Meteorology, Climate and Environment Research to Integrated City Services. *Urban Clim.* 23, 330–341. doi:10.1016/j.ulclim.2017.05.004
- Barlage, M., Miao, S., and Chen, F. (2016). Impact of Physics Parameterizations on High-Resolution Weather Prediction over Two Chinese Megacities. *J. Geophys. Res. Atmos.* 121, 4487–4498. doi:10.1002/2015JD024450
- Bartos, M., Park, H., Zhou, T., Kerkez, B., and Vasudevan, R. (2019). Windshield Wipers on Connected Vehicles Produce High-Accuracy Rainfall Maps. *Sci. Rep.* 9, 170. doi:10.1038/s41598-018-36282-7
- Båserud, L., Lussana, C., Nipen, T. N., Seierstad, I. A., Oram, L., and Aspelien, T. (2020). TITAN Automatic Spatial Quality Control of Meteorological *In-Situ* Observations. *Adv. Sci. Res.* 17, 153–163. doi:10.5194/asr-17-153-2020
- Bassett, R., Cai, X., Chapman, L., Heaviside, C., Thornes, J. E., Muller, C. L., et al. (2016). Observations of Urban Heat Island Advection from a High-Density Monitoring Network. *Q. J. R. Meteorol. Soc.* 142, 2434–2441. doi:10.1002/qj.2836
- Bassett, R., Cai, X., Chapman, L., Heaviside, C., and Thornes, J. E. (2017). The Effects of Heat Advection on UK Weather and Climate Observations in the Vicinity of Small Urbanized Areas. *Boundary-layer Meteorol.* 165, 181–196. doi:10.1007/s10546-017-0263-0
- Bechtel, B., Demuzere, M., Sismanidis, P., Fenner, D., Brousse, O., Beck, C., et al. (2017). Quality of Crowdsourced Data on Urban Morphology—The Human Influence Experiment (HUMINEX). *Urban Sci.* 1, 15. doi:10.3390/urbansci1020015
- Bechtel, B., Demuzere, M., and Stewart, I. D. (2020). A weighted accuracy measure for land cover mapping: Comment on Johnson et al. local climate zone (LCZ) map accuracy assessments should account for land cover physical characteristics that affect the local thermal environment. *remote sens.* 11, 2420. doi:10.3390/rs1111769
- Beck, C., Straub, A., Breitner, S., Cyrys, J., Philipp, A., Rathmann, J., et al. (2018a). Air Temperature Characteristics of Local Climate Zones in the Augsburg Urban Area (Bavaria, Southern Germany) under Varying Synoptic Conditions. *Urban Clim.* 25, 152–166. doi:10.1016/j.ulclim.2018.04.007
- Beck, H. E., Zimmermann, N. E., McVicar, T. R., Vergopolan, N., Berg, A., and Wood, E. F. (2018b). Present and Future Köppen-Geiger Climate Classification Maps at 1-km Resolution. *Sci. Data* 5, 1–12. doi:10.1038/sdata.2018.214
- Bell, S., Cornford, D., and Bastin, L. (2015). How Good Are Citizen Weather Stations? Addressing a Biased Opinion. *Weather* 70, 75–84. doi:10.1002/wea.2316
- Bornstein, R. D. (1968). Observations of the Urban Heat Island Effect in New York City. *J. Appl. Meteorol.* 7, 575–582. doi:10.1175/1520-0450(1968)007<0575:OOTUHI>2.0.CO;2
- Bornstein, R., and Lin, Q. (2000). Urban Heat Islands and Summertime Convective Thunderstorms in Atlanta: Three Case Studies. *AtmosEnviron.* 34, 507–516. doi:10.1016/S1352-2310(99)00374-X
- Bottyán, Z., Kircsi, A., Szegedi, S., and Unger, J. (2005). The Relationship between Built-Up Areas and the Spatial Development of the Mean Maximum Urban Heat Island in Debrecen, Hungary. *Int. J. Climatol.* 25, 405–418. doi:10.1002/joc.1138
- Brousse, O., Georganos, S., Demuzere, M., Dujardin, S., Lennert, M., Linard, C., et al. (2020). Can We Use Local Climate Zones for Predicting Malaria Prevalence across Sub-saharan African Cities. *Environ. Res. Lett.* 15, 124051. doi:10.1088/1748-9326/abc996
- Chapman, L., Bell, C., and Bell, S. (2017). Can the Crowdsourcing Data Paradigm Take Atmospheric Science to a New Level? A Case Study of the Urban Heat Island of London Quantified Using Netatmo Weather Stations. *Int. J. Climatol.* 37, 3597–3605. doi:10.1002/joc.4940
- Chapman, L., Muller, C. L., Young, D. T., Warren, E. L., Grimmond, C. S. B., Cai, X. M., et al. (2015). The Birmingham Urban Climate Laboratory: An Open Meteorological Test Bed and Challenges of the Smart City. *Bull. Am. Meteorol. Soc.* 96, 1545–1560. doi:10.1175/BAMS-D-13-00193.1

- Chwala, C., and Kunstmann, H. (2019). Commercial Microwave Link Networks for Rainfall Observation: Assessment of the Current Status and Future Challenges. *WIREs Water* 6, 1–20. doi:10.1002/wat2.1337
- Clarke, J. F. (1969). Nocturnal Urban Boundary Layer over Cincinnati, Ohio. *Mon. Weather Rev.* 97, 582–589. doi:10.1175/1520-0493(1969)097<0582:nubloc>2.3.co;2
- Cox, W. (2017). *Demographia World Urban Areas*. Belleville, Illinois: World Agglomerations. 13th Annu. Available at: <http://www.demographia.com/db-worldua.pdf>.
- de Vos, L., Leijnse, H., Overeem, A., and Uijlenhoet, R. (2017). The Potential of Urban Rainfall Monitoring with Crowdsourced Automatic Weather Stations in Amsterdam. *Hydrol. Earth Syst. Sci.* 21, 765–777. doi:10.5194/hess-21-765-2017
- de Vos, L. W., Drost, A. M., Zander, M. J., Overeem, A., Leijnse, H., Heusinkveld, B. G., et al. (2020). Hydrometeorological Monitoring Using Opportunistic Sensing Networks in the Amsterdam Metropolitan Area. *Bull. Am. Meteorol. Soc.* 101, E167–E185. doi:10.1175/BAMS-D-19-0091.1
- de Vos, L. W., Leijnse, H., Overeem, A., and Uijlenhoet, R. (2019). Quality Control for Crowdsourced Personal Weather Stations to Enable Operational Rainfall Monitoring. *Geophys. Res. Lett.* 46, 8820–8829. doi:10.1029/2019GL083731
- Demuzere, M., Hankey, S., Mills, G., Zhang, W., Lu, T., and Bechtel, B. (2020). Combining Expert and Crowd-Sourced Training Data to Map Urban Form and Functions for the continental US. *Sci. Data* 7, 1–13. doi:10.1038/s41597-020-00605-z
- Demuzere, M., Kittner, J., and Bechtel, B. (2021). LCZ Generator: A Web Application to Create Local Climate Zone Maps. *Front. Environ. Sci.* 9. doi:10.3389/fenvs.2021.637455
- Dienst, M., Lindén, J., and Esper, J. (2018). Determination of the Urban Heat Island Intensity in Villages and its Connection to Land Cover in Three European Climate Zones. *Clim. Res.* 76, 1–15. doi:10.3354/crc01522
- Dienst, M., Lindén, J., Saladié, O., and Esper, J. (2019). Detection and Elimination of UHI Effects in Long Temperature Records from Villages – A Case Study from Tivissa, Spain. *Urban Clim.* 27, 372–383. doi:10.1016/j.ulclim.2018.12.012
- Dixon, P. G., and Mote, T. L. (2003). Patterns and Causes of Atlanta's Urban Heat Island–Initiated Precipitation. *J. Appl. Meteorol.* 42, 1273–1284. doi:10.1175/1520-0450(2003)042<1273:pacoau>2.0.co;2
- Drost, A. M., Heusinkveld, B. G., Fenner, D., and Steeneveld, G. J. (2020). Assessing the Potential and Application of Crowdsourced Urban Wind Data. *Q. J. R. Meteorol. Soc.* 146, 2671–2688. doi:10.1002/qj.3811
- Drost, A. M., Pape, J. J., Overeem, A., Leijnse, H., Steeneveld, G. J., Van Delden, A. J., et al. (2017). Crowdsourcing Urban Air Temperatures through Smartphone Battery Temperatures in São Paulo, Brazil. *J. Atmos. Ocean. Technol.* 34, 1853–1866. doi:10.1175/JTECH-D-16-0150.1
- Ellis, K. N., Hathaway, J. M., Mason, L. R., Howe, D. A., Epps, T. H., and Brown, V. M. (2015). Summer Temperature Variability across Four Urban Neighborhoods in Knoxville, Tennessee, USA. *Theor. Appl. Climatol.* 127, 701–710. doi:10.1007/s00704-015-1659-8
- Emmanuel, R. (2021). Urban Microclimate in Temperate Climates: a Summary for Practitioners. *Build. Cities* 2, 402–410. doi:10.5334/bc.109
- Feichtinger, M., de Wit, R., Goldenits, G., Kolejka, T., Hollósi, B., Žuvela-Aloise, M., et al. (2020). Case-study of Neighborhood-Scale Summertime Urban Air Temperature for the City of Vienna Using Crowd-Sourced Data. *Urban Clim.* 32, 1–12. doi:10.1016/j.ulclim.2020.100597
- Fenner, D., Holtmann, A., Meier, F., Langer, I., and Scherer, D. (2019). Contrasting Changes of Urban Heat Island Intensity during Hot Weather Episodes. *Environ. Res. Lett.* 14, 124013. doi:10.1088/1748-9326/ab506b
- Fenner, D., Meier, F., Bechtel, B., Otto, M., and Scherer, D. (2017). Intra and Inter 'local Climate Zone' Variability of Air Temperature as Observed by Crowdsourced Citizen Weather Stations in Berlin, Germany. *Meteorol. Z.* 26, 525–547. doi:10.1127/metz/2017/0861
- Fenner, D., Meier, F., Scherer, D., and Polze, A. (2014). Spatial and Temporal Air Temperature Variability in Berlin, Germany, during the Years 2001–2010. *Urban Clim.* 10, 308–331. doi:10.1016/j.ulclim.2014.02.004
- Fernandez Milan, B., and Creutzig, F. (2015). Reducing Urban Heat Wave Risk in the 21st century. *Curr. Opin. Environ. Sustain.* 14, 221–231. doi:10.1016/j.cosust.2015.08.002
- Franck, U., Kruger, M., Schwarz, N., Grossmann, K., Roder, S., and Schlink, U. (2013). Heat Stress in Urban Areas: Indoor and Outdoor Temperatures in Different Urban Structure Types and Subjectively Reported Well-Being during a Heat Wave in the City of Leipzig. *Meteorol. Z.* 22, 167–177. doi:10.1127/0941-2948/2013/0384
- Gabriel, K. M. A., and Endlicher, W. R. (2011). Urban and Rural Mortality Rates during Heat Waves in Berlin and Brandenburg, Germany. *Environ. Pollut.* 159, 2044–2050. doi:10.1016/j.envpol.2011.01.016
- Garbero, V., Milelli, M., Buccignani, E., Mercogliano, P., Varentsov, M., Rozinkina, I., et al. (2021). Evaluating the Urban Canopy Scheme TERRA\_URB in the COSMO Model for Selected European Cities. *Atmosphere (Basel)* 12, 237. doi:10.3390/atmos12020237
- Gardes, T., Schoetter, R., Hidalgo, J., Long, N., Marquès, E., and Masson, V. (2020). Statistical Prediction of the Nocturnal Urban Heat Island Intensity Based on Urban Morphology and Geographical Factors - an Investigation Based on Numerical Model Results for a Large Ensemble of French Cities. *Sci. Total Environ.* 737, 139253. doi:10.1016/j.scitotenv.2020.139253
- Grassmann, T., Napoli, A., Meier, F., and Fenner, D. (2018). Quality Control for Crowdsourced Data from CWS. doi:10.14279/depositone-6740.3
- Gregg, J. W., Jones, C. G., and Dawson, T. E. (2003). Urbanization Effects on Tree Growth in the Vicinity of New York City. *Nature* 424, 183–187. doi:10.1038/nature01728
- Haberlandt, U., and Sester, M. (2010). Areal Rainfall Estimation Using Moving Cars as Rain Gauges - A Modelling Study. *Hydrol. Earth Syst. Sci.* 14, 1139–1151. doi:10.5194/hess-14-1139-2010
- Han, J. Y., Baik, J. J., and Lee, H. (2014). Urban Impacts on Precipitation. *Asia-Pacific J. Atmos. Sci.* 50, 17–30. doi:10.1007/s13143-014-0016-7
- Hart, M. A., and Sailor, D. J. (2009). Quantifying the Influence of Land-Use and Surface Characteristics on Spatial Variability in the Urban Heat Island. *Theor. Appl. Climatol.* 95, 397–406. doi:10.1007/s00704-008-0017-5
- Heaviside, C., Cai, X.-M., and Vardoulakis, S. (2015). The Effects of Horizontal Advection on the Urban Heat Island in Birmingham and the West Midlands, United Kingdom during a Heatwave. *Q. J. R. Meteorol. Soc.* 141, 1429–1441. doi:10.1002/qj.2452
- Heusinkveld, B. G., Steeneveld, G. J., Hove1, L. W. A. v., Jacobs, C. M. J., and Holtslag, A. A. M. (2014). Spatial Variability of the Rotterdam Urban Heat Island as Influenced by Urban Land Use. *J. Geophys. Res. Atmos.* 119, 677–692. doi:10.1002/2012JD019399.Received
- Jiang, S., Huang, F., Zhan, W., Bechtel, B., Liu, Z., Demuzere, M., et al. (2021). Mapping Local Climate Zones: A Bibliometric Meta- Analysis and Systematic Review. *OSF Prepr.*, 1–106. doi:10.31219/osf.io/c2bez
- Kislov, A. V., Varentsov, M. I., Gorlach, I. A., and Alekseeva, L. I. (2017). "Heat Island" of the Moscow Agglomeration and the Urban-Induced Amplification of Global Warming [in Russian]. *Mosc. Univ. Vestnik. Ser. Geogr.* 5, 12–19.
- Kwok, Y. T., Schoetter, R., Lau, K. K., Hidalgo, J., Ren, C., Pigeon, G., et al. (2019). How Well Does the Local Climate Zone Scheme Discern the thermal Environment of Toulouse (France)? an Analysis Using Numerical Simulation Data. *Int. J. Climatol.* 39, 5292–5315. doi:10.1002/joc.6140
- Leconte, F., Bouyer, J., Claverie, R., and Pétrissans, M. (2015). Using Local Climate Zone Scheme for UHI Assessment: Evaluation of the Method Using mobile Measurements. *Build. Environ.* 83, 39–49. doi:10.1016/j.buildenv.2014.05.005
- Lelovics, E., Unger, J., Gál, T., and Gál, C. V. (2014). Design of an Urban Monitoring Network Based on Local Climate Zone Mapping and Temperature Pattern Modelling. *Clim. Res.* 60, 51–62. doi:10.3354/cr01220
- Lemonsu, A., and Masson, V. (2002). Simulation of a Summer Urban Breeze over Paris. *Boundary-layer Meteorol.* 104, 463–490. doi:10.1023/A:1016509614936
- Li, Y., Schubert, S., Kropp, J. P., and Rybski, D. (2020). On the Influence of Density and Morphology on the Urban Heat Island Intensity. *Nat. Commun.* 11, 2647. doi:10.1038/s41467-020-16461-9
- Lokoshchenko, M. A., Korneva, I. A., Kochin, A. V., Dubovetsky, A. Z., Novitsky, M. A., and Razin, P. Y. (2016). Vertical Extension of the Urban Heat Island above Moscow. *Dokl. Earth Sci.* 466, 70–74. doi:10.1134/S1028334X16010128
- Lokoshchenko, M. A. (2017). Urban Heat Island and Urban Dry Island in Moscow and Their Centennial Changes. *J. Appl. Meteorol. Climatol.* 56, 2729–2745. doi:10.1175/JAMC-D-16-0383.1
- Lokoshchenko, M. A. (2014). Urban 'heat Island' in Moscow. *Urban Clim.* 10, Part 3, 550–562. doi:10.1016/j.ulclim.2014.01.008
- Mahoney, W. P., and O'Sullivan, J. M. (2013). Realizing the Potential of Vehicle-Based Observations. *Bull. Am. Meteorol. Soc.* 94, 1007–1018. doi:10.1175/BAMS-D-12-00044.1
- Mandement, M., and Caumont, O. (2020). Contribution of Personal Weather Stations to the Observation of Deep-Convection Features Near the Ground. *Nat. Hazards Earth Syst. Sci.* 20, 299–322. doi:10.5194/nhess-20-299-2020

- Manoli, G., Fatichi, S., Schläpfer, M., Yu, K., Crowther, T. W., Meili, N., et al. (2019). Magnitude of Urban Heat Islands Largely Explained by Climate and Population. *Nature* 573, 55–60. doi:10.1038/s41586-019-1512-9
- Martilli, A., Roth, M., Chow, W. T. L., Demuzere, M., Lipson, M., and Scott, E. (2020). Summer Average Urban-Rural Surface Temperature Differences Do Not Indicate the Need for Urban Heat Reduction. *OSF Prepr.* doi:10.31219/osf.io/8gnbf
- Mass, C. F., and Madaus, L. E. (2014). Surface Pressure Observations from Smartphones: A Potential Revolution for High-Resolution Weather Prediction. *Bull. Am. Meteorol. Soc.* 95, 1343–1349. doi:10.1175/BAMS-D-13-00188.1
- Meier, F., Fenner, D., Grassmann, T., Otto, M., and Scherer, D. (2017). Crowdsourcing Air Temperature from Citizen Weather Stations for Urban Climate Research. *Urban Clim.* 19, 170–191. doi:10.1016/j.uclim.2017.01.006
- Messer, H., Zinevich, A., and Alpert, P. (2006). Environmental Monitoring by Wireless Communication Networks. *Science* 312 (5774), 713. doi:10.1126/science.1120034
- Milošević, D., Savić, S., Kresojia, M., Lužanin, Z., Šećerov, I., Arsenović, D., et al. (2021). Analysis of Air Temperature Dynamics in the “Local Climate Zones” of Novi Sad (Serbia) Based on Long-Term Database from an Urban Meteorological Network. *Int. J. Biometeorol.* doi:10.1007/s00484-020-02058-w
- Mironova, V., Shartova, N., Beljaev, A., Varentsov, M., and Grishchenko, M. (2019). Effects of Climate Change and Heterogeneity of Local Climates On the Development of Malaria Parasite (*Plasmodium vivax*) in Moscow Megacity Region. *Int. J. Environ. Res. Public Health* 16, 694. doi:10.3390/ijerph16050694
- Muller, C. L., Chapman, L., Grimmond, C. S. B., Young, D. T., and Cai, X. (2013). Sensors and the City: A Review of Urban Meteorological Networks. *Int. J. Climatol.* 33, 1585–1600. doi:10.1002/joc.3678
- Napoly, A., Grassmann, T., Meier, F., and Fenner, D. (2018). Development and Application of a Statistically-Based Quality Control for Crowdsourced Air Temperature Data. *Front. Earth Sci.* 6, 1–16. doi:10.3389/feart.2018.00118
- Nazarian, N., Liu, S., Kohler, M., Lee, J. K. W., Miller, C., Chow, W. T., et al. (2020). Project Coolbit: Can Your Watch Predict Heat Stress and thermal comfort Sensation. *Environ. Res. Lett.* 16, 034031. doi:10.1088/1748-9326/ab130
- Nipen, T. N., Seierstad, I. A., Lussana, C., Kristiansen, J., and Hov, Ø. (2020). Adopting Citizen Observations in Operational Weather Prediction. *Bull. Am. Meteorol. Soc.* 101, E43–E57. doi:10.1175/BAMS-D-18-0237.1
- Oke, T. R. (1973). City Size and the Urban Heat Island. *Atmos. Environ. Pergamon Pres* 7, 769–779. doi:10.1016/0004-6981(73)90140-6
- Oke, T. R., Mills, G., Christen, A., and Voogt, J. A. (2017). *Urban Climates*. Cambridge: Cambridge University Press. doi:10.1017/9781139016476
- Oke, T. R. (1995). “The Heat Island of the Urban Boundary Layer: Characteristics, Causes and Effects,” in *Wind Climate in Cities* (Dordrecht: Springer Netherlands), 81–107. doi:10.1007/978-94-017-3686-2\_5
- Orlanski, L. (1975). A Rational Subdivision of Scale for Atmospheric Processes. *Bull. Am. Meteorol. Soc.* 56, 527–530.
- Oswald, E. M., Rood, R. B., Zhang, K., Gronlund, C. J., O’Neill, M. S., White-Newsome, J. L., et al. (2012). An Investigation into the Spatial Variability of Near-Surface Air Temperatures in the Detroit, Michigan, Metropolitan Region. *J. Appl. Meteorol. Climatol.* 51, 1290–1304. doi:10.1175/JAMC-D-11-0127.1
- Overeem, A., Leijnse, H., and Uijlenhoet, R. (2013a). Country-wide Rainfall Maps from Cellular Communication Networks. *Proc. Natl. Acad. Sci. U. S. A.* 110, 2741–2745. doi:10.1073/pnas.1217961110
- Overeem, A., Robinson, J. C. R., Leijnse, H., Steeneveld, G. J., Horn, B. K. P., and Uijlenhoet, R. (2013b). Crowdsourcing Urban Air Temperatures from Smartphone Battery Temperatures. *Geophys. Res. Lett.* 40, 4081–4085. doi:10.1002/grl.50786
- Pacifini, M., Rama, F., and de Castro Marins, K. R. (2019). Analysis of Temperature Variability within Outdoor Urban Spaces at Multiple Scales. *Urban Clim.* 2, 90–104. doi:10.1016/j.uclim.2018.11.003
- Quanz, J. A., Ulrich, S., Fenner, D., Holtmann, A., and Eimermacher, J. (2018). Micro-scale Variability of Air Temperature within a Local Climate Zone in Berlin, Germany, during Summer. *Climate* 6, 5. doi:10.3390/cl6010005
- Richard, Y., Emery, J., Dudek, J., Pergaud, J., Chateau-Smith, C., Zito, S., et al. (2018). How Relevant Are Local Climate Zones and Urban Climate Zones for Urban Climate Research? Dijon (France) as a Case Study. *Urban Clim.* 26, 258–274. doi:10.1016/j.uclim.2018.10.002
- Rivin, G. S., Rozinkina, I. A., Vil'fand, R. M., Kiktev, D. B., Tudrii, K. O., Blinov, D. V., et al. (2020). Development of the High-Resolution Operational System for Numerical Prediction of Weather and Severe Weather Events for the Moscow Region. *Russ. Meteorol. Hydrol.* 45, 455–465. doi:10.3103/S1068373920070018
- Samsonov, T. E., and Trigub, K. S. (2018). Mapping of Local Climate Zones of Moscow City. *Geod. Cartogr.* 936, 14–25. doi:10.22389/0016-7126-2018-936-6-14-25
- Samsonov, T. E., and Varentsov, M. I. (2020). Computation of City-Descriptive Parameters for High-Resolution Numerical Weather Prediction in Moscow Megacity in the Framework of the COSMO Model. *Russ. Meteorol. Hydrol.* 45, 515–521. doi:10.3103/S1068373920070079
- Samsonov, T., Koshelev, S., Walther, D., and Jenny, B. (2019). Automated Placement of Supplementary Contour Lines. *Int. J. Geogr. Inf. Sci.* 33, 2072–2093. doi:10.1080/13658816.2019.1610965
- Sangiorgio, V., Fiorito, F., and Santamouris, M. (2020). Development of a Holistic Urban Heat Island Evaluation Methodology. *Sci. Rep.* 10, 1–13. doi:10.1038/s41598-020-75018-4
- Scott, A. A., Zaitchik, B., Waugh, D. W., and O’Meara, K. (2017). Intraurban Temperature Variability in Baltimore. *J. Appl. Meteorol. Climatol.* 56, 159–171. doi:10.1175/JAMC-D-16-0232.1
- Shi, Y., Lau, K. K. L., Ren, C., and Ng, E. (2018). Evaluating the Local Climate Zone Classification in High-Density Heterogeneous Urban Environment Using mobile Measurement. *Urban Clim.* 25, 167–186. doi:10.1016/j.uclim.2018.07.001
- Skarbit, N., Stewart, I. D., Unger, J., and Gál, T. (2017). Employing an Urban Meteorological Network to Monitor Air Temperature Conditions in the ‘local Climate Zones’ of Szeged, Hungary. *Int. J. Climatol.* 37, 582–596. doi:10.1002/joc.5023
- Steeneveld, G. J., Koopmans, S., Heusinkveld, B. G., Hove, L. W. A. Van, and Holtslag, A. A. M. (2011). Quantifying Urban Heat Island Effects and Human comfort for Cities of Variable Size and Urban Morphology in the Netherlands. *J. Geophys. Res.* 116, 1–14. doi:10.1029/2011JD015988
- Stewart, I. D., Oke, T. R., and Krayenhoff, E. S. (2014). Evaluation of the ‘Local Climate Zone’ Scheme Using Temperature Observations and Model Simulations. *Int. J. Climatol.* 1080, 1062–1080. doi:10.1002/joc.3746
- Stewart, I. D., and Oke, T. R. (2012). Local Climate Zones for Urban Temperature Studies. *Bull. Am. Meteorol. Soc.* 93, 1879–1900. doi:10.1175/BAMS-D-11-00019.1
- Stewart, I. D. (2019). Why Should Urban Heat Island Researchers Study History. *Urban Clim.* 30, 100484. doi:10.1016/j.uclim.2019.100484
- Straub, A., Berger, K., Breitner, S., Cyrys, J., Geruschkat, U., Jacobbeit, J., et al. (2019). Statistical Modelling of Spatial Patterns of the Urban Heat Island Intensity in the Urban Environment of Augsburg, Germany. *Urban Clim.* 29, 100491. doi:10.1016/j.uclim.2019.100491
- Svensson, M. K., and Eliasson, I. (2002). Diurnal Air Temperatures in Built-Up Areas in Relation to Urban Planning. *Landscape Urban Plan.* 61, 37–54. doi:10.1016/S0169-2046(02)00076-2
- Szymański, M., and Kryza, M. (2009). GIS-based Techniques for Urban Heat Island Spatialization. *Clim. Res.* 38, 171–187. doi:10.3354/cr00780
- Tan, J., Zheng, Y., Tang, X., Guo, C., Li, L., Song, G., et al. (2010). The Urban Heat Island and its Impact on Heat Waves and Human Health in Shanghai. *Int. J. Biometeorol.* 54, 75–84. doi:10.1007/s00484-009-0256-x
- Tardivo, G., and Berti, A. (2012). A Dynamic Method for gap Filling in Daily Temperature Datasets. *J. Appl. Meteorol. Climatol.* 51, 1079–1086. doi:10.1175/JAMC-D-11-0117.1
- Theeuwes, N. E., Steeneveld, G. J., Ronda, R. J., and Holtslag, A. A. M. (2017). A Diagnostic Equation for the Daily Maximum Urban Heat Island Effect for Cities in Northwestern Europe. *Int. J. Climatol.* 37, 443–454. doi:10.1002/joc.4717
- van Hove, L. W. A., Jacobs, C. M. J., Heusinkveld, B. G., Elbers, J. A., Van Driel, B. L., and Holtslag, A. A. M. (2015). Temporal and Spatial Variability of Urban Heat Island and thermal comfort within the Rotterdam Agglomeration. *Build. Environ.* 83, 91–103. doi:10.1016/j.buildenv.2014.08.029
- Varentsov, M. I., Grishchenko, M. Y., and Wouters, H. (2019). Simultaneous Assessment of the Summer Urban Heat Island in Moscow Megacity Based on *In Situ* Observations, thermal Satellite Images and Mesoscale Modeling. *Geogr. Environ. Sustain.* 12, 74–95. doi:10.24057/2071-9388-2019-10

- Varentsov, M. I., Konstantinov, P. I., and Samsonov, T. E. (2017). Mesoscale Modelling of the Summer Climate Response of Moscow Metropolitan Area to Urban Expansion. *IOP Conf. Ser. Earth Environ. Sci.* 96, 012009. doi:10.1088/1755-1315/96/1/012009
- Varentsov, M. I., Konstantinov, P. I., Shartova, N. V., Samsonov, T. E., Kargashin, P. E., Varentsov, A. I., et al. (2020a). Urban Heat Island of the Moscow Megacity: the Long-Term Trends and New Approaches for Monitoring and Research Based on Crowdsourcing Data. *IOP Conf. Ser. Earth Environ. Sci.* 606, 012063. doi:10.1088/1755-1315/606/1/012063
- Varentsov, M., Samsonov, T., and Demuzere, M. (2020b). Impact of Urban Canopy Parameters on a Megacity's Modelled Thermal Environment. *Atmosphere (Basel)*. 11, 1349. doi:10.3390/atmos11121349
- Varentsov, M., Wouters, H., Platonov, V., and Konstantinov, P. (2018). Megacity-Induced Mesoclimatic Effects in the Lower Atmosphere: A Modeling Study for Multiple Summers over Moscow, Russia. *Atmosphere (Basel)* 9, 50. doi:10.3390/atmos9020050
- Venter, Z. S., Brousse, O., Esau, I., and Meier, F. (2020). Hyperlocal Mapping of Urban Air Temperature Using Remote Sensing and Crowdsourced Weather Data. *Remote Sens. Environ.* 242, 111791. doi:10.1016/j.rse.2020.111791
- Verdonck, M. L., Demuzere, M., Hooyberghs, H., Beck, C., Cyrys, J., Schneider, A., et al. (2018). The Potential of Local Climate Zones Maps as a Heat Stress Assessment Tool, Supported by Simulated Air Temperature Data. *Landscape Urban Plan.* 178, 183–197. doi:10.1016/j.landurbplan.2018.06.004
- Vulova, S., Meier, F., Fenner, D., Nouri, H., and Kleinschmit, B. (2020). Summer Nights in Berlin, Germany: Modeling Air Temperature Spatially with Remote Sensing, Crowdsourced Weather Data, and Machine Learning. *IEEE J. Sel. Top. Appl. Earth Obs. Remote Sens.* 13, 5074–5087. doi:10.1109/JSTARS.2020.3019696
- Wang, Q., Hang, J., Fan, Y., and Li, Y. (2020). Urban Plume Characteristics under Various Wind Speed, Heat Flux, and Stratification Conditions. *Atmos. Environ.* 239, 117774. doi:10.1016/j.atmosenv.2020.117774
- Wolters, D., and Brandsma, T. (2012). Estimating the Urban Heat Island in Residential Areas in the Netherlands Using Observations by Weather Amateurs. *J. Appl. Meteorol. Climatol.* 51, 711–721. doi:10.1175/JAMC-D-11-0135.1
- Wouters, H., De Ridder, K., Demuzere, M., Lauwaet, D., and Van Lipzig, N. P. M. (2013). The Diurnal Evolution of the Urban Heat Island of Paris: A Model-Based Case Study during Summer 2006. *Atmos. Chem. Phys.* 13, 8525–8541. doi:10.5194/acp-13-8525-2013
- Yushkov, V. P., Kurbatova, M. M., Varentsov, M. I., Lezina, E. A., Kurbatov, G. A., Miller, E. A., et al. (2019). Modeling an Urban Heat Island during Extreme Frost in Moscow in January 2017. *Izv. Atmos. Ocean. Phys.* 55, 389–406. doi:10.1134/S0001433819050128
- Zemtsov, S., Shartova, N., Varentsov, M., Konstantinov, P., Kidyaeva, V., Shchur, A., et al. (2020). Intraurban Social Risk and Mortality Patterns during Extreme Heat Events: A Case Study of Moscow, 2010–2017. *Health Place* 66, 102429. doi:10.1016/j.healthplace.2020.102429
- Zhang, D.-L., Shou, Y.-X., Dickerson, R. R., and Chen, F. (2011). Impact of Upstream Urbanization on the Urban Heat Island Effects along the Washington–Baltimore Corridor. *J. Appl. Meteorol. Climatol.* 50, 2012–2029. doi:10.1175/JAMC-D-10-05008.1
- Zhou, B., Rybski, D., and Kropp, J. P. (2017). The Role of City Size and Urban Form in the Surface Urban Heat Island. *Sci. Rep.* 7, 4791. doi:10.1038/s41598-017-04242-2
- Zinevich, A., Messer, H., and Alpert, P. (2009). Frontal Rainfall Observation by a Commercial Microwave Communication Network. *J. Appl. Meteorol. Climatol.* 48, 1317–1334. doi:10.1175/2008JAMC2014.1
- Conflict of Interest:** The authors declare that the research was conducted in the absence of any commercial or financial relationships that could be construed as a potential conflict of interest.
- Publisher's Note:** All claims expressed in this article are solely those of the authors and do not necessarily represent those of their affiliated organizations, or those of the publisher, the editors, and the reviewers. Any product that may be evaluated in this article, or claim that may be made by its manufacturer, is not guaranteed or endorsed by the publisher.
- Copyright © 2021 Varentsov, Fenner, Meier, Samsonov and Demuzere. This is an open-access article distributed under the terms of the Creative Commons Attribution License (CC BY). The use, distribution or reproduction in other forums is permitted, provided the original author(s) and the copyright owner(s) are credited and that the original publication in this journal is cited, in accordance with accepted academic practice. No use, distribution or reproduction is permitted which does not comply with these terms.



# CrowdQC+—A Quality-Control for Crowdsourced Air-Temperature Observations Enabling World-Wide Urban Climate Applications

Daniel Fenner<sup>1,2\*</sup>, Benjamin Bechtel<sup>1</sup>, Matthias Demuzere<sup>1</sup>, Jonas Kittner<sup>1</sup> and Fred Meier<sup>3</sup>

<sup>1</sup>Urban Climatology, Department of Geography, Faculty of Geosciences, Ruhr University Bochum, Bochum, Germany, <sup>2</sup>Chair of Environmental Meteorology, Institute of Earth and Environmental Sciences, Faculty of Environment and Natural Resources, University of Freiburg, Freiburg, Germany, <sup>3</sup>Chair of Climatology, Institute of Ecology, Technische Universität Berlin, Berlin, Germany

## OPEN ACCESS

### Edited by:

Tomas Halenka,  
Charles University, Czechia

### Reviewed by:

Tirthankar Chakraborty,  
Yale University, United States  
Jiannan Wang,  
Simon Fraser University, Canada

### \*Correspondence:

Daniel Fenner  
[daniel.fenner@meteo.uni-freiburg.de](mailto:daniel.fenner@meteo.uni-freiburg.de)

### Specialty section:

This article was submitted to  
Interdisciplinary Climate Studies,  
a section of the journal  
Frontiers in Environmental Science

Received: 04 June 2021

Accepted: 02 November 2021

Published: 03 December 2021

### Citation:

Fenner D, Bechtel B, Demuzere M, Kittner J and Meier F (2021)  
CrowdQC+—A Quality-Control for  
Crowdsourced Air-Temperature  
Observations Enabling World-Wide  
Urban Climate Applications.  
*Front. Environ. Sci.* 9:720747.  
doi: 10.3389/fenvs.2021.720747

In recent years, the collection and utilisation of crowdsourced data has gained attention in atmospheric sciences and citizen weather stations (CWS), i.e., privately-owned weather stations whose owners share their data publicly via the internet, have become increasingly popular. This is particularly the case for cities, where traditional measurement networks are sparse. Rigorous quality control (QC) of CWS data is essential prior to any application. In this study, we present the QC package “CrowdQC+,” which identifies and removes faulty air-temperature (*ta*) data from crowdsourced CWS data sets, i.e., data from several tens to thousands of CWS. The package is a further development of the existing package “CrowdQC.” While QC levels and functionalities of the predecessor are kept, CrowdQC+ extends it to increase QC performance, enhance applicability, and increase user-friendliness. Firstly, two new QC levels are introduced. The first implements a spatial QC that mainly addresses radiation errors, the second a temporal correction of the data regarding sensor-response time. Secondly, new functionalities aim at making the package more flexible to apply to data sets of different lengths and sizes, enabling also near-real time application. Thirdly, additional helper functions increase user-friendliness of the package. As its predecessor, CrowdQC+ does not require reference meteorological data. The performance of the new package is tested with two 1-year data sets of CWS data from hundreds of “Netatmo” CWS in the cities of Amsterdam, Netherlands, and Toulouse, France. Quality-controlled data are compared with data from networks of professionally-operated weather stations (PRWS). Results show that the new package effectively removes faulty data from both data sets, leading to lower deviations between CWS and PRWS compared to its predecessor. It is further shown that CrowdQC+ leads to robust results for CWS networks of different sizes/densities. Further development of the package could include testing the suitability of CrowdQC+ for other variables than *ta*, such as air pressure or specific humidity, testing it on data sets from other background climates such as tropical or desert cities, and to incorporate added filter functionalities for further improvement. Overall, CrowdQC+ could lead the way to utilise CWS data in world-wide urban climate applications.

**Keywords:** crowdsourcing, quality control, citizen weather station, private weather station, urban climate, Netatmo, Amsterdam, Toulouse

## INTRODUCTION

Cities modify atmospheric conditions and amongst these alterations the urban heat island (UHI) phenomenon, i.e., generally higher temperatures within the city compared to its rural surroundings, is likely the best documented one (Arnfield 2003; Oke et al., 2017; Stewart 2019). Despite high variability in atmospheric conditions within cities due to heterogeneity in underlying surface cover, morphology, thermal properties, and anthropogenic heat emissions (Oke et al., 2017), there is a dearth of observations to monitor these. While a growing number of cities is now equipped with dedicated urban climate observation networks (see review by Muller et al., 2013), mostly run by research institutions [e.g., Amsterdam, Netherlands (Ronda et al., 2017), Berlin, Germany (Fenner et al., 2014; Langer et al., 2021), Birmingham, United Kingdom (Chapman et al., 2015; Warren et al., 2016), Novi Sad, Serbia (Šćerov et al., 2019), Szeged, Hungary (Lelovics et al., 2014; Skarbit et al., 2017)], for the broad majority of urban regions across the globe little to none is known about their urban climate conditions through observations.

In recent years, the collection and utilisation of vast amounts of data via crowdsourcing, i.e., the collection of data from non-traditional sources via the internet (Muller et al., 2015), has gained much attention. Such non-traditional, opportunistic sources of data are, e.g., smartphones (e.g., Overeem et al., 2013b; Mass and Madaus 2014; Droste et al., 2017), smart wearable devices (Nazarian et al., 2021), cars (e.g., Haberlandt and Sester 2010; Bartos et al., 2019), commercial microwave links (e.g., Messer et al., 2006; Overeem et al., 2013a; Chwala and Kunstmann 2019), and privately-owned weather stations, called citizen weather stations (CWS) in the following (e.g., Steeneveld et al., 2011; Wolters and Brandsma 2012; Bell et al., 2013; Madaus et al., 2014; Chapman et al., 2017; de Vos et al., 2017; Venter et al., 2021). Each type of these data sources alone or multiple combined can be used in different meteorological and climatological applications, such as weather forecast (e.g., Mass and Madaus, 2014; Nipen et al., 2020), operational weather monitoring (e.g., de Vos et al., 2019), mesoscale model evaluation (e.g., Hammerberg et al., 2018), hydrometeorological analyses and modelling (e.g., Smiatek et al., 2017; de Vos et al., 2020), high-resolution mapping of air temperature (e.g., Venter et al., 2020; Vulova et al., 2020; Zumwald et al., 2021), thermal-comfort assessment (Nazarian et al., 2021), and urban climate investigations (e.g., Fenner et al., 2017, 2019; Droste et al., 2020; Feichtinger et al., 2020). The potential of CWS data is especially large for cities, where population density and thus also CWS network density is high and where traditional meteorological observations are sparse.

By investigating CWS data and crowdsourced data sets of air-temperature (*ta*) measurements, Bell et al. (2015) and Meier et al. (2017) identified different sources of uncertainties or errors. These are issues related to metadata (e.g., incorrect, incomplete), the device design (flaws of the station that lead to inaccurate measurements, e.g., radiative errors, slow response), installation (e.g., CWS set up inappropriately near building walls), calibration (e.g., constant offsets or sensor drift

over time), and communication and software errors (lead to missing data) (Bell et al., 2015; Meier et al., 2017). For other variables than *ta*, other sources of uncertainty may also arise [see, e.g., de Vos et al. (2019) for precipitation, and Droste et al. (2020) for wind speed]. Design flaws leading to radiative errors and to slow sensor-response times are common among many different types of CWS (Bell 2015). This holds particularly true for the Netatmo CWS (<https://www.netatmo.com/en-us/weather>), a popular CWS especially in Europe. Due to its compact built form and its aluminum shell with poor ventilation and without a proper radiation screen it is particularly affected by both types of errors (Meier et al., 2017; Büchau 2018). Despite the abundance of CWS, especially in urban areas, crowdsourced CWS data sets can hence not be used in urban climate research without prior rigorous quality control (QC).

To address sources of uncertainties associated with CWS data and to remove erroneous data from a data set of crowdsourced CWS observations, a number of studies has developed QC procedures, either relying on reference data from professionally-operated weather stations (PRWS), or using statistical approaches that are independent of additional meteorological observations. Several QC procedures for CWS that make use of PRWS data have been developed, all with different complexity and focusing on different variables: for *ta* (e.g., Bell 2015; Meier et al., 2017; Hammerberg et al., 2018; Cornes et al., 2020), for precipitation (Bárdossy et al., 2021), for wind speed (Droste et al., 2020; Chen et al., 2021), and for multiple variables (Clark et al., 2018; Mandement and Caumont 2020). Recently, Båserud et al. (2020) introduced an automatic QC package for *ta* and precipitation, which aims at identifying possibly faulty values from meteorological observations based on a series of (spatial) tests. The applicability of that specific QC is highlighted by the fact that it is implemented in the operational weather forecast of the Norwegian Meteorological Service (Båserud et al., 2020; Nipen et al., 2020).

One core potential benefit of CWS data is their availability in regions where traditional and high-quality meteorological observations are sparse or even non-existing. Hence, a QC that is independent of such additional data makes it particularly useful for application in such areas and transferable across regions. For precipitation from CWS, de Vos et al. (2019) developed an automatic QC that can be applied in (near-)real time for operational weather monitoring. For *ta*, Chapman et al. (2017), e.g., used a relatively simple statistical approach of mean and standard deviation to filter potentially faulty measurements from CWS in London, United Kingdom. Napoly et al. (2018) developed a more comprehensive QC for *ta*, also working without reference meteorological data and being available as a package in R (R Core Team 2021) under the name of “CrowdQC” (Grassmann et al., 2018). CrowdQC is a statistically-based QC with four main and three optional QC levels that are applied sequentially, removing erroneous data based on the assumption that the whole crowd of CWS knows more than each individual station

(“wisdom of the crowd”). Since its release, CrowdQC has successfully been applied in a number of studies to quality-control CWS *ta* data for further analyses (e.g., Fenner et al., 2019; Feichtinger et al., 2020; Venter et al., 2020, 2021; Vulova et al., 2020; Benjamin et al., 2021; Potgieter et al., 2021; Zumwald et al., 2021). Its large-scale applicability was only recently demonstrated by the study of Venter et al. (2021), using CrowdQC to quality-control data from >50,000 CWS in 342 urban regions in Europe for a summer month.

While CrowdQC already provides good performance regarding identifying and removing possibly faulty values in the CWS data set (Napoly et al., 2018), Feichtinger et al. (2020), e.g., identified that when applying CrowdQC for Vienna, Austria, radiative errors remained in the filtered data set. Similar issues were reported by Venter et al. (2021). To address the remaining radiative errors, Feichtinger et al. (2020) introduced additional filter levels, adopting filter functions developed by Meier et al. (2017). These additional filter functions rely on measurements of global radiation and *ta* data from PRWS. Further, Feichtinger et al. (2020) had to collect and quality-control a whole month of CWS data, even though their investigation period lasted only eleven days during that month. This was due to the functionality of CrowdQC, which only worked on a fixed monthly basis and not being flexible towards periods of other lengths.

While radiative errors have been addressed by the various QC procedures available for CWS data, none of them has tried to address errors due to slow sensor response. Sensor-response times are dependent on the type of sensor, its built form, radiation shield, location, and weather conditions, which makes it non-trivial to implement such a correction for crowdsourced CWS data. The question is, whether it is nonetheless possible to reduce such errors due to slow sensor response, in absence of additional meta data and other meteorological observations. Since Netatmo CWS are all built identically, it might be possible to reduce errors in a crowdsourced data set of hundreds of these CWS in a simplified manner by correcting the data with a uniform time constant.

This study introduces and describes CrowdQC+ as a further development of CrowdQC. CrowdQC+ builds on its predecessor, keeping the QC concepts, software and QC design, and existing QC levels. The core aim of CrowdQC+ is to retain the existing applicability of CrowdQC, i.e., providing a QC for CWS data that is independent of reference meteorological data, thus exploiting the “wisdom of the crowd” and being applicable universally around the world. The main idea of CrowdQC+ is that there is trustworthy information in a large group of individual measurements, which can be used to check individual values. With several enhancements and added functionalities, the aim of CrowdQC+ is to increase applicability and performance of the QC, effectively removing faulty data while retaining as much data as possible. The core enhancement of CrowdQC+ is the introduction of two new QC levels: The first implements a spatial QC that mainly addresses radiative errors, the second a temporal correction of the data regarding sensor-response time.

Besides, a number of modifications and bug fixes to the existing package are implemented, as well as several helper functions that target the user-friendliness of the package.

The following sections aim at providing an overview of the open-source package CrowdQC+ with its additional functionalities and extensions. Both CrowdQC and CrowdQC+ are applied to two data sets in Amsterdam (Netherlands) and Toulouse (France), where PRWS data exist, used as benchmark. In the end, two applications highlight the applicability of CWS data in urban climate research.

## DATA AND METHODS

### Data

#### Cities and Investigation Periods

Two cities were selected for this study: Amsterdam (52.37°N, 4.89°E) and Toulouse (43.60°N, 1.44°E). **Figure 1** displays both regions and corresponding weather stations, **Table 1** provides a brief overview of the cities and the respective investigation periods. Both investigation periods cover 1 year: 2019 and 2020 for Amsterdam and Toulouse, respectively. The cities and investigation periods were selected due to the availability of reference data from PRWS for comparison with CWS data, relatively dense CWS networks, different background climates, and different city settings.

Amsterdam lies in the north of the Netherlands and is strongly influenced by maritime air from the North Sea (distance to coast <50 km). In addition, the surroundings contain large waterbodies (to the north-east of the city) and canals are found throughout the city centre region. The region of interest (ROI) for Amsterdam (cf. definition of ROI in *Station Selection* section) has a flat topography, with an altitude approximately at mean sea level. Central areas of the city are mainly composed of LCZ 2 (compact midrise). Surrounding these areas, LCZ 6 (open low-rise) and 8 (large low-rise) dominate the built-up areas, natural surroundings of the city are mainly composed of LCZ D (low plants) and G (water) (**Figure 1A**).

Toulouse is an inland city in the south of France, approximately 80 km north/north-east of the Pyrenees mountain range. The river Garonne runs through the city. Overall, topography is flat, with a mean ROI altitude of approximately 150 m above mean sea level (amsl). Central parts of Toulouse are composed of LCZ 2 and 5 (open midrise), while largest built-up areas consist of LCZ 6, 8, and 9 (sparsely built). Natural landcover surrounding the city is mainly LCZ D and A (dense trees) (**Figure 1B**).

#### Citizen Weather Stations and Crowdsourcing

Data from CWS were collected from the Netatmo network (<https://weathermap.netatmo.com/>) via the company’s Application Programming Interface API (<https://dev.netatmo.com/>).

The Netatmo CWS is a smart device, sold by the French company “Netatmo.” The station consists of an indoor and an

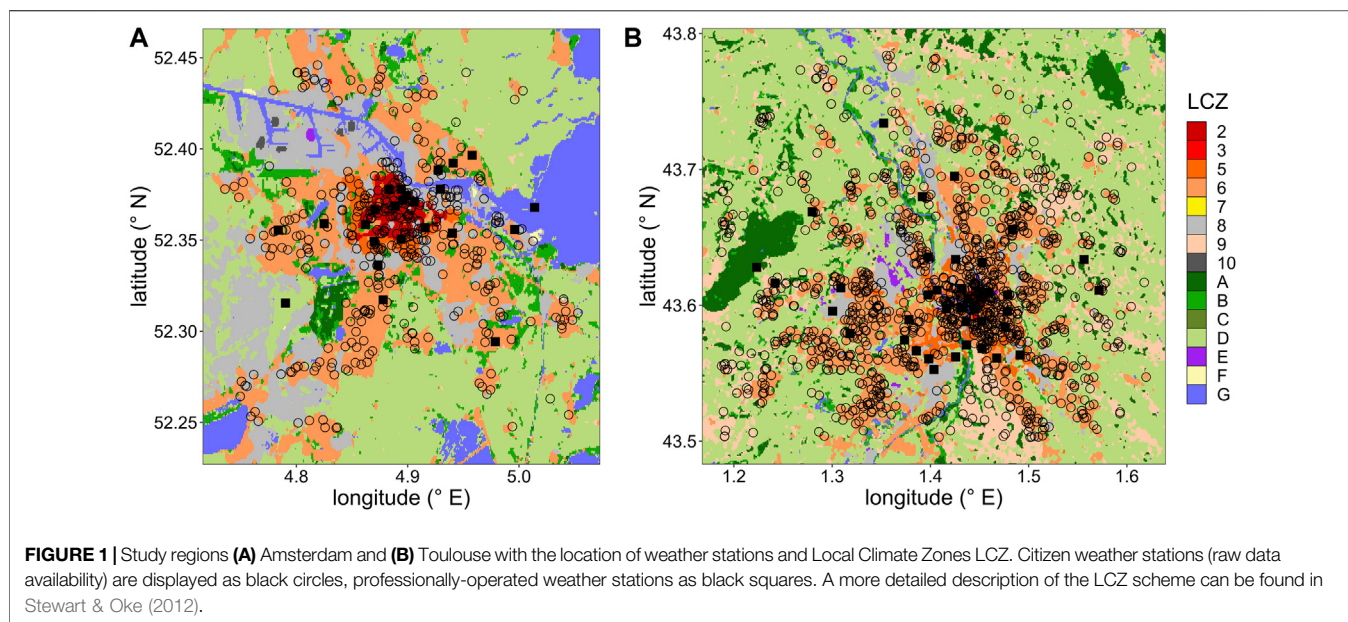


**TABLE 1 |** Overview of the professionally-operated weather stations in each city used in the investigations. KGC: Köppen-Geiger classification after Beck et al. (2018b). KNMI, Koninklijk Nederlands Meteorologisch Instituut–Royal Netherlands Meteorological Institute; AAMS, Amsterdam Atmospheric Meteorological Supersite (Ronda et al., 2017).

City	KGC	Period	Network/Provider	Number of stations <sup>a</sup>	Temporal resolution (minutes)	Sensor	Accuracy (K)
Amsterdam	Cfb	01/01–31/12/2019	KNMI	1	60	Pt500 (active ventilation)	0.1
			AAMS	23	5	Decagon VP-3 (active ventilation with global radiation >100 W m <sup>-2</sup> )	<0.5
Toulouse	Cfa	01/01–31/12/2020	Toulouse Métropole/Météo France	38	15	Davis Vantage Pro II ISS (natural ventilation)	0.3

<sup>a</sup>In analyses, after QC, aggregation, and clipped to each cities' ROI.

outdoor module, each enclosed by a cylindrical shell made of aluminium. Upon purchase, Netatmo CWS do not contain a proper radiation shield such as lamella-type radiation screens, making it prone to shortwave radiative errors if set up in unshaded locations. Additional radiation screens can be fitted to the sensor but are likely only found at a marginal percentage of Netatmo CWS, since the company does not offer such a screen. The outdoor module measures *ta* (specified accuracy  $\pm 0.3$  K,  $-40^{\circ}\text{C}$  to  $65^{\circ}\text{C}$ ) and relative humidity at 5-min resolution. Data is automatically and wirelessly sent to the Netatmo server, from which the owner can retrieve the data. If the owner consents to share the data, the outdoor measurements are publicly shared and can be retrieved via the API at no cost. Meier et al. (2017) investigated the accuracy of the sensor, showing that the specified accuracy is met for the tested range  $0^{\circ}\text{C}$ – $30^{\circ}\text{C}$ , with only a small positive bias at  $0^{\circ}\text{C}$ . Fenner (2020) further showed that even after several years in the field the sensors did not show a systematic drift and still met the specified accuracy.

CWS *ta* data was crowdsourced at an hourly resolution using the “getmeasure” API endpoint. Beforehand, station metadata (station identifier, latitude, longitude, altitude) were collected and

updated regularly using the “getpublicdata” API endpoint, retrieving new metadata and comparing it to previously-obtained metadata. Each CWS received a unique internal station ID. If a change in position for an existing CWS was detected, a new internal station ID was assigned to this CWS, in order to keep the time series consistent (similar to Meier et al., 2017). Metadata for each CWS are limited to geographical position and altitude, and no further information regarding, e.g., a possible additional radiation shield or the specific setup of the sensor are available from the Netatmo API. This is in contrast to other CWS platforms such as Weather Underground (<https://www.wunderground.com/pws/overview>) or the Weather Observations Website (<https://www.wow.metoffice.gov.uk/>), where such metadata can be provided by station owners and which can then be obtained by API users. However, the Netatmo network surpasses other CWS platforms regarding network density, especially in Europe, and offers the advantage of a consistent station design and sensor quality throughout the whole network.

Netatmo CWS data are one-hourly mean values. Netatmo time stamps obtained from the API were valid for the beginning

of each aggregation interval, which was modified (+3600 s/+1 h) to represent the end of each interval. Then, CWS data were prepared for the QC according to the requirements of the CrowdQC and CrowdQC+ packages, resulting in a data table (Dowle and Srinivasan 2021) with column names as required by the packages [*ta*, time information, station ID, and corresponding coordinates (latitude, longitude)].

### Professionally-Operated Weather Stations and Quality Control

Data from PRWS were collected from different institutions for both cities. The respective temporal availability, temporal resolution, instrumentation, and number of stations are displayed in **Table 1**. Data from these PRWS are especially suitable for our purpose, as networks in both cities cover extended areas with stations being located in a variety of local settings, yet with a focus on city-centre regions where CWS data are also especially dense (**Figure 1**). PRWS data for Amsterdam from the Amsterdam Atmospheric Meteorological Supersite (AAMS, Ronda et al., 2017) have previously been used in the evaluation of and comparison with CWS data (e.g., de Vos et al., 2020; Droste et al., 2020). PRWS data from the network in Toulouse was already used in the study by Napoly et al. (2018) to evaluate the performance of CrowdQC, yet with a much lower number of sites than in this study. Sensors of both PRWS networks are installed on lampposts or street signs at a height of approximately 3–4 m above ground level.

Data from PRWS were quality-controlled to remove unrealistic values. The QC steps and corresponding thresholds were adapted from several sources (Shafer et al., 2000; Zahumenský 2004; Fiebrich et al., 2010; Estévez et al., 2011; Cerlini et al., 2020). The QC consisted of four individual tests, all working on the individual station level:

- 1) Gross-error limit test: All values outside the range [-40°C, 60°C] were flagged as FALSE.
- 2) Spike-dip/step test (temporal consistency): If the difference between a value and its previous value was above a threshold value, this value was flagged as FALSE. The threshold was adapted to the temporal resolution of the data (5-min resolution: 6 K, 15-min resolution: 10 K, 1-hourly resolution: 20 K).
- 3) Persistence test (temporal consistency): If a value persisted for a certain period of time, these values were flagged as FALSE. The threshold was adapted to the temporal resolution of the data (5-min resolution: 2 h, 15-min resolution: 3 h, 1-hourly resolution: 6 h).
- 4) Manual visual check: This last step was performed to identify any additional flawed data based on a visual inspection of each time series.

The QC tests were always applied at the highest available temporal resolution at each station. If any of the tests failed (FALSE flag), this value was set to missing value. After QC, all data were aggregated to hourly mean values. A minimum of >80% of valid data per hour had to be available for the aggregation, otherwise this value was set to missing value.

Further, each month of a station was only kept if >80% of hourly data were valid.

### Local Climate Zone Maps

For each city, an LCZ map (**Figure 1**) was produced using the LCZ Generator (Demuzere et al., 2021, <https://lcz-generator.rub.de/>). This web application translates the default WUDAPT protocol (Bechtel et al., 2015; Ching et al., 2018) into a cloud-based web application, thereby using all recent advancements of LCZ mapping as described in Bechtel et al. (2019) and Demuzere et al. (2019a,b; 2020).

## Methods

### Station Selection

A ROI was set for each city. Each ROI extended from the minimum to the maximum in common geographical coverage among the PRWS and CWS networks (based on latitude and longitudes of all stations), adding (subtracting) 0.05° to the maximum (minimum) latitude and longitude. Only stations within each ROI were selected for further analyses (**Figure 1**). The ROI for Amsterdam (506.54 km<sup>2</sup>) is about half the size of that for Toulouse (1,130.90 km<sup>2</sup>), while the maximum network density in time for raw CWS data (calculated per hourly data availability) is similar for both cities with 0.85 CWS/km<sup>2</sup> and 0.86 CWS/km<sup>2</sup> for Amsterdam and Toulouse, respectively.

### Height Correction

For comparisons among stations after QC, *ta* data were corrected for elevation differences among stations to a reference height per city, using the environmental lapse rate of -0.0065 K m<sup>-1</sup>. The reference height was set to the mean of the elevation of all PRWS in each city, rounded to the nearest integer value (Amsterdam: 3 m amsl, Toulouse: 155 m amsl). The elevation of each station was extracted from the nearest grid-point value from the hole-filled Shuttle Radar Topographic Mission SRTM data (Jarvis et al., 2008). Additionally, the sensor height was considered in the height correction, using the available metadata for PRWS and assuming a uniform sensor height for the CWS of 2 m above ground level, as in Fenner et al. (2017).

### Classification of Stations to Local Climate Zones

All CWS available in the ROI were considered in the application of CrowdQC and CrowdQC+. For comparison between CWS and PRWS, an LCZ was assigned to each station following Fenner et al. (2017) and Varentsov et al. (2021), using the geographical position of each station and the LCZ maps. First, the nearest-pixel LCZ value was assigned to each station. Second, for a buffer with a radius of 250 m around each station, the surface-cover fraction of the modal LCZ was calculated (using pixels of the LCZ map). Third, a weighted surface-cover LCZ fraction in the same buffer was calculated (Varentsov et al., 2021), applying “similarity weights” (**Figure 3B** in Bechtel et al., 2020) between the modal LCZ and all other grid points (LCZ pixels) within the buffer.

Only those stations (CWS and PRWS) were considered if 1) the nearest-pixel LCZ was identical to the modal LCZ in the buffer, 2) the modal LCZ covered a surface fraction within the

buffer of >0.5, and 3) the weighed-LCZ fraction of the modal LCZ was  $\geq 0.75$ . This procedure was applied to select only those stations that are located in homogeneous surroundings regarding the LCZ scheme, to obtain a locally-representative signal (Fenner et al., 2017).

## Statistics

Four statistical metrics were calculated to compare CWS with PRWS *ta* data.

Mean deviation MD:

$$MD = \frac{1}{N} \sum_{i=1}^N |ta_{i,CWS} - ta_{i,PRWS}|$$

where  $ta_{i,CWS}$  and  $ta_{i,PRWS}$  are *ta* at CWS and PRWS, respectively, at time *i*.

Mean absolute deviation MAD:

$$MAD = \frac{1}{N} \sum_{i=1}^N |ta_{i,CWS} - ta_{i,PRWS}|$$

Root-mean-square deviation RMSD:

$$RMSD = \sqrt{\frac{1}{N} \sum_{i=1}^N (ta_{i,CWS} - ta_{i,PRWS})^2}$$

Centred root-mean-square deviation cRMSD (Taylor 2001):

$$cRMSD = \sqrt{\frac{1}{N} \sum_{i=1}^N \left[ \left( ta_{i,CWS} - \overline{ta}_{CWS} \right) - \left( ta_{i,PRWS} - \overline{ta}_{PRWS} \right) \right]^2}$$

where  $\overline{ta}_{CWS}$  and  $\overline{ta}_{PRWS}$  are temporal mean *ta* across the whole investigation period at CWS and PRWS, respectively.

For comparisons when these statistical metrics were calculated per PRWS (e.g., Table 3), all CWS within a 2000 m radius around each PRWS, belonging to the same LCZ as the PRWS (cf. *Classification of Stations to Local Climate Zones* section), where firstly identified (Amsterdam: 200 CWS from 531 in the original data retained, Toulouse: 497 CWS from originally 1,354). Secondly, the metrics were calculated for each of these CWS-PRWS pairs and then averaged per PRWS. Lastly, the metrics were averaged across all PRWS for city-scale results. This approach was chosen in order to have an as direct as possible comparison between the two types of networks, even though a large percentage of CWS was omitted. If the statistical metrics were calculated on the network basis, i.e., averaging *ta* per network first and then calculating the metrics, overall lower deviations were obtained (not shown).

## DESCRIPTION OF CROWDQC+

CrowdQC+ is an improved version of the existing CrowdQC R package (Grassmann et al., 2018; Napolé et al., 2018), implementing several additional or modified functionalities. In

the following, all available functions are briefly described. Focus is given to the additions and modifications of CrowdQC+. Table 2 provides an overview of the QC levels and additional functions that are available.

As in CrowdQC, a data table with CWS data and meta data is used as input in CrowdQC+. Each QC level adds an additional column to the data table with boolean flag values TRUE (QC level passed) and FALSE (QC level failed). Only values flagged TRUE in the previous QC level are used in the subsequent level.

## Main Quality-Control Levels

### m1–Metadata Check

In QC level m1, function *cqcpc\_m1* performs a metadata check based on available latitude and longitude values and removes stations with identical values (similar also to filter A0 in Meier et al., 2017). This function is unchanged compared to CrowdQC and primarily targets CWS that were faultily installed by the user with automatic assignment of geographic coordinates based on the IP address of the user's internet connection. This error is a common feature in data sets of Netatmo CWS.

### m2–Distribution Check

In main QC level m2 the distribution of *ta* at each time step for the whole ROI is checked and values that are statistical outliers at the lower and upper ends of the distribution are removed. Respective cut-off values can be specified by the user. This QC level primarily targets radiative errors that lead to unrealistically high *ta* values, and errors due to CWS installed indoors, showing, e.g., lower *ta* during daytime than CWS installed outdoors. A height correction, i.e., lapse-rate adjustment of *ta*, can be applied (default: TRUE) to account for elevation differences in the data set. Compared to CrowdQC, where only the environmental lapse rate could be applied, *cqcpc\_m2* now provides the option to the user to specify any lapse rate in the height correction. Then, a normal distribution is assumed in QC level m2 to calculate critical values for flagging outliers at the lower and upper ends of the distribution at each time step. Yet, if the available number of stations is low (<100, value discussed in *Effect of Different Distribution Functions in m2* section), the assumption of normal distribution may no longer hold. In such a case, critical values can be more robustly calculated assuming a Student-t distribution (Gosset, 1908). This functionality (parameter "t\_distribution") was added in CrowdQC+.

### m3–Data Validity

Main QC level m3 checks each station for the amount of values that were flagged FALSE in QC level m2. If too many values (default: 20%) are flagged FALSE in a certain period of time, it is assumed that this station is to erroneous to be kept. In CrowdQC this period of time was fixed to monthly episodes. In CrowdQC+, *cqcpc\_m3* offers the possibility to specify any period of time ("duration") for this check. The user can also choose to use the complete data set ("complete = TRUE").

### m4–Temporal Correlation

In QC level m4, a temporal correlation between each station and the median of all stations is carried out for a specified period of

**TABLE 2** | Overview of the quality control QC levels and additional functions available in CrowdQC+. Italic lines mark functions that were modified regarding their functionality compared to the original CrowdQC, bold lines mark functions that were added in CrowdQC+.

Level	Details	Modification to CrowdQC	Comment	Default values
Main QC levels				
m1	Lat/Lon check			
m2	Distribution check	Student-t distribution possible, other lapse rate possible		cutOff = 1 low = 0.01, high = 0.95, heightCorrection = T, lapse_rate = 0.0065, t_distribution = F
m3	Validity	Other time span possible		
m4	Temporal correlation	Other time span possible		
<b>m5</b>	<b>Spatial buddy check</b>	<b>New</b>	<b>With(-out) height correction, with(-out) elevation check, removing/keeping isolated stations</b>	<b>radius = 3000, n_buddies = 5, alpha = 0.1, heightCorrection = T, lapse_rate = 0.0065, check_elevation = T, max_elev_diff = 100, keep_isolated = FALSE</b>
Optional QC levels				
o1	Interpolation			maxLength = 1
o2	Daily validity			cutOff = 0.8
o3	Duration validity	Other time span possible		cutOff = 0.8, monthly basis
<b>o4</b>	<b>Sensor lag</b>	<b>New</b>	<b>Known sensor lag</b>	<b>no default</b>
Additional functions				
	<b>Input check</b>	<b>New</b>	<b>Tests for column names, temporal coverage, data regularity, geographical extent, number of stations</b>	
	<b>Padding</b>	<b>New</b>	<b>Make regular and complete for each station</b>	
	<b>Add digital elevation model</b>	<b>New</b>	<b>Automatic download of elevation data possible</b>	
	<b>height</b>			
	<b>Output statistics</b>	<b>New</b>	<b>Data availability after each QC level</b>	

time. As in QC level m3, this was formerly set to correlations per month. In *cqcp\_m4*, analogously to *cqcp\_m3*, any period of time can be specified or the complete data set can be used (default: month). If the complete data set or the specified duration is short (sample size <100) considering the temporal resolution of the data set, the correlation is still calculated, yet a warning is given. This QC level primarily targets CWS that are set up indoors and thus show a weak temporal correlation with the median of all CWS, which are assumed to be installed outdoors.

### m5—Spatial Buddy Check

This new main QC level m5 performs a spatial buddy check, i.e., an outlier detection within the neighbourhood of a station. Analogously to QC level m2, it is assumed that a (large) number of individual observations contain robust information, justifying that individual stations can be flagged as erroneous when deviating too much from spatially adjacent stations. This QC level aims at identifying faulty values that remained after all previous QC steps, primarily single unrealistically high values due to radiative errors. The QC level is comparable to the spatial buddy check implemented in the TITAN package (Båserud et al., 2020). There, mean and standard deviation are calculated across the buddies to then identify statistical outliers. For CrowdQC+, it was decided to apply the same robust statistics in the buddy check as in QC level m2, i.e., median and Q<sub>n</sub> estimator (Rousseeuw and Croux, 1993), the latter being an efficient alternative of the

median absolute deviation, instead of the arithmetic mean and standard deviation. CWS data sets typically contain outliers that could affect these statistics, while median and Q<sub>n</sub>/median absolute deviation are less influenced by them.

In *cqcp\_m5*, the spatial neighbours, i.e., buddies, of each station are first identified within a given radius (default: 3000 m). If a sufficiently large number of neighbours with valid data are available (default: five), median and Q<sub>n</sub> are calculated per time step, excluding the station that is checked. Then, comparable to the check in *cqcp\_m2* (see Napoly et al., 2018 for the detailed description), a z-score Z is calculated as

$$Z = \frac{|ta_{i,j} - \text{median}(ta_{i,\text{buddies}})|}{Q_n(ta_{i,\text{buddies}})}$$

where *ta<sub>i,j</sub>* is the *ta* value at time *i* and station *j*, and *ta<sub>i,buddies</sub>* are the *ta* values of the buddies at time *i*. Based on the Student-t distribution and a specified significance level *a* (default: 0.1), critical cut-off values (two-tailed approach, default: *a* = 0.1, which translates to probabilities of 0.05 and 0.95 at the lower and upper tail of the distribution, respectively) are calculated per station and time step. All values for which *Z* < cut-off and for which the number of buddies is sufficiently high are flagged as TRUE, otherwise FALSE. Additionally, a second column “isolated” is added to the data table, indicating whether (flag “isolated” = FALSE) or not (flag “isolated” = TRUE) enough buddies are present for each station.

In order to avoid the influence of vertical temperature gradients in this check, the data can be corrected for height differences using a lapse-rate adjustment, as in *cqcp\_m2* (default: TRUE). This is done prior to the statistical calculations detailed above. Additionally, and independently from the height correction, the user can specify that only stations within the radius are considered, if their elevation does differ too much from the elevation of the station that is checked (default: 100 m elevation difference).

Since at least the specified number of buddies/valid observations has to be present within the given radius, QC level m5 also flags isolated stations (flag “m5” = FALSE). While this will lead to the exclusion of stations and negatively affect spatial coverage, it provides greater trust in the overall quality-controlled data set, since data from individual CWS are doubtful in absence of comprehensive metadata (Fenner et al., 2017; Napoly et al., 2018). Nonetheless, for certain applications or especially where network density is low, it might be desirable to keep these isolated stations, which an optional parameter allows (“*keep\_isolated* = TRUE”).

By setting the minimum number of buddies to a low number or specifying a large radius, the user has the possibility to adjust this to the region under investigation, depending on, e.g., network density.

## Optional Quality-Control Levels

After the main QC levels, four optional levels are included in CrowdQC+. Altogether, they aim at further improving data quality, yet are not considered essential. The benefits of these levels depend on the specific application.

### **o1–Temporal Interpolation**

In optional QC level o1, function *cqcp\_o1* carries out a temporal linear interpolation for missing values between the two closest valid values in a time series. This function is unchanged compared to CrowdQC and aims at increasing data availability by having as continuous time series as possible.

### **o2–Daily Validity**

For robust calculation of daily values, function *cqcp\_o2* checks if a predefined fraction (default: 0.8) of valid values is available at each station on each calendar day. Again, this QC level is unchanged compared to CrowdQC.

### **o3–Validity in Time Period**

Optional QC level o3 was modified compared to CrowdQC to handle other time spans than full months, to be consistent with the main QC levels m3 and m4. Function *cqcp\_o3* checks if a predefined fraction (default: 0.8) of valid values is available at each station during the specified duration.

### **o4–Correction for Time Constant**

The optional QC level o4 was introduced in CrowdQC+ in order to correct values for a known time constant  $\tau$  of the sensor at each station.  $\tau$  is typically defined as the time that a sensor needs to respond to approximately 63% of a step change in conditions (here: *ta*). Typical high-quality sensors deployed in

meteorological measurement networks have  $\tau$  values of a few seconds. However, CWS might suffer from design flaws, leading to a slow response time of the sensor (Bell et al., 2015). Netatmo sensors, e.g., have a slow thermal response due to their compact form and cylindrical enclosure, as noted by previous works (Meier et al., 2017; Büchau 2018).

In function *cqcp\_o4*, a time-constant corrected air temperature *ta\_corr* is calculated (similar to Miloshevich et al., 2004 for humidity):

$$ta_{corr_i} = \frac{ta_i - \left( ta_{i-1} * e^{-(t_i - t_{i-1})/\tau} \right)}{1 - e^{-(t_i - t_{i-1})/\tau}}$$

where *ta<sub>i</sub>* is the *ta* value at time *t<sub>i</sub>*, *ta<sub>i-1</sub>* the *ta* value at the previous time step *t<sub>i-1</sub>*, *e* Euler’s number, and  $\tau$  the time constant.

In CrowdQC+ it is assumed that  $\tau$  is the same for all stations and that it is constant, regardless of weather conditions. In the correction itself, it is assumed that a step change in air temperature happens from one time step to the next. The correction is applied to the original values (“*ta*”) and not to the interpolated values obtained in QC level o1 (“*ta\_int*”). Hence, the correction can be applied after any QC level. Diverging from all other QC levels, no additional flag variable with TRUE/FALSE values is added to the data table during *cqcp\_o4*. The user can thus select the corrected values at any QC level. In addition, *cqcp\_o4* is not carried out with any default values, as the time constant is specific to each possible sensor type. CrowdQC+ is, however, not limited or specific to any type of station or sensor.

## Additional Functions

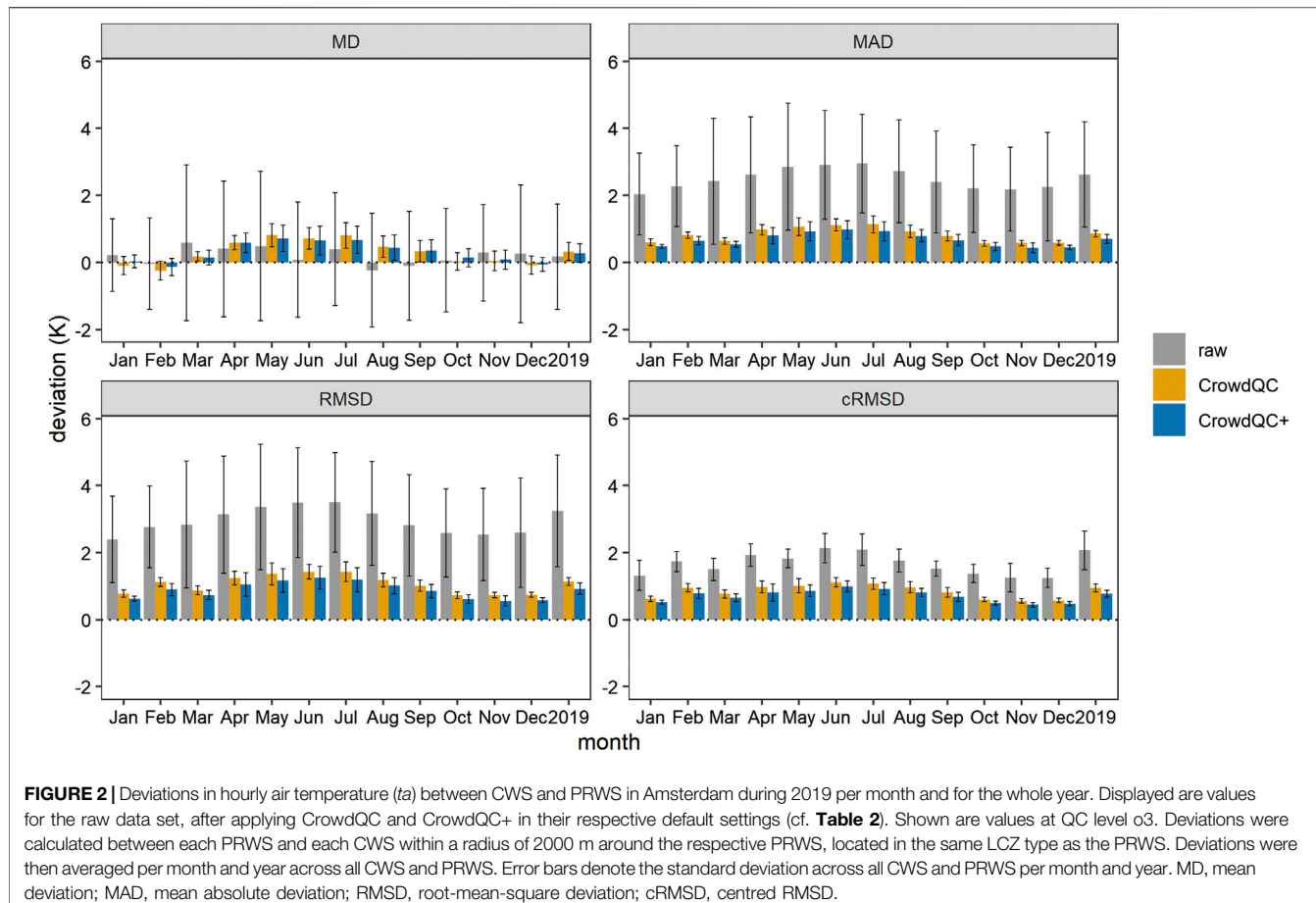
On top of the actual QC functions, four additional functions are implemented in CrowdQC+ to provide the user with support in preparing the input data for the QC and to obtain quick statistics on data availability at each QC level. These functions do not carry out actual QC of the data.

### **Input Check**

The *cqcp\_check\_input* function checks the input data table for compliance with CrowdQC+ and can be used before starting the actual QC functions. Five individual tests are performed to check that 1) all relevant columns (“*p\_id*”, “*time*”, “*ta*”, “*lon*”, “*lat*”) are present, 2) the temporal coverage of all stations is identical, 3) data for all stations are at the same temporal resolution and regular, 4) the geographical extent is not too large (<100 km×100 km), and 5) the absolute number of available stations is sufficiently high. The function prints information regarding these tests in the console or to an output file, or outputs the results of the tests as a list. The latter output is especially useful in automated workflows. The function further provides hints to the user to resolve errors in case some of the tests fail.

### **Padding**

The padding function *cqcp\_padding* makes sure that all stations cover the same period of time with the same temporal resolution



and is helpful in the preparation of the data for CrowdQC+. For a specified temporal resolution, data at each station is set to the nearest, next upper, or previous lower time step. If multiple values per time step are present, the mean is calculated across these. This function is especially useful if, e.g., the original station data have gaps, do not cover the same period of time, or have time stamps that are not regular.

### Adding Digital Elevation Model Height

If the user does not have elevation information at each station available but wants to apply the height correction of the measurement data in main QC levels m2 and m5, *cqcp\_add\_dem\_height* adds data from a digital elevation model (DEM) to each station. Any DEM data can be provided by the user via a RasterLayer object or a path to a GeoTIFF. If none of the two is given, SRTM data is downloaded automatically via the *getData* function from the *raster* package (Hijmans 2021). The downloaded data can be cropped to the extent of the CWS data and stored as a GeoTIFF. Note that SRTM data is only available between 60°N and 56°S. In case the region under investigation is located outside that range the user should make use of other available DEM data sets, e.g., the “Multi-Error-Removed Improved-Terrain DEM (MERIT DEM)” (Yamazaki et al., 2017).

### Output Statistics

After CrowdQC+ was carried out, *cqcp\_output\_statistics* provides basic statistics, i.e., the absolute number of valid observations, the percentage of valid observations compared to the raw data, and the number of unique stations with at least one valid observation after each QC level. The information is printed to the console or to an output file. This function is for illustrative purposes to the user to see, e.g., what effect the choice of a different threshold in one of the QC functions has on data availability.

## RESULTS AND ANALYSES OF NEW FUNCTIONALITIES

In this section, mainly the results for Amsterdam are shown as figures and tables. Similar figures and tables for Toulouse can be found in **Supplementary Material A** and will be referred to in the following sub-sections.

### Overall Performance and Comparison With CrowdQC

Comparing overall deviations between CWS and PRWS in Amsterdam, both QC packages show a strong improvement in all statistical metrics along the annual cycle compared to the raw

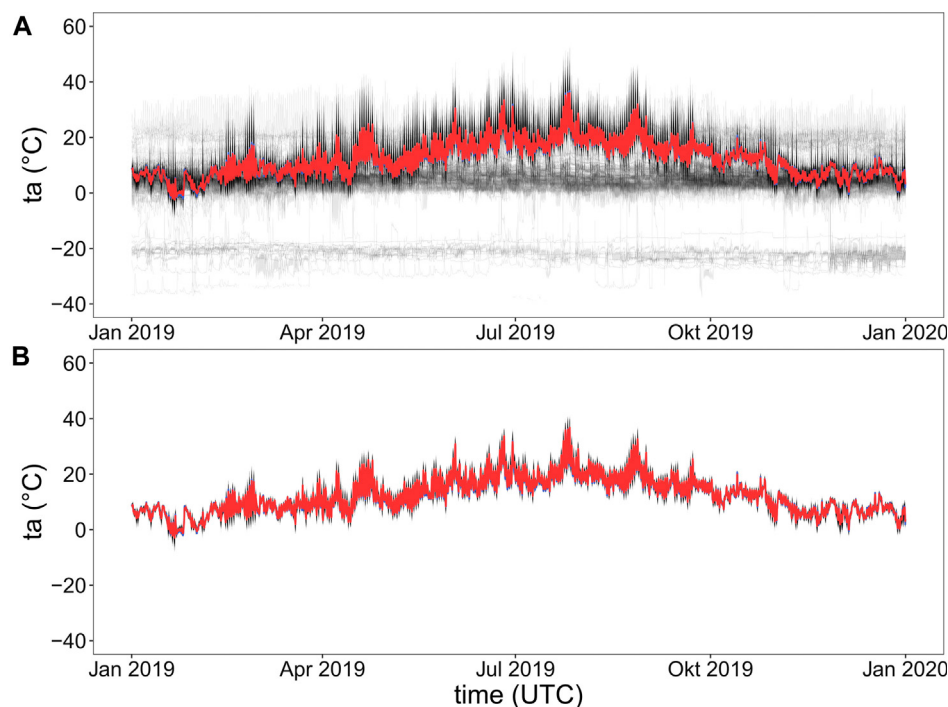


**FIGURE 3 |** Hourly air temperature ( $ta$ ) in Amsterdam during 2019. Each grey line corresponds to data from a single CWS, the red line displays the spatial median across all CWS, the blue line the median across all PRWS (barely visible as similar to red line). Sub-figure **(A)** shows raw CWS data, sub-figure **(B)** CWS data at QC level m5 of CrowdQC+ with default settings (cf. **Table 2**).

data, except for MD (**Figure 2**). MD is higher after applying the QC packages compared to the raw data. This is due to the fact that a large number of CWS in Amsterdam show values just above  $0^{\circ}\text{C}$  and around  $-20^{\circ}\text{C}$  (**Figure 3A**) at the raw data level. These stations are likely set up indoors in refrigerated warehouses or fridges, as they also display no distinct annual cycle but display relatively constant values. Similar features were noticed by Meier et al. (2017) for likely indoor stations in Berlin, which showed relatively constant values around  $20^{\circ}\text{C}$ . After applying the QC functions, both data sets are cleaned of these outliers by misplaced CWS (**Figure 3B, Supplementary Figure S2**).

Overall, positive deviations are visible in CWS  $ta$  compared to PRWS  $ta$  (**Figure 2, Supplementary Figure S1**), as noted in previous studies (e.g., Chapman et al., 2017; Meier et al., 2017; Napoly et al., 2018; Venter et al., 2021). Deviations are reduced after application of CrowdQC and CrowdQC+, with stronger reduction for Amsterdam than for Toulouse. Statistical metrics further show that while CrowdQC already provides a strong improvement compared to the raw data, CrowdQC+ provides further improvement with overall lower deviations than CrowdQC (**Figure 2, Supplementary Figure S1**). Improvements are stronger during the warmer months of the year for all metrics in Amsterdam and more variable for Toulouse (**Supplementary Figure S1**). Comparing both cities, Amsterdam shows generally lower deviations than Toulouse and displays a more distinct annual cycle with higher deviations during summer compared to winter months (**Figure 2**).

The overall better performance of CrowdQC+ is, however, accompanied with lower data availability after QC (**Table 3**). QC level m1 already reduced data availability by 30% and removed 163 CWS for Amsterdam. The high percentage of invalid values at QC level m1 is specific to the Amsterdam CWS data set and much higher than for Toulouse (**Table 3**) and what was found for Berlin, Germany (Meier et al., 2017; Napoly et al., 2018). In fact, most of these removed CWS in Amsterdam with invalid latitude and longitude values as defined by QC level m1 show no distinct annual cycle in  $ta$  (not shown) and are thus likely set up indoors. QC filters m2 and m5 (CrowdQC+) further reduced data availability by approximately 10% in both cities. Due to the reduction in data availability in QC level m5, roughly 20% of the raw CWS data at nearly 200 CWS are retained after QC level o3 with CrowdQC+ in Amsterdam, compared to 41% from 281 CWS with CrowdQC (**Table 3**). For Toulouse, the difference in data availability after QC level o3 between CrowdQC and CrowdQC+ is similar, with approximately 55% and nearly 30%, respectively.

**Figure 4** shows mean  $ta$  differences between CWS and PRWS along annual and diurnal cycles in 2019 with the stations grouped by LCZ type. Across all LCZ a distinctive pattern is visible, which is related to the diurnal cycles of  $ta$  and incoming shortwave radiation. Higher differences are generally found after midday during the months April to September with highest differences in the late afternoon in summer, while for other times differences are generally lower and consistent. The CWS data set is thus likely still influenced by radiative errors induced by the design of the

**TABLE 3** | Percentage of CWS hourly data availability and number of available CWS (given in brackets) at each QC level in Amsterdam (2019) and Toulouse (2020) after application of CrowdQC and CrowdQC+ in their respective default settings (cf. **Table 2**). Values for CrowdQC+ for QC levels m5 to o3 are given with isolated stations in QC level m5 removed (first values per field) and retained (second values per field, italic).

QC level	Amsterdam		Toulouse	
	CrowdQC	CrowdQC+	CrowdQC	CrowdQC+
raw	100.0 [531]		100.0 [1354]	
m1	69.4 [368]		92.0 [1214]	
m2	59.9 [362]		82.5 [1214]	
m3	59.4 [354]		82.2 [1185]	
m4	58.2 [332]		81.4 [1170]	
m5		47.1 [324]/48.9 [332]		69.2 [1146]/ 70.6 [1163]
o1	58.5 [332]	47.8 [324]/49.6 [332]	81.8 [1170]	70.2 [1146]/ 71.5 [1163]
o2	53.0 [331]	36.9 [323]/38.5 [331]	72.4 [1165]	52.6 [1123]/ 53.8 [1140]
o3	41.0 [281]	20.7 [197]/22.1 [205]	54.9 [971]	29.5 [700]/ 30.5 [715]

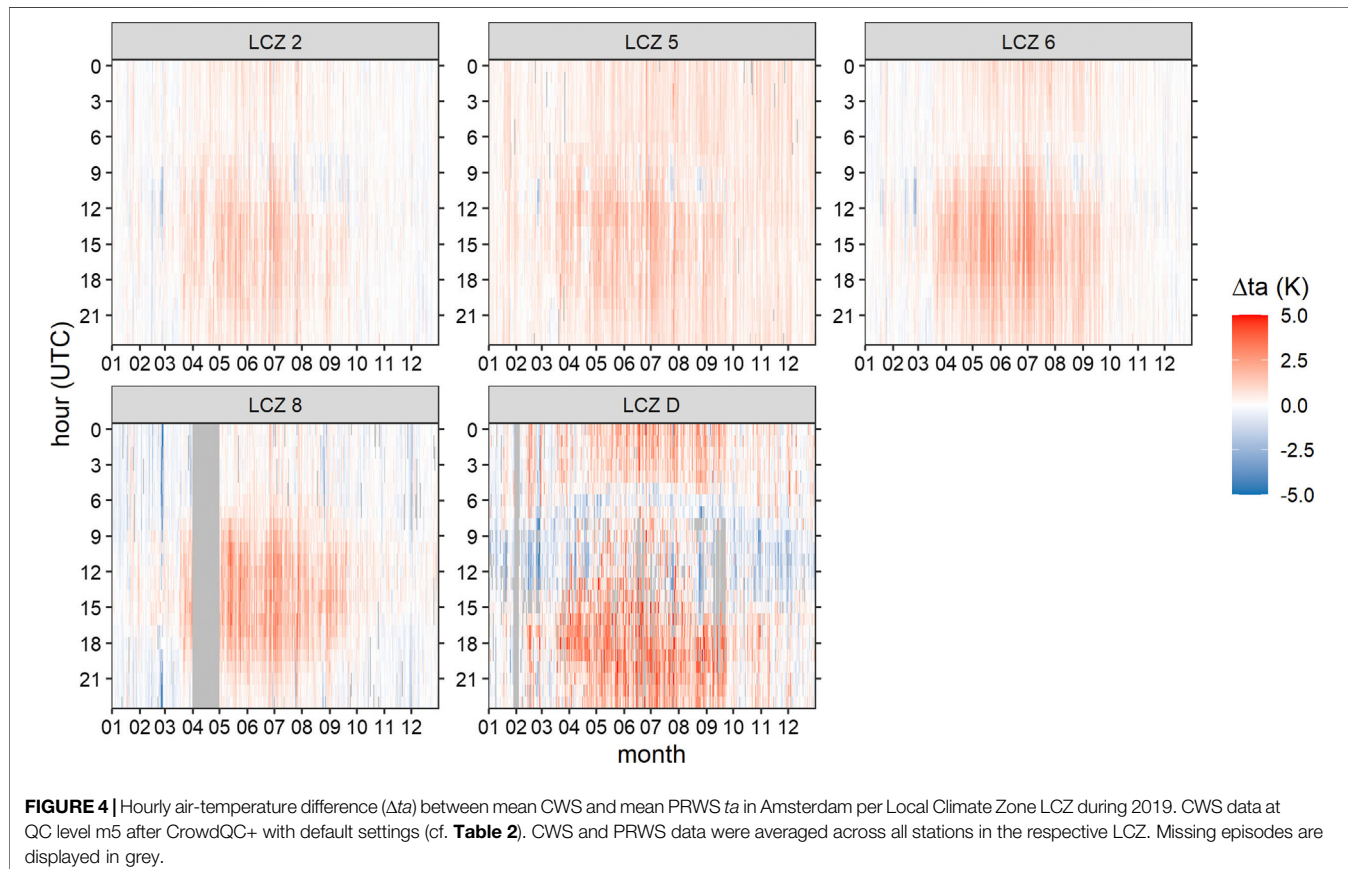


**FIGURE 4** | Hourly air-temperature difference ( $\Delta t_a$ ) between mean CWS and mean PRWS  $t_a$  in Amsterdam per Local Climate Zone LCZ during 2019. CWS data at QC level m5 after CrowdQC+ with default settings (cf. **Table 2**). CWS and PRWS data were averaged across all stations in the respective LCZ. Missing episodes are displayed in grey.

Netatmo CWS without a proper radiation shield and the setup of CWS in unshaded locations, leading to these higher differences. This might impair analyses of daytime  $t_a$  conditions in cities when absolute values are of relevance, yet might be of lower relevance when calculating spatial differences among (groups of) CWS, as in, e.g., UHI analyses. Night-time differences are lower and consistent both in time (along annual cycle) and space (across LCZ types), underlining the high applicability of Netatmo CWS in urban climate investigations that focus on night-time. Other types of CWS might be less influenced by

radiative errors during daytime due to a better design with lamella-type radiation shields and would thus allow for more reliable daytime analyses. Yet, they might show other deficiencies such as a systematic bias or a sensor drift over time, which have not been observed for Netatmo CWS (Meier et al., 2017; Fenner 2020).

LCZ D displays a different pattern with higher deviations during night-time and late afternoon and negative differences during winter, spring, and autumn months during daytime (**Figure 4**). This pattern resembles typical urban heat island

characteristics along annual and diurnal cycles (compare, e.g., Fenner et al., 2014; Skarbit et al., 2017). This could indicate that the CWS in LCZ D in Amsterdam contain an “urban” signal in their *ta* data (due to a set up close to buildings, compared to the PRWS in LCZ D, Schiphol airport. Note though that this PRWS is likely also not completely uninfluenced by man-made surfaces, considering its setup on the airport ground between runways. Another possible reason for this pattern could be related to advective effects. While Schiphol airport is located upwind of Amsterdam (most south-western PRWS in **Figure 1A**, main wind direction along the annual cycle south-west, not shown), most CWS located in LCZ D are located downwind of built-up areas. Advection of warm air from cities to the surroundings has been reported by observational (e.g., Brandsma et al., 2003; Bassett et al., 2016, 2017) and modelling studies (e.g., Zhang et al., 2012; Heaviside et al., 2015; Bassett et al., 2019).

For Toulouse, mean *ta* differences between CWS and PRWS along annual and diurnal cycles in 2020 per LCZ type show a different pattern with higher positive deviations during night-time and generally near-zero to negative deviations during daytime (**Supplementary Figure S3**). To understand these differences, it needs noting that there is a systematic difference in the setup of stations between the CWS and the PRWS network. While CWS are likely located in all kinds of settings, ranging from setups close to building walls and within street canyons to more open settings in residential gardens, the majority of PRWS is located in open areas with little shade. This difference in the setup leads to two possible effects, likely both acting at the same time, which could explain the pattern found. Firstly, *ta* conditions are different at the sites. CWS located in street canyons and shaded environments experience less radiative heating of the air during daytime than open areas where the PRWS are set up and thus measure lower *ta*. During night-time, due to reduced sky view factors (SVF) at CWS sites compared to the more open PRWS sites, cooling of the air is hindered, leading to higher *ta*. This is similar to the first hypothesis brought forward above to explain the deviation for LCZ D in Amsterdam (**Figure 4**). Secondly, radiative errors contribute to the deviations. Even though the PRWS are of much higher quality than the CWS, especially regarding the station design (Netatmo CWS with aluminium shell around the sensor with little ventilation, Davis Vantage Pro with lamella-type radiation shield, naturally ventilated), the type of PRWS used is not free of radiative errors (Cernes et al., 2020). Comparing the radiation biases of two Davis Vantage Pro with natural ventilation, one in a rural setting with relatively unobstructed airflow and one in a more enclosed residential setting, Cernes et al. (2020) found that measurements at the site in the residential setting experienced radiative errors of >1 K during midday and the warmer months of the year, compared to ≤0.6 K at the rural site. It was suggested that this difference is due to increased airflow at the rural site that aided the ventilation of the radiation screen, reducing radiative errors.

Based on these results and since the majority of PRWS in Toulouse are located in urban, yet open settings with little shading, radiative errors can be expected. On the other hand, radiative errors in the CWS data set should largely be reduced by

the QC. Further, hypothesising that the majority of CWS is located in shaded environments, the network of quality-controlled CWS contains less radiative errors during daytime which could then, in the end, lead to the deviations that were found (**Supplementary Figure S3**). Positive deviations between CWS and PRWS *ta* for Toulouse during night-time might also be linked to differences in setup. At locations close to building walls, where CWS are typically installed, *ta* might be higher during night-time than further away from the wall, yet predominantly for walls that were exposed to solar radiation during the day (Nakamura and Oke 1988). The hypotheses brought forward require further systematic investigations, yet go beyond the scope of this study.

Note that all displayed deviations between CWS and PRWS are not all errors of the CWS data set with respect to the PRWS data. Firstly, variation in *ta* can be expected in the 2000 m radius around each PRWS (used in the calculations of the deviations), even if located in the same LCZ type as the PRWS. Secondly, deviations in *ta* are likely due to differences in the setup of stations. CWS are typically installed closer to buildings than PRWS, leading to differences in exposure and micro-scale settings at each site, which affect *ta* (Chapman et al., 2017; Fenner et al., 2017).

## Effect of Different Durations

In QC levels m3, m4, and o3 different durations can be defined in the filter applications. To investigate their influence on overall *ta* deviations, six experiments were run, applying durations from 3 days to the complete data set (1 year) (**Table 4, Supplementary Table S1**). Overall, differences in deviations between the experiments are small, indicating a robust behaviour of the QC regarding this parameter. When looking at the best results per metric and variable (bold numbers in **Table 4** and **Supplementary Table S1**), choosing the complete data set shows generally best performance. However, using the complete data set at QC level o3 for a 1-year data set reduces final data availability to about 13% of hourly data (compared to the raw data) from 58 CWS in Amsterdam and to nearly 15% from 157 CWS in Toulouse. This is mainly due to QC level o3, checking for data availability per station for the specified duration and flagging a complete station with FALSE in case of not enough valid values (default: fraction of 0.8, i.e., 80% data availability). With marginally higher deviations, but retaining a much higher fraction of data after QC, the use of a shorter duration could be advisable (**Table 4, Supplementary Table S1**). Based on the obtained results, we recommend to use a duration between 7 days and 1 month. Shorter durations, one the one hand, lead to less robust correlations in QC level m4 with hourly data (sample size at best 72), leading to overall higher deviations. Longer deviations, on the other hand, lead to much more data being excluded, with only a marginal benefit in terms of deviations to PRWS data.

Setting parameter “*complete = TRUE*” is especially useful in cases when only a shorter period of time is under investigation. Further, it could be useful in near-real time applications, when data shall be quality-controlled and used in operational weather monitoring. In such a case, the user could provide data for the past, e.g., 14 days to the QC and use this complete data set for the QC.

**TABLE 4** | Mean annual deviations in hourly air temperature (*ta*) and in aggregated daily values of mean (*ta\_mean*), maximum (*ta\_max*), and minimum (*ta\_min*) between CWS and PRWS in Amsterdam, and remaining data availability during 2019 after applying CrowdQC+ in its default setting (cf. **Table 2**). Displayed are values at QC level o3 with different “durations” (in QC levels m3, m4, o3). Bold values mark best results per metric and variable, italic values second best. Deviations were calculated between each PRWS and each CWS within a radius of 2000 m around the respective PRWS, located in the same LCZ type as the PRWS. Deviations were then averaged across all CWS and PRWS. MD, mean deviation; MAD, mean absolute deviation; RMSD, root-mean-square deviation; cRMSD, centred RMSD.

Metric	Variable	3 days	7 days	14 days	21 days	1 month	Complete
MD (K)	<i>ta</i>	0.32	<b>0.27</b>	0.28	0.29	0.28	0.32
	<i>ta_mean</i>	0.30	<b>0.25</b>	0.27	0.27	0.26	0.31
	<i>ta_max</i>	0.50	0.45	0.46	0.48	<b>0.44</b>	0.48
	<i>ta_min</i>	0.33	<b>0.30</b>	0.35	0.33	0.32	<b>0.30</b>
MAD (K)	<i>ta</i>	0.76	0.70	0.69	0.70	0.70	<b>0.64</b>
	<i>ta_mean</i>	0.61	0.56	0.55	0.55	0.55	<b>0.52</b>
	<i>ta_max</i>	0.93	0.88	0.88	0.90	0.87	<b>0.82</b>
	<i>ta_min</i>	0.77	0.69	0.70	0.68	0.69	<b>0.58</b>
RMSD (K)	<i>ta</i>	1.01	0.92	0.91	0.92	0.92	<b>0.87</b>
	<i>ta_mean</i>	0.75	0.68	0.68	0.67	0.67	<b>0.65</b>
	<i>ta_max</i>	1.20	1.14	1.14	1.15	1.13	<b>1.11</b>
	<i>ta_min</i>	0.93	0.83	0.84	0.83	0.83	<b>0.72</b>
cRMSD (K)	<i>ta</i>	0.83	0.77	0.77	0.77	0.77	<b>0.75</b>
	<i>ta_mean</i>	0.52	0.49	0.48	<b>0.47</b>	0.48	0.50
	<i>ta_max</i>	0.95	0.91	0.90	<b>0.89</b>	0.90	0.93
	<i>ta_min</i>	0.58	0.54	0.53	0.54	0.55	<b>0.51</b>
Data availability	% of raw data	26.7	24.9	23.0	22.0	20.7	13.1
	No. of CWS	303	268	244	227	197	58

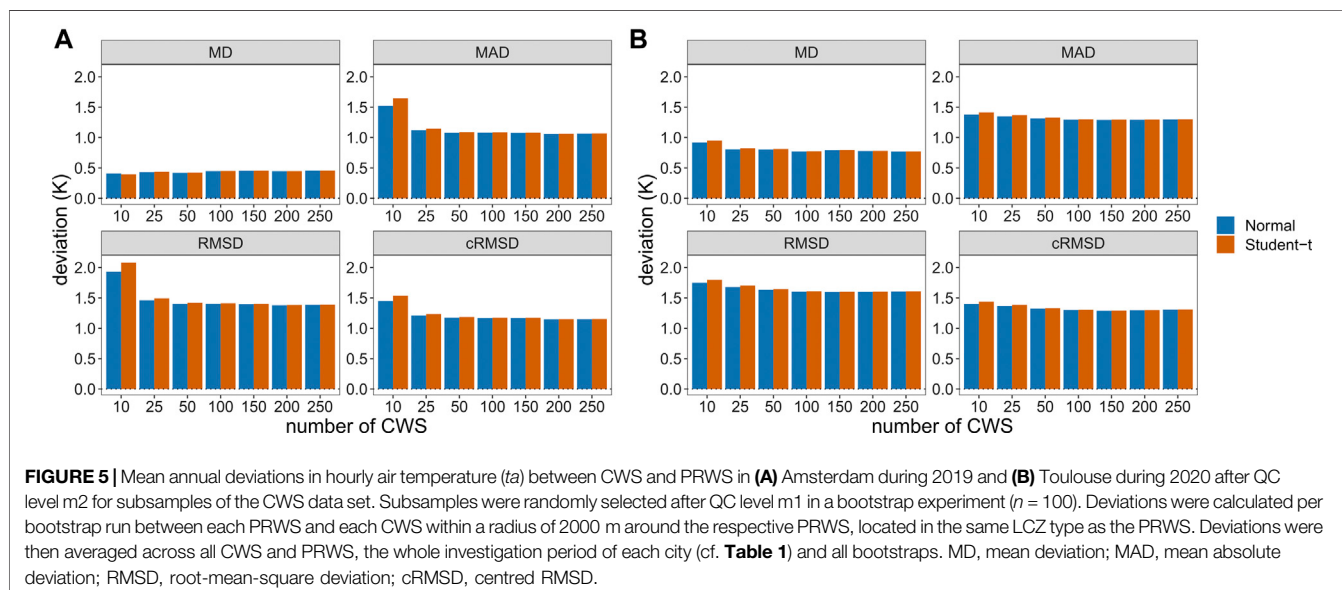


**FIGURE 5** | Mean annual deviations in hourly air temperature (*ta*) between CWS and PRWS in **(A)** Amsterdam during 2019 and **(B)** Toulouse during 2020 after QC level m2 for subsamples of the CWS data set. Subsamples were randomly selected after QC level m1 in a bootstrap experiment ( $n = 100$ ). Deviations were calculated per bootstrap run between each PRWS and each CWS within a radius of 2000 m around the respective PRWS, located in the same LCZ type as the PRWS. Deviations were then averaged across all CWS and PRWS, the whole investigation period of each city (cf. **Table 1**) and all bootstraps. MD, mean deviation; MAD, mean absolute deviation; RMSD, root-mean-square deviation; cRMSD, centred RMSD.

## Effect of Different Distribution Functions in m2

To test the effect of using the normal distribution or the Student-t distribution when calculating the critical cut-off values in QC level m2, the following experiment was run. After applying QC level m1 and removing all CWS that only provide invalid data after this QC level for each city’s investigation period, a bootstrap approach was chosen to randomly select a subsample of a specified number of CWS from each city’s data set. Then, QC level m2 was carried out, once assuming the normal distribution (parameter “*t\_distribution = FALSE*,” default in *cqcp\_m2*) and

once assuming the Student-t distribution (parameter “*t\_distribution = TRUE*”). Afterwards, deviations between CWS and PRWS at QC level m2 were calculated for both data sets for the whole investigation period as described at the end of *Statistics* section. Finally, deviations were averaged across the number of bootstraps ( $n = 100$ ). Seven subsample sizes were chosen in the experiment: 10, 25, 50, 100, 150, 200, and 250.

**Figure 5** displays the results of the experiment for both cities. Deviations are highest when ten CWS were randomly selected in the bootstrap runs in both cities. With a higher number of CWS, deviations are lower and relatively similar when comparing the

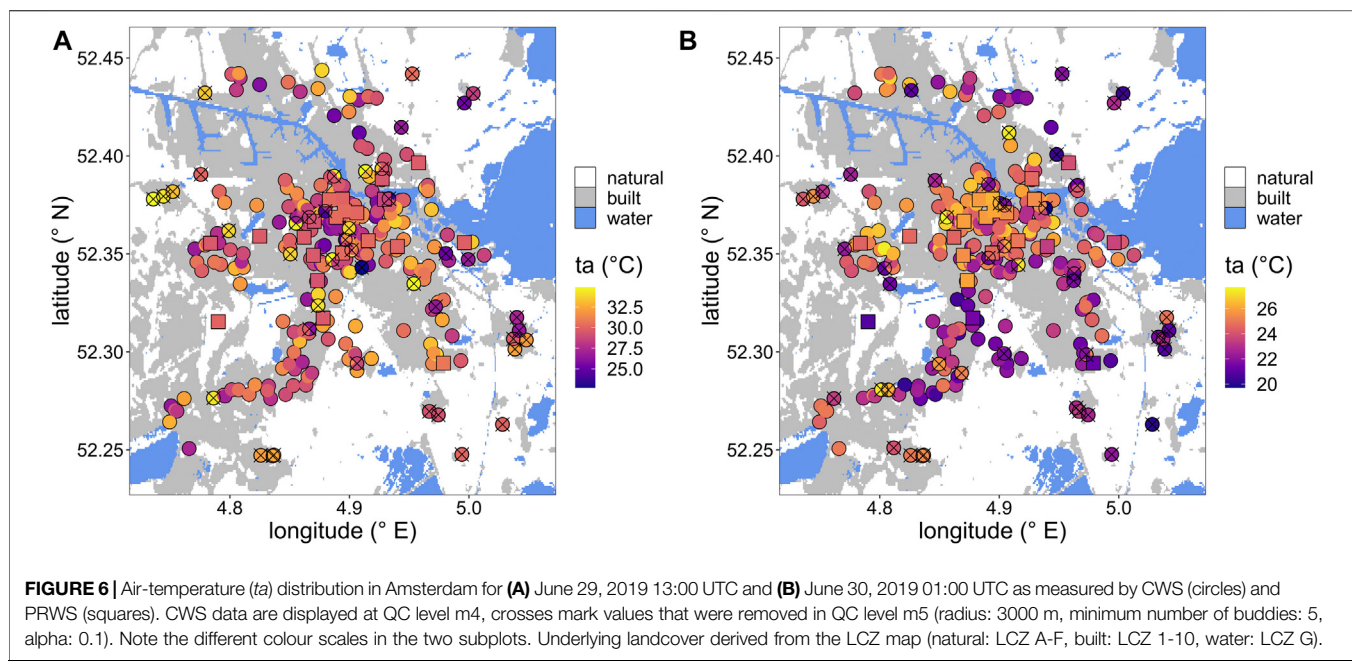


**FIGURE 6** | Air-temperature ( $ta$ ) distribution in Amsterdam for **(A)** June 29, 2019 13:00 UTC and **(B)** June 30, 2019 01:00 UTC as measured by CWS (circles) and PRWS (squares). CWS data are displayed at QC level m4, crosses mark values that were removed in QC level m5 (radius: 3000 m, minimum number of buddies: 5, alpha: 0.1). Note the different colour scales in the two subplots. Underlying landcover derived from the LCZ map (natural: LCZ A-F, built: LCZ 1-10, water: LCZ G).

sample sizes. For both distribution functions deviations are overall similar when  $\geq 100$  CWS were selected. Generally, deviations are lower for the assumption of a normal distribution. Differences in deviations between the two distributions are small but more distinct for a low number of CWS ( $\leq 50$  CWS, **Figure 5**).

These results firstly show the robustness of QC level m2 to the underlying assumption of distribution for a range of CWS sample sizes. Secondly, it shows that even for CWS networks with a relatively low number of stations per city such as 50–100 CWS, CrowdQC+ yields comparable deviations in the quality-controlled data set compared to networks with more CWS. This highlights the applicability of CrowdQC+ for cities with different CWS network sizes/densities. The fact that assuming a Student-t distribution for the calculation of cut-off values in QC level m2 leads to higher deviations, particularly for low number of CWS, can be explained by the fact that the Student-t distribution assumes heavier tails than the normal distribution. This leads to lower (higher) critical Z-scores for the lower (upper) tail of the distribution, which in turn leads to less values being excluded in QC level m2 when assuming a Student-t distribution.

Based on the results, we suggest to apply the Student-t distribution in QC level m2 if data sets of  $< 100$  stations are checked. Considering the statistical hypothesis behind this QC level, the use of the Student-t distribution leads to statistically more robust cut-off values. As a side effect, it will lead to less values being excluded from the already small data set.

## Buddy Check

To illustrate the effect of the buddy check in QC level m5, **Figure 6** and **Supplementary Figure S4** exemplarily display the  $ta$  distribution in Amsterdam and Toulouse, respectively, for a day- and night-time situation during a hot summer day. Both figures show that those values that deviate too much from

the stations in the immediate surroundings are identified and removed in QC level m5. Additionally, isolated sites are identified and removed, as their quality cannot be assessed due to the lack of available neighbours. In regions where the CWS data set is heterogeneous, the filter retains all values. Here, the  $ta$  distribution within the radius is wide and none of the values can be considered a statistical outlier.

In order to highlight the effect of QC level m5 for longer periods of time, **Figures 7, 8** display data for Amsterdam for the whole year 2019 (cf. **Supplementary Figures S5, S6** for Toulouse). **Figure 7** displays scatter plots between PRWS and CWS  $ta$  at levels m4 and m5. At the individual PRWS level (**Figures 7A,B**), as well as considering the whole network of stations (**Figures 7C,D**), deviations between PRWS and CWS are reduced in all four statistical metrics after QC level m5. Deviations after applying QC level m5 are especially lower for daily maximum  $ta$  (**Figure 7**), compared to daily mean, daily minimum, and hourly  $ta$  (all not shown). Hence, higher  $ta$  in CWS data during daytime, likely resulting from radiative errors, are now better filtered with the new spatial buddy check. Summarizing, using information from neighbouring CWS to filter likely faulty values in the whole data set is beneficial, also highlighted by others (e.g., de Vos et al., 2019; Båserud et al., 2020; Nipen et al., 2020; Chen et al., 2021).

**Figure 8** further highlights that the improvement in the statistical metrics is consistently found along the annual cycle, with strongest improvement in the warmer months of the year (April–August), when deviations are higher compared to the rest of the months. Overall, MD is approximately 1 K during summer and  $< 0.3$  K during winter at QC levels m4 and m5, being within the specified accuracy of the Netatmo sensor (Meier et al., 2017). For Toulouse, MD is relatively constant throughout the year and always  $< 1$  K (**Supplementary Figure S5**). MAD and RMSD are higher, yet  $\leq 1.5$  K after QC level m5

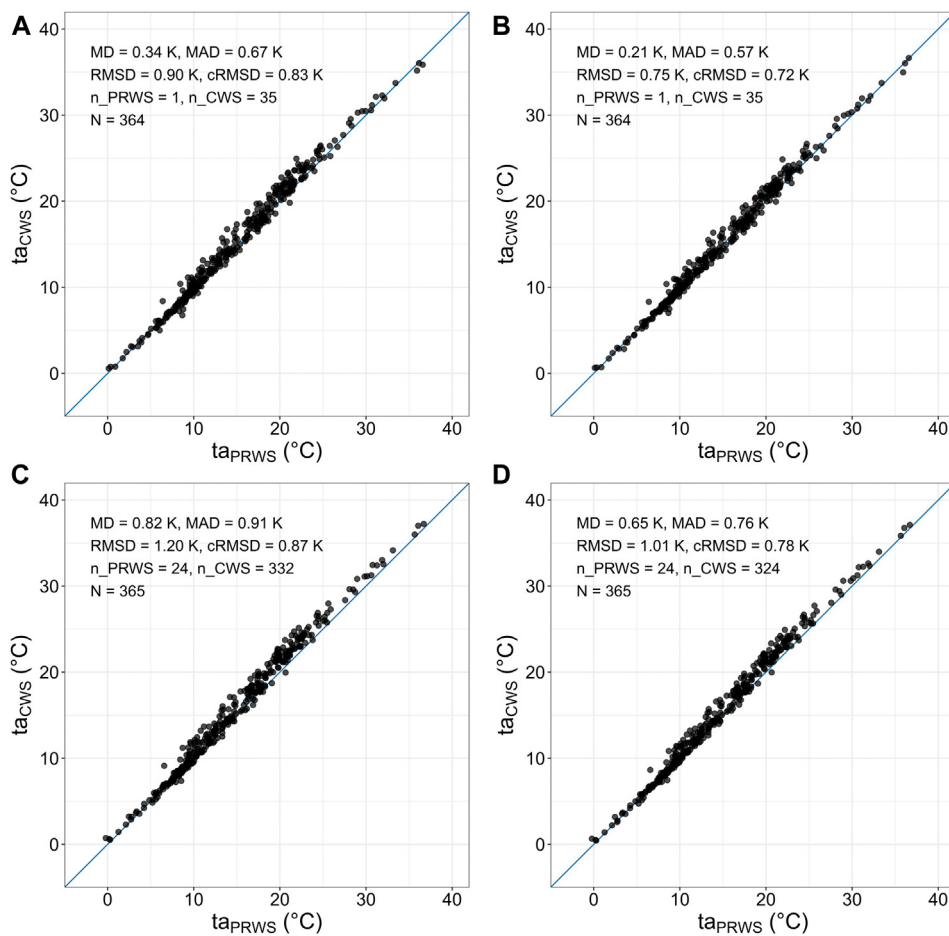


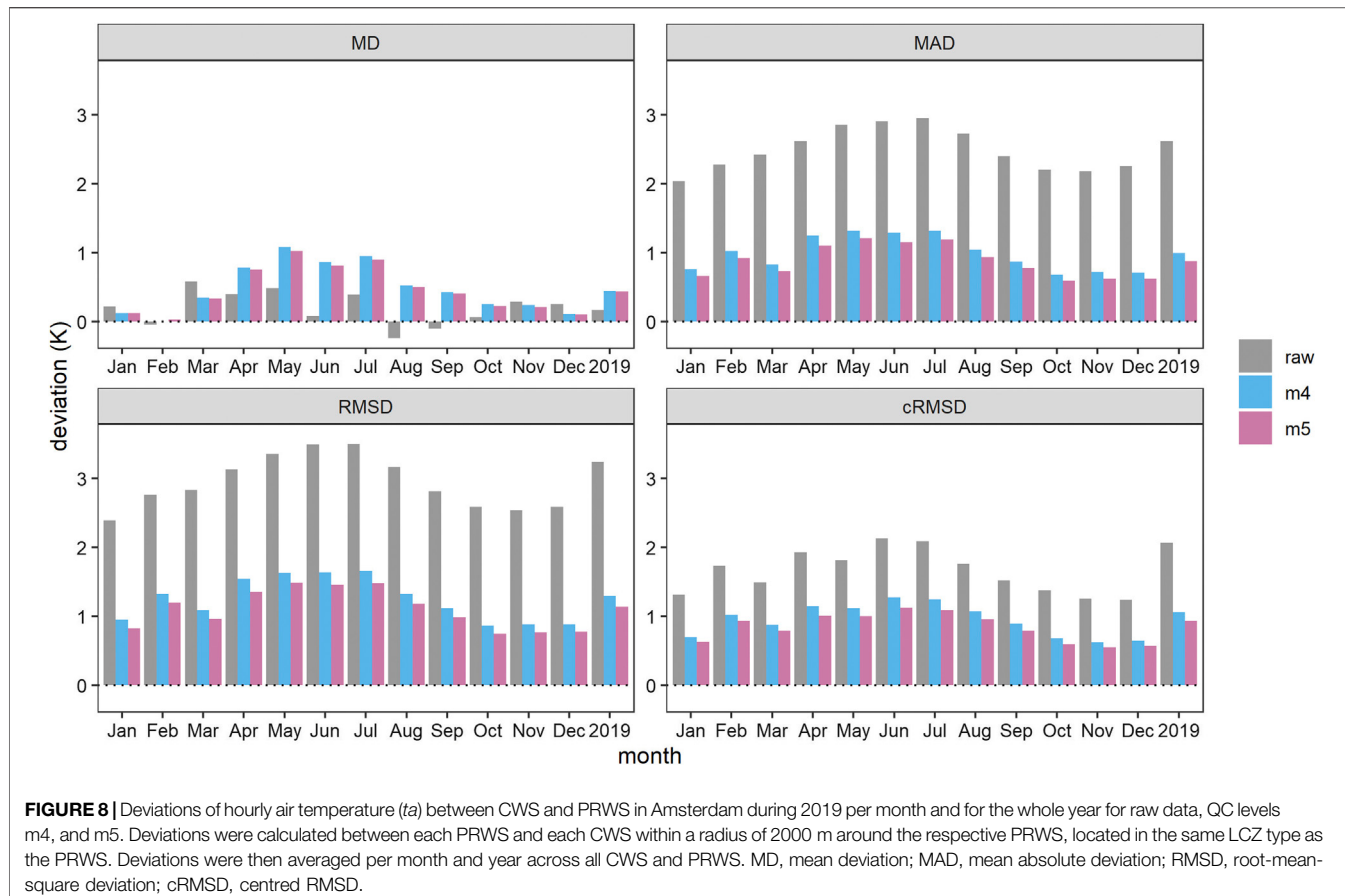
**FIGURE 7 |** Relation between daily maximum air temperature ( $ta$ ) at PRWS and CWS in Amsterdam during 2019. **(A)** and **(B)** for one PRWS (station “2229”; 52.3719°N, 4.89568°E) and the mean of all CWS within a 2000 m radius around the PRWS in the same LCZ type (2—compact midrise). **(C)** and **(D)** as the mean across all PRWS and all CWS. **(A)** and **(C)** display CWS  $ta$  at QC level m4, **(B)** and **(D)** CWS  $ta$  at QC level m5. MD, mean deviation; MAD, mean absolute deviation; RMSD, root-mean-square deviation; cRMSD, centred RMSD; n\_PRWS, number of PRWS; n\_CWS, number of CWS; N, number of daily values.

in all months. cRMSD shows that the unsystematic deviation between CWS and PRWS is between 0.6 and 1.3 K in the monthly means after QC level m5 in Amsterdam and Toulouse. Annual averages show that mean CWS  $ta$  data on a city scale is ~0.5 and ~0.8 K higher than PRWS data after the main QC levels for Amsterdam and Toulouse, respectively (Figure 8, Supplementary Figure S6).

In its current form, the buddy check neglects any spatial gradient in  $ta$  in its calculations. Within cities, horizontal gradients in  $ta$  might arise in particular from elevation differences among stations on mountain slopes or due to differences in land cover/land use. While the former is addressed in CrowdQC+ with the height correction being carried out, plus the additional check for elevation differences among buddies, the latter is difficult to implement without additional information on underlying surface characteristics. Here, the concept of LCZs might be a suitable candidate to characterise a station in terms of its local surroundings. Such an (optional) addition could be a further extension of CrowdQC+ in the future, yet requires in-depths investigations and might

impair subsequent LCZ-based analyses. Per default, a radius of 3000 m is used in QC level m5, which is based on tests for the two investigated cities (not shown) and similar to recommendations by Båserud et al. (2020). In cities with heterogeneous surface cover and morphology, a smaller radius might be more appropriate, as  $ta$  will hence be “patchier,” especially during dry, cloud-free, and calm conditions that promote spatial  $ta$  gradients (e.g., Parry 1956; Oke 1973; Erell and Williamson 2007; van Hove et al., 2015; Arnds et al., 2017; Fenner et al., 2017; Beck et al., 2018a). Analogously, for urban regions with extensive and homogeneous surface cover and morphology, a larger radius could be applied.

The buddy check is the computationally most expensive of the QC levels. For data sets from several hundred or few thousands of CWS and for extended periods of time such as a year (as in this study), this filter might take several minutes. For near-real time applications such as operational  $ta$  monitoring at (half-) hourly resolution this would not be an issue, if a data set of the past, e.g., 14 days is used to perform the complete QC. Further developments of CrowdQC+ will focus on the improvement of



this QC level in order to reduce the time spent to perform the buddy check.

### Time-Constant Correction

Büchau (2018) determined  $\tau$  of the Netatmo sensor (investigating in total seven Netatmo stations) by conducting cooldown and warmup tests in a laboratory environment. He determined a mean  $\tau$  across the sensors of 22.46 and 26.89 min for the two experiments, respectively (Figure 2.3 a and b in Büchau 2018). Based on these results, we apply a mean of these two values in the time-constant correction, using  $\tau = 1480.5$  s. The effect of the time-constant correction is illustrated in the following.

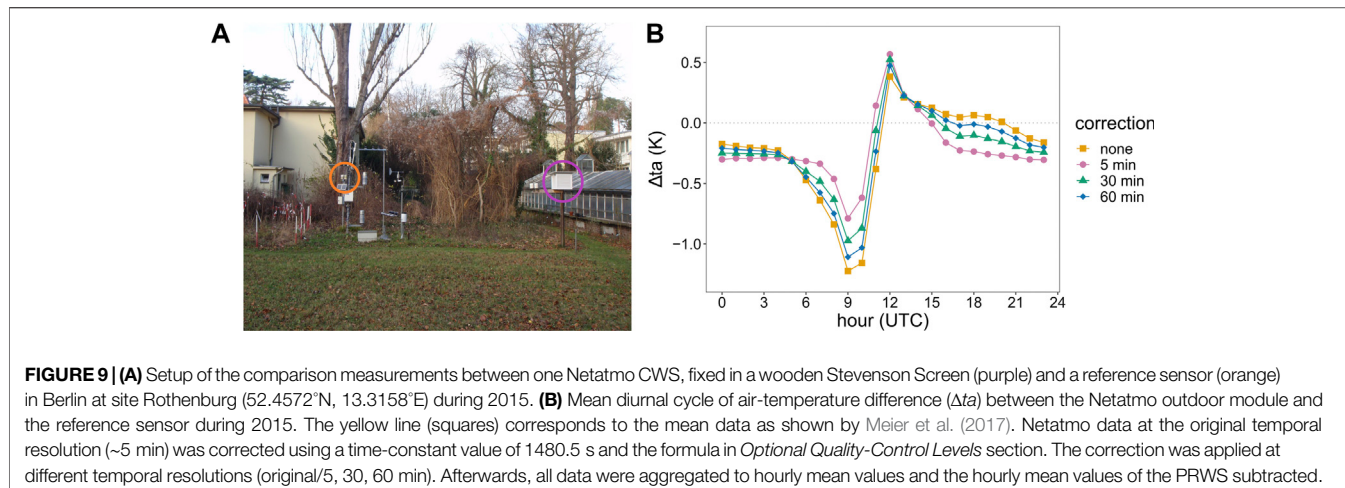
### Comparison Measurements With One Netatmo Sensor

Firstly, we investigate data from a 1-year long comparison measurement in Berlin in 2015 between one Netatmo sensor and a reference sensor (Campbell Scientific CS215, accuracy  $\pm 0.4$  K in range 5–40°C). Both sensors were set up at 2 m above ground level, the Netatmo sensor inside a wooden Stevenson Screen, the reference sensor inside a small lamella-type radiation shield, actively ventilated during sunlit periods (Figure 9A). Netatmo data was collected at the original 5-min resolution (approximately) from the user interface of Netatmo, reference data was sampled at 1-min resolution. This data set was previously used in the study by Meier et al. (2017). Figure 9B

shows a distinct diurnal cycle in the mean deviation between the two sensors. While in the morning hours after sunrise the Netatmo sensor displays lower mean values than the reference sensor, it shows higher values in the early afternoon.

Figure 9B further shows the benefit of applying the time-constant correction ( $\tau = 1480.5$  s) to the Netatmo data. If the correction is applied at the original temporal resolution of the Netatmo sensor, the correction reduces the mean hourly deviation in the morning hours by 0.5 K, yet increases the deviation at noon by 0.2 K. The correction further leads to a more “stable” deviation between the two sensors during afternoon and night-time hours at approximately –0.3 K, likely showing a systematic bias. The remaining stronger mean negative and positive deviations in the morning and at noon, respectively, are likely partly due to the slower thermal response of the Stevenson Screen (Bryant 1968; Brandsma and van der Meulen 2008; Harrison 2010) in which the Netatmo sensor was placed, compared to the small lamella-type radiation shield of the reference sensor (actively ventilated during sunlit times).

When using the Netatmo API, different temporal resolutions for obtaining the data can be specified, ranging from the original resolution at approximately 5 min, over 30 and 60 min to 3 h, 1 day, 1 week, or 1 month (<https://dev.netatmo.com/apidocumentation/weather#getmeasure>). Thus, Figure 9B also



displays the effect of the time-constant correction applied at 30- and 60-min data. For this, the original Netatmo data was aggregated to mean values for the respective temporal resolution prior to correction. With decreasing temporal resolution, the effect of the time-constant correction also decreases.

While for hourly resolution the time-constant correction provides only a marginal difference, it is worthwhile to apply in temporally higher-resolution data of the Netatmo sensor and likely also other sensors with similarly large time constants.

### Effects in City-Wide Data

Secondly, applying the time-constant correction to the hourly data set in Amsterdam and Toulouse, minor to no differences between the corrected and uncorrected data set with respect to the statistical metrics are found (**Supplementary Table S2**). For daily maximum  $ta$  the time-constant correction leads to higher deviations, while for daily minimum  $ta$  overall lower deviations are found. Statistical metrics for daily mean and hourly  $ta$  are not affected.

In its current form, QC level o4 assumes the same value for  $\tau$  for all CWS and hence only works meaningfully with one type of CWS in the data set. A possible future development of CrowdQC+ and improvement of this QC level could be to include information on the type of CWS, thus enabling the correction of different types of CWS with regard to sensor lag in the same data set.

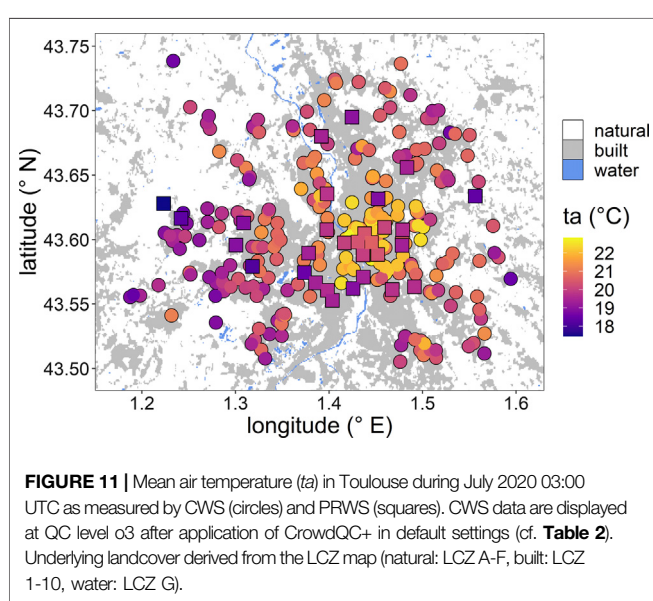
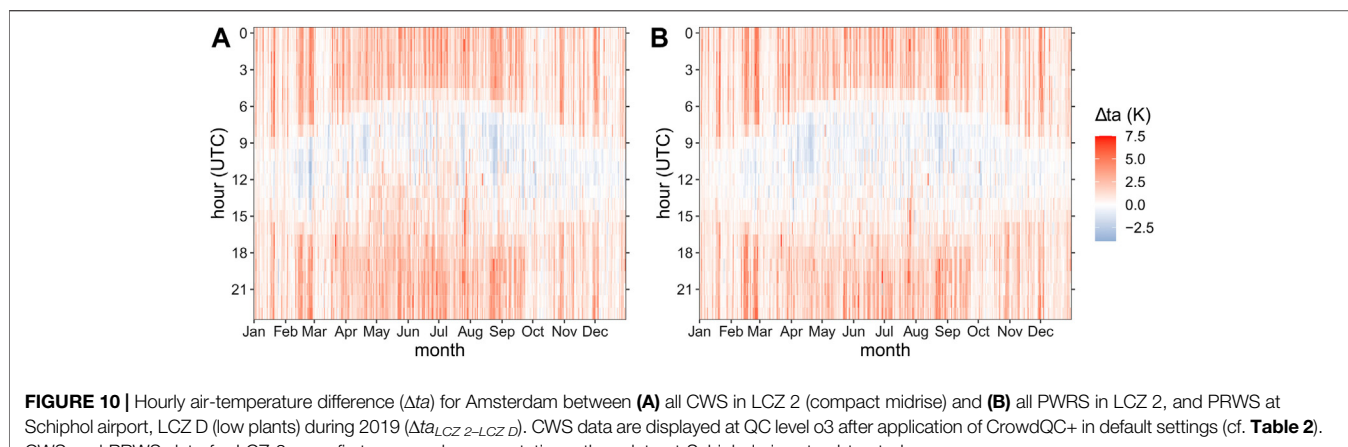
## APPLICATIONS OF THE QUALITY-CONTROLLED DATA

To highlight the usability of quality-controlled CWS data for urban climate studies, two applications are put forward.

In the first application, the annual and diurnal cycle in  $ta$  difference ( $\Delta ta$ ) between two LCZ types is displayed for Amsterdam, comparable to typical UHI analyses. **Figure 10** displays  $\Delta ta$  between LCZ 2, as the mean across the quality-

controlled CWS (**Figure 10A**) and across PRWS data (**Figure 10B**), and the Schiphol airport PRWS. We follow the approach by de Vos et al. (2020) and use the airport station as the “rural” reference for both networks, acknowledging that this is not a true rural reference site. Both sub-figures show the characteristic cycles in  $\Delta ta$  between urban and rural environments that is found for mid-latitude cities, i.e., higher values during night-time and the warmer months of the year, and lower values during daytime (Oke et al., 2017). Yet, distinctive episodes with higher and lower  $\Delta ta$  than this typical pattern are also found (visible in the vertical stripe-like pattern), being related to the specific weather conditions during this year. Two of such “stripes” are particularly prominent in the second half of February 2019 with large positive  $\Delta ta$  during night-time, being episodes of unusually high  $ta$  in Amsterdam with clear skies and no precipitation (not shown). Such conditions promote distinct local-scale  $\Delta ta$  (e.g., Parry 1956; Oke 1973; Erell and Williamson 2007; van Hove et al., 2015; Arnds et al., 2017; Fenner et al., 2017; Beck et al., 2018a) Finally, **Figure 10** highlights the strong agreement between both networks when comparing both sub-figures. This underlines the suitability of CWS data for quasi-climatological analyses, if a multitude of quality-controlled CWS are available.

In the second application (**Figure 11**), night-time  $ta$  distribution for the month of July 2020 is displayed for Toulouse. July 2020 was a month with heatwave-like conditions and only marginal rain. **Figure 11** shows a distinct night-time UHI for Toulouse of several K in the monthly mean, both for CWS and PRWS data. Highest  $ta$  was recorded in central districts of Toulouse with generally decreasing  $ta$  towards the outskirts and rural areas, comparable to model results from Kwok et al. (2019). Further, the systematic difference between CWS and PRWS data is visible (**Figure 11**). The application highlights the benefit of using CWS data for mapping of meteorological conditions due to their high density and spatial distribution. Yet, the imbalance between number of CWS in built-up areas and natural settings is also prominent (Chapman et al., 2017; Fenner et al., 2017; Meier et al., 2017; Feichtinger et al., 2020).



## CONCLUSION

The availability of CWS data in theoretically every region of the world makes this data source an interesting choice for scientists and practitioners to gain information on atmospheric conditions. This holds even more true for cities, where atmospheric conditions are highly heterogeneous and traditional measurement networks are sparse. Yet, the data come with a number of uncertainties and errors, which require targeted QC procedures.

In this study, the QC package CrowdQC+ was presented, which is a further development of the existing package CrowdQC. CrowdQC+ extends that package and adds several additions and functionalities, i.e., 1) a further QC level for additional spatial filtering to mainly address remaining radiative errors, 2) an option to correct CWS data for slow sensor response, 3) modifications to the existing QC levels to enhance applicability, and 4) additional functionalities for increased user-friendliness. The package is primarily designed to quality-control air-temperature data from CWS. As its predecessor, CrowdQC+ works without any meteorological reference data and

can thus be applied in basically every (urban) region with CWS data, enabling large-scale urban climate studies based on CWS data.

Applying CrowdQC+ to two data sets from Netatmo CWS of 1 year for Amsterdam and Toulouse, and comparing the CWS data to data from PRWS, it is shown that CrowdQC+ effectively removes erroneous data and provides an improvement compared to CrowdQC. Deviations between CWS and PRWS data on the city-scale level and per station are lower after applying CrowdQC+ than using CrowdQC in both investigated cities in all seasons, highlighting the additional value of the newly-introduced functionalities. Yet, deviations between CWS and PRWS data remain, which are likely linked to remaining faulty values not identified by the QC, but also to differences in network designs, sensor qualities, and station setups. The trade-off of the reduced deviations and thus increased QC performance of CrowdQC+ compared to CrowdQC is a lower data availability after applying the QC. It is further shown that CrowdQC+ can be applied to CWS data sets of different size, that data sets of different duration can be quality-controlled, and that the newly added functionalities of the package enable the QC to be applied in operational mode for near-real time applications.

This study aims to be a step ahead in a continuous development and enhancement of the package, retaining the core of the QC, which is the applicability in regions without reference meteorological observations. CrowdQC+ is an open-source tool under active development (<https://github.com/dafenner/CrowdQCplus>), collaboration and participation in further developments of the package are welcome. Future work could focus on the evaluation of the QC with regard to other variables such as air pressure or humidity, which can also be crowdsourced from CWS. Testing the QC on CWS data sets of, e.g., tropical or desert cities would also be of high value to understand its performance in different background climates. Furthermore, future studies could investigate the performance of the QC when applied to crowdsourced data sets composed of measurements by different types of CWS.

## DATA AVAILABILITY STATEMENT

CrowdQC+ v1.0.0, as described in this paper, is available as an R package as Supplementary Material. The latest version of CrowdQC+ and the possibility to submit issues is available at <https://github.com/>

dafenner/CrowdQCplus. Publicly available datasets were analyzed in this study. This data can be found here: Netatmo CWS data can freely be obtained via the company's API at <https://dev.netatmo.com/>. SRTM digital elevation data is freely available at [https://srtm.cgiar.org](https://srtm.csi.cgiar.org). PRWS data for Toulouse is freely available at <https://data.toulouse-metropole.fr/explore/dataset/stations-meteo-en-place/table/>. PRWS data for Amsterdam from the AAMS are available upon request from Gert-Jan Steeneveld or Bert Heusinkveld at Wageningen University & Research. Data from the KNMI can freely be obtained at <https://dataplatform.knmi.nl/>.

## AUTHOR CONTRIBUTIONS

All authors designed the study. JK, BB, and MD collected the CWS data, DF assembled PRWS data and processed all data used. All authors contributed to the design of the package, DF did the programming of the package. DF carried out all analyses and mainly wrote the manuscript. All authors discussed the results and contributed to the writing of the manuscript.

## FUNDING

This work was conducted in the context of project ENLIGHT, funded by the German Research Foundation (DFG) under grant No.

## REFERENCES

- Arndt, D., Böhner, J., and Bechtel, B. (2017). Spatio-Temporal Variance and Meteorological Drivers of the Urban Heat Island in a European City. *Theor. Appl. Climatol.* 128 (1), 43–61. doi:10.1007/s00704-015-1687-4
- Arnfield, A. J. (2003). Two Decades of Urban Climate Research: a Review of Turbulence, Exchanges of Energy and Water, and the Urban Heat Island. *Int. J. Climatol.* 23 (1), 1–26. doi:10.1002/joc.859
- Bárdossy, A., Seidel, J., and El Hachem, A. (2021). The Use of Personal Weather Station Observations to Improve Precipitation Estimation and Interpolation. *Hydrol. Earth Syst. Sci.* 25, 583–601. doi:10.5194/hess-25-583-2021
- Bäserud, L., Lussana, C., Nipen, T. N., Seierstad, I. A., Oram, L., and Aspelien, T. (2020). TITAN Automatic Spatial Quality Control of Meteorological *In-Situ* Observations. *Adv. Sci. Res.* 17, 153–163. doi:10.5194/asr-17-153-2020
- Bartos, M., Park, H., Zhou, T., Kerkez, B., and Vasudevan, R. (2019). Windshield Wipers on Connected Vehicles Produce High-Accuracy Rainfall Maps. *Sci. Rep.* 9 (1), 170. doi:10.1038/s41598-018-36282-7
- Bassett, R., Cai, X., Chapman, L., Heaviside, C., Thornes, J. E., Muller, C. L., et al. (2016). Observations of Urban Heat Island Advection from a High-Density Monitoring Network. *Q.J.R. Meteorol. Soc.* 142 (699), 2434–2441. doi:10.1002/qj.2836
- Bassett, R., Cai, X., Chapman, L., Heaviside, C., and Thornes, J. E. (2017). The Effects of Heat Advection on UK Weather and Climate Observations in the Vicinity of Small Urbanized Areas. *Boundary-layer Meteorol.* 165 (1), 181–196. doi:10.1007/s10546-017-0263-0
- Bassett, R., Cai, X., Chapman, L., Heaviside, C., and Thornes, J. E. (2019). Semi-idealized Urban Heat Advection Simulations Using the Weather Research and Forecasting Mesoscale Model. *Int. J. Climatol.* 39 (3), 1345–1358. doi:10.1002/joc.5885
- Bechtel, B., Alexander, P., Böhner, J., Ching, J., Conrad, O., Feddeema, J., et al. (2015). Mapping Local Climate Zones for a Worldwide Database of the Form and Function of Cities. *Ijgi* 4, 199–219. doi:10.3390/ijgi4010199
- Bechtel, B., Alexander, P. J., Beck, C., Böhner, J., Brousse, O., Ching, J., et al. (2019). Generating WUDAPT Level 0 Data - Current Status of Production and Evaluation. *Urban Clim.* 27, 24–45. doi:10.1016/j.ulclim.2018.10.001
437467569. The Amsterdam Atmospheric Monitoring Supersite (AAMS) has been financially supported by the Amsterdam Institute for Advanced Metropolitan Solutions (AMS) under grant VIR16002 and the NWO/eScience grant 027.012.103.

## ACKNOWLEDGMENTS

We thank all CWS owners who shared their data publicly. Tom Grassmann is thanked for sharing ideas and code in the development of CrowdQC+. We are grateful to Gert-Jan Steeneveld and Bert Heusinkveld at Wageningen University & Research (WUR) for sharing of and support with the PRWS data in Amsterdam. We further thank Guillaume Dumas at the Centre national de la recherche scientifique (CNRS) for support with the PRWS data in Toulouse. We acknowledge the WUDAPT contributors Julia Hidalgo and Ran Wang for providing the LCZ training areas for Toulouse and Amsterdam, respectively.

## SUPPLEMENTARY MATERIAL

The Supplementary Material for this article can be found online at: <https://www.frontiersin.org/articles/10.3389/fenvs.2021.720747/full#supplementary-material>

- Cerlini, P. B., Silvestri, L., and Saraceni, M. (2020). Quality Control and gap-filling Methods Applied to Hourly Temperature Observations over central Italy. *Meteorol. Appl.* 27 (3), e1913. doi:10.1002/met.1913
- Chapman, L., Muller, C. L., Young, D. T., Warren, E. L., Grimmond, C. S. B., Cai, X.-M., et al. (2015). The Birmingham Urban Climate Laboratory: An Open Meteorological Test Bed and Challenges of the Smart City. *Bull. Am. Meteorol. Soc.* 96, 1545–1560. doi:10.1175/BAMS-D-13-00193.1
- Chapman, L., Bell, C., and Bell, S. (2017). Can the Crowdsourcing Data Paradigm Take Atmospheric Science to a New Level? A Case Study of the Urban Heat Island of London Quantified Using Netatmo Weather Stations. *Int. J. Climatol.* 37 (9), 3597–3605. doi:10.1002/joc.4940
- Chen, J., Saunders, K., and Whan, K. (2021). Quality Control and Bias Adjustment of Crowdsourced Wind Speed Observations. *QJR Meteorol. Soc.* 147, 3647–3664. doi:10.1002/qj.4146
- Ching, J., Mills, G., Bechtel, B., See, L., Feddema, J., Wang, X., et al. (2018). World Urban Database and Access Portal Tools (WUDAPT), an urban weather, climate and environmental modeling infrastructure for the Anthropocene. *Bull. Am. Meteorol. Soc.* 99, 1907–1924. doi:10.1175/bams-d-16-0236.1
- Chwala, C., and Kunstmann, H. (2019). Commercial Microwave Link Networks for Rainfall Observation: Assessment of the Current Status and Future Challenges. *WIREs Water* 6 (2), e1337. doi:10.1002/wat2.1337
- Clark, M. R., Webb, J. D. C., and Kirk, P. J. (2018). Fine-scale Analysis of a Severe Hailstorm Using Crowd-Sourced and Conventional Observations. *Met. Apps* 25 (3), 472–492. doi:10.1002/met.1715
- Cornes, R. C., Dirksen, M., and Sluiter, R. (2020). Correcting Citizen-science Air Temperature Measurements across the Netherlands for Short Wave Radiation Bias. *Meteorol. Appl.* 27, e1814. doi:10.1002/met.1814
- de Vos, L., Leijnse, H., Overeem, A., and Uijlenhoet, R. (2017). The Potential of Urban Rainfall Monitoring with Crowdsourced Automatic Weather Stations in Amsterdam. *Hydroclim. Earth Syst. Sci.* 21 (2), 765–777. doi:10.5194/hess-21-765-2017
- de Vos, L. W., Leijnse, H., Overeem, A., and Uijlenhoet, R. (2019). Quality Control for Crowdsourced Personal Weather Stations to Enable Operational Rainfall Monitoring. *Geophys. Res. Lett.* 46 (15), 8820–8829. doi:10.1029/2019gl083731
- de Vos, L. W., Droste, A. M., Zander, M. J., Overeem, A., Leijnse, H., Heusinkveld, B. G., et al. (2020). Hydrometeorological Monitoring Using Opportunistic Sensing Networks in the Amsterdam Metropolitan Area. *Bull. Am. Meteorol. Soc.* 101, E167–E185. doi:10.1175/bams-d-19-0091.1
- Demuzere, M., Bechtel, B., Middel, A., and Mills, G. (2019a). Mapping Europe into Local Climate Zones. *PLoS One* 14 (4), e0214474. doi:10.1371/journal.pone.0214474
- Demuzere, M., Bechtel, B., and Mills, G. (2019b). Global Transferability of Local Climate Zone Models. *Urban Clim.* 27, 46–63. doi:10.1016/j.uclim.2018.11.001
- Demuzere, M., Hankey, S., Mills, G., Zhang, W., Lu, T., and Bechtel, B. (2020). Combining Expert and Crowd-Sourced Training Data to Map Urban Form and Functions for the continental US. *Sci. Data* 7, 264. doi:10.1038/s41597-020-00605-z
- Demuzere, M., Kittner, J., and Bechtel, B. (2021). LCZ Generator: A Web Application to Create Local Climate Zone Maps. *Front. Environ. Sci.* 9, 637455. doi:10.3389/fenvs.2021.637455
- Dowle, M., and Srinivasan, A. (2021). data.table: Extension of `data.Frame'. R package version 1.13.0. Available at: <https://CRAN.R-project.org/package=data.table>. (Accessed November 12, 2021).
- Droste, A. M., Pape, J. J., Overeem, A., Leijnse, H., Steeneveld, G. J., Van Delden, A. J., et al. (2017). Crowdsourcing Urban Air Temperatures through Smartphone Battery Temperatures in São Paulo, Brazil. *J. Atmos. Ocean. Tech.* 34 (9), 1853–1866. doi:10.1175/JTECH-D-16-0150.1
- Droste, A. M., Heusinkveld, B. G., Fenner, D., and Steeneveld, G. J. (2020). Assessing the Potential and Application of Crowdsourced Urban Wind Data. *QJR Meteorol. Soc.* 146 (731), 2671–2688. doi:10.1002/qj.3811
- Erell, E., and Williamson, T. (2007). Intra-urban Differences in Canopy Layer Air Temperature at a Mid-latitude City. *Int. J. Climatol.* 27, 1243–1255. doi:10.1002/joc.1469
- Estévez, J., Gavilán, P., and Giráldez, J. V. (2011). Guidelines on Validation Procedures for Meteorological Data from Automatic Weather Stations. *J. Hydrol.* 402 (1-2), 144–154. doi:10.1016/j.jhydrol.2011.02.031
- Feichtinger, M., de Wit, R., Goldenits, G., Kolejka, T., Hollósi, B., Žuvela-Aloise, M., et al. (2020). Case-study of Neighborhood-Scale Summertime Urban Air Temperature for the City of Vienna Using Crowd-Sourced Data. *Urban Clim.* 32, 100597. doi:10.1016/j.uclim.2020.100597
- Fenner, D., Meier, F., Scherer, D., and Polze, A. (2014). Spatial and Temporal Air Temperature Variability in Berlin, Germany, during the Years 2001–2010. *Urban Clim.* 10 (2), 308–331. doi:10.1016/j.uclim.2014.02.004
- Fenner, D., Meier, F., Bechtel, B., Otto, M., and Scherer, D. (2017). Intra and Inter 'local Climate Zone' Variability of Air Temperature as Observed by Crowdsourced Citizen Weather Stations in Berlin, Germany. *Meteorol. Z.* 26 (5), 525–547. doi:10.1127/metz/2017/0861
- Fenner, D., Holtmann, A., Meier, F., Langer, I., and Scherer, D. (2019). Contrasting Changes of Urban Heat Island Intensity during Hot Weather Episodes. *Environ. Res. Lett.* 14 (12), 124013. doi:10.1088/1748-9326/ab506b
- Fenner, D. (2020). *Heatwaves and Urban thermal Climates in Berlin, Germany*. Berlin, Germany: Technische Universität Berlin. PhD Thesis. doi:10.14279/depositonce-10378
- Feebrich, C. A., Morgan, C. R., McCombs, A. G., Hall, P. K., Jr., and McPherson, R. A. (2010). Quality Assurance Procedures for Mesoscale Meteorological Data. *J. Atmos. Ocean. Tech.* 27 (10), 1565–1582. doi:10.1175/2010JTECHA1433.1
- Gosset, W. S. (1908). The Probable Error of a Mean. *Biometrika* 6 (1), 1–25. doi:10.2307/2331554
- Grassmann, T., Napol, A., Meier, F., and Fenner, D. (2018). Quality Control for Crowdsourced Data from CWS. (Accessed November 12, 2021). doi:10.14279/depositonce-6740.3
- Haberlandt, U., and Sester, M. (2010). Areal Rainfall Estimation Using Moving Cars as Rain Gauges - a Modelling Study. *Hydroclim. Earth Syst. Sci.* 14 (7), 1139–1151. doi:10.5194/hess-14-1139-2010
- Hammerberg, K., Brousse, O., Martilli, A., and Mahdavi, A. (2018). Implications of Employing Detailed Urban Canopy Parameters for Mesoscale Climate Modelling: a Comparison between WUDAPT and GIS Databases over Vienna, Austria. *Int. J. Climatol.* 38 (S1), e1241–e1257. doi:10.1002/joc.5447
- Harrison, R. G. (2010). Natural Ventilation Effects on Temperatures within Stevenson Screens. *QJR Meteorol. Soc.* 136 (646), 253–259. doi:10.1002/qj.537
- Heaviside, C., Cai, X. M., and Vardoulakis, S. (2015). The Effects of Horizontal Advection on the Urban Heat Island in Birmingham and the West Midlands, United Kingdom during a Heatwave. *QJR Meteorol. Soc.* 141 (689B), 1429–1441. doi:10.1002/qj.2452
- Hijmans, R. J. (2021). Raster: Geographic Data Analysis and Modeling. R package version 3.3-13. Available at: <https://CRAN.R-project.org/package=raster>. (Accessed November 12, 2021).
- Jarvis, A., Reuter, H. I., Nelson, A., and Guevara, E. (2008). Hole-filled Seamless SRTM Data V4. International Centre for Tropical Agriculture CIAT. available from: <https://srtm.csi.cgiar.org>. (Accessed November 12, 2021).
- Kwok, Y. T., Schoetter, R., Lau, K. K. L., Hidalgo, J., Ren, C., Pigeon, G., et al. (2019). How Well Does the Local Climate Zone Scheme Discern the thermal Environment of Toulouse (France)? an Analysis Using Numerical Simulation Data. *Int. J. Climatol.* 39 (14), 5292–5315. doi:10.1002/joc.6140
- Langer, I., Fakharizadehshirazi, E., and Werner, J. (2021). Spatial Variation of Physiologically Equivalent Temperature in Different Local Climate Zones of a Large City during a Hot Spell. *Meteorol. Z.* 30 (2), 115–125. doi:10.1127/metz/2020/0996
- Lelevics, E., Unger, J., Gál, T., and Gál, C. (2014). Design of an Urban Monitoring Network Based on Local Climate Zone Mapping and Temperature Pattern Modelling. *Clim. Res.* 60, 51–62. doi:10.3354/cr01220
- Madaus, L. E., Hakim, G. J., and Mass, C. F. (2014). Utility of Dense Pressure Observations for Improving Mesoscale Analyses and Forecasts. *Mon. Weather Rev.* 142 (7), 2398–2413. doi:10.1175/mwr-d-13-00269.1
- Mandement, M., and Caumont, O. (2020). Contribution of Personal Weather Stations to the Observation of Deep-Convection Features Near the Ground. *Nat. Hazards Earth Syst. Sci.* 20, 299–322. doi:10.5194/nhess-20-299-2020
- Mass, C. F., and Madaus, L. E. (2014). Surface Pressure Observations from Smartphones: A Potential Revolution for High-Resolution Weather Prediction? *Bull. Am. Meteorol. Soc.* 95, 1343–1349. doi:10.1175/BAMS-D-13-00188.1
- Meier, F., Fenner, D., Grassmann, T., Otto, M., and Scherer, D. (2017). Crowdsourcing Air Temperature from Citizen Weather Stations for Urban Climate Research. *Urban Clim.* 19, 170–191. doi:10.1016/j.uclim.2017.01.006
- Messer, H., Zinevich, A., and Alpert, P. (2006). Environmental Monitoring by Wireless Communication Networks. *Science* 312 (5774), 713. doi:10.1126/science.1120034

- Miloshevich, L. M., Paukkunen, A., Vömel, H., and Oltmans, S. J. (2004). Development and Validation of a Time-Lag Correction for Vaisala Radiosonde Humidity Measurements. *J. Atmos. Oceanic Technol.* 21 (9), 1305–1327. doi:10.1175/1520-0426(2004)021<1305:davota>2.0.co;2
- Muller, C. L., Chapman, L., Grimmond, C. S. B., Young, D. T., and Cai, X. (2013). Sensors and the City: a Review of Urban Meteorological Networks. *Int. J. Climatol.* 33 (7), 1585–1600. doi:10.1002/joc.3678
- Muller, C. L., Chapman, L., Johnston, S., Kidd, C., Illingworth, S., Foody, G., et al. (2015). Crowdsourcing for Climate and Atmospheric Sciences: Current Status and Future Potential. *Int. J. Climatol.* 35 (11), 3185–3203. doi:10.1002/joc.4210
- Nakamura, Y., and Oke, T. R. (1988). Wind, Temperature and Stability Conditions in an East-West Oriented Urban canyon. *Atmos. Environ.* (1967) 22 (12), 2691–2700. doi:10.1016/0004-6981(88)90437-4
- Napoly, A., Grassmann, T., Meier, F., and Fenner, D. (2018). Development and Application of a Statistically-Based Quality Control for Crowdsourced Air Temperature Data. *Front. Earth Sci.* 6, 118. doi:10.3389/feart.2018.00118
- Nazarian, N., Liu, S., Kohler, M., Lee, J. K. W., Miller, C., Chow, W. T. L., et al. (2021). Project Coolbit: Can Your Watch Predict Heat Stress and thermal comfort Sensation? *Environ. Res. Lett.* 16 (3), 034031. doi:10.1088/1748-9326/abd130
- Nipen, T. N., Seierstad, I. A., Lussana, C., Kristiansen, J., and Hov, Ø. (2020). Adopting Citizen Observations in Operational Weather Prediction. *Bull. Amer. Meteorol. Soc.* 101, E43–E57. doi:10.1175/bams-d-18-0237.1
- Oke, T. R., Mills, G., Christen, A., and Voogt, J. A. (2017). *Urban Climates*. Cambridge, United Kingdom: Cambridge University Press. doi:10.1017/9781139016476
- Oke, T. R. (1973). City Size and the Urban Heat Island. *Atmos. Environ.* (1967) 7 (8), 769–779. doi:10.1016/0004-6981(73)90140-6
- Overeem, A., Leijnse, H., and Uijlenhoet, R. (2013a). Country-wide Rainfall Maps from Cellular Communication Networks. *Proc. Natl. Acad. Sci.* 110 (8), 2741–2745. doi:10.1073/pnas.1217961110
- Overeem, A., Robinson, J. C., Leijnse, H., Steeneveld, G. J., P. Horn, B. K., and Uijlenhoet, R. (2013b). Crowdsourcing Urban Air Temperatures from Smartphone Battery Temperatures. *Geophys. Res. Lett.* 40, 4081–4085. doi:10.1002/grl.50786
- Parry, M. (1956). Local Temperature Variations in the Reading Area. *Q.J.R. Met. Soc.* 82 (351), 45–57. doi:10.1002/qj.49708235105
- Potgieter, J., Nazarian, N., Lipson, M. J., Hart, M. A., Ulpiani, G., Morrison, W., et al. (2021). Combining High-Resolution Land Use Data with Crowdsourced Air Temperature to Investigate Intra-urban Microclimate. *Front. Environ. Sci.* 9, 720323. doi:10.3389/fenvs.2021.720323
- R Core Team (2021). *R: A Language and Environment for Statistical Computing*. Vienna, Austria: R Foundation for Statistical Computing. URL: <https://www.R-project.org/>.
- Ronda, R. J., Steeneveld, G. J., Heusinkveld, B. G., Attema, J. J., and Holtslag, A. A. M. (2017). Urban Finescale Forecasting Reveals Weather Conditions with Unprecedented Detail. *Bull. Am. Meteorol. Soc.* 98 (12), 2675–2688. doi:10.1175/BAMS-D-16-0297.1
- Rousseeuw, P. J., and Croux, C. (1993). Alternatives to the Median Absolute Deviation. *J. Am. Stat. Assoc.* 88 (424), 1273–1283. doi:10.1080/01621459.1993.10476408
- Šećerov, I. B., Savić, S. M., Milošević, D. D., Arsenović, D. M., Dolinaj, D. M., and Popov, S. B. (2019). Progressing Urban Climate Research Using a High-Density Monitoring Network System. *Environ. Monit. Assess.* 191 (2), 89. doi:10.1007/s10661-019-7210-0
- Shafer, M. A., Fiebrich, C. A., Arndt, D. S., Fredrickson, S. E., and Hughes, T. W. (2000). Quality Assurance Procedures in the Oklahoma Mesonet. *J. Atmos. Oceanic Technol.* 17 (4), 474–494. doi:10.1175/1520-0426(2000)017<0474:qapito>2.0.co;2
- Skarbit, N., Stewart, I. D., Unger, J., and Gál, T. (2017). Employing an Urban Meteorological Network to Monitor Air Temperature Conditions in the 'local Climate Zones' of Szeged, Hungary. *Int. J. Climatol.* 37 (S1), 582–596. doi:10.1002/joc.5023
- Smiatek, G., Keis, F., Chwala, C., Fersch, B., and Kunstmann, H. (2017). Potential of Commercial Microwave Link Network Derived Rainfall for River Runoff Simulations. *Environ. Res. Lett.* 12 (3), 034026. doi:10.1088/1748-9326/aa5f46
- Steeneveld, G. J., Koopmans, S., Heusinkveld, B. G., van Hove, L. W. A., and Holtslag, A. A. M. (2011). Quantifying Urban Heat Island Effects and Human comfort for Cities of Variable Size and Urban Morphology in the Netherlands. *J. Geophys. Res.* 116 (D20), D20129. doi:10.1029/2011JD015988
- Stewart, I. D. (2019). Why Should Urban Heat Island Researchers Study History? *Urban Clim.* 30, 100484. doi:10.1016/j.uclim.2019.100484
- Stewart, I. D., and Oke, T. R. (2012). Local climate zones for urban temperature studies. *Bull. Am. Meteorol. Soc.* 93 (12), 1879–1900. doi:10.1175/BAMS-D-11-00019.1
- Taylor, K. E. (2001). Summarizing Multiple Aspects of Model Performance in a Single Diagram. *J. Geophys. Res.* 106 (D7), 7183–7192. doi:10.1029/2000JD900719
- van Hove, L. W. A., Jacobs, C. M. J., Heusinkveld, B. G., Elbers, J. A., van Driel, B. L., and Holtslag, A. A. M. (2015). Temporal and Spatial Variability of Urban Heat Island and thermal comfort within the Rotterdam Agglomeration. *Build. Environ.* 83, 91–103. doi:10.1016/j.buildenv.2014.08.029
- Varentsov, M., Fenner, D., Meier, F., Samsonov, T., and Demuzere, M. (2021). Quantifying Local- and Meso-Scale Drivers of Moscow's Urban Heat Island with Reference and Crowdsourced Observations. *Frontiers in Environmental Science*. doi:10.3389/fenvs.2021.716968
- Venter, Z. S., Brousse, O., Esau, I., and Meier, F. (2020). Hyperlocal Mapping of Urban Air Temperature Using Remote Sensing and Crowdsourced Weather Data. *Remote Sens. Environ.* 242, 111791. doi:10.1016/j.rse.2020.111791
- Venter, Z. S., Chakraborty, T., and Lee, X. (2021). Crowdsourced Air Temperatures Contrast Satellite Measures of the Urban Heat Island and its Mechanisms. *Sci. Adv.* 7 (22), eabb9569. doi:10.1126/sciadv.eabb9569
- Vulova, S., Meier, F., Fenner, D., Nouri, H., and Kleinschmit, B. (2020). Summer Nights in Berlin, Germany: Modeling Air Temperature Spatially with Remote Sensing, Crowdsourced Weather Data, and Machine Learning. *IEEE J. Sel. Top. Appl. Earth Observ. Remote Sens.* 13, 5074–5087. doi:10.1109/jstars.2020.3019696
- Warren, E. L., Young, D. T., Chapman, L., Muller, C., Grimmond, C. S. B., and Cai, X.-M. (2016). The Birmingham Urban Climate Laboratory-A High Density, Urban Meteorological Dataset, from 2012–2014. *Sci. Data* 3, 160038. doi:10.1038/sdata.2016.38
- Wolters, D., and Brandsma, T. (2012). Estimating the Urban Heat Island in Residential Areas in the Netherlands Using Observations by Weather Amateurs. *J. Appl. Meteorol. Clim.* 51 (4), 711–721. doi:10.1175/JAMC-D-11-0135.1
- Yamazaki, D., Ikeshima, D., Tawatari, R., Yamaguchi, T., O'Loughlin, F., Neal, J. C., et al. (2017). A High-Accuracy Map of Global Terrain Elevations. *Geophys. Res. Lett.* 44 (11), 5844–5853. doi:10.1002/2017gl072874
- Zahumenský, I. (2004). *Guidelines on Quality Control Procedures for Data from Automatic Weather Stations*. Document CIMO/OPAG-SURFACE/ET ST\&MT-1/Doc.6.1(2). Geneva, Switzerland: World Meteorological Organization.
- Zhang, D.-L., Shou, Y.-X., Dickerson, R. R., and Chen, F. (2011). Impact of Upstream Urbanization on the Urban Heat Island Effects along the Washington-Baltimore Corridor. *J. Appl. Meteorol. Clim.* 50 (10), 2012–2029. doi:10.1175/jamc-d-10-05008.1
- Zumwald, M., Knüsel, B., Bresch, D. N., and Knutti, R. (2021). Mapping Urban Temperature Using Crowd-Sensing Data and Machine Learning. *Urban Clim.* 35, 100739. doi:10.1016/j.uclim.2020.100739

**Conflict of Interest:** The authors declare that the research was conducted in the absence of any commercial or financial relationships that could be construed as a potential conflict of interest.

The reviewer (TC) declared a past co-authorship with one of the authors (BB) to the handling Editor.

**Publisher's Note:** All claims expressed in this article are solely those of the authors and do not necessarily represent those of their affiliated organizations, or those of the publisher, the editors and the reviewers. Any product that may be evaluated in this article, or claim that may be made by its manufacturer, is not guaranteed or endorsed by the publisher.

Copyright © 2021 Fenner, Bechtel, Demuzere, Kittner and Meier. This is an open-access article distributed under the terms of the Creative Commons Attribution License (CC BY). The use, distribution or reproduction in other forums is permitted, provided the original author(s) and the copyright owner(s) are credited and that the original publication in this journal is cited, in accordance with accepted academic practice. No use, distribution or reproduction is permitted which does not comply with these terms.



# SmartAirQ: A Big Data Governance Framework for Urban Air Quality Management in Smart Cities

Akshara Kaginalkar<sup>1,2\*</sup>, Shamita Kumar<sup>2</sup>, Prashant Gargava<sup>3</sup>, Neelesh Kharkar<sup>1</sup> and Dev Niyogi<sup>4,5,6</sup>

<sup>1</sup>Centre for Development of Advanced Computing, Pune, India, <sup>2</sup>Institute of Environment Education and Research, Bharati Vidyapeeth Deemed University, Pune, India, <sup>3</sup>Central Pollution Control Board, New Delhi, India, <sup>4</sup>Center for Excellence in Disaster Mitigation and Management, Indian Institute of Technology Roorkee, Roorkee, India, <sup>5</sup>Department of Geological Sciences, Jackson School of Geosciences, The University of Texas at Austin, Austin, TX, United States, <sup>6</sup>Department of Civil, Architectural, and Environmental Engineering, Cockrell School of Engineering, The University of Texas at Austin, Austin, TX, United States

## OPEN ACCESS

### Edited by:

Negin Nazarian,  
University of New South Wales,  
Australia

### Reviewed by:

Jovan Pantelic,  
KU Leuven, Belgium  
Arjan Marten Droste,  
Wageningen University and Research,  
Netherlands

### \*Correspondence:

Akshara Kaginalkar  
akshara@cdac.in

### Specialty section:

This article was submitted to  
Environmental Informatics and Remote  
Sensing,  
a section of the journal  
*Frontiers in Environmental Science*

Received: 28 September 2021

Accepted: 23 February 2022

Published: 08 April 2022

### Citation:

Kaginalkar A, Kumar S, Gargava P,  
Kharkar N and Niyogi D (2022)  
SmartAirQ: A Big Data Governance  
Framework for Urban Air Quality  
Management in Smart Cities.  
*Front. Environ. Sci.* 10:785129.  
doi: 10.3389/fenvs.2022.785129

Rapid urbanization across the world has put an enormous burden on our environment. Cities from developing countries, in particular, are experiencing high air pollution levels. To address this challenge, the new WHO global air quality guidelines and various nations are mandating cities to implement clean air measures. However, these implementations are largely hindered by limited observations, siloed city operations, absence of standard processes, inadequate outreach, and absence of collaborative urban air quality management (UAQM) governance. The world is experiencing transformative changes in the way we live. The 4th industrial revolution technologies of artificial intelligence, Internet of Things, big data, and cloud computing bridge gaps between physical, natural, and personal entities. Globally, smart cities are being promulgated on the premise that technologies and data aid in improving urban services. However, in many instances, the smart city programs and UAQM services may not be aligned, thereby constraining the cumulative advantage in building urban resilience. Considering the potential of these technologies as enablers of environmental sustainability, a conceptual urban computing framework "SmartAirQ" for UAQM is designed. This interdisciplinary study outlines the SmartAirQ components: 1) data acquisition, 2) communication and aggregation, 3) data processing and management, 4) intelligence, 5) application service, 6) high-performance computing- (HPC-) cloud, and 7) security. The framework has integrated science cloud and urban services aiding in translating scientific data into operations. It is a step toward collaborative, data-driven, and sustainable smart cities.

**Keywords:** urban computing, frontier technologies, data governance, AI, cloud computing, machine learning, smart cities, air pollution

**Abbreviations:** ANN, artificial neural network; AOD, aerosol optical depth; AQI, air quality index; AR, augmented reality; BC, black carbon; CCTV, close circuit tv; CFD, computational fluid dynamics; CO, carbon monoxide; CUDA, compute unified device architecture; DALY, disability-adjusted life years; GDP, gross development; GHG, greenhouse gas; GIS, geographical information system; GPS, global positioning system; HDFS, Hadoop Data File System; HPC, high-performance computing; OC, organic carbon; QA/QC, quality assurance and quality control; RF, random forest; RFID, radio frequency identification; RTI, right to information; SDG, sustainable development goals; SVM, support vector machine; VOC, volatile organic compound; VR, virtual reality; WRF, weather research and forecast.

## 1 INTRODUCTION

Globally, growing economic opportunities fuel rapid urbanization (United Nations, 2019). While aiding the economy, this growth is affecting the environment and living. For instance, air pollution is among the top five global causes of mortality (WHO, 2018; Lelieveld et al., 2020). At the same time, short- and long-term pollution exposure have severe health impacts, such as chronic respiratory diseases, asthma, cancer, and dementia (Balakrishnan et al., 2019). For emerging economies, this burden is unproportionate (Landrigan et al., 2018; Anenberg et al., 2019). For example, air pollution is a major health emergency in India, with 1.67 million deaths, accounting for 17.8% of total deaths (Pandey, 2021). Over 100 Indian cities exceed the National Air Quality and WHO standards (CPCB, 2019). This air pollution burden has translated into incremental health expenses, causing a loss of about \$95 billion, amounting to a 3% of Indian GDP in 2019 (CII, Dalberg, 2021). Recently, the COVID-19 pandemic has exacerbated it (Achakulwisut et al., 2019; Khan et al., 2021).

Governmental programs, such as the national clean air program and smart city initiatives, are steps toward addressing these challenges (India Smart City, 2015; CPCB, 2019). However, these programs often run in parallel, thereby diminishing the opportunity to synchronize the activities toward the common goal of improving quality of life. Though pollution mitigation policies are defined, a significant gap remains when implementing them (UNEP, 2021). Consequently, smart cities struggle to show sustainability benefits (Komninos et al., 2015; Parisar, 2020). With less than a decade remaining for Sustainable Development Goals 2030, there is an urgent need for overarching solutions for cities.

Data-driven solutions are important for monitoring the progress toward sustainability goals. Its criticality is reflected in the statement of the United Nations Secretary-General in 2018, “The availability of quality, accessible, open, timely and disaggregated data is vital for evidence based decision-making and the full implementation of the 2030 Agenda and realization of its ambitions of leaving no one behind.” Accordingly, integrated impact and data-based environmental services are increasingly promoted (Baklanov et al., 2018; González et al., 2021). These services entail seamless access to interdisciplinary data and processing resources for different stakeholders (Bibri and Krogstie, 2020).

Such a service, urban air quality management (UAQM), encompasses multi-sectorial functions, data and information exchanges on pollution sources, mitigation, health burden, socioeconomic impacts, and policy formulation. For its effectiveness, real-time and near-real-time data communication is required. However, these data are often created in silos or not available in cross-sectorial usable form, necessitating integrated data governance translating data into knowledgeable information. Despite the number of smart city concepts, research on urban data governance for sustainable development is underestimated (Paskaleva et al., 2017).

Smart city technologies, such as the 4th industrial revolution (4IR) technologies of Internet of Things (IoT), artificial

intelligence (AI), and cloud computing, are providing solutions to these problems by ubiquitous data creation, efficient predictive and prescriptive analysis, and effective information dissemination (ITU, 2015; Mabkhot, 2021). In this context, urban computing (UC) is an emerging theme connecting urban sensing, data, and city services such as environment, transport, energy, and economy, bringing insights into sustainable operations (Kindberg et al., 2007; ITU 2020; Lytras et al., 2020).

Given the significant role of UC in urban sustainability, this study provides a conceptual framework for next-generation UAQM as part of ongoing interdisciplinary research on developing environmental cyberinfrastructure such as the system of systems (Kaginalkar et al., 2022). The ultimate objective is to provide a cross-sector data governance ecosystem for smart cities built from the UC framework derived from our understanding of empirical evidence of 4IR technology applications (Kaginalkar et al., 2021) and participative research (Kaginalkar et al., in preparation).

The study presents the design of SmartAirQ—an UC framework with multi-sector real-time and strategic data governance and technology integration. SmartAirQ is a hybrid cross-sector data framework with varied stakeholders/users, such as researchers (atmosphere, air quality, health, economics, machine learning (ML), and information technology), governance (policymaker, municipality environment department, and regulatory boards), citizens, and non-governmental organizations as end users. The system has a high-end distributed backend data and computing ecosystem and user-specific decision support system (DSS), disseminating easily understandable information. Although the framework is described with Indian smart cities, the FAIR (Findable, Accessible, Interoperable, Reusable) data-based architecture is scalable across world cities (Wilkinson et al., 2016). With worldwide air pollution concerns, SmartAirQ has broad relevance and is likely to be suitable for emerging cities (Pinder et al., 2019).

Due to the space limitation, this study focuses on the data governance and framework features. This study is organized as follows: **Section 2** discusses the air quality and smart city context, **Section 3** describes the methodology, **Section 4** discusses the SmartAirQ building blocks considered for the design, **Section 5** presents the derived conceptual SmartAirQ architecture, and **Section 6** has representative use cases, highlighting the data flow and stakeholder actions. This study is summarized in **Section 7**.

## 2 THE CONTEXT

Urban air pollution is influenced by geography, meteorology, morphology, natural events, and anthropogenic activities (Oke et al., 2017). Apart from local impact, long-range transport contributes to pollution and climate change (Baklanov et al., 2016). The UAQM is determined by the information on hyper-local pollutant source-concentration, its residency period, transport from other regions, and pollution impacts on socioeconomic conditions.

Managing the urban air quality is a cross-functional process, from identifying emission sources to actual removal from the atmosphere for protecting human beings (Julia et al., 2015). UAQM is often supported by scientific research, policies, continuous assessment of mitigation measures, and awareness programs (Baklanov et al., 2020). It has close linkages with other city functions, such as solid waste management, traffic, infrastructure, health, industry, urban planning, and social welfare, requiring timely access to multivariate data. Improvement in its effectiveness necessitates city governments for capacity building of data governance and intelligent decision-making (UNEP, 2021).

In this context of urban governance, globally, smart cities are promulgated as engines of urban resiliency, attracting the attention of researchers, practitioners, and governments (Albino et al., 2015). Often, in these smart cities, information and communication technology is considered an enabler for social, economic, and environmental transitions and collaborative governance (Nam and Pardo, 2011). A number of studies have attributed technology key characteristics to these transitions to smart cities, such as big data (Hashem et al., 2016; Paskaleva et al., 2017; Bibri and Krogstie, 2020), IoT (Zanella et al., 2014; Ahlgren et al., 2016), AI (Azevedo Guedes et al., 2018; Allam and Dhunny, 2019), cloud computing (Khan et al., 2015), crowdsourcing (Stojanovic et al., 2016; Alvear et al., 2018), software architecture (Viqueira et al., 2020; Majumdar et al., 2021), and city services (Lv et al., 2018; Badii et al., 2019). Despite these studies, standardization of UAQM data acquisition, advanced data processing, and stakeholder participation methods are limited (Creutzig et al., 2019).

In this context, India's smart city mission provides an opportune platform for environmental data governance (India Smart City, 2015). Even though the mission is expected to address environmental sustainability, there is a disconnect between the smart city services and plans mandated by the national clean air program (CPCB, 2019). Moreover, current smart cities are driven by technology vendors or built infrastructure and have a limited focus on environmental services (Randhawa and Kumar, 2017; Smith et al., 2019). Even through some air quality information portals with *in situ*<sup>1</sup> data, low-cost sensors (LCS),<sup>2</sup> and model data for a few Indian cities (Beig et al., 2015; Jena et al., 2021) are available, a multi-functional participative DSS across the value chain of UAQM is not yet evident (Parisar, 2020; Verma, 2021). Consequently, cities face implementation ambiguity, siloed operations of stakeholders, and limited progress toward pollution reduction. These gaps necessitate a data and technology ecosystem enabling seamless cross-sector functions.

UC plays a multi-faceted role in UAQM with operation digitalization, real-time data acquisition, data processing, and dissemination. For instance, IoT helps cities access granular city data by connecting physical systems and humans seamlessly (Toma et al., 2019). Fast data processing with AI and HPC-cloud services enables real-time data analytics and metadata

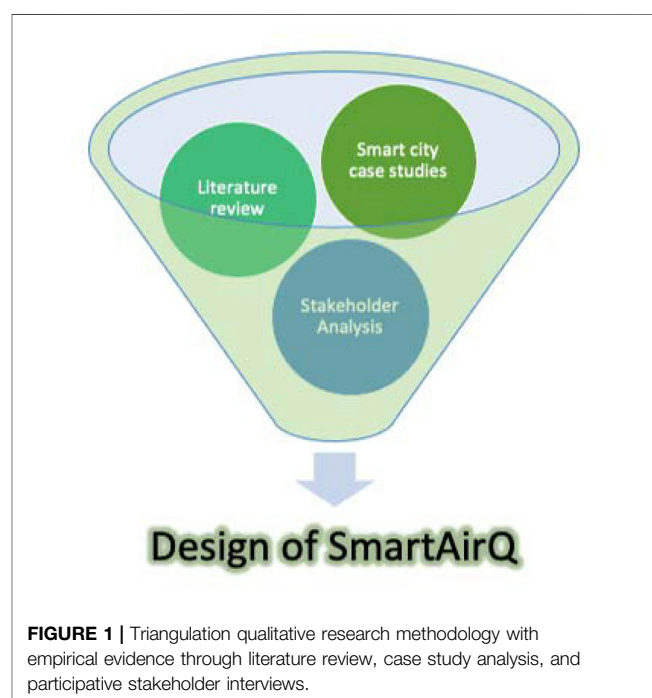
sharing (Bibri, 2019). Above all, the open data priorities of smart cities are bringing values to cyber-physical-governance-human systems by accessing and hyper-looping back the data for further intelligence building (Wilkinson et al., 2016; Allam and Dhunny, 2019). Considering this potential, this study discusses design aspects of an institutionalized framework as a smart city service tool for data governance and individual decisions.

### 3 METHODOLOGY

The methodology is built to help answer the following research questions:

- (1) What are the different data elements of UAQM in the context of emerging smart cities and the value they bring in as an interoperable system?
- (2) How can technologies be optimally connected for cross-sector data acquisition, aggregation, processing, modeling, stakeholder participation, and dissemination?
- (3) What can be the overarching design of UC-enabled UAQM as a standard platform, scalable across smart cities?

To address these questions, we adopted the triangulation method (**Figure 1**) of qualitative analysis by developing convergence evidence of causal relationships (Yin, 2016; Sekayi and Kennedy, 2017). It includes systematic framework analysis of UC evidence through literature review (Given, 2008), smart city case studies (Baškarada, 2014), and empirical insights through stakeholder analysis (Reed et al., 2009). Involving stakeholders in designing the environmental solutions is increasingly adopted as an effective way of co-production of climate services bringing the



<sup>1</sup><https://app.cpcbccr.com/CCR/#/CAAQM-Dashboard-all/CAAQM-Landing>

<sup>2</sup><https://ncap.carboncopy.info/CAAQMS/>.

synergetic research-practice-research perspective (Lim et al., 2018; Vincent et al., 2018; Fragomeni et al., 2020). In accordance, we followed an idealized design approach, wherein “information on the futuristic system” is sought from the users, leading to product realization (Ballejos and Montagna, 2011).

UAQM involves national, regional, and local cross-sector stakeholders. These can be classified as follows: 1) those that have a role in environmental governance and policies; 2) those who are enablers and solution providers broadly referred to as researchers and practitioners; and 3) those impacted by the decisions and solutions (e.g., industry and citizens). Eliciting stakeholder requirements and perception on data and technologies, we conducted focus interviews with ten participants, including members from national and state regulatory agencies, doctors, air quality modelers, policymakers, non-governmental organizations, National Green Tribunal members, and city environment managers. The participants were selected using purposive sampling by identifying the experts through their current role and prior project experience of authors with the experts. The interviews had the following broad questions:

- (1) What are the functional inter-linkages between the stakeholders and how and which data are typically used or shared?
- (2) What are the technical requirements and challenges faced while performing the air quality functions?
- (3) How do stakeholders view the integration of smart city and UAQM services?

The interview responses were transcribed and coded with MAXQDA software by applying thematic typology (Kaginalkar et al., in preparation). It was found that UAQM in Indian cities has a strong dependence on interagency coordination, requiring knowledge and a decision-sharing ecosystem. The interview synthesis highlighted cross-sector gaps and data challenges and generated insights on the next generation UAQM with 4IR technologies. For example, an urgent need for intelligent cross-sectorial data access, such as real-time vehicular distribution on the road, was felt by the modelers. On one side, there is plethora of data being generated, on the other side, there is general sentiment that due to the limited access of the meta data, stakeholders can not perform air quality data analysis effectively. For instance, one non-governmental organization member shared that though 15-minute monitoring data is available from the pollution control board site, extracting the quality controlled data for specific locality or duration is time-consuming. The discussions also drew attention to the fact that though technology companies deploy sensors and servers in smart cities, the data and facilities are not available in real time as integrated application platforms to all the stakeholders.

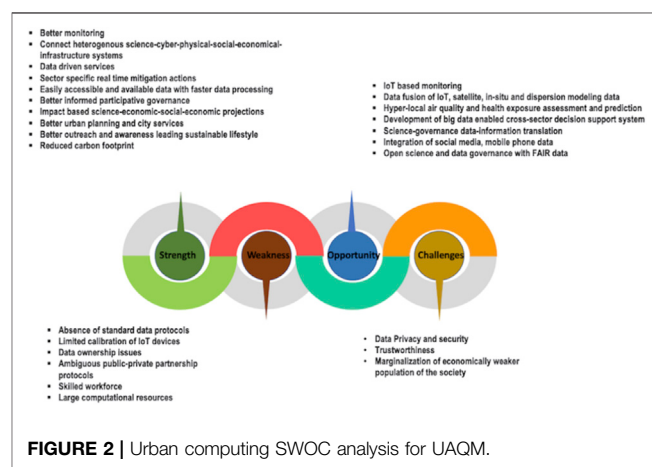
The city environment manager response showed that current technology usage in UAQM is generally limited to administration, rather than its active use as an enabling tool for planning, controlling pollution, and communicating decisions among stakeholders. The participative research also highlighted

the need for sub-scale monitoring and exposure data, computational resources, interoperability issues due to data heterogeneity and difficulty in translating complex scientific data into user understandable information. Though all the stakeholders found potential in IoT and big data analytics for data-driven UAQM, the non-alignment of smart city plans and clean air program was a major gap. A manuscript detailing the stakeholder analysis method and its outcome will be available by Kaginalkar et al. (in preparation). The research synthesis led to strength, weakness, opportunities, and challenges (SWOC) analysis of UC offerings (**Figure 2**). The summary is presented in this section.

### 3.1 Strengths

Augmenting the traditional monitoring methods, data fusion of *in situ*, IoT, model, and satellite data typically yields better spatiotemporal mapping (Lau et al., 2019). Hyper-local emission source estimation and concentration prediction using multiscale models aid in neighborhood-scale pollution mitigation and outreach (Jena et al., 2021). LCS, wearable devices, social media, and smartphones enable citizen participation (Skjetne and Liu, 2017; Nyhan et al., 2019; Yarza et al., 2020). AI methods improve LCS calibration and model prediction performance and facilitate the integration of newer data sources and faster processing (Bellinger et al., 2017; McGovern et al., 2017; Zimmerman et al., 2018; Ameer et al., 2019). The high-granularity data from the LCS typically has uncertainty and may have limited utility for daily real-time pollutant level predictions. However, they can be advantageous in “fit-for-the-purpose” approaches, for example, building awareness, education, exposure reduction, air quality model validation, source apportionment, epidemiological studies, and hot spot identification (WHO, 2021).

The inherent uncertainty in high-resolution numerical model data is augmented by coupling with ML for bias correction and pattern analysis (Cho et al., 2020; Ma et al., 2020). For this, HPC-cloud services provide cost-effective urban informatics solutions (Molthan et al., 2014).



### 3.2 Weakness

IoT-based monitoring is yet to mature due to calibration and maintenance issues. Standardizing sensor measurements and communication protocols with data privacy needs more effort (Syed et al., 2021). At the same time, fully AI-based methods still face trustworthiness and ethical issues. Complex higher granularity models and huge databases demand large HPC resources to predict sub-local air quality (Michalakes, 2020). IoT and social media smart city data is affected by confidentiality, data leakage, and access control issues (Toma et al., 2019).

### 3.3 Opportunities

The ubiquitous and fast processing characteristics make UC a candidate for UAQM. Interoperable data options, improvements in air quality predictions and services, and the ability to connect cyber-physical systems with the city's socioeconomic-infrastructure systems that include natural and anthropogenic feedbacks provide opportunities to develop better smart cities through governance actions (Mondschein et al., 2021). Examples include graded action plans for pollution reduction, prompting systems to pause production (e.g., open burning in the underprivileged neighborhood) or changes in traffic flow patterns. Such aspects can be integrated within the Smart City environmental service framework.

Shared computational and data platform through cloud services aids developers in designing participative governance. The large urban covariate data with deciphering capability of structured and unstructured data of AI are bringing insights by including newer observations. For example, sentiment analysis of social media aiding understanding of mental health impact of pollution (Zheng et al., 2019). The open data and ubiquitous technologies enable citizen participation in environmental governance (Constant, 2018; English et al., 2018).

### 3.4 Threats

Data-driven service has a major threat to data privacy and security in smart cities (Cui et al., 2018; Ismagilova et al., 2020). Misuse and biased data interpretation can lead to a skewed decision. Black box AI methods face trust issues. Better anonymization and cyber security procedures with improved authentication, encryption algorithm, and blockchain methods may serve the purpose (Ghraibeh et al., 2017).

Faster technological growth with newer solutions can sometimes hamper developmental completeness, for example, a newer processor in the market or enhance ML algorithms. This can be augmented with modular technical enhancements, wherein the architecture can have flexible component connections with the interface layers.

The study findings are characterized and organized into various components; cross-sector processes, data interoperability, and user attributes. We then applied the multi-case analysis method by mapping gaps, challenges' actionable knowledge, and technology solutions to stakeholder attributes. This approach combined multiple monitoring methods, state-of-the-art multiscale and multi-sector data and models on HPC-cloud platforms, source apportionment methods, satellite data extraction, data processing, data management, and dissemination.

## 4 BUILDING BLOCKS

This section seeks an answer to the first research question of "What are the different data elements of UAQM in the context of emerging smart cities and the value they bring in as an interoperable system?"

Increasingly, urban aspects are reflected in the form of digital information enabling city functions in a more coordinated way. This digital information creation has a life cycle with value creation at each stage (GPAI, 2020) and enhancing partnerships among stakeholders, supported by data and technologies deriving knowledge and executing meaningful decisions (Figure 3).

UAQM stakeholders need cross-sector data access (Table 1). The stakeholders/users of SmartAirQ, including state and national regulatory agencies, multidisciplinary researchers, non-governmental organizations, city environment managers, local municipal departments, smart city IT centers, and industry, have varied data usage patterns (Tables 1–4). The UAQM users strongly rely on timely access to the information existing in the form of instrument data, written records, laboratory samples, complex model output, and governmental reports. This section gives a spectrum of scientific and administrative data and the associated technologies useful for accessing, processing, and disseminating it.

### 4.1 Data

Many of the urban datasets are part of open data portals of national and local governments, global websites of scientific data, Internet, and smart city platforms. They have spatiotemporal heterogeneity with different spatial scales (sub-local, local, regional, national, and global), temporal scales (minutes, hourly, daily, weekly, monthly, and annual), types (structured and unstructured), and domains (scientific, social, economics, infrastructure, and governance) (Supplementary Material). The real-time, historical data and metadata are classified into four main types considering the static and dynamic nature of the data: 1) city characteristics, 2) monitoring and observations, 3) modeling, and 4) city services (Figure 4).

#### 4.1.1 City Characteristics

These define city static/semi-static data such as demography, morphology, Land Use Land Cover (LULC), urban planning, climatic conditions, industry, and socioeconomic characteristics (Supplementary Table S1). Geographical details of the city are required, as the location of the city determines air pollution dispersion patterns, for example, coastal city or city in a valley. For understanding and modeling the pollutant formation and its dispersion, morphological data such as road type and length, building type, height, and density and trees is required (Cárdenas Rodríguez et al., 2016). Realistic representation of urban LULC also aids in simulating the planetary boundary layer structure, calculating the thermodynamic and air pollutant transport functions (Sun et al., 2020). Satellite-derived LULC classification, for example, from Landsat and Sentinel, is a viable source for capturing sub-scale granularity and temporal transitions (Saraswat et al., 2017).

A city's socioeconomic information such as projected population growth, residential area, business hubs, recreation areas, and industry location contribute to the anthropogenic emission source

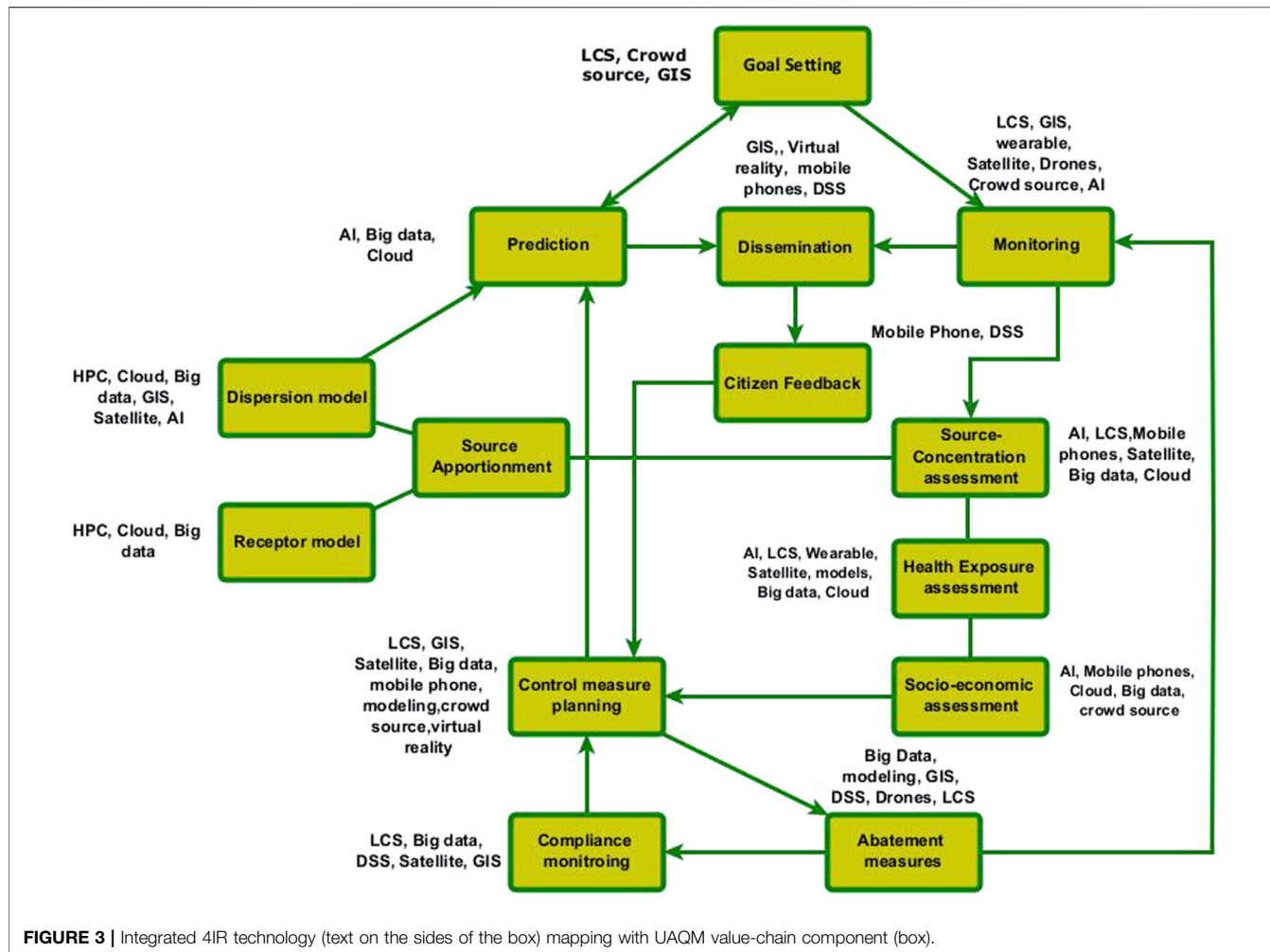


**FIGURE 3 |** Integrated 4IR technology (text on the sides of the box) mapping with UAQM value-chain component (box).

identification (Guttikunda et al., 2013). Geo-referenced ward-wise shapefiles and point shapefiles are part of the city's geospatial database. Geographical information system (GIS) data such as place of interest, roads, buildings, location layers, and hospital information are important components of the interactive DSS.

#### 4.1.2 Monitoring and Observations

These are classified depending on the mode of observation (**Supplementary Table S2**).

##### 4.1.2.1 In Situ

This includes real-time and historical daily manual and continuous monitoring stations from regulatory agencies<sup>3</sup> and research programs (Beig et al., 2015). Recently, smart city LCS data are available in the public domain<sup>4</sup>. Monitoring datasets also include pollution data on specific events, such as music events, rallies, dust storms (Kedia et al., 2018), correlating human activities and observations from airshed regions.

Monitoring is augmented by periodic instrument maintenance information. The quality control data with calibration information such as sensor type, aggregated network information, gateway node, sensor ID, location, parameters to be tested, statistical analysis, missing values, error flags, and number of operational stations are classified in the calibration datasets of SmartAirQ (Chu et al., 2020; Sahu et al., 2021).

Ground and remote satellite data complement the sparse monitoring data (Martin, 2008). For instance, data from TROMPMI over Sentinel-5P gives daily high-resolution coverage for pollutant measurements (Sentinel-5P). Another example is that satellite data retrieved PM<sub>2.5</sub> is used in operational UAQM (Geng et al., 2021; Jena et al., 2021). In addition to pollutants, satellite images of dust, wildfire data help understand the emission sources (Engel-Cox et al., 2004).

Continuous emission monitoring system (CEMS) data from industries is accessed by regulatory agencies for compliance and mitigation actions. Control measure reports include compliance data of periodic site visits (e.g., power plants). Non-numeric data, such as information on inspection of laboratory infrastructure, show cause or closure notice to polluters and environmental

<sup>3</sup><https://prana.cpcb.gov.in/#/home>.

<sup>4</sup><https://iudx.org.in/>.

**TABLE 1 |** User-specific decision support system functionalities.

Stakeholder	Application service use cases
City environment manager	<ul style="list-style-type: none"> <li>• Ward-wise emission source-concentration data analysis—past and future projection</li> <li>• Road segment real-time emission load and concentration information with a pollution heat map</li> <li>• Low emission zone area and tax planning</li> <li>• Ward-wise AQI trend analysis</li> <li>• Control measure efficacy analysis with GIS plots for applicability and expected % reduction</li> <li>• Current and model prediction data-based graded action plan for mitigation</li> <li>• Current and future reduction objectives</li> <li>• Urban planning with other city departments with “what-if” spatiotemporal scenario model output for pollution reduction and health impact assessment</li> <li>• Access past and current emission source and pollution data for tree plantation</li> <li>• Access to health exposure data for compliance (e.g., ban on open burning)</li> <li>• Access to pollution heat maps for planning new monitoring station</li> <li>• Use of drones for pollution abatement in a hotspot area</li> <li>• Sensor calibration data</li> <li>• PUC database</li> </ul>
Health professional	<ul style="list-style-type: none"> <li>• Vulnerable patient treatment with reduced pollution exposure advisory</li> <li>• Asthma trigger alert</li> <li>• Mental health analysis and advisory</li> <li>• “What-if” scenario pollution exposure and disease correlation analysis</li> </ul>
City transport department	<ul style="list-style-type: none"> <li>• “What-if” scenario model output for route planning</li> <li>• Design of low emission zones</li> <li>• Directing traffic to alternate routes in extreme pollution episodes through command and control</li> <li>• Transport service authorization linked to PUC certification</li> <li>• Planning multi-modal trips minimizing air pollution</li> </ul>
City energy department	<ul style="list-style-type: none"> <li>• Dynamic carbon footprint driven energy costing</li> <li>• Access to urban heat island data and energy usage for demand-supply management</li> <li>• Pollution scenario-based energy pricing</li> <li>• Future energy scenarios and GHG emissions of the city</li> </ul>
Traffic department	<ul style="list-style-type: none"> <li>• Less polluted route navigation advisory</li> <li>• Emission-pollution data-based congestion management</li> <li>• PUC database</li> </ul>
Urban planner	<ul style="list-style-type: none"> <li>• What-if scenario-green space planning</li> <li>• Planning waste management sites based on pollution heat maps</li> <li>• What if scenario analysis for walkway and cycle track planning</li> <li>• New building permission based on the pollution footprints</li> <li>• Infrastructure related control measure efficacy analysis</li> </ul>
Infrastructure department	<ul style="list-style-type: none"> <li>• What-if scenario-building permission based on UHI and emission projections</li> <li>• Low emission zone planning based on pollution trend analysis and hotspot information</li> </ul>
Regulatory agencies	<ul style="list-style-type: none"> <li>• Emission standard compliance data analysis</li> <li>• New industry approval based on what-if scenario of emission projections</li> <li>• Local and non-local emission source characterization data analysis</li> <li>• Trend analysis of toxic air pollutants (e.g., benzene 3-butadiene and formaldehyde)</li> <li>• COVID lockdown city pollution impact trend</li> <li>• Legal cases database and impact analysis</li> </ul>
Health department	<ul style="list-style-type: none"> <li>• Ward-wise pollution exposure data</li> <li>• Vulnerable population information</li> <li>• Ward-wise disease burden</li> <li>• Hospital records</li> <li>• Creating awareness campaigns</li> </ul>
Researchers	<ul style="list-style-type: none"> <li>• Source apportionment data analysis—sub-scale source characterization</li> <li>• Multiscale/multi-sector model workflow selection and execution</li> <li>• Future scenario modeling and assessment</li> <li>• Sub-scale dispersion model skill analysis</li> <li>• Hybrid numerical model and AI model for prediction skill improvement</li> <li>• Health exposure assessment with “what-if” emission reduction scenarios</li> <li>• Sharing of model data with other covariate researchers (e.g., air quality data with health assessment researchers)</li> <li>• Work with city environment department to translate scientific data into information</li> </ul>

(Continued on following page)

**TABLE 1 | (Continued)** User-specific decision support system functionalities.

Stakeholder	Application service use cases
Citizens	<ul style="list-style-type: none"> <li>Air pollution current and future information on a pollution heat map with data and infographics</li> <li>Control measure trend analysis</li> <li>Long-term location specific pollution trend analysis for residence selection</li> <li>Outdoor exercise/activity planning based on sub-scale pollution exposure data projection</li> <li>Geo-fencing based hotspot pollution alert on mobile app</li> <li>Selection of less polluted mobility option</li> <li>Pollution footprint calculation based on mobility choice</li> <li>Less polluted route navigation advisory</li> <li>Emission zone based congestion tax warning on mobile app/city billboards</li> <li>Contribution to monitoring with crowdsourced data feeds</li> <li>Emission and pollution status awareness through AR/VR using city data</li> <li>Reporting of polluting event, e.g., open burning in the locality along with geocoding or photos</li> </ul>
Industry	<ul style="list-style-type: none"> <li>Contributing CEMS data</li> <li>Receiving alerts for reduced production in the event of extreme pollution</li> <li>Contribute the emission monitoring data</li> <li>Access pollution data information for future planning</li> <li>Control measure model scenarios for clean technology adoption</li> </ul>
Non-governmental agencies	<ul style="list-style-type: none"> <li>Governance mitigation action advocacy based on pollution trend analysis</li> <li>Control measure efficacy analysis</li> <li>Outreach for sustainable lifestyle adaption</li> <li>Pollution awareness for reduced exposure actions</li> <li>Contribution to city pollution reduction goal setting using monitoring, control measure data, and current and future efficacy projections</li> </ul>

clearance records of industry, building, and commercial establishments such as malls, and public hearing records from critical governance database (Verma, 2021).

#### 4.1.2.2 Field Campaign

This includes special study or campaign datasets such as emission inventory (EI), specific emission source impact (e.g., construction-based pollutant level), and health impact assessment data such as mortality, emergency visits, and affected population. Granular EI has activity data from emission sources multiplied by emission factor to give emission loads in each city grid for various pollutants (**Supplementary Tables S5, S8**). Periodic EI with activity data of anthropogenic sources: mobility, open burning, residential heating, diesel generators, traffic, vehicle type, restaurants, business activities, and natural sources such as wildfire and dust storm are required for source attribution, dispersion modeling, and mitigation assessment (Dalvi et al., 2006; Behera et al., 2011).

In addition, the UAQM data repository includes historical monitoring datasets and metadata such as short- and long-term control measure impact efficacy analysis. Source apportionment datasets with laboratory reports and receptor models characterizing the city emission sources with source profiles are needed for planning mitigation actions (Mircea et al., 2020). A health exposure assessment database is prepared with disease characterization attributed to particular air pollutants and hospital records (Braithwaite et al., 2019; Katoto et al., 2021). It also includes newer sources of personal physiological impact information from wearable devices (Ranscombe, 2019).

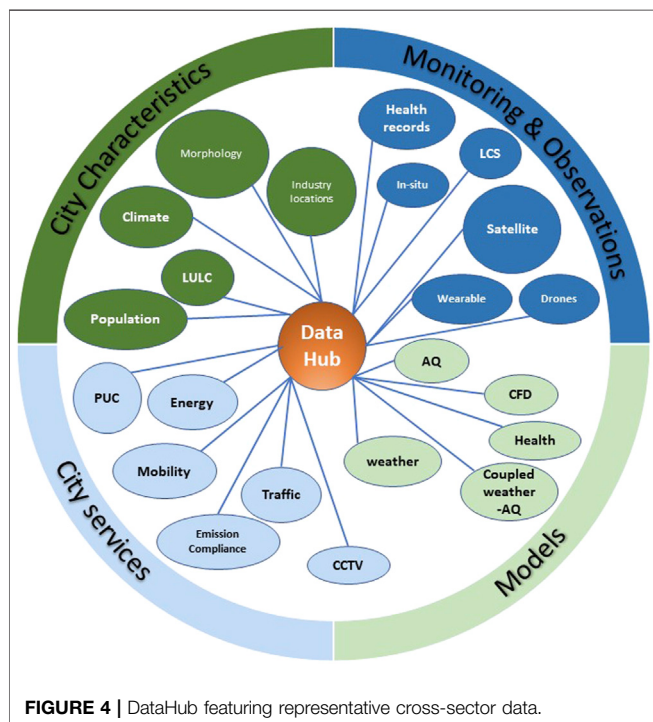
#### 4.1.2.3 Crowdsourcing

This includes two types of observations: 1) pollution sensing using LCS and mobile phones and 2) health impact information through wearable devices, mobile phones, and social media. These are further classified as passive and active data (Ghermandi and Sinclair, 2019). Examples of passive data include social media streaming (sky images, emission source photos, Tweets, and sentiments), smartphone activity data, google activity data, and citizen feedback, for example, extreme pollution event, traffic congestion, and open burning from these datasets (Jiang et al., 2015; Charitidis et al., 2019). Examples of active data include specific purposes, for example, pollution impact on vulnerable population such as school or focused study of control measure efficacy (Wu Y. C. et al., 2015; Alexeff et al., 2018; Castell et al., 2018; Dirks et al., 2018). It also includes data streaming from crowdsourced LCS websites.<sup>5</sup>

#### 4.1.3 Modeling

Modeling data is used for three major purposes: understanding the pollution sources, assessing their impacts, and predicting future conditions. These datasets can be long (1–3 months), medium (3–10 days), short (1–3 days), and nowcasting (6–12 h). It includes multiscale (global, regional, and local) weather prediction, real-time and future projection air quality model data, multi-observation atmospheric and chemical data assimilation, health impact, emission factors, and chemical

<sup>5</sup>[openaq.org](https://openaq.org), <https://ncap.carboncopy.info/caaqms/>.



profiles (Baklanov and Zhang, 2020) (**Supplementary Table S3**). Meteorology data consist of wind speed, direction, turbulence, surface and boundary layer temperature, precipitation, humidity, cloud cover, reflectivity, boundary layer depth, and mixing height affecting pollutant concentration. Boundary layer and lower mixing heights influence the pollutant concentration, and wind speed and direction are responsible for its transport (Oke et al., 2017).

Source apportionment data generated in campaign mode with chemical mass balance models giving source characterization estimates of particulate matter with ions, metals, carbon-specific composition data, and chemical profiles of different emission sources (Pipalatkar et al., 2014; Gargava and Rajagopalan, 2016) form a critical database.

Health exposure assessment model data with mortality, morbidity, and disability-adjusted life years prediction information (Fotopoulos et al., 2016) are the most critical data required for policy decisions and mitigation efficacy analysis. In addition, information on bio air allergens transmissions combined with chemical pollution forms a health database for clinical advisory (Klein et al., 2012).

#### 4.1.4 City services

These databases include static and dynamic data generated by city service departments or national ministries. It consists of fuel type information, vehicle emission standards, sector-wise emission standards, emission factors, daily road segment traffic count, CCTV images, energy demand-supply data, mobility data from smartcards, hospital records, congestion information, different LCS certification data, pollution under control data, smartphone

activity data from vendors, Twitter feeds, multi-modal ridership system, route navigation, control measures implementation current and future plans, types of emissions sources to which they are applied and its socioeconomic impact, yearly urban environmental status report, industry regularization reports, air quality Right to Information responses from government departments, and hazardous waste management data (Verma, 2021) (**Supplementary Table S4**).

## 4.2 Technologies

Before answering the second research question of “How can technologies be optimally connected for cross-sector data acquisition, aggregation, processing, modeling, stakeholder participation, and dissemination?” we first discuss the technology potential in this section. The 4IR technologies, in addition to traditional technologies, enable seamless access of cross-sector data (**Section 4.1**) and faster processing of data.

### 4.2.1 IoT

IoT with ubiquitous measurements and faster communication enables more granular and better-informed decisions. We consider two types of IoT devices in SmartAirQ: LCS and wearable devices.

LCS provide cheaper and more flexible monitoring options complimenting the expensive reference-grade stations (Hagan et al., 2019). Its flexibility to mount on multiple platforms aids in capturing dynamic pollution characteristics for campaign studies (Apte et al., 2017). SmartAirQ considers LCS for non-regulatory monitoring, hotspots identification, pollution impact assessment on a vulnerable population, awareness, selection of location for regulatory stations, citizen sensing, health exposure assessment, and control measure efficacy analysis (Morawska et al., 2018).

IoT-based wearable devices enable cost-effective epidemiological and individual exposure assessment (Haghi et al., 2018). Wearable devices aid practitioners in the personalized treatment of pollution-related allergies and respiratory diseases (Piedrahita et al., 2014). SmartAirQ will enable the processing of health parameters data derived from crowdsourced data with data privacy and security protocols.

### 4.2.2 Smartphones

SmartAirQ processes smartphone mobility data to predict traffic-related pollution levels to quantify neighborhood-scale mitigation and geotagged photos for exposure guidance (Donaire-Gonzalez et al., 2016; Gately et al., 2017). They are also effective via media for crowdsourcing LCS data, photos, awareness, and real-time data dissemination through mobile App.

<sup>8</sup><https://catalogue.iudx.org.in/>.

**TABLE 2 |** Extreme pollution alert use case.

SmartAirQ plane	Use case processes	Actors/enabling service
Data acquisition	<ul style="list-style-type: none"> <li>- Monitoring sub-service accesses</li> <li>- <i>In situ</i>, smart city LCS data, crowdsourced LCS, satellite data</li> <li>- Haze images from phone</li> <li>- Twitter and Facebook posts</li>   <li>- Hotspot pre simulated model scenario data</li> <li>- Past extreme pollution observation data</li> <li>- GIS data</li> <li>- Traffic sensors and CCTV images</li> <li>- Covariate data from city data repository and smart city services</li> <li>- Hyper-scale air quality model and hotspot CFD model prediction data</li> <li>- Hotspot pollution level training datasets</li> <li>- Data from transport models</li> <li>- Control measures action repository</li> <li>- City socioeconomic data with demographic data</li> </ul>	Regulatory agency Meteorology service IUDX <sup>4</sup> City municipality data service (smart city command and control centre) Scientific platform Social media analytics Big data repository
Data communication and aggregation	<ul style="list-style-type: none"> <li>- Internet, WiFi, Bluetooth, ftp using National Knowledge network</li> <li>- Data wrangling and normalization with uniform gridding</li> <li>- Monitoring and modeling data classification</li> </ul>	Smart city communication service Edge processing IoT broker services
Data processing and Management	<ul style="list-style-type: none"> <li>- Data calibration using ML methods</li> <li>- Pollution heat maps with exceedance data calculation</li> <li>- Correlation of pollution levels with emission source information such as industry, dust, traffic, CCTV, route information, open burning, solid waste</li> <li>- Impact data correlation such as vulnerable population, traffic pattern using OpenStreetMap</li> </ul>	Data analytics service City environment manager
Intelligence	<ul style="list-style-type: none"> <li>-Pollution heat maps with monitoring data and ML methods</li> <li>-AQI calculation using NO<sub>x</sub>, SO<sub>2</sub>, CO<sub>2</sub>, O<sub>3</sub>, PM<sub>10</sub>, and PM<sub>2.5</sub> data of previous day observation, air quality model predicted data, weather observations, and ML methods</li> <li>-Flagging off of extreme polluted current and predicted areas using data mining and pattern recognition algorithm operated on pre-calculated CFD model scenarios on city environment department interface</li> <li>-User-specific advisory preparation based on ML driven intelligence advisory using model predicted data, covariate data such as traffic flow, solid waste, industry emission, economy, weather, vulnerable population, social information, cost-benefit data of various control scenarios with their spatiotemporal data analysis</li> </ul>	AI services
Application services	<ul style="list-style-type: none"> <li>- City environment engineer triggers the three-tier graded action plan to application plane using control measure service module mapped with predicted pollutions for implementing graded action: immediate, in 3 days and 10 days</li> <li>- Control measure implementation advisory is shared with different service interfaces in push mode, such as transport department gets an advisory alert on its dashboard for real-time rerouting of traffic; based on pollution load on road sectors automatic traffic signal synchronization for congestion management; and emission zone surcharge display through phone navigation or billboard display for citizens, highly polluted industries and their location</li> <li>- Automated messaging alerts are disseminated via email, websites, Facebook, twitter, radio, mobile app through publishing service</li> <li>- Extreme pollution location with AQI and alert is communicated to health practitioners as shared service</li> <li>- Citizens access the alerts, AQI information in the local language, and the pollution heat map through mobile phone or portal or city displays for planning outdoor activities</li> </ul>	Intelligence service  service  City environment Manager  Traffic Department  Industry pollution regulation authority Health professionals Citizens

#### 4.2.3 Social Media

Social media provides a new avenue to gather pollution information (Wang et al., 2017; Charitidis et al., 2019). The best practice example shared in the stakeholder interview,

showed that the real time traffic information extracted from the Google mobility data can help city transport planners with better public bus fleet management. The semantic analysis of tweets can be used for mental health impact analysis (Du et al.,

**TABLE 3 |** Model as a Service HPC-cloud use case.

SmartAirQ plane	Use case processes	Actor/enabling service
Data acquisition	<ul style="list-style-type: none"> <li>- <i>In situ</i>, smart city LCS, satellite data (MODIS, LandSAT) initial and boundary conditions from global ensemble weather forecast model</li> <li>- Chemical boundary conditions from the global Mozart model</li> <li>- Global and local EI</li> <li>- Satellite-derived fire EI</li> <li>- Population data</li> <li>- Hospital health records</li> <li>- Transport model data</li> </ul>	Regulatory agencies, meteorology agencies for global model initial conditions
Data communication and aggregation	<ul style="list-style-type: none"> <li>- ftp, API, internet</li> <li>- Data wrangling with data classification</li> <li>- Data calibration using ML methods</li> <li>- Uniform gridding using land use regression methods</li> <li>- Temporal classification (24 h average/8 h average)</li> <li>- Units synchronization</li> </ul>	Intelligence plane, cloud services
Data processing and management	<ul style="list-style-type: none"> <li>- Weather and chemical data assimilation of satellite, <i>in situ</i> and smart city LCS monitoring data</li> <li>- LCZ using WUDAPT tool (Ching et al., 2018)</li> <li>- Regional WRF-Chem simulation for airshed region using EI and meteorology data (<b>Figure 5</b>)</li> <li>- “What-if” scenario simulation with integrated WRF-Chem, bio weather, health exposure assessment model, and transport model</li> <li>- Selection of computing resources using HPC-cloud service workflow</li> <li>- Simulated data model repository with lossless compression</li> </ul>	Air quality researcher, health researcher
Intelligence plane	<ul style="list-style-type: none"> <li>- Data fusion of <i>in situ</i>, LCS, and satellite monitoring data using ML methods</li> <li>- Mapping of real-time gridded data with pre-calculated hotspot air quality simulations of CFD model with data from WRF-Chem model as input</li> <li>- Applying ML-based bias correction to CFD model output for improving prediction accuracy</li> <li>- Best fit selection using ML method such K-NN using previous years' daily data for training and previous day air quality and weather observation is selected for accurate data prediction and for creating future projection pollution heat maps using GIS</li> <li>- AQI calculation using model</li> <li>- Linking air quality model output with transport model output for creating polluted route information</li> </ul>	Hybrid modeling service, city municipality data service (smart city command and control center)
Application service	<ul style="list-style-type: none"> <li>- Model simulated gridded predicted and control scenario projection data mapping to place of interest with pollution heat map</li> <li>- Visualization using 3D animation and VR software to view the pollution transport across the city, e.g., in a densely built area</li> <li>- Uploading of model-simulated data onto the DSS and dashboard service</li> <li>- Selection of less polluted data service</li> </ul>	National, regional, and local regulatory board members, citizen

2016; Upadhyay and Upadhyay, 2017; Zheng et al., 2019). These datasets, in addition to other data in SmartAirQ DSS, enable city managers to plan, evaluate the mitigation, and build awareness.

#### 4.2.4 Satellite

Satellite data give concentration information along the column of satellite sensors and on the ground. Geostationary satellite datasets from NASA AQUA/MERRA MODIS and Sentinel-5P, NOAA GOES-R, Hamamury, and CALLIPSO give continuous remote sensed observations of AOD, PM<sub>2.5</sub>, PM<sub>10</sub>, OC, BC, NO<sub>2</sub>, SO<sub>2</sub>, NH<sub>3</sub>, CO, VOC, and dust, aiding in emission trend analysis, filling the observation gaps, sub-scale health exposure, and identifying non-local sources (Wiedinmyer et al., 2011; Kulkarni et al., 2020). NASA

Landsat datasets characterize LULC features, source apportionment, and extreme events (Gupta et al., 2006; Jena et al., 2021). SmartAirQ has satellite-based LULC data creation; data fusion of *in situ*, LCS, drones, ground sun photometer, and satellite data to create granular pollution maps; and data assimilation in models, industry compliance, and health impact assessment (Lau et al., 2019). Recently, 1 km PM2.5 MODIS retrieved datasets for two decades for India will be accessed through SmartAirQ (Dey et al., 2020).

#### 4.2.5 Crowdsourcing

Citizen science brings an opportunity to conduct participative governance, including policy design, awareness, and impact assessment (Mahajan et al., 2020; Lepenies and Zakari, 2021).

**TABLE 4 |** Multi-variate data analysis use case.

SmartAirQ plane	Use case processes	Actors/enabling service
Data acquisition	<ul style="list-style-type: none"> <li>- Smartphone activity data (Google activity data), GPS data, CCTV images, <i>in situ</i>, smart city LCS and weather observation data, traffic sensor, toll/emission zone RFID data through real-time streaming</li> <li>- Social media posts, images</li> <li>- Transport model data</li> </ul>	<ul style="list-style-type: none"> <li>- IUDX<sup>8</sup></li> <li>- Regulatory agencies, meteorological institutes</li> <li>- Smart city traffic management service</li> <li>- Crowdsourcing</li> </ul>
Data communication and aggregation	<ul style="list-style-type: none"> <li>- ftp, API, internet, WiFi, Bluetooth, cellular network</li> <li>- Data wrangling with data classification</li> <li>- Data calibration using ML methods</li> <li>- Uniform gridding using land use regression methods</li> <li>- Temporal classification (24 h average/8 h average)</li> <li>- Units synchronization</li> </ul>	<ul style="list-style-type: none"> <li>- Smart city ICT centre (command and control centre)</li> </ul>
Data processing and management	<ul style="list-style-type: none"> <li>- Real-time traffic data from sensors and CCTV images are accessed and tagged with date, time, geospatial parameters</li> <li>- The data are dynamically classified with image processing for classifying 2, 3, 4W, buses, trucks, number plate recognition using ML methods. The data also include crowdsourced congestion images shared by citizens from smartphones and extracted from social media posts</li> <li>- Using the gridded monitoring and traffic data, real-time traffic emission estimates are prepared. These data along with EI and dispersion model output are used to create pollution load estimates along all road sectors. These estimates are then correlated with satellite data extracted from AOD. Together, gridded dataset is created by pollution load across the city grid</li> </ul>	<ul style="list-style-type: none"> <li>- Data fusion service citizens</li> </ul>
Intelligence plane	<ul style="list-style-type: none"> <li>- Hyper-local gridded pollution heat map is created using data fusion of different monitoring source data</li> <li>- Data fusion methods are also applied for curating traffic data from traffic sensors, CCTV images, toll data, and modeling data</li> <li>- Using GPS navigation data, the travel time estimation of different routes with start and destination points are created using covariate data from the GPS data and ML methods and pollution route with time to travel dataset are created</li> <li>- Geofencing with emission zone calculation</li> </ul>	<ul style="list-style-type: none"> <li>- AI services</li> </ul>
Application service	<ul style="list-style-type: none"> <li>- The alert information is pushed through mobile navigation app for drivers to choose the routes</li> <li>- Geofencing application alerts citizen about hotspot areas nearby and advise to take actions such as wearing mask</li> <li>- Updated pollution maps on web portal and mobile app</li> <li>- Emission zone toll charge activation</li> </ul>	<ul style="list-style-type: none"> <li>- DSS service</li> <li>- State regulatory agencies</li> <li>- City environment department</li> <li>- Smart city command and control centre</li> <li>- Traffic police department</li> <li>- Citizens</li> </ul>

SmartAirQ enables crowdsourced emission-pollution monitoring through LCS, mobile phone photos, and health impact data acquisition.

#### 4.2.6 Big Data and AI/ML

With the data mining of scientific and governance data, the urban big data has utility in context-aware data-driven services such as UAQM (Rathore et al., 2018). The UAQM data have big data characteristics of large volume, variety with heterogenous data, velocity with faster data processing, variability due to covariate data dependency, and veracity with data privacy and security (Fazziki et al., 2015; Octaviano et al., 2020). SmartAirQ data architecture builds on the big data principles and technologies such as Hadoop/MongoDB, SPARK, for real-time data processing using cloud computing (Asgari et al., 2017; Huang et al., 2018; Silva et al., 2018).

Hitherto, pollution studies and operational services were limited to *in situ* observations and coarser models. With the capability to interpret structured and unstructured data, ML methods are used for data mining of large data by training the data and pattern recognition. By building diagnostic, descriptive, prescriptive, and predictive models from it, they enable better actions (Sebestyén et al., 2021). For instance, Liu et al. (2021) developed a correlation analysis of PM10, SO<sub>2</sub>, NO<sub>2</sub>, and O<sub>3</sub> and showed improvement in prediction data efficiency up to 86% by applying regression models with reference-grade data and other covariate data, such as meteorology using artificial neural network. SmartAirQ uses such ML methods across UAQM lifecycle, namely, random forest in improving LCS calibration (Zimmerman et al., 2018), data fusion (Johansson et al., 2015; Lau et al., 2019), parametrization (Wang et al., 2019), bias correction (Haupt et al., 2021; Xu et al., 2021), extracting information from

unstructured data (Zheng et al., 2019), epidemiology (Bellinger et al., 2017), and data sharing within the IoT devices (Ravi et al., 2017).

#### 4.2.7 Cloud Computing

The computing concept increasingly transitions to “moving analysis to the data” rather than “data to analysis.” SmartAirQ has cloud services with Data as a Service (DaaS), Model as a Service (MaaS), and Platform as a Service (PaaS) connecting to IoT devices, real-time and legacy data, models, and model output to provide last mile services (Liu et al., 2017). It supports data reusability through standardized data workflows, user-specific metadata creation, and sharing. SmartAirQ architecture has service orchestration tools linking with smart city services such as transport, health, economy, and energy. The technology stack has cloud services and processing tools (**Supplementary Table S6**).

#### 4.2.8 Models

Modeling is an important tool for understanding environmental processes and predicting future conditions. SmartAirQ includes HPC-cloud service with cross-sector, multiscale statistical, and numerical models such as weather, global, regional, and local air quality models and health impact assessment models (Baklanov and Zhang, 2020). The top-down source apportionment method with receptor modeling compares chemical and physical sample properties with emission sources giving the type of the source and its contribution information used in campaign mode (Gargava and Rajagopalan, 2016).

The urban scale dispersion models use downscaled data of initial and boundary conditions, emissions, observational data assimilation, and chemical and physical equation calculations, such as 3D turbulence, convection, boundary layer calculations, transport, and urban heat island influences (Li H. et al., 2020; Ghude et al., 2020; Ramacher et al., 2021). Hyper-local computational fluid dynamics (CFD) models capture pollutant flow around buildings and ventilation coefficient (Santiago et al., 2017). SmartAirQ includes health exposure assessment methods to understand the cause-effect and the disease burden (Smith et al., 2017; Ramos et al., 2018).

#### 4.2.9 Decision Support System

Worldwide, DSS with model-based prediction and information systems are gaining importance in air quality governance activities (AirNow; Baklanov et al., 2020; LondonAir; Molina et al., 2019). For example, Zheng et al. (2015) developed an air quality prediction system using machine learning algorithm application on current and past air quality and covariate data such as point of interest, meteorology, traffic flow, and roads. By integrating traditional data sources such as ground observation and chemistry models with satellite, social media, and LCS data, a prototype for hyper-local air pollution DSS (APDSS) for Hong Kong has advanced data analytics and mining methods (Leung et al., 2018). Through highlighting the importance of health risks,

the SMURBS<sup>6</sup> system has an urban atlas derived from the fusion of satellite data and sub-local exposure assessment data, real-time LCS calibration tool, and emergency action module for industrial accidents with data fusion of CAMS model, citizen observatory, Sentinel-5P and MODIS data, and real-time source apportionment. However, these modules appear as independent components, and an integrated DSS facility is not evident. Furthermore, very few of these go beyond the information portal and include interactive data communication leveraging the 4IR technology for sectorial decisions (Zheng et al., 2015; Leung et al., 2018; Che et al., 2020).

The proposed SmartAirQ framework has not only the best of the above features but also a multi-user secure and interactive science cloud and linked operational service facility harnessing cross-sector pollution mitigation and its integrated assessment, including socioeconomic impacts supported by multiscale modeling and data governance.

## 5 SmartAirQ ARCHITECTURE

The triangulation method synthesis addresses the third research question of What can be the overarching design of UC-enabled UAQM as a standard platform, scalable across smart cities?

The literature prompts increasing interest in smart city architecture (Santana et al., 2017; Habibzadeh et al., 2019). However, its application context is often generic in nature or addresses a single aspect of technology such as big data, IoT, or AI (Fazziki et al., 2015; Ang and Seng, 2016; Dwevedi et al., 2018). The SmartAirQ outlined in this study incorporates integrated multiple 4IR technology applications by considering two major aspects: scientific ecosystem and governance services executed through HPC-cloud resources.

The SmartAirQ has utilities for national, regional, and local users with bi-directional knowledge exchanges between governance-governance (among different functional agencies), citizens-governance (active participation and feedback), and governance-citizens (dissemination). It builds on the living lab concept, i.e., 1) creating value for stakeholders, 2) considering end users as active partners, and 3) creating open processes for interconnected socio-technological systems (Jensen and Campbell, 2019; Steuri et al., 2020).

SmartAirQ system has a cloud-based plug-play ecosystem for data analytics, modeling, aggregation, and user-specific information built on advanced HPC resources and 4IR technologies. It supports a data platform to create, simulate, contribute, integrate, and disseminate data and metadata, enabling cross-sector applications of pollution reduction actions and policies (**Figure 5**). The SmartAirQ is designed around modularity and flexibility as technology leapfrogs.

SmartAirQ has adopted multiple data planes typology with service-oriented architecture (Habibzadeh et al., 2019). Some planes operate independently and some as cross-functional

<sup>6</sup><https://smurbs.eu/solutions/>.

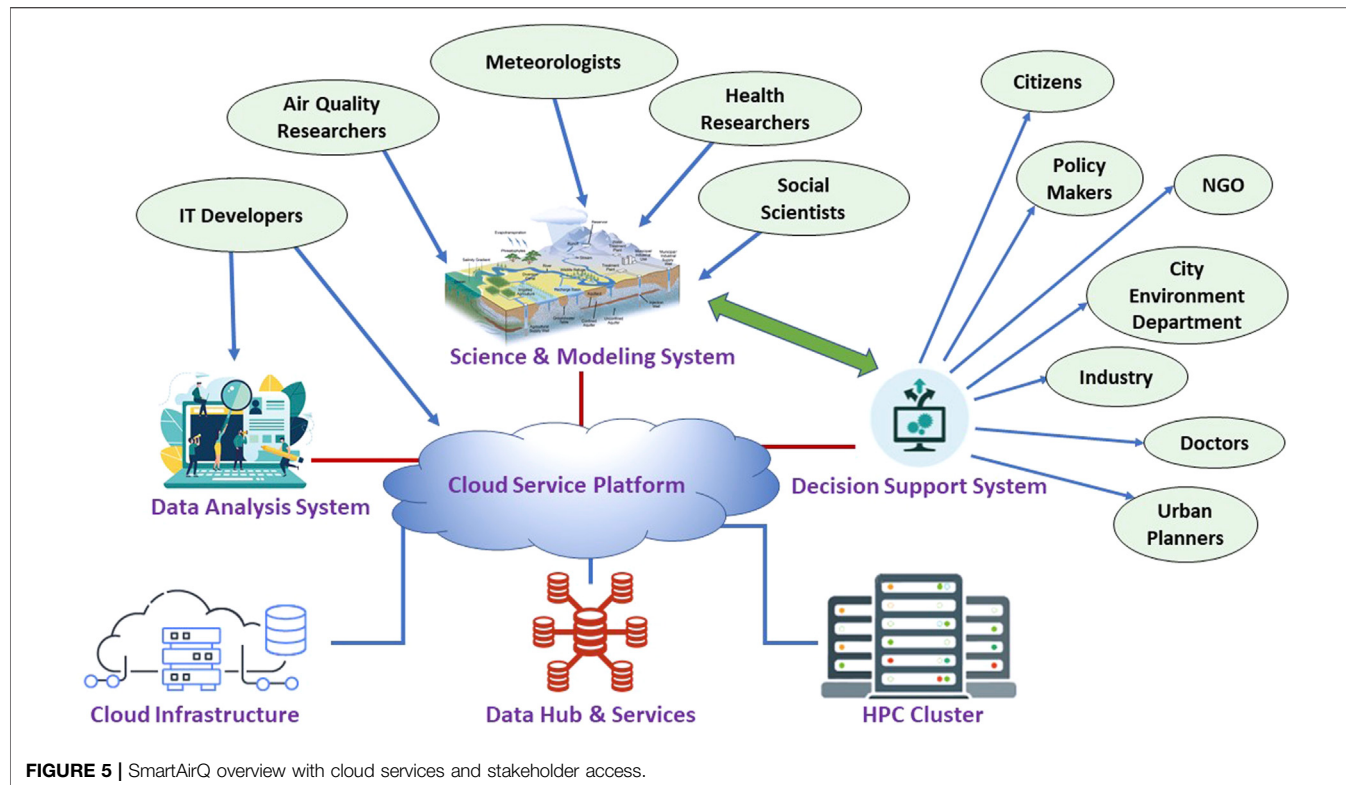


**FIGURE 5 |** SmartAirQ overview with cloud services and stakeholder access.

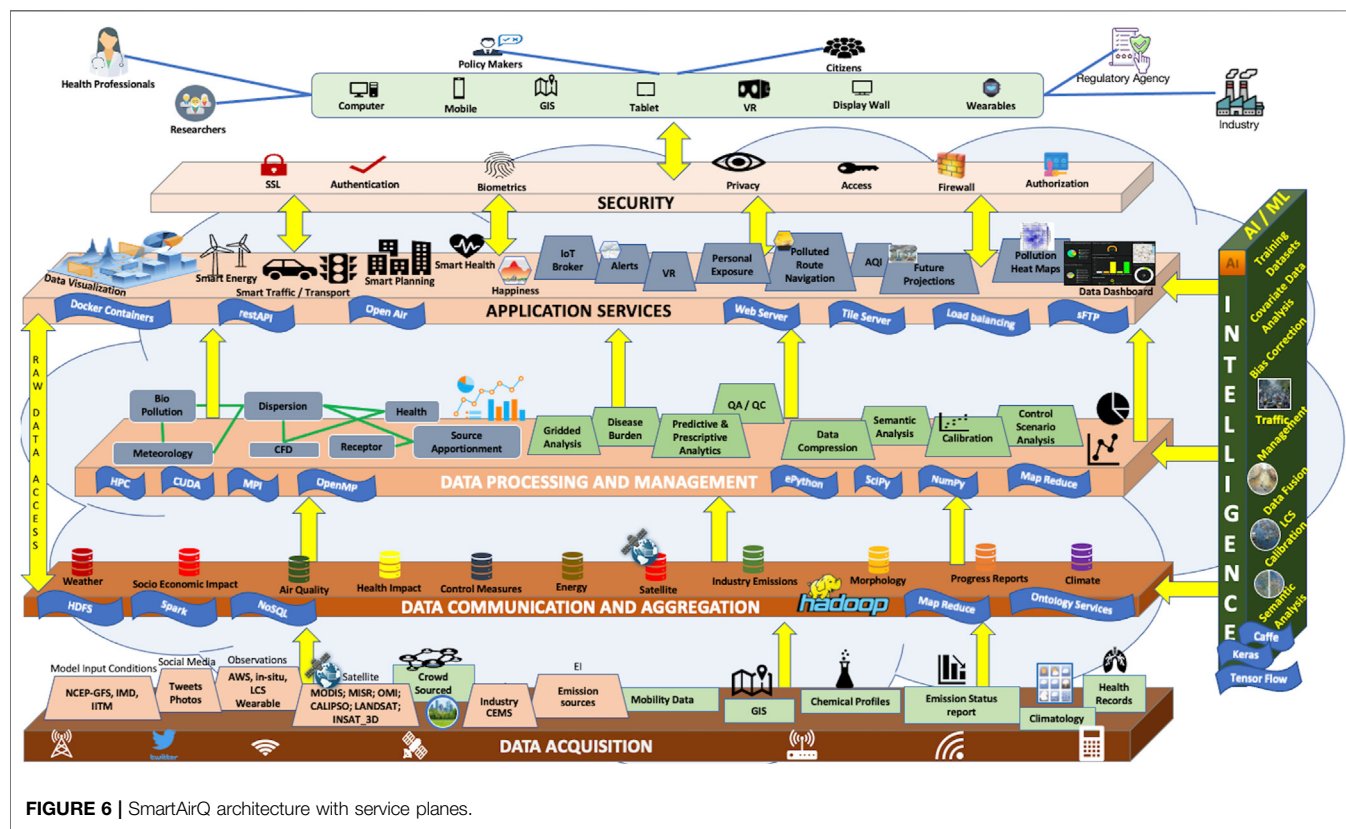


**FIGURE 6 |** SmartAirQ architecture with service planes.

services (**Figure 6**). The data planes are characterized as (DI) data acquisition plane, (DII) communication and aggregation plane, (DIII) data processing and management plane, and (DIV) application service plane with visualization. These planes are supported by three cross-functional planes: (DA) intelligence plane, (DB) data security and privacy, and (DC) HPC-cloud service.

## 5.1 Data Acquisition Plane (DI)

Cross-sector data is collected from varied sources such as *in situ* stations, LCS, weather observations, wearable devices, smartphones, social media, different model outputs, government records, city infrastructures, people, radars, surveys, satellites, and GIS (**Section 4.1**). Each dataset has different formats, access types, measurement intervals, and time scales such as real-time, past, and future data (**Supplementary Table S7**). These datasets are accessed through open websites, ftp protocols, or service interfaces to IoT devices or other smart city databases through RestAPI and Spark streaming for social media or data portals. Acquired data are mapped to Open Geospatial Consortium (OGC) standards (van der Schaaf and Herzog, 2015) and IoT standards such as SensorThingsAPI (Kotsev et al., 2018).

The data undergoes quality checks by removing garbage data, range validation, missing values, and removing outliers. The basic statistical methods such as root mean square error, correlation coefficient, and mean bias are applied to check the data quality. The LCS data is correlated with co-located reference-grade stations for accuracy purpose. This plane has provision for citizens to submit crowdsourced monitoring and impact data. The data is anonymized with a coding key.

## 5.2 Communication and Aggregation Plane (DII)

This plane connects data from the acquisition plane to the cloud environment. For real-time processing, low latency and high throughput bandwidth is critical. The data from various sources are communicated to the cloud layer through WiFi, 4G/5G network, internet, Bluetooth, or FTP. The data transmission from the IoT network is facilitated by a gateway using a wireless sensor network and IoT service broker.

Then, the data are compressed or decompressed, stored, normalized, and classified. It is classified as raw data or metadata with data format information using data standards (WCCD, 2021). The data classification has multiple ontologies, such as parameter-wise, emission source types, ward-wise, geotagged photos and tweets, exposure types, same temporal interval, or same functionality datasets, for example, global, regional, and urban weather, air quality model output, and control measure scenarios. Data interoperability considers various levels such as physical parameter, syntax, semantic, pragmatic, dynamicity, spatial, temporal intervals, and data constraints (Laniak et al., 2013). The interoperability is achieved through the sensor web framework of Open

Geospatial Consortium, Web coverage service standards, and API.

This layer has APIs for sharing the data with other smart city services to process and manage interoperability issues.

## 5.3 Data Processing and Management Plane (DIII)

This plane connects data from the communication plane and creates metadata in response to the query from the application service plane. It performs multi-functional processing using mash-up web services methods (described below) with service and user interface orchestration for integrating different city services using the Hadoop environment (Atrouche et al., 2015). The processing includes predictive, prescriptive, and inferential analysis. This plane also has database management and storage services using the HPC-cloud platform. The cloud services are supported by Kubernetes and Docker tools. This plane encompasses a variety of data processing methods presented below.

### 5.3.1 Calibration

The monitoring data quality is improved by calibration methods, such as range test, based on local climatic conditions by mining historical extremes; single sensor and sensor network spatial calibration using linear regression coefficients with reference-grade sensors and land use data (Masiol et al., 2018; Chu et al., 2020); and persistence testing applied by calculating standard deviation below the critical threshold, least square regression (Morawska et al., 2018; Hagan et al., 2019), and multiple regression trees (Simmhan et al., 2019). It also includes CEMS sensor location calibration against standards deployment protocols. This layer has statistical methods to fill gaps in real-time and monitoring data either using historical data mining or co-located station data.

### 5.3.2 Data analytics

The application query triggers different data processing methods, including pollutant trend analysis, correlation, regression, multivariate data analysis of weather, air quality, transport, health exposure, energy cause-effect analysis, and interpolation to create uniform gridded datasets. The statistical analysis is performed using openAir libraries (Carslaw and Ropkins, 2012). This layer includes control measure efficacy analysis in preventing and reducing polluting incidences, such as “what-if” analysis change in vehicle emission standards and the impact on air pollution levels in a region. Pollution heat maps of all the criteria pollutants are processed for uniform gridding across the city using the inverse-distance-weighting method and calculated from past, current, or future data created from pollution data fusion (**Section 5.4**).

This plane enables real-time micro-environment exposure calculation based on real-time pollution data (**Section 5.4**), mobility data, social media, wearable device data, and pushing alerts or advisories through the application service plane.

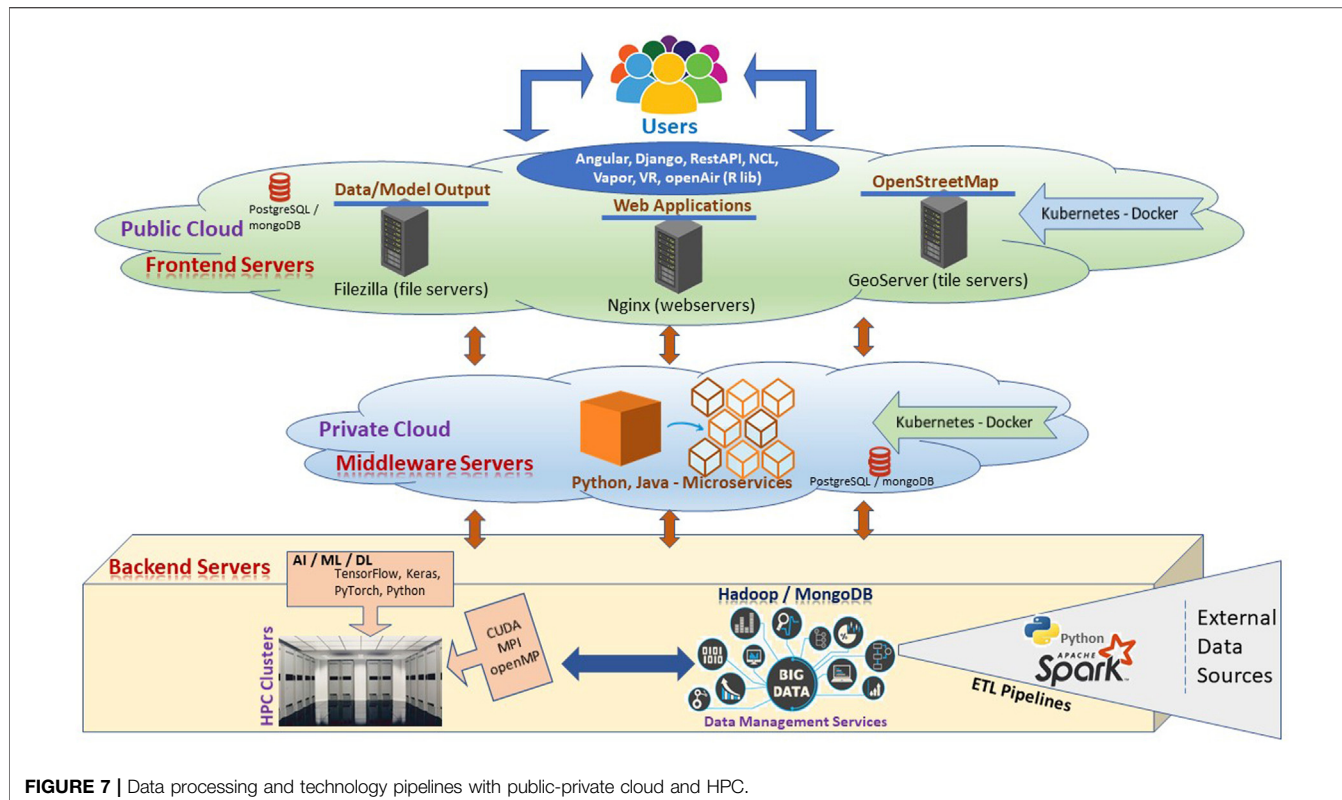


**FIGURE 7 |** Data processing and technology pipelines with public-private cloud and HPC.

### 5.3.3 Crowdsourced Data Processing

This layer conducts quality for the LCS as per the crowdsourcing standards (EPA, 2015; Capineri et al., 2016). Social media posts are processed with natural language processing with taxonomy, language filters, and semantic connections using ML methods (Charitidis et al., 2019; Jiang et al., 2019). The classified data is then mapped to create pollution data and impact database. Local climatic zones (LCZ) with GIS are an important consideration due to their ability to detail the localized LULC (natural and anthropogenic) influences such as building height, building cluster, open spaces, vegetation on pollutant concentration, and dispersion (Wu J. et al., 2015; Shi et al., 2019). Standardized LCZ classification methods and tools, such as World Urban Database and Access Portal Tools (WUDAPT), aid in better representation of LULC using crowdsourced morphological data (Ching et al., 2018).

### 5.3.4 Air Quality Index Calculation

From the observation data, aggregated AQI is calculated for awareness purposes with six categories: good, satisfactory, moderately polluted, poor, very poor, and severe. AQ sub-index and health breakpoints are evolved for eight pollutants (PM<sub>10</sub>, PM<sub>2.5</sub>, NO<sub>2</sub>, SO<sub>2</sub>, CO, O<sub>3</sub>, NH<sub>3</sub>, and Pb). AQI are predicted using past and current AQI, past and current weather and model data, social media feeds, and ML (Kosmidis et al., 2018; Castelli et al., 2020). SmartAirQ system has query-based access to sub-local AQI values using GIS visualization and advisory in infographics form for easy

understanding of impacted community and citizens, such as the decision regarding school closure during extreme pollution situation in Delhi.<sup>7</sup>

### 5.3.5 Workflow Orchestration

In response to the application service triggers, this layer transforms the query requirements, connects different data analytics components, allocates the cloud resources, and automates the input-processing-output tasks with service-oriented architecture services (Zanella et al., 2014). It involves multiple job management with scripting and streaming processing for real-time data access, batch processing, and process optimization for DaaS, PaaS, and MaaS. The MaaS connecting multi-sector model workflows with preprocessing, simulations, and post-processing with model data exchanges has OpenMI2.0 framework (Harpham et al., 2019). The workflows run through the public and private cloud (Figure 7).

- (1) Public cloud: end users will directly interact with the hosted services that will expose various web applications developed with angular, Django/spring boot framework. It will facilitate users with data visualization using NCL graphics, Vapor, and data analytics using openAir R libraries. OpenStreetMap used in visualization will be exposed via GeoServer, and data can be downloaded via ftp servers.

<sup>7</sup><https://timesofindia.indiatimes.com/city/delhi/air-pollution-delhi-schools-to-remain-shut-for-physical-classes-till-further-orders/articleshow/87831917.cms>.

- (2) Private cloud: it will include middleware servers that host several python, java-based microservices deployed as Docker containers, which will be managed by Kubernetes.

### 5.3.6 Modeling

Various modeling interfaces can be integrated within the UAQM (Kaginalkar et al., 2022). The modeling service layer has global weather forecast models and global, regional, and urban air quality models, such as source apportionment, statistical and simple box dispersion and complex chemical transport models, street-level CFD models, bioweather models, health exposure assessment and socioeconomics impact evaluation models (Baklanov and Zhang, 2020). The models are used for source-concentration estimates, future predictions, and what-if control scenario projections. The model workflow has data containers for data acquisition of 1) global data weather forecast and chemistry model datasets; 2) global, regional, and local EI datasets; 3) air quality observations from regulatory stations, LCS, and satellite 4) LULC data derived from LANDSAT datasets; and 5) weather and air quality observations.

SmartAirQ prototype module consists of regional and urban WRF, WRF-Chem model (Grell et al., 2005), and CFD model OPENFOAM<sup>9</sup>. CFD modeling workflows can be invoked in two streams: 1) running online CFD models for the entire city and 2) running CFD models for hotspots as precalculated scenarios and then pattern matching of real-time data using ML methods. It also includes executing the regional-urban-Gaussian dispersion model, such as AERMOD (Cimorelli et al., 2005) to identify multiple hot spots and create sector-specific graded action plans. Users can select further data prediction improvement methods such as hybrid modeling with lognormal/log-logistic statistical distribution model (Julia et al., 2017) for episodic cases or by running AI models (**Section 5.4**).

Further, sub-local air quality models can be coupled with health exposure models such as AirQ (AirQ+) and BENMAP (USEPA, 2014) for estimating exposure and “what-if” scenarios. The model simulated data can be invoked through the query system of the application service plane DSS (**Section 5.5**).

The model's accuracy is improved by atmospheric and chemical data assimilation, data fusion methods, and bias correction using hybrid numeric and ML models. The air quality models are executed in ensembles with different initial conditions. The air quality models are supported by evaluation tools for validation with observation data, such as AMET (USEPA, 2016). The compute workloads needed for various simulations and AI/ML engines using several libraries, such as MPI, openMP, TensorFlow, Keras, CUDA, will be executed on HPC clusters (**Figure 7**).

### 5.3.7 Database Management

Efficient data storage is critical in urban environment data management as, every day, huge amounts of data are created and processed. For example, daily three-day forecast Pune city

with 500 m WRF model generates ~17 GB, whereas ten-day forecast for 400 m WRF-Chem model with a larger national capital region of Delhi using chemical data assimilation attributes to 210 GB. This layer is responsible for storing and arranging data with spatiotemporal, sector-specific, impact-specific labeling. It includes a raw data and metadata repository with a periodic storage policy (e.g., few datasets); weather and air quality observations are required as climatology information for past trend analysis or training ML models. For optimal storage, considering the end-user function of the data, lossy or lossless compression techniques are adopted depending on the data accuracy requirements. SmartAirQ leverages distributed data access, wherein data will not always be stored at a centralized location but organized on multiple physical or virtual infrastructures. The repository also includes information on apps, different model configurations, scripts, and data connection between different models as workflows. Data management services will have a big data framework using Hadoop/MongoDB, which will house the data needed for SmartAirQ. It will also have extraction transformation load (ETL) channels implemented in spark, python, to ingest data into the data store (**Figure 7**).

## 5.4 Intelligence Plane (DA)

This plane runs across all the above planes with AI methods, improving the UAQM functionality and providing value addition to the underlying technologies.

### 5.4.1 LCS and Model Data Calibration

ML-based calibration methods such as support vector machine, random forest, K-nearest neighbor, and geospatial kriging are applied to LCS data and covariate data to improve the accuracy (Maag et al., 2018; Zoest et al., 2020).

### 5.4.2 Data Fusion

Overcoming the limitations of various monitoring methods, data fusion processes monitoring data from *in situ* data, campaign study data, satellite data, chemical transport models, and smart city air quality LCS data using ML methods to create gridded datasets of PM<sub>2.5</sub>, PM<sub>10</sub>, NO<sub>2</sub>, CO<sub>2</sub>, SO<sub>2</sub>, and O<sub>3</sub> (Li et al., 2017; Schneider et al., 2020; Viqueira et al., 2020).

Data fusion is executed in two ways: offline and real-time. Generally, in the offline mode, data used in specific campaigns are fused to create a newer dataset. For example, LCS, drones data, and mobile LCS data on vehicles are combined to create an emission source spatiotemporal map. These datasets are then used to train the dataset for real-time feature extraction in data fusion methods (Lau et al., 2019; Geng et al., 2021). Then, the data created by data fusion method is compared with the in-situ station data.

### 5.4.3 Cross-Sector Data Processing

Pollution reduction is dependent on emission source-concentration information. Building scale LULC data is prepared using satellite data and ML methods (Kerins et al., 2020). This layer performs spatial (roads, buildings, place of interest, and types of roads) and temporal classifiers based on

<sup>9</sup><https://www.openfoam.com>.

artificial neural network and regression methods on cross-variate data training models to improve pollutant concentration predictability (Zheng et al., 2015). In this layer, ML methods K-nearest neighbor and long short-term memory are applied for traffic density assessment by vehicle count from traffic sensor data, trajectory analysis, and visual classification from CCTV images from smart city command and control data services for congestion prediction (Majumdar et al., 2021). These datasets are linked to pollutant level datasets and GIS data for less polluted route navigation and emission zone surcharge advisory on the mobile app.

LCS and social media data are used to identify emission sources and control measures. This layer includes content extraction and pattern recognition using natural language processing and semantic analysis using ML methods (Zheng et al., 2019). Data are then correlated to pollution concentration data to predict future AQI and health impact assessment data to be used by city managers and by health practitioners (Yan et al., 2019). Satellite-derived emission source data and pollutant and LULC data are correlated with CEMS data for compliance monitoring (Kurinji and Ganguly, 2020).

This plane has provision for health impact data processing using hospital records, traffic sensor data, mobile phone activity data, wearable device data, ridership data, real-time and historical meteorology data, social media, and gridded pollution data generated from the data fusion layer and using ML methods such as random forest, support vector machine, and multiple regression methods giving pollution exposure information at a location and time (Hu et al., 2014; Masiol et al., 2018).

#### 5.4.4 Hybrid Models

ML methods are applied to air quality models, such as WRF-Chem, to improve predictability by bias correction and for faster processing (Ma et al., 2020). The processing is executed using Keras, TensorFlow, PyTorch, NumPy, python scripts, and CUDA environment.

The data processing pipelines involve various tools and libraries, as shown in **Figure 7 (Supplementary Table S6)**.

### 5.5 Application Service Plane (DIV)

Data processed in previous planes is accessed through a service layer of the decision support system. This multi-user interactive layer is activated through a GUI with query system, scheduler, GIS, and data orchestration through the portal or mobile app service (**Table 1**). The application services include sector-specific raw data and metadata access and visualization. Public services include alerts, pollution monitoring data, pollutant comparison between different locations, exceptional events, future prediction, and control scenario projection in the form of pollution concentration maps, infographics, and virtual reality such as dispersion trend analysis in a hotspot area. The pollution maps created through data fusion of IoT data, model output, and satellite, mapped with interactive GIS, enable citizens to access localized pollution information through the query system, such as deciding to reduce exposure (e.g., avoiding outdoor exercise at selected location and time).

This smart city system has varied connotations for different stakeholders, for example, for air quality researchers, improving the accuracy of model prediction using high-resolution models executed on advanced HPC systems or using innovative methods using 4IR technology for reducing pollution impact. In contrast, for non-governmental agencies, it can be vulnerable location metadata derived from daily station data for advocacy purposes or sub-local AQI information to school authorities.

#### 5.5.1 Visualization

Data visualization with GIS is an inherent component of the city's digital platform and DSS. Its usage runs across all the components of SmartAirQ, from EI development to dissemination services (Dalvi et al., 2006; Badach et al., 2020). WebGIS allows full view of the city, standardized data access, interactive location-specific query, and navigation (Gkatzoflias et al., 2013). SmartAirQ architecture considers it a vertical plane running across all other service planes.

Visual representation of data is triggered by user query or sector-specific action in the form of infographics, plots, 3D animation, augmented reality and virtual reality (AR/VR), time-series graphs, trend analysis, correlation, exceedance, prediction information, industry compliance reports, and AQI display (Elbir et al., 2010; Li W. et al., 2020). The dynamic visualization includes interactive navigation displaying pollutant information along all the routes with an expected time of arrival information. The application service has a restful API for data exchanges. The scientific plots are viewed through Vapor/NCL.

### 5.6 Data Privacy and Security Plane (DB)

As soon as the data are accessed, they are anonymized with system-driven ID and personal or system-specific details, such as department name, and the authority name is coded into the independent key by applying cryptography algorithms (Toma et al., 2019). The data has multi-layer authorization. In an example of a collaborative research case, first, the researcher creates EI with activity data and emission factors in their own restricted space. Second, the researcher provides permission to access this derived EI data to the authorized member from the city environment department through a password protection mechanism. In the future, blockchain methods for secure data communications can be explored (Benedict et al., 2019).

## 6 USE CASES

Moving now from theory to practice, we present use-case scenarios that illustrate the applicability of the SmartAirQ framework in UAQM functions.

These use cases present the cross-sector functionality orchestration and decision services specific to the user category. The consolidated actions undergo step-wise data translation through different planes and technology applications. The examples of use cases are drawn from

**Table 1.** These use cases have stakeholders, users, and smart city service components as actors. This section discusses the example of the use case of emission control measure mitigation. Additional use cases are presented in Tables 2–4.

## 6.1 Emission Control Measure Mitigation Process Flow

### 6.1.1 Description

For pollution mitigation and its efficacy assessment, large data must be brought together, linked, and inferred in the context in which it is applied, which requires an efficient database management system maneuvering cross-sector data and metadata.

In this use case, the control measures selection process is instrumented by a local environment manager, considering the business as usual scenario or future scenario projection data analytics. It accesses the pre-simulated future projections using dispersion models.

### 6.1.2 Data and Functionality Pathways

Emission factors and EI activity data generated from source apportionment studies are uploaded by researchers through the data acquisition plane (Figure 8). The system applies data wrangling and data classification methods by data mining of source categories and sub-categories. The city environment manager selects business as usual scenarios and control scenarios. The data are processed in the data processing plane with a calculation of emission load, reduction factor, and applicability ratio. Based on the query and user-selected pollutant type, source type from the area, point or line, scenario type, such as the closure of construction work in a fixed time or banning diesel vehicles, emission factor selection, and analytics mode, such as emission load in kg/year or ton/day, a cumulated scenario is generated (Figure 9). The backend calculations are executed using WRF-Chem and AERMOD models projected simulations using cloud resources, and analytics is conducted using R libraries.

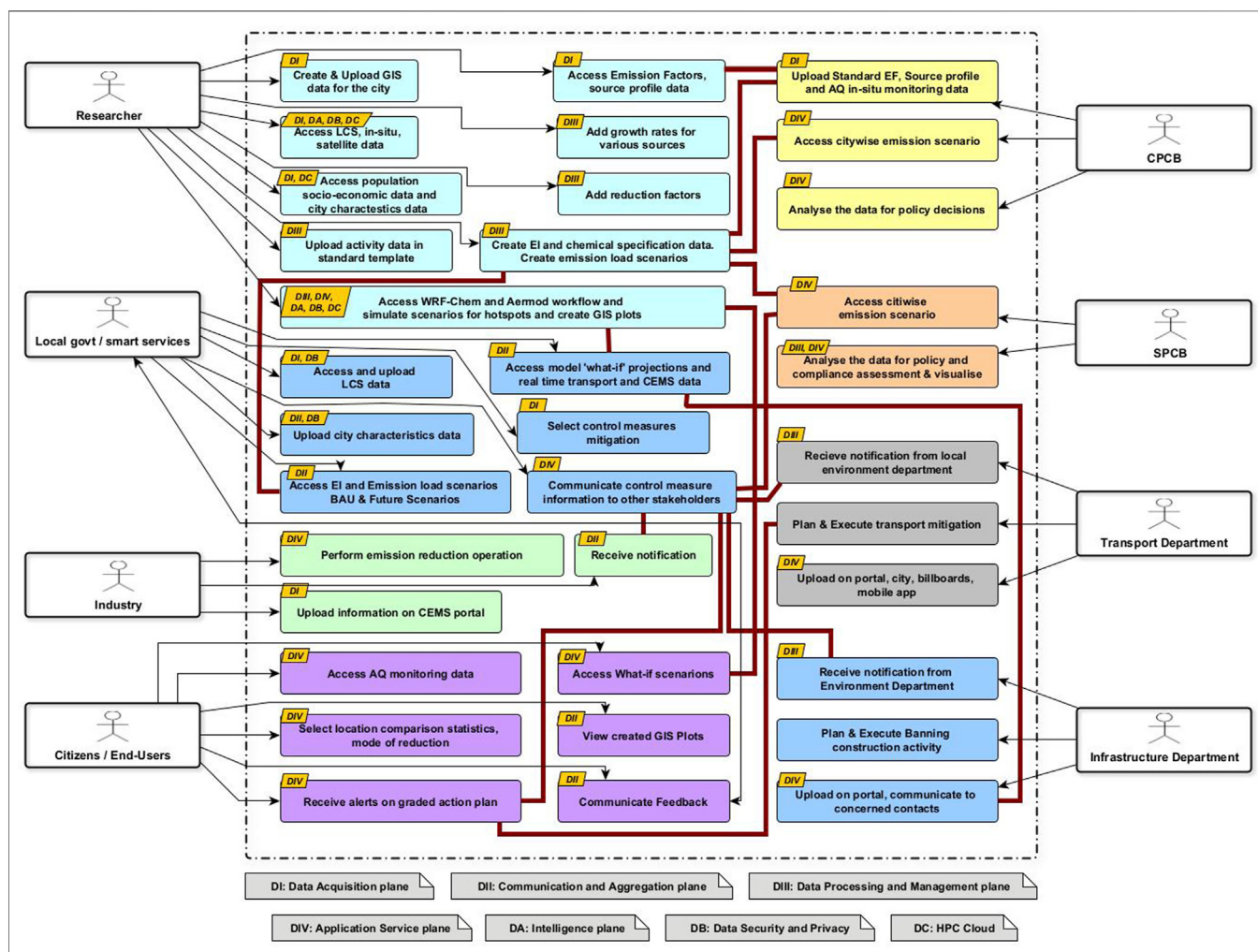


**FIGURE 8 |** Cross-sector stakeholder functions for control scenarios orchestrated through the SmartAirQ planes.

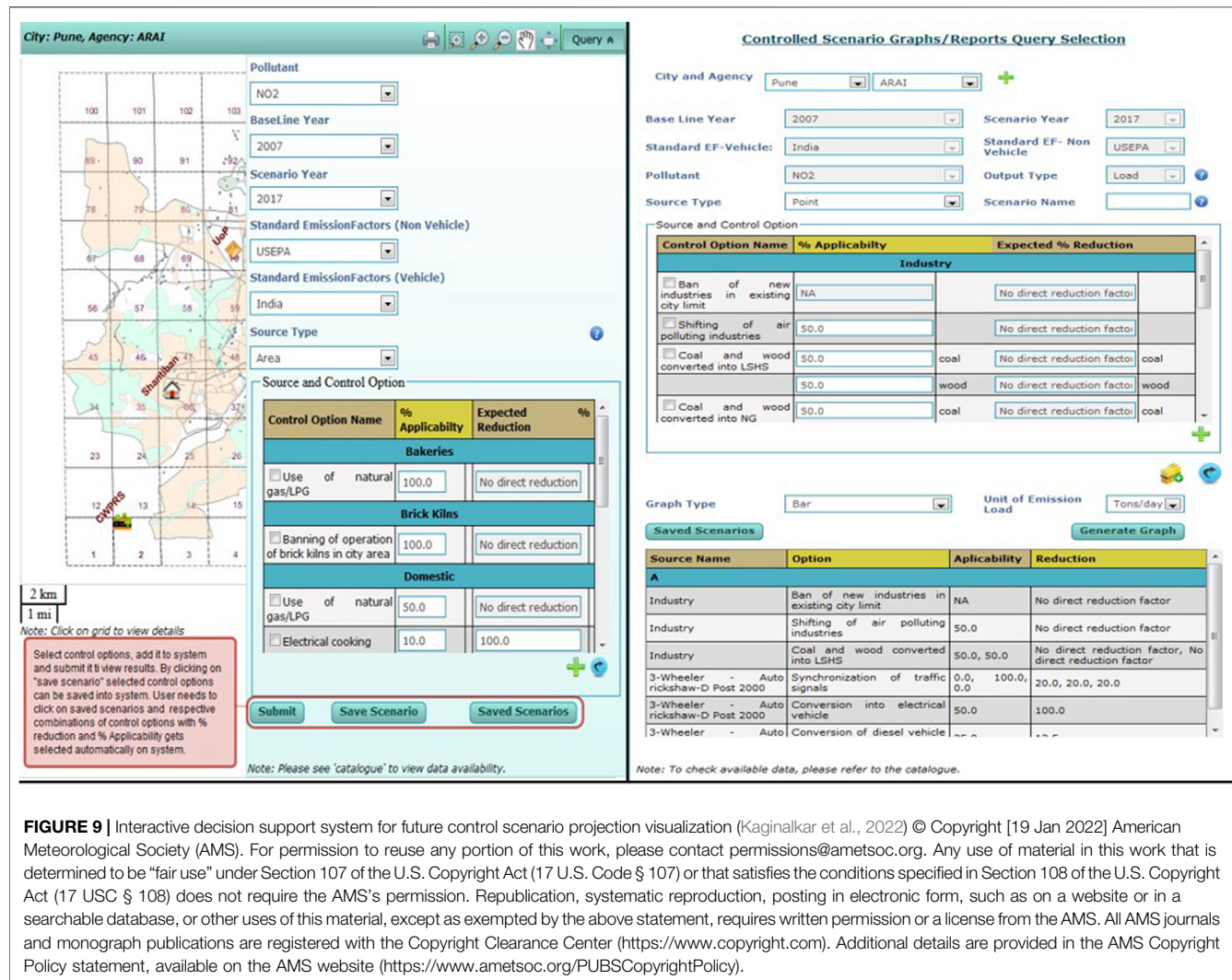


**FIGURE 9 |** Interactive decision support system for future control scenario projection visualization (Kaginalkar et al., 2022) © Copyright [19 Jan 2022] American Meteorological Society (AMS). For permission to reuse any portion of this work, please contact permissions@ametsoc.org. Any use of material in this work that is determined to be “fair use” under Section 107 of the U.S. Copyright Act (17 U.S. Code § 107) or that satisfies the conditions specified in Section 108 of the U.S. Copyright Act (17 USC § 108) does not require the AMS’s permission. Republication, systematic reproduction, posting in electronic form, such as on a website or in a searchable database, or other uses of this material, except as exempted by the above statement, requires written permission or a license from the AMS. All AMS journals and monograph publications are registered with the Copyright Clearance Center (<https://www.copyright.com>). Additional details are provided in the AMS Copyright Policy statement, available on the AMS website (<https://www.ametsoc.org/PUBSCopyrightPolicy>).

### 6.1.3 Outcome

The total % reduction is displayed either as plots or GIS-based heat maps (Figure 9). In the decision chain, the manager links the data with energy, transport, traffic, infrastructure department, and state pollution control board members. The concerned stakeholders view the applicability and feasibility of control measures with interactive pollutant, source, control scenarios selection, comparison between two locations, and so forth. The selected control measures are then implemented by respective stakeholders.

### 6.2 Extreme Pollution

This use case involves an extreme pollution event in a city. In response, the orchestration of services from the city environment manager, traffic manager, scientists, citizens, and SmartAirQ middleware services are executed, as shown in Table 2.

### 6.3 Modeling

In real-time operations, there can be a trade-off between models due to computational complexity. This use case involves scientists

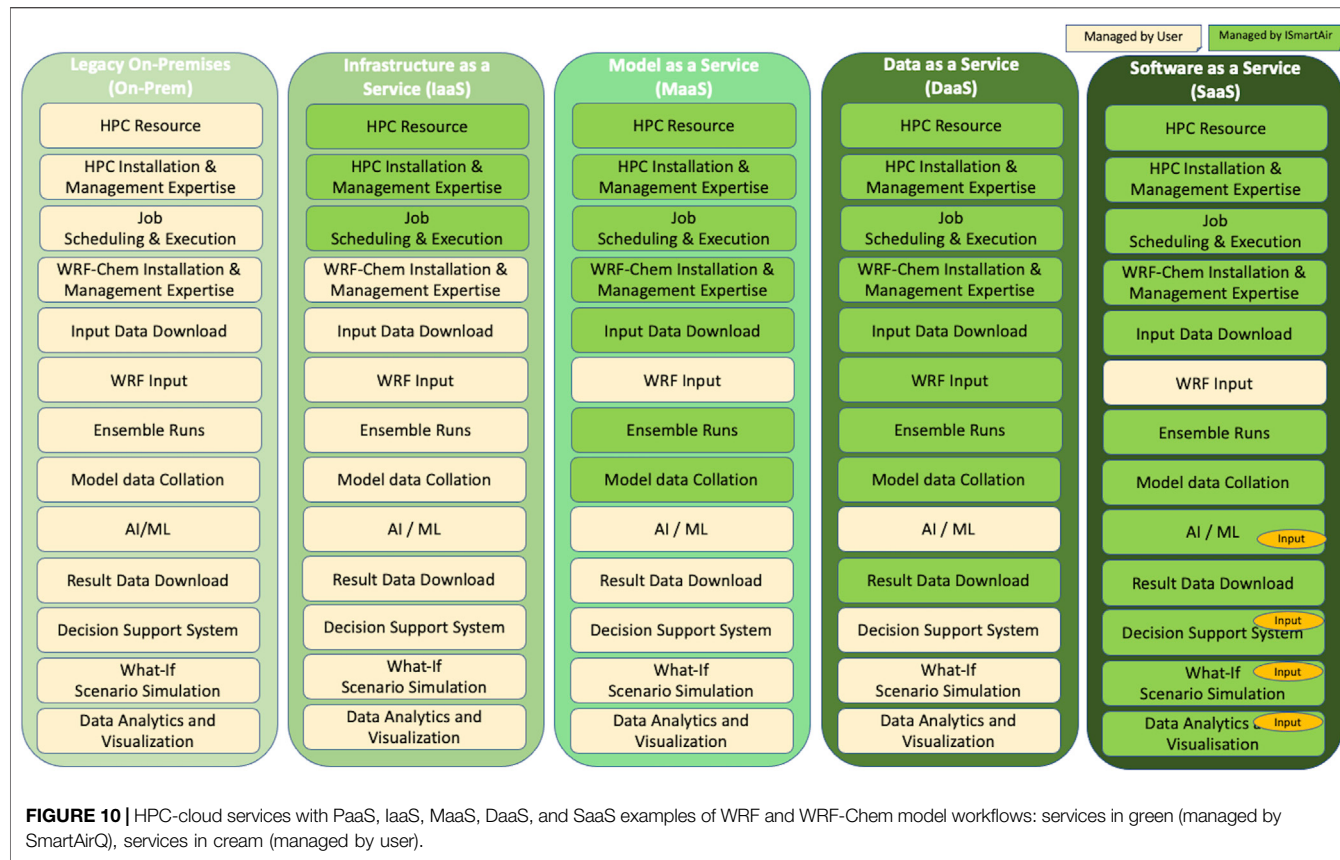
running model workflows (Table 3) using standard operating procedures at different entry points on HPC-cloud (Figure 10).

### 6.4 Traffic Management

This involves data processing and management, intelligence plane, smart city service, and citizens as actors (Table 4).

## 7 SUMMARY

For successful environmental services in smart cities, seamless data exchanges and their systematic interpretation for cross-sectorial decisions are essential. UAQM is a multidimensional service involving policy formulation, monitoring, prediction, awareness, enforcement, health impact assessment, and mitigation. In the backdrop of NCAP and India’s smart city mission, it is imperative to develop an integrated open data and smart city information ecosystem for UAQM.



This study presented SmartAirQ, a conceptual integrated data governance and 4IR technology framework for air quality smart city service. It is primarily for researchers, policymakers, and governance to enable actions for end-users such as non-governmental organizations, citizens, and health practitioners. The big data and cloud platform built within SmartAirQ provide scalable, interoperable, sustainable, and affordable solutions for scientific and last-mile services. The cloud services enable participative UAQM governance with data reuse and shared computing resources, reducing the carbon footprint.

The data governance architecture opens up avenues to formulate, implement, and evaluate control measures for future actions and in real time at various scales and sectors. SmartAirQ facilitates the inclusion of newer data and citizen science information into the governance realm with monitoring, exposure information, and perception. Its predictive hybrid numerical and AI modeling system enables cause (source apportionment) to effect (air quality prediction) to impact (health assessment models) value chain for hyper-local pollution risk reduction. It brings two critical components under UAQM data governance: cross-sector data with the computing ecosystem and stakeholders as co-producers/co-owners of data.

Well-defined data governance, harmonizing disparate data, is the first step toward sustainable smart cities. With ever-increasing urban data, a framework such as SmartAirQ is an exemplary co-created smart city service with context-dependent solutions for environmental issues that go beyond the monitoring and modeling data information portal. The SmartAirQ flexible architecture is scalable across world cities, aiding in efforts toward Sustainable development goals.

Although this conceptual framework is designed for ambient urban air pollution, our follow-up work will report on the interaction between the ambient and indoor air quality and system deployment experiences.

The recent WHO global air quality guidelines (WHO, 2021) call for technologically driven, science-society collaborative actions for pollution reduction. The SmartAirQ framework is apt to facilitate these translations for an effective UAQM.

## AUTHOR CONTRIBUTIONS

AK conceptualized and developed the manuscript with formal analysis. AK and NK contributed to the visualization. SK, PG, and DN contributed to the review and revision of the draft.

## ACKNOWLEDGMENTS

AK acknowledges the support of colleagues from C-DAC, Pune, and faculty of Institute of Environment Education and Research, Bharati Vidyapeeth Deemed University, Pune, India. AK acknowledges the participation of the stakeholders in the research. AK and NK thank the National Supercomputing Mission program, India. DN acknowledges India DST National Network Program on Urban Climate, US NSF, and the NASA Interdisciplinary Sciences program. Authors appreciate

the time and efforts of the editor and the reviewers for their valuable suggestion to improve the quality of the paper.

## SUPPLEMENTARY MATERIAL

The Supplementary Material for this article can be found online at: <https://www.frontiersin.org/articles/10.3389/fenvs.2022.785129/full#supplementary-material>

## REFERENCES

- Achakulwisut, P., Brauer, M., Hystad, P., and Anenberg, S. C. (2019). Global, National, and Urban Burdens of Paediatric Asthma Incidence Attributable to Ambient NO<sub>2</sub> Pollution: Estimates from Global Datasets. *Lancet Planet. Health.* 3, e166–e178. doi:10.1016/s2542-5196(19)30046-4
- Ahlgren, B., Hidell, M., and Ngai, E. C.-H. (2016). Internet of Things for Smart Cities: Interoperability and Open Data. *IEEE Internet Comput.* 20, 52–56. doi:10.1109/mic.2016.124
- AirNow. Home Page | AirNow.Gov. [WWW Document]. URL Available at: <https://www.airnow.gov/> (accessed 9/10, 20)
- AirQ+. AirQ+: Software Tool for Health Risk Assessment of Air Pollution. [WWW Document]. URL Available at: <https://www.euro.who.int/en/health-topics/environment-and-health/air-quality/activities/airq-software-tool-for-health-risk-assessment-of-air-pollution> (accessed 22/7, 21).
- Albino, V., Berardi, U., and Dangelico, R. M. (2015). Smart Cities: Definitions, Dimensions, Performance, and Initiatives. *J. Urban Technology.* 22, 3–21. doi:10.1080/10630732.2014.942092
- Alexeff, S. E., Roy, A., Shan, J., Liu, X., Messier, K., Apte, J. S., et al. (2018). High-resolution Mapping of Traffic Related Air Pollution with Google Street View Cars and Incidence of Cardiovascular Events within Neighborhoods in Oakland, CA. *Environ. Health.* 17, 38. doi:10.1186/s12940-018-0382-1
- Allam, Z., and Dhunny, Z. A. (2019). On Big Data, Artificial Intelligence and Smart Cities. *Cities.* 89, 80–91. doi:10.1016/j.cities.2019.01.032
- Alvear, O., Calafate, C. T., Cano, J.-C., and Manzoni, P. (2018). Crowdsensing in Smart Cities: Overview, Platforms, and Environment Sensing Issues. *Sensors* 18 (2), 460. doi:10.3390/s18020460
- Ameer, S., Shah, M. A., Khan, A., Song, H., Maple, C., Islam, S. U., et al. (2019). Comparative Analysis of Machine Learning Techniques for Predicting Air Quality in Smart Cities. *IEEE Access* 7, 128325–128338. doi:10.1109/access.2019.2925082
- Anenberg, S. C., Achakulwisut, P., Brauer, M., Moran, D., Apte, J. S., and Henze, D. K. (2019). Particulate Matter-Attributable Mortality and Relationships with Carbon Dioxide in 250 Urban Areas Worldwide. *Sci. Rep.* 9, 11552–11556. doi:10.1038/s41598-019-48057-9
- Ang, L.-M., and Seng, K. P. (2016). Big Sensor Data Applications in Urban Environments. *Big Data Res.* 4, 1–12. doi:10.1016/j.bdr.2015.12.003
- Apte, J. S., Messier, K. P., Gani, S., Brauer, M., Kirchstetter, T. W., Lunden, M. M., et al. (2017). High-Resolution Air Pollution Mapping with Google Street View Cars: Exploiting Big Data. *Environ. Sci. Technol.* 51, 6999–7008. doi:10.1021/acs.est.7b00891
- Asgari, M., Farnagh, M., and Ghaemi, Z. (2017). “Predictive Mapping of Urban Air Pollution Using Apache Spark on a Hadoop Cluster,” in Proceedings of the 2017 International Conference on Cloud and Big Data Computing, ICCBCD 2017 (London, United Kingdom: Association for Computing Machinery), 89–93. doi:10.1145/3141128.3141131
- Atrouche, A., Idoughi, D., and David, B. (2015). “A Mashup-Based Application for the the Smart City Problematic,” in *Human-Computer Interaction: Interaction Technologies. HCI 2015. Lecture Notes in Computer Science*. Editor M. Kurosu. (Cham: Springer), 9170. doi:10.1007/978-3-319-20916-6\_63
- Azevedo Guedes, A., Carvalho Alvarenga, J., Dos Santos Sgarbi Goulart, M., Rodriguez y Rodriguez, M., and Pereira Soares, C. (2018). Smart Cities: The Main Drivers for Increasing the Intelligence of Cities. *Sustainability* 10, 3121. doi:10.3390/su10093121
- Badach, J., Voordeckers, D., Nyka, L., and Van Acker, M. (2020). A Framework for Air Quality Management Zones - Useful GIS-Based Tool for Urban Planning: Case Studies in Antwerp and Gdańsk. *Building Environ.* 174, 106743. doi:10.1016/j.buildenv.2020.106743
- Badii, C., Bellini, P., Difino, A., Nesi, P., Pantaleo, G., and Paolucci, M. (2019). MicroServices Suite for Smart City Applications. *Sensors*. 19, 4798. doi:10.3390/s19214798
- Baklanov, A., Cárdenas, B., Lee, T.-c., Leroyer, S., Masson, V., Molina, L. T., et al. (2020). Integrated Urban Services: Experience from Four Cities on Different Continents. *Urban Clim.* 32, 100610. doi:10.1016/j.ulclim.2020.100610
- Baklanov, A., Grimmond, C. S. B., Carlson, D., Terblanche, D., Tang, X., Bouchet, V., et al. (2018). From Urban Meteorology, Climate and Environment Research to Integrated City Services. *Urban Clim.* 23, 330–341. doi:10.1016/j.ulclim.2017.05.004
- Baklanov, A., Molina, L. T., and Gauss, M. (2016). Megacities, Air Quality and Climate. *Atmos. Environ.* 126, 235–249. doi:10.1016/j.atmosenv.2015.11.059
- Baklanov, A., and Zhang, Y. (2020). Advances in Air Quality Modeling and Forecasting. *Glob. Transitions.* 2, 261–270. doi:10.1016/j.glt.2020.11.001
- Balakrishnan, K., Dey, S., Gupta, T., Dhaliwal, R. S., Brauer, M., Cohen, A. J., et al. (2019). The Impact of Air Pollution on Deaths, Disease burden, and Life Expectancy across the States of India: The Global Burden of Disease Study 2017. *Lancet Planet. Health.* 3, e26–e39. doi:10.1016/S2542-5196(18)30261-4
- Ballejos, L. C., and Montagna, J. M. (2011). Modeling Stakeholders for Information Systems Design Processes. *Requirements Eng.* 16, 281–296. doi:10.1007/s00766-011-0123-2
- Baškarada, S. (2014). Qualitative Case Study Guidelines. *The Qualitative Report.* 19, 1–18. doi:10.46743/2160-3715/2014.1008
- Behera, S. N., Sharma, M., Dikshit, O., and Shukla, S. P. (2011). GIS-Based Emission Inventory, Dispersion Modeling, and Assessment for Source Contributions of Particulate Matter in an Urban Environment. *Water Air Soil Pollut.* 218, 423–436. doi:10.1007/s11270-010-0656-x
- Beig, G., Chate, D. M., Sahu, S. K., Parkhi, N. S., Srinivas, R., Kausar, S., et al. (2015). System of Air Quality Forecasting and Research (SAFAR – India). *WMO GAW* 217, 51. [https://mce2.org/wmogurme/images/reports/GAW\\_217%20\(SAFAR\).pdf](https://mce2.org/wmogurme/images/reports/GAW_217%20(SAFAR).pdf).
- Bellinger, C., Mohamed Jabbar, M. S., Zaïane, O., and Osornio-Vargas, A. (2017). A Systematic Review of Data Mining and Machine Learning for Air Pollution Epidemiology. *BMC Public Health* 17, 907. doi:10.1186/s12889-017-4914-3
- Benedict, S., Rumaise, P., and Kaur, J. (2019). “IoT Blockchain Solution for Air Quality Monitoring in SmartCities,” in 2019 IEEE International Conference on Advanced Networks and Telecommunications Systems (ANTS), 1–6. doi:10.1109/ANTS47819.2019.9118148
- Bibri, S. E., and Krogstie, J. (2020). The Emerging Data-Driven Smart City and its Innovative Applied Solutions for Sustainability: the Cases of London and Barcelona. *Energy Inform* 3, 5. doi:10.1186/s42162-020-00108-6
- Bibri, S. E. (2019). The Sciences Underlying Smart Sustainable Urbanism: Unprecedented Paradigmatic and Scholarly Shifts in Light of Big Data Science and Analytics. *Smart Cities* 2, 179–213. doi:10.3390/smartcities2020013
- Braithwaite, I., Zhang, S., Kirkbride, J. B., Osborn, D. P. J., and Hayes, J. F. (2019). Air Pollution (Particulate Matter) Exposure and Associations with Depression, Anxiety, Bipolar, Psychosis and Suicide Risk: A Systematic Review and Meta-Analysis. *Environ. Health Perspect.* 127, 126002. doi:10.1289/EHP4595
- Capineri, C., Haklay, M., Huang, H., Antoniou, V., Kettunen, J., Ostermann, F., et al. (2016). “Introduction,” in *European Handbook of Crowdsourced*

- Geographic Information.* Editors C. Capineri, M. Haklay, H. Huang, V. Antoniou, J. Kettunen, and F. Ostermann. (London: Ubiquity Press), 1–11. doi:10.5334/bax.a
- Cárdenas Rodríguez, M., Dupont-Courtade, L., and Oueslati, W. (2016). Air Pollution and Urban Structure Linkages: Evidence from European Cities. *Renew. Sustainable Energ. Rev.* 53, 1–9. doi:10.1016/j.rser.2015.07.190
- Carlaw, D. C., and Ropkins, K. (2012). Openair - An R Package for Air Quality Data Analysis. *Environ. Model. Softw.* 27–28, 52–61. doi:10.1016/j.envsoft.2011.09.008
- Castell, N., Schneider, P., Grossberndt, S., Fredriksen, M. F., Sousa-Santos, G., Vogt, M., et al. (2018). Localized Real-Time Information on Outdoor Air Quality at Kindergartens in Oslo, Norway Using Low-Cost Sensor Nodes. *Environ. Res.* 165, 410–419. doi:10.1016/j.enres.2017.10.019
- Castelli, M., Clemente, F. M., Popović, A., Silva, S., and Vanneschi, L. (2020). A Machine Learning Approach to Predict Air Quality in California. *Complexity* 2020, 8049504. doi:10.1155/2020/8049504
- Charitidis, P., Papadopoulos, S., Apostolidis, L., and Kompatsiaris, I. (2019). “Social media Monitoring Tools for Air Quality Accounts,” in IEEE/WIC/ACM International Conference on Web Intelligence - Companion Volume, WI ’19 Companion (Thessaloniki, Greece: Association for Computing Machinery), 215–222. doi:10.1145/3358695.3361106
- Che, W., Frey, H. C., Fung, J. C. H., Ning, Z., Qu, H., Lo, H. K., et al. (2020). PRAISE-HK: A Personalized Real-Time Air Quality Informatics System for Citizen Participation in Exposure and Health Risk Management. *Sustainable Cities Soc.* 54, 101986. doi:10.1016/j.scs.2019.101986
- Ching, J., Mills, G., Bechtel, B., See, L., Feddema, J., Wang, X., et al. (2018). WUDAPT: An Urban Weather, Climate, and Environmental Modeling Infrastructure for the Anthropocene. *Bull. Amer. Meteorol. Soc.* 99, 1907–1924. doi:10.1175/bams-d-16-0236.1
- Cho, D., Yoo, C., Im, J., and Cha, D. H. (2020). Comparative Assessment of Various Machine Learning-Based Bias Correction Methods for Numerical Weather Prediction Model Forecasts of Extreme Air Temperatures in Urban Areas. *Earth Space Sci.* 7, e2019EA000740. doi:10.1029/2019EA000740
- Chu, H.-J., Ali, M. Z., and He, Y.-C. (2020). Spatial Calibration and PM2.5 Mapping of Low-Cost Air Quality Sensors. *Sci. Rep.* 10, 22079. doi:10.1038/s41598-020-79064-w
- CII, Dalberg (2021). Air Pollution and its Impact on Business - The Silent Pandemic. Available at: <https://www.cleanairfund.org/publication/economic-impacts-india/>.
- Cimorelli, A. J., Perry, S. G., Venkatram, A., Weil, J., Paine, R. J., Wilson, R. B., et al. (2005). AERMOD: A Dispersion Model for Industrial Source Applications. Part I: General Model Formulation and Boundary Layer Characterization. *J. Appl. Meteorol.* 44 (5), 682–693. doi:10.1175/JAM2227.1
- Constant, N. (2018). “Role of Citizen Science in Air Quality Monitoring,” in *Urban Pollution* (John Wiley & Sons), 303–312. doi:10.1002/9781119260493.ch23
- CPCB (2019). Report : National clear Air Programme. [WWW Document]. URL Available at: [http://moef.gov.in/wp-content/uploads/2019/05/NCAP\\_Report.pdf](http://moef.gov.in/wp-content/uploads/2019/05/NCAP_Report.pdf)
- Creutzig, F., Lohrey, S., Bai, X., Baklanov, A., Dawson, R., Dhakal, S., et al. (2019). Upscaling Urban Data Science for Global Climate Solutions. *Glob. Sustainability* 2, e2. doi:10.1017/sus.2018.16
- Cui, L., xie, G., Qu, Y., Gao, L., and yang, Y. (2018). Security and Privacy in Smart Cities: Challenges and Opportunities. *IEEE Access* 6, 46134–46145. doi:10.1109/ACCESS.2018.2853985
- Dalvi, M., Beig, G., Patil, U., Kaginalkar, A., Sharma, C., and Mitra, A. P. (2006). A GIS Based Methodology for Gridding of Large-Scale Emission Inventories: Application to Carbon-Monoxide Emissions over Indian Region. *Atmos. Environ.* 40, 2995–3007. doi:10.1016/j.atmosenv.2006.01.013
- Dey, S., Purohit, B., Balyan, P., Dixit, K., Bali, K., Kumar, A., et al. (2020). A Satellite-Based High-Resolution (1-km) Ambient PM2.5 Database for India over Two Decades (2000–2019): Applications for Air Quality Management. *Remote Sensing* 12, 3872. doi:10.3390/rs12233872
- Dirks, K., Salmon, J., and Talbot, N. (2018). Air Pollution Exposure in Walking School Bus Routes: A New Zealand Case Study. *Int. J. Environ. Res. Public Health* 15, 2802. doi:10.3390/ijerph15122802
- Donaire-Gonzalez, D., Valentín, A., de Nazelle, A., Ambros, A., Carrasco-Turigas, G., Seto, E., et al. (2016). Benefits of Mobile Phone Technology for Personal Environmental Monitoring. *JMIR Mhealth Uhealth.* 4, e126. doi:10.2196/mhealth.5771
- Dwevedi, R., Krishna, V., and Kumar, A. (2018). Environment and Big Data: Role in Smart Cities of India. *Resources* 7, 64. doi:10.3390/resources7040064
- Elbir, T., Mangir, N., Kara, M., Simsir, S., Eren, T., and Ozdemir, S. (2010). Development of a GIS-Based Decision Support System for Urban Air Quality Management in the City of Istanbul. *Atmos. Environ.* 44, 441–454. doi:10.1016/j.atmosenv.2009.11.008
- Engel-Cox, J. A., Hoff, R. M., and Haymet, A. D. J. (2004). Recommendations on the Use of Satellite Remote-Sensing Data for Urban Air Quality. *J. Air Waste Management Assoc.* 54, 1360–1371. doi:10.1080/10473289.2004.10471005
- English, P. B., Richardson, M. J., and Garzón-Galvis, C. (2018). From Crowdsourcing to Extreme Citizen Science: Participatory Research for Environmental Health. *Annu. Rev. Public Health* 39, 335–350. doi:10.1146/annurev-publhealth-040617-013702
- EPA (2015). Citizen Science Opportunities for Monitoring Air Quality. Available at: [https://www.epa.gov/sites/default/files/2015-06/documents/citizen\\_science\\_air\\_monitoring\\_factsheet\\_march\\_2015.pdf](https://www.epa.gov/sites/default/files/2015-06/documents/citizen_science_air_monitoring_factsheet_march_2015.pdf)
- Fazziki, A. E., Sadiq, A., Ouarzazi, J., and Sadgal, M. (2015). “A Multi-Agent Framework for a Hadoop Based Air Quality Decision Support System,” in *CAiSE Industry Track*.
- Topopoulou, E., Zafeiropoulos, A., Papaspyros, D., Hasapis, P., Tsoli, G., Bouras, T., et al. (2016). Linked Data Analytics in Interdisciplinary Studies: The Health Impact of Air Pollution in Urban Areas. *IEEE Access* 4, 149–164. doi:10.1109/access.2015.2513439
- Fragomeni, M. B. A., Bernardes, S., Shepherd, J. M., and Rivero, R. (2020). A Collaborative Approach to Heat Response Planning: A Case Study to Understand the Integration of Urban Climatology and Land-Use Planning. *Urban Clim.* 33, 100653. doi:10.1016/j.ulclim.2020.100653
- Gargava, P., and Rajagopalan, V. (2016). Source Apportionment Studies in Six Indian Cities—Drawing Broad Inferences for Urban PM10 Reductions. *Air Qual. Atmos. Health* 9, 471–481. doi:10.1007/s11869-015-0353-4
- Gately, C. K., Hutyra, L. R., Peterson, S., and Sue Wing, I. (2017). Urban Emissions Hotspots: Quantifying Vehicle Congestion and Air Pollution Using mobile Phone GPS Data. *Environ. Pollut.* 229, 496–504. doi:10.1016/j.envpol.2017.05.091
- Geng, G., Xiao, Q., Liu, S., Liu, X., Cheng, J., Zheng, Y., et al. (2021). Tracking Air Pollution in China: Near Real-Time PM2.5 Retrievals from Multisource Data Fusion. *Environ. Sci. Technol.* 55, 12106–12115. doi:10.1021/acs.est.1c01863
- Gharaibeh, A., Salahuddin, M., Hussini, S., Khreishah, A., Khalil, I., Guizani, M., et al. (2017). Smart Cities: A Survey on Data Management, Security and Enabling Technologies. *IEEE Communications Surveys & Tutorials*, 1. doi:10.1109/COMST.2017.2736886
- Ghermandi, A., and Sinclair, M. (2019). Passive Crowdsourcing of Social media in Environmental Research: A Systematic Map. *Glob. Environ. Change* 55, 36–47. doi:10.1016/j.gloenvcha.2019.02.003
- Khude, S. D., Jena, C., Kumar, R., Debnath, S., Soni, V., Nanjundiah, R. S., et al. (2020). “Development of a High-Resolution (400 M) Operational Air Quality Early Warning System for Delhi, India through Integrated Chemical Data Assimilation,” in EGU General Assembly Conference Abstracts, EGU General Assembly Conference Abstracts, 12876.
- Given, L. (2008). *The SAGE Encyclopedia of Qualitative Research Methods*, Vols. 1–0. Thousand Oaks, CA: SAGE Publications, Inc. doi:10.4135/9781412963909
- Gkatzoflias, D., Mellios, G., and Samaras, Z. (2013). Development of a Web GIS Application for Emissions Inventory Spatial Allocation Based on Open Source Software Tools. *Comput. Geosciences* 52, 21–33. doi:10.1016/j.cageo.2012.10.011
- González, J. E., Ramamurthy, P., Bornstein, R. D., Chen, F., Bou-Zeid, E. R., Ghandehari, M., et al. (2021). Urban Climate and Resiliency: A Synthesis Report of State of the Art and Future Research Directions. *Urban Clim.* 38, 100858. doi:10.1016/j.ulclim.2021.100858
- GPAI (2020). Data Governance Working Group A Framework Paper for GPAI’s Work on Data Governance. Available at: <https://gpai.ai/projects/data-governance/>
- Grell, G. A., Peckham, S. E., Schmitz, R., McKeen, S. A., Frost, G., Skamarock, W. C., et al. (2005). Fully Coupled “Online” Chemistry within the WRF Model. *Atmos. Environ.* 39, 6957–6975. doi:10.1016/j.atmosenv.2005.04.027
- Gulia, S., Nagendra, S. M. S., and Khare, M. (2017). A System Based Approach to Develop Hybrid Model Predicting Extreme Urban NO X and PM 2.5 Concentrations. *Transportation Res. D: Transport Environ.* 56, 141–154. doi:10.1016/j.trd.2017.08.005

- Guilia, S., Shiva Nagendra, S. M., Khare, M., and Khanna, I. (2015). Urban Air Quality Management-A Review. *Atmos. Pollut. Res.* 6, 286–304. doi:10.5094/apr.2015.033
- Gupta, P., Christopher, S. A., Wang, J., Gehrig, R., Lee, Y., and Kumar, N. (2006). Satellite Remote Sensing of Particulate Matter and Air Quality Assessment over Global Cities. *Atmos. Environ.* 40, 5880–5892. doi:10.1016/j.atmosenv.2006.03.016
- Guttikunda, S. K., and Calori, G. (2013). A GIS Based Emissions Inventory at 1 Km × 1 Km Spatial Resolution for Air Pollution Analysis in Delhi, India. *Atmos. Environ.* 67, 101–111. doi:10.1016/j.atmosenv.2012.10.040
- Habibzadeh, H., Kaptan, C., Soyata, T., Kantarci, B., and Boukerche, A. (2019). Smart City System Design: A Comprehensive Study of the Application and Data Planes. *ACM Comput. Surv.* 52, 41. doi:10.1145/3309545
- Hagan, D. H., Gani, S., Bhandari, S., Patel, K., Habib, G., Apte, J. S., et al. (2019). Inferring Aerosol Sources from Low-Cost Air Quality Sensor Measurements: A Case Study in Delhi, India. *Environ. Sci. Technol. Lett.* 6, 467–472. doi:10.1021/acs.estlett.9b00393
- Haghif, M., Stoll, R., and Thurow, K. (2018). A Low-Cost, Standalone, and Multi-Tasking Watch for Personalized Environmental Monitoring. *IEEE Trans. Biomed. Circuits Syst.* 12, 1144–1154. doi:10.1109/tbcas.2018.2840347
- Harpham, Q. K., Hughes, A., and Moore, R. V. (2019). Introductory Overview: The OpenMI 2.0 Standard for Integrating Numerical Models. *Environ. Model. Softw.* 122, 104549. doi:10.1016/j.envsoft.2019.104549
- Hashem, I. A. T., Chang, V., Anuar, N. B., Adewole, K., Yaqoob, I., Gani, A., et al. (2016). The Role of Big Data in Smart City. *Int. J. Inf. Management* 36, 748–758. doi:10.1016/j.ijinfomgt.2016.05.002
- Haupt, S. E., Chapman, W., Adams, S. V., Kirkwood, C., Hosking, J. S., Robinson, N. H., et al. (2021). Towards Implementing Artificial Intelligence post-processing in Weather and Climate: Proposed Actions from the Oxford 2019 Workshop. *Philos. Trans. A. Math. Phys. Eng. Sci.* 379, 20200091. doi:10.1098/rsta.2020.0091
- Hu, K., Davison, T., Rahman, A., and Sivaraman, V. (2014). “Air Pollution Exposure Estimation and Finding Association with Human Activity Using Wearable Sensor Network,” in Proceedings of the MLSDA 2014 2nd Workshop on Machine Learning for Sensory Data Analysis (Australia: MLSDA’14. Association for Computing Machinery, Gold Coast, Australia QLD), 48–55. doi:10.1145/2689746.2689749
- Huang, Y., Zhao, Q., Zhou, Q., and Jiang, W. (2018). Air Quality Forecast Monitoring and its Impact on Brain Health Based on Big Data and the Internet of Things. *IEEE Access* 6, 78678–78688. doi:10.1109/access.2018.2885142
- India Smart City (2015). Smart Cities Mission Statements and Guidelines. [WWW Document]. URL. Available at: [http://smartcities.gov.in/upload/uploadfiles/files/SmartCityGuidelines\(1\).pdf](http://smartcities.gov.in/upload/uploadfiles/files/SmartCityGuidelines(1).pdf).
- Ismagilova, E., Hughes, L., Rana, N. P., and Dwivedi, Y. K. (2020). Security, Privacy and Risks within Smart Cities: Literature Review and Development of a Smart City Interaction Framework. *Inf. Syst. Front.* doi:10.1007/s10796-020-10044-1
- ITU (2015). Report: ICT4SDG: Fast-Forward Progress, Leveraging Tech to Achieve Global Goals. [WWW Document]. URL. Available at: [https://www.itu.int/en/sustainable-world/Documents/Fast-forward\\_progress\\_report\\_414709%20FINAL.pdf](https://www.itu.int/en/sustainable-world/Documents/Fast-forward_progress_report_414709%20FINAL.pdf).
- ITU (2020). Frontier Technologies to Protect the Environment and Tackle Climate Change. [WWW Document]. URL. Available at: <http://staging.itu.int/en/publications/Documents/tsb/2020-Frontier-Technologies-to-Protect-the-Environment-and-Tackle-Climate-Change/files/basic-html/index.html> (accessed 12 12, 20).
- Jena, C., Ghude, S. D., Kumar, R., Debnath, S., Govardhan, G., Soni, V. K., et al. (2021). Performance of High Resolution (400 M) PM2.5 Forecast over Delhi. *Sci. Rep.* 11, 4104. doi:10.1038/s41598-021-83467-8
- Jensen, D., and Campbell, J. (2019). *The Case for a Digital Ecosystem for the Environment: Bringing Together Data, Algorithms and Insights for Sustainable Development*. doi:10.13140/RG.2.2.10387.73764
- Jiang, J.-Y., Sun, X., Wang, W., and Young, S. (2019). “Enhancing Air Quality Prediction with Social Media and Natural Language Processing,” in Proceedings of the 57th Annual Meeting of the Association for Computational Linguistics. (Florence, Italy: Association for Computational Linguistics), 2627–2632. doi:10.18653/v1/p19-1251
- Jiang, W., Wang, Y., Tsou, M.-H., and Fu, X. (2015). Using Social Media to Detect Outdoor Air Pollution and Monitor Air Quality Index (AQI): A Geo-Targeted Spatiotemporal Analysis Framework with Sina Weibo (Chinese Twitter). *Plos One* 10, e0141185. doi:10.1371/journal.pone.0141185
- Johansson, L., Epitropou, V., Karatzas, K., Karppinen, A., Wanner, L., Vrochidis, S., et al. (2015). Fusion of Meteorological and Air Quality Data Extracted from the Web for Personalized Environmental Information Services. *Environ. Model. Softw.* 64, 143–155. doi:10.1016/j.envsoft.2014.11.021
- Kaginalkar, A., Ghude, S. D., Mohanty, U. C., Mujumdar, P., Bhakare, S., Darbari, H., et al. (2022). Integrated Urban Environmental System of Systems for Weather Ready Cities in India. *Bull. Am. Meteorol. Soc.* 103, E54–E76. doi:10.1175/BAMS-D-20-0279.1
- Kaginalkar, A., Kumar, S., Gargava, P., and Niyogi, D. (2021). Kaginalkar, A., Kumar, S., Gargava, P., Niyogi, D., 2021. Review of urban computing in air quality management as smart city service: An integrated IoT, AI, and cloud technology perspective. *Urban Climate* 39, 100972. <https://doi.org/10.1016/j.jclim.2021.100972>. Review of Urban Computing in Air Quality Management as Smart City Service: An Integrated IoT, AI, and Cloud Technology Perspective. *Urban Clim.* 39, 100972. doi:10.1016/j.jclim.2021.100972
- Katoto, P. D. M. C., Brand, A. S., Bakan, B., Obadia, P. M., Kuhangana, C., Kayembe-Kitenge, T., et al. (2021). Acute and Chronic Exposure to Air Pollution in Relation with Incidence, Prevalence, Severity and Mortality of COVID-19: a Rapid Systematic Review. *Environ. Health* 20, 41. doi:10.1186/s12940-021-00714-1
- Kerins, P., Nilson, E., Mackres, E., Rashid, T., Guzder-Williams, B., and Brumby, S. (2020). *Spatial Characterization of Urban Land Use through Machine Learning*. Technical Note. Washington, DC: World Resources Institute. Available online at: <https://www.wri.org/publication/spatialcharacterization-urban-land-use>.
- Khan, A., Khorat, S., Khatun, R., Doan, Q.-V., Nair, U. S., and Niyogi, D. (2021). Variable Impact of COVID-19 Lockdown on Air Quality across 91 Indian Cities. *Earth Interactions* 25, 57–75. doi:10.1175/ ei-d-20-0017.1
- Khan, Z., Anjum, A., Soomro, K., and Tahir, M. A. (2015). Towards Cloud Based Big Data Analytics for Smart Future Cities. *J. Cloud Comp.* 4, 2. doi:10.1186/s13677-015-0026-8
- Kindberg, T., Chalmers, M., and Paulos, E. (2007). Guest Editors’ Introduction: Urban Computing. *IEEE Pervasive Comput.* 6, 18–20. doi:10.1109/mprv.2007.57
- Klein, T., Kukkonen, J., Bossioli, E., Baklanov, A., Vik, A., Agnew, P., et al. (2012). Interactions of Physical, Chemical, and Biological Weather Calling for an Integrated Approach to Assessment, Forecasting, and Communication of Air Quality. *Ambio* 41 (8), 851–864. doi:10.1007/s13280-012-0288-z
- Kominos, N., Bratsas, C., Kominos, N., Bratsas, C., Kakderi, C., and Tsarchopoulos, P. (2015). Smart City Ontologies: Improving the Effectiveness of Smart City Applications. *J. Smart Cities* 1, 1–16. doi:10.18063/jsc.2015.01.001
- Kosmidis, E., Syropoulou, P., Tekes, S., Schneider, P., Spyromitros-Xioufis, E., Riga, M., et al. (2018). hackAIR: Towards Raising Awareness about Air Quality in Europe by Developing a Collective Online Platform. *Ijgi* 7, 187. doi:10.3390/ijgi7050187
- Kotsev, A., Schleidt, K., Liang, S., Van der Schaaf, H., Khalafbeigi, T., Grellet, S., et al. (2018). Extending INSPIRE to the Internet of Things through SensorThings API. *Geosciences* 8, 221. doi:10.3390/geosciences8060221
- Kulkarni, S. H., Ghude, S. D., Jena, C., Karumuri, R. K., Sinha, B., Sinha, V., et al. (2020). How Much Does Large-Scale Crop Residue Burning Affect the Air Quality in Delhi? *Environ. Sci. Technol.* 54, 4790–4799. doi:10.1021/acs.est.0c00329
- Kurinji, S. L., and Ganguly, T. (2020). *Managing India’s Air Quality Through an Eye in the Sky*. New Delhi: Council on Energy, Environment and Water. <https://www.ceew.in/publications/satellite-air-quality-monitoring-and-remote-pollution-sensing-india>.
- Landigan, P. J., Fuller, R., Acosta, N. J. R., Adeyi, O., Arnold, R., Basu, N. N., et al. (2018). The Lancet Commission on Pollution and Health. *The Lancet* 391, 462–512. doi:10.1016/s0140-6736(17)32345-0
- Laniak, G. F., Olchin, G., Goodall, J., Voinov, A., Hill, M., Glynn, P., et al. (2013). Integrated Environmental Modeling: A Vision and Roadmap for the Future. *Environ. Model. Softw.* 39, 3–23. doi:10.1016/j.envsoft.2012.09.006
- Lau, P. L. B., Marakkalage, H., Zhou, Y., Ul Hassan, N., Yuen, C., Zhang, M., et al. (2019). A Survey of Data Fusion in Smart City Applications. *Inf. Fusion* 52, 357. doi:10.1016/j.inffus.2019.05.004

- Lelieveld, J., Pozzer, A., Pöschl, U., Fnais, M., Haines, A., and Münzel, T. (2020). Loss of Life Expectancy from Air Pollution Compared to Other Risk Factors: a Worldwide Perspective. *Cardiovasc. Res.* 116, 1910–1917. doi:10.1093/cvr/cvaa025
- Lepenies, R., and Zakari, I. S. (2021). Citizen Science for Transformative Air Quality Policy in Germany and Niger. *Sustainability* 13, 3973. doi:10.3390/su13073973
- Leung, Y., Leung, K.-S., Wong, M.-H., Mak, T., Cheung, K.-Y., Lo, L.-Y., et al. (2018). An Integrated Web-Based Air Pollution Decision Support System - a Prototype. *Int. J. Geographical Inf. Sci.* 32, 1787–1814. doi:10.1080/13658816.2018.1460752
- Li, H., Sodoudi, S., Liu, J., and Tao, W. (2020). Temporal Variation of Urban Aerosol Pollution Island and its Relationship with Urban Heat Island. *Atmos. Res.* 241, 104957. doi:10.1016/j.atmosres.2020.104957
- Li, W., Batty, M., and Goodchild, M. F. (2020). Real-time GIS for Smart Cities. *Int. J. Geographical Inf. Sci.* 34, 311–324. doi:10.1080/13658816.2019.1673397
- Li, T., Shen, H., Yuan, Q., Zhang, X., and Zhang, L. (2017). Estimating Ground-Level PM2.5 by Fusing Satellite and Station Observations: A Geo-Intelligent Deep Learning Approach. *Geophys. Res. Lett.* 44 (11), 985–1011. doi:10.1002/2017gl075710
- Lim, C., Kim, K.-J., and Maglio, P. P. (2018). Smart Cities with Big Data: Reference Models, Challenges, and Considerations. *Cities* 82, 86–99. doi:10.1016/j.cities.2018.04.011
- Liu, B., Zhao, Q., Jin, Y., Shen, J., and Li, C. (2021). Application of Combined Model of Stepwise Regression Analysis and Artificial Neural Network in Data Calibration of Miniature Air Quality Detector. *Sci. Rep.* 11, 3247. doi:10.1038/s41598-021-82871-4
- Liu, X., Nielsen, P. S., Heller, A., and Giannou, P. (2017). “SciCloud: A Scientific Cloud and Management Platform for Smart City Data,” in 2017 28th International Workshop on Database and Expert Systems Applications (DEXA), 27–31.
- LondonAir (n.d.). London Air Quality Network Air Quality Forecast for London. [WWW Document]. URL. Available at: <https://www.londonair.org.uk/Londonair/Forecast/> (accessed 9 10, 20).
- Lv, Z., Li, X., Wang, W., Zhang, B., Hu, J., and Feng, S. (2018). Government Affairs Service Platform for Smart City. *Future Generation Computer Syst.* 81, 443–451. doi:10.1016/j.future.2017.08.047
- Lytras, M. D., Visvizi, A., Torres-Ruiz, M., Damiani, E., and Jin, P. (2020). IEEE Access Special Section Editorial: Urban Computing and Well-Being in Smart Cities: Services, Applications, Policymaking Considerations. *IEEE Access* 8, 72340–72346. doi:10.1109/access.2020.2988125
- Ma, J., Yu, Z., Qu, Y., Xu, J., and Cao, Y. (2020). Application of the XGBoost Machine Learning Method in PM2.5 Prediction: A Case Study of Shanghai. *Aerosol Air Qual. Res.* 20, 128–138. doi:10.4209/aaqr.2019.08.0408
- Maag, B., Zhou, Z., and Thiele, L. (2018). A Survey on Sensor Calibration in Air Pollution Monitoring Deployments. *IEEE Internet Things J.* 5, 4857–4870. doi:10.1109/jiot.2018.2853660
- Mabkhot, M., Ferreira, P., Maffei, M., Podrzaj, P., Madziel, M., Antonelli, D., et al. (2021). Mapping Industry 4.0 Enabling Technologies into United Nations Sustainability Development Goals. *Sustainability* 13, 2560. doi:10.3390/su13052560
- Mahajan, S., Kumar, P., Pinto, J. A., Riccetti, A., Schaaf, K., Campodon, G., et al. (2020). A Citizen Science Approach for Enhancing Public Understanding of Air Pollution. *Sustainable Cities Soc.* 52, 101800. doi:10.1016/j.scs.2019.101800
- Majumdar, S., Subhani, M. M., Roullier, B., Anjum, A., and Zhu, R. (2021). Congestion Prediction for Smart Sustainable Cities Using IoT and Machine Learning Approaches. *Sustainable Cities Soc.* 64, 102500. doi:10.1016/j.scs.2020.102500
- Martin, R. V. (2008). Satellite Remote Sensing of Surface Air Quality. *Atmos. Environ.* 42, 7823–7843. doi:10.1016/j.atmosenv.2008.07.018
- Masiol, M., Žíková, N., Chalupa, D. C., Rich, D. Q., Ferro, A. R., and Hopke, P. K. (2018). Hourly Land-Use Regression Models Based on Low-Cost PM Monitor Data. *Environ. Res.* 167, 7–14. doi:10.1016/j.envres.2018.06.052
- McGovern, A., Elmore, K. L., Gagne, D. J., Haupt, S. E., Karstens, C. D., Lagerquist, R., et al. (2017). Using Artificial Intelligence to Improve Real-Time Decision-Making for High-Impact Weather. *Bull. Amer. Meteorol. Soc.* 98, 2073–2090. doi:10.1175/bams-d-16-0123.1
- Michalakes, J. (2020). “HPC for Weather Forecasting,” in *Parallel Algorithms in Computational Science and Engineering*. Editors A. Gramma and A. H. Sameh (Cham: Springer International Publishing), 297–323. doi:10.1007/978-3-030-43736-7\_10
- Mircea, M., Calori, G., Pirovano, G., and Belis, C. A. (2020). *European Guide on Air Pollution Source Apportionment for Particulate Matter with Source Oriented Models and Their Combined Use with Receptor Models*. EUR 30082 EN. Luxembourg: Publications Office of the European Union. 2020, ISBN 978-92-76-10698-2.
- Molina, L. T., Velasco, E., Retama, A., and Zavala, M. (2019). Experience from Integrated Air Quality Management in the Mexico City Metropolitan Area and Singapore. *Atmosphere* 10, 512. doi:10.3390/atmos10090512
- Molthan, A. L., Case, J. L., Venner, J., Schroeder, R., Checchi, M. R., Zavodsky, B. T., et al. (2015). Clouds in the Cloud: Weather Forecasts and Applications within Cloud Computing Environments. *Bull. Amer. Meteorol. Soc.* 96, 1369–1379. doi:10.1175/BAMS-D-14-00013.1
- Mondschein, J., Clark-Ginsberg, A., and Kuehn, A. (2021). Smart Cities as Large Technological Systems: Overcoming Organizational Challenges in Smart Cities through Collective Action. *Sustainable Cities Soc.* 67, 102730. doi:10.1016/j.jscs.2021.102730
- Morawska, L., Thai, P. K., Liu, X., Asumadu-Sakyi, A., Ayoko, G., Bartonova, A., et al. (2018). Applications of Low-Cost Sensing Technologies for Air Quality Monitoring and Exposure Assessment: How Far Have They Gone? *Environ. Int.* 116, 286–299. doi:10.1016/j.envint.2018.04.018
- Nam, T., and Pardo, T. A. (2011). “Conceptualizing Smart City with Dimensions of Technology, People, and Institutions,” in Proceedings of the 12th Annual International Digital Government Research Conference: Digital Government Innovation in Challenging Times (College Park, Maryland, USA: Dgo '11. Association for Computing Machinery), 282–291. doi:10.1145/2037556.2037602
- Nyhan, M. M., Kloog, I., Britter, R., Ratti, C., and Koutrakis, P. (2019). Quantifying Population Exposure to Air Pollution Using Individual Mobility Patterns Inferred from mobile Phone Data. *J. Expo. Sci. Environ. Epidemiol.* 29, 238–247. doi:10.1038/s41370-018-0038-9
- Octaviano, C., Ramirez, F., Araiza, O., Nieto, I., Conteiras, A., Ruiz, U., et al. (2020). Data for Climate Action Challenge : Electro-Mobility: Cleaning Mexico City's Air with Transformational Climate Policies Through Big Data Pattern Analysis in Traffic & Social Mobility. [WWW Document]. URL. Available at: <http://www.dataforclimateaction.org/meet-the-winners/>.
- Oke, T. R., Mills, G., Christen, A., and Voogt, J. A. (2017). *Urban Climates*. Cambridge: Cambridge University Press. doi:10.1017/9781139016476
- Pandey, A., Brauer, M., Cropper, M. L., Balakrishnan, K., Mathur, P., Dey, S., et al. (2021). Health and Economic Impact of Air Pollution in the States of India: the Global Burden of Disease Study 2019. *Lancet Planet. Health* 5, e25–e38. doi:10.1016/S2542-5196(20)30298-9
- Parisar (2020). Clearing the Haze. Available at: <https://www.parisar.org/what-we-do/air-quality/advocacy/new-report-clearing-the-haze-an-analysis-of-air-quality-improvements-in-six-smart-cities-in-maharashtra>.
- Paskaleva, K., Evans, J., Martin, C., Linjordet, T., Yang, D., and Karvonen, A. (2017). Data Governance in the Sustainable Smart City. *Informatics* 4, 41. doi:10.3390/informatics4040041
- Piedrahita, R., Xiang, Y., Masson, N., Ortega, J., Collier, A., Jiang, Y., et al. (2014). The Next Generation of Low-Cost Personal Air Quality Sensors for Quantitative Exposure Monitoring. *Atmos. Meas. Tech.* 7, 3325–3336. doi:10.5194/amt-7-3325-2014
- Pinder, R. W., Klopp, J. M., Kleiman, G., Hagler, G. S. W., Awe, Y., and Terry, S. (2019). Opportunities and Challenges for Filling the Air Quality Data gap in Low- and Middle-Income Countries. *Atmos. Environ.* 215, 116794. doi:10.1016/j.atmosenv.2019.06.032
- Pipalatkar, P., Khaparde, V. V., Gajghate, D. G., and Bawase, M. A. (2014). Source Apportionment of PM2.5 Using a CMB Model for a Centrally Located Indian City. *Aerosol Air Qual. Res.* 14, 1089–1099. doi:10.4209/aaqr.2013.04.0130
- Ramacher, M. O. P., Kakouri, A., Speyer, O., Feldner, J., Karl, M., Timmermans, R., et al. (2021). The UrbEm Hybrid Method to Derive High-Resolution Emissions for City-Scale Air Quality Modeling. *Atmosphere* 12, 1404. doi:10.3390/atmos12111404
- Ramos, F., Trilles, S., Muñoz, A., and Huerta, J. (2018). Promoting Pollution-free Routes in Smart Cities Using Air Quality Sensor Networks. *Sensors* 18, 2507. doi:10.3390/s18082507

- Randhawa, A., and Kumar, A. (2017). Exploring Sustainability of Smart Development Initiatives in India. *Int. J. Sustainable Built Environ.* 6, 701–710. doi:10.1016/j.ijsbe.2017.08.002
- Ranscombe, P. (2019). Wearable Technology for Air Pollution. *Lancet Respir. Med.* 7, 567–568. doi:10.1016/s2213-2600(19)30151-1
- Rathore, M. M., Paul, A., Hong, W.-H., Seo, H., Awan, I., and Saeed, S. (2018). Exploiting IoT and Big Data Analytics: Defining Smart Digital City Using Real-Time Urban Data. *Sustainable Cities Soc.* 40, 600–610. doi:10.1016/j.scs.2017.12.022
- Ravi, D., Wong, C., Lo, B., and Yang, G. Z. (2017). A Deep Learning Approach to On-Node Sensor Data Analytics for Mobile or Wearable Devices. *IEEE J. Biomed. Health Inform.* 21, 56–64. doi:10.1109/JBHI.2016.2633287
- Reed, M. S., Graves, A., Dandy, N., Posthumus, H., Hubacek, K., Morris, J., et al. (2009). Who's in and Why? A Typology of Stakeholder Analysis Methods for Natural Resource Management. *J. Environ. Manage.* 90, 1933–1949. doi:10.1016/j.jenvman.2009.01.001
- Rivas, I., Beddows, D. C. S., Amato, F., Green, D. C., Järvi, L., Hueglin, C., et al. (2020). Source Apportionment of Particle Number Size Distribution in Urban Background and Traffic Stations in Four European Cities. *Environ. Int.* 135, 105345. doi:10.1016/j.envint.2019.105345
- Sahu, R., Nagal, A., Dixit, K. K., Unnibhavi, H., Mantravadi, S., Nair, S., et al. (2020). Robust Statistical Calibration and Characterization of Portable Low-Cost Air Quality Monitoring Sensors to Quantify Real-Time O<sub>3</sub> and NO<sub>2</sub> Concentrations in Diverse Environments. *Atmos. Measur. Tech.* 14, 37–52. doi:10.5194/amt-14-37-2021
- Santana, E. F. Z., Chaves, A. P., Gerosa, M. A., Kon, F., and Milojicic, D. S. (2018). Software Platforms for Smart Cities. *ACM Comput. Surv.* 50, 1–37. doi:10.1145/3124391
- Santiago, J. L., Borge, R., Martin, F., de la Paz, D., Martilli, A., Lumbreras, J., et al. (2017). Evaluation of a CFD-Based Approach to Estimate Pollutant Distribution within a Real Urban Canopy by Means of Passive Samplers. *Sci. Total Environ.* 576, 46–58. doi:10.1016/j.scitotenv.2016.09.234
- Saraswat, I., Mishra, R. K., and Kumar, A. (2017). Estimation of PM10 Concentration from Landsat 8 OLI Satellite Imagery over Delhi, India. *Remote Sensing Appl. Soc. Environ.* 8, 251–257. doi:10.1016/j.rsase.2017.10.006
- Schneider, R., Vicedo-Cabrera, A., Sera, F., Masselot, P., Stafigoggia, M., de Hoogh, K., et al. (2020). A Satellite-Based Spatio-Temporal Machine Learning Model to Reconstruct Daily PM2.5 Concentrations across Great Britain. *Remote Sensing* 12, 3803. doi:10.3390/rs12223803
- Sebestyén, V., Czvetkó, T., and Abonyi, J. (2021). The Applicability of Big Data in Climate Change Research: The Importance of System of Systems Thinking. *Front. Environ. Sci.* 9, 70. doi:10.3389/fenvs.2021.619092
- Sebayi, D., and Kennedy, A. (2017). Qualitative Delphi Method: A Four Round Process with a Worked Example. *Qual. Rep.* 22, 2755–2763. doi:10.46743/2160-3715/2017.2974
- Sentinel-5P. Sentinel-5P TROPOMI User Guide - Sentinel Online - Sentinel. [WWW Document]. URL Available at: <https://sentinel.esa.int/web/sentinel/user-guides/sentinel-5p-tropomi> (accessed 11 5, 21).
- Shi, Y., Ren, C., Lau, K. K.-L., and Ng, E. (2019). Investigating the Influence of Urban Land Use and Landscape Pattern on PM2.5 Spatial Variation Using mobile Monitoring and WUDAPT. *Landscape Urban Plann.* 189, 15–26. doi:10.1016/j.landurbplan.2019.04.004
- Silva, B., Khan, M., Jung, C., Seo, J., Muhammad, D., Han, J., et al. (2018). Urban Planning and Smart City Decision Management Empowered by Real-Time Data Processing Using Big Data Analytics. *Sensors* 18, 2994. doi:10.3390/s18092994
- Simmhan, Y., Nair, S., Monga, S., Sahu, R., Dixit, K., Sutaria, R., et al. (2019). "SATVAM: Toward an IoT Cyber-Infrastructure for Low-Cost Urban Air Quality Monitoring," in 2019 15th International Conference on eScience (eScience). Presented at the 2019 15th International Conference on eScience (eScience), 57–66. doi:10.1109/econference.2019.900014
- Skjetne, E., and Liu, H.-Y. (2017). Traffic Maps and Smartphone Trajectories to Model Air Pollution, Exposure and Health Impact. *J. Environ. Prot.* 08, 1372–1392. doi:10.4236/jep.2017.811084
- Smith, R. B., Fecht, D., Gulliver, J., Beevers, S. D., Dajnak, D., Blangiardo, M., et al. (2017). Impact of London's Road Traffic Air and Noise Pollution on Birth Weight: Retrospective Population Based Cohort Study. *BMJ* 359, j5299. doi:10.1136/bmj.j5299
- Smith, R. M., Pathak, P. A., and Agrawal, G. (2019). India's "smart" Cities mission: A Preliminary Examination into India's Newest Urban Development Policy. *J. Urban Aff.* 41, 518–534. doi:10.1080/07352166.2018.1468221
- Steuri, B., Bender, S., and Cortekar, J. (2020). Successful User-Science Interaction to Co-develop the New Urban Climate Model PALM-4U. *Urban Clim.* 32, 100630. doi:10.1016/j.ulclim.2020.100630
- Stojanovic, D., Predic, B., Predic, B., and Stojanovic, N. (2016). "Mobile Crowd Sensing for Smart Urban Mobility," in *European Handbook of Crowdsourced Geographic Information* (Ubiquity Press), 371–382. doi:10.5334/bax.aa
- Sun, W., Liu, Z., Zhang, Y., Xu, W., Lv, X., Liu, Y., et al. (2020). Study on Land-Use Changes and Their Impacts on Air Pollution in Chengdu. *Atmosphere* 11, 42. doi:10.3390/atmos11010042
- Syed, A. S., Sierra-Sosa, D., Kumar, A., and Elmaghriby, A. (2021). IoT in Smart Cities: A Survey of Technologies, Practices and Challenges. *Smart Cities* 4, 429–475. doi:10.3390/smartcities4020024
- Toma, C., Alexandru, A., Popa, M., and Zamfirou, A. (2019). IoT Solution for Smart Cities' Pollution Monitoring and the Security Challenges. *Sensors* 19, 3401. doi:10.3390/s19153401
- UNEP (2021). *Measuring Progress: Environment and the SDGs*. Nairobi: United Nations Environment Programme Nairobi. Available at: <https://www.unep.org/resources/publication/measuring-progress-environment-and-sdgs>.
- United Nations (2019). "Department of Economics and Social Affairs, Population Division (2019), World Urbanization Prospects: The 2018 Revision," in *World Urbanization Prospects: The 2018 Revision (ST/ESA/SER.A/420)*. New York, NY: United Nations.
- Upadhyay, N., and Upadhyay, S. (2017). #RighttoBreathe Why Not? Social Media Analysis of the Local in the Capital City of India. *Proced. Computer Sci.* 108, 2542–2546. doi:10.1016/j.procs.2017.05.017
- USEPA (2014). Environmental Benefits Mapping and Analysis Program - Community Edition. (BenMAP-CE) [WWW Document]. US EPA. URL Available at: <https://www.epa.gov/benmap> (accessed 9 10, 20).
- USEPA (2016). The Atmospheric Model Evaluation Tool. [WWW Document]. URL Available at: <https://www.epa.gov/cmaq/atmospheric-model-evaluation-tool> (accessed 22 9, 21).
- van der Schaaf, H., and Herzog, R. (2015). "Mapping the OGC SensorThings API onto the OpenIoT Middleware," in *Interoperability and Open-Source Solutions for the Internet of Things, Lecture Notes in Computer Science*. Editors I. Podnar Žarko, K. Pripužić, and M. Serrano (Cham: Springer International Publishing), 62–70. doi:10.1007/978-3-319-16546-2\_6
- van Zoest, V., Osei, F. B., Hoek, G., and Stein, A. (2020). Spatio-temporal Regression Kriging for Modelling Urban NO<sub>2</sub> Concentrations. *Int. J. Geographical Inf. Sci.* 34, 851–865. doi:10.1080/13658816.2019.1667501
- Verma, S. (2021). *Transparency Index: Rating of Pollution Control Boards on Public Disclosure*. New Delhi: Centre for Science and Environment. Available at: <https://www.cseindia.org/transparency-index-rating-of-pollution-control-boards-on-public-disclosure-10936>.
- Vincent, K., Daly, M., Scannell, C., and Leathes, B. (2018). What Can Climate Services Learn from Theory and Practice of Co-production? *Clim. Serv.* 12, 48–58. doi:10.1016/j.ciser.2018.11.001
- Viqueira, J. R. R., Villarroyo, S., Mera, D., and Taboada, J. A. (2020). Smart Environmental Data Infrastructures: Bridging the Gap between Earth Sciences and Citizens. *Appl. Sci.* 10, 856. doi:10.3390/app10030856
- Wang, J., Balaprakash, P., and Kotamarthi, R. (2019). Fast Domain-Aware Neural Network Emulation of a Planetary Boundary Layer Parameterization in a Numerical Weather Forecast Model. *Geosci. Model. Dev.* 12, 4261–4274. doi:10.5194/gmd-12-4261-2019
- Wang, Y.-d., Fu, X.-k., Jiang, W., Wang, T., Tsou, M.-H., and Ye, X.-y. (2017). Inferring Urban Air Quality Based on Social media. *Comput. Environ. Urban Syst.* 66, 110–116. doi:10.1016/j.compenvurbsys.2017.07.002
- WCCD (2021). World Council on City Data [WWW Document]. World Council on City Data. URL Available at: <https://www.dataforcities.org> (accessed 21 9, 21).
- WHO (2021). New WHO Global Air Quality Guidelines Aim to Save Millions of Lives from Air Pollution. [WWW Document]. URL Available at: <https://www.who.int/news-room/22-09-2021-new-who-global-air-quality-guidelines-aim-to-save-millions-of-lives-from-air-pollution> (accessed 923, 21).

- WHO (2018). Burden of Disease from Ambient Air Pollution. [WWW Document]. Available at: [https://www.who.int/airpollution/data/AAP\\_BoD\\_results\\_May2018\\_final.pdf](https://www.who.int/airpollution/data/AAP_BoD_results_May2018_final.pdf).
- Wiedinmyer, C., Akagi, S. K., Yokelson, R. J., Emmons, L. K., Al-Saadi, J. A., Orlando, J. J., et al. (2011). The Fire INventory from NCAR (FINN): a High Resolution Global Model to Estimate the Emissions from Open Burning. *Geosci. Model. Dev.* 4, 625–641. doi:10.5194/gmd-4-625-2011
- Wilkinson, M. D., Dumontier, M., Aalbersberg, I. J., Appleton, G., Axton, M., Baak, A., et al. (2016). The FAIR Guiding Principles for Scientific Data Management and Stewardship. *Sci. Data* 3, 160018. doi:10.1038/sdata.2016.18
- Wu, J., Xie, W., Li, W., and Li, J. (2015). Effects of Urban Landscape Pattern on PM2.5 Pollution-A Beijing Case Study. *PLoS one* 10, e0142449. doi:10.1371/journal.pone.0142449
- Wu, Y. C., Lin, Y. C., Yu, H. L., Chen, J. H., Chen, T. F., Sun, Y., et al. (2015). Association between Air Pollutants and Dementia Risk in the Elderly. *Alzheimer's Demen. Diagn. Assess. Dis. Monit.* 1, 220–228. doi:10.1016/j.dadm.2014.11.015
- Xu, M., Jin, J., Wang, G., Segers, A., Deng, T., and Lin, H. X. (2021). Machine Learning Based Bias Correction for Numerical Chemical Transport Models. *Atmos. Environ.* 248, 118022. doi:10.1016/j.atmosenv.2020.118022
- Yan, L., Duarte, F., Wang, D., Zheng, S., and Ratti, C. (2019). Exploring the Effect of Air Pollution on Social Activity in China Using Geotagged Social media Check-In Data. *Cities* 91, 116–125. doi:10.1016/j.cities.2018.11.011
- Yarza, S., Hassan, L., Shtein, A., Lesser, D., Novack, L., Katra, I., et al. (2020). Novel Approaches to Air Pollution Exposure and Clinical Outcomes Assessment in Environmental Health Studies. *Atmosphere* 11, 122. doi:10.3390/atmos11020122
- Yin, R. K. (2016). *Qualitative Research from Start to Finish*. New York: Guilford Press.
- Zanella, A., Bui, N., Castellani, A., Vangelista, L., and Zorzi, M. (2014). Internet of Things for Smart Cities. *IEEE Internet Things J.* 1, 22–32. doi:10.1109/JIOT.2014.2306328
- Zheng, S., Wang, J., Sun, C., Zhang, X., and Kahn, M. E. (2019). Air Pollution Lowers Chinese Urbanites' Expressed Happiness on Social media. *Nat. Hum. Behav.* 3, 237–243. doi:10.1038/s41562-018-0521-2
- Zheng, Y., Yi, X., Li, M., Li, R., Shan, Z., Chang, E., et al. (2015). "Forecasting Fine-Grained Air Quality Based on Big Data," in Proceedings of the 21th ACM SIGKDD International Conference on Knowledge Discovery and Data Mining, KDD '15 (Sydney, NSW, Australia: Association for Computing Machinery), 2267–2276. doi:10.1145/2783258.2788573
- Zimmerman, N., Presto, A. A., Kumar, S. P. N., Gu, J., Hauryliuk, A., Robinson, E. S., et al. (2018). A Machine Learning Calibration Model Using Random Forests to Improve Sensor Performance for Lower-Cost Air Quality Monitoring. *Atmos. Meas. Tech.* 11, 291–313. doi:10.5194/amt-11-291-2018
- Conflict of Interest:** The authors declare that the research was conducted in the absence of any commercial or financial relationships that could be construed as a potential conflict of interest.
- Publisher's Note:** All claims expressed in this article are solely those of the authors and do not necessarily represent those of their affiliated organizations or those of the publisher, the editors, and the reviewers. Any product that may be evaluated in this article, or claim that may be made by its manufacturer, is not guaranteed or endorsed by the publisher.
- Copyright © 2022 Kaginalkar, Kumar, Gargava, Kharkar and Niyogi. This is an open-access article distributed under the terms of the Creative Commons Attribution License (CC BY). The use, distribution or reproduction in other forums is permitted, provided the original author(s) and the copyright owner(s) are credited and that the original publication in this journal is cited, in accordance with accepted academic practice. No use, distribution or reproduction is permitted which does not comply with these terms.



# Urban Climate Informatics: An Emerging Research Field

Ariane Middel<sup>1,2,3\*</sup>, Negin Nazarian<sup>4,5,6</sup>, Matthias Demuzere<sup>7</sup> and Benjamin Bechtel<sup>7</sup>

<sup>1</sup>School of Arts, Media and Engineering (AME), Arizona State University, Tempe, AZ, United States, <sup>2</sup>School of Computing and Augmented Intelligence (SCAI), Arizona State University, Tempe, AZ, United States, <sup>3</sup>Urban Climate Research Center (UCRC), Arizona State University, Tempe, AZ, United States, <sup>4</sup>School of Built Environment, University of New South Wales, Sydney, NSW, Australia, <sup>5</sup>City Futures Research Centre, University of New South Wales, Sydney, NSW, Australia, <sup>6</sup>ARC Centre of Excellence for Climate Extreme, Sydney, NSW, Australia, <sup>7</sup>Department of Geography, Urban Climatology Group, Ruhr-University Bochum, Bochum, Germany

## OPEN ACCESS

### Edited by:

Marco Casazza,  
University of Salerno, Italy

### Reviewed by:

Iryna Dronova,  
University of California, Berkeley,  
United States

Lyndon Mark Olaguera,  
Ateneo de Manila University,  
Philippines

Jennifer Ann Salmond,  
The University of Auckland,  
New Zealand

### \*Correspondence:

Ariane Middel  
Ariane.middel@asu.edu

### Specialty section:

This article was submitted to  
Environmental Informatics and Remote  
Sensing,  
a section of the journal  
Frontiers in Environmental Science

Received: 01 February 2022

Accepted: 13 April 2022

Published: 02 May 2022

### Citation:

Middel A, Nazarian N, Demuzere M and  
Bechtel B (2022) Urban Climate  
Informatics: An Emerging  
Research Field.  
*Front. Environ. Sci.* 10:867434.  
doi: 10.3389/fenvs.2022.867434

The scientific field of urban climatology has long investigated the two-way interactions between cities and their overlying atmosphere through *in-situ* observations and climate simulations at various scales. Novel research directions now emerge through recent advancements in sensing and communication technologies, algorithms, and data sources. Coupled with rapid growth in computing power, those advancements augment traditional urban climate methods and provide unprecedented insights into urban atmospheric states and dynamics. The emerging field introduced and discussed here as Urban Climate Informatics (UCI) takes on a multidisciplinary approach to urban climate analyses by synthesizing two established domains: urban climate and climate informatics. UCI is a rapidly evolving field that takes advantage of four technological trends to answer contemporary climate challenges in cities: advances in sensors, improved digital infrastructure (e.g., cloud computing), novel data sources (e.g., crowdsourced or big data), and leading-edge analytical algorithms and platforms (e.g., machine learning, deep learning). This paper outlines the history and development of UCI, reviews recent technological and methodological advances, and highlights various applications that benefit from novel UCI methods and datasets.

**Keywords:** urban climate informatics (UCI), research agenda, novel data sources and sensors, big data, artificial intelligence

## 1 INTRODUCTION

### From Thermometers to Big Data: The Rise of Urban Climate Informatics

Rapid urbanization is one of the defining features of the 21st century with substantial global environmental impact compounded by climate change (Georgescu et al., 2013; Krayenhoff et al., 2018; Masson et al., 2020b; Zhao et al., 2021). In cities, the combined effects of population growth and climatic changes threaten urban livability through urban overheating (Nazarian et al., under review), hazardous air quality (Chapman S. et al., 2017; Broadbent et al., 2020), increased energy consumption, and extreme weather (Willems et al., 2012) (Li et al., 2020b) with widespread health, socioeconomic, and ecological impacts. In response to these challenges, numerous subfields of urban climatology have evolved over the last century to carefully document, examine, and model urban climate at various scales.

Sensors and observational methods have traditionally been developed to assess built environment impacts on local air temperature (Stewart, 2019) and quantify intra- and inter-urban variability in the urban canopy layer (Núñez-Peiró et al., 2021; Potgieter et al., 2021). Early weather and climate observations were motivated by pragmatic needs, e.g., to support agriculture or shipping, while the invention of the thermometer and the barometer in the early 17th century enabled systematic recording of weather conditions. In the late 18th century, the Societas Meteorologica Palatina established an observational network of calibrated instruments and an observation protocol (“Mannheimer Stunden”), which enabled scientific climatic studies. The approach aimed to encourage collaborative data collection by providing calibrated sensors at no cost (Neves et al., 2017). Although participation was limited to academic institutions and companies, the philosophy resonates with modern crowdsourcing and citizen science projects. Synoptic weather analysis required real-time data exchange, which became possible 50 years later with the invention of the telegraph. The first weather map with data from 22 stations was displayed at the World Exhibition in London in 1851.

Temperature maps became widely available with advances in thermal remote sensing, which provides high-resolution surface temperature distributions (Voogt and Oke, 2003; Zhan et al., 2013; Stewart et al., 2021). In the 20th century, advancements in aviation permitted unprecedented atmospheric 3D observations, and in 1960, the launch of the first weather satellite TIROS (Television and InfraRed Observation Satellite) opened a new age of meteorology.

Technological progress has also impacted the field of urban climatology. While research in the early 20th century concentrated on Europe and was mostly descriptive, rapidly increasing computational power in the late 20th and early 21st century significantly advanced quantitative and systematic scientific approaches in the Anglo-American realm (Mills, 2014). Numerical and climate modeling at building to regional scales produced urban climate parameters at high spatial and temporal resolution/coverage and facilitated what-if analyses (Hamdi et al., 2020). At the same time, model outputs and their availability to the research community increased with computing and storage capacity.

Most certainly, big and fine-resolution urban datasets have rapidly evolved with transmission rates exceeding 0.1 Petabyte per day (Reichstein et al., 2019). This trend was driven by increased availability, accuracy, and resolution of sensors and datasets as well as changes in data policy. In remote sensing, for instance, NASA and ESA granted free access to data archives, which enabled new techniques such as time series analysis and multi-sensor data fusion (Wulder et al., 2012).

Despite tremendous technological progress in research, the application of traditional micrometeorological theory to urban areas is still limited by the complexity and heterogeneity of the built environment (Mills, 2014). Conventional observation methods often fall short in providing fine-resolution spatial and temporal urban data, which highlights the need for denser observation networks and novel data sources. Additionally, urban climate studies have traditionally ignored “human factors” that

lead to personal exposures to environmental stressors (Kuras et al., 2017; Okonkwo et al., 2017; Nazarian and Lee, 2021). Lastly, the risks for people and infrastructure are arguably more important than the geographic extent and magnitude of the hazard for planning and emergency response purposes, thus requiring direct access to highly localized information on human mobility (Moore and Obradovich, 2020).

## The Cornerstones of Urban Climate Informatics

**Urban Climate Informatics (UCI)** is an evolving research field that originates from two established domains: *Urban Climate* (concerned with interactions between a city and the atmosphere) and *Climate Informatics* (research combining climate science with approaches from statistics, machine learning, and data mining) (Monteleoni et al., 2016). While Climate Informatics focuses on computational approaches in climate science, UCI takes a broader, multidisciplinary approach. **UCI aims to explore and understand complex urban climate systems and human-environment interactions through new technological, methodological, and systems thinking approaches. It embraces more integrated and human-centric methods to address urban climate challenges that are enabled by novel sensing, non-traditional datasets, crowdsourcing, big data, digital infrastructure, advanced analytics, and artificial intelligence.**

Four emerging technologies and methods can be noted as the cornerstones of UCI (Figure 1). First, recent **advancements in environmental sensing** have resulted in lower sensor size and power consumption at reduced sensor costs. More importantly, improvements in wireless data transmission (using various methods such as Wifi, 5G, and LoRaWAN) and location awareness of devices have enabled Internet-of-Things (IoT) sensing, contributing to real-time and ubiquitous data collection. Second, in addition to environmental datasets that are actively collected by sensors, **new urban datasets** from various sources emerge. These novel datasets include detailed information on three-dimensional and heterogeneous urban configurations as well as incidental and public domain data that can be extracted from social media or the web. The availability of organic datasets, such as mobility patterns in cities, further contributed to understanding the population exposure and impact of urban climate challenges (Li and Wang, 2021). At the same time, a stronger emphasis on citizen engagement and technology-use in daily activities has evolved over the last decade. Driven by commercial trends (e.g., home automation sensors, smartwatches, wearables) and solutions that are non-expert friendly, citizen science data collection has become mainstream and is implemented in education, entertainment, and social activities (Caluwaerts et al., 2021). This contributes to ubiquitous and crowdsourced data collection beyond the academic community (Irwin, 2018), further enabling more realistic and human-centric solutions to urban climate challenges. Third, **state-of-the-art analytical algorithms and computer systems** have entered urban climate analytics, providing an opportunity for more sophisticated data

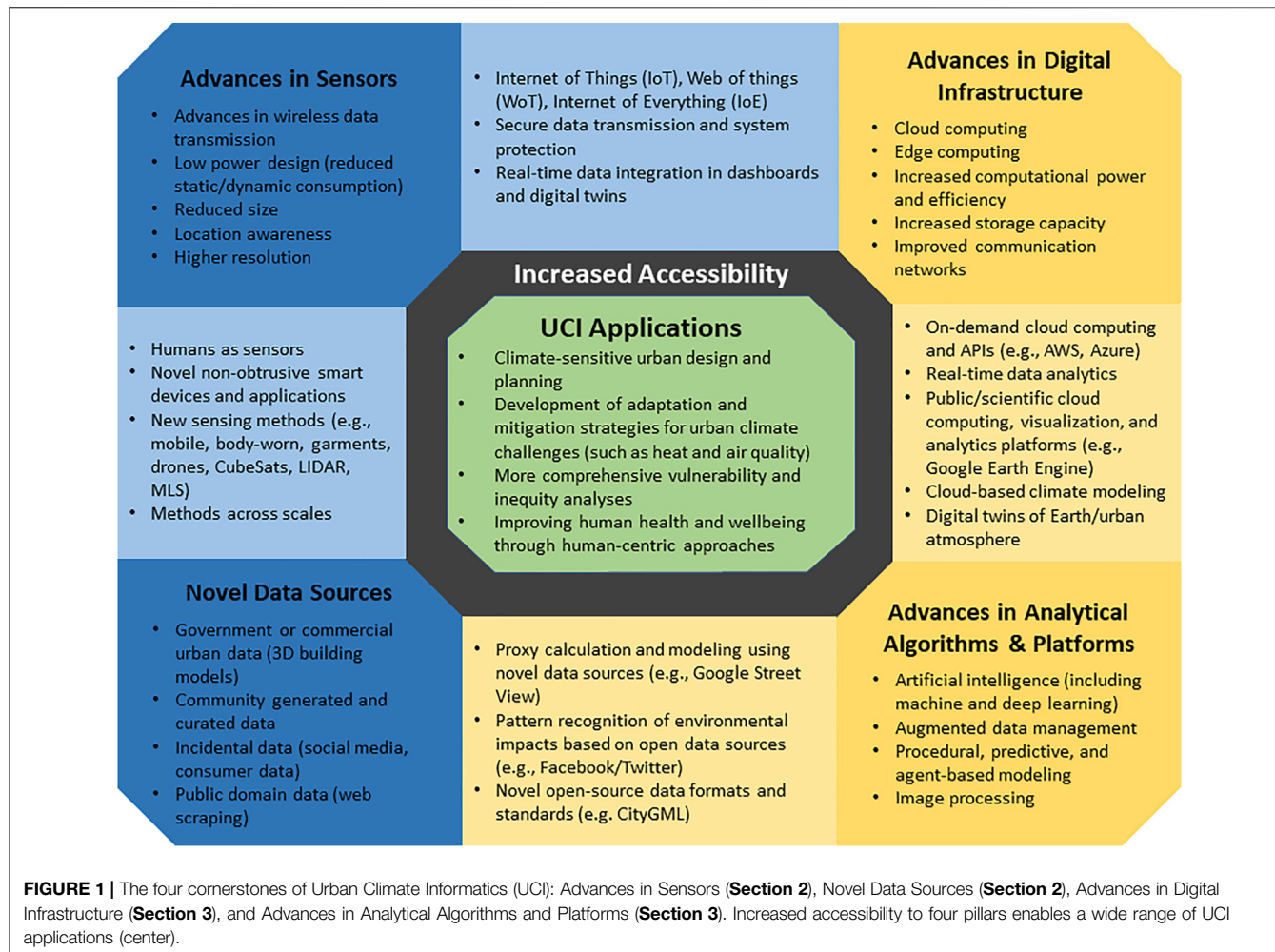


**FIGURE 1 |** The four cornerstones of Urban Climate Informatics (UCI): Advances in Sensors (**Section 2**), Novel Data Sources (**Section 2**), Advances in Digital Infrastructure (**Section 3**), and Advances in Analytical Algorithms and Platforms (**Section 3**). Increased accessibility to four pillars enables a wide range of UCI applications (center).

analyses, computational methods, and modeling approaches. Artificial Intelligence (AI, including Machine and Deep Learning) has been instrumental in characterizing urban areas into local climate zones or climatic maps (Bechtel and Daneke, 2012; Xu et al., 2019; Demuzere et al., 2021; Demuzere et al., 2022), which are paramount for observational and modeling efforts in urban climatology. Lastly, the **accessibility of digital infrastructures** for storage, analytics, and communication of results have transformed various approaches, enabling global-scale analyses of urban climate parameters such as surface and air temperatures (Peng et al., 2012; Chakraborty and Lee, 2019; Venter et al., 2021).

Collectively, novel data sources, sensors, and computing methods have led to a paradigm shift in urban climate analyses, significantly changing “how” we do science and expanding research questions directed at the urban atmosphere and its residents. This shift includes moving beyond the traditional focus on city-atmosphere interactions and tackling challenges of the Anthropocene, including climate change, urban overheating, poor air quality, and climate injustice. Most notably, four trends can be observed: 1) urban climate research has moved towards comprehensive analyses of the

dynamics of urban climate and human-environment interactions at fine temporal and spatial scales; 2) the research focus has shifted from an assessment of local atmospheric conditions in a city vs its rural surroundings (traditional UHI definition) towards intra-urban hazard distribution and human thermal exposure assessments; 3) highly accurate, expensive, high-maintenance weather stations and air quality sensors operated by experts are complemented by educational or operational, lower-cost tools and data that were acquired for non-urban climate purposes; 4) urban climate research teams have become interdisciplinary spanning a wide range of expertise, from architects and engineers to urban planners, computer scientists, and local government representatives, which allows more complex, solutions-oriented analyses from health sciences to social justice and equity; and 5) research results are better communicated to non-experts through new platforms and visualizations (e.g., websites, social media, dashboards) to maximize broader societal impact.

UCI has the potential to overcome current gaps and challenges in urban climatology, which include but are not limited to 1) a lack of human processes (e.g., anthropogenic heat, people's movement) in urban modeling; 2) observations that are not

representative of atmospheric processes and human exposures across space and time (e.g., for long-term climate studies or model validation); and 3) limited data availability (e.g., urban canopy parameters, urban morphology) and computing power for urban climate modeling (Masson et al., 2020a; González et al., 2021). This paper outlines the key trends in the development of UCI, discussing novel technological and methodological advances that enable future directions in urban climate research. The following sections provide a general overview of the UCI field as well as examples and discussions of novel sensing and data sources (**Section 2**) as well as advancement in data processing (**Section 3**).

## 2 NOVEL SENSORS AND DATA SOURCES

One of the key catalysts for the UCI field is the emergence of novel and more expansive datasets resulting from several interconnected developments, most importantly advances in sensor solutions, communication technologies, and data acquisition methods. Here, we detail how advancements in sensors (**Section 2.1**), ensuing novel acquisition methods (**Section 2.2**), and datasets (**Section 2.3**) have been used to understand and address urban climate challenges.

### 2.1 Advancement in Sensors and Communication Technologies

Advances in environmental sensing have greatly increased the availability, resolution, and quality of observational data for urban climate research. In the last decade, a major shift was seen from research-grade sensors operated by experts to low-cost devices, e.g., for citizen-scientists. New technologies not only allowed sensing units to record a more comprehensive set of parameters (such as standard meteorology, air quality, UV, and noise), but also removed limiting factors in continuously monitoring the built environment, such as power supply (source and consumption) and sensor size. The sensor technology revolution resulted in smaller sensors that could easily be mounted to existing structures, required less energy (or were sustained through solar panels), and eventually, were cheaper. This process is similarly seen in satellite/remote sensing, where the emergence of CubeSats has led to miniaturized satellites for space research that have high potential to enhance observations for urban climate applications (González et al., 2021).

Such advances are further complemented with novel wireless and ubiquitous communication technologies, such as WiFi, 3G/4G/5G, and LoRaWan. While previous data-loggers required a technician to connect to the sensor and (often manually) transfer the data for further processing, wireless communication enables automatic and seamless transitions of data from multiple devices to servers. Removing the communication and scaling barrier has led to the emergence of Internet-of-Things (IoT), where physical sensors are connected to digital infrastructure and real-time analytics (**Sections 2.1** and **2.2**); Web-of-Things (WoT), where sensors and everyday objects are fully integrated into the web; and

Internet of Everything (IoE), with all-round connectivity, intelligence, and cognition beyond computers, tablets and smartphones.

Advances in sensors and communication methods greatly contribute to observational studies in UCI. Low-cost sensors with seamless data communication allow scientists, practitioners, and citizens to utilize numerous sensors in a variety of urban spaces with different user behaviors. Instead of using sparsely-placed outdoor sensors to determine heat, weather, or air quality, fine-grained and multi-parameter IoT sensor networks have been successful in depicting the spatial and temporal heterogeneity of environmental quality in educational, commercial, and residential buildings and their outdoor surroundings (Palacios Temprano et al., 2020; Luo et al., 2021; Ulpiani et al., 2021). In addition to covering a larger spatial area and determining hotspots of environmental stressors (Schneider et al., 2017), IoT sensor networks contribute to predictive models for weather (Chavan and Momin, 2017), energy consumptions (Cheng et al., 2021) and air pollution exposures (Xiaojun et al., 2015; Zhang and Woo, 2020); assist in determining the impact of surface cover and urban design on microclimate (Pfautsch and Tjoelker, 2020); and further raise citizen awareness on urban environmental challenges. Lastly, advancement in sensor solutions and communication methods lead to novel data acquisition methods in cities.

### 2.2 Data Acquisition Methods

As existing sensing technologies improve over time, urban climate science further benefits from emerging data acquisition techniques. Novel observation methods take advantage of new sensors and digital literacy of urban residents. Observations range from mobile sensors mounted on various devices and humans to crowdsourcing and volunteered geographic information (VGI), where citizens and distributed private sensors provide a source of geographic and environmental data (See et al., 2016). These methods have long been neglected in atmospheric sciences, mostly due to knowledge gaps and justified concerns in data quality and standardization (Muller et al., 2015). However, these novel data sources are predestined for urban analyses because they are typically collected in the most populated places: cities.

#### Mobile Sensing and “Humans as Sensors”

Traditional urban climate research uses observational datasets that determine inter- and intra-urban variabilities of climatic parameters. As sensors have become smaller, wireless, and more power-efficient, it is more feasible to gather such data through mobile sensing, where the primary goal is increased coverage at reduced costs. This has led to four measurement categories: 1) portable weather stations, 2) vehicle-based sensors, 3) smartphones, and 4) wearable and nearable devices.

Portable weather stations are moved through urban environments using garden carts (Middel and Krayenhoff, 2019; Middel et al., 2021), golf carts (Häb et al., 2015), or cargo bikes (Heusinkveld et al., 2014; Rajkovich and Larsen, 2016). Measurement campaigns often utilize research-grade weather stations and monitor a comprehensive set of parameters, providing valuable spatial data particularly in the

face of extreme heat events. However, mobile sensors lack the medium- or long-term temporal resolution of fixed sensors and, more importantly, need post-processing methods to address prolonged sensor response time in common weather stations (Häb et al., 2015). Additionally, data outputs of mobile measurements are often in time-series format, while the sensors are non-stationary. The changing atmospheric conditions impact observations that should be corrected through time-detrending (Parlow and Foken, 2021). Lastly, mobile sensors are subject to anthropogenic influences such as heat from traffic and space heating/cooling equipment. Accordingly, mobile data should be enriched with detailed metadata to comprehensively interpret the observations.

Similar to portable weather stations, sensors mounted on vehicles such as buses (Kang et al., 2016; Seidel et al., 2016), trash trucks (deSouza et al., 2020), and cars (Ferwati et al., 2018) have been used to traverse cities. Vehicle-based data are prone to the same challenges as portable weather stations. Low-cost (and therefore less accurate) sensors are frequently deployed due to size and communication limits, yet they allow to assess behavioral patterns and human-centric exposure to environmental stressors such as air quality and heat (Fugiglando et al., 2018).

Mobile phones have become an attractive data source for human-scale urban climate information, as there are currently 6.64 billion smartphone users in the world today. Various studies have used phone battery temperature as a proxy for air temperature to map thermal conditions in cities (Overeem et al., 2013; Droste et al., 2017b). Data uncertainty increases with solar radiation exposure (Cabrera et al., 2021), more extreme weather, and precipitation, because the smartphone is most likely enclosed. Although smartphone data for environmental modeling are yet to be validated and scaled beyond academic assessments, the importance of gathering continuous, real-time feedback from urban dwellers should not be underestimated. Assessing urban climate impact requires more in-depth focus on humans exposed to environmental stressors in cities. Accordingly, smartphone applications collecting data on the human experience (e.g., thermal comfort vote and noise/pollution discomfort) can obtain critical data points to augment environmental parameters (Lassen et al., 2021).

Recent urban climate studies have used wearables and nearable sensors for data collection. Here, we define wearables as smart devices (e.g., smart watches, sensor patches, smart clothing) that are worn by participants to obtain environmental parameters (e.g., air temperature and humidity) and physiological responses or behavioral patterns and activities. Nearables refer to (low-cost) sensors carried by individuals or placed in the immediate environment of people. The National Science Experiment in Singapore (low-cost wireless SENSG devices (Wilhelm et al., 2016) is probably the largest deployments of wearables, with 50,000 sensors carried by students for assessment of thermal comfort among other objectives (Monnot et al., 2016; Happle et al., 2017). Wearable sensors have been used to combine all three (environmental, physiological, and behavioral) factors and have shown promising results in predicting heat stress (Nazarian et al., 2021) and obtaining non-obtrusive, real-time feedback (Jayathissa et al., 2019). As sensors are frequently moved between indoor and outdoor settings, pocket

and palms, and are also influenced by the device CPU load, interpretation of the data requires more in-depth investigations.

## Crowdsourcing and Citizen Science

Crowdsourcing, i.e., collection of atmospheric data from non-traditional distributed sources, has evolved as a cost-efficient alternative for monitoring urban climates. While the use of crowdsourced data in atmospheric sciences was in its infancy half a decade ago (Muller et al., 2015), it has reached adolescence quickly. Since 2015, a growing body of crowdsourcing literature has focused on citizen weather station (CWS) data from privately-owned, non-professional, low-cost stations connected to the Internet. Early studies focused on network air temperature (Bell et al., 2015; Chapman L. et al., 2017; Fenner et al., 2017; Meier et al., 2017), but more recent analyses added other atmospheric parameters including precipitation (De Vos et al., 2017; Bardossy et al., 2021), air pressure (de Vos et al., 2020), and wind speed (Droste et al., 2020). While the data quality of individual stations remains low, many insights have been gained on error sources, quality control, and filtering algorithms (Meier et al., 2017; Hammerberg et al., 2018; Napolý et al., 2018; de Vos et al., 2019; Mandement and Caumont, 2020; Fenner et al., 2021). This development is dynamic, and the uncertainty in crowdsourced CWS data much depends on the parameter of interest and the network density, but confidence increases that robust parameter estimates can be derived for spatial averages or climatology. Other crowdsourcing sensors of high interest are cars (Bröring et al., 2015; Bonczak and Kontokosta, 2019) and smartphones, which have been used to observe air pressure (Mass and Madaus, 2014; de Vos et al., 2020) and air temperature (Overeem et al., 2013; Droste et al., 2017a), amongst others (see previous section).

A major driver of advancements in crowdsourcing is the growing number of applications. CWS have been used to analyze urban heat islands (Meier et al., 2017; Varentsov et al., 2021; Venter et al., 2021), hailstorms (Clark et al., 2018), and deep convection (Mandement and Caumont, 2020); for high-resolution mapping of air temperature (Venter et al., 2020; Vulova et al., 2020; Zumwald et al., 2021); to derive boundary conditions for urban-climate models (Jin et al., 2021); and for operational weather forecasts (Nipen et al., 2020). Furthermore, CWS data have been combined with novel datasets emerging in UCI (Section 2.3) such as high-resolution 3D urban models, such that we better understand the role of urban design and land cover on urban microclimate (Potgieter et al., 2021). Since crowdsourced data allow new types of analyses and improve the accuracy of short-term forecasts, they have slowly gained acceptance in the climatology community, but concerns about data quality remain. For centuries, climatologists have developed and advanced standards and protocols to make observations comparable between places and decades; in the future, much of this rigor must be applied to the quality control and filtering algorithms of crowdsourced data.

## Unmanned Aerial Vehicles

Observations from unmanned aerial vehicles (UAVs) are at the smallest scale of remote sensing for monitoring land surface dynamics. Unmanned aerial systems (UASs) produce high

spatial resolution data, sufficiently detailed to make field-level decisions, and fill the gap between satellite and *in-situ*, near-ground observations (Emilien et al., 2021). The genesis of UAS dates back to 1849 and was, for a long time, driven by military needs (Rakha and Gorodetsky, 2018). In the early 1970s, Konrad et al. (1970) pioneered the use of UAVs in meteorology to study the dynamics of the convective process, which requires fine-scale data on the temporal and spatial structure of the atmosphere. To overcome limitations of available platforms at that time (e.g., balloons, towers, and full-sized aircraft), the authors developed and tested a small, radio-controlled aircraft with meteorological sensing instrumentation as a versatile measurement platform. Over the next decades, technical developments facilitated more frequent uses of UAVs in atmospheric research. For example, Leuenberger et al. (2020) evaluated the assimilation of boundary layer observations gathered by “Meteodrones” into the numerical weather prediction system at Meteoswiss and found that the drone observations improved fog prediction. Chilson et al. (2019) proposed an automated 3D mesonet based on autonomous UAS stations to observe atmospheric profiles similar to standard “mesonets”, which consist of surface-based, *in-situ* stations. Although this work is in its infancy, a 3D network could significantly enhance our monitoring capacity of environmental variables in the lower atmosphere, improve our understanding of atmospheric boundary layer processes, and improve high-impact numerical weather prediction. Despite the low cost and resolution advantages, drones still have limited use in climatology, because they require additional sensors beyond RGB imagery, and flight durations are short (Yavaşlı, 2020).

Yet, UAVs have proven to be useful in an urban climate context, as shown by Rakha and Gorodetsky (2018). Their comprehensive review of thermal drones for energy audits highlights that the increased accessibility, efficiency, and safety of drones expedites the improvement and retrofitting of aging and energy-inefficient building stock and infrastructure. This finding is corroborated by Bayomi et al. (2021), who collected thermal drone data to calibrate a building energy model for improved performance and to assess building material degradation, thermal bridging, and insulation failures. In recent years, UAVs have been increasingly deployed to measure 3D urban form (Gevaert et al., 2017) and to monitor *in-situ* air quality (Kuuluvainen et al., 2018), but limitations such as flight duration, payload capacity, and sensor dimensions, accuracy, and sensitivity remain (Villa et al., 2016).

### 2.3 Datasets

New emerging datasets are key for representing realistic, heterogeneous urban environments while driving insight into the exposure of urban residents to climate challenges. These datasets are obtained through planned processes gathering information on defined research questions (***purposeful*** data) such as LiDAR point clouds, or secondary outcomes of technological processes and platforms used in urban areas (***organic*** data) such as social media data. The source, intention, and method of data collection further dominate whether the dataset is ***structured***, or more importantly, can be

***activated*** for use in climate analyses (i.e., used to develop insights or devise action). While the unprecedented ***volume*** of data is offering exciting opportunities for better understanding and quantifying urban climate challenges, the ***velocity*** (rate at which the data are generated), ***veracity*** (truthfulness, accuracy, and quality of data), and ***ownership*** (access to, possession of, and responsibility for data) creates significant challenges for data use in climate research and application. For instance, while data policies of authorities have become considerably more open over the past decade, data generated by citizens are often legally “owned” by private companies, thus their long-term availability depends on business interests and success. The challenges of data ownership are manifested in access to 3D urban models, where the development of Data as a Service (DaaS) prohibits their dissemination for modeling or observational studies. Lastly, new datasets raise novel challenges with respect to privacy, most seen in human-scale data collection. Here, we detail three novel data types that have been successfully collected and used for urban climate analyses and discuss limitations in research and application.

### Big Data

Detailed, accurate 3D information on a city’s composition, configuration, and morphology is key for urban climate analyses and applications. The wide variety of building types, architectural features, construction materials, and the distribution of vegetation govern the interactions between the city and its surrounding atmosphere (Middel et al., 2014; Oke et al., 2017; Ching et al., 2018). Traditionally, 3D city models and urban form parameters have been established using photogrammetry (processing optical stereo imagery) or high-resolution satellite images (Masson et al., 2020a). More recent approaches use large point clouds (next section) or procedural modeling (Nishida et al., 2018) to automatically generate cityscapes (Ching et al., 2019a). In the advent of big data, researchers started to repurpose large datasets that were originally collected for non-urban-climate purposes, such as street level photography. Street View image repositories from Google, Baidu, Mapillary, Tencent have increasingly become available and been used to characterize the built environment using machine learning (feature detection and image segmentation) (Keralis et al., 2020). A street canyon perspective is more human-centric than bird’s eye view imagery, which is particularly important for human thermal comfort, health, and behavioral studies (Middel et al., 2019). Past research has used Street View images to quantify street greenery (Li et al., 2017; Lu, 2019), building age (Li et al., 2018), building floor count (Iannelli and Dell’Acqua, 2017), sidewalks and crosswalks (Hara et al., 2013; Berriel et al., 2017), urban land use (Zhang et al., 2017), and sky view factors (Middel et al., 2018; Zeng et al., 2018; Nice et al., 2020). Street level images have also been used to conduct virtual neighborhood audits to assess walkability (Yin and Wang, 2016), bikeability (Arellana et al., 2020), traffic safety (Mooney et al., 2016), physical activity (Griew et al., 2013), and human health (Keralis et al., 2020). Lastly, Street View images have been linked to urban climate parameters such as surface temperature (Zhang et al., 2019) and air quality (Apte

et al., 2017). While street level imagery offers remote access to urban form, design, and function, many providers have recently restricted free image downloads. Other known constraints include limited spatial and temporal availability (i.e., the user does not have control over image acquisition season, date, time, and location), images are usually taken in the center of the road, not on the sidewalk, and they do not provide insight into backyards. Yet, with more and more users volunteering geographic information, uploading crowdsourced photography, and more companies entering the mapping market, Street View products will remain a valuable big data source for urban climates studies.

### LiDAR Point Clouds

Urban areas affect the atmosphere via their built materials, distinct surface cover and urban structure. The latter refers to the 3D urban morphology, or urban form, that determines albedo and aerodynamic roughness, and controls radiative exchange and airflow (Oke et al., 2017). With advances in remote sensing, LiDAR (Light Detection And Ranging) systems have become a well-established alternative to stereo photogrammetry for generating digital urban models. Point clouds from airborne, mobile, or terrestrial LiDAR yield 3D urban form at unprecedented spatial resolution (Yan et al., 2015; Bonczak and Kontokosta, 2019). Wang et al. (2018) reviewed urban reconstruction algorithms for point cloud data, evaluated their performance in modeling architectural elements (e.g., buildings, roads, bridges, power lines, trees), and highlighted the generation of 3D city models with multiple levels of detail (LoDs). In this context, CityGML by the Open Geospatial Consortium has emerged as a widely accepted standard for describing the representation, storage, and exchange of digital 3D city and landscape models (Gröger and Plümer, 2012). Higher levels of detail require more data storage, and as such, pathways are currently explored on how to represent multiple levels of detail (LoDs) while optimizing storage. This relates to the urban-scale space exploration (Lafarge, 2015) and the concept of “fit-for-purpose” urban data as advertised by the World Urban Database and Access Portal Tools project (WUDAPT, Ching et al., 2018, 2019; Bechtel et al., 2019) that aims to find an optimal solution across scales as a tradeoff between data complexity and model accuracy.

Point clouds have myriad urban climate applications. Urech et al. (2020) used LiDAR to reconstruct digital 3D landscapes and devised a framework to generate future landscape scenarios by manipulating the point cloud. This information was subsequently used to inform the Discrete Anisotropic Radiative Transfer (DART) model that estimates the 3D radiative budget of urban and natural landscapes, and to assess changes in thermal comfort in a neighborhood in Singapore. Dissegna et al. (2019) calculated the leaf area density (LAD) of urban trees from terrestrial LiDAR scans to quantify the contribution of vegetation to the radiative budget of a city, which can mitigate the urban heat island (UHI) effect and ultimately contribute to the development of climate resilient urban spaces. Other studies used airborne LiDAR data to map urban vegetation and LAD in Vienna, Austria (Höfle et al., 2012) and Gothenburg, Sweden

(Klingberg et al., 2017), thereby indicating the important ecological characteristics of urban vegetation that influence urban climate through shading and transpiration cooling and air quality through air pollutant deposition. The Urban Multi-scale Environmental Predictor (UMEP), an urban climate service tool (Lindberg et al., 2018), combines models and approaches for fine-scale climate simulations. The tool includes modules to derive digital surface models (DSM) and canopy digital surface models (CDSM) from airborne LiDAR and has recently been used in various heat exposure and mitigation studies across the globe (Aminipour et al., 2019; Kong et al., 2022).

Reviewing the latest advances of LiDAR-based mobile mapping systems, Wang et al. (2020) identified challenges related to reliable positioning, the need for more sophisticated deep-learning architectures to classify point clouds, and AI challenges to comprehensively understand semantics of complex urban streetscapes. Nevertheless, the authors envision that point clouds will give rise to a new category of geo-big data and will play an important role in future monitoring, detection, and modeling tasks.

### Social Media

In the era of information and communications technology, urban geolocated social media data (SMD) offer new opportunities to indirectly measure the impact of hazards on society, to advance understanding of complex urban dynamics, and to support decision-making for sustainability transformations (Ilieva and McPhearson, 2018; Creutzig et al., 2019). SMD from Flickr, Twitter, Foursquare, Facebook, Instagram, etc. have the potential to fill important data gaps that prevent researchers and practitioners from understanding human-environment interactions. During the first IPCC Cities and Climate Science Conference in Edmonton, Canada (Bai et al., 2018; Frantzeskaki et al., 2019), SMD indicators of social, ecological, and infrastructural change were highlighted in a series of synthesis statements on the role, potential, and research gaps of nature-based solutions for climate adaptation and mitigation. Grasso et al. (2017) argue that micro-blogging platforms such as Twitter may be used as a distributed network of mobile sensors that react to external events by exchanging messages. They found significant associations between the daily increase in tweets and extreme temperatures during a 2015 summer heat wave in Italy, indicating that the daily volume of Twitter messages can indicate local heatwave impacts, improve preparedness measures at the regional and local level, and thus reduce heat vulnerability. Young et al. (2021) came to a similar conclusion when studying Twitter data to detect different scales of response and varying attitudes towards heat waves in the United Kingdom (United Kingdom), the United States of America (US), and Australia. They performed a sentiment analysis, i.e., the field of natural language processing that aims to extract the attitude conveyed in a body of text. The United Kingdom and US had similar levels of positivity during the heatwave, while Australians were more negative, with a significant sentiment increase as temperature decreased. By quantitatively reviewing 169 studies that use data from social media and social networking sites to better

understand human-environment interactions (Ghermandi and Sinclair, 2019), suggest that SMD offers unprecedented opportunities in terms of data volume, scale of analysis, and real-time monitoring. At the same time, challenges remain, including the integration of different types of information in data matching, the development of quality assurance procedures and ethical codes, an improved integration with existing methods, and the assurance of long-term, free, and easy-to-access provision of public social media data (Ghermandi and Sinclair, 2019).

### 3 ADVANCEMENTS IN DATA PROCESSING

The emergence of new digital infrastructure and analytics algorithms and platforms is a major driver of UCI. Cloud storage and computing allow bigger data volumes to be stored outside of the sphere of physical storage and processed directly in the cloud. Furthermore, novel analysis methods (e.g., AI or edge computing) complement previous advancements and remove some privacy and security concerns of previous approaches that analyzed the impact of urban climate on residents.

#### 3.1 Algorithms

Climate is increasingly becoming a data problem (Jones, 2017). For example, the compressed climate model output for the sixth Coupled Model Intercomparison Project (CMIP6) is estimated at 18 Peta Bytes, which is five times the size of the CMIP5 archive (Balaji et al., 2018). The research field “Climate Informatics” encourages collaborations between climate scientists and machine learning researchers to help bridge the gap between data and understanding and to accelerate discovery in climate science (Monteleoni et al., 2016; Huntingford et al., 2019). Machine Learning (ML) techniques have been used to find complex patterns and networks in large data, insights that might otherwise depend on expert judgment or physical-based rules (Jones, 2017). ML also speeds up the development of parameterizations in weather and climate models (or their sub-components, e.g., land surface models), either by completely replacing physically-based parameterizations by data-driven neural networks or by harnessing ML to calibrate or “tune” the many free parameters involved in their formulation (Couvreur et al., 2021; Hourdin et al., 2021; Pal and Sharma, 2021). In urban climate studies, the use of ML or other artificial intelligence (AI) techniques such as deep learning has been primarily used to derive urban form and land cover from image datasets. Ma et al. (2019) reviewed 200 remote sensing studies and found that deep learning was predominantly used in urban applications. Xu et al. (2019) employed convolutional neural networks (CNNs) and ground-level images to classify urban areas into climate zones, while Zhou et al. (2021) and Yoo et al. (2019) used deep learning, CNN, and random forest to map LCZs from remotely sensed images. Deep learning has also been used to predict air pollution in urban areas using satellite data (Lee et al., 2021) and Street View images (Suel et al., under review). Venter et al. (2020) applied a random forest model to Sentinel, Landsat, LiDAR, and crowd-sourced air temperature measurements to model hyper-local urban air temperature

distribution concluding that the resulting maps can complement and validate traditional urban canopy models.

#### 3.2 Digital Infrastructure and Platforms

##### Platforms for Big Earth Observation Data

As discussed in the introduction, many urban climate studies rely on remotely sensed Earth Observation (EO) data, which has become increasingly more available, accurate, and fine-scaled. EO products are frequently used to assess the surface urban heat island (SUHI), perform land cover classifications, and provide input for models of urban surface-atmosphere exchange (Voogt and Oke, 2003). Many EO datasets are delivered on a daily basis, providing a massive amount of remotely sensed data that places us in an age of big EO data (Chi et al., 2016). Over the last decade, cutting-edge platforms have been developed to support a new generation of spatial data infrastructure based on cloud computing, distributed systems, MapReduce systems, and web services. These systems address challenges related to big EO data management heterogeneity, storage, processing, analytics, visualization, sharing, and applications (Li et al., 2020c). Importantly, the development of data infrastructure enables the application of data standards to data layers developed by diverse stakeholders and addresses challenges regarding data interoperability and integration. In their review, Gomes et al. (2020) define “platforms for big EO data management and analysis” as computational solutions that provide functionalities for data management, storage, and access; that allow processing on the server side without having to download large datasets; and that provide a certain level of data and processing abstractions for EO community users and researchers. Seven platforms currently match this definition: Google Earth Engine (GEE) (Gorelick et al., 2017), Sentinel Hub (Sinergise, 2018), Open Data Cube (Open Data Cube, 2021), System for Earth Observation Data Access, Processing and Analysis for Land Monitoring (SEPAL, FAO, 2021), OpenEO (Pebesma et al., 2017), the JRC Earth Observation Data and Processing Platform (JEODPP, Soille et al., 2018), and pipsCloud (Wang L. et al., 2018; Gomes et al., 2020). GEE is probably the most widely used platform in urban climate studies.

Amani et al. (2020) reviewed 450 GEE-related journal articles and found 40 papers on urban topics, including urban planning, development and extent; urban morphology; and urban temperature and heat island studies. For example, Cheng et al. (2018) and Zhang et al. (2020) used GEE to develop global maps of manmade impervious areas. Li M. et al. (2020) mapped urban 3D building structure, i.e., building footprint, height, and volume, for Europe, the United States, and China using random forest models in GEE. Huang et al. (2018) and Duan et al. (2019) used GEE to map urban green spaces and urban forests in China using Landsat and Sentinel-2 imagery, respectively. In a series of papers, Demuzere et al. (2019a, 2019b, 2020, 2021) converted the off-line single-city Local Climate Zone (LCZ) mapping strategy (Stewart and Oke, 2012; Bechtel et al., 2015) into a GEE-based procedure that allows for the creation of continental-scale LCZ maps, including a web-application (LCZ generator, <https://lcz-generator.rub.de/>) that makes LCZ mapping fast and easy. Bechtel et al. (2019b) assessed the SUHI from MODIS and

Landsat against LCZ maps for 50 global cities, and Chakraborty and Lee (2019) computed the SUHI from MODIS for over 9500 urban clusters and examined how vegetation controls spatiotemporal SUHI variability. Benz et al. (2017) analyzed global shallow groundwater temperatures by processing and integrating land surface temperatures, evapotranspiration data, and snow cover in GEE. The availability of LCZ mapping has also enabled a consistent comparison with three-dimensional urban data (**Section 2.3**) for different cities, providing detailed city-descriptive input parameters for climate models (Lipson et al., under review).

Big Earth data and related platforms introduced disruptive changes in EO data management and analysis (Sudmanns et al., 2019). Yet, despite their advancements, challenges remain. For example, Gomes et al. (2020) report that none of the investigated platforms offer all ten required EO capabilities presented by Camara et al. (2016) and Ariza-Porras et al. (2017). Besides technical challenges, organizational and political challenges exist that are partly unsolved or not discussed, such as security issues (e.g., storing datasets or algorithms on non-proprietary platforms) or increasing costs for developing and maintaining such platforms. These issues lead to the question whether Big EO data platforms will continue to provide reliable data and services in the future (Sudmanns et al., 2019).

### Cloud Computing

In recent years, cloud computing services have become increasingly affordable. Third-party providers such as Amazon Web Services (AWS), Microsoft Azure, and Google Cloud host and maintain scalable computing infrastructure, i.e., customers are only charged for the infrastructure they use. Several recent urban climate studies have used cloud computing for modeling sky view factors (Dirksen et al., 2019), to run WRF (Goga et al., 2018), simulate microclimate with ENVI-met (Crank et al., under review), and predict neighborhood air pollution (Triscone et al., 2016). Cloud services also gain popularity in crowdsourcing and IoT applications. For example, Fauzandi et al. (2021) designed and implemented a low-cost sensor system for UHI observations using AWS, and Kulkarni et al. (under review) used an AWS database to store biometeorological observations and people counts from an IoT device in a public park. Similar to Big EO data platforms, cloud computing has limitations related to server availability (e.g., downtime during service outages), security, and privacy. Cloud computing also offers limited control and flexibility because the infrastructure is managed by the service provider, not the urban climate researcher, and is often tied to a specific vendor (the service provider). Despite these limitations, it is expected that cloud computing will play a major role in UCI as simulations become more complex and datasets increase in size.

## 4 CONCLUSION AND OUTLOOK

The field of urban climate has greatly advanced our understanding of city-atmosphere interactions since the first weather map was created in the mid-19th century. Driven by sensing and modeling physical phenomena, urban climate

research in the past decade has integrated multidisciplinary methods and practices complementing the core principles in atmospheric science. UCI parallels this development, embracing various scientific disciplines such as data science, geospatial analyses, urban design, health, and policy. A clear paradigm shift can be seen from focusing on city-atmosphere interactions to tackling grand challenges of the Anthropocene, including climate change, urban overheating, poor air quality, and climate injustice. New advancements enabled by UCI offer unprecedented opportunities to understand these grave problems and support a variety of applications.

UCI facilitates the development of adaptation and mitigation strategies for urban climate challenges by pushing the boundaries of observational networks, model resolution, and domain size to yield unprecedented details on hazard distribution. High resolution 3D city data paired with detailed thermal properties of the urban fabric enable urban climatologists to answer questions about optimal tree placement, the amount of available shade, and heat retention in urban canyons. Digital twins—virtual city models integrating various datasets, real-time sensing, and predictive models of underlying atmospheric processes—are on the rise and will eventually allow analyses of complex city-atmosphere interactions at fine temporal and spatial scales. Although still in their infancy, Digital Twins have already been used to support collaborative and participatory urban planning and aid in hyper-local air pollution mitigation (Dembski et al., 2020). The City of Zurich uses Digital Twins to simulate urban climate, noise, air pollution, and create future scenarios for decision-making (Schrotter and Hürzeler, 2020).

Computational steering (interactively changing parameters during simulation) has the potential to transform how we parameterize and run urban climate models. The future of urban climate may even be in the cloud! In parallel, as sensing capabilities grow, cities will become smarter through sensors embedded in the urban fabric. These future directions in UCI research and application are instrumental in achieving the vision of climate-sensitive urban design and planning.

In recent years, the focus of urban climate has shifted from UHI studies towards intra-urban hazard distribution and human thermal exposure assessments. Emerging research aims to combine climate analyses with various urban data layers to achieve more comprehensive vulnerability and inequity analyses. For example, Harlan et al. (2006) investigated heat-related health inequalities related to microclimate considering socioeconomic status, ethnicity data, and urban form and configuration descriptors. Results showed that residents in hotter neighborhoods were more vulnerable because of fewer resources to cope with heat. Servadio et al. (2019) analyzed health outcomes and air pollution exposure in Atlanta using various data layers and found that areas with majority African-American populations exhibited significantly higher exposure to poor air quality. Considering the social dimensions of atmospheric impacts in neighborhoods allows to further identify “hotspots” with vulnerable populations that are unproportionally affected by hazards. This is further enabled by novel digital communication platforms (such as public data dashboards) that use simplified

data visualizations as well as easily comprehensible metrics and indicators to communicate the relevance of urban climate data for urban dwellers. The contributions of UCI to public engagement not only bridge the communication gap and inform residents about the extent of urban climate challenges, but also enable people to make individual decisions that can minimize exposure to environmental stressors in cities. Lastly, the emergence of “humans as sensors” and citizen science in UCI is key to not only inform urban dwellers, but also devise the most effective solutions for improving human health and wellbeing in the face of increased climate challenges.

Novel approaches always entail barriers that need to be overcome, and UCI is no exception. With respect to novel sensors and data sources, guidelines and best practices must be established to guarantee standardized methods for crowdsourcing, IoT sensing, data curation, processing, storage, and metadata documentation. In addition, long-term availability of data must be secured. While public entities have recently adopted more open data policies, citizen-science generated data are often legally owned by private companies and dependent on short-term business interests. Another emerging concern is data privacy, which needs careful consideration at the design phase of any implementation.

While big, unprecedented data sets offer exciting opportunities to better understand the Earth System, our data collection ability currently outweighs our usage and analysis capacity. Too often, available data are not activated, leaving behind unused potential. Moving forward, the focus should not only be on new data collection but also drawing meaningful insight from data sets already available. Also, with inflating raw data, processing chains require higher attention, highlighting the important role of open-source quality control packages.

Finally, as human-centric data collection through mobile devices becomes more mainstream, the digital divide must be addressed. While smart technology enables wide-scale, human-centric data collection, more affluent areas will have more access to those technologies, further contributing to urban climate inequity.

## REFERENCES

- Alvarez-Vanhardt, E., Corpetti, T., and Houet, T. (2021). UAV & Satellite Synergies for Optical Remote Sensing Applications: A Literature Review. *Sci. Remote Sens.* 3, 100019. doi:10.1016/j.srs.2021.100019
- Amani, M., Ghorbanian, A., Ahmadi, S. A., Kakooei, M., Moghimi, A., Mirmazloumi, S. M., et al. (2020). Google Earth Engine Cloud Computing Platform for Remote Sensing Big Data Applications: A Comprehensive Review. *IEEE J. Sel. Top. Appl. Earth Obs. Remote Sens.* 13, 5326–5350. doi:10.1109/JSTARS.2020.3021052
- Aminipour, M., Knudby, A. J., Krayenhoff, E. S., Zickfeld, K., and Middel, A. (2019). Modelling the Impact of Increased Street Tree Cover on Mean Radiant Temperature across Vancouver’s Local Climate Zones. *Urban For. Urban Green.* 39, 9–17. doi:10.1016/j.ufug.2019.01.016
- Apte, J. S., Messier, K. P., Gani, S., Brauer, M., Kirchstetter, T. W., Lunden, M. M., et al. (2017). High-Resolution Air Pollution Mapping with Google Street View Cars: Exploiting Big Data. *Environ. Sci. Technol.* 51, 6999–7008. doi:10.1021/acs.est.7b00891

Cities are living, breathing ecosystems that include physical, socio-economical, and behavioral processes. UCI seeks to understand and respond to such complex, dynamic human-environment interactions through novel technological, methodological, and systems thinking approaches, achieving more integrated and human-centric assessments of urban climate challenges in future research and application. Moving forward, UCI will undoubtedly shape the urban climate research agenda for upcoming decades and positively impact fundamental, applied, and policy-relevant research.

## DATA AVAILABILITY STATEMENT

The original contributions presented in the study are included in the article/Supplementary Material, further inquiries can be directed to the corresponding author.

## AUTHOR CONTRIBUTIONS

AM conceived the idea and presented it as a keynote at EGU. All authors refined the definition of UCI, reviewed and organized literature, developed the UCI figure, and wrote and edited the final manuscript.

## FUNDING

This research was funded by the National Science Foundation, grant number CMMI-1942805 (CAREER: Human Thermal Exposure in Cities - Novel Sensing and Modeling to Build Heat-Resilience). MD and BB are supported by the ENLIGHT project, funded by the German Research Foundation (DFG) under grant No. 437467569. Any opinions, findings, and conclusions or recommendations expressed in this material are those of the authors and do not necessarily reflect the views of the sponsoring organizations.

- Arellana, J., Saltarín, M., Larrañaga, A. M., González, V. I., and Henao, C. A. (2020). Developing an Urban Bikeability Index for Different Types of Cyclists as a Tool to Prioritise Bicycle Infrastructure Investments. *Transp. Res. Part A Policy Pract.* 139, 310–334. doi:10.1016/j.tra.2020.07.010
- Ariza-Porras, C., Bravo, G., Villamizar, M., Moreno, A., Castro, H., Galindo, G., et al. (2017). CDCol: A Geoscience Data Cube that Meets Colombian Needs. *Commun. Comput. Inf. Sci.* 735, 87–99. doi:10.1007/978-3-319-66562-7\_7/FIGURES/3
- Bai, X., Dawson, R. J., Ürge-Vorsatz, D., Delgado, G. C., Salisu Barau, A., Dhakal, S., et al. (2018). Six Research Priorities for Cities and Climate Change. *Nature* 555, 23–25. doi:10.1038/d41586-018-02409-z
- Balaji, V., Taylor, K. E., Juckes, M., Lawrence, B. N., Durack, P. J., Lautenschlager, M., et al. (2018). Requirements for a Global Data Infrastructure in Support of Cmp6. *Geosci. Model Dev.* 11, 3659–3680. doi:10.5194/gmd-11-3659-2018
- Bárdossy, A., Seidel, J., and El Hachem, A. (2021). The Use of Personal Weather Station Observations to Improve Precipitation Estimation and Interpolation. *Hydrol. Earth Syst. Sci.* 25, 583–601. doi:10.5194/HESS-25-583-2021

- Bayomi, N., Nagpal, S., Rakha, T., and Fernandez, J. E. (2021). Building Envelope Modeling Calibration Using Aerial Thermography. *Energy Build.* 233, 110648. doi:10.1016/j.enbuild.2020.110648
- Bechtel, B., Alexander, P., Böhner, J., Ching, J., Conrad, O., Feddema, J., et al. (2015). Mapping Local Climate Zones for a Worldwide Database of the Form and Function of Cities. *Ijgi* 4, 199–219. doi:10.3390/ijgi4010199
- Bechtel, B., Alexander, P. J., Beck, C., Böhner, J., Brousse, O., Ching, J., et al. (2019a). Generating WUDAPT Level 0 Data - Current Status of Production and Evaluation. *Urban Clim.* 27, 24–45. doi:10.1016/j.ulim.2018.10.001
- Bechtel, B., and Daneke, C. (2012). Classification of Local Climate Zones Based on Multiple Earth Observation Data. *IEEE J. Sel. Top. Appl. Earth Obs. Remote Sens.* 5, 1191–1202. doi:10.1109/JSTARS.2012.2189873
- Bechtel, B., Demuzere, M., Mills, G., Zhan, W., Sismanidis, P., Small, C., et al. (2019b). SUHI Analysis Using Local Climate Zones—Comparison of 50 Cities. *Urban Clim.* 28, 100451. doi:10.1016/j.ulim.2019.01.005
- Bell, S., Cornford, D., and Bastin, L. (2015). How Good Are Citizen Weather Stations? Addressing a Biased Opinion. *Weather* 70, 75–84. doi:10.1002/wea.2316
- Benz, S. A., Bayer, P., and Blum, P. (2017). Global Patterns of Shallow Groundwater Temperatures. *Environ. Res. Lett.* 12, 034005. doi:10.1088/1748-9326/aa5fb0
- Berriel, R. F., Rossi, F. S., de Souza, A. F., and Oliveira-Santos, T. (2017). Automatic Large-Scale Data Acquisition via Crowdsourcing for Crosswalk Classification: A Deep Learning Approach. *Comput. Graph.* 68, 32–42. doi:10.1016/j.cag.2017.08.004
- Bonczak, B., and Kontokosta, C. E. (2019). Large-scale Parameterization of 3D Building Morphology in Complex Urban Landscapes Using Aerial LiDAR and City Administrative Data. *Comput. Environ. Urban Syst.* 73, 126–142. doi:10.1016/j.compenvurbsys.2018.09.004
- Broadbent, A. M., Krayenhoff, E. S., and Georgescu, M. (2020). The Motley Drivers of Heat and Cold Exposure in 21st Century US Cities. *Proc. Natl. Acad. Sci. U.S.A.* 117, 21108–21117. doi:10.1073/pnas.2005492117
- Bröring, A., Remke, A., Stasch, C., Autermann, C., Rieke, M., and Möllers, J. (2015). enviroCar: A Citizen Science Platform for Analyzing and Mapping Crowd-Sourced Car Sensor Data. *Trans. GIS* 19, 362–376. doi:10.1111/tgis.12155
- Cabrera, A. N., Droste, A., Heusinkveld, B. G., and Steeneveld, G.-J. (2021). The Potential of a Smartphone as an Urban Weather Station—An Exploratory Analysis. *Front. Environ. Sci.* 9, 344. doi:10.3389/fenvs.2021.673937
- Caluwaerts, S., Top, S., Vergauwen, T., Wauters, G., De Ridder, K., Hamdi, R., et al. (2021). Engaging Schools to Explore Meteorological Observational Gaps. *Bull. Am. Meteorol. Soc.* 102, E1126–E1132. doi:10.1175/BAMS-D-20-0051.1
- Camara, G., Assis, L. F., Ribeiro, G., Ferreira, K. R., Llapa, E., Vinhas, L., et al. (2016) 2016. Big Earth Observation Data Analytics. *Proc. 5th ACM SIGSPATIAL Int. Work. Anal. Big Geospatial Data, BigSpatial*, 1–6. doi:10.1145/3006386.3006393
- Chakraborty, T., and Lee, X. (2019). A Simplified Urban-Extent Algorithm to Characterize Surface Urban Heat Islands on a Global Scale and Examine Vegetation Control on Their Spatiotemporal Variability. *Int. J. Appl. Earth Observation Geoinformation* 74, 269–280. doi:10.1016/j.jag.2018.09.015
- Chapman, L., Bell, C., and Bell, S. (2017a). Can the Crowdsourcing Data Paradigm Take Atmospheric Science to a New Level? A Case Study of the Urban Heat Island of London Quantified Using Netatmo Weather Stations. *Int. J. Climatol.* 37, 3597–3605. doi:10.1002/joc.4940
- Chapman, S., Watson, J. E. M., Salazar, A., Thatcher, M., and McAlpine, C. A. (2017b). The Impact of Urbanization and Climate Change on Urban Temperatures: a Systematic Review. *Landsc. Ecol.* 32, 1921–1935. doi:10.1007/s10980-017-0561-4
- Chavan, G., and Momin, B. (2017) 2017. An Integrated Approach for Weather Forecasting over Internet of Things: A Brief Review. *Proc. Int. Conf. IoT Soc. Mob. Anal. Cloud, I-SMAC*, 83–88. doi:10.1109/I-SMAC.2017.8058291
- Cheng, G., Yang, C., Yao, X., Guo, L., and Han, J. (2018). When Deep Learning Meets Metric Learning: Remote Sensing Image Scene Classification via Learning Discriminative CNNs. *IEEE Trans. Geosci. Remote Sens.* 56, 2811–2821. doi:10.1109/TGRS.2017.2783902
- Cheng, Y. L., Lim, M. H., and Hui, K. H. (2022). Impact of Internet of Things Paradigm towards Energy Consumption Prediction: A Systematic Literature Review. *Sustain. Cities Soc.* 78, 103624. doi:10.1016/j.scs.2021.103624
- Chi, M., Plaza, A., Benediktsson, J. A., Sun, Z., Shen, J., and Zhu, Y. (2016). Big Data for Remote Sensing: Challenges and Opportunities. *Proc. IEEE* 104, 2207–2219. doi:10.1109/JPROC.2016.2598228
- Chilson, P. B., Bell, T. M., Brewster, K. A., Britto Hupsel de Azevedo, G., Carr, F. H., Carson, K., et al. (2019). Moving towards a Network of Autonomous UAS Atmospheric Profiling Stations for Observations in the Earth's Lower Atmosphere: The 3D Mesonet Concept. *Sensors* 19, 2720. doi:10.3390/s19122720
- Ching, J., Aliaga, D., Mills, G., Masson, V., See, L., Neophytou, M., et al. (2019a). Pathway Using WUDAPT's Digital Synthetic City Tool towards Generating Urban Canopy Parameters for Multi-Scale Urban Atmospheric Modeling. *Urban Clim.* 30, 100459. doi:10.1016/j.ulim.2019.100527
- Ching, J., Aliaga, D., Mills, G., Masson, V., See, L., Neophytou, M., et al. (2019b). Pathway Using WUDAPT's Digital Synthetic City Tool towards Generating Urban Canopy Parameters for Multi-Scale Urban Atmospheric Modeling. *Urban Clim.* 28, 100459. doi:10.1016/j.ulim.2019.100459
- Ching, J., Mills, G., Bechtel, B., See, L., Feddema, J., Wang, X., et al. (2018). WUDAPT: An Urban Weather, Climate, and Environmental Modeling Infrastructure for the Anthropocene. *Bull. Am. Meteorol. Soc.* 99, 1907–1924. doi:10.1175/BAMS-D-16-0236.1
- Clark, M. R., Webb, J. D. C., and Kirk, P. J. (2018). Fine-scale Analysis of a Severe Hailstorm Using Crowd-Sourced and Conventional Observations. *Mater. Apps* 25, 472–492. doi:10.1002/met.1715
- Couvreux, F., Hourdin, F., Williamson, D., Roehrig, R., Volodina, V., Villefranque, N., et al. (2021). Process-Based Climate Model Development Harnessing Machine Learning: I. A Calibration Tool for Parameterization Improvement. *J. Adv. Model. Earth Syst.* 13, e2020MS002217. doi:10.1029/2020MS002217
- Creutzig, F., Lohrey, S., Bai, X., Baklanov, A., Dawson, R., Dhakal, S., et al. (2019). Upscaling Urban Data Science for Global Climate Solutions. *Glob. Sustain.* 2, doi:10.1017/sus.2018.16
- De Vos, L., Leijnse, H., Overeem, A., and Uijlenhoet, R. (2017). The Potential of Urban Rainfall Monitoring with Crowd-sourced Automatic Weather Stations in Amsterdam. *Hydrol. Earth Syst. Sci.* 21, 765–777. doi:10.5194/hess-21-765-2017
- de Vos, L. W., Droste, A. M., Zander, M. J., Overeem, A., Leijnse, H., Heusinkveld, B. G., et al. (2020). Hydrometeorological Monitoring Using Opportunistic Sensing Networks in the Amsterdam Metropolitan Area. *Bull. Am. Meteorol. Soc.* 101, E167–E185. doi:10.1175/BAMS-D-19-0091.1
- Dembski, F., Wößner, U., Letzgus, M., Ruddat, M., and Yamu, C. (2020). Urban Digital Twins for Smart Cities and Citizens: The Case Study of Herrenberg, Germany. *Sustainability* 202012, 2307. doi:10.3390/SU12062307
- Demuzere, M., Bechtel, B., Middel, A., and Mills, G. (2019a). Mapping Europe into Local Climate Zones. *PLoS One* 14, e0214474. doi:10.1371/journal.pone.0214474
- Demuzere, M., Bechtel, B., and Mills, G. (2019b). Global Transferability of Local Climate Zone Models. *Urban Clim.* 27, 46–63. doi:10.1016/j.ulim.2018.11.001
- Demuzere, M., Hankey, S., Mills, G., Zhang, W., Lu, T., and Bechtel, B. (2020). Combining Expert and Crowd-Sourced Training Data to Map Urban Form and Functions for the Continental US. *Sci. Data* 7, 1–13. doi:10.1038/s41597-020-00605-z
- Demuzere, M., Kittner, J., and Bechtel, B. (2021). LCZ Generator: A Web Application to Create Local Climate Zone Maps. *Front. Environ. Sci.* 9, 637455. doi:10.3389/fenvs.2021.637455
- Demuzere, M., Kittner, J., Martilli, A., Mills, G., Moede, C., Stewart, I. D., et al. (2022). A Global Map of Local Climate Zones to Support Earth System Modelling and Urban Scale Environmental Science. *Earth Syst. Sci. Data Discuss.* [Preprint]. doi:10.5194/essd-2022-92
- deSouza, P., Anjomshoaa, A., Duarte, F., Kahn, R., Kumar, P., and Ratti, C. (2020). Air Quality Monitoring Using Mobile Low-Cost Sensors Mounted on Trash-Trucks: Methods Development and Lessons Learned. *Sustain. Cities Soc.* 60, 102239. doi:10.1016/j.scs.2020.102239
- Dirksen, M., Ronda, R. J., Theeuwes, N. E., and Pagani, G. A. (2019). Sky View Factor Calculations and its Application in Urban Heat Island Studies. *Urban Clim.* 30, 100498. doi:10.1016/j.ulim.2019.100498
- Dissegna, M. A., Yin, T., Wei, S., Richards, D., and Grêt-Regamey, A. (2019). 3-D Reconstruction of an Urban Landscape to Assess the Influence of Vegetation in the Radiative Budget. *Forests* 10, 700. doi:10.3390/f10080700

- Droste, A. M., Heusinkveld, B. G., Fenner, D., and Steeneveld, G. J. (2020). Assessing the Potential and Application of Crowdsourced Urban Wind Data. *QJR Meteorol. Soc.* 146, 2671–2688. doi:10.1002/qj.3811
- Droste, A. M., Pape, J. J., Overeem, A., Leijnse, H., Steeneveld, G. J., Van Delden, A. J., et al. (2017a). Crowdsourcing Urban Air Temperatures through Smartphone Battery Temperatures in São Paulo, Brazil. *J. Atmos. Ocean. Technol.* 34, 1853–1866. doi:10.1175/JTECH-D-16-0150.1
- Droste, A. M., Pape, J. J., Overeem, A., Leijnse, H., Steeneveld, G. J., Van Delden, A. J., et al. (2017b). Crowdsourcing Urban Air Temperatures through Smartphone Battery Temperatures in São Paulo, Brazil. *J. Atmos. Ocean. Technol.* 34, 1853–1866. doi:10.1175/JTECH-D-16-0150.1
- Duan, Q., Tan, M., Guo, Y., Wang, X., and Xin, L. (2019). Understanding the Spatial Distribution of Urban Forests in China Using Sentinel-2 Images with Google Earth Engine. *Forests* 10, 729. doi:10.3390/f10090729
- Fauzandi, F. I., Retnowati, Y., Tamba, J. D., Husni, E. M., Yusuf, R., and Yahya, B. N. (2021). “Design and Implementation of Low Cost IoT Sensor System for Urban Heat Island Observation,” in *Design and Implementation of Low Cost IoT Sensor System for Urban Heat Island Observation*, 1–6. doi:10.1109/iceei52609.2021.9611099
- Fenner, D., Bechtel, B., Demuzere, M., Kittner, J., and Meier, F. (2021). CrowdQC+-A Quality-Control for Crowdsourced Air-Temperature Observations Enabling World-wide Urban Climate Applications. *Front. Environ. Sci.* 9, 553. doi:10.3389/fenvs.2021.720747
- Fenner, D., Meier, F., Bechtel, B., Otto, M., and Scherer, D. (2017). Intra and Inter ‘local Climate Zone’ Variability of Air Temperature as Observed by Crowdsourced Citizen Weather Stations in Berlin, Germany. *metz* 26, 525–547. doi:10.1127/metz/2017/0861
- Ferwati, S., Skelhorn, C., Shandas, V., Voelkel, J., Shawish, A., and Ghanim, M. (2018). Analysis of Urban Heat in a Corridor Environment - the Case of Doha, Qatar. *Urban Clim.* 24, 692–702. doi:10.1016/j.ulcim.2017.08.008
- Frantzeskaki, N., McPhearson, T., Collier, M. J., Kendal, D., Bulkeley, H., Dumitru, A., et al. (2019). Nature-based Solutions for Urban Climate Change Adaptation: Linking Science, Policy, and Practice Communities for Evidence-Based Decision-Making. *Bioscience* 69, 455–466. doi:10.1093/biosci/biz042
- Fugigladio, U., Santucci, D., Bojic, I., Santi, P., Cheung, T. C. T., Schiavon, S., et al. (2018). “Developing Personal Thermal Comfort Models for the Control of HVAC in Cars Using Field Data,” in *Proceedings of 10th Windsor Conference: Rethinking Comfort*, 442–450. Available at: <https://escholarship.org/uc/item/7vj0s2ht> (Accessed January 30, 2022).
- Georgescu, M., Moustakou, M., Mahalov, A., and Dudhia, J. (2013). Summer-time Climate Impacts of Projected Megapolitan Expansion in Arizona. *Nat. Clim. Change* 3, 37–41. doi:10.1038/nclimate1656
- Gevaert, C. M., Persello, C., Sliuzas, R., and Vosselman, G. (2017). Informal Settlement Classification Using Point-Cloud and Image-Based Features from UAV Data. *ISPRS J. Photogrammetry Remote Sens.* 125, 225–236. doi:10.1016/j.isprsjprs.2017.01.017
- Ghermandi, A., and Sinclair, M. (2019). Passive Crowdsourcing of Social Media in Environmental Research: A Systematic Map. *Glob. Environ. Change* 55, 36–47. doi:10.1016/j.GLOENVCHA.2019.02.003
- Goga, K., Parodi, A., Ruiu, P., and Terzo, O. (2018). Performance Analysis of WRF Simulations in a Public Cloud and HPC Environment. *Adv. Intell. Syst. Comput.* 611, 384–396. doi:10.1007/978-3-319-61566-0\_35
- Gomes, V., Queiroz, G., and Ferreira, K. (2020). An Overview of Platforms for Big Earth Observation Data Management and Analysis. *Remote Sens.* 12, 1253. doi:10.3390/RS12081253
- González, J. E., Ramamurthy, P., Bornstein, R. D., Chen, F., Bou-Zeid, E. R., Ghandehari, M., et al. (2021). Urban Climate and Resiliency: A Synthesis Report of State of the Art and Future Research Directions. *Urban Clim.* 38, 100858. doi:10.1016/j.UCLIM.2021.100858
- Gorelick, N., Hancher, M., Dixon, M., Ilyushchenko, S., Thau, D., and Moore, R. (2017). Google Earth Engine: Planetary-Scale Geospatial Analysis for Everyone. *Remote Sens. Environ.* 202, 18–27. doi:10.1016/j.rse.2017.06.031
- Grasso, V., Crisci, A., Morabito, M., Nesi, P., and Pantaleo, G. (2017). Public Crowdsensing of Heat Waves by Social Media Data. *Adv. Sci. Res.* 14, 217–226. doi:10.5194/asr-14-217-2017
- Griew, P., Hillsdon, M., Foster, C., Coombes, E., Jones, A., and Wilkinson, P. (2013). Developing and Testing a Street Audit Tool Using Google Street View to Measure Environmental Supportiveness for Physical Activity. *Int. J. Behav. Nutr. Phys. Act.* 10, 1–7. doi:10.1186/1479-5868-10-103
- Gröger, G., and Plümer, L. (2012). CityGML - Interoperable Semantic 3D City Models. *ISPRS J. Photogrammetry Remote Sens.* 71, 12–33. doi:10.1016/j.isprsjprs.2012.04.004
- Hab, K., Middel, A., Ruddell, B. L., and Hagen, H. (2015). TraVis - A Visualization Framework for Mobile Transect Data Sets in an Urban Microclimate Context. *IEEE Pac. Vis. Symp.* 2015, 167–174. doi:10.1109/PACIFICVIS.2015.7156374
- Häb, K., Ruddell, B. L., and Middel, A. (2015). Sensor Lag Correction for Mobile Urban Microclimate Measurements. *Urban Clim.* 14, 622–635. doi:10.1016/j.ulcim.2015.10.003
- Hamdi, R., Kusaka, H., Doan, Q.-V., Cai, P., He, H., Luo, G., et al. (2020). The State-Of-The-Art of Urban Climate Change Modeling and Observations. *Earth Syst. Environ.* 4, 631–646. doi:10.1007/s41748-020-00193-3
- Hammerberg, K., Brousse, O., Martilli, A., and Mahdavi, A. (2018). Implications of Employing Detailed Urban Canopy Parameters for Mesoscale Climate Modelling: a Comparison between WUDAPT and GIS Databases over Vienna, Austria. *Int. J. Climatol.* 38, e1241–e1257. doi:10.1002/joc.5447
- Happle, G., Wilhelm, E., Fonseca, J. A., and Schlueter, A. (2017). Determining Air-Conditioning Usage Patterns in Singapore from Distributed, Portable Sensors. *Energy Procedia* 122, 313–318. doi:10.1016/j.egypro.2017.07.328
- Hara, K., Le, V., and Froehlich, J. (2013). Combining Crowdsourcing and Google Street View to Identify Street-Level Accessibility Problems. *Conf. Hum. Factors Comput. Syst. - Proc.*, 631–640. doi:10.1145/2470654.2470744
- Harlan, S. L., Brazel, A. J., Prashad, L., Stefanov, W. L., and Larsen, L. (2006). Neighborhood Microclimates and Vulnerability to Heat Stress. *Soc. Sci. Med.* 63, 2847–2863. doi:10.1016/j.socscimed.2006.07.030
- Heusinkveld, B. G., Steeneveld, G. J., Van Hove, L. W. A., Jacobs, C. M. J., and Holtslag, A. A. M. (2014). Spatial Variability of the Rotterdam Urban Heat Island as Influenced by Urban Land Use. *J. Geophys. Res. Atmos.* 119, 677–692. doi:10.1002/2012JD019399
- Höfle, B., Hollaus, M., and Hagenauer, J. (2012). Urban Vegetation Detection Using Radiometrically Calibrated Small-Footprint Full-Waveform Airborne LiDAR Data. *ISPRS J. Photogrammetry Remote Sens.* 67, 134–147. doi:10.1016/j.isprsjprs.2011.12.003
- Hourdin, F., Williamson, D., Rio, C., Couvreux, F., Roehrig, R., Villefranche, N., et al. (2021). Process-Based Climate Model Development Harnessing Machine Learning: II. Model Calibration from Single Column to Global. *J. Adv. Model. Earth Syst.* 13, e2020MS002225. doi:10.1029/2020MS002225
- Huang, C., Yang, J., and Jiang, P. (2018). Assessing Impacts of Urban Form on Landscape Structure of Urban Green Spaces in China Using Landsat Images Based on Google Earth Engine. *Remote Sens.* 10, 1569. doi:10.3390/rs10101569
- Huntingford, C., Jeffers, E. S., Bonsall, M. B., Christensen, H. M., Lees, T., and Yang, H. (2019). Machine Learning and Artificial Intelligence to Aid Climate Change Research and Preparedness. *Environ. Res. Lett.* 14, 124007. doi:10.1088/1748-9326/ab4e55
- Iannelli, G., and Dell’Acqua, F. (2017). Extensive Exposure Mapping in Urban Areas through Deep Analysis of Street-Level Pictures for Floor Count Determination. *Urban Sci.* 1, 16. doi:10.3390/urbansci1020016
- Ilieva, R. T., and McPhearson, T. (2018). Social-media Data for Urban Sustainability. *Nat. Sustain.* 1, 553–565. doi:10.1038/s41893-018-0153-6
- Irwin, A. (2018). No PhDs Needed: How Citizen Science Is Transforming Research. *Nature* 562, 480–482. doi:10.1038/d41586-018-07106-5
- Jayathissa, P., Quintana, M., Sood, T., Nazarian, N., and Miller, C. (2019). Is Your Clock-Face Cozie? A Smartwatch Methodology for the *In-Situ* Collection of Occupant Comfort Data. *J. Phys. Conf. Ser.* 1343, 012145. doi:10.1088/1742-6596/1343/1/012145
- Jin, L., Schubert, S., Fenner, D., Meier, F., and Schneider, C. (2021). Integration of a Building Energy Model in an Urban Climate Model and its Application. *Boundary-Layer Meteorol.* 178, 249–281. doi:10.1007/s10546-020-00569-y
- Jones, N. (2017). How Machine Learning Could Help to Improve Climate Forecasts. *Nature* 548, 379. doi:10.1038/548379a
- Kang, L., Poslad, S., Wang, W., Li, X., Zhang, Y., and Wang, C. (2016) 2016. A Public Transport Bus as a Flexible Mobile Smart Environment Sensing Platform for IoT. *Proc. - 12th Int. Conf. Intell. Environ. IE*, 1–8. doi:10.1109/IE.2016.71
- Keralis, J. M., Javanmardi, M., Khanna, S., Dwivedi, P., Huang, D., Tasdizen, T., et al. (2020). Health and the Built Environment in United States Cities: Measuring Associations Using Google Street View-Derived Indicators of the

- Built Environment. *BMC Public Health* 20, 1–10. doi:10.1186/s12889-020-8300-1
- Klingberg, J., Konarska, J., Lindberg, F., Johansson, L., and Thorsson, S. (2017). Mapping Leaf Area of Urban Greenery Using Aerial LiDAR and Ground-Based Measurements in Gothenburg, Sweden. *Urban For. Urban Green.* 26, 31–40. doi:10.1016/j.ufug.2017.05.011
- Konrad, T. G., Hill, M. L., Rowland, J. R., and Meyer, J. H. (1970). A Small, Radio-Controlled Aircraft as A Platform for Meteorological Sensors. *Apl. Tech. Dig.*, 11–19.
- Krayenhoff, E. S., Moustaqi, M., Broadbent, A. M., Gupta, V., and Georgescu, M. (2018). Diurnal Interaction between Urban Expansion, Climate Change and Adaptation in US Cities. *Nat. Clim. Change* 8, 1097–1103. doi:10.1038/s41558-018-0320-9
- Kuras, E. R., Richardson, M. B., Calkins, M. M., Ebi, K. L., Hess, J. J., Kintziger, K. W., et al. (2017). Opportunities and Challenges for Personal Heat Exposure Research. *Environ. Health Perspect.* 125, 085001. doi:10.1289/EHP556
- Kuuluvainen, H., Poikkinen, M., Järvinen, A., Kuula, J., Irlala, M., Dal Maso, M., et al. (2018). Vertical Profiles of Lung Deposited Surface Area Concentration of Particulate Matter Measured with a Drone in a Street Canyon. *Environ. Pollut.* 241, 96–105. doi:10.1016/j.envpol.2018.04.100
- Lafarge, F. (2015). “Some New Research Directions to Explore in Urban Reconstruction,” 2015 Joint Urban Remote Sensing Event (JURSE), 1–4. doi:10.1109/JURSE.2015.7120488
- Lassen, N., Josefson, T., and Goia, F. (2021). Design and In-Field Testing of a Multi-Level System for Continuous Subjective Occupant Feedback on Indoor Climate. *Build. Environ.* 189, 107535. doi:10.1016/j.buildenv.2020.107535
- Lee, A., Jeong, S., Joo, J., Park, C.-R., Kim, J., and Kim, S. (2021). Potential Role of Urban Forest in Removing PM2.5: A Case Study in Seoul by Deep Learning with Satellite Data. *Urban Clim.* 36, 100795. doi:10.1016/j.uclim.2021.100795
- Leuenberger, D., Haefele, A., Omanovic, N., Fengler, M., Martucci, G., Calpini, B., et al. (2020). Improving High-Impact Numerical Weather Prediction with Lidar and Drone Observations. *Bull. Am. Meteorol. Soc.* 101, E1036–E1051. doi:10.1175/BAMS-D-19-0119.1
- Li, M., Koks, E., Taubenböck, H., and van Vliet, J. (2020a). Continental-scale Mapping and Analysis of 3D Building Structure. *Remote Sens. Environ.* 245, 111859. doi:10.1016/j.rse.2020.111859
- Li, X., Ratti, C., and Seiferling, I. (2017). Mapping Urban Landscapes along Streets Using Google Street View. *Lect. Notes Geoinf. Cartogr.*, 341–356. doi:10.1007/978-3-319-57336-6\_24
- Li, X., and Wang, G. (2021). Examining Runner’s Outdoor Heat Exposure Using Urban Microclimate Modeling and GPS Trajectory Mining. *Comput. Environ. Urban Syst.* 89, 101678. doi:10.1016/j.compenvurbsys.2021.101678
- Li, Y., Chen, Y., Rajabifard, A., Khoshelham, K., and Aleksandrov, M. (2018). Estimating Building Age from Google Street View Images Using Deep Learning. *Leibniz Int. Proc. Inf. LIPIcs* 114. doi:10.4230/LIPIcs.GIScience.2018.40
- Li, Y., Fowler, H. J., Argüeso, D., Blenkinsop, S., Evans, J. P., Lenderink, G., et al. (2020b). Strong Intensification of Hourly Rainfall Extremes by Urbanization. *Geophys. Res. Lett.* 47, e2020GL088758. doi:10.1029/2020GL088758
- Li, Y., Yu, M., Xu, M., Yang, J., Sha, D., Liu, Q., et al. (2020c). Big Data and Cloud Computing. *Man. Digit. Earth*, 325–355. doi:10.1007/978-981-32-9915-3\_9
- Lindberg, F., Grimmond, C. S. B., Gabey, A., Huang, B., Kent, C. W., Sun, T., et al. (2018). Urban Multi-Scale Environmental Predictor (UMEP): An Integrated Tool for City-Based Climate Services. *Environ. Model. Softw.* 99, 70–87. doi:10.1016/j.envsoft.2017.09.020
- Lu, Y. (2019). Using Google Street View to Investigate the Association between Street Greenery and Physical Activity. *Landsc. Urban Plan.* 191, 103435. doi:10.1016/j.landurbplan.2018.08.029
- Luo, M., Hong, Y., and Pantelic, J. (2021). Determining Building Natural Ventilation Potential via IoT-Based Air Quality Sensors. *Front. Environ. Sci.* 9, 144. doi:10.3389/fenvs.2021.634570
- Ma, K., Tang, X., Ren, Y., and Wang, Y. (2019). Research on the Spatial Pattern Characteristics of the Taihu Lake “Dock Village” Based on Microclimate: A Case Study of Tangli Village. *Sustainability* 11, 368. doi:10.3390/su11020368
- Mandement, M., and Caumont, O. (2020). Contribution of Personal Weather Stations to the Observation of Deep-Convection Features Near the Ground. *Nat. Hazards Earth Syst. Sci.* 20, 299–322. doi:10.5194/nhess-20-299-2020
- Mass, C. F., and Madaus, L. E. (2014). Surface Pressure Observations from Smartphones: A Potential Revolution for High-Resolution Weather Prediction? *Bull. Am. Meteorol. Soc.* 95, 1343–1349. doi:10.1175/BAMS-D-13-00188.1
- Masson, V., Heldens, W., Bocher, E., Bonhomme, M., Bucher, B., Burmeister, C., et al. (2020a). City-descriptive Input Data for Urban Climate Models: Model Requirements, Data Sources and Challenges. *Urban Clim.* 31, 100536. doi:10.1016/j.uclim.2019.100536
- Masson, V., Lemonsu, A., Hidalgo, J., and Voogt, J. (2020b). Urban Climates and Climate Change. *Annu. Rev. Environ. Resour.* 45, 411–444. doi:10.1146/annurev-environ-012320-083623
- Meier, F., Fenner, D., Grassmann, T., Otto, M., and Scherer, D. (2017). Crowdsourcing Air Temperature from Citizen Weather Stations for Urban Climate Research. *Urban Clim.* 19, 170–191. doi:10.1016/j.uclim.2017.01.006
- Middel, A., AlKhaleed, S., Schneider, F. A., Hagen, B., and Coseo, P. (2021). 50 Grades of Shade. *Bull. Am. Meteorol. Soc.*, 1–35. doi:10.1175/bams-d-20-0193.1
- Middel, A., Häb, K., Brazel, A. J., Martin, C. A., and Guhathakurta, S. (2014). Impact of Urban Form and Design on Mid-afternoon Microclimate in Phoenix Local Climate Zones. *Landsc. Urban Plan.* 122, 16–28. doi:10.1016/j.landurbplan.2013.11.004
- Middel, A., and Krayenhoff, E. S. (2019). Micrometeorological Determinants of Pedestrian Thermal Exposure during Record-Breaking Heat in Tempe, Arizona: Introducing the MaRTy Observational Platform. *Sci. Total Environ.* 687, 137–151. doi:10.1016/j.scitotenv.2019.06.085
- Middel, A., Lukasczyk, J., Maciejewski, R., Demuzere, M., and Roth, M. (2018). Sky View Factor Footprints for Urban Climate Modeling. *Urban Clim.* 25, 120–134. doi:10.1016/j.uclim.2018.05.004
- Middel, A., Lukasczyk, J., Zakrzewski, S., Arnold, M., and Maciejewski, R. (2019). Urban Form and Composition of Street Canyons: A Human-Centric Big Data and Deep Learning Approach. *Landsc. Urban Plan.* 183, 122–132. doi:10.1016/j.landurbplan.2018.12.001
- Mills, G. (2014). Urban Climatology: History, Status and Prospects. *Urban Clim.* 10, 479–489. doi:10.1016/j.uclim.2014.06.004
- Monnot, B., Wilhelm, E., Piliouras, G., Zhou, Y., Dahlmeier, D., Lu, H. Y., et al. (2016). Inferring Activities and Optimal Trips: Lessons from Singapore’s National Science Experiment. *Adv. Intell. Syst. Comput.* 426, 247–264. doi:10.1007/978-3-319-29643-2\_19
- Monteleoni, C., Schmidt, G. A., Alexander, F., Niculescu-Mizil, A., Steinhaeuser, K., Tippett, M., et al. (2016). Climate Informatics. *Comput. Intell. Data Anal. Sustain. Dev.*, 81–126. doi:10.1201/b14799-8
- Mooney, S. J., DiMaggio, C. J., Lovasi, G. S., Neckerman, K. M., Bader, M. D. M., Teitler, J. O., et al. (2016). Use of Google Street View to Assess Environmental Contributions to Pedestrian Injury. *Am. J. Public Health* 106, 462–469. doi:10.2105/AJPH.2015.302978
- Moore, F. C., and Obradovich, N. (2020). Using Remarkability to Define Coastal Flooding Thresholds. *Nat. Commun.* 11, 1–8. doi:10.1038/s41467-019-13935-3
- Muller, C. L., Chapman, L., Johnston, S., Kidd, C., Illingworth, S., Foody, G., et al. (2015). Crowdsourcing for Climate and Atmospheric Sciences: Current Status and Future Potential. *Int. J. Climatol.* 35, 3185–3203. doi:10.1002/joc.4210
- Napoly, A., Grassmann, T., Meier, F., and Fenner, D. (2018). Development and Application of a Statistically-Based Quality Control for Crowdsourced Air Temperature Data. *Front. Earth Sci.* 6, 118. doi:10.3389/feart.2018.00118
- Nazarian, N., and Lee, J. K. (2021). Personal Assessment of Urban Heat Exposure: A Systematic Review. *Environ. Res. Lett.* 16, 033005. doi:10.1088/1748-9326/abdf30
- Nazarian, N., Liu, S., Kohler, M., Lee, J. K. W., Miller, C., Chow, W. T. L., et al. (2021). Project Coolbit: Can Your Watch Predict Heat Stress and Thermal Comfort Sensation? *Environ. Res. Lett.* 16, 034031. doi:10.1088/1748-9326/abdf30
- Nice, K. A., Wijnands, J. S., Middel, A., Wang, J., Qiu, Y., Zhao, N., et al. (2020). Sky Pixel Detection in Outdoor Imagery Using an Adaptive Algorithm and Machine Learning. *Urban Clim.* 31, 100572. doi:10.1016/j.uclim.2019.100572
- Nipen, T. N., Seierstad, I. A., Lussana, C., Kristiansen, J., and Hov, Ø. (2020). Adopting Citizen Observations in Operational Weather Prediction. *Bull. Am. Meteorol. Soc.* 101, E43–E57. doi:10.1175/BAMS-D-18-0237.1
- Nishida, G., Bousseau, A., and Aliaga, D. G. (2018). Procedural Modeling of a Building from a Single Image. *Comput. Graph. Forum* 37, 415–429. doi:10.1111/cgf.13372
- Núñez-Poiré, M., Sánchez-Guevara Sánchez, C., and Neila González, F. J. (2021). Hourly Evolution of Intra-urban Temperature Variability across the Local

- Climate Zones. The Case of Madrid. *Urban Clim.* 39, 100921. doi:10.1016/j.ulclim.2021.100921
- Oke, T. R., Mills, G., Christen, A., and Voogt, J. A. (2017). *Urban Climates*. Online Publication: Cambridge University Press, 1–525. doi:10.1017/9781139016476
- Okkon, E. O., Yli-Tuomi, T., Turunen, A. W., Taimisto, P., Pennanen, A., Vuotsis, I., et al. (2017). Particulates and Noise Exposure during Bicycle, Bus and Car Commuting: A Study in Three European Cities. *Environ. Res.* 154, 181–189. doi:10.1016/j.envres.2016.12.012
- Open Data Cube (2022). Open Source. Available at: <https://www.opendatacube.org/> (Accessed January 30, 2022).
- Overeem, A., R. Robinson, J. C., Steeneveld, G. J., P. Horn, B. K., Uijlenhoet, R., and Uijlenhoet, R. (2013). Crowdsourcing Urban Air Temperatures from Smartphone Battery Temperatures. *Geophys. Res. Lett.* 40, 4081–4085. doi:10.1002/grl.50786
- Pal, S., and Sharma, P. (2021). A Review of Machine Learning Applications in Land Surface Modeling. *Earth* 2, 174–190. doi:10.3390/earth2010011
- Palacios Temprano, J., Eichholz, P., Willeboordse, M., and Kok, N. (2020). Indoor Environmental Quality and Learning Outcomes: Protocol on Large-Scale Sensor Deployment in Schools. *BMJ Open* 10, e031233. doi:10.1136/bmjopen-2019-031233
- Parlow, E., and Foken, T. (2021). *Ground-based Mobile Measurement Systems*. Springer Handbooks, 1351–1367. doi:10.1007/978-3-030-52171-4\_50Ground-based Mobile Measurement Systems
- Pebesma, E., Wagner, W., Schramm, M., Von Beringe, A., Paulik, C., Neteler, M., et al. (2017). OpenEO - a Common, Open Source Interface between Earth Observation Data Infrastructures and Front-End Applications. 57. [Accessed January 31, 2022]. doi:10.5281/zenodo.1065474
- Peng, S., Piao, S., Ciais, P., Friedlingstein, P., Ottle, C., Bréon, F.-M., et al. (2012). Surface Urban Heat Island across 419 Global Big Cities. *Environ. Sci. Technol.* 46, 696–703. doi:10.1021/es2030438
- Pfautsch, S., and Tjoelker, A. R. (2020). The Impact of Surface Cover and Tree Canopy on Air Temperature in Western Sydney 140. doi:10.26183/BK6D-1466
- Potgieter, J., Nazarian, N., Lipson, M. J., Hart, M. A., Ulpiani, G., Morrison, W., et al. (2021). Combining High-Resolution Land Use Data with Crowdsourced Air Temperature to Investigate Intra-urban Microclimate. *Front. Environ. Sci.* 9, 385. doi:10.3389/fenvs.2021.720323
- Rajkovich, N., and Larsen, L. (2016). A Bicycle-Based Field Measurement System for the Study of Thermal Exposure in Cuyahoga County, Ohio, USA. *Ijerph* 13, 159. doi:10.3390/ijerph13020159
- Rakha, T., and Gorodetsky, A. (2018). Review of Unmanned Aerial System (UAS) Applications in the Built Environment: Towards Automated Building Inspection Procedures Using Drones. *Automation Constr.* 93, 252–264. doi:10.1016/j.autcon.2018.05.002
- Reichstein, M., Camps-Valls, G., Stevens, B., Jung, M., Denzler, J., Carvalhais, N., et al. (2019). Deep Learning and Process Understanding for Data-Driven Earth System Science. *Nature* 566, 195–204. doi:10.1038/s41586-019-0912-1
- Schneider, P., Castell, N., Vogt, M., Dauge, F. R., Lahoz, W. A., and Bartonova, A. (2017). Mapping Urban Air Quality in Near Real-Time Using Observations from Low-Cost Sensors and Model Information. *Environ. Int.* 106, 234–247. doi:10.1016/j.envint.2017.05.005
- Schrotter, G., and Hürzeler, C. (2020). The Digital Twin of the City of Zurich for Urban Planning. *Pfg* 88, 99–112. doi:10.1007/S41064-020-00092-2/FIGURES/14
- See, L., Mooney, P., Foody, G., Bastin, L., Comber, A., Estima, J., et al. (2016). Crowdsourcing, Citizen Science or Volunteered Geographic Information? the Current State of Crowdsourced Geographic Information. *ISPRS Int. J. Geo-Information* 5, 55. doi:10.3390/ijgi5050055
- Seidel, J., Ketzler, G., Bechtel, B., Thies, B., Philipp, A., Böhner, J., et al. (2016). Mobile Measurement Techniques for Local and Micro-scale Studies in Urban and Topo-Climatology. *Erde* 147, 15–39. doi:10.12854/erde-147-2
- SEPAL (2022). FAO. Available at: <https://github.com/openforis/sepal> (Accessed January 30, 2022).
- Servadio, J. L., Lawal, A. S., Davis, T., Bates, J., Russell, A. G., Ramaswami, A., et al. (2019). Demographic Inequities in Health Outcomes and Air Pollution Exposure in the Atlanta Area and its Relationship to Urban Infrastructure. *J. Urban Health* 96, 219–234. doi:10.1007/S11524-018-0318-7/TABLES/4
- Sinergise (2018). Sentinel Hub. *Eo Brows*. Available at: <https://apps.sentinel-hub.com/eo-browser/?lat=41.9000&lng=12.5000&zoom=10> (Accessed January 30, 2022).
- Soille, P., Burger, A., De Marchi, D., Kempeneers, P., Rodriguez, D., Syrris, V., et al. (2018). A Versatile Data-Intensive Computing Platform for Information Retrieval from Big Geospatial Data. *Future Gener. Comput. Syst.* 81, 30–40. doi:10.1016/j.future.2017.11.007
- Stewart, I. D., Krayenhoff, E. S., Voogt, J. A., Lachapelle, J. A., Allen, M. A., and Broadbent, A. M. (2021). Time Evolution of the Surface Urban Heat Island. *Earth's Future* 9, e2021EF002178. doi:10.1029/2021EF002178
- Stewart, I. D., and Oke, T. R. (2012). Local Climate Zones for Urban Temperature Studies. *Bull. Am. Meteorol. Soc.* 93, 1879–1900. doi:10.1175/BAMS-D-11-00019.1
- Stewart, I. D. (2019). Why Should Urban Heat Island Researchers Study History? *Urban Clim.* 30, 100484. doi:10.1016/j.ulclim.2019.100484
- Sudmanns, M., Tiede, D., Lang, S., Bergstedt, H., Trost, G., Augustin, H., et al. (2019). Big Earth Data: Disruptive Changes in Earth Observation Data Management and Analysis? 13, 832–850. doi:10.1080/17538947.2019.1585976
- Triscone, G., Abdennadher, N., Balistreri, C., Donzé, O., Greco, D., Haas, P., et al. (2016). Computational Fluid Dynamics as a Tool to Predict the Air Pollution Dispersion in a Neighborhood - a Research Project to Improve the Quality of Life in Cities. *Int. J. SDP* 11, 546–557. doi:10.2495/SDP-V11-N4-546-557
- Ulpiani, G., Nazarian, N., Zhang, F., and Pettit, C. J. (2021). Towards a Living Lab for Enhanced Thermal Comfort and Air Quality: Analyses of Standard Occupancy, Weather Extremes, and COVID-19 Pandemic. *Front. Environ. Sci.* 9, 556. doi:10.3389/fenvs.2021.725974
- Urech, P. R. W., Dissegna, M. A., Girot, C., and Grêt-Regamey, A. (2020). Point Cloud Modeling as a Bridge between Landscape Design and Planning. *Landscape Urban Plan.* 203, 103903. doi:10.1016/j.landurbplan.2020.103903
- Varentsov, M., Fenner, D., Meier, F., Samsonov, T., and Demuzere, M. (2021). Quantifying Local and Mesoscale Drivers of the Urban Heat Island of Moscow with Reference and Crowdsourced Observations. *Front. Environ. Sci.* 9, 543. doi:10.3389/fenvs.2021.716968
- Venter, Z. S., Brousse, O., Esau, I., and Meier, F. (2020). Hyperlocal Mapping of Urban Air Temperature Using Remote Sensing and Crowdsourced Weather Data. *Remote Sens. Environ.* 242, 111791. doi:10.1016/j.rse.2020.111791
- Venter, Z. S., Chakraborty, T., and Lee, X. (2021). Crowdsourced Air Temperatures Contrast Satellite Measures of the Urban Heat Island and its Mechanisms. *Sci. Adv.* 7. doi:10.1126/sciadv.abb9569
- Villa, T., Gonzalez, F., Miljkovic, B., Ristovski, Z., and Morawska, L. (2016). An Overview of Small Unmanned Aerial Vehicles for Air Quality Measurements: Present Applications and Future Prospectives. *Sensors* 16, 1072. doi:10.3390/s16071072
- Voogt, J. A., and Oke, T. R. (2003). Thermal Remote Sensing of Urban Climates. *Remote Sens. Environ.* 86, 370–384. doi:10.1016/S0034-4257(03)00079-8
- Vos, L. W., Leijnse, H., Overeem, A., and Uijlenhoet, R. (2019). Quality Control for Crowdsourced Personal Weather Stations to Enable Operational Rainfall Monitoring. *Geophys. Res. Lett.* 46, 8820–8829. doi:10.1029/2019GL083731
- Vulova, S., Meier, F., Fenner, D., Nouri, H., and Kleinschmit, B. (2020). Summer Nights in Berlin, Germany: Modeling Air Temperature Spatially with Remote Sensing, Crowdsourced Weather Data, and Machine Learning. *IEEE J. Sel. Top. Appl. Earth Obs. Remote Sens.* 13, 5074–5087. doi:10.1109/JSTARS.2020.3019696
- Wang, C., Wen, C., Dai, Y., Yu, S., and Liu, M. (2020). Urban 3D Modeling with Mobile Laser Scanning: a Review. *Virtual Real. Intelligent Hardw.* 2, 175–212. doi:10.1016/j.vrih.2020.05.003
- Wang, L., Ma, Y., Yan, J., Chang, V., and Zomaya, A. Y. (2018a). pipsCloud: High Performance Cloud Computing for Remote Sensing Big Data Management and Processing. *Future Gener. Comput. Syst.* 78, 353–368. doi:10.1016/j.future.2016.06.009
- Wang, R., Peethambaran, J., and Chen, D. (2018b). LiDAR Point Clouds to 3-D Urban Models\$: A Review. *IEEE J. Sel. Top. Appl. Earth Obs. Remote Sens.* 11, 606–627. doi:10.1109/JSTARS.2017.2781132
- Wilhelm, E., Siby, S., Zhou, Y., Ashok, X. J. S., Jayasuriya, M., Foong, S., et al. (2016). Wearable Environmental Sensors and Infrastructure for Mobile Large-Scale Urban Deployment. *IEEE Sensors J.* 16, 8111–8123. doi:10.1109/JSEN.2016.2603158

- Willem, P., Arnbjerg-Nielsen, K., Olsson, J., and Nguyen, V. T. V. (2012). Climate Change Impact Assessment on Urban Rainfall Extremes and Urban Drainage: Methods and Shortcomings. *Atmos. Res.* 103, 106–118. doi:10.1016/j.atmosres.2011.04.003
- Wulder, M. A., Masek, J. G., Cohen, W. B., Loveland, T. R., and Woodcock, C. E. (2012). Opening the Archive: How Free Data Has Enabled the Science and Monitoring Promise of Landsat. *Remote Sens. Environ.* 122, 2–10. doi:10.1016/j.rse.2012.01.010
- Xiaojun, C., Xianpeng, L., and Peng, X. (2015). IOT-based Air Pollution Monitoring and Forecasting System. *Int. Conf. Comput. Comput. Sci. ICCCS*, 257–260. doi:10.1109/ICCACS.2015.7361361
- Xu, G., Zhu, X., Tapper, N., and Bechtel, B. (2019). Urban Climate Zone Classification Using Convolutional Neural Network and Ground-Level Images. *Prog. Phys. Geogr. Earth Environ.* 43, 410–424. doi:10.1177/0309133319837711
- Yan, W. Y., Shaker, A., and El-Ashmawy, N. (2015). Urban Land Cover Classification Using Airborne LiDAR Data: A Review. *Remote Sens. Environ.* 158, 295–310. doi:10.1016/j.rse.2014.11.001
- Yavaşlı, D. D. (2020). Drone Applications in Geography: Game of Drones. *Curr. Stud. Soc. Sci. II* 8, 117. Available at: [https://www.researchgate.net/publication/344839834\\_Drone\\_Applications\\_in\\_Geography\\_Game\\_of\\_Drones](https://www.researchgate.net/publication/344839834_Drone_Applications_in_Geography_Game_of_Drones) (Accessed January 30, 2022).
- Yin, L., and Wang, Z. (2016). Measuring Visual Enclosure for Street Walkability: Using Machine Learning Algorithms and Google Street View Imagery. *Appl. Geogr.* 76, 147–153. doi:10.1016/j.apgeog.2016.09.024
- Yoo, C., Han, D., Im, J., and Bechtel, B. (2019). Comparison between Convolutional Neural Networks and Random Forest for Local Climate Zone Classification in Mega Urban Areas Using Landsat Images. *ISPRS J. Photogrammetry Remote Sens.* 157, 155–170. doi:10.1016/j.isprsjprs.2019.09.009
- Young, J. C., Arthur, R., Spruce, M., and Williams, H. T. P. (2021). Social Sensing of Heatwaves. *Sensors* 21, 3717. doi:10.3390/s21113717
- Zeng, L., Lu, J., Li, W., and Li, Y. (2018). A Fast Approach for Large-Scale Sky View Factor Estimation Using Street View Images. *Build. Environ.* 135, 74–84. doi:10.1016/j.buildenv.2018.03.009
- Zhan, W., Chen, Y., Zhou, J., Wang, J., Liu, W., Voogt, J., et al. (2013). Disaggregation of Remotely Sensed Land Surface Temperature: Literature Survey, Taxonomy, Issues, and Caveats. *Remote Sens. Environ.* 131, 119–139. doi:10.1016/j.rse.2012.12.014
- Zhang, D., and Woo, S. S. (2020). Real Time Localized Air Quality Monitoring and Prediction through Mobile and Fixed IoT Sensing Network. *IEEE Access* 8, 89584–89594. doi:10.1109/ACCESS.2020.2993547
- Zhang, W., Li, W., Zhang, C., Hanink, D. M., Li, X., and Wang, W. (2017). Parcel-based Urban Land Use Classification in Megacity Using Airborne LiDAR, High Resolution Orthoimagery, and Google Street View. *Comput. Environ. Urban Syst.* 64, 215–228. doi:10.1016/j.compenvurbsys.2017.03.001
- Zhang, X., Liu, L., Wu, C., Chen, X., Gao, Y., Xie, S., et al. (2020). Development of a Global 30 M Impervious Surface Map Using Multisource and Multitemporal Remote Sensing Datasets with the Google Earth Engine Platform. *Earth Syst. Sci. Data* 12, 1625–1648. doi:10.5194/esd-12-1625-2020
- Zhang, Y., Middel, A., and Turner, B. L. (2019). Evaluating the Effect of 3D Urban Form on Neighborhood Land Surface Temperature Using Google Street View and Geographically Weighted Regression. *Landscape Ecol.* 34, 681–697. doi:10.1007/s10980-019-00794-y
- Zhao, L., Oleson, K., Bou-Zeid, E., Kravchenko, E. S., Bray, A., Zhu, Q., et al. (2021). Global Multi-Model Projections of Local Urban Climates. *Nat. Clim. Chang.* 11, 152–157. doi:10.1038/s41558-020-00958-8
- Zhou, Y., Wei, T., Zhu, X., and Collin, M. (2021). A Parcel-Based Deep-Learning Classification to Map Local Climate Zones from Sentinel-2 Images. *IEEE J. Sel. Top. Appl. Earth Obs. Remote Sens.* 14, 4194–4204. doi:10.1109/JSTARS.2021.3071577
- Zumwald, M., Knüsel, B., Bresch, D. N., and Knutti, R. (2021). Mapping Urban Temperature Using Crowd-Sensing Data and Machine Learning. *Urban Clim.* 35, 100739. doi:10.1016/j.uclim.2020.100739
- Conflict of Interest:** The authors declare that the research was conducted in the absence of any commercial or financial relationships that could be construed as a potential conflict of interest.
- Publisher's Note:** All claims expressed in this article are solely those of the authors and do not necessarily represent those of their affiliated organizations, or those of the publisher, the editors and the reviewers. Any product that may be evaluated in this article, or claim that may be made by its manufacturer, is not guaranteed or endorsed by the publisher.
- Copyright © 2022 Middel, Nazarian, Demuzere and Bechtel. This is an open-access article distributed under the terms of the Creative Commons Attribution License (CC BY). The use, distribution or reproduction in other forums is permitted, provided the original author(s) and the copyright owner(s) are credited and that the original publication in this journal is cited, in accordance with accepted academic practice. No use, distribution or reproduction is permitted which does not comply with these terms.



# MaRTiny—A Low-Cost Biometeorological Sensing Device With Embedded Computer Vision for Urban Climate Research

Karthik K. Kulkarni<sup>1</sup>, Florian A. Schneider<sup>2</sup>, Tejaswi Gowda<sup>3</sup>, Suren Jayasuriya<sup>1,3\*</sup> and Ariane Middel<sup>3,4</sup>

<sup>1</sup>School of Electrical, Computer and Energy Engineering, Arizona State University, Tempe, AZ, United States, <sup>2</sup>School of Sustainability, College of Global Futures, Arizona State University, Tempe, AZ, United States, <sup>3</sup>School of Arts, Media and Engineering, Arizona State University, Tempe, AZ, United States, <sup>4</sup>School of Computing and Augmented Intelligence, Arizona State University, Tempe, AZ, United States

## OPEN ACCESS

### Edited by:

Adam Schlosser,  
Massachusetts Institute of  
Technology, United States

### Reviewed by:

Giuseppe Riccio,  
University of Naples Federico II, Italy  
Juan Angel Acero Alejandro,  
Singapore-MIT Alliance for Research  
and Technology (SMART), Singapore

### \*Correspondence:

Suren Jayasuriya  
sjayasur@asu.edu

### Specialty section:

This article was submitted to  
Interdisciplinary Climate Studies,  
a section of the journal  
Frontiers in Environmental Science

Received: 31 January 2022

Accepted: 15 April 2022

Published: 12 May 2022

### Citation:

Kulkarni KK, Schneider FA, Gowda T,  
Jayasuriya S and Middel A (2022)

MaRTiny—A Low-Cost  
Biometeorological Sensing Device  
With Embedded Computer Vision for  
Urban Climate Research.

Front. Environ. Sci. 10:866240.  
doi: 10.3389/fenvs.2022.866240

Extreme heat puts tremendous stress on human health and limits people's ability to work, travel, and socialize outdoors. To mitigate heat in public spaces, thermal conditions must be assessed in the context of human exposure and space use. Mean Radiant Temperature (MRT) is an integrated radiation metric that quantifies the total heat load on the human body and is a driving parameter in many thermal comfort indices. Current sensor systems to measure MRT are expensive and bulky (6-directional setup) or slow and inaccurate (globe thermometers) and do not sense space use. This engineering systems paper introduces the hardware and software setup of a novel, low-cost thermal and visual sensing device (MaRTiny). The system collects meteorological data, concurrently counts the number of people in the shade and sun, and streams the results to an Amazon Web Services (AWS) server. MaRTiny integrates various micro-controllers to collect weather data relevant to human thermal exposure: air temperature, humidity, wind speed, globe temperature, and UV radiation. To detect people in the shade and Sun, we implemented state of the art object detection and shade detection models on an NVIDIA Jetson Nano. The system was tested in the field, showing that meteorological observations compared reasonably well to MaRTy observations (high-end human-biometeorological station) when both sensor systems were fully sun-exposed. To overcome potential sensing errors due to different exposure levels, we estimated MRT from MaRTiny weather observations using machine learning (SVM), which improved RMSE. This paper focuses on the development of the MaRTiny system and lays the foundation for fundamental research in urban climate science to investigate how people use public spaces under extreme heat to inform active shade management and urban design in cities.

**Keywords:** mean radiant temperature (MRT), thermal sensing, shade detection, urban microclimate, urban heat

## 1 INTRODUCTION

The year 2020 marks the Earth's warmest 10-year period with an average increase in global temperature of 1.3 °C above pre-industrial levels. Extreme heat and related heat waves put tremendous stress on individuals' health and well-being and limits their ability to work, travel, and socialize in outdoor settings. Globally, extreme heat and associated heat wave events are occurring more frequently and longer (Masson-Delmotte et al., 2021). Future trends of urban warming indicate the need for adaption measures to promote resilience in the population. The outdoor urban environment is a complex arrangement of urban forms and materials that impact how heat is experienced by pedestrians at the microscale. In hot, dry cities pedestrian comfort is strongly dictated by the availability of shade (Middel et al., 2014; Colter et al., 2019). Pedestrian may respond to microscale outdoor conditions by changing their walking path from Sun to shade or vice versa based on their heat exposure.

The most common way to report urban heat is air temperature, which has been shown to be insufficient to quantify personal heat exposure (Harlan et al., 2006; Kuras et al., 2017). A more human-centric metric that emphasizes the heat load on the human body is the Mean Radiant Temperature (MRT). MRT objectively quantifies the total short- and longwave radiation the human body is exposed to at a given location and time (Kántor and Unger, 2011). This includes longwave radiation emitted from surrounding surfaces, such as asphalt parking lots or concrete walls, and shortwave radiation from the Sun. MRT roughly equals air temperature in the shade but can be 30 °C higher in the Sun, making a person feel much less comfortable when it is hot. In warm, dry climates such as the desert city of Phoenix, Arizona in the USA, MRT is the heat metric that best describes how people experience heat (Middel et al., 2016). MRT is also a crucial input parameter for calculating outdoor human thermal comfort indices such as PET (Höppe, 1999) and UTCI (Jendritzky et al., 2012).

MRT has been successfully used in urban climate and human biometeorology research to predict heat-related mortality and outperformed air temperature as predictor (Thorsson et al., 2014). Using computer simulations, MRT was estimated to assess the impact of tree planting strategies on human thermal exposure under climate change in Vancouver, Canada (Aminipour et al., 2019) and to perform thermal comfort routing in Tempe, Arizona, USA (Middel et al., 2017). Observational studies have quantified the benefit of shade for thermal comfort of different shade types including trees, engineered structures, and urban form (Lee et al., 2018; Middel et al., 2021). Accurate, high resolution MRT measurements require expensive equipment, such as the biometeorological instrument platform MaRTy (Middel and Krayenhoff, 2019), but lower-cost alternatives such as the gray 38 mm globe thermometers and cylindrical thermometers have been developed (Thorsson et al., 2006; Brown, 2019; Vanos et al., 2021).

Active shade management in cities is important, especially in the Southwestern US, to provide shade where people work, travel, and socialize outdoors, because cooling benefits are hyperlocal.

While a large body of literature has investigated shade and microclimate in hot regions (Ali-Toudert and Mayer, 2007; Emmanuel et al., 2007; Shashua-Bar et al., 2009; Coutts et al., 2016), little information exists on how people use public spaces and when and where they are exposed to outdoor heat. We close this gap by developing a novel low-cost, portable, smart IoT weather station (MaRTiny) that can measure passively the local meteorological conditions, the heat exposure at the given location and count people in the shade and Sun. Connecting hyperlocal meteorological conditions with space use data captured by a camera reveals behavioral patterns of shade and Sun preferences that vary by time of day, location, and ambient conditions. MaRTiny, as a passive sensor package, designed for hot, dry climates, can provide local heat exposure, such as MRT, and space use data without using external database.

Our contributions can be summarized as follows:

1. **MaRTiny Weather Station**—A low-cost and compact IoT weather station that records air temperature, relative humidity, globe temperature, and wind speed at 1-min intervals. Globe temperature was converted to MRT using an empirical model in the literature and compared with high-end MRT measurements, resulting in a root mean square error (RMSE) of 10.0°C for observed 6-directional measurements vs globe temperature measurements.
2. **MaRTiny Vision System**—A low-cost, low-powered, compact and smart vision system driven by state-of-the-art AI algorithms. This system counts pedestrian and is also capable of identifying if a pedestrian is under the cooling effect of shade. From our observations, we calculate a precision of 95% for pedestrian detection and an accuracy of 80% for shade detection.
3. **Machine Learning based MRT**—We developed a novel machine learning model that relies only on a few meteorological parameters and is robust to changes in its surrounding environment. This model corrects errors introduced by the low-cost IoT sensor, such as slow response time, shape, color and material inconsistencies, etc., and predicts MRT with an accuracy of RMSE = 4°C.

This research paper is focused on the engineering and development of a low-cost, portable IoT weather stations for MRT measurement. The study does not focus on a large-scale scientific study of human exposure in outdoor spaces, but rather the engineering and data science challenges of estimating MRT with a combined hardware-software system.

## 2 BACKGROUND AND RELATED WORK

### 2.1 Mean Radiant Temperature Sensing

MRT is typically determined with integral radiation measurements using the so-called 6-directional method (Höppe, 1992). Three net radiometers are orthogonally setup to measure the longwave and shortwave radiation in six directions. The radiative fluxes are then summarized into a temperature value using the Stefan-Boltzmann Law:

$$MRT = \sqrt[4]{\frac{\sum_{i=1}^6 W_i (a_k K_i + a_l L_i)}{a_l \sigma}} - 273.15 \quad (1)$$

where  $K_i$  and  $L_i$  are the directional shortwave and longwave radiation fluxes, respectively;  $a_k$  and  $a_l$  are absorption coefficients for short- and long wave radiation fluxes, respectively;  $\sigma$  is the Stefan-Boltzmann constant; and  $W_i$  are factors that weigh the directional fluxes to match the cylindrical shape of the human standing body (0.06 is used for sensors pointing up and down, 0.22 for lateral sensors). This method is limited by cost with three net radiometers that cost \$5k each.

A more affordable but less accurate method to estimate MRT is using a black globe thermometer. Globe thermometers such as the Kestrel Heat Stress meter (\$500) have been used to quantify the heat load of pedestrians, athletes, and outdoor workers in various studies (Johansson et al., 2014). Thorsson et al. (2006) developed a low-cost globe thermometer using a thermocouple in a gray ping pong ball (<\$100). The acrylic gray color of the globe almost matches the average albedo of the combination of the human skin and clothing to reliably estimate MRT (Olesen et al., 1989; Thorsson et al., 2006). Albedo variations based on clothing and skin color are large between people and cannot simply be represented by one color alone, hence this gray globe can provide an accurate estimate for the average combined albedo which can be used as a reference.

Various convection coefficients have been developed for globe thermometers to improve MRT estimations from globe temperature (Oliveira et al., 2019; Manavvi and Rajasekar, 2020; Acero et al., 2021; Alfano et al., 2021). Those coefficients are usually derived under specific outdoor conditions and cannot be generalized easily. Here, we will use an empirical model for acrylic gray globe temperature  $T_g$  developed by Vanos et al. (2021) in Phoenix, AZ based on air temperature  $T_a$ , wind speed  $V_a$ , globe thermometer diameter  $D = 38mm$ , and emissivity  $\epsilon = 0.97$  of the globe:

$$MRT = \left\{ \left( (1.6T_g - 0.339T_a - 8.69 + 273.15)^4 + (0.24 + 2.08V_a^{0.5} + 1.14V_a^{0.667}) (1.6T_g - 0.339T_a - 8.69 - T_a)10^8 \right) \right\}^{1/4} - 273.15 \quad (2)$$

## 2.2 MRT Modeling

Due to limited sensing resources, MRT measurements across space and time are usually sparse. To address this gap, microclimate and radiation models calculate MRT using information on the built form and meteorological data. For example, RayMan (Matzarakis et al., 2010) is a point-based, single location model that requires hemispherical fisheye photos as input and calculates MRT based on the horizon limitation and standard weather information. ENVI-met (Bruse and Fleer, 1998) is a 3D gridded computational fluid dynamics (CFD) model in urban climates studies to assess heat at the neighborhood level. ENVI-met and RayMan calculate MRT based on Sun position to calculate the direct solar radiation and other radiative fluxes. However, Crank et al. (2020) found that both models do not perform well in extreme heat cases and struggle with complex urban forms. Acero and Herranz-Pascual (2015) also report deviations in MRT simulations from globe thermometer readings, especially under clear sky conditions, and Krüger et al.

(2014) found that all approaches discussed above (ENVI-met, RayMan, and globe thermometer observations) overestimate MRT when compared to ISO calculations. Currently, no model can accurately estimate MRT in the absence of detailed urban form parameters.

## 2.3 Pedestrian Counting

Much research has been developed for pedestrian counting and crowd estimation. Sensor-based techniques (Zappi et al., 2010; Wahl et al., 2012; Raykov et al., 2016; Lau et al., 2018) use passive infrared (PIR) and proximity sensors to monitor moving pedestrians. Although these setups are compact and low-cost, they have a low accuracy and misclassify often, and work best only under certain environmental conditions. Alternatively, network-based techniques (Kjærgaard et al., 2012; Weppner and Lukowicz, 2013; Depatla et al., 2015) use Bluetooth and WiFi networks for crowd sensing.

Recently, machine learning techniques low-level image feature extraction methods (Chen et al., 2013, 2012), such as Haar cascade (Viola and Jones, 2001) and HOG (Histogram of Oriented Gradient) (Dalal and Triggs, 2005; Yao et al., 2020) combined with regression models like SVM (Support Vector Machine) (Yao et al., 2020) or detectors like AdaBoost (Viola and Snow, 2003). State-of-the-art methods leverage deep convolutional neural networks for crowd estimation using individual detection (Wu and Nevatia, 2005; Brostow and Cipolla, 2006; Wang and Wang, 2011; Stewart et al., 2016; Liu et al., 2019) and using perspective maps (Chan et al., 2008; Lempitsky and Zisserman, 2010; Zhang et al., 2015).

Further, there are works revolving around analysis of crowd behaviour in urban areas (Hoogendoorn and Bovy, 2004; Hashimoto et al., 2016; Lee, 2020) and their relation with thermal comfort (Arens and Bosselmann, 1989; Givoni et al., 2003; Eliasson et al., 2007; Eom and Nishihori, 2021). We do not aim to outperform any existing pedestrian counting techniques, but to combine them with a weather station as a single setup.

## 2.4 Research Gaps

In summary, thermal exposure measurements in tandem with public space use assessments are crucial for active shade management in cities, but accurate MRT measurement setups are expensive and bulky. Low-cost systems such as gray globe thermometers have been developed but are not connected to the cloud for easy data storage and analysis. In addition, such low-cost sensors can suffer from over- and under-estimation of MRT at various times of the day as noted in previous literature. None of the existing MRT sensing platforms have vision capabilities, and space use is often assessed through time-consuming manual observations. Finally, physics-based MRT models require detailed 3D data of the urban environment to model radiation flux densities and sun-exposure. Our MaRTiny system aims to address all these gaps.

## 3 SYSTEM OVERVIEW

The MaRTiny system is a compact, Internet-of-Things (IoT), low-cost sensing and vision/recording/surveying platform (see

**Figure 1**). Its primary functionality is to measure MRT for a given sun-exposed location using off-the-shelf meteorological sensors and a custom-made globe thermometer. MaRTiny measures air temperature, relative humidity, wind speed, and globe temperature, which are used to calculate MRT (see Eq. (2)). In addition, MaRTiny is outfitted with a camera to detect and count people in the shade and Sun. This data helps analyze pedestrian behavior in public spaces (e.g. identifying the number of people who utilize shade, umbrella, bicycles and transportation etc). Privacy is preserved by only storing quantitative metrics (e.g. pedestrian count) and discarding the captured images after analysis.

The entire system transmits data to a cloud database via WiFi. It is powered by a single power source of 20 W which is split among different components according to their power ratings. MaRTiny was built under \$200 using different micro-controllers and AI edge devices. MaRTiny is envisioned to be a useful scientific platform to capture MRT data and correlate it with pedestrian behavior in outdoor settings at a fraction of the size/cost of existing solutions. No active human labor is needed for data collection which helps save funds, time, and heat exposure for researchers.

### 3.1 MaRTiny Weather Station

MaRTiny has four types of sensors to collect meteorological data every minute—multiple temperature probes/thermometers, UV sensor, humidity sensor, and anemometer (wind speed sensor) (see **Figure 2** and **Table 1** and **Table 2** for details). Two temperature probes are utilized for globe and air temperature respectively. Globe temperature is measured using a gray ping-pong ball attached on top of its probe. The globe's gray color almost matches the albedo of the human skin. The globe thermometer and the derived MRT emulate the omnidirectional thermal exposure for a human body as a

function of radiation, air temperature, and velocity, and thus are an accurate low-cost solution to net radiometers (Thorsson et al., 2006). Air temperature is measured using a downward hanging white cup that shades the attached temperature probe. The white cup reflects most of the solar radiation instead of absorbing it to provide an air temperature “free” from the influence of solar radiations. The UV sensor is used to measure the UV intensity and train the machine learning model to estimate MRT based on all measured parameters. MaRTiny is powered by a DC adapter of 5V/4A, which is shared by both systems (weather station and vision system). The anemometer is supplied with 9 V power by stepping up the primary voltage source. This setup can be easily scaled with more sensors without compromising on space and power. In practice, low-cost sensors are subject to noise and variation, which can yield errors in MRT estimation using Eq. (2) as we show later in **Section 5**. To solve this problem, we introduce a machine learning model to robustly estimate MRT despite these inaccuracies.

### 3.2 MaRTiny Vision

Along with meteorological parameters, MaRTiny requires vision capabilities including object detection and identification as well as shade detection in outdoor areas. We leverage the NVIDIA Jetson Nano, a low-cost and low-powered edge device to run state-of-the-art deep learning models. The Jetson Nano features an ARM-based micro-processor built with a Nvidia V100 GPU programmed through Nvidia's low level API TensorRT engine. It has configurable power consumption modes of 5W and 10 W. As we perform computationally heavy tasks, we have configured the Jetson Nano to 10 W mode. To capture video, we utilize a compact MIPI (Mobile Industry Processor Interface) camera and stream the data to the Jetson Nano using a gstreamer pipeline. Vision data is sent to AWS via an external USB WiFi on-board. In



**FIGURE 1 |** Top view of MaRTiny setup. Jetson Nano is attached with cooling Fan along with camera and WiFi module. Arduino boards are connected to different meteorological sensors.

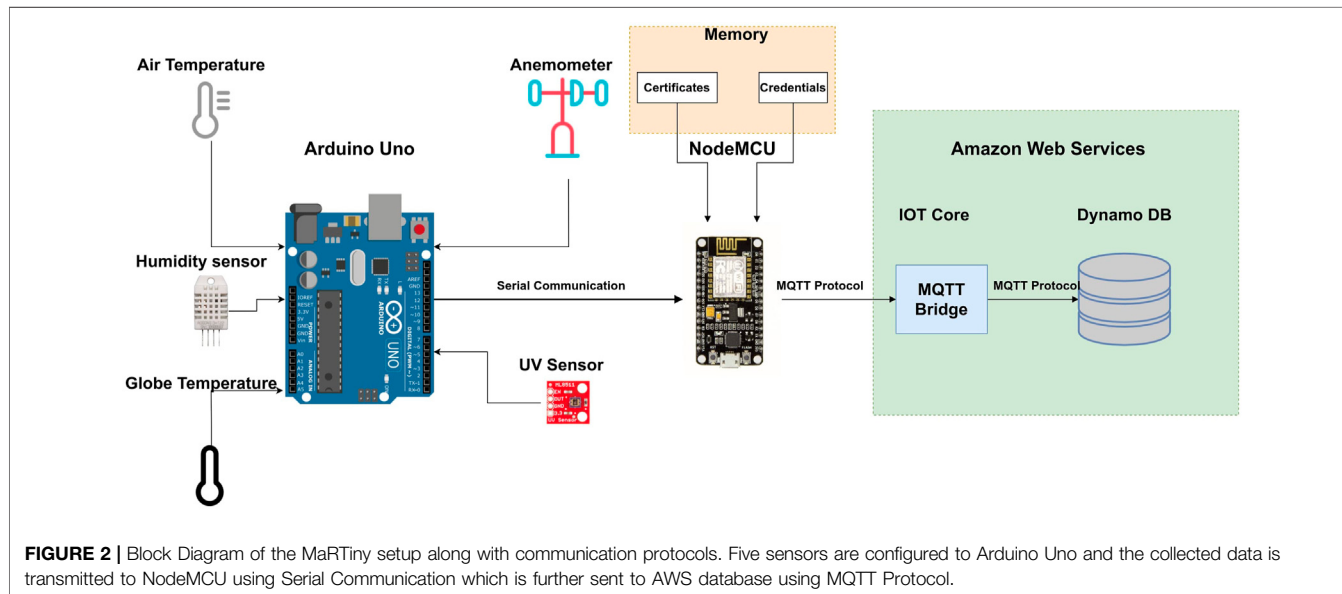


**TABLE 1 |** List of meteorological parameters measured by MaRTiny.

#### Meteorological parameters

Parameter	Description	Unit
Ta	Temperature of the surrounding air	°C
Tg	Temperature in the gray globe	°C
UV	Medium and long wave UV radiation	mW/cm <sup>2</sup>
RH	Relative Humidity	%
WS	Wind speed	m/s

the next section, we describe in detail our deep learning networks to detect pedestrians in shade.

### 3.3 Data Logging and Communication

To read meteorological sensor data, we use an Arduino Uno microcontroller. The Uno board communicates with a NodeMCU micro-controller featuring an ESP8266 architecture that has an inbuilt WiFi module, flash memory, and supports the PEM (Privacy Enhanced Mail) file system (see Figure 2). Sensor data are continuously read in a loop by the Uno with a small 1 ms delay to avoid overheating. Data are collected in a buffer, and an average is calculated for every minute, which is then transmitted to the NodeMCU board. The Uno acquires around 80 readings per minute. Both boards communicate via the serial communication protocol UART (universal Asynchronous Receiver/Transmitter).

The NodeMCU communicates securely with the online database. We utilize AWS DynamoDB, a NoSQL flexible database that can handle unstructured data. All the necessary security PEM files are stored in the NodeMCU's flash memory for authentication of MaRTiny. Using these files, NodeMCU establishes a communication path with AWS through the MQTT protocol, an extremely lightweight publish/subscribe messaging protocol

**TABLE 2 |** List of electrical MaRTiny parts, costs, and meteorological sensor accuracies.

#### Part List

Sensor	Part no	Cost (\$)	Accuracy
Temperature Probe	DS18B20	9	±0.5 °C from -10 °C to +85 °C
Humidity Sensor	DHT22	5	2–5% from 0 to 100%
UV Sensor	ML8511	5	1%
Anemometer	Adafruit	40	worst case 1 m/s
Arduino	Uno	20	
Node MCU	ESP8266	7	
CSI Camera	IMX219	20	
Nvidia Jetson	Jetson Nano	108	

designed for IoT. Once the communication is established, Node MCU waits for bytes of data to be received from the Uno board. Sensor data collected by Uno is sent to NodeMCU via serial communication every minute, which is then transmitted to DynamoDB using the MQTT protocol.

## 4 MACHINE LEARNING ALGORITHM DEVELOPMENT

### 4.1 Machine Learning for Accurate MRT Estimation

As MaRTiny is a low-cost, compact alternative to the MaRTy sensing platform (Middel and Krayenhoff, 2019; Middel et al., 2020, 2021), the replacement of highly accurate sensors has drawbacks including less accuracy and sensor lag (Häb et al., 2015). We noticed these inaccuracies caused serious errors in the calculated MRT values (Figure 7). In particular, MRT was sensitive to the positioning and orientation of the MaRTiny relative to MaRTy (e.g. the MaRTiny was shaded in one of the

test, which resulted in lower MRT values, while MaRTy's net radiometers were partially sun-exposed).

To overcome this limitation, we formulate MRT estimation as a supervised learning problem. This requires labeled ground-truth MRT values to be provided in correspondence with our less robust meteorological sensor data. In **Section 5**, we discuss data collection consisting of paired MaRTy and MaRTiny measurements to create this labeled data. This allows us to train a machine learning model to estimate MRT accurately from MaRTiny sensor data. We explored both traditional machine learning methods using a support vector machine (SVM) as well as a deep learning-based artificial neural network. These two algorithms are versatile and well-known in machine learning as they satisfy universal approximation theorems (Cybenko, 1989; Hammer and Gersmann, 2002). In particular, we observed an SVM with RBF (Radial Basis Function) kernel achieved the highest accuracy on our evaluation dataset in **Section 5**. This method is also computationally lightweight and can be easily deployed on the Jetson Nano for performing inference, i.e. the process of using a trained machine learning algorithm to make a prediction.

## 4.2 People and Shade Detection

### 4.2.1 Shadow Detection

To perform shadow detection in an image, we use the deep learning model Bi-directional Feature Pyramid with Recurrent Attention Residual Modules (BDRAR) (Zhu et al., 2018), visualized in the upper branch of **Figure 3**. BDRAR network takes a single image as input and outputs a binary shadow map as output in an end-to-end manner. First, it leverages a convolutional neural network (CNN) to extract feature maps at different spatial resolutions. It then employs two series of recurrent attention residual modules to fully exploit global and

local context for these feature maps. The features captured by shallow layers exploit shadow details in the local regions and the features captured by deep layers understand the overall shadow region of the image. **Figure 4** provides an example of shadow maps produced by the network.

### 4.2.2 Object Detection

For object detection, we utilize the state-of-the-art YOLOv3 network (AleyAB, 2016) visualized in the lower branch of **Figure 3**. The model is trained on 80 different classes of the Microsoft COCO dataset. The YOLOv3 algorithm can be built using two different frameworks - DarkNet and MobileNet (Redmon et al., 2016). The MobileNet framework is computationally light but has low accuracy, hence we decided to use the Darknet framework. YOLOv3 has a mAP (mean Average purpose) of around 57 (Redmon and Farhadi, 2018) and has been proven to be efficient in crowd places (Hsu et al., 2020). Since the YOLOv3-darknet model is large and computationally expensive to run on the NVIDIA Jetson Nano, we converted it into a simple neural graph using Nvidia's TensorRT. This allowed the model to run successfully on the Nano with a application-sufficient frame-rate of 4fps.

### 4.2.3 Pedestrian in Shade Detection

An image is a 2D representation of the 3D world, so it is difficult to determine the exact location of a pedestrian on the ground and their distance from the camera. We introduce a simple approach to identify pedestrians in shade without determining their position in 3D space. First, a binary shadow map from BDRAR indicating the presence of shade per pixel is computed periodically (in our case, every 15 min as shade does not vary significantly). For every MIPI camera frame, YOLOv3 outputs objects with their bounding boxes consisting

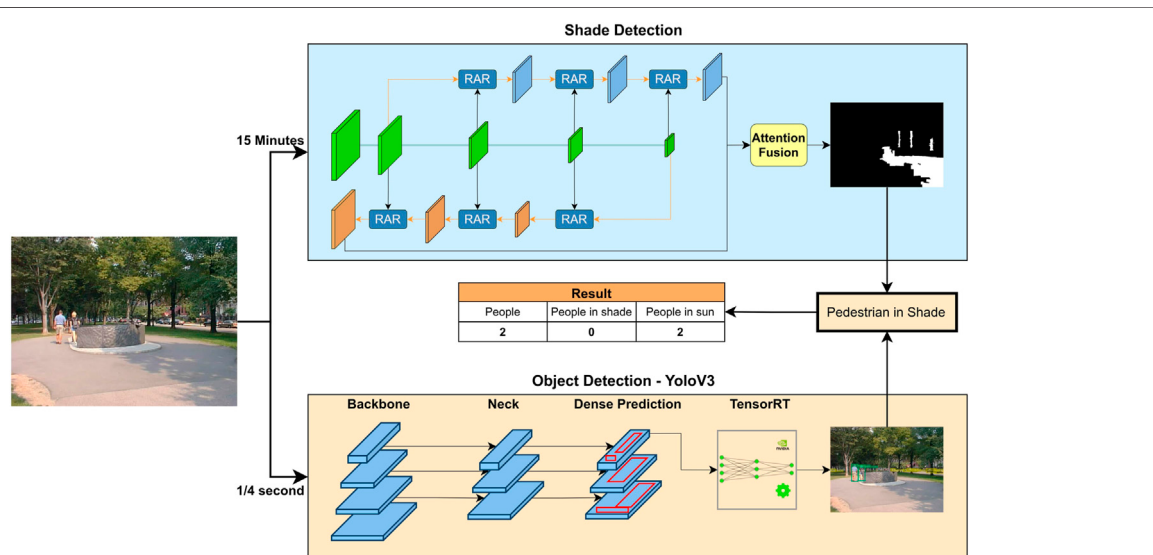


**FIGURE 3** | System Overview of the MaRTiny Vision using different types of Neural Networks. The top network represents BDRAR network, responsible for shade detection and the bottom network represents Yolov3. Shade map and bounding box of pedestrian is fed into the pedestrian algorithm to check number of people in shade and sun.



**FIGURE 4 |** Examples of shadow maps produced by BDRAR network. Note how the network works well for dark pixels without mistaking them for shade effect.

of pixel coordinates for the corners. Our algorithm calculates the IOU (Intersection over Union) of the bounding box with the shade map. We consider a person to be in shade if 40% of the bounding box region is inside the shade map (i.e.  $IOU = 0.4$ ).

Calculating IOU without considering the pedestrian's position with respect to shade can lead to errors. For example, in **Figure 5**, one person is sun-exposed and the other person is in the shade. The IOU of the bounding box with the shadow map equals 60% in the first case and 40% in the second case. The IOU for the first case is high due to background shade and shadow cast by the person's body. This is the most common type of error that occurs at different orientations of a person; therefore, it is necessary to distinguish between shade from a person and shade from the surroundings. Our algorithm first checks if the bounding box edge is in the shade. A person does not have to be completely in shade to feel the cooling effect, hence we consider only the bottom half i.e. 50% of the bounding box as a ROI (Region of Interest). We then calculate the IOU between this region and the shadow map. An IOU of 80% (which implies an IOU of 40% of the complete bounding box) is considered as the optimum value for a person to experience the cooling effects of shade. The ROI and IOU can change based on the environment and application. Pedestrian count under Sun and shade along with other relevant counts (umbrellas, pets, and bicycles) are reported to the online database, and the frame with identifying features is discarded. This allows our device to preserve the privacy of the individuals being observed which is necessary for public deployment.

## 5 SYSTEM EVALUATION

### 5.1 Data Collection

For evaluation, we collected a custom dataset of ground truth MRT values for two sun-exposed outdoor locations for 3 days in

Tempe, Arizona, United States. For validation purposes, the MaRTy human-biometeorological platform (Middel and Krayenhoff, 2019) was paired with the MaRTiny system for simultaneous data logging. **Figure 6** illustrates the paired setup, the top box corresponding to MaRTiny and the bottom setup corresponds to MaRTy. We can clearly see the difference in scale between both the setups. In addition, an image dataset was collected for evaluating object and shade detection. Images from the MIPI camera were stored at random intervals along with the bounding boxes of the interested objects. Ground truth bounding boxes were drawn manually using tools such as AlexyAB, (2016); Tosmonav, (2020) for 30 images consisting of around 50 different objects. Precision and Recall for each object were calculated and then used to calculate mAP (mean Average Precision). The same images were used to evaluate shade detection using IOU (Intersection Over Union) metrics. Small video snippets were stored at random intervals which helped to cross-verify the number of people in a given time frame. All the images and videos were stored in an AWS S3 bucket and were deleted after testing.

### 5.2 MRT Estimation

We first evaluated the performance of MaRTiny in estimating MRT values. We utilize **Eq. 2** with the sensor data on-board to calculate MRT. MaRTy logs data every 2 s, and MaRTiny stores data every minute, hence we calculated 1-min averages for comparison. Ground truth MRT was calculated using **Eq. 1**. **Figure 7** shows MaRTiny MRT results in green and MaRTy's ground truth calculation in red. A significant error in MaRTiny's estimation of MRT was found in the mornings with an MSE of around  $10^{\circ}\text{C}$ . The error is due to the spatial offset between the two devices, which caused the gray globe thermometer of the MaRTiny sensor to be partially shaded by a nearby palm tree in the mornings while MaRTy's net radiometers were sun-exposed. A palm tree has a narrow shadow pattern covering only portions of the whole MaRTy and MaRTiny setup (see

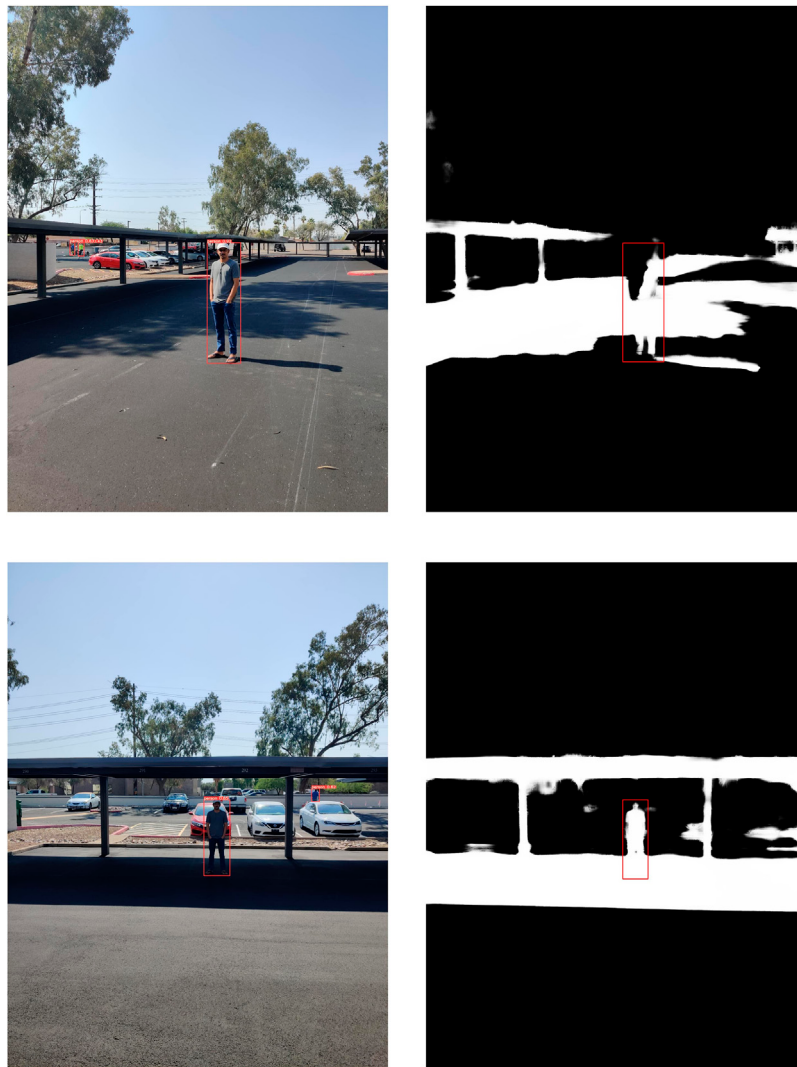


**FIGURE 5** | Images of a person with bounding box and shadow map of the surrounding. Using our algorithm, we can detect that the person in the first image is sun-exposed and the person in the second scenario is in shade.

**Figure 6).** For a detailed discussion of limitations, please see **section 6** (Discussion and Limitations).

To overcome these issues, we utilized our supervised learning approach using both SVM and ANN. Machine learning models were trained on selected meteorological parameters - air temperature, globe temperature, humidity and UV intensity, which were comparatively more accurate and less prone to noise. We used around 12,000 data points for training and 3,000 for testing from a range of dates, times, and locations in the sensing period. These training points were fed as vectors into the scikit-learn package in Python for training SVMs and ANNs. 5-fold cross-validation was used to tune model hyperparameters such as learning rate. A separate dataset for evaluation consisted of around 700 data points from a single location collected in a day as is the usual application for this algorithm.

Since there is a non-linear relation of globe temperature and air temperature with MRT given in Eq. 2, machine learning models need to understand complex non-linear relations between these parameters. A SVM with RBF kernel and a neural network with ReLU (Rectified Linear Unit) activation function are example of such models. In **Table 3**, we present a comparison of SVMs with three different kernels and a traditional artificial neural network (ANN). We report the Root Mean Square Error (RMSE) for both the testing and evaluation datasets. Note that the results of linear and polynomial SVM kernels justify our earlier assumption and the results of SVM with RBF kernel as well as the ANN achieved the best performance in quantitative metrics. From **Figure 8** we can see the performance of SVM with RBF kernel, which is almost linear with the ground truth.

We trained our ANN on a i7 CPU. We set our learning rate  $\alpha$  to 0.001, which took around 5 min and 300 epochs to converge.



**FIGURE 6 |** MaRTiny and MaRTy setup. The top white box corresponds to MaRTiny and the entire bottom setup corresponds to MaRTy.

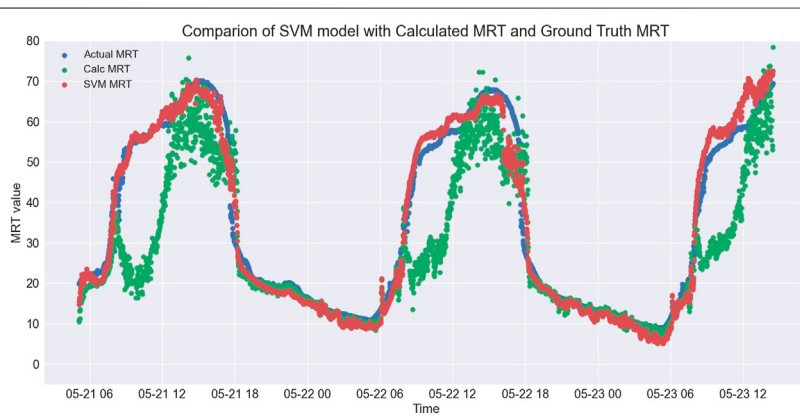


**FIGURE 7 |** Part I: Performance of MaRTiny weather station along with trained ML model tested between 05-21-2021 to 05-23-2021 in Tempe, Arizona. Comparison of calculated MRT values with SVM model. Note the dips in the calculation due to the shading effects of the environment experienced by the MaRTiny system, which is corrected by the SVM Model.

**TABLE 3 |** Performance of different supervised machine learning models for MRT estimation.

Machine Learning Algorithms for MRT		
Algorithm	RMS-Test	RMS-Eval
SVM-Linear	16.8	20.2
SVM-Poly	12.0	10.0
SVM-RBF	4.6	3.9
ANN	3.2	3.8

Although this model performs slightly better on the test dataset than the SVM-RBF model, performance is identical on the evaluation dataset. The SVM model is also computationally lighter and can be easily trained and deployed on edge devices such as Jetson Nano.

### 5.3 Shade and Object Detection

For object detection, we leverage the YOLOv3 architecture (Redmon and Farhadi, 2018). While not a state-of-the-art object detector, this model is computationally lightweight in comparison to more modern object detection models. Further,

the object detector needed to be compatible with both the TensorRT engine which we utilize on the NVIDIA Jetson board as well as the Python dependencies and packages necessary to run BDRAR as well as itself. Future research could investigate the optimal choice of object detector with shade detection (or a joint-model) for enhanced application performance. Although the model is out-of-box, we wanted to evaluate its performance in the environment suitable for the MaRTiny device and hence, we collected a small custom dataset and evaluated performance on these images. This evaluation on custom dataset should only be considered as a secondary evaluation while we still refer the reader to the main evaluation mentioned in the original study (Redmon and Farhadi, 2018) for the full performance of the object detector.

The standard evaluation metric used for any object detection is mAP (mean Average Precision). Bounding boxes were manually drawn using the tool for the dataset consisting of 30 images and IOU was calculated with the bounding boxes predicted by our model. Precision and recall is calculated for a series of different IOU thresholds ranging from 0.5 to 0.95. A precision-recall graph is constructed and the area under this graph provides us the mAP value of around 55%, which is close to the value reported in their study (Redmon and Farhadi, 2018). For our application IOU threshold of 0.5 gives us the optimal results. We also achieved an Average Precision of more than 85% for the class of Pedestrian, which is important for our application (**Figure 9**).

Evaluation of shadow detection is done on a per pixel basis, which is a binary evaluation method. A dataset consisting of 30 shade images was collected from different location and time. We manually annotated these images using the tool Tosmonav, (2020). We use the pre-trained BDRAR model to evaluate these images and calculated IOU of the shadow map with the ground truth and found a precision of 90%. This is not the most effective method to calculate model accuracy due to the irregular shapes, human error in annotation and small dataset and hence we also refer readers to the evaluation metrics of the original paper (Zhu et al., 2018). We evaluate our pedestrian in shade detection algorithm on a custom dataset of 50 images collected using MaRTiny. We have manually compared the detected values from our

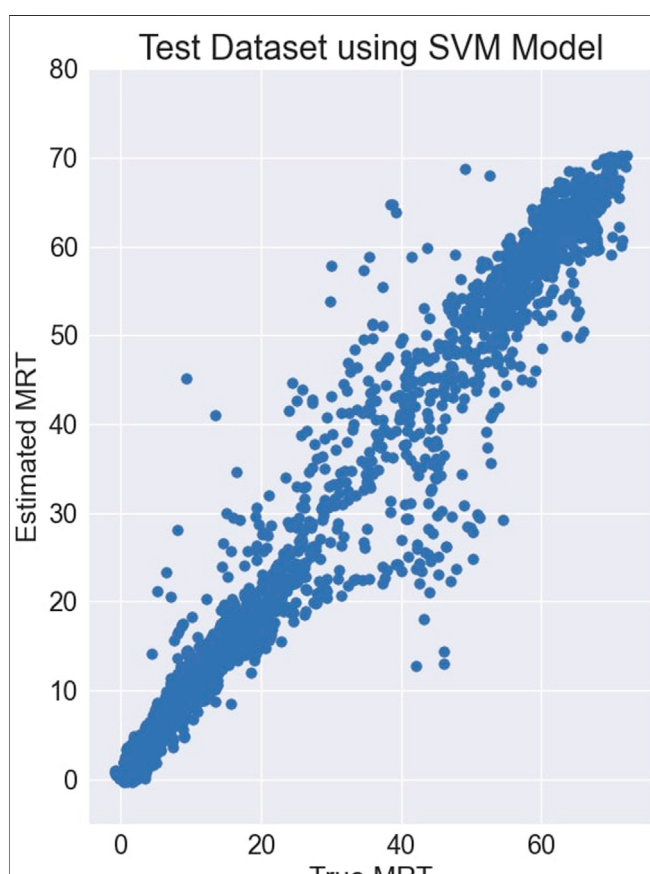


**FIGURE 8 |** Part II: Performance of MaRTiny weather station along with trained ML model tested between 05-21-2021 to 05-23-2021 in Tempe, Arizona. Performance of SVM Model on test dataset, which is almost linear with ground truth.

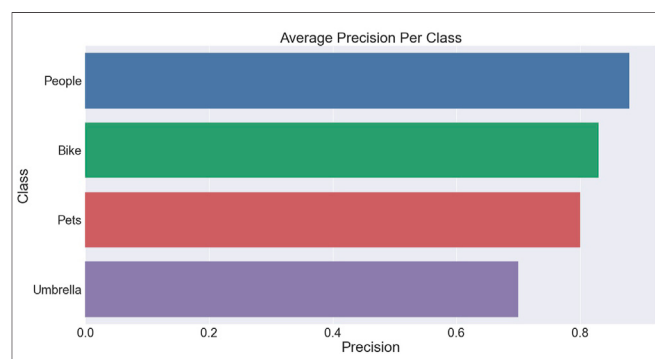


**FIGURE 9 |** The graph shows the performance of object detection on different classes of images collected during evaluation.



**FIGURE 10** | Example of Pedestrian detection along with masks using Yolov3 algorithm (left) and MaRTiny performing pedestrian detection in shade and sun (right).

algorithm with the ground truth and plotted a confusion matrix to obtain an accuracy of around 80%. Test data consisted of different shading effects and relative positions of pedestrian. Since this kind of testing has not been carried out before, our result can act as a baseline for future tests. The accuracy can be improved on edge cases where pedestrian is partially exposed to Sun at different orientations. **Figure 10** and **Figure 11** provides examples of MaRTiny Vision where YOLOv3 detects different objects and works along with BDRAR to determine if a pedestrian is in shade or sun.

## 6 DISCUSSION AND LIMITATIONS

This systems engineering study introduced a novel low-cost device that combines meteorological sensing with computer vision to estimate MRT and space use. While previous work has mainly focused on assessing the accuracy and precision of various sensors and on advancing MRT simulation tools, our contribution focuses on developing a low-cost hardware and software setup that can be used by non-experts such as city staff and citizen scientists. We also explored the use of state-of-



**FIGURE 11** | Sample images of Shade Detection and Pedestrian Counting. The top two rows are example of shade map estimation carried at different time and environments (Trees, Buildings, Empty Spaces) and last row has sample images captured by MaRTiny for Object Detection (Pedestrian and Bike).

the-art machine learning techniques to improve MRT estimation from low-cost sensors.

This article introduces the setup of the novel MaRTiny system to monitor biometeorological conditions and people's use of public spaces with changing weather conditions. An empirical study must follow to collect robust data over a long period of time to systematically analyze the relationship between thermal conditions and space usage. In addition, the MaRTiny biometeorological setup must be fully calibrated against NIST certified sensors before deployment, as it is built using off-the-shelf sensors with low accuracy (see **Table 2**).

While an RMSE of 10 °C between 6-directional MRT observations and globe temperature derived MRT may seem large, it is on the order of magnitude of errors reported by other authors and quite common for outdoor MRT measurements in heterogeneous built environments. Acero et al. (2021) found an RMSE of 7.4 °C for the standard ISO7726 coefficient between the 6-directional setup and a standard black globe. Vanos et al. (2021) found an average difference of  $-1.6 \pm 7.2$  °C between an acrylic gray globe and integral radiation measurements on a solar roof that was not subject to shading from the surrounding built environment. Most recently, Lee et al. (2022) reported a large mean difference of 13.2–21.6°C on sunny days between globe thermometer MRT and traditional MRT measurements.

Globe thermometers have various shortcomings, mostly related to the indirect measurement of incident radiative fluxes, which is highly sensitive to globe size, shape, material properties/assumptions, color, and wind speed (Vanos et al., 2021). Guo et al. (2018) and Chen et al. (2014) found significant impacts of wind speed on MRT obtained from globe thermometers, and Teitelbaum et al. (2020) point to errors from free convection. Globe thermometers also have a long response time (Nikolopoulou et al., 1999) that grows with globe diameter. MaRTinies are operated in stationary settings, which reduces the error, but they will not be able to respond quickly to changing cloud conditions. Lastly, globe thermometers are known to overestimate MRT during high incoming solar radiation periods and an underestimate at low solar elevation (Thorsson et al., 2006; Acero and Herranz-Pascual, 2015; Vanos et al., 2021).

The presented machine learning model is a proof-of-concept and is not a reliable MRT predictor in its current state. Our work demonstrates the potential of SVM models for MRT estimation but requires future data collection with identical micrometeorological conditions for all sensors, ideally for a full year, to build a robust model. The RMSE we calculated for our two testing days is high due to a palm tree that shaded the globe thermometer during the morning hours. RMSE is <4°C when the morning hours are discarded. We included those hours in our proof-of-concept to illustrate that a SVM model can overcome errors that are introduced by sensor setup. However, for a robust SVM model that can be used in a scientific study, all sensors should be subject to the same micrometeorological (shading) conditions.

With respect to the vision system, the BDRAR network exhibits minor inaccuracies in the shadow map estimation and

Yolov3. Although it performs well when detecting pedestrians in crowds, it struggles when an individual person occludes another person in the video feed. The shade detection works well but can misclassify a person as shaded or sun-exposed when intersecting the position of a person with the shadow mask, because the algorithm does not take into account the 3-dimensional nature of the shade and person in the scene.

## 7 CONCLUSION

Advancements in sensor technology have led to smaller, more portable, and more affordable sensors that facilitate low-cost sensing for many applications. In the domain of urban climate, low-cost sensing has gained popularity for crowdsourcing and citizen science studies, but is also increasingly used to build IoT sensor networks, for example, to monitor air pollution (Xiaojun et al., 2015) or thermal conditions in occupational settings (Sulzer et al., 2022).

MaRTiny leverages edge devices that are low-cost, low-powered, and yet computationally capable of running state-of-the-art machine learning algorithms. Integrating a vision system and people detection into the biometeorological sensing system enables in-depth analyses of how weather and microclimate conditions impact people's walking behavior in public spaces, including the use of shaded and sun-exposed areas. Once calibrated, the system will be deployed in City of Tempe parks and at playgrounds to inform municipal decision-making on targeted investments for cooling infrastructure in public spaces. The MaRTiny system is an example of how the emerging field of Urban Climate Informatics can support heat mitigation efforts through non-traditional observational methodologies.

## DATA AVAILABILITY STATEMENT

The raw data supporting the conclusions of this article will be made available by the authors, without undue reservation.

## AUTHOR CONTRIBUTIONS

KK designed and built the system, designed the algorithms and software, analyzed data from experiments, and helped write and edit the manuscript. FS assisted with hardware prototyping and data collection for both the MaRTiny and MaRTy setups as well as writing/revising the paper. TG helped with initial project discussions/conception. SJ helped supervise the project especially with machine learning and computer vision algorithms and helped write and edit the paper. AM conceived of the project idea, supervised the project, and helped write and edit the paper.

## FUNDING

This research was funded by the National Science Foundation (NSF), grant number CMMI-1942805 (CAREER: Human

Thermal Exposure in Cities - Novel Sensing and Modeling to Build Heat-Resilience), NSF CNS-1951928 (Understanding Heat Resiliency via Physiological, Mental, and Behavioral Health Factors for Indoor and Outdoor Urban Environments), and DEB-1832016 (Central Arizona-Phoenix

## REFERENCES

- Acero, J. A., Dissegna, A., Tan, Y. S., Tan, A., and Norford, L. K. (2021). Outdoor Performance of the Black Globe Temperature Sensor on a Hot and Humid Tropical Region. *Environ. Technol.*, 1–13. doi:10.1080/09593330.2021.1989057
- Acero, J. A., and Herranz-Pascual, K. (2015). A Comparison of Thermal Comfort Conditions in Four Urban Spaces by Means of Measurements and Modelling Techniques. *Build. Environ.* 93, 245–257. doi:10.1016/j.buildenv.2015.06.028
- [Dataset] AlexeyAB (2016). YOLO\_mark. Available at: [https://github.com/AlexeyAB/Yolo\\_mark](https://github.com/AlexeyAB/Yolo_mark).
- Alfano, F. R. D., Dell'isola, M., Ficco, G., Palella, B. I., and Riccio, G. (2021). On the Measurement of the Mean Radiant Temperature by Means of Globes: An Experimental Investigation under Black Enclosure Conditions. *Build. Environ.* 193, 107655. doi:10.1016/j.buildenv.2021.107655
- Ali-Toudert, F., and Mayer, H. (2007). Thermal Comfort in an East-West Oriented Street Canyon in Freiburg (Germany) Under Hot Summer Conditions. *Theor. Appl. Climatol.* 87, 223–237. doi:10.1007/s00704-005-0194-4
- Aminipouri, M., Rayner, D., Lindberg, F., Thorsson, S., Knudby, A. J., Zickfeld, K., et al. (2019). Urban Tree Planting to Maintain Outdoor Thermal Comfort Under Climate Change: The Case of Vancouver's Local Climate Zones. *Build. Environ.* 158, 226–236. doi:10.1016/j.buildenv.2019.05.022
- Arens, E., and Bosselmann, P. (1989). Wind, Sun and Temperature-Predicting the Thermal Comfort of People in Outdoor Spaces. *Build. Environ.* 24, 315–320. doi:10.1016/0360-1323(89)90025-5
- Brostow, G. J., and Cipolla, R. (2006). *Unsupervised Bayesian Detection of Independent Motion in Crowds*. USA: IEEE Computer Society.
- Brown, R. D. (2019). Correcting the Error in Measuring Radiation Received by a Person: Introducing Cylindrical Radiometers. *Sensors* 19, 5085. doi:10.3390/s19235085
- Bruse, M., and Fleer, H. (1998). Simulating Surface-Plant-Air Interactions inside Urban Environments with a Three Dimensional Numerical Model. *Environ. Model. Softw.* 13, 373–384. doi:10.1016/S1364-8152(98)00042-5
- Chan, A. B., Zhang-Sheng John Liang, J., and Vasconcelos, N. (2008). “Privacy Preserving Crowd Monitoring: Counting People without People Models or Tracking,” in *Computer Vision and Pattern Recognition*. doi:10.1109/CVPR.2008.4587569
- Chen, K., Gong, S., Xiang, T., and Chang Loy, C. (2013). “Cumulative Attribute Space for Age and Crowd Density Estimation,” in Proceedings of the IEEE Conference on Computer Vision and Pattern Recognition (CVPR). doi:10.1109/cvpr.2013.319
- Chen, K., Loy, C. C., Gong, S., and Xiang, T. (2012). “Feature Mining for Localised Crowd Counting,” in Proceedings of the British Machine Vision Conference (BMVA Press), 21. doi:10.5244/C.26.21
- Chen, Y.-C., Lin, T.-P., and Matzarakis, A. (2014). Comparison of Mean Radiant Temperature from Field Experiment and Modelling: a Case Study in Freiburg, Germany. *Theor. Appl. Climatol.* 118, 535–551. doi:10.1007/s00704-013-1081-z
- Colter, K. R., Middel, A. C., and Martin, C. A. (2019). Effects of Natural and Artificial Shade on Human Thermal Comfort in Residential Neighborhood Parks of Phoenix, Arizona, USA. *Urban For. Urban Green.* 44, 126429. doi:10.1016/j.ufug.2019.126429
- Coutts, A. M., White, E. C., Tapper, N. J., Beringer, J., and Livesley, S. J. (2016). Temperature and Human Thermal Comfort Effects of Street Trees across Three Contrasting Street Canyon Environments. *Theor. Appl. Climatol.* 124, 55–68. doi:10.1007/s00704-015-1409-y
- Crank, P. J., Middel, A., Wagner, M., Hoots, D., Smith, M., and Brazel, A. (2020). Validation of Seasonal Mean Radiant Temperature Simulations in Hot Arid Urban Climates. *Sci. Total Environ.* 749, 141392. doi:10.1016/j.scitotenv.2020.141392
- Long-Term Ecological Research Program CAP LTER). Any opinions, findings, and conclusions or recommendations expressed in this material are those of the authors and do not necessarily reflect the views of the sponsoring organizations.
- Cybenko, G. (1989). Approximation by Superpositions of a Sigmoidal Function. *Math. Control Signal Syst.* 2, 303–314. doi:10.1007/BF02551274
- Dalal, N., and Triggs, B. (2005). “Histograms of Oriented Gradients for Human Detection,” in 2005 IEEE Computer Society Conference on Computer Vision and Pattern Recognition (CVPR'05), 886–893. doi:10.1109/CVPR.2005.177
- Depatla, S., Muralidharan, A., and Mostofi, Y. (2015). Occupancy Estimation Using Only WiFi Power Measurements. *IEEE J. Sel. Areas Commun.* 33, 1381–1393. doi:10.1109/JSAC.2015.2430272
- Eliasson, I., Knez, I., Westerberg, U., Thorsson, S., and Lindberg, F. (2007). Climate and Behaviour in a Nordic City. *Landsc. Urban Plan.* 82, 72–84. doi:10.1016/j.landurbplan.2007.01.020
- Emmanuel, R., Rosenlund, H., and Johansson, E. (2007). Urban Shading—A Design Option for the Tropics? A Study in Colombo, Sri Lanka. *Int. J. Climatol.* 27, 1995–2004. doi:10.1002/joc.1609
- Eom, S., and Nishihori, Y. (2021). How Weather and Special Events Affect Pedestrian Activities: Volume, Space, and Time. *Int. J. Sustain. Transp.* 0, 1–31. doi:10.1080/15568318.2021.1897907
- Givoni, B., Noguchi, M., Saaroni, H., Pochter, O., Yaacov, Y., Feller, N., et al. (2003). Outdoor Comfort Research Issues. *Energy Build.* 35, 77–86. doi:10.1016/S0378-7788(02)00082-8
- Guo, H., Teitelbaum, E., Houchois, N., Bozlar, M., and Meggers, F. (2018). Revisiting the Use of Globe Thermometers to Estimate Radiant Temperature in Studies of Heating and Ventilation. *Energy Build.* 180, 83–94. doi:10.1016/j.enbuild.2018.08.029
- Häb, K., Ruddell, B. L., and Middel, A. (2015). Sensor Lag Correction for Mobile Urban Microclimate Measurements. *Urban Clim.* 14, 622–635. doi:10.1016/j.uclim.2015.10.003
- Hammer, B., and Gersmann, K. (2003). A Note on the Universal Approximation Capability of Support Vector Machines. *Neural Process. Lett.* 17, 43–53. doi:10.1023/A:1022936519097
- Harlan, S. L., Brazel, A. J., Prashad, L., Stefanov, W. L., and Larsen, L. (2006). Neighborhood Microclimates and Vulnerability to Heat Stress. *Soc. Sci. Med.* 63, 2847–2863. doi:10.1016/j.soscimed.2006.07.030
- Hashimoto, Y., Gu, Y., Hsu, L.-T., Iryo-Asano, M., and Kamijo, S. (2016). A Probabilistic Model of Pedestrian Crossing Behavior at Signalized Intersections for Connected Vehicles. *Transp. Res. Part C Emerg. Technol.* 71, 164–181. doi:10.1016/j.trc.2016.07.011
- Hoogendoorn, S. P., and Bovy, P. H. L. (2004). Pedestrian Route-Choice and Activity Scheduling Theory and Models. *Transp. Res. Part B Methodol.* 38, 169–190. doi:10.1016/S0191-2615(03)00007-9
- Höpke, P. (1992). A New Procedure to Determine the Mean Radiant Temperature Outdoors. *Wetter und Leben* 44, 147–151.
- Höpke, P. (1999). The Physiological Equivalent Temperature – a Universal Index for the Biometeorological Assessment of the Thermal Environment. *Int. J. Biometeorology* 43, 71–75. doi:10.1007/s004840050118
- Hsu, Y. W., Chen, Y. W., and Perng, J. W. (2020). Estimation of the Number of Passengers in a Bus Using Deep Learning. *Sensors (Basel)* 20, 2178. doi:10.3390/s20082178
- Jendritzky, G., de Dear, R., and Havenith, G. (2012). UTCI—why Another Thermal Index? *Int. J. Biometeorol.* 56, 421–428. doi:10.1007/s00484-011-0513-7
- Johansson, E., Thorsson, S., Emmanuel, R., and Krüger, E. (2014). Instruments and Methods in Outdoor Thermal Comfort Studies – the Need for Standardization. *Urban Clim.* 10, 346–366. doi:10.1016/j.uclim.2013.12.002
- Kántor, N., and Unger, J. (2011). The Most Problematic Variable in the Course of Human-Biometeorological Comfort Assessment – the Mean Radiant Temperature. *Central Eur. J. Geosciences* 3, 90–100. doi:10.2478/s13533-011-0010-x
- Kjaergaard, M. B., Wirz, M., Roggen, D., and Troster, G. (2012). “Mobile Sensing of Pedestrian Flocks in Indoor Environments Using WiFi Signals,” in 2012 IEEE International Conference on Pervasive Computing and Communications, PerCom. doi:10.1109/PerCom.2012.6199854

- Krüger, E. L., Minella, F. O., and Matzarakis, A. (2014). Comparison of Different Methods of Estimating the Mean Radiant Temperature in Outdoor Thermal Comfort Studies. *Int. J. Biometeorol.* 58, 1727–1737. doi:10.1007/s00484-013-0777-1
- Kuras, E. R., Richardson, M. B., Calkins, M. M., Ebi, K. L., Hess, J. J., Kintziger, K. W., et al. (2017). Opportunities and Challenges for Personal Heat Exposure Research. *Environ. Health Perspect.* 125, 085001. doi:10.1289/EHP556
- Lau, B. P. L., Wijerathne, N., Ng, B. K. K., and Yuen, C. (2018). Sensor Fusion for Public Space Utilization Monitoring in a Smart City. *IEEE Internet Things J.* 5, 473–481. doi:10.1109/JIOT.2017.2748987
- Lee, H., Jo, S., and Park, S. (2022). A Simple Technique for the Traditional Method to Estimate Mean Radiant Temperature. *Int. J. Biometeorol.* 66, 521–533. doi:10.1007/s00484-021-02213-x
- Lee, I., Voogt, J., and Gillespie, T. (2018). Analysis and Comparison of Shading Strategies to Increase Human Thermal Comfort in Urban Areas. *Atmosphere* 9, 91. doi:10.3390/atmos9030091
- Lee, J. M. (2020). Exploring Walking Behavior in the Streets of New York City Using Hourly Pedestrian Count Data. *Sustainability* 12, 7863. doi:10.3390/su12197863
- Lempitsky, V., and Zisserman, A. (2010). “Learning to Count Objects in Images.”, *Advances in Neural Information Processing Systems*. Editors J. Lafferty, C. Williams, J. Shawe-Taylor, R. Zemel, and A. Culotta (Curran Associates, Inc.), 23.
- Liu, W., Salzmann, M., and Fua, P. (2019). “Context-aware Crowd Counting,” in Proceedings of the IEEE/CVF Conference on Computer Vision and Pattern Recognition (CVPR). doi:10.1109/cvpr.2019.00524
- Manavvi, S., and Rajasekar, E. (2020). Estimating Outdoor Mean Radiant Temperature in a Humid Subtropical Climate. *Build. Environ.* 171, 106658. doi:10.1016/j.buildenv.2020.106658
- Masson-Delmotte, V., Zhai, P., Pirani, A., Connors, S., Péan, C., Berger, S., et al. (2021). *Ipccl, 2021: Climate Change 2021: The Physical Science Basis. Contribution of Working Group I to the Sixth Assessment Report of the Intergovernmental Panel on Climate Change*. Cambridge University Press. Available at : <https://www.ipcc.ch/report/sixth-assessment-report-working-group-i/>
- Matzarakis, A., Rutz, F., and Mayer, H. (2010). Modelling Radiation Fluxes in Simple and Complex Environments: Basics of the RayMan Model. *Int. J. Biometeorol.* 54, 131–139. doi:10.1007/s00484-009-0261-0
- Middel, A., AlKhaleed, S., Schneider, F. A., Hagen, B., and Coseo, P. (2021). 50 Grades of Shade. *Bull. Am. Meteorological Soc.* 1, 1–35. doi:10.1175/bams-d-20-0193.1
- Middel, A., Häb, K., Brazel, A. J., Martin, C. A., and Guhathakurta, S. (2014). Impact of Urban Form and Design on Mid-afternoon Microclimate in Phoenix Local Climate Zones. *Landsc. Urban Plan.* 122, 16–28. doi:10.1016/j.landurbplan.2013.11.004
- Middel, A., and Krayenhoff, E. S. (2019). Micrometeorological Determinants of Pedestrian Thermal Exposure during Record-Breaking Heat in Tempe, Arizona: Introducing the Marty Observational Platform. *Sci. Total Environ.* 687, 137–151. doi:10.1016/j.scitotenv.2019.06.085
- Middel, A., Lukasczyk, J., and Maciejewski, R. (2017). Sky View Factors from Synthetic Fisheye Photos for Thermal Comfort Routing-A Case Study in Phoenix, Arizona. *Urban Planning* 2, 19–30. doi:10.17645/up.v2i1.855
- Middel, A., Selover, N., Hagen, B., and Chhetri, N. (2016). Impact of Shade on Outdoor Thermal Comfort-A Seasonal Field Study in Tempe, Arizona. *Int. J. Biometeorol.* 60, 1849–1861. doi:10.1007/s00484-016-1172-5
- Middel, A., Turner, V. K., Schneider, F. A., Zhang, Y., and Stiller, M. (2020). Solar Reflective Pavements-A Policy Panacea to Heat Mitigation? *Environ. Res. Lett.* 15, 064016. doi:10.1088/1748-9326/ab87d4
- Nikolopoulou, M., Baker, N., and Steemers, K. (1999). Improvements to the Globe Thermometer for Outdoor Use. *Archit. Sci. Rev.* 42, 27–34. doi:10.1080/00038628.1999.9696845
- Olesen, B., Rosendahl, J., Kalisperis, L., Summers, L. H., and Steinman, M. (1989). Methods for Measuring and Evaluating the Thermal Radiation in a Room. *Ashrae Trans.* 95, 1028–1044.
- Oliveira, A. V. M., Raimundo, A. M., Gaspar, A. R., and Quintela, D. A. (2019). Globe Temperature and its Measurement: Requirements and Limitations. *Ann. Work Expo. Health* 63, 743–758. doi:10.1093/annweh/wxz042
- Raykov, Y., Ozer, E., Dasika, G., Boukouvalas, A., and Little, M. (2016). “Predicting Room Occupancy with a Single Passive Infrared (Pir) Sensor through Behavior Extraction,” in UbiComp 2016 - Proceedings of the 2016 ACM International Joint Conference on Pervasive and Ubiquitous Computing (United States: ACM), 1016–1027. 2016 ACM International Joint Conference on Pervasive and Ubiquitous Computing, UbiComp 2016 ; Conference date: 12-09-2016 Through 16-09-2016.
- Redmon, J., Divvala, S. K., Girshick, R. B., and Farhadi, A. (2016). “You Only Look once: Unified, Real-Time Object Detection,” in 2016 IEEE Conference on Computer Vision and Pattern Recognition (CVPR), 779. doi:10.1109/cvpr.2016.91
- Redmon, J., and Farhadi, A. (2018). YOLOv3: An Incremental Improvement. *arXiv*, ArXiv abs/1804.02767. doi:10.48550/ARXIV.1804.02767
- Shashua-Bar, L., Pearlmutter, D., and Erell, E. (2009). The Cooling Efficiency of Urban Landscape Strategies in a Hot Dry Climate. *Landsc. urban Plan.* 92, 179–186. doi:10.1016/j.landurbplan.2009.04.005
- Stewart, R., Andriluka, M., and Ng, A. Y. (2016). “End-to-End People Detection in Crowded Scenes,” in Proceedings of the IEEE Conference on Computer Vision and Pattern Recognition (CVPR). doi:10.1109/cvpr.2016.255
- Sulzer, M., Christen, A., and Matzarakis, A. (2022). A Low-Cost Sensor Network for Real-Time Thermal Stress Monitoring and Communication in Occupational Contexts. *Sensors* 22, 1828. doi:10.3390/s22051828
- Teitelbaum, E., Chen, K. W., Meggers, F., Guo, H., Houchois, N., Pantelic, J., et al. (2020). Globe Thermometer Free Convection Error Potentials. *Sci. Rep.* 10, 2652–2713. doi:10.1038/s41598-020-59441-1
- Thorsson, S., Honjo, T., Lindberg, F., Eliasson, I., and Lim, E.-M. (2007). Thermal Comfort and Outdoor Activity in Japanese Urban Public Places. *Environ. Behav.* 39, 660–684. doi:10.1177/0013916506294937
- Thorsson, S., Rocklöv, J., Konarska, J., Lindberg, F., Holmer, B., Dousset, B., et al. (2014). Mean Radiant Temperature - A Predictor of Heat Related Mortality. *Urban Clim.* 10, 332–345. doi:10.1016/j.ulclim.2014.01.004
- [Dataset] Tosmonav (2020). Cvat. Available at: <https://github.com/openvinotoolkit/cvat>.
- Vanos, J. K., Rykaczewski, K., Middel, A., Vecellio, D. J., Brown, R. D., and Gillespie, T. J. (2021). Improved Methods for Estimating Mean Radiant Temperature in Hot and Sunny Outdoor Settings. *Int. J. Biometeorol.* 65, 967–983. doi:10.1007/s00484-021-02131-y
- Viola, P., Jones, M. J., and Snow, D. (2003). “Detecting Pedestrians Using Patterns of Motion and Appearance,” in Proceedings Ninth IEEE International Conference on Computer Vision, 734. doi:10.1109/ICCV.2003.1238422
- Viola, P., and Jones, M. (2001). “Rapid Object Detection Using a Boosted Cascade of Simple Features,” in Proceedings of the 2001 IEEE Computer Society Conference on Computer Vision and Pattern Recognition. CVPR. doi:10.1109/CVPR.2001.990517
- Wahl, F., Milenkovic, M., and Amft, O. (2012). “A Distributed Pir-Based Approach for Estimating People Count in Office Environments,” in 2012 IEEE 15th International Conference on Computational Science and Engineering, 640–647. doi:10.1109/ICCSE.2012.92
- Wang, M., and Wang, X. (2011). Automatic Adaptation of a Generic Pedestrian Detector to a Specific Traffic Scene. *CVPR*, 3401–3408. doi:10.1109/CVPR.2011.5995698
- Weppner, J., and Lukowicz, P. (2013). “Bluetooth Based Collaborative Crowd Density Estimation with Mobile Phones,” in 2013 IEEE International Conference on Pervasive Computing and Communications, PerCom, 193–200. doi:10.1109/PerCom.2013.6526732
- Wu, B., and Nevatia, R. (2005). Detection of Multiple, Partially Occluded Humans in a Single Image by Bayesian Combination of Edgelet Part Detectors. *Tenth IEEE Int. Conf. Comput. Vis.* 1, 90–97. doi:10.1109/iccv.2005.74
- Xiaojun, C., Xianpeng, L., and Peng, X. (2015). “Iot-based Air Pollution Monitoring and Forecasting System,” in 2015 International Conference on Computer and Computational Sciences (ICCCS), 257–260. doi:10.1109/icccs.2015.7361361
- Yao, Y., Zhang, X., Liang, Y., Zhang, X., Shen, F., and Zhao, J. (2020). “A Real-Time Pedestrian Counting System Based on Rgb-D,” in 2020 12th International Conference on Advanced Computational Intelligence (ICACI), 110. doi:10.1109/ICACI49185.2020.9177816
- Zappi, P., Farella, E., and Benini, L. (2010). Tracking Motion Direction and Distance with Pyroelectric Ir Sensors. *IEEE Sensors J.* 10, 1486–1494. doi:10.1109/JSEN.2009.2039792

- Zhang, C., Li, H., Wang, X., and Yang, X. (2015). "Cross-scene Crowd Counting via Deep Convolutional Neural Networks," in Proceedings of the IEEE Conference on Computer Vision and Pattern Recognition (CVPR). doi:10.1109/cvpr.2015.7298684
- Zhu, L., Deng, Z., Hu, X., Fu, C.-W., Xu, X., Qin, J., et al. (2018). "Bidirectional Feature Pyramid Network with Recurrent Attention Residual Modules for Shadow Detection," in *ECCV 2018. Lecture Notes in Computer Science*. doi:10.1007/978-3-030-01231-1\_8

**Conflict of Interest:** The authors declare that the research was conducted in the absence of any commercial or financial relationships that could be construed as a potential conflict of interest.

**Publisher's Note:** All claims expressed in this article are solely those of the authors and do not necessarily represent those of their affiliated organizations, or those of the publisher, the editors and the reviewers. Any product that may be evaluated in this article, or claim that may be made by its manufacturer, is not guaranteed or endorsed by the publisher.

Copyright © 2022 Kulkarni, Schneider, Gowda, Jayasuriya and Middel. This is an open-access article distributed under the terms of the Creative Commons Attribution License (CC BY). The use, distribution or reproduction in other forums is permitted, provided the original author(s) and the copyright owner(s) are credited and that the original publication in this journal is cited, in accordance with accepted academic practice. No use, distribution or reproduction is permitted which does not comply with these terms.



# A Transformation in City-Descriptive Input Data for Urban Climate Models

Mathew J. Lipson<sup>1\*</sup>, Negin Nazarian<sup>2,3,4</sup>, Melissa A. Hart<sup>2</sup>, Kerry A. Nice<sup>5</sup> and Brooke Conroy<sup>2,6</sup>

<sup>1</sup>ARC Centre of Excellence for Climate System Science, University of New South Wales, Sydney, NSW, Australia, <sup>2</sup>ARC Centre of Excellence for Climate Extremes, University of New South Wales, Sydney, NSW, Australia, <sup>3</sup>School of Built Environment, University of New South Wales, Sydney, NSW, Australia, <sup>4</sup>City Futures Research Centre, University of New South Wales, Sydney, NSW, Australia, <sup>5</sup>Transportation, Health and Urban Design Research Lab, Faculty of Architecture, Building, and Planning, University of Melbourne, Melbourne, VIC, Australia, <sup>6</sup>School of Earth and Environmental Sciences, University of Wollongong, Wollongong, NSW, Australia

## OPEN ACCESS

**Edited by:**

Marco Casazza,  
University of Salerno, Italy

**Reviewed by:**

Saskia Buchholz,  
German Weather Service, Germany  
Andrea Zonato,  
University of Trento, Italy  
Merja H. Tölle,  
University of Kassel, Germany  
Jack Katzfey,  
CSIRO Oceans and Atmosphere,  
Australia

**\*Correspondence:**

Mathew J. Lipson  
m.lipson@unsw.edu.au

**Specialty section:**

This article was submitted to  
Environmental Informatics and Remote  
Sensing,  
a section of the journal  
*Frontiers in Environmental Science*

**Received:** 31 January 2022

**Accepted:** 06 June 2022

**Published:** 06 July 2022

**Citation:**

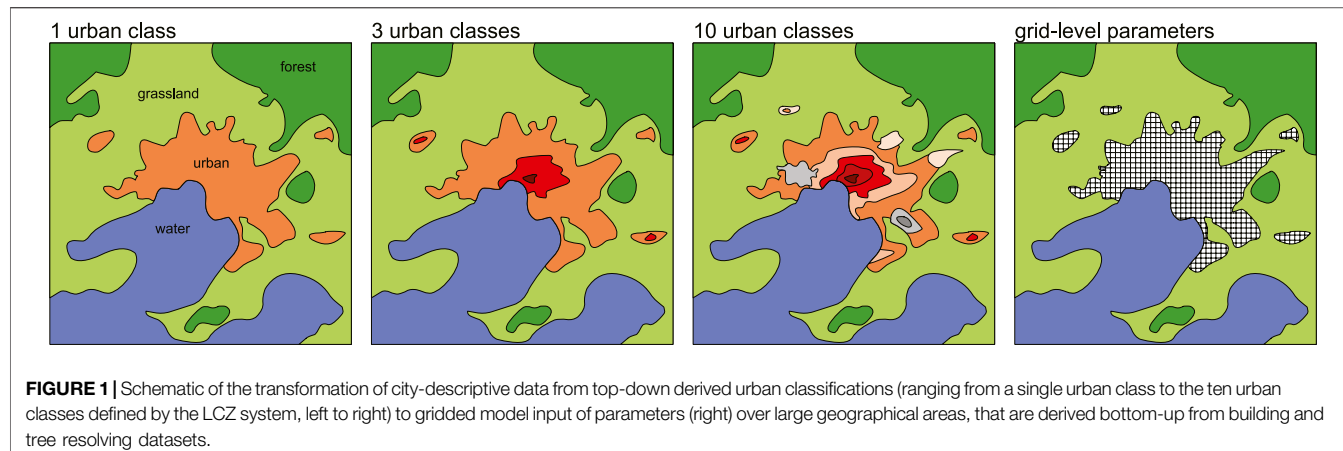
Lipson MJ, Nazarian N, Hart MA, Nice KA and Conroy B (2022) A Transformation in City-Descriptive Input Data for Urban Climate Models. *Front. Environ. Sci.* 10:866398.  
doi: 10.3389/fenvs.2022.866398

In urban climate studies, datasets used to describe urban characteristics have traditionally taken a class-based approach, whereby urban areas are classified into a limited number of typologies with a resulting loss of fidelity. New datasets are becoming increasingly available that describe the three-dimensional structure of cities at sub-metre micro-scale resolutions, resolving individual buildings and trees across entire continents. These datasets can be used to accurately determine local characteristics without relying on classes, but their direct use in numerical weather and climate modelling has been limited by their availability, and because they require processing to conform to the required inputs of climate models. Here, we process building-resolving datasets across large geographical extents to derive city-descriptive parameters suitable as common model inputs at resolutions more appropriate for local or meso-scale modelling. These parameter values are then compared with the ranges obtained through the class-based Local Climate Zone framework. Results are presented for two case studies, Sydney and Melbourne, Australia, as open access data tables for integration into urban climate models, as well as codes for processing high-resolution and three-dimensional urban datasets. We also provide an open access 300 m resolution building morphology and surface cover dataset for the Sydney metropolitan region (approximately 5,000 square kilometres). The use of building resolving data to derive model inputs at the grid scale better captures the distinct heterogenous characteristics of urban form and fabric compared with class-based approaches, leading to a more accurate representation of cities in climate models. As consistent building-resolving datasets become available over larger geographical extents, we expect bottom-up approaches to replace top-down class-based frameworks.

**Keywords:** urban, climate, model, spatial, data, open, morphology

## 1 INTRODUCTION

A transformation is underway in how urban form and fabric are described for urban climate modelling and observation studies. For the last 50 years, datasets used in urban environment or climate studies have typically described urban areas using types or classes in a “top-down” approach, whereby regions of a city, and sometimes surrounds, are classified based on a limited number of



urban surface and land-use characteristics (e.g., Masson et al., 2003; Jackson et al., 2010; Stewart and Oke, 2012; Demuzere et al., 2020). In more recent years, very high resolution (sub-metre) urban datasets have become increasingly available that resolve the characteristics of individual buildings and trees over entire cities, regions and continents (PSMA Australia, 2020; Biljecki et al., 2021; Sirkko et al., 2021).

These new building-resolving datasets are transforming the way cities can be represented in urban climate models, as spatial dataset parameters are no longer tied to a class type but can be defined for each model grid at any resolution from the “bottom-up” (Figure 1). Where available, these new datasets can be used to produce direct inputs for climate modelling studies at the grid level, or to inform locally appropriate parameter choices in traditional class approaches. The transition to a bottom-up approach, however, is ongoing as many regions do not have access to this urban element-resolving data, and many urban climate models are designed to rely on a class approach when defining urban area characteristics (Masson et al., 2020).

Enhanced accuracy in the representation of urban areas in climate modelling is vital. Cities experience the dual burden of global warming from increased greenhouse gas emissions, and localised warming due to urbanization. This urban heat differs not only from the non-urbanised surrounds but also spatially within a city due to differences in urban density and surfaces. To fully understand the interaction between climates of cities and assess the role of both current and future urbanization in urban climate challenges, it is important for this intra-urban variability to be captured when modelling a city’s climate (Martilli et al., 2020; Potgieter et al., 2021).

Accurate representation of urban areas requires description of four categories of features in both the urbanized areas and surrounds: a) form (urban and vegetated morphology), fabric (materials and surface cover), function (land use and anthropogenic effects), and regional geographic factors (topography and distance from water). Due to computational costs, however, mesoscale models are unable to resolve all urban features while modelling atmospheric processes spanning the entire region. Instead, urban canopy models are defined that assume simplified building geometry in a “building-averaged”

approach. The most common geometrical assumptions used in urban models are bulk (1-dimensional), canyon (2-dimensional) or block array (3-dimensional) (Nazarian, 2022). Different modelling assumptions then require different types of morphological and surface cover inputs (outlined in Table 1), further distinguished by the representation of sub-models for vegetation impact and/or thermal comfort characteristics within the street canopy. Accurate urban descriptions are of even greater importance with local and micro-scaled modelling (at sub 10 m resolutions) and in three dimensions, with models such as PALM (Fröhlich and Matzarakis, 2020), ENVI-met (Bruse, 1999), VTUF-3D (Nice et al., 2018), and SOLWEIG/UMEP (Lindberg et al., 2018), as the improved model input can result in more realistic output.

Historically, urban areas have been captured in models *via* land use classification. This is often done by just one urban land type, where different urban regions are represented with a constant set of parameters. Single class approaches have been used in both global models (if urban areas are represented) (Li et al., 2016; Katzfey et al., 2020) and in mesoscale models (Argüeso et al., 2014). Moving beyond one urban land-use class, cities in global or mesoscale models have also been classified on levels of urban density (Ma et al., 2018; Oleson and Feddema, 2020) or by dividing urban areas into different categories such as residential, commercial, and industrial (Chen et al., 2016). These methods provide information on urban form and/or function but fidelity is limited by the number of defined classes.

In a key development, Stewart and Oke (2012) proposed Local Climate Zones (LCZ). LCZs classify city form, fabric, and function into 10 urban classes, and non-urban land cover types into seven classes. The primary motivation for developing LCZs was to improve the description of sites in observational studies in a move away from the historical urban-rural differentiation when investigating urban heat. The classification has been widely used to determine appropriate urban and rural sites for traditional urban heat island intensity calculations (Siu and Hart, 2013) and to explore variability in intra-urban air temperatures in observation studies (Núñez-Péiró et al., 2021; Potgieter et al., 2021).

**TABLE 1 |** City-descriptive parameters for various modelling purposes.

Model type	Input parameters
Urban canopy models	
Bulk (slab) model	Built fraction, roughness length
Canyon model	Plan area density (or building fraction), aspect (or height-to-width) ratio, mean building height, building height standard deviation, displacement height, roughness length
Block array model	Plan area density (or building fraction), wall area density, mean building height, building height standard deviation, displacement height, roughness length
Sub-models	
Vegetation model	Tree fraction, low vegetation (grass/shrubs) fraction, bare earth fraction, water fraction, tree canopy height, roughness length
Thermal comfort model	Sky view factor, roughness length, displacement height, roughness length

LCZs have also become commonly used in urban climate modelling, with LCZ classes being integrated into urban land cover classification in mesoscale models (Brousse et al., 2016; Zonato et al., 2020). World Urban Database and Access Portal Tools (Ching et al., 2018), a community led initiative to collect worldwide data on urban form, fabric and function, at its lowest level of detail produces LCZ maps of cities and their surrounding areas. The maps are produced *via* users classifying small subsections of a city as training data, which are then used in machine learning algorithms to classify the entire region of interest. More recently, WUDAPT workflows have been streamlined into open, online services (e.g., the LCZ Generator; Demuzere et al., 2021).

A limitation of the LCZ approach in the context of numerical modelling is that LCZ parameters are provided as a range of values with substantial overlap between classes, while urban canopy models typically accept explicitly defined values. Common methods of dealing with these challenges include using the midpoints of the LCZ range proposed in Stewart and Oke (2012) for each LCZ used (Mughal et al., 2019), or setting the parameters for LCZ ranges using additional datasets that provide local knowledge (Hirsch et al., 2021).

These traditional top-down approaches, although useful for widespread analyses where data may be lacking, have limitations in that there is often a level of local knowledge or estimation required when setting parameter values, and that outputs are not likely to be consistent between different users and regions. New urban datasets are emerging that directly characterize the 3D urban form produced *via* methods such as LiDAR and aerial photography observations. Among these high-resolution datasets is the emergence of 3D building models that provide comprehensive representation of built environments in cities across large geographical extents (Biljecki et al., 2016; Biljecki et al., 2021). These novel datasets allow a bottom-up assessment of parameters required to accurately represent intra-urban variability in urban form in climate models, and some have been used to configure models at city-scales (e.g., Simón-Moral et al., 2020). Potential datasets include very high-resolution (~1 m) surface cover data, three-dimensional building or tree data, as well as incidental and public domain data that can be extracted from social media or the web, contributing to a multi-disciplinary approach to urban climate research, i.e., urban climate informatics (Middel et al., 2022). Coverage of suitable bottom-up datasets, especially at a global

scale, remains a challenge. Global datasets of high-resolution impervious surface maps (Zhang et al., 2020; Sun et al., 2022) or urban dwellings (e.g., the Global Urban Footprint (GUF) (Esch et al., 2012)) are becoming available but lack important characteristics such as land cover types and feature heights. The Copernicus Land Monitoring Service updates the CORINE Land Cover dataset (Büttner, 2014) providing 27 land cover classes at 6-year intervals but only provides coverage of Europe (39 countries). Some promising global morphology datasets derived from satellite data have begun to be reported (Esch et al., 2022), but as of writing are not yet publicly available.

In this paper, we use high-resolution, element-resolving datasets to 1) create maps which define actual urban form through the different urban parameters necessary for urban climate models, gridded to appropriate scales, without the fidelity limitations of class approaches and 2) improve traditional class-based approach parameter choices with local data. We use the Australian cities of Sydney and Melbourne as case studies and describe how to extract precise and localized ranges of model parameters using the continental-scale Geoscape datasets (PSMA Australia, 2020) of individual building geometry with ~1 m accuracy (Geoscape Buildings v2.0, 2020), 2 m land surface (Geoscape Surface Cover v1.6, 2020) and tree characteristics (Geoscape Trees v1.6, 2020). These parameter values are then compared with those calculated by the LCZ method (Stewart and Oke, 2012) *via* a distribution assessment and presented as data tables for integration into urban climate models.

## 2 MATERIALS AND METHODS

This section details the city-descriptive data used and processed in this analysis. Two data sources are considered: 1) Local Climate Zone (LCZ) maps which represent a top-down approach for characterizing urban neighbourhoods based on local urban form, and 2) the Geoscape datasets that represent the bottom-up method for detailing three-dimensional form at the level of individual buildings and trees. While the LCZ maps are defined and developed at local scales, building-resolving datasets require reprocessing to resolutions suitable for observation and modelling studies. The list of urban parameters that are available through processing both data

**TABLE 2** | List and symbols of urban parameters available through LCZ maps and our bottom-up method (BUM) using building and tree resolving datasets. The name of each parameter in the final processed dataset is also shown.

	Parameters used in urban climate modelling	Symbol	LCZ	BUM	Parameter name
Surface cover attributes	Building fraction (or plan area density)	$\lambda_p$	Yes	Yes	building_fraction
	Tree fraction	$\lambda_{vt}$	No	Yes	tree_fraction
	Low vegetation fraction (grass, shrubs etc.)	$\lambda_{vl}$	No	Yes	lowveg_fraction
	Water fraction	$\lambda_{wa}$	No	Yes	water_fraction
	Bare earth fraction	$\lambda_{be}$	No	Yes	bareearth_fraction
	Impervious surface fraction excluding buildings, as defined in Stewart and Oke, (2012)	$\lambda_{rf}$	Yes	Yes	roadpath_fraction
	Total built fraction (including buildings, roads)	$\lambda_{tb}$	No	Yes	total_builtin
	Total pervious fraction (including vegetation, water, bare earth)	$\lambda_{tp}$	Yes	Yes	total_pervious
Morphology attributes	Frontal area density	$\lambda_f$	No	Yes	frontal_density
	Wall area density	$\lambda_w$	No	Yes	wall_density
	Building height (mean) (noted in Stewart and Oke, (2012) as "height of roughness elements" for urban LCZ 1-10)	$H_{avg}$	Yes	Yes	building_height
	Building height (maximum)	$H_{max}$	No	Yes	building_height_max
	Building height (standard deviation)	$H_{std}$	No	Yes	building_height_std
	Tree height (mean) (noted in Stewart and Oke, (2012) as "height of roughness elements" for natural LCZ A-F)	$HT_{avg}$	Yes	Yes	tree_height
	Tree height (standard deviation)	$HT_{std}$	No	Yes	tree_height_std
	Terrain roughness class	—	Yes	No	—
	Sky view factor	$\psi$	Yes	Yes	skyview_factor
	Canyon aspect (or height-to-width) ratio	$h/w$	Yes	Yes	height_to_width
	Roughness length Macdonald et al. (1998)	$Z_{0,mac}$	No	Yes	roughness_mac
	Roughness length Kanda et al. (2013)	$Z_{0,kan}$	No	Yes	roughness_kanda
	Displacement height Macdonald et al. (1998)	$Z_{d,mac}$	No	Yes	displacement_mac
	Displacement height Kanda et al. (2013)	$Z_{d,kan}$	No	Yes	displacement_kanda
Thermal attributes	Surface admittance	$\mu$	Yes	No	—
	Surface albedo	$\alpha$	Yes	No	—
	Anthropogenic heat output	$Q_F$	Yes	No	—

sources are included in **Table 2**. These parameters cover a range of inputs required by urban climate models pertaining to surface cover, morphology, canopy attribute, and thermal attributes (**Table 1**).

Sydney and Melbourne greater regions are selected for this analysis as they represent the largest metropolitan areas in Australia with a population of 5.4 and 5.1 million, respectively (census data obtained by Australian Bureau of Statistics in June 2020). The climate subtype of Sydney and Melbourne is classified as temperate with warm summers and cool winters, according to the modified Köppen-Geiger classification system used by the Australian Bureau of Meteorology and based on a standard 30-year climatology (1961–1990) (Bureau of Meteorology, 2021).

## 2.1 Local Climate Zone Datasets

To provide a standardized landscape classification for both Sydney and Melbourne, maps of local climate zones (LCZs) at 100 m resolution are obtained from the LCZ Generator tool (Demuzere et al., 2021) as part of the WUDAPT initiative (Bechtel et al., 2015; Ching et al., 2018). The LCZ Generator is available as a web-based platform that enables the LCZ mapping of global cities using freely available satellite imagery and machine learning algorithms. The LCZ classification requires valid training areas (obtained using local insight) as input parameters and uses an automated cross-validation approach (Bechtel et al., 2019) to provide an accuracy assessment.

The resulting LCZ maps of Sydney and Melbourne are shown in **Figures 2, 3**, respectively (Conroy, 2021; Nazarian, 2022). There were 13 LCZs identified in greater Sydney (8 built-up and five natural classes) with three dominating built-up categories: sparsely built, open low-rise, and compact low-rise (**Figure 2A**). In greater Melbourne, 14 LCZs were classified (8 built-up and six natural classes) with open low-rise and sparsely built areas representing more than 80% of the built up LCZs (**Figure 3-left**). The higher percentage of low plants in greater Melbourne can be explained by the larger number of local farms in the area. A higher percentage of compact low-rise neighbourhoods in Sydney is observed in older inner-city suburbs that are often water-bound and in the proximity of the central business district areas. Overall, both cities only have a small percentage of compact LCZs presented (19 and 6% of built-up LCZs for greater Sydney and Melbourne, respectively) a consequence of the low-density suburban sprawl which comprises most Australian cities.

## 2.2 Geoscape Derived Datasets

### 2.2.1 Land Cover Data

An independent high resolution dataset of two-dimensional land cover (Geoscape Surface Cover v1.6, 2020) was used to define surface cover fractions and enable comparison with the LCZ approach. The Geoscape surface data consists of 10 surface type categories at 2 m resolution, collected through remote sensing between 2017 and 2019, with coverage of all Australian towns and cities with populations greater than 200 persons. Coverage

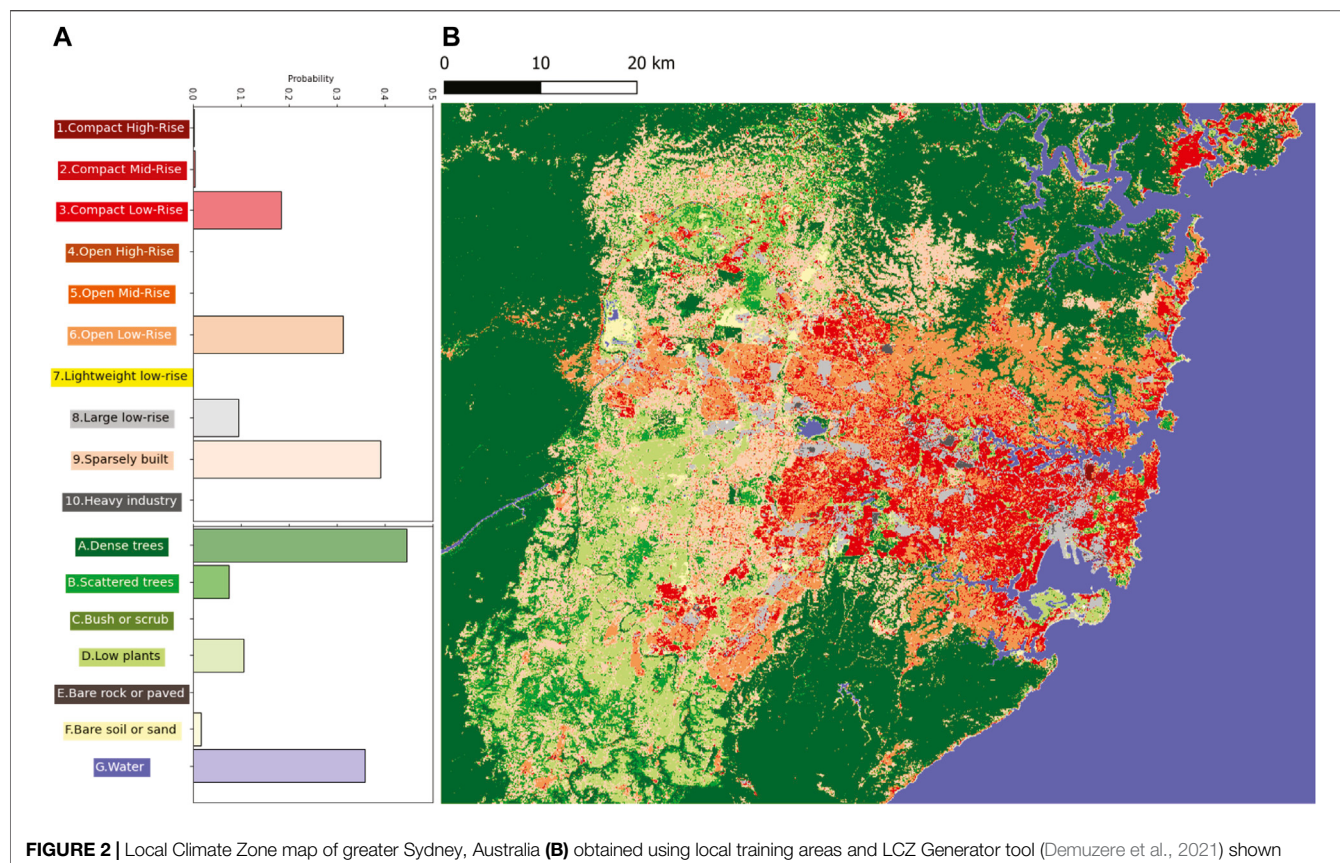


**FIGURE 2 |** Local Climate Zone map of greater Sydney, Australia (B) obtained using local training areas and LCZ Generator tool (Demuzere et al., 2021) shown together with the histogram distribution of LCZ classes across the area (A).

outside of urban areas is also available at 30 m resolution across the Australian continent (not used). Accuracy of land cover classification is greater than 90% (Geoscape Surface Cover v1.6, 2020). Using the 2 m urban data for two Australian cities, Sydney and Melbourne, we resample the ten Geoscape surface classes into six primary categories and two secondary categories (Table 3) at 100 m resolution. Cloud and shadow categories are not retained but are used to rescale other fractions so that primary and secondary categories each sum to 1 within grids.

### 2.2.2 Morphology Data

Three-dimensional morphology data are derived from the datasets of buildings (Geoscape Buildings v2.0, 2020) and trees (Geoscape Trees v1.6, 2020). The buildings data consist of geolocated outlines of buildings within Australia with area greater than 9 m<sup>2</sup> (approximately 15 million buildings), along with associated building metadata such as roof height. Trees data are raster-based with canopy height at 2 m resolution. Buildings and Trees datasets were collected through remote sensing (predominantly between 2017 and 2019) and processed through automated and manual processes using satellite-derived Digital Surface Model (DSM) or Digital Elevation Model (DEM) and aerial-derived stereo digitisation information. Vertical accuracy is approximately 0.1 m for aerial and 1 m for satellite derived building and tree heights.

Horizontal accuracy is approximately 0.2 m for aerial and 2.5 m for satellite derived positioning (Geoscape Buildings v2.0, 2020; Geoscape Trees v1.6, 2020).

With these datasets we derive a range of gridded morphological statistics that are commonly used in urban modelling and observational studies (source code available in **Supplementary Material**). First, we calculate each building's external wall area by multiplying building perimeter with building height (defined here as the average of building roof and eave heights), and each building's frontal area is calculated by averaging the cross-sectional area of a building in two cardinal directions. These building-specific parameters are then used to calculate gridded statistics.

The gridded mean, maximum and standard deviations of building height ( $H_{avg}$ ,  $H_{max}$ ,  $H_{std}$ ) are calculated, with building footprint area used to weight  $H_{avg}$  so that buildings with larger plan area have greater influence on grid height statistics. Wall area density ( $\lambda_w$ ) is calculated by summing the building wall area within a grid and divided by the grid plan area. Frontal area density ( $\lambda_f$ ) is calculated by summing building frontal areas and dividing by grid plan area (Grimmond and Oke, 1999).

For gridded values, the centroid of a building is used to assign the grid in which the building parameters will be placed. Trees are treated differently, as the underlying canopy height data are as rasterised canopy height at 2 m resolution. Tree-related

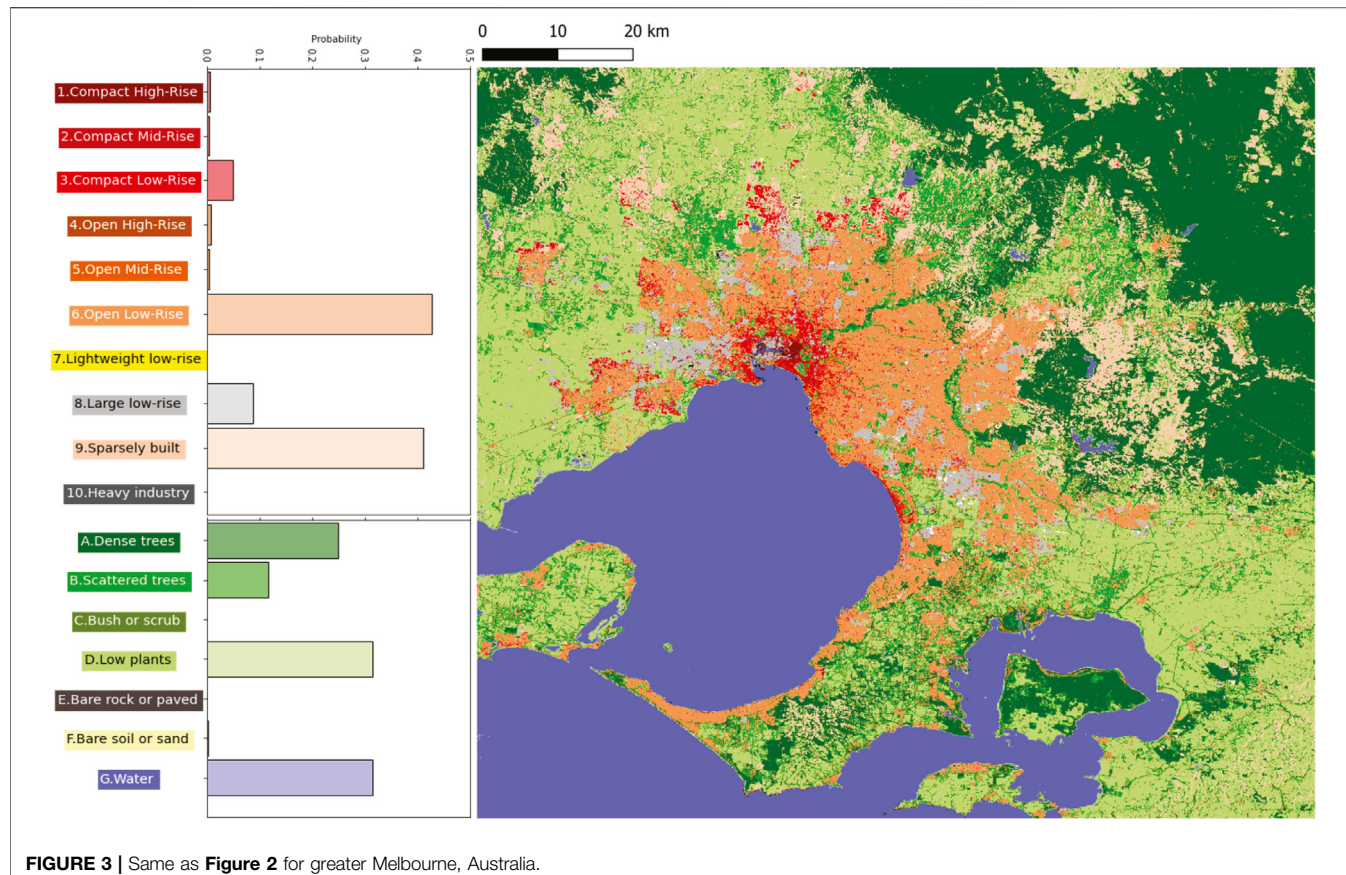


**TABLE 3 |** Surface cover categories for the original Geoscape data and the derived dataset.

<b>Geoscape surface cover classes</b>	<b>Derived dataset</b>	
	<b>Dataset primary classes</b>	<b>Dataset secondary classes</b>
Buildings	Building_fraction	Total_built
Road and Path	Roadpath_fraction	Total_built
Built-up Areas	Roadpath_fraction	Total_built
Trees	Tree_fraction	Total_pervious
Grass	Lowveg_fraction	Total_pervious
Unspecified Vegetation	Lowveg_fraction	Total_pervious
Bare Earth	Bareearth_fraction	Total_pervious
Water	Water_fraction	Total_pervious
Swimming Pool	Water_fraction	Total_pervious
Cloud	(Used to rescale other fractions)	(Used to rescale other fractions)
Shadow	(Used to rescale other fractions)	(Used to rescale other fractions)

parameters mean height ( $HT_{ave}$ ) and standard deviation of height ( $HT_{std}$ ) are therefore derived from any part of a tree which falls within a 100 m grid.

Some urban models, such as TARGET (Broadbent et al., 2019) or UT&C (Meili et al., 2020), use inputs such as canyon aspect ratio ( $h/w$ ) or sky view factor ( $\psi$ ) for configuration. Although difficult to define for typical real-world urban areas (Masson et al., 2020), these parameters can easily be derived from established parameters if the simplified geometric assumptions inherent in many urban models are used. For example, for a repeating two-

dimensional street canyon geometry, canyon aspect ratio is (Masson et al., 2020):

$$h/w = \frac{\lambda_w}{2(1 - \lambda_p)}, \quad (1)$$

where  $\lambda_p$  is the plan area density. Similarly, sky view factor can be calculated as (Masson et al., 2020):

$$\psi = \sqrt{(h/w)^2 + 1} - h/w. \quad (2)$$

In this dataset  $h/w$  and  $\psi$  are calculated in this way, enabling their use as inputs for urban models which use infinite canyon geometry assumptions. For models relying on different geometric assumptions,  $H_{avg}$ ,  $\lambda_p$  and  $\lambda_w$  should be used, as these parameters relate directly to their real world analogues (Masson et al., 2020).

To calculate momentum fluxes and wind profiles, some models require aerodynamic roughness lengths ( $z_0$ ) and/or zero-plane displacement height ( $z_d$ ). Many practitioners have derived empirical relations for these aerodynamic characteristics based on morphological inputs (Grimmond and Oke, 1999). Two methods commonly used in models are Macdonald et al. (1998) and Kanda et al. (2013). Calculations proposed by Macdonald et al. (indicated by subscript *mac*) are derived from wind tunnel studies using a matrix of bluff bodies with constant height and spacing. Kanda et al. (indicated by subscript *kan*) incorporated data from computational fluid dynamic simulations in domains with more realistic city geometry, and accounts for building height variability as well as average and maximum heights.

Using Macdonald et al. (1998), the zero-plane displacement height  $z_{d,mac}$  and roughness length  $z_{0,mac}$  are

$$z_{d,mac} = [1 + A^{-\lambda_p}(\lambda_p - 1)]H_{avg} \quad (3)$$

$$z_{0,mac} = \left[ \left( 1 - \frac{z_{d,mac}}{H_{avg}} \right) \exp \left[ - \left\{ 0.5\beta \frac{C_D}{\kappa^2} \left( 1 - \frac{z_{d,mac}}{H_{avg}} \right) \lambda_f \right\}^{-0.5} \right] \times H_{avg} \right] \quad (4)$$

where  $A = 4.43$ ,  $\beta = 1.0$  (for staggered arrays),  $C_D = 1.2$  (drag coefficient),  $\kappa = 0.4$  (von Karman constant).

Using Kanda et al. (2013), the zero-plane displacement height  $z_{d,kan}$  and roughness length  $z_{0,kan}$  are

$$z_{d,kan} = [c_0 X^2 + (a_0 \lambda_p^{b_0} - c_0)X]H_{max}, \quad (5)$$

$$z_{0,kan} = (b_1 Y^2 + c_1 Y + a_1)z_{0,mac}, \quad (6)$$

where  $a_1 = 0.71$ ,  $b_1 = 20.21$ ,  $c_1 = -0.77$ ,  $a_0 = 1.29$ ,  $b_0 = 0.36$ ,  $c_0 = -0.17$ , and

$$X = \frac{H_{std} + H_{avg}}{H_{max}}, 0 \leq X \leq 1.0, \quad (7)$$

$$Y = \frac{\lambda_p H_{std}}{H_{avg}}, Y \geq 0. \quad (8)$$

Macdonald and Kanda derivations of  $z_d$  and  $z_0$  are derived for each grid.

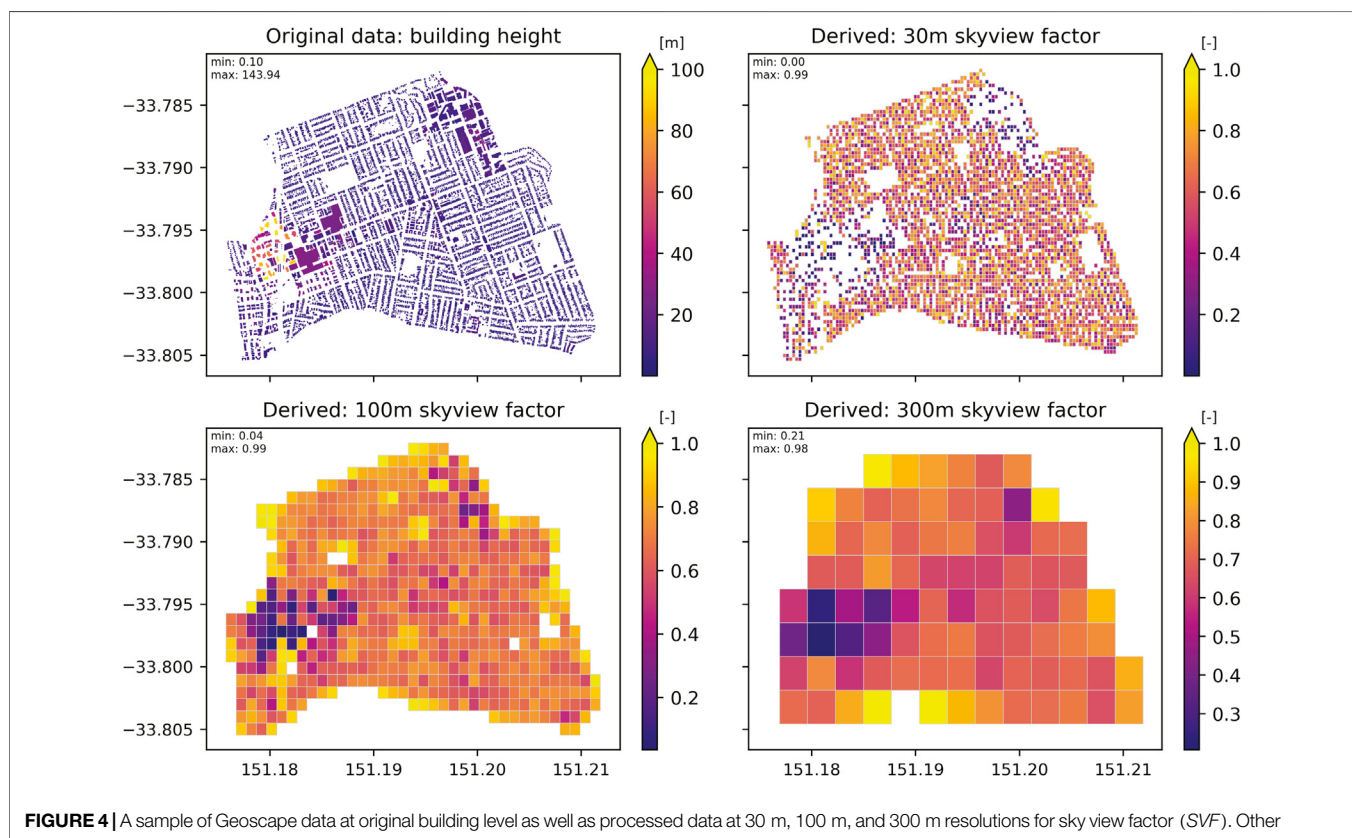
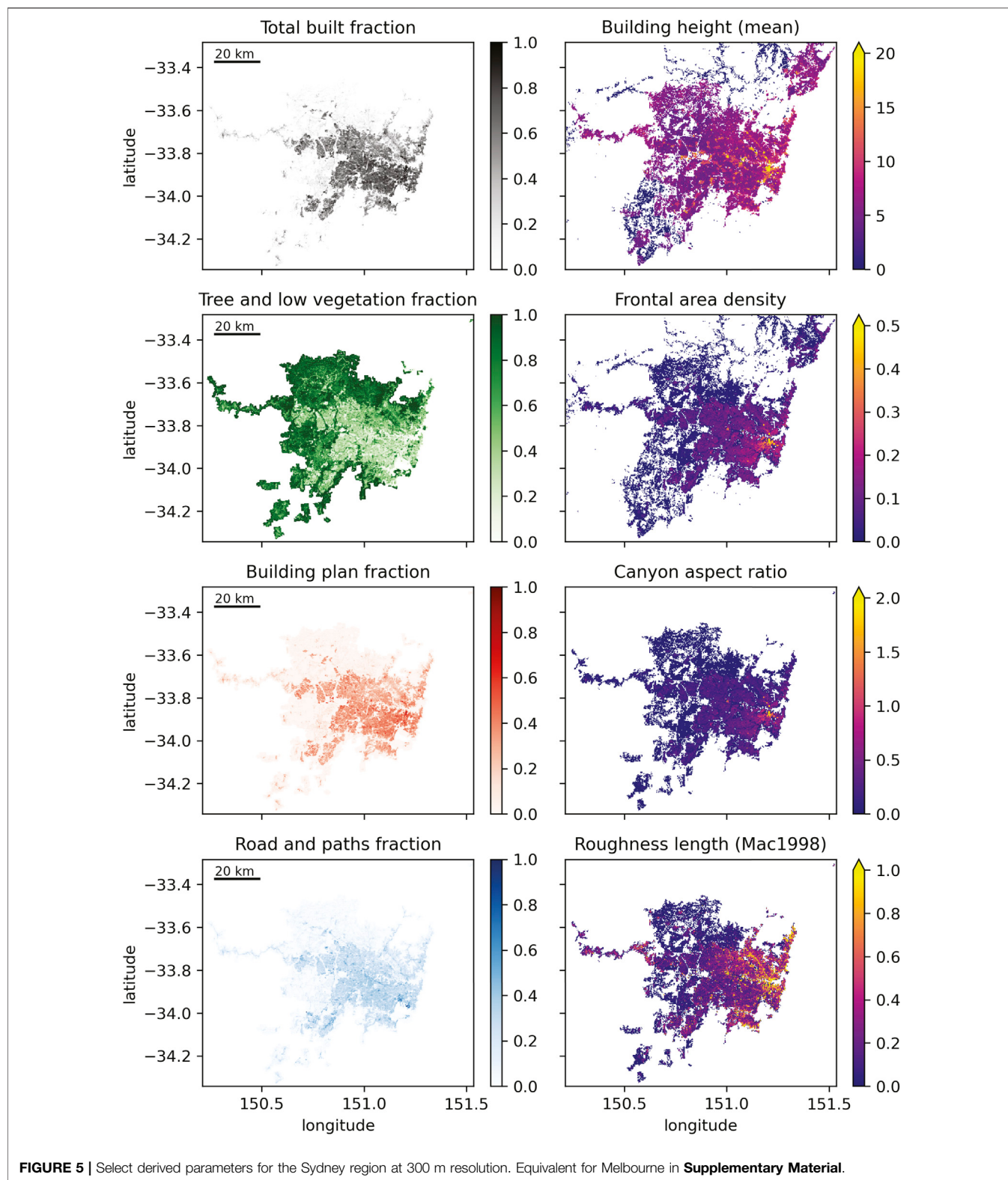


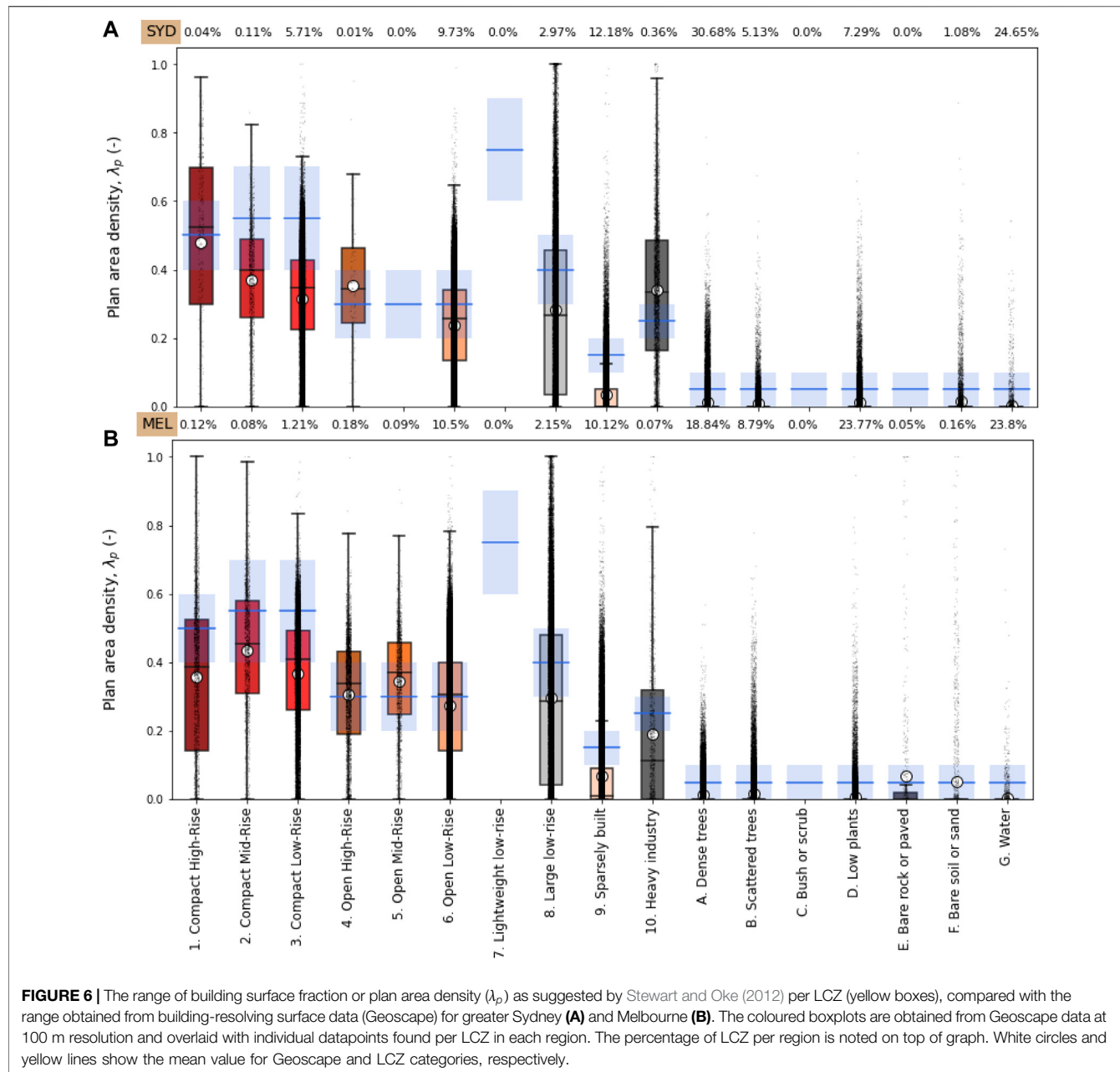
**FIGURE 4 |** A sample of Geoscape data at original building level as well as processed data at 30 m, 100 m, and 300 m resolutions for sky view factor (SVF). Other variables shown in **Supplementary Material**.



### 2.2.3 Processing and Resolution

We produce output at three resolutions (30, 100, and 300 m) to obtain gridded maps of city-descriptive parameters listed in

**Table 2.** **Figure 4** shows how different resolutions impact calculations of gridded sky view factor from the high-resolution building height data for a freely available sample



of the Sydney data (<https://geoscape.com.au/get-sample/>). Figure 5 shows spatial maps of Sydney at 100 m resolution for a selection of the derived parameters. Our source code for producing outputs are included in **Supplementary Material**. We also make openly available a 300 m resolution derived dataset for the Greater Sydney region (Lipson et al., 2022), with outputs available in NETCDF and TIFF formats.

Surface cover fractions are calculated by summing all 2 m land cover categorical cells within each 30, 100 or 300 m grid, and dividing by the total cell instances within the larger grid. Gridded morphology characteristics are calculated by

averaging (or finding the maximum and minimum) values for individual buildings where their footprint centroid falls within a grid.

When processing Geoscape data, the grid resolution has a critical impact on the calculated morphology parameters (Figure 4). While higher resolution may be desirable for some use cases (e.g., micro climate modelling), high resolution may not be appropriate for parameters intended to represent neighbourhood-scale characteristics. For example, canyon height-to-width ratio ( $h/w$ ) and sky view factor ( $\psi$ ) (Eqs 1, 2) have less coverage at the highest

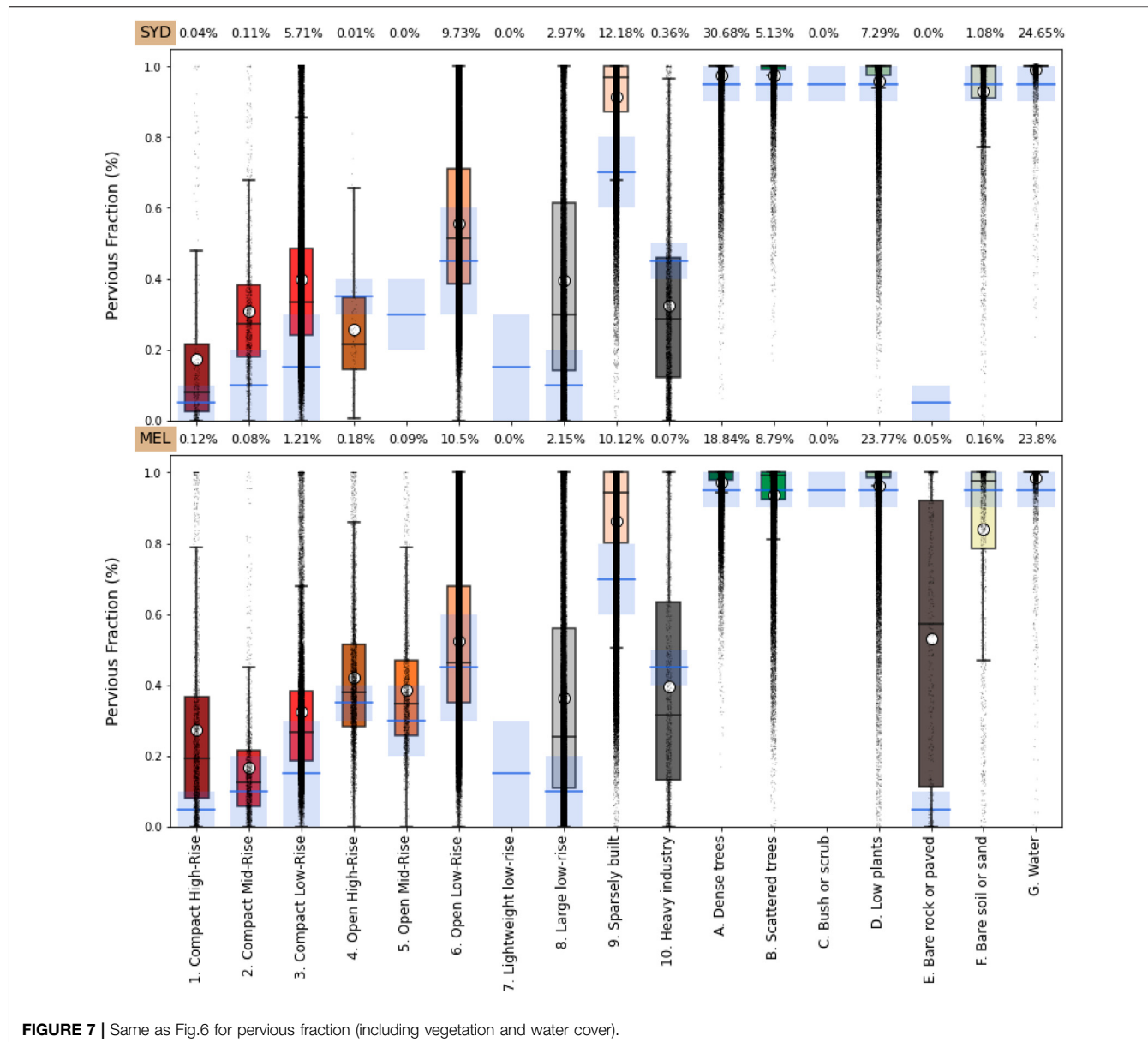


**FIGURE 7 |** Same as Fig.6 for pervious fraction (including vegetation and water cover).

resolutions (30 m) because they are undefined where building fraction covers the entire grid cell (**Figure 4**). Where a building footprint falls across multiple grid cells, our algorithm places the calculated parameters for building footprint and wall area in the grid cell that holds the centroid of building. This assumption makes it feasible to efficiently derive maps across large geographical areas, but leads to greater errors at higher resolution. This is because the morphology characteristics of a large building are assigned to a single grid cell, leading to underestimation or undefined morphology parameters in adjacent grids at high resolutions.

One alternative method is to divide each building that falls within multiple grids into smaller buildings with shared walls. This solution, however, increases the computational cost by

more than 250 times in our small-scale tests, which meant it was not feasible to implement across a large geographic area such as Sydney. This solution also leads to overestimation of external wall area properties and associated parameters such as  $\lambda_w$ ,  $\lambda_f$ ,  $h/w$  and  $\psi$ , so was not further utilised in this study. Another alternative is to use building footprints to define amorphous polygons around each building block, then calculate average  $\lambda_f$  for each polygon through a series of intersecting lines (Simón-Moral et al., 2020). This method however does not overcome the problems associated with dividing properties of larger blocks into multiple grid cells except through computationally expensive intersection methods.

The most appropriate output resolution will depend on the use case and available computational resources. Stewart and

Oke (2012) define the intended scale of LCZs as spanning hundreds of metres to several kilometres in horizontal scale. For our comparison between Geoscape and LCZ outputs we used 100 m resolution to align with the native resolution of the LCZ generator output (Demuzere et al., 2021). Additional plots of parameter/resolution sensitivity (as in Figure 4) and for Melbourne outputs (as in Figure 5) are available in Supplementary Material (Supplementary Figures S2–S5) showing gridded building footprint fractions, pervious fractions, mean building heights, and canyon aspect ratios calculated from the high-resolution building footprint and building height data.

## 2.2.4 Comparison of LCZ With Derived Morphology Maps

Fine-grained data on urban form and fabric can inform numerical climate models which rely on categorical urban classifications. Through the WUDAPT project, several mesoscale climate models—including Weather Research Forecasting (WRF)—are now able to incorporate LCZ maps at 100–1,000 m resolutions (e.g., Brousse et al., 2016). Typically, the dominant LCZ type within a model grid is used to determine model parameters. More realistic inter-grid variability may be achieved by interpolating LCZ parameter values from higher-resolution maps to the model grid (Zonato et al., 2020). In either case, providing locally appropriate

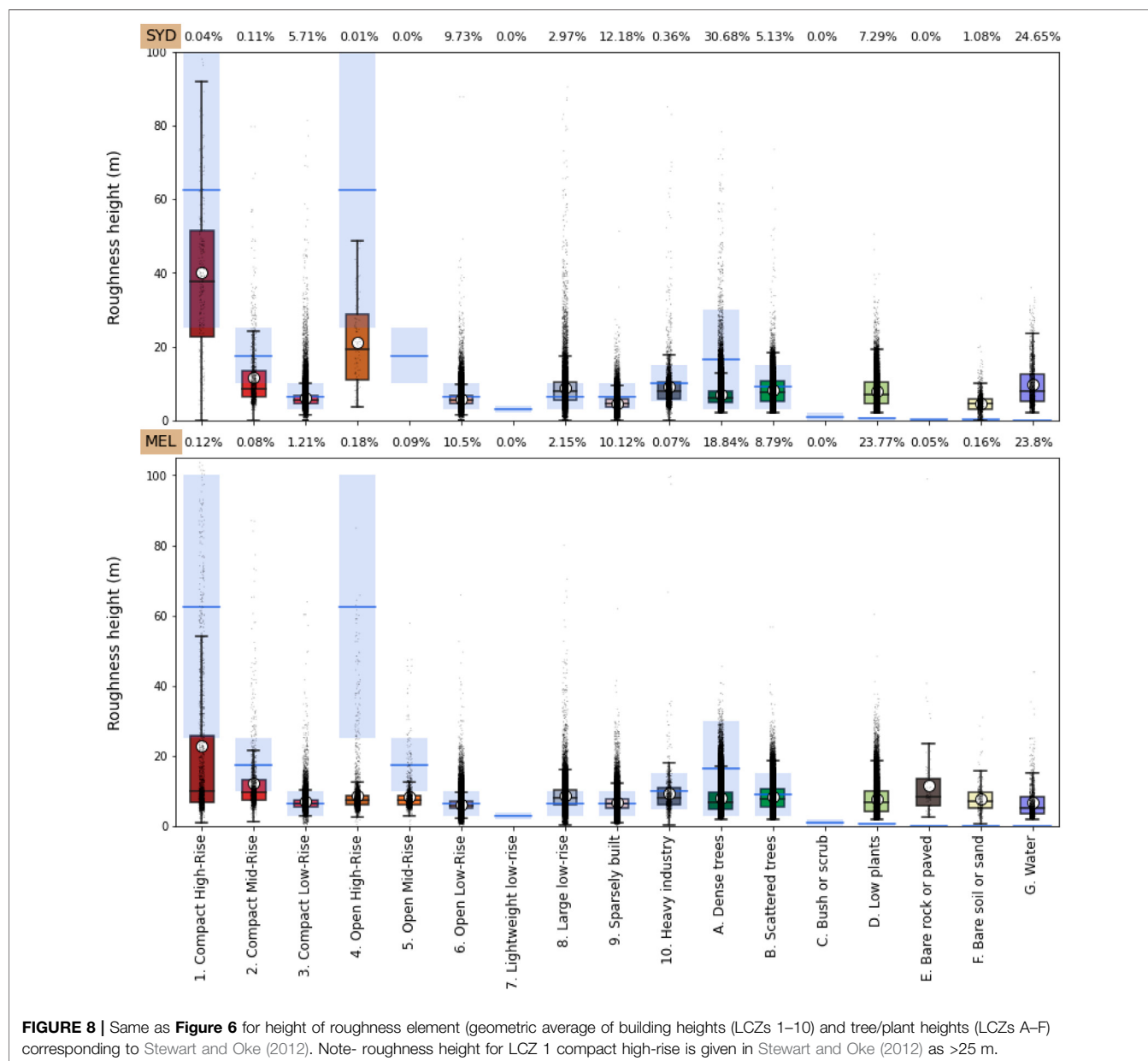


**FIGURE 8 |** Same as Figure 6 for height of roughness element (geometric average of building heights (LCZs 1–10) and tree/plant heights (LCZs A–F) corresponding to Stewart and Oke (2012). Note- roughness height for LCZ 1 compact high-rise is given in Stewart and Oke (2012) as >25 m.

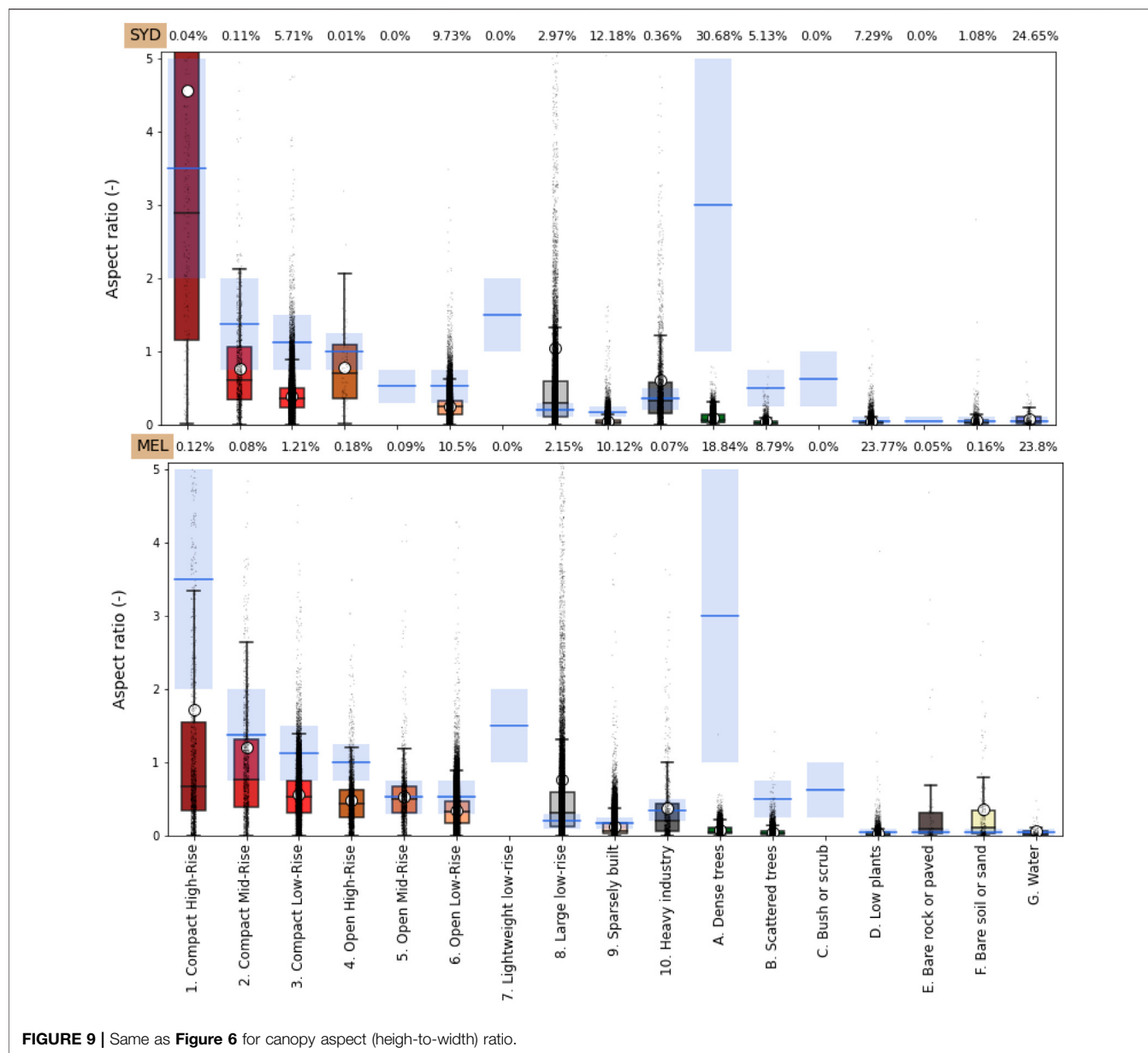


**FIGURE 9 |** Same as **Figure 6** for canopy aspect (height-to-width) ratio.

parameter values for each LCZ class has the potential to improve model performance compared with using generic LCZ characteristics.

To find locally appropriate LCZ characteristics, the coordinates of Geoscape-derived data are matched with LCZ maps at 100 m resolution. The Geoscape dataset is then grouped based on the corresponding grid's LCZ categorization. Results are shown with a boxplot visualization, indicating mean and median values as well as data frequency distribution in each LCZ. The recommended parameter range and mean value for each LCZ class (Stewart and Oke, 2012) is also shown. This comparison focuses on six out of seven geometric and surface cover parameters defined for LCZs, covering pervious and impervious surface fraction, plan area density, sky view factor and height of roughness

elements. Terrain roughness class is not included as it is not available through the Geoscape dataset.

### 3 RESULTS

**Figures 6–10** compare the recommended parameter ranges defined by Stewart and Oke (2012) for each LCZ class with local values obtained from the Geoscape surface cover, building and tree data for greater Sydney and Melbourne.

For plan area density (**Figure 6**), the recommended LCZ range by Stewart and Oke (2012) shows reasonable agreement with the bottom-up data, although local values for both Sydney and Melbourne are generally lower. The difference is greatest in

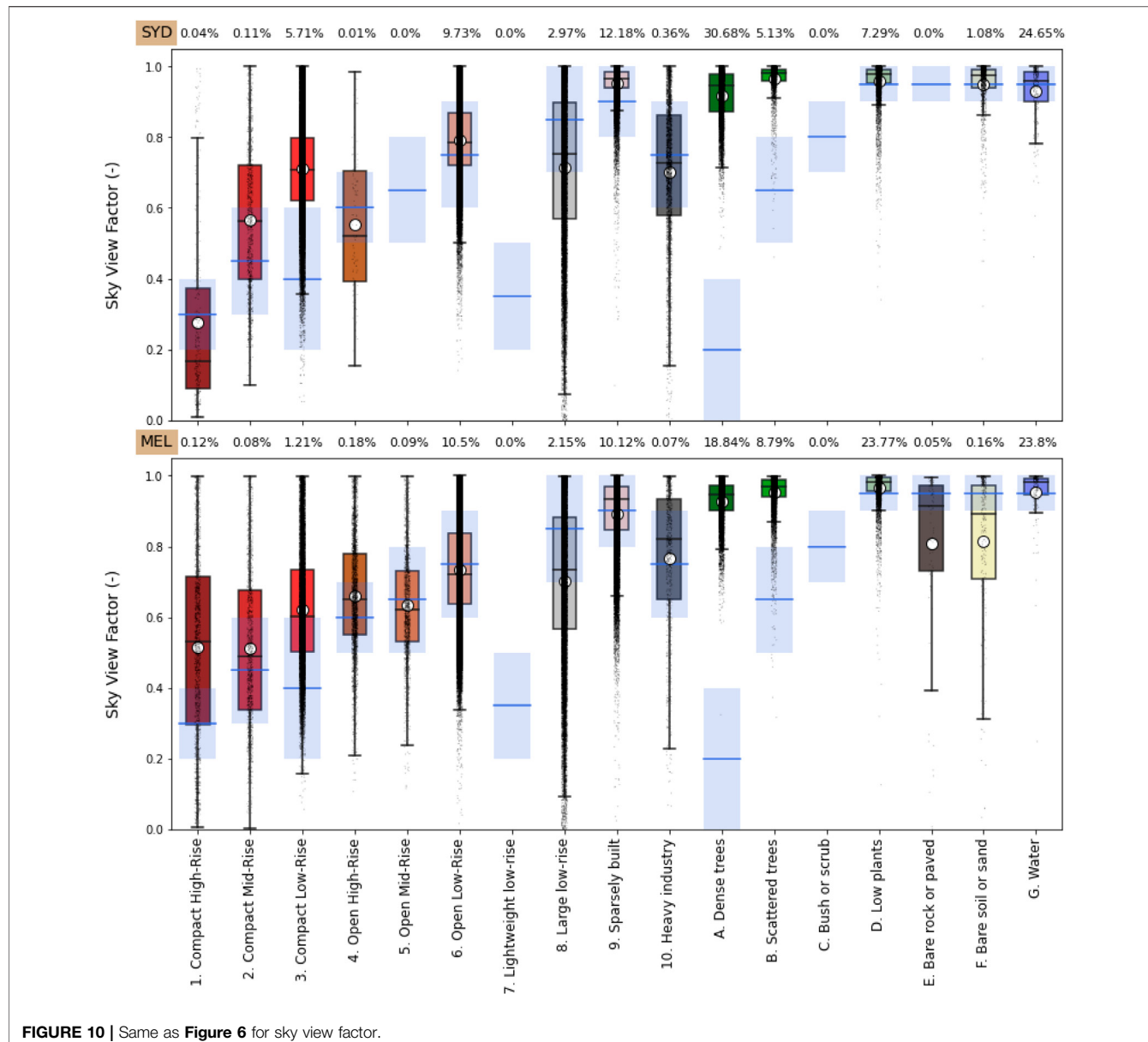


**FIGURE 10 |** Same as **Figure 6** for sky view factor.

compact mid-rise (LCZ2), compact low-rise (LCZ3), large low-rise (LCZ8) and sparsely-built (LCZ9). The lower than recommended plan area density is seen consistently in both cities. This indicates that, although the WUDAPT instructions to derive LCZ classes were followed (including training data provided by local experts), differences with the original LCZ definitions can occur. The significant number of outliers in **Figure 6** (and **Figures 7–10**) indicate the large variability of morphology characteristics within an LCZ class, as well as possible misclassification from the LCZ process.

Comparing the pervious fraction (**Figure 7**), the locally derived values are higher than recommended LCZ ranges in almost all built-up densities, except heavy industry. This difference is seen in both cities. Overall, this indicates that Australian cities have a higher percentage of vegetation and

water even in compact neighbourhoods compared with LCZ-based definitions. Greater disparity occurs in categories for which there are few identified cells within the domain, for example LCZ1 (Compact high-rise) and LCZ4 (Open high-rise). For the natural land covers, good agreement is seen between both datasets.

**Figure 8** compares the height of roughness elements in both datasets, as defined by Stewart and Oke (2012) as the geometric average of building heights in urban LCZ (LCZ 1–10) and tree/plant height for natural LCZs (LCZ A–F). The mean roughness height is significantly lower than the recommended range for the high-rise LCZ categories (LCZ 1 and LCZ3), particularly in Melbourne. This is likely because of different notions of what comprises a compact or open high-rise neighbourhood in Australian cities, and because compact and open high-rise

**TABLE 4** | City-descriptive parameters for Melbourne and Sydney for **built-up** local climate zones (LCZ 1-10). Mean values are calculated with gridded morphology and surface cover obtained from building-resolving 3D dataset (Geoscape) for each LCZ within each city's map.

	LCZ 1		LCZ 2		LCZ 3		LCZ 4		LCZ 5		LCZ 6		LCZ 7		LCZ 8		LCZ 9		LCZ 10	
	SYD	MEL	SYD	MEL	SYD	MEL	SYD	MEL	SYD	MEL	SYD	MEL	SYD	MEL	SYD	MEL	SYD	MEL	SYD	MEL
Mean building height (m)	40.06	22.91	11.61	12.18	6.15	6.96	21.12	8.76	8.38	5.88	6.24		8.80	8.61	4.54	6.74	9.06	9.31		
Max building height (m)	54.97	29.90	16.43	16.18	8.46	9.32	27.89	11.56	11.20	8.10	8.55		10.55	9.75	5.86	8.47	10.78	11.11		
Standard deviation of building height (m)	18.13	8.81	3.95	4.01	1.73	1.88	8.61	2.66	2.49	1.66	1.85		2.55	2.10	1.48	2.34	2.49	2.80		
Wall area density (-)	2.49	1.26	0.82	0.92	0.45	0.60	0.91	0.59	0.62	0.34	0.43		0.46	0.46	0.08	0.19	0.47	0.40		
Frontal area density (-)	0.67	0.37	0.24	0.25	0.13	0.17	0.26	0.16	0.17	0.10	0.12		0.13	0.12	0.02	0.05	0.13	0.11		
Mean tree height (m)	15.50	8.55	9.30	7.26	6.83	5.31	11.09	6.67	6.75	7.49	6.22		7.89	6.33	8.20	9.13	7.92	5.98		
Standard deviation of tree height (m)	6.72	4.02	4.04	2.77	3.30	2.06	4.49	3.08	3.09	3.98	2.89		3.23	2.19	4.08	4.26	3.30	2.20		
Plan area density (-)	0.48	0.36	0.37	0.44	0.32	0.37	0.35	0.31	0.34	0.24	0.27		0.28	0.30	0.04	0.07	0.34	0.19		
Tree fraction (-)	0.04	0.07	0.16	0.05	0.14	0.08	0.11	0.18	0.19	0.25	0.18		0.07	0.03	0.26	0.22	0.09	0.04		
Low vegetation fraction (-)	0.02	0.10	0.08	0.06	0.18	0.16	0.08	0.19	0.16	0.25	0.30		0.13	0.19	0.55	0.55	0.13	0.14		
Water fraction (-)	0.07	0.06	0.02	0.01	0.01	0.00	0.01	0.02	0.00	0.01	0.00		0.05	0.00	0.01	0.01	0.02	0.08		
Bare earth fraction (-)	0.05	0.05	0.05	0.04	0.06	0.08	0.05	0.03	0.03	0.05	0.04		0.15	0.14	0.09	0.09	0.09	0.14		
Impervious fraction (-) Stewart and Oke, (2012)	0.35	0.37	0.32	0.40	0.29	0.31	0.39	0.27	0.27	0.21	0.20		0.32	0.34	0.05	0.07	0.34	0.41		
Total built fraction (-)	0.83	0.73	0.69	0.83	0.60	0.68	0.74	0.58	0.61	0.44	0.47		0.60	0.64	0.09	0.14	0.67	0.60		
Total pervious fraction (-)	0.17	0.27	0.31	0.17	0.40	0.32	0.26	0.42	0.39	0.56	0.53		0.40	0.36	0.91	0.86	0.33	0.40		
Canopy aspect ratio (-)	4.56	1.72	0.77	1.20	0.38	0.56	0.78	0.49	0.53	0.25	0.34		1.05	0.76	0.05	0.13	0.61	0.38		
Sky view factor (-)	0.28	0.52	0.57	0.51	0.71	0.62	0.55	0.66	0.63	0.79	0.73		0.71	0.70	0.95	0.89	0.70	0.77		
Mean Roughness Height (m) Stewart and Oke, (2012)	40.06	22.91	11.61	12.18	6.15	6.96	21.12	8.76	8.38	5.88	6.24		8.80	8.61	4.54	6.74	9.06	9.31		
Displacement height (m) Macdonald et al. (1998)	32.21	16.25	7.21	8.50	3.54	4.37	12.31	4.82	4.97	2.72	3.22		5.27	5.33	0.81	1.67	5.48	4.24		
Roughness length (m) Macdonald et al. (1998)	2.52	1.76	0.84	0.61	0.30	0.29	1.98	0.63	0.46	0.31	0.29		0.40	0.29	0.14	0.32	0.43	0.62		
Displacement height (m) Kanda et al. (2013)	60.96	28.34	13.61	15.12	6.82	7.97	25.08	9.37	9.29	5.79	6.61		9.61	9.04	3.06	5.28	9.60	8.95		
Roughness length (m) Kanda et al. (2013)	3.77	2.22	0.79	0.65	0.25	0.24	1.95	0.49	0.37	0.24	0.24		0.37	0.25	0.13	0.29	0.37	0.45		

**TABLE 5 |** City-descriptive parameters for Melbourne and Sydney for **natural** local climate zones (LCZ A-G). Mean values are calculated with gridded morphology and surface cover obtained from building-resolving 3D dataset (Geoscape) for each LCZ within each city's map.

	LCZ A		LCZ B		LCZ C		LCZ D		LCZ E		LCZ F		LCZ G	
	SYD	MEL	SYD	MEL	SYD	MEL	SYD	MEL	SYD	MEL	SYD	MEL	SYD	MEL
Mean building height (m)	6.29	8.97	3.71	5.71			4.24	4.89	11.68	4.56	7.74	8.15	6.17	
Max building height (m)	8.86	11.45	5.82	6.39			5.67	5.31	12.26	5.56	8.59	9.67	6.63	
Standard deviation of building height (m)	2.46	3.96	1.67	1.79			1.53	1.45	3.40	1.34	2.06	2.60	1.18	
Wall area density (-)	0.14	0.14	0.05	0.09			0.07	0.06	0.42	0.09	0.30	0.13	0.09	
Frontal area density (-)	0.04	0.04	0.01	0.02			0.02	0.02	0.12	0.03	0.08	0.04	0.03	
Mean tree height (m)	6.92	7.97	8.22	8.39			7.80	7.69	5.94	7.48	6.25	9.61	6.64	
Standard deviation of tree height (m)	3.45	4.09	4.03	3.58			3.49	2.86	2.13	3.00	2.09	3.61	2.19	
Plan area density (-)	0.01	0.01	0.01	0.02			0.01	0.01	0.07	0.01	0.05	0.00	0.00	
Tree fraction (-)	0.72	0.62	0.29	0.16			0.11	0.04	0.01	0.03	0.02	0.02	0.01	
Low vegetation fraction (-)	0.22	0.33	0.60	0.66			0.70	0.78	0.07	0.32	0.28	0.01	0.03	
Water fraction (-)	0.02	0.01	0.02	0.02			0.06	0.03	0.30	0.17	0.07	0.96	0.90	
Bare earth fraction (-)	0.02	0.01	0.06	0.10			0.09	0.12	0.15	0.40	0.47	0.01	0.04	
Impervious fraction (-) Stewart and Oke, (2012)	0.01	0.01	0.02	0.05			0.03	0.03	0.40	0.06	0.11	0.01	0.01	
Total built fraction (-)	0.02	0.03	0.02	0.06			0.04	0.04	0.47	0.07	0.16	0.01	0.02	
Total pervious fraction (-)	0.98	0.97	0.98	0.94			0.96	0.96	0.53	0.93	0.84	0.99	0.98	
Canopy aspect ratio (-)	0.09	0.08	0.04	0.05			0.04	0.04	8.87	0.06	0.36	0.08	0.06	
Sky view factor (-)	0.92	0.93	0.97	0.95			0.96	0.97	0.81	0.95	0.81	0.93	0.95	
Mean Roughness Height (m) Stewart and Oke, (2012)	6.92	7.97	8.22	8.39			7.80	7.69	11.68	4.56	7.74	9.61	6.64	
Displacement height (m) Macdonald et al. (1998)	1.28	1.27	0.57	0.79			0.70	0.57	5.27	0.87	3.48	1.35	1.17	
Roughness length (m) Macdonald et al. (1998)	0.37	0.56	0.14	0.18			0.15	0.11	0.86	0.17	0.31	0.53	0.33	
Displacement height (m) Kanda et al. (2013)	4.98	6.12	2.91	3.26			2.97	2.63	9.21	3.12	7.16	5.14	2.87	
Roughness length (m) Kanda et al. (2013)	0.36	0.51	0.16	0.18			0.17	0.12	0.52	0.16	0.29	0.53	0.13	

neighbourhoods in Australian cities are less homogenous, i.e., high-rise buildings are surrounded by a range of different buildings with variable heights. This heterogeneity in the grids classified as “high-rise” consequently reduces the mean roughness height. The difference between the two maps is less pronounced in mid-rise LCZs, while LCZs with low building heights (such as compact/open/large low rise, sparsely built, and heavy industry) closely follow the recommended LCZ ranges. For natural land cover, when roughness height is calculated based on tree height (Stewart and Oke 2012), the bottom-up approach gives results within the recommended range for trees, but overestimates roughness element height in LCZs with low vegetation or no vegetation. This again could be caused by real urban heterogeneous surfaces including a scattering of higher roughness elements.

Two morphological parameters are also compared: Canopy aspect ratio (**Figure 9**) and sky view factor (**Figure 10**). These calculations are based on the assumption of a repeating, two-dimensional canyon geometry (**Section 2.2**) and depend on the calculated plan area and wall density (Masson et al., 2020) ( $\lambda_p$  and  $\lambda_w$ , respectively). These assumptions and resultant parameters do not account for vegetation. Accordingly, the comparison between these datasets are focused on built-up LCZs. In both Sydney and Melbourne, canopy aspect ratio in the majority of built-up LCZs is lower than the recommended range. This is because of the generally lower plan area density of locally defined categories (**Figure 6**), and because vegetation is not accounted for in our calculation of sky view (**Eq. 2**).

Although these results highlight some differences with recommended LCZ parameter values, the outputs provide valuable input data for urban climate models. The defined

LCZ maps, when used to configure a model in Sydney or Melbourne, can now be informed with accurate local parameter values for each class. As such, we provide tables of urban LCZs (LCZ1-10; **Table 4**) and natural LCZs (LCZ A-G; **Table 5**) for both Sydney and Melbourne for use in future modelling exercises. Mean values are calculated by comparing LCZ maps with 100 m morphology and surface cover data derived from Geoscape datasets. These provide a more accurate representation of local surface cover and morphology than the mid-point of the recommended LCZ ranges from Stewart and Oke (2012).

## 4 DISCUSSION

Numerical urban analysis has been experiencing two critical transformations in the last decade. First, new datasets are being generated using novel methods describing urban form, fabric, and function at higher resolutions than previously achieved (Mills et al., 2021). Second, the growth of computing power—roughly doubling every 2 years (Leiserson et al., 2020)—has enabled more sophisticated models to resolve urban processes at higher resolutions. Nonetheless, many urban modelling studies have been unable to represent true intra-urban variabilities because they rely on class-based approaches to describe urban surface parameters.

In this paper, we presented a methodology to derive city-descriptive data for urban climate models using sub-metre resolution datasets which resolve individual urban elements. We have produced new gridded datasets which do not rely on classes. In addition, we have been able to complement established

methods by updating default class-based parameters with those derived from local characteristics.

The code and examples for processing data layers are provided as **Supplementary Material**, enabling future city-descriptive maps to be developed for other regions using Geoscape data, as well as informing other studies with similar building-resolving datasets. The derived land cover and morphology dataset for the Greater Sydney region at 300 m resolution is made openly available (Lipson et al. 2022).

All building-resolving data contain errors which depend on the collection and processing methods. The base Geoscape data used here has a vertical accuracy of  $\pm 0.1$  m for aerial and  $\pm 1$  m for satellite derived building and tree heights (Geoscape Buildings v2.0, 2020; Geoscape Trees v1.6, 2020). The horizontal accuracy is  $\pm 0.2$  m for aerial and  $\pm 2.5$  m for satellite derived building positioning (although consistent translational errors minimise errors in the derived morphology characteristics). In comparison with top-down methods, the mid-range building height values for LCZs can differ with the Geoscape-derived values by dozens of metres (**Figure 8**), well outside the range of Geoscape errors. Top-down methods remain valuable where building-resolving data is unavailable.

The strength of the methodology described here is manifold. First, the building resolving data used is derived in a consistent manner at continental scales. Such large-scale and consistent datasets reduce uncertainties associated with class-based approaches which rely on ad-hoc human training and machine learning. Ad-hoc or inconsistent training data can lead to incorrect classification (Bechtel et al., 2017; Stewart, 2018), while machine learning inherently obscures the algorithm's decision-making processes, making replication or adaptation difficult. Second, class-based approaches can omit some parameters required by numerical modelling systems. Our bottom-up method provides additional parameters for defining the form of urban areas and surrounds that are important for quantify the impact of mitigation strategies using modelling approaches (Krayenhoff et al., 2021). Lastly, the traditional class-based approach is limited by the fidelity of class system (i.e., the number of defined classes) while the bottom-up approach described here capture the unique characteristics of a city's fabric and form by detailing variability at the grid scale. This is a methodological difference; instead of defining more subclasses at increasingly high fidelity and defining their recommended parameters, the properties of urban morphology can be captured from the building scale and applied at the desired resolution directly, enabling a more accurate characterization of real urban form in urban climate models.

The methods detailed here provide a useful approach for obtaining critical city-descriptive parameters for climate models, but several limitations persist. First, common geometric assumption used to calculate some morphology parameters (such as canopy height to width ratio and sky view factor) fall short in representing realistic urban configurations (as discussed in **Section 2.2.3**). Second, a method for resampling categorical class-based maps (the

LCZ system) to different resolutions is not well-established in the literature, limiting the comparison of values at different resolutions. Thirdly, the data for large datasets may be remotely sensed and incorporated over time, and so should be updated regularly to account for rapid urbanization processes and changes in urban land cover and use. Furthermore, a key challenge in implementing this methodology relate to the availability of high-resolution datasets that resolve individual buildings and trees. Consistent and complete global high-resolution datasets are not yet publicly available. These challenges are likely to decrease as more data becomes available, though being significantly affected by different local data policy and resources (Mills et al., 2021). Finally, we still have limited available information on urban fabric and function, even at local scales. A description of the spatial distribution of materiality, for instance, is hard to achieve and hard to implement in models in a realistic way. These issues require more detailed attention in the future.

## DATA AVAILABILITY STATEMENT

The datasets presented in this study can be found in online repositories. The names of the repository/repositories and accession number(s) can be found in the article. The 300 m surface characteristics dataset is openly available for the Sydney region at: <https://doi.org/10.5281/zenodo.6579061>

## AUTHOR CONTRIBUTIONS

ML, NN, and MH conceived the study. BC and NN created the LCZ maps, with input from MH. ML wrote code to process Geoscape datasets and associated figures. NN wrote code to compare LCZ and Geoscape-derived outputs and associated figures. KN provided input for Melbourne data for comparison. NN, MH, and ML wrote the manuscript, with input from KN and BC.

## FUNDING

This research was supported by the Australian Research Council (ARC) Centre of Excellence for Climate System Science (Grant CE110001028), the ARC Centre of Excellence for Climate Extremes (Grant CE170100023). KN is supported by NHMRC/UKRI grant (1194959).

## ACKNOWLEDGMENTS

We gratefully acknowledge the Australian Urban Research Infrastructure Network (AURIN) and Geoscape Australia for providing the datasets necessary for this study, drawing on Geoscape Buildings, Surface Cover and Trees datasets, © Geoscape Australia, 2020: <https://geoscape.com.au/legal/data/>

copyright-and-disclaimer/. With thanks to William Morrison, Sue Grimmond, Song Chen and Pratiman Patel for useful discussions on processing methods.

## SUPPLEMENTARY MATERIAL

The Supplementary Material for this article can be found online at: <https://www.frontiersin.org/articles/10.3389/fenvs.2022.866398/full#supplementary-material>

## REFERENCES

- Argüeso, D., Evans, J. P., Fita, L., and Bormann, K. J. (2014). Temperature Response to Future Urbanization and Climate Change. *Clim. Dyn.* 42, 2183–2199. doi:10.1007/s00382-013-1789-6
- Bechtel, B., Alexander, P., Böhner, J., Ching, J., Conrad, O., Feddema, J., et al. (2015). Mapping Local Climate Zones for a Worldwide Database of the Form and Function of Cities. *ISPRS Int. J. Geo-Inf.* 4, 199–219. doi:10.3390/ijgi4010199
- Bechtel, B., Alexander, P. J., Beck, C., Böhner, J., Brousse, O., Ching, J., et al. (2019). Generating WUDAPT Level 0 Data - Current Status of Production and Evaluation. *Urban Clim.* 27, 24–45. doi:10.1016/j.uclim.2018.10.001
- Bechtel, B., Demuzere, M., Sismanidis, P., Fenner, D., Brousse, O., Beck, C., et al. (2017). Quality of Crowdsourced Data on Urban Morphology—The Human Influence Experiment (HUMINEX). *Urban Sci.* 1, 15. doi:10.3390/urbansci1020015
- Biljecki, F., Chew, L. Z. X., Milojevic-Dupont, N., and Creutzig, F. (2021). Open Government Geospatial Data on Buildings for Planning Sustainable and Resilient Cities. *ArXiv*. Preprint 210704023 Cs. doi:10.48550/arXiv.2107.04023
- Biljecki, F., Ledoux, H., and Stoter, J. (2016). An Improved LOD Specification for 3D Building Models. *Comput. Environ. Urban Syst.* 59, 25–37. doi:10.1016/j.compenvurbsys.2016.04.005
- Broadbent, A. M., Coutts, A. M., Nice, K. A., Demuzere, M., Kravchenko, E. S., Tapper, N. J., et al. (2019). The Air-Temperature Response to Green/blue-infrastructure Evaluation Tool (TARGET v1.0): an Efficient and User-Friendly Model of City Cooling. *Geosci. Model Dev.* 12, 785–803. doi:10.5194/gmd-12-785-2019
- Brousse, O., Martilli, A., Foley, M., Mills, G., and Bechtel, B. (2016). WUDAPT, an Efficient Land Use Producing Data Tool for Mesoscale Models? Integration of Urban LCZ in WRF over Madrid. *Urban Clim.* 17, 116–134. doi:10.1016/j.uclim.2016.04.001
- Bruse, M. (1999). *The Influences of Local Environmental Design on Microclimate-Development of a Prognostic Numerical Model ENVI-Met for the Simulation of Wind, Temperature and Humidity Distribution in Urban Structures*. Germany: University of Bochum.
- Bureau of Meteorology (2021). Australia's Official Weather Forecasts & Weather Radar - Bureau of Meteorology. Available at: <http://www.bom.gov.au/> (Accessed December 15, 2021).
- Büttner, G. (2014). "CORINE Land Cover and Land Cover Change Products," in *Land Use and Land Cover Mapping in Europe: Practices & Trends Remote Sensing and Digital Image Processing*. Editors I. Manakos and M. Braun (Dordrecht: Springer Netherlands), 55–74. doi:10.1007/978-94-007-7969-3\_5
- Chen, G., Zhao, L., and Mochida, A. (2016). Urban Heat Island Simulations in Guangzhou, China, Using the Coupled WRF/UCM Model with a Land Use Map Extracted from Remote Sensing Data. *Sustainability* 8, 628. doi:10.3390/su8070628
- Ching, J., Mills, G., Bechtel, B., See, L., Feddema, J., Wang, X., et al. (2018). WUDAPT: An Urban Weather, Climate, and Environmental Modeling Infrastructure for the Anthropocene. *Bull. Am. Meteorol. Soc.* 99, 1907–1924. doi:10.1175/BAMS-D-16-0236.1
- Conroy, B. (2021). WUDAPT Level 0 Training Data for Melbourne (Australia, Commonwealth of), Submitted to the LCZ Generator. LCZ Gener. Available at: <https://lcz-generator.rub.de/factsheets/>
- Supplementary Figure S1 |** Select derived parameters for the Melbourne region.
- Supplementary Figure S2 |** Building footprint fraction at 30, 100, 300 m resolutions for a sample region in Sydney.
- Supplementary Figure S3 |** Total pervious fraction at 30, 100, 300 m resolutions for a sample region in Sydney.
- Supplementary Figure S4 |** Mean building height at 30, 100, 300 m resolutions for a sample region in Sydney.
- Supplementary Figure S5 |** Canyon aspect ratio at 30, 100, 300 m resolutions for a sample region in Sydney.
- d2aa6b283cdc6bf2dd372bfdcd5612d2219a690/d2aa6b283cdc6bf2dd372bfdcd5612d2219a690\_factsheet.html (September 12, 2021).
- Demuzere, M., Hankey, S., Mills, G., Zhang, W., Lu, T., and Bechtel, B. (2020). Combining Expert and Crowd-Sourced Training Data to Map Urban Form and Functions for the Continental US. *Sci. Data* 7, 264. doi:10.1038/s41597-020-00605-z
- Demuzere, M., Kittner, J., and Bechtel, B. (2021). LCZ Generator: A Web Application to Create Local Climate Zone Maps. *Front. Environ. Sci.* 9, 112. doi:10.3389/fenvs.2021.637455
- Esch, T., Brzoska, E., Dech, S., Leutner, B., Palacios-Lopez, D., Metz-Marconcini, A., et al. (2022). World Settlement Footprint 3D - A First Three-Dimensional Survey of the Global Building Stock. *Remote Sens. Environ.* 270, 112877. doi:10.1016/j.rse.2021.112877
- Esch, T., Taubenböck, H., Roth, A., Heldens, W., Felbier, A., Thiel, M., et al. (2012). TanDEM-X Mission-New Perspectives for the Inventory and Monitoring of Global Settlement Patterns. *J. Appl. Remote Sens.* 6, 061702. doi:10.1111/j.1.JRS.061702
- Fröhlich, D., and Matzarakis, A. (2020). Calculating Human Thermal Comfort and Thermal Stress in the PALM Model System 6.0. *Geosci. Model Dev.* 13, 3055–3065. doi:10.5194/gmd-13-3055-2020
- Geoscape Buildings v2.0 (2020). *Geoscape Buildings v2.0*. Griffith, ACT, Australia: PSMA Australia.
- Geoscape Surface Cover v1.6 (2020). *Geoscape Surface Cover v1.6*. Griffith, ACT, Australia: PSMA Australia.
- Geoscape Trees v1.6 (2020). *Geoscape Trees v1.6*. Griffith, ACT, Australia: PSMA Australia.
- Grimmond, C. S. B., and Oke, T. R. (1999). Aerodynamic Properties of Urban Areas Derived from Analysis of Surface Form. *J. Appl. Meteor.* 38, 1262–1292. doi:10.1175/1520-0450(1999)038<1262:apouad>2.0.co;2
- Hirsch, A. L., Evans, J. P., Thomas, C., Conroy, B., Hart, M. A., Lipson, M., et al. (2021). Resolving the Influence of Local Flows on Urban Heat Amplification during Heatwaves. *Environ. Res. Lett.* 16, 064066. doi:10.1088/1748-9326/ac0377
- Jackson, T. L., Feddema, J. J., Oleson, K. W., Bonan, G. B., and Bauer, J. T. (2010). Parameterization of Urban Characteristics for Global Climate Modeling. *Ann. Assoc. Am. Geogr.* 100, 848–865. doi:10.1080/00045608.2010.497328
- Kanda, M., Inagaki, A., Miyamoto, T., Gryschka, M., and Raasch, S. (2013). A New Aerodynamic Parametrization for Real Urban Surfaces. *Boundary-Layer Meteorol.* 148, 357–377. doi:10.1007/s10546-013-9818-x
- Katzfey, J., Schlünzen, H., Hoffmann, P., and Thatcher, M. (2020). How an Urban Parameterization Affects a High-resolution Global Climate Simulation. *Q.J.R. Meteorol. Soc.* 146, 3808–3829. doi:10.1002/qj.3874
- Kravchenko, E. S., Broadbent, A. M., Zhao, L., Georgescu, M., Middel, A., Voogt, J. A., et al. (2021). Cooling Hot Cities: a Systematic and Critical Review of the Numerical Modelling Literature. *Environ. Res. Lett.* 16, 053007. doi:10.1088/1748-9326/abdcf1
- Leiserson, C. E., Thompson, N. C., Emer, J. S., Kuszmaul, B. C., Lampson, B. W., Sanchez, D., et al. (2020). There's Plenty of Room at the Top: What Will Drive Computer Performance after Moore's Law? *Science* 368, eaam9744. doi:10.1126/science.aam9744
- Li, D., Malyshev, S., and Sheviakova, E. (2016). Exploring Historical and Future Urban Climate in the Earth System Modeling Framework: 1. Model Development and Evaluation: Urban Climate in Earth System Models. *J. Adv. Model. Earth Syst.* 8, 917–935. doi:10.1002/2015MS000578

- Lindberg, F., Grimmond, C. S. B., Gabey, A., Huang, B., Kent, C. W., Sun, T., et al. (2018). Urban Multi-Scale Environmental Predictor (UMEP): An Integrated Tool for City-Based Climate Services. *Environ. Model. Softw.* 99, 70–87. doi:10.1016/j.envsoft.2017.09.020
- Lipson, M., Nazarian, N., Hart, M. A., Nice, K. A., and Conroy, B. (2022). *Urban Form Data for Climate Modelling: Sydney at 300 M Resolution Derived from Building-Resolving and 2 M Land Cover Datasets*. Sydney: Zenodo. doi:10.5281/ZENODO.6579061
- Ma, S., Pitman, A., Yang, J., Carouge, C., Evans, J. P., Hart, M., et al. (2018). Evaluating the Effectiveness of Mitigation Options on Heat Stress for Sydney, Australia. *J. Appl. Meteorol. Climatol.* 57, 209–220. doi:10.1175/JAMC-D-17-0061.1
- Macdonald, R. W., Griffiths, R. F., and Hall, D. J. (1998). An Improved Method for the Estimation of Surface Roughness of Obstacle Arrays. *Atmos. Environ.* 32, 1857–1864. doi:10.1016/S1352-2310(97)00403-2
- Martilli, A., Krayenhoff, E. S., and Nazarian, N. (2020). Is the Urban Heat Island Intensity Relevant for Heat Mitigation Studies? *Urban Clim.* 31, 100541. doi:10.1016/j.ulim.2019.100541
- Masson, V., Champeaux, J.-L., Chauvin, F., Meriguet, C., and Lacaze, R. (2003). A Global Database of Land Surface Parameters at 1-km Resolution in Meteorological and Climate Models. *J. Clim.* 16, 1261–1282. doi:10.1175/1520-0442-16.9.1261
- Masson, V., Heldens, W., Bocher, E., Bonhomme, M., Bucher, B., Burmeister, C., et al. (2020). City-descriptive Input Data for Urban Climate Models: Model Requirements, Data Sources and Challenges. *Urban Clim.* 31, 100536. doi:10.1016/j.ulim.2019.100536
- Meili, N., Manoli, G., Burlando, P., Bou-Zeid, E., Chow, W. T. L., Coutts, A. M., et al. (2020). An Urban Ecohydrological Model to Quantify the Effect of Vegetation on Urban Climate and Hydrology (UT&C v1.0). *Geosci. Model Dev.* 13, 335–362. doi:10.5194/gmd-13-335-2020
- Middel, A., Nazarian, N., Bechtel, B., and Demuzere, M. (2022). Urban Climate Informatics: an Emerging Research Field. *Front. Environ. Sci. Rev.* 10, 867434. doi:10.3389/fenvs.2022.867434
- Mills, G., Ching, J., and Bechtel, B. (2021). “Characterising Urban Morphology for Urban Climate Modelling,” in *Urban Climate Science for Planning Healthy Cities Biometeorology*. Editors C. Ren and G. McGregor (Cham: Springer International Publishing), 339–354. doi:10.1007/978-3-030-87598-5\_15
- Mughal, M. O., Li, X. X., Yin, T., Martilli, A., Brousse, O., Dissegna, M. A., et al. (2019). High-Resolution, Multilayer Modeling of Singapore’s Urban Climate Incorporating Local Climate Zones. *J. Geophys. Res. Atmos.* 124, 7764–7785. doi:10.1029/2018JD029796
- Nazarian, N. (2022). WUDAPT Level 0 Training Data for Sydney (Australia, Commonwealth of), Submitted to the LCZ Generator. LCZ Gener. Available at: [https://lcz-generator.rub.de/factsheets/3530917846fefde7c17637092c9b98a2378053e0/3530917846fefde7c17637092c9b98a2378053e0\\_factsheet.html](https://lcz-generator.rub.de/factsheets/3530917846fefde7c17637092c9b98a2378053e0/3530917846fefde7c17637092c9b98a2378053e0_factsheet.html) (January 27, 2022).
- Nice, K. A., Coutts, A. M., and Tapper, N. J. (2018). Development of the VTUF-3D v1.0 Urban Micro-climate Model to Support Assessment of Urban Vegetation Influences on Human Thermal Comfort. *Urban Clim.* 24, 1052–1076. doi:10.1016/j.ulim.2017.12.008
- Núñez-Péiró, M., Sánchez-Guevara Sánchez, C., and Neila González, F. J. (2021). Hourly Evolution of Intra-urban Temperature Variability across the Local Climate Zones. The Case of Madrid. *Urban Clim.* 39, 100921. doi:10.1016/j.ulim.2021.100921
- Oleson, K. W., and Feddema, J. (2020). Parameterization and Surface Data Improvements and New Capabilities for the Community Land Model Urban (CLMU). *J. Adv. Model. Earth Syst.* 12, e2018MS00158. doi:10.1029/2018MS001586
- Potgieter, J., Nazarian, N., Lipson, M. J., Hart, M. A., Ulpiani, G., Morrison, W., et al. (2021). Combining High-Resolution Land Use Data with Crowdsourced Air Temperature to Investigate Intra-urban Microclimate. *Front. Environ. Sci.* 9, 385. doi:10.3389/fenvs.2021.720323
- PSMA Australia (2020). Geoscape | Location Data with Depth. Geoscape Aust. Available at: <https://geoscape.com.au/> (Accessed December 15, 2021).
- Simón-Moral, A., Dipankar, A., Roth, M., Sánchez, C., Velasco, E., and Huang, X. Y. (2020). Application of MORUSES Single-layer Urban Canopy Model in a Tropical City: Results from Singapore. *QJR Meteorol. Soc.* 146, 576–597. doi:10.1002/qj.3694
- Sirkko, W., Kashubin, S., Ritter, M., Annkah, A., Bouchareb, Y. S. E., Dauphin, Y., et al. (2021). Continental-scale Building Detection from High Resolution Satellite Imagery. *arXiv*. Preprint. doi:10.48550/arXiv.2107.12283
- Siu, L. W., and Hart, M. A. (2013). Quantifying Urban Heat Island Intensity in Hong Kong SAR, China. *Environ. Monit. Assess.* 185, 4383–4398. doi:10.1007/s10661-012-2876-6
- Stewart, I. (2018). Developing a Field Guide to Identify Local Climate Zones in Cities. in *Special Session on World Urban Database and Access Portal Tools (WUDAPT) I*. New York: American Meteorological Society. Available at: <https://ams.confex.com/ams/ICUC10/meetingapp.cgi/Paper/342085>
- Stewart, I. D., and Oke, T. R. (2012). Local Climate Zones for Urban Temperature Studies. *Bull. Am. Meteorol. Soc.* 93, 1879–1900. doi:10.1175/bams-d-11-00019.1
- Sun, Z., Du, W., Jiang, H., Weng, Q., Guo, H., Han, Y., et al. (2022). Global 10-m Impervious Surface Area Mapping: A Big Earth Data Based Extraction and Updating Approach. *Int. J. Appl. Earth Observation Geoinformation* 109, 102800. doi:10.1016/j.jag.2022.102800
- Zhang, X., Liu, L., Wu, C., Chen, X., Gao, Y., Xie, S., et al. (2020). Development of a Global 30 m Impervious Surface Map Using Multisource and Multitemporal Remote Sensing Datasets with the Google Earth Engine Platform. *Earth Syst. Sci. Data* 12, 1625–1648. doi:10.5194/essd-12-1625-2020
- Zonato, A., Martilli, A., Di Sabatino, S., Zardi, D., and Giovannini, L. (2020). Evaluating the Performance of a Novel WUDAPT Averaging Technique to Define Urban Morphology with Mesoscale Models. *Urban Clim.* 31, 100584. doi:10.1016/j.ulim.2020.100584

**Conflict of Interest:** The authors declare that the research was conducted in the absence of any commercial or financial relationships that could be construed as a potential conflict of interest.

**Publisher's Note:** All claims expressed in this article are solely those of the authors and do not necessarily represent those of their affiliated organizations, or those of the publisher, the editors and the reviewers. Any product that may be evaluated in this article, or claim that may be made by its manufacturer, is not guaranteed or endorsed by the publisher.

Copyright © 2022 Lipson, Nazarian, Hart, Nice and Conroy. This is an open-access article distributed under the terms of the Creative Commons Attribution License (CC BY). The use, distribution or reproduction in other forums is permitted, provided the original author(s) and the copyright owner(s) are credited and that the original publication in this journal is cited, in accordance with accepted academic practice. No use, distribution or reproduction is permitted which does not comply with these terms.



# Resolving Radiant: Combining Spatially Resolved Longwave and Shortwave Measurements to Improve the Understanding of Radiant Heat Flux Reflections and Heterogeneity

Coleman Merchant<sup>1\*</sup>, Forrest Meggers<sup>1\*</sup>, Miaomiao Hou<sup>2,3</sup>, Dorit Aviv<sup>2</sup>, Florian Arwed Schneider<sup>4</sup> and Ariane Middel<sup>5,6</sup>

<sup>1</sup> Princeton School of Architecture and the Andlinger Center for Energy and the Environment, Princeton University, Princeton, NJ, United States, <sup>2</sup> Weitzman School of Design, University of Pennsylvania, Philadelphia, PA, United States, <sup>3</sup> College of Architecture and Urban Planning, Tongji University, Shanghai, China, <sup>4</sup> School of Sustainability, Arizona State University, Tempe, AZ, United States, <sup>5</sup> School of Arts, Media and Engineering, Arizona State University, Tempe, AZ, United States, <sup>6</sup> School of Computing and Augmented Intelligence, Arizona State University, Tempe, AZ, United States

## OPEN ACCESS

### Edited by:

Jennifer Ann Salmon, The University of Auckland, New Zealand

### Reviewed by:

Dahai Qi,

Université de Sherbrooke, Canada  
Xiangfei Kong,  
Hebei University of Technology, China

### \*Correspondence:

Coleman Merchant  
[cbm5@princeton.edu](mailto:cbm5@princeton.edu)  
Forrest Meggers  
[fmeggers@princeton.edu](mailto:fmeggers@princeton.edu)

### Specialty section:

This article was submitted to  
Health and Cities,  
a section of the journal  
Frontiers in Sustainable Cities

Received: 04 February 2022

Accepted: 17 May 2022

Published: 22 July 2022

### Citation:

Merchant C, Meggers F, Hou M, Aviv D, Schneider FA and Middel A (2022) Resolving Radiant: Combining Spatially Resolved Longwave and Shortwave Measurements to Improve the Understanding of Radiant Heat Flux Reflections and Heterogeneity. *Front. Sustain. Cities* 4:869743. doi: 10.3389/frsc.2022.869743

We introduce and demonstrate new measurement and modeling techniques to fully resolve the spatial variation in shortwave and longwave radiant heat transfer in the outdoor environment. We demonstrate for the first time a way to directly resolve the shortwave radiant heat transfer from terrestrial reflected and diffuse sky components along with the standard direct solar radiation using an adapted thermopile array and ray-tracing modeling techniques validated by 6-direction net radiometer. Radiant heat transfer is a major component of heat experienced in cities. It has significant spatial variability that is most easily noticed as one moves between shade and direct solar exposure. But even on a cloudy and warm day the invisible longwave infrared thermal radiation from warm surfaces makes up a larger fraction of heat experienced than that caused by convection with surrounding air. Under warm or hot climate conditions in cities, radiant heat transfer generally accounts for the majority of heat transfer to people. Both the shortwave (visible/solar) and the longwave (infrared/thermal) have significant spatial variation. We demonstrate sensor methods and data analysis techniques to resolve how these radiant fluxes can change the heat experienced by  $>1 \text{ kW m}^{-2}$  across small distances. The intense solar shortwave radiation is easily recognized outdoors, but longwave is often considered negligible. Longwave radiation from heat stored in urban surfaces is more insidious as it can cause changes invisible to the eye. We show how it changes heat experienced by  $>200 \text{ W m}^{-2}$ . These variations are very common and also occur at the scale of a few meters.

**Keywords:** radiant heat transfer, thermal sensors, urban heat, longwave, shortwave, thermopile array

## INTRODUCTION AND BACKGROUND

The measurement of heat impacts on people in the built environment is critical to understanding and addressing issues of human health, climate, and urban design. Climate change is increasing average temperatures across the globe, with the most recent Intergovernmental Panel on Climate Change (IPCC) assessment reporting a higher average temperature increase across the last century

of  $1.59^{\circ}\text{C}$  over land compared to ocean, and additionally stating that cities will intensify human-induced warming locally (IPCC, 2021). Heat is also increasing even more in urban areas due to radiative trapping and anthropogenic emissions of heat (Oke, 1982). These temperature increases all represent surface air temperatures. As we and others have shown, surface temperatures can easily be  $>30^{\circ}\text{C}$  warmer than air temperatures reaching extremes above  $60^{\circ}\text{C}$  (Yang and Li, 2015; Meggers et al., 2016; Middel and Krayenhoff, 2019; Aviv et al., 2021). We argue that the direct radiant heat transfer from these hot surfaces not only add to the heat experienced from warmer urban air temperatures, but actually have significantly larger impacts than the warmer air on urban dwellers. In this paper we will demonstrate new techniques that produce novel results describing the complex longwave, shortwave, and reflecting components of radiant heat transfer as it bounces through the urban environment independent of air temperature.

The general population largely associates heat with air temperatures, but in warm climates the majority of heat experienced by people in the urban environment is in the form of radiant heat transfer (Hoppe, 1992; Thorsson et al., 2007; Johansson et al., 2014; Middel et al., 2014; Lindberg et al., 2016). We have built human body heat models (Teitelbaum et al., 2020), and built experimental radiant pavilions (Chen et al., 2020; Teitelbaum et al., 2022), which have both demonstrated how as air temperatures approach skin temperature the body's necessary metabolic heat rejection can become almost completely dependent on radiant heat transfer. We argue it is therefore critical to explore new ways to model and measure radiant heat transfer that include its complex geometric and spectral properties.

## Background

Radiant heat transfer is the exchange of heat by the emission and absorption of electromagnetic radiation between surfaces. Governed by blackbody radiation physics described by Planck, the temperature of surfaces drives the emission of thermal radiation, including between people and their surroundings. Radiant heat transfer occurs across the full spectrum of radiation, and as the emission is related to temperatures there are two dominant modes of radiant heat experienced: solar shortwave radiation and terrestrial longwave radiation. The sun, at around  $5000\text{ K}$ , emits shortwave light peaking around  $0.5\text{--}1$  micron wavelengths that we have evolved to see with our eyes, but that also brings around  $1\text{ kW m}^{-2}$  to the surface of the Earth. The Earth, including those of us existing on it, are only around  $300\text{K}$  and therefore emit largely in the longwave wavelengths of  $8\text{--}15$  micron, creating a dynamic exchange between surfaces on the planet that is invisible to the human eye.

For shortwave radiation there is an intuitive association of heat felt from the intense solar direct beam, and an understanding that black materials (low albedo and heat absorption) will absorb more of this heat than white materials (high albedo and heat reflection). The longwave radiation is not visible to the human eye and it is not transmitted via an intense direct beam, but rather is diffusely emitted and exchanged between surfaces, which makes the view factor to surrounding

surfaces and their varying temperatures critical in understanding radiant heat impacts. While finding shade from the sun is an obvious strategy to reduce radiant heat, it is nearly impossible for a human to adapt to the diffuse longwave heat surrounding them in the urban environment. In addition, even in the shade the diffuse shortwave radiation that diffusely reflects off high-albedo surfaces is also non-trivial.

In this paper we build on previous work that strives to better characterize the invisible longwave radiant heat along with the shortwave components coming from all directions. As demonstrated by the work of the mobile human-biometeorological station (MaRTy cart) experimentally in previous work at Arizona State University (ASU) in Tempe, Arizona (Middel and Krayenhoff, 2019), we can measure precisely the longwave and shortwave radiation using the 6-direction net radiometer setup, and move through a variety of locations demonstrating that lateral longwave and shortwave radiation dominate heat experienced with invisible longwave being the dominant flux. This work showed that MRT reached above  $75^{\circ}\text{C}$ , and that these sites were above asphalt or concrete. It also demonstrated the benefits of green surfaces like trees in reducing sky view factor and Mean Radiant Temperature (MRT). The 6-direction radiometer method provides averaged directional readings of the  $\text{W m}^{-2}$  of radiation, but does not resolve the specific surfaces. In previous work at Princeton the Spherical Motion Average Radiant Temperature (SMaRT) sensor was developed to scan and map longwave radiant heat emission from surfaces with a high resolution thermal array, which enabled analysis of the exact sources of radiant heat and resolving the exact location of hot surfaces and their geometry relative to potential occupants in space (Teitelbaum et al., 2016, 2017; Houchois et al., 2019). With this work we were able to show how radiant heat can vary significantly across surfaces, and also to calculate the distribution of MRT at any point in space as a function of the highly resolved surrounding surface temperatures and geometries measured by the sensor. This showed that indoor surfaces often varied by more than  $10^{\circ}\text{C}$  and MRT could vary by  $> 2^{\circ}\text{C}$  when moving just 2 feet (60 cm) in a standard heated office. The Princeton and ASU team initially brought the MaRTy cart and the SMaRT sensor platforms together to explore potential methods combining the high precision and high resolution aspects of each system in a 1-day experimental campaign in Philadelphia on the Temple University campus (Aviv et al., 2021). As there were gaps in data produced by the systems, a simulation technique was added from collaborators at Penn that was informed by the results from both systems to create spatial characterizations of the urban environment that built on previous ray tracing techniques for longwave heat transfer (Aviv, 2019; Aviv et al., 2022). The modeling techniques became integrated as a tool for data reduction and analysis from the two sensor platforms, which helped to generate results that created a data-driven mapping of varying MRT throughout an outdoor space in the collaborative paper that showed for the first time a method to combine high resolution surface temperatures showing variations in MRT in space that could be validated against precise net radiometer measurements (Aviv et al., 2021).

The measurement and modeling of shortwave are both improved in this paper. Modeling the radiative exchanges on and within urban surfaces can be done several ways. Some studies on urban climate have integrated ray tracing techniques into the urban canopy model. A neighborhood-scale multi-layer urban canopy model (MUCM) combined with ray tracing methods was developed to account for shortwave and longwave radiation exchange in the urban canyon, but it is based on the two-dimensional canyon geometry and thus not feasible to use a detailed three-dimensional geometry model as the input (Krayenhoff et al., 2013). Doan and Kusaka (2019) introduced a new MUCM also combined with a ray-tracing algorithm to represent both shortwave and longwave radiative processes on urban surfaces. The urban geometry model considers buildings and vegetation land as bulks with thermal properties. Based on the urban canyon model, Rosado et al. (2017) proposed an urban canyon albedo model (UCAM) to calculate the amount of radiant flux accounting for three reflection bounces, and the results demonstrated the need to use the actual urban geometry for more accurate studies. Another approach is using a ray tracing model directly. A three-dimensional numerical model based on ray tracing methods was developed by Yang and Li (2015) to predict a detailed urban surface temperature distribution. The urban geometry model consists of normalized cells, representing different abstracted scenarios of building density, height and arrangements. The aforementioned work took reflection and urban albedo as important parameters when testing different scenarios. There are also studies investigating the influence of shortwave reflections on the energy balance (Vallati et al., 2018; Ali-Toudert, 2021). As an approach that can support detailed urban geometry model, the solar and longwave environmental irradiance geometry (SOLWEIG) model can simulate spatial variations of three-dimensional radiation fluxes in complex urban settings with building digital elevation model as input (Lindberg et al., 2008; Lindberg and Grimmond, 2011) and has been tested in cases of different cities. For example, Chen et al. (2016) employed the SOLWEIG model to simulate the radiant heat flux densities in several urban settings in Shanghai, which showed good agreement with the six directional radiant flux density measurements. Research on more land cover types and the exact contribution of reflection on the radiant heat flux are required.

In the field of solar radiation measurement studies have been carried out using novel combinations of sensors to better resolve sky radiation as demonstrated in published work (Blum et al., 2022). Here a precise pyranometer was combined with a sky imager to improve the resolution of the precise data from the pyranometer. These sky imagers are inherently limited in their accuracy due to their use of a CMOS sensor which does not respond proportionally to  $\text{Wm}^{-2}$  of irradiance because of their limited spectral response.

## Objective

The objective of this paper was to address some of the limitations of the initial collaboration combining the MaRTy, SMaRT, and ray tracing simulations (Aviv et al., 2021), and to carry out a more extensive field campaign to test and demonstrate

improvements to the methods. A significant limitation in the first study was the inability of the SMaRT sensor to resolve any shortwave radiation as well as to record high resolution longwave scans in a short enough time period for the 1-day campaign, which resulted in significantly lower resolution images.

This study uses an updated version of the SMaRT sensor, the SMaRT Shortwave and Longwave (SMaRT-SL) that records 360° shortwave and longwave panoramic images, which is deployed alongside the MaRTy cart across locations at ASU in Tempe, Arizona for two hot clear days. It uses an updated modeling technique to better address shortwave sky radiation as well as reflections. We aimed to produce results that help better characterize through measurement and modeling the relevance of both the diffuse shortwave reflections along with the longwave emissions at a high geometric resolution. We hope this will provide a more clear picture of how the built environment, and its planned and designed landscapes and buildings, have easily-overlooked radiant relationships to the heat experienced by urban dwellers.

Measuring radiant heat transfer is critical to understanding urban heat, yet this highly variable phenomenon remains often unexamined and underappreciated in its role affecting people. Improving characterization of this phenomenon and moreover, making new tools and techniques more available to urban planners, designers, and architects will create new opportunities to better address challenges of urban heat. We argue these exchanges have many nuances including highly complex and variable heat impacts on people as they move through the geometry of the urban fabric.

## METHODOLOGY

### Experimental Setup and Locations

Experiments were carried out on May 18 and 19, 2021 on the ASU campus in Tempe Arizona. On each day the MaRTy cart and SMaRT-SL sensor platforms were set up at different locations in  $\sim 2$  h increments between 8:00 am and 5:30 pm. Readings were recorded from each device, panoramic photos (see Figure 1) were taken of the sites, and the albedo and emissivity of the surfaces were estimated.

There were five sites tested (see Figure 1). These varied in conditions from grass to concrete with varying levels of sky exposure. These were selected to try to achieve a variety of representative scenarios with varying sky, sun, horizon, ground cover, and ground temperature. The five sites were tested across 2 days. One site was measured on both days to have a reference (Hayden Lawn).

First, the SMaRT-SL sensor took one complete measurement which took  $\sim 16\text{--}17$  min to complete. Second, MaRTy is placed at the same location and measures for  $\sim 1$  min which includes 20 s to account for the sensor lag of the net radiometers and temperature sensor. Deploying and measuring with both MaRTy cart and SMaRT-SL sensor requires just below 20 min per location. Measuring three locations requires  $\sim 1$  h including the walk between locations.

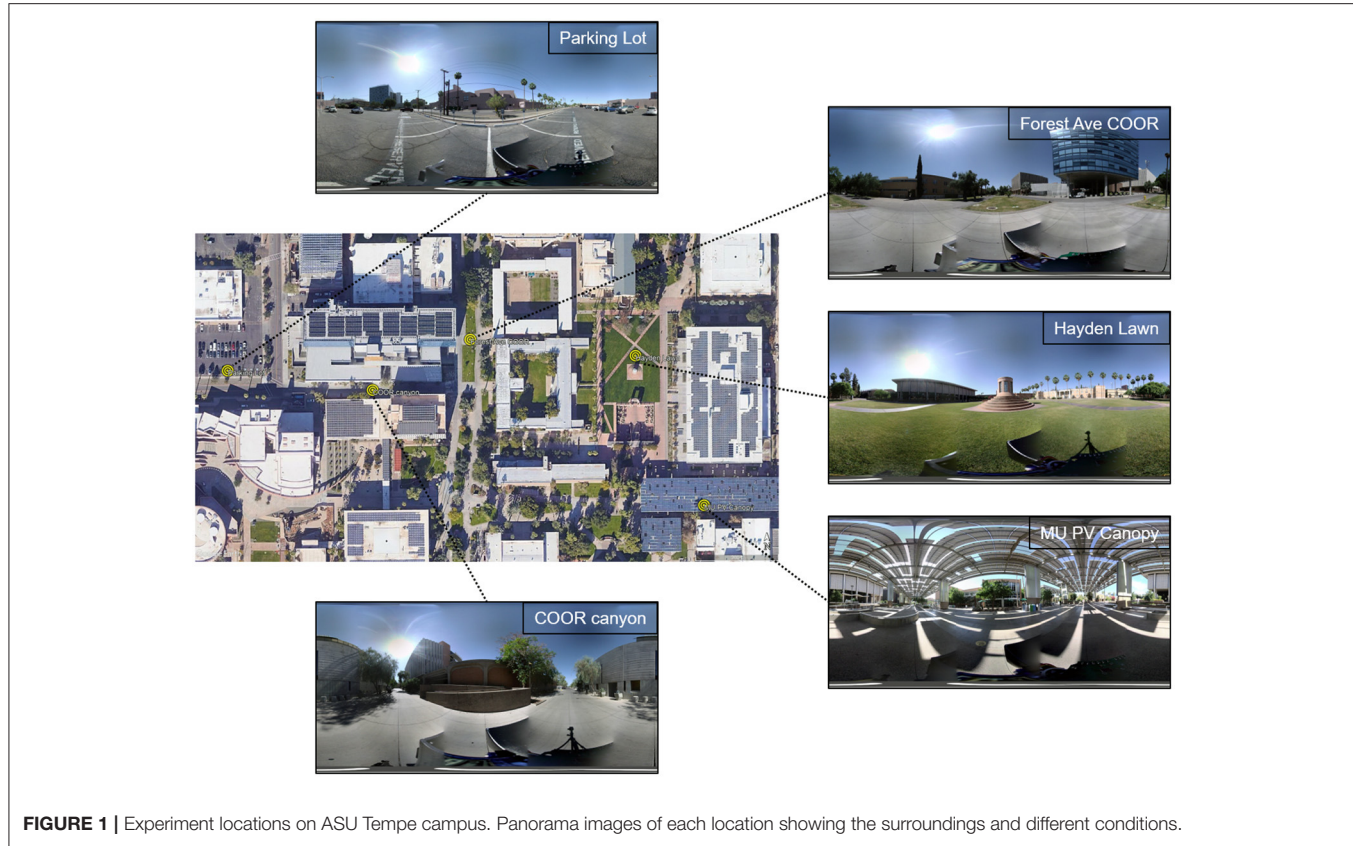


**FIGURE 1 |** Experiment locations on ASU Tempe campus. Panorama images of each location showing the surroundings and different conditions.

On the first day, May 18th, the sensors were deployed in three locations (1) The Hayden lawn, a large open grass field, (2) The MU PV Canopy, an outdoor seating area under a large PV shade structure; (3) The Forest Ave COOR, a concrete open area in front of the Lattie F. Coor Hall at ASU. Five measurements were made at Hayden lawn, Six at the MUPV Canopy, and four measurements were made at Forest Ave COOR all spaced ~2 h apart with the Hayden and MU PV starting between 8 and 9 am with the MU PV having an additional data collection between 9 and 10 am due to data loss between 8 and 9 am.

On the second day, May 19th, the sensors were rotated through three locations, again (1) Hayden lawn (reference location), (2) Parking lot, an open area dominated by asphalt concrete, and (3) COOR canyon, a concrete walkway between buildings near the Coor Hall.

## MaRTy Cart Mobile Net Radiometer Platform

The MaRTy cart setup is the same as described in our previous collaboration (Aviv et al., 2021), and as detailed in a first experiment at ASU in Tempe (Middel and Krayenhoff, 2019). It is a human-biometeorological platform (**Figure 2**), which was custom-built to be a mobile platform that is easily moved from location to location.

The MaRTy sensor platform records location (lat/lon, °), air temperature (°C); relative humidity (RH%); wind speed ( $\text{m}\cdot\text{s}^{-1}$ ); longwave ( $\text{Wm}^{-2}$ ) and shortwave ( $\text{Wm}^{-2}$ ) radiant flux densities in a 6-directional Hukseflux NR-01 net radiometer setup. It

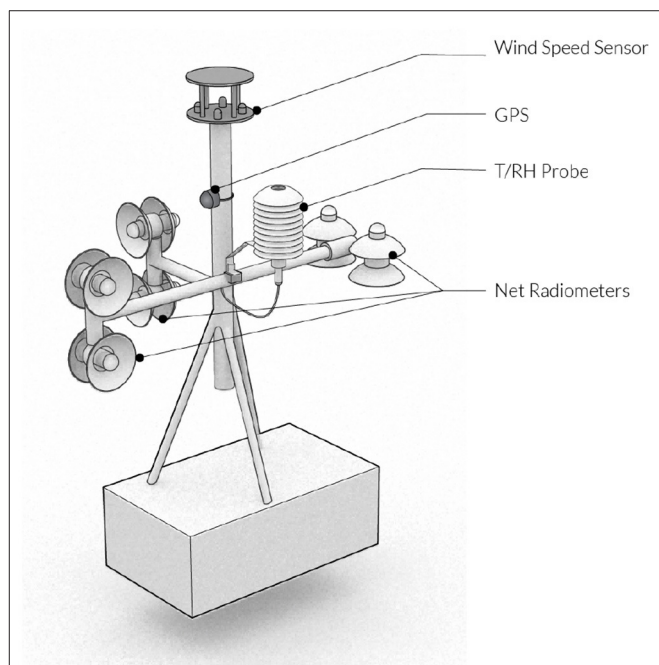


**FIGURE 2 |** The MaRTy cart sensor platform.

determines MRT from combining net radiometer readings of directional shortwave and longwave radiation, weighting each direction according to angular factors of a standing person as per

**TABLE 1** | Apogee sensor specifications.

	<b>SL-510 Pyrgeometer</b>	<b>SP-510 Pyranometer</b>
Calibration uncertainty	5%	5%
Measurement repeatability	<1%	1%
Long-term drift	<2% per year	<2% per year
Non-linearity	<1%	<1%
Spectral range	5–30 $\mu\text{m}$	385–2,105 nm
Temperature response	<5% from –15 to 45°C	<5% from –15–45°C
Window heating offset	<10 $\text{W} \cdot \text{m}^{-2}$	<2 $\text{W} \cdot \text{m}^{-2}$
Uncertainty in daily total	5%	5%

Equation 1:

$$T_{MRT} = \sqrt[4]{\frac{\sum_{i=1}^6 W_i (a_k K_i + a_l L_i)}{a_l * \sigma}} - 273.15K \quad (1)$$

where  $a_k = 0.70$  and  $a_l = 0.97$  are the unitless absorption coefficients for short-wave and longwave radiant flux densities,  $\sigma$  is the Stefan-Boltzmann constant in  $\text{W m}^{-2} \text{K}^{-4}$ , and the unitless angular weighting factors of  $W_i = 0.06$  for the up and down facing sensors and  $W_i = 0.22$  for the sensors pointing in each cardinal direction.

## SMaRT-SL Short and Longwave Mapping

We build on previous work developing a scanning mean radiant temperature sensor (SMaRT) sensor. The new expanded version includes short and longwave (SMaRT-SL) thermopile array detectors. It is composed of four directional radiative energy sensors mounted on a 2-axis rotation stage, capable of 360 degrees of motion in the azimuthal direction and 180 degrees of motion in elevation for on-demand full spherical coverage of all four sensors. In this implementation, servos are used to drive reduction gears on each rotation stage, allowing for high directional accuracy and power and communication cable pass-throughs inside the centers of the reduction gears. The system is controlled by an Arduino DUE microcontroller.

The sensor package consists of: an Apogee Instruments SP-510 Thermopile pyranometer, an Apogee Instruments SL-510 pyrgeometer, a Heimann HTPA 80x64d R2 L10.5/0.95 F7.7HiC thermopile array thermal camera, and a novel custom-made thermopile array shortwave camera using a HTPA 80x64d R2 L0 FCaF2 thermopile sensor. The novel addition of this shortwave (here meaning UV to SWIR sensitivity) thermopile camera to the conventional longwave IR thermal camera allows for explicit directional and spatial quantification of all significant radiative components of thermal comfort. The single-value pyranometer and pyrgeometer measurements are then used as comparative reference signals, and the pyranometer was additionally used for initial calibration of the sensitivity coefficient of the shortwave thermopile sensor.

The Apogee Instruments pyranometer and pyrgeometer are measured using an ADS1115 16 bit precision, differential ADC with a resolution of 3.9  $\mu\text{V}$ . The pyrgeometer thermistor channel is read with a standard 12-bit ADC for a resolution of 0.8 mV. The sensor specifications and errors are shown in **Table 1**.

The Heimann HTPA 80x64d R2 L10.5/0.95 F7.7HiC thermopile array has 5,120 elements, and a field of view of  $\sim 39$  by 31 degrees. The f/0.95 lens has a LWP coating with a cut-on ( $\text{Tr: } 5\%$ ) at  $7.7 \mu\text{m} \pm 0.3 \mu\text{m}$ . The accuracy is  $\pm 3\% |\text{TO} - \text{TA}|$  or  $\pm 3\text{K}$  (whatever is larger) for object temperatures  $< 300^\circ\text{C}$  and ambient temperatures from 5 to  $50^\circ\text{C}$ , and the NETD is 140 mK@1Hz.

The shortwave thermopile array sensor combines a lensless, unfiltered thermopile array with a VIS-NIR coated achromatic optical float glass lens pair. The result is a low-resolution camera with near-flat spectral response from 375 to 2500 nm. The HTPA 80x64d R2 L0 FCaF2 thermopile sensor has an  $\sim 1\text{ mm}$  thick CaF<sub>2</sub> window to seal the device, which provides nearly flat bandpass response across the  $200 \mu\text{m}$  to  $\sim 10,000 \mu\text{m}$  range. The focusing lens is a N-BAF10/N-SF5 achromatic pair with 14 mm focal length and 12.5 mm diameter for an f-number of 1.15. A VIS-NIR (400–1,000 nm) anti-reflection coating reduces glare across the primary portion of the spectrum, and has a 50% signal range from 375 to 2,650 nm. A rectangular lens hood further reduces lens flare, an on-going issue due to the strength of the direct beam sun. Finally, a servo actuated shutter-flap is used to darken the device for zeroing and calibration of thermal offsets. See **Figure 3** for a cutaway 3-D model of the shortwave sensor.

The SMaRT-SL can complete a full set of measurements over a 15 min period. Upon power up, the tripod base is used to align the sensor in the North direction. Next, the sensor rotates to the Up, North, East, South, West and Down directions, pausing at each for  $\sim 30$  s to record the Apogee Instruments Pyranometer and Pyrgeometer readings, creating a full 6-direction net radiometer measurement with only two sensors. After this 6 direction measurement is completed, the shutter is closed on the SW thermopile camera and the raw voltage outputs of the thermopile are read and averaged over  $\sim 30$  s. This provides the baseline signal level offset due to the temperature dependent longwave IR emission of the optical elements. After this calibration is run, the device begins the panoramic scan, achieving full spherical coverage from 70 images with small overlaps over about 8 min. After the panorama is completed, a followup SWIR camera calibration and 6 direction net radiometry is taken.

## SMaRT-SL Sensor Image Processing

The SMaRT-SL sensor raw data, in the form of a collection of images, is post-processed to create a Lambert cylindrical equal-area projection of the full scene. This process distributes, upscales, smooths and averages the overlapping images, and also serves the important role of evenly distributing pixel data points to have equal solid-angle view factors. The image pixels are binned and spaced at integer values in a discrete uniform distribution in the horizontal and vertical dimensions in the final projection, assuring that in 3D vector space every pixel value in the projection image has an equal solid-angle view factor. A matrix of corresponding 3D vector coordinates is saved with

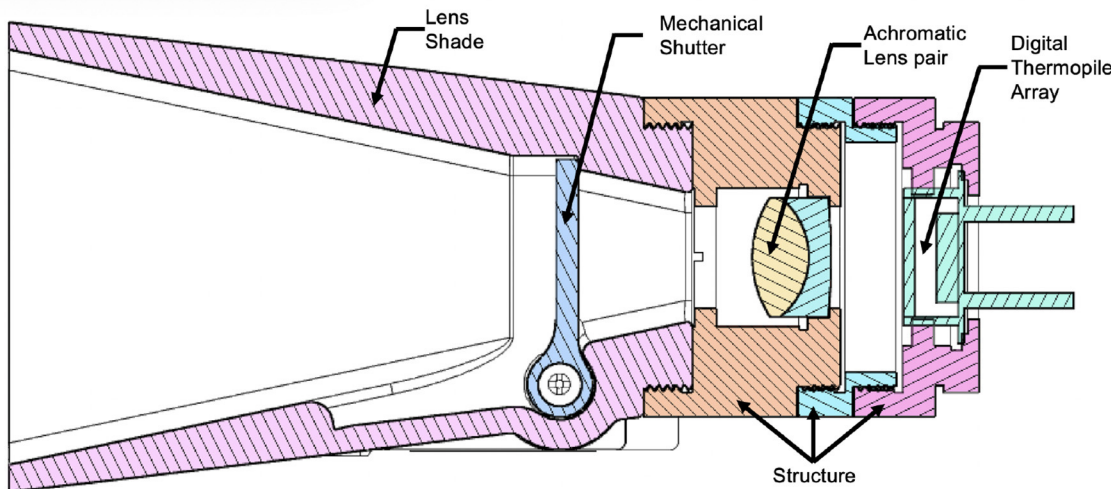


**FIGURE 3 |** Shortwave sensor cross section, with shutter in closed position. Adaptable system using c-mount components, and 3D printed lens shade.

the image, allowing further calculations to then be done in the projection space utilizing this even point spread.

To generate the planar irradiance values for a given direction from the SMaRT-SL data, virtual pyranometer and pyrgeometer models were used to generate singular numbers. The 3D vector coordinates of the pixels were used to apply Lambert's cosine law to weight the data points within view of the simulated plane. This allowed the generation of not only cardinal direction planar irradiance values to match the experimental pyranometer and pyrgeometer data, but of any arbitrary plane direction as well.

A further insight made possible by both the unique resolution and paired sensor setup of the SMaRT-SL allowed for very accurate classification of any given pixel in the projection of the scene as having either terrestrial, sky, or direct solar origins. This was made possible by using logic that paired the longwave and shortwave images: if the longwave reading was more than  $25^{\circ}\text{C}$  below ambient temperature the reading was classified as "sky," if the shortwave was above  $1,000 \text{ W}\cdot\text{sr}^{-1}\cdot\text{m}^{-2}$  the reading was classified as "direct sun," and all other points were classified as "ground." This method proved quite robust, however further testing and refinement of the process may be required for scenes with significant cloud cover. **Figure 4** demonstrates the technique's ability to classify trees, buildings and the overall varying horizon line. This classification allows for both the quantification in any given measurement of the individual contributions of direct and reflected sources, as well as calculation of statistics such as Diffuse Horizontal Irradiance (DHI) and Direct Normal Irradiance (DNI).

## Simulation Methods

For shortwave irradiance simulation, a ray-tracing model was constructed using Honeybee (version 0.66), a validated environmental plugin in the Rhino/Grasshopper algorithmic 3D modeling platform. With the inputs of the location (Phoenix, USA,  $33^{\circ}25' \text{ N}$ ,  $111^{\circ}56' \text{ W}$ ), the dates and times of the

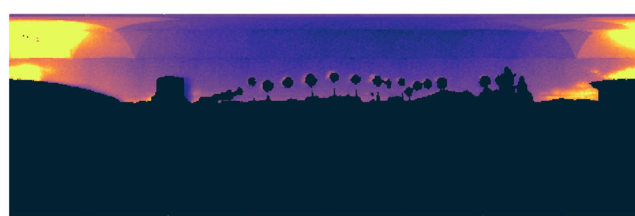


**FIGURE 4 |** Demonstration of pixel categorization at Hayden Lawn on summed longwave and shortwave irradiance image where pixels classified as "ground" are blacked out.

experiments (8 am-4 pm, May 18th and 19th, 2021), and the direct normal irradiance and diffuse horizontal irradiance, the model firstly generates the sky matrix for each simulation case. The resolution for determining the sun's location is 1 hour. The sun path and the sun location during the experiments are shown as **Figure 5A**. The hourly global horizontal irradiance was collected in a weather station of the Arizona Meteorological Network, which is located in the central Phoenix and around 16 kilometers away from the experimental sites. However, the meteorological data does not include direct normal irradiance and diffuse horizontal irradiance. In order to estimate the aforementioned two parameters, the Typical Meteorological Years (TMY) dataset provided by ISD (US NOAA's Integrated Surface Database) contains the irradiance data and was used as reference. Based on the combination of the two sources, the estimated direct normal irradiance and diffuse horizontal irradiance were calibrated.

For the geometric modeling, the 3D model of buildings, land surfaces of different types and trees were built and the reflectivity coefficients of all surfaces were assigned based on measurements at each site after experiments with an ASD

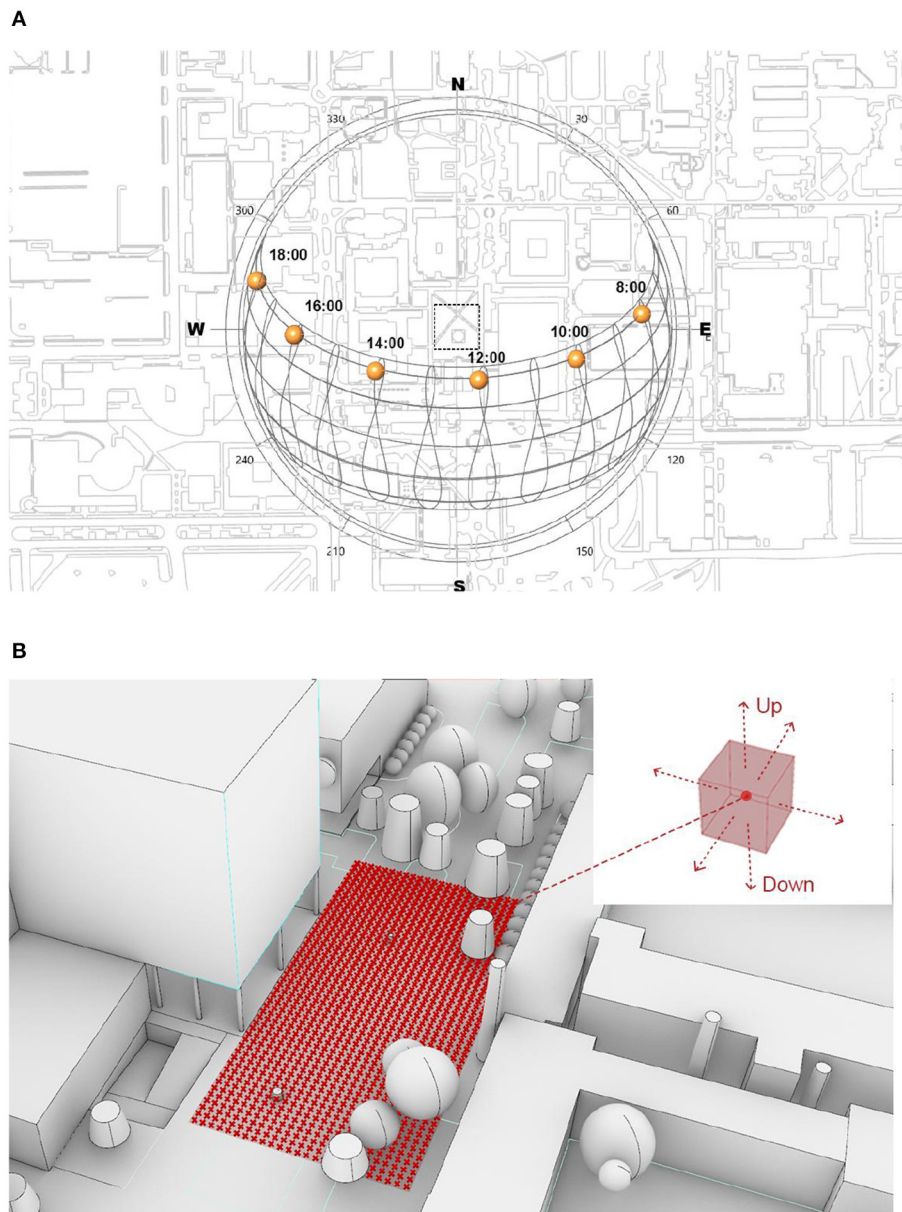


**FIGURE 5 | (A)** The sun path and sun locations during the measurements; **(B)** Sample points distribution of Forest Ave site.

FieldSpec 4 Spectroradiometer, with reflectivity values averaged over the 350–2,500 nm wavelength measurement range: 0.11 for asphalt ground, 0.2–0.25 for pavement, 0.5 for vegetation, 0.3 for gravel, 0.4 for photovoltaic panels, 0.3 for concrete, 0.15 for brick, 0.2 for trees. For each simulation case, a spatial map showing the mean spherical irradiance variation was created with a testing plane at the height of 1.1 m above the ground representing the centroid of humans and the testing points were generated in the resolution of 1 m. Boxes centered on the testing points were separated into six surfaces for plane irradiance calculation and the results correspond to the east, west, south, north, upward and downward orientations, respectively

(**Figure 5B**). Based on these inputs, the RADIANCE engine embedded in Honeybee was used to build a ray-tracing model for irradiance simulation (Ward, 1994). The plane irradiance of all testing boxes' surfaces can be calculated, based on which the mean spherical irradiance was calculated using a cubic method. This simulation technique has been developed in our previous studies (Hou et al., 2021).

In order to investigate the reflectivity of the surrounding environment and its influence on the irradiance received on the ground, a parallel set of simulations was conducted for each case with the reflectivity coefficients of all surrounding surfaces as 0 while keeping other settings unchanged. The parallel test still

includes the indirect irradiance from the sky rather than from the surfaces in the built environment such as building envelopes, since the maximum number of diffuse bounces computed by the indirect calculation were four for all cases.

## RESULTS

We have selected sets of results from the five locations to best illustrate the novel data that can be resolved by combining these techniques. The full datasets will be made available and submitted as data-in-brief and posted to a github repository ([chaos-laboratory/Resolving-Radiant-2022-Paper-Data](#)). We selected illustrative datasets collected from the Forest Ave site next to the COOR building, the Hayden Lawn, and the MUPV shade canopy. These provide a range of shortwave and longwave conditions that expose the role of longwave outdoors, and terrestrial sources of reflected shortwave, both of which are often assumed to be small relative to direct sky solar radiation. We show that they are not only significant, but that they have highly variable distributions that affect the heat experienced by people across short areas, and make shaded areas capable of significant heat stress.

### Longwave and Shortwave Radiant Energy Spherical Panoramas

We first present the results of the longwave and shortwave high resolution scans collected by the SMaRT-SL platform. We have false-colored the images similar to thermal imaging, but in this case the gradient is representing the  $\text{W} \cdot \text{sr}^{-1} \cdot \text{m}^{-2}$  coming from that direction. For each site, Forest Ave in **Figure 6**, Hayden Lawn in **Figure 7**, and MUPV in **Figure 8** we also include a visible panorama for reference to make it easier to interpret the sources and structures that appear in the radiant panoramas. Each image is a full 360 degree panorama, and the significant variation in thermal radiation is clear. In the case of Forest Ave in **Figure 6** there are images for two times, one at 11 am and one at 3 pm. The shortwave changes dramatically from 11 am to 3 pm as the sun passes behind the COOR building and creates a large shaded area. Still there remain non-insignificant sources of reflected shortwave that are of similar, and in some areas greater, than the diffuse sky intensity. The longwave image is also very interesting for Forest Ave as the building plays a significant role as a heat source as does the hot concrete on the ground. At 2 pm the shade creates an obvious reduction in shortwave, but although the longwave has reduced without the direct heating from the sun on the surfaces, it still represents a significantly high source of radiant heat, and in the case of the building, it is blocking what would otherwise be thermally cool longwave sky.

The Hayden lawn data is representative of large open areas. The shortwave data again illustrates the significant reflection from the surrounding surfaces. Here the longwave component is more significant as the major shift in temperature from the grass to the concrete causes a major change in the radiant heat. The radiant heat from the grass surfaces is about 10–20% lower than the concrete surfaces. This shift in heat of going from standing on the lawn to standing on concrete would be equivalent to the air

temperature changing by several degrees. The SMaRT-SL sensor data allows us to not only calculate the radiant temperature fields in main directions, but to now visualize the role that all designed surfaces in an environment play in the thermal load placed on people using the spaces.

The MUPV canopy presents one of the most interesting radiant datasets for our high resolution measurement case study. The variation of openings in the canopy and the significant heating of the panels cause unique shortwave and longwave conditions. While the overall amount of shortwave is certainly reduced by the canopy shading, there is still significant amounts of shortwave that arrives through the gaps in the canopy. This can largely be avoided by users as needed because the hot spots clearly register in the visible image, but we noted that our measurements even across a few inches could be dramatically influenced by the highly variable shadows cast by the system, and passing through the space users would still experience these small spaces of shortwave radiation as well as the reflections from them which are generally not considered heat source but nevertheless have an effect.

What is more critical and fully unseen is the added longwave heat emitted by the panels as they are heated in the sun and radiate down in the longwave. The shaded canopy actually blocks out the sky with a surface that is as hot as hot pavement. While blocking the sun is critical to mitigate shortwave, the rest of the sky acts as an important longwave radiant heat sink. The SMaRT-SL system can clearly display both the significant longwave radiant heat from the panels, and then also show how the sky's potential as a longwave radiant sink, or cooler, is also obstructed by the panels.

### Longwave Directional Irradiance

Next we present the results for the longwave data resolved across principle directions for the various instruments for comparison in **Figure 9**. We acquired longwave data similar to our previous work (Aviv et al., 2021) taking readings using the standard net radiometer measurements from MaRTy. For the SMaRT-SL sensor an improved array detector enabled more rapid acquisition of high resolution longwave panoramas, which addressed one of the issues in the first collaboration with MaRTy where the SMaRT-SL scans took more than 30 min and had limited resolution. The longwave results are in **Figure 9** for data from the MaRTy cart and from the processed SMaRT-SL sensor longwave array, with the fraction from the sky and from the ground illustrated in a stacked bar. The Apogee Pyrrometer that was mounted on SMaRT-SL for additional verification did not produce accurate data, most likely due to overheating in the hot Arizona temperatures.

The longwave data shows consistently higher values for the terrestrial down direction, up to  $615 \text{ W} \cdot \text{m}^{-2}$  for the ground on Forest Ave, and the sky in the up direction has lower values as expected, at  $366 \text{ W} \cdot \text{m}^{-2}$  for the sky on Forest Ave. This MUPV canopy significantly increases the up directions longwave irradiance due to the high temperature PV panel canopy. So while providing shade, the PV canopy actually has the highest longwave heat impact in the scene. One can also see temporally the effect of the Forest Ave COOR building shading the ground in the

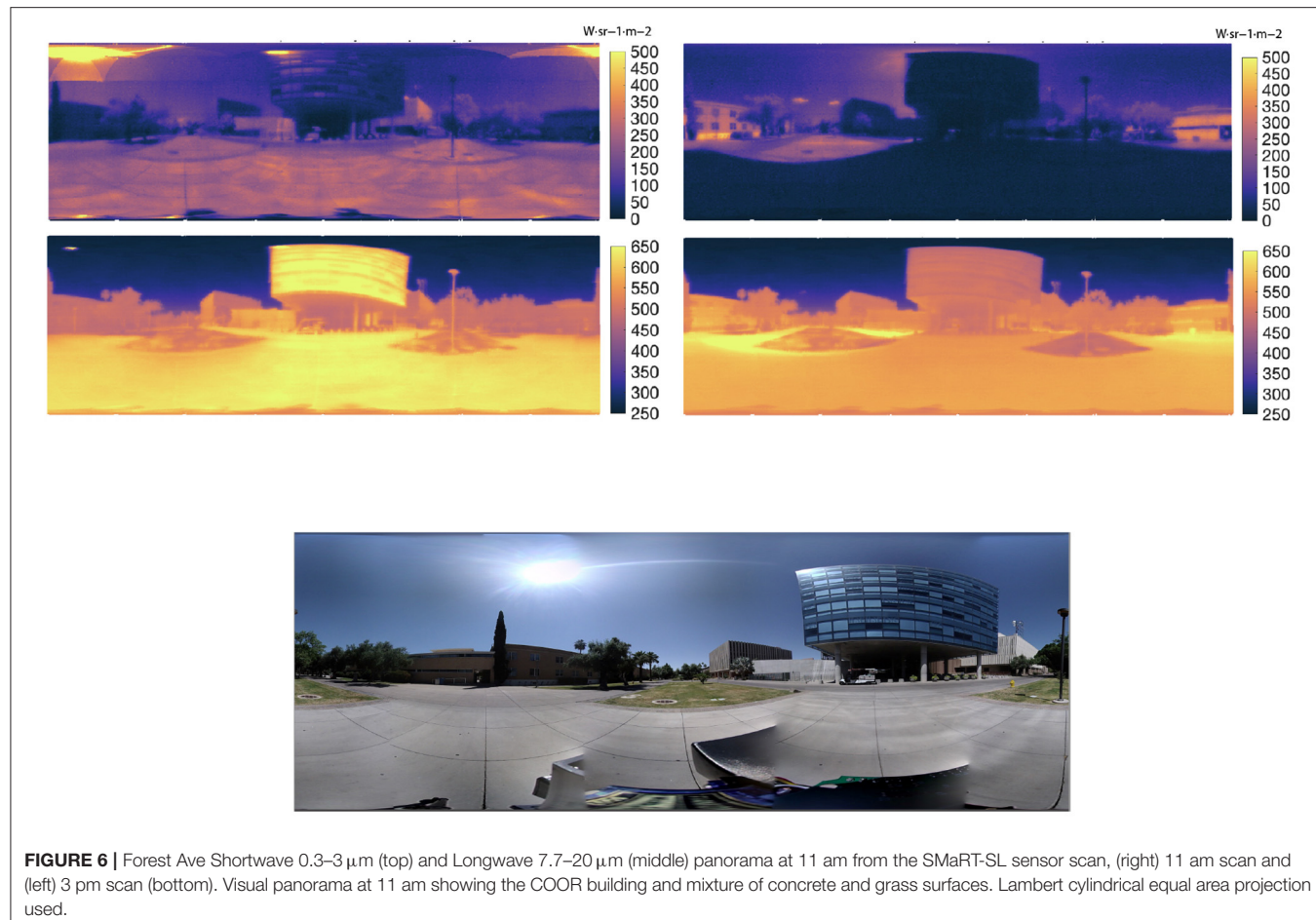


**FIGURE 6 |** Forest Ave Shortwave 0.3–3  $\mu\text{m}$  (top) and Longwave 7.7–20  $\mu\text{m}$  (middle) panorama at 11 am from the SMaRT-SL sensor scan, (right) 11 am scan and (left) 3 pm scan (bottom). Visual panorama at 11 am showing the COOR building and mixture of concrete and grass surfaces. Lambert cylindrical equal area projection used.

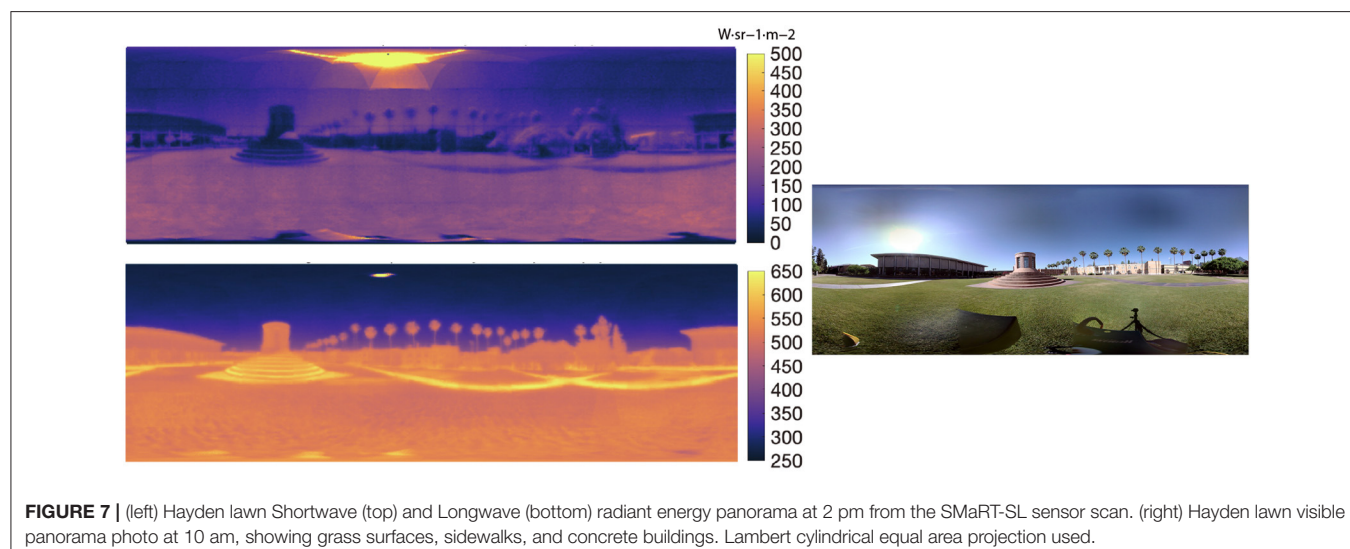


**FIGURE 7 |** (left) Hayden lawn Shortwave (top) and Longwave (bottom) radiant energy panorama at 2 pm from the SMaRT-SL sensor scan. (right) Hayden lawn visible panorama photo at 10 am, showing grass surfaces, sidewalks, and concrete buildings. Lambert cylindrical equal area projection used.

afternoon causing a reduction in the longwave, while similarly to the MUPV canopy causing increased longwave in the UP direction due to the presence of the hot building and reduced view to the cooler sky.

There is good agreement between the MaRTy and SMaRT-SL data, with the biggest discrepancy coming from the up direction where the significant sky portion may not be read with the same spectral sensitivity by the detectors due to filter cutoffs of the

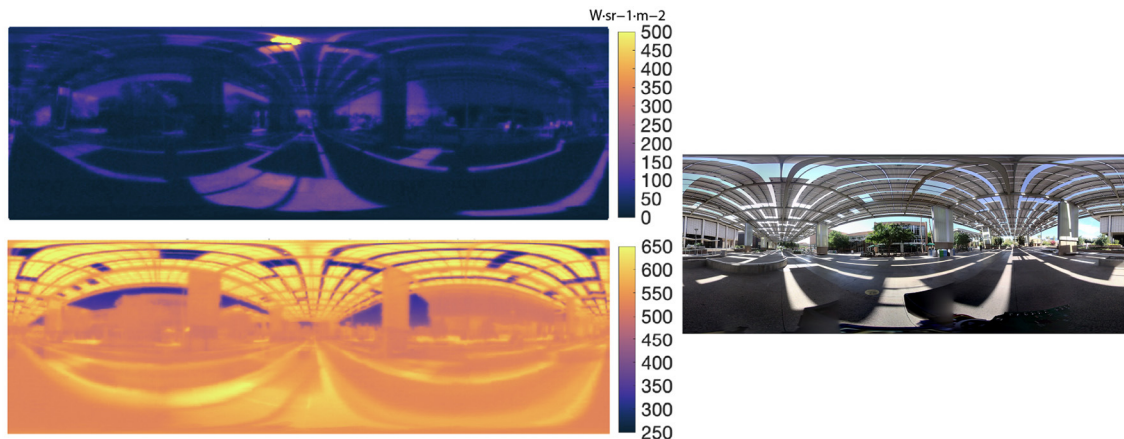


**FIGURE 8 |** (left) MUPV canopy shortwave (top) and longwave (bottom) radiant energy panorama at 2 pm from SMaRT-SL sensor scan, showing the significant longwave heat. (right) MUPV canopy visible panorama photo at 10 am. Lambert cylindrical equal area projection used.

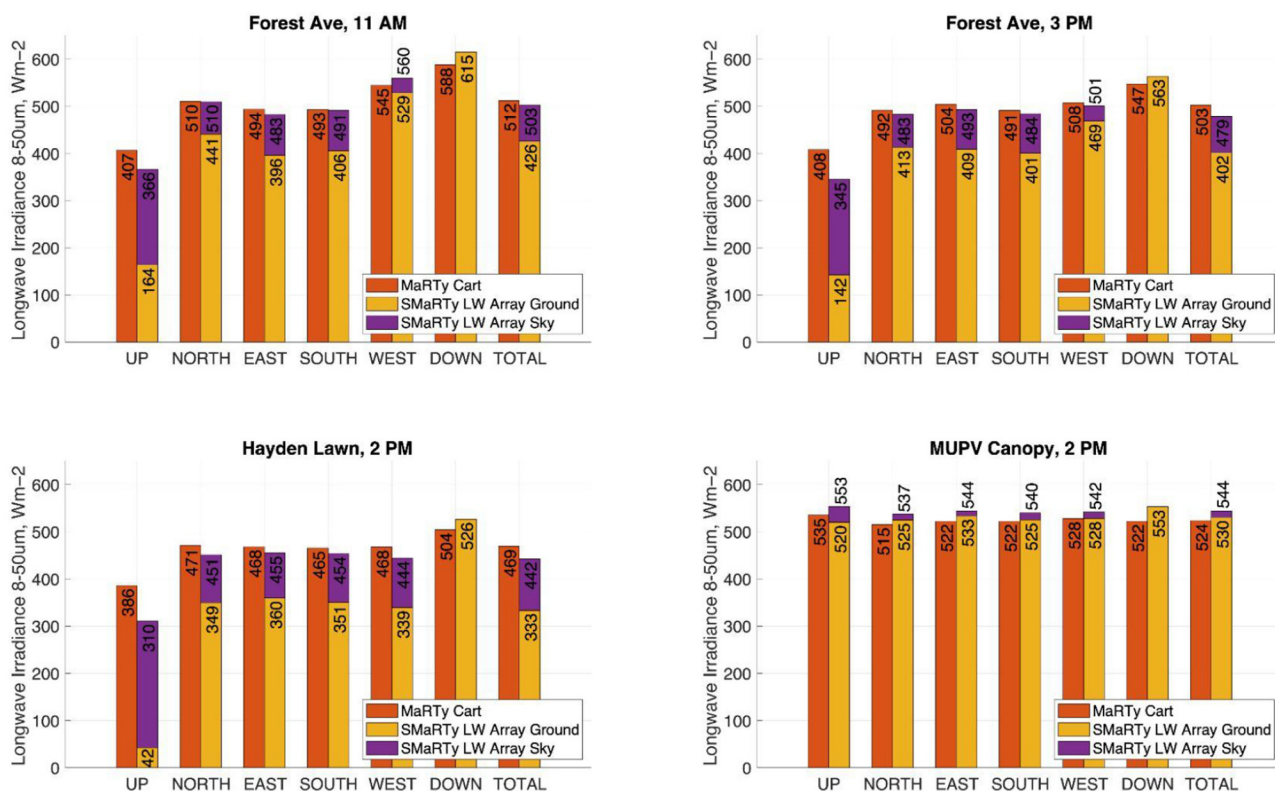


**FIGURE 9 |** Longwave radiation,  $\text{W} \cdot \text{m}^{-2}$ , measured at 11 am and 3 pm at Forest Ave by the COOR, and at 2 pm at the Hayden Lawn and at the MUPV Canopy. Planar Irradiance values are from each direction and the overall average, from the MaRTy cart (left bar) and the SMaRT-SL array (right bar). The SMaRT data is broken into sky and ground components by utilizing its greater degree of resolution.

longwave sensors components, as well as differing error modes such as self heating. Generally an increased sky fraction caused the SMaRT-SL reading to be reduced compared to the MaRTy reading. Still, the results are a significant improvement over our previous work with the two systems (Aviv et al., 2021).

## Shortwave Directional and Total Irradiance

The shortwave imaging data present another important extension from our previous work. The results of the new SMaRT-SL shortwave array sensor also show relatively good agreement for Forest Ave at 10 am and Hayden lawn at 2 pm as shown in

**Figure 10.** In this case we also have additional comparative data from the Apogee Pyrometer mounted on SMaRT-SL and from the shortwave simulation carried out to compare results from the SMaRT-SL array broken down into sky and reflected surfaces. The Forest Ave 3 pm and MUPV data are both shown on different scales because there was not direct sunlight, and in particular that limited the shortwave intensity for the Forest Ave 3 pm data. It has a maximum of just over  $100 \text{ W} \cdot \text{m}^{-2}$ , but in the morning in the sun it was nearly  $1,000 \text{ W} \cdot \text{m}^{-2}$  in the upward sky direction. The MUPV data illustrates the intense local variations possible due to the PV panel shading—small differences in the physical size and location of the sensors yields highly variable results. Hayden Lawn illustrates how the reflected portion is both dominating and significant in the north and east directions—due the clear skies, the diffuse shortwave radiation from the sky is quite low. The comparison of Forest Ave at 11 am and 3 pm shows the significant differences of shading. On Forest Ave the sun went behind the building at 3 pm. both in the upwards and downwards directions, with a further marked change of the reflected portions in the cardinal directions dominating the overall radiative load. The variation among the data at Forest Ave at 3 pm is likely due to the increased difficulty of parsing out the much lower overall signals from an accurate accounting of the roughly  $450 \text{ W} \cdot \text{m}^{-2}$  incident on the thermopile sensors due to the radiant temperature of the longwave-emitting, shortwave transparent lens system. A similar error mode can be found in low intensity pyranometer measurements.

A significant conclusion borne out by both the simulation and the SMaRT-SL sensor data is in the significance of the reflected portion of the spectrum to the overall radiative load. For the respective datasets shown in **Figure 10**, a simple accounting comparing the up and down pyranometer data shows the downwards reflected portion as 22.5, 18.2, 21, and 2.8% of the upwards direction, compared to a more accurate accounting of the ratio of the total spherical irradiance as 32.4, 45.9, 33.5, and 36.7% by an average of the SMaRT-SL and simulation data. The simple pyranometer comparison belies the significance of the reflections to the overall radiative heat transfer in lacking a more precise way of accounting for reflections. Furthermore, the accounting of reflections not just in the downwards direction holds significance for human thermal comfort, as the downwards direction has lesser impact on a standing human form (Rizzo et al., 1991).

## Shortwave Reflected Radiant Heat

**Figure 11** shows the variation in the fraction of reflected shortwave. Here we have data taken directly from the SMaRT-SL as well as from the simulation, which were both able to resolve shortwave arriving from the sky and direct sun as well as shortwave reflected off terrestrial surfaces. There is again relatively good agreement between simulation and the sensor. The discrepancies arise when the scene is shaded and there is more significant variation at the site of the measurement.

Improving the measurement and understanding of shortwave reflections is of particular interest because in practice the reflection of shortwave radiation off of terrestrial surfaces is often considered insignificant relative to the direct solar and

sky radiation. The reflected sources of radiation ranged from 10 to 70% of the total, with the open Hayden lawn receiving a more consistent range of 25–35%. In addition, one can see both the temporal and directional dependencies of the reflected shortwave. Across the three locations, reflected shortwave was a strong component of the total radiative heat load, with certain local conditions like highly reflective buildings causing it to even become the dominant portion. By breaking the data down by direction, one can see that a simple accounting of the shortwave as simply being driven by direct radiation from the sky is highly incomplete. Furthermore, the significant variations seen in this data show the importance of more accurate and spatially resolved accountings provided by the SMaRT-SL and simulation methods to better understand the complex influences of the reflected radiative sources.

The north, south, east, and west directions provide insights into how the sun reflects off of different surfaces throughout the day, and to the high variability of heat experienced from the non-direct sources of shortwave radiation. In all cases the down direction clearly only provided reflection, but interestingly the up direction was not just direct and included reflections as well. These were caused by adjacent buildings and in particular the PV canopy site had significant reflection.

For **Figure 11A** at Forest Ave, the mean spherical irradiance keeps decreasing from 11 am (when it reaches the peak  $320.4 \text{ W} \cdot \text{m}^{-2}$ ). The percentage of reflected portion in the mean spherical irradiance remains around 30%, with the highest as 32.9% at 3 pm and lowest as 26.5% at 5 pm. The avenue in the south-north direction has a high H/W ratio with buildings on both sides. Clusters of trees are on the north side. The concrete pavement and grass are reflective. From the east the reflected percentage increases and reaches the peak 83.2% ( $58.1 \text{ W} \cdot \text{m}^{-2}$ ) at 3 pm, when the direct sun ray comes from the southwest direction and is reflected by the brick buildings, trees, grass and the concrete pavement. From the west the reflected percentage is high in the morning and reaches the peak 91.6% ( $119.8 \text{ W} \cdot \text{m}^{-2}$ ) at 11 am, and keeps decreasing after that, when the direct sun ray comes from the southeast direction and is reflected by the building with glass facade and the concrete pavement on the west side. From the north the irradiance reaches the peak 88.0% ( $110.5 \text{ W} \cdot \text{m}^{-2}$ ) also at 11 am, and has a decreasing trend afterwards. From the south the reflection percentage decreases to the lowest at 1 pm, and increases after that. The reflection percentage at around 4 pm (~47%) is lower than that in the lawn (51.3%) and under the PV (62.3%). For the two open sites, the reflectance of the concrete pavement in the avenue is lower than that of grass in the lawn. The space under the PV shading structure has a brick building and trees on the south side which may contribute to irradiance from the south direction through multiple bounces, resulting in a higher reflection percentage.

For **Figure 11B** at the MUPV, the Mean spherical irradiance does not fluctuate much during the day, with the highest as  $89.1 \text{ W} \cdot \text{m}^{-2}$  at 12 pm and lowest as  $56.9 \text{ W} \cdot \text{m}^{-2}$  at 4 pm. The percentage of reflected portion in the mean spherical irradiance does not vary much either, with the highest as 37.4% at 12 pm and lowest as 30.3% at 8 am. The irradiance from the upward direction ( $224.4 \text{ W} \cdot \text{m}^{-2}$ ) is lower than that in the lawn

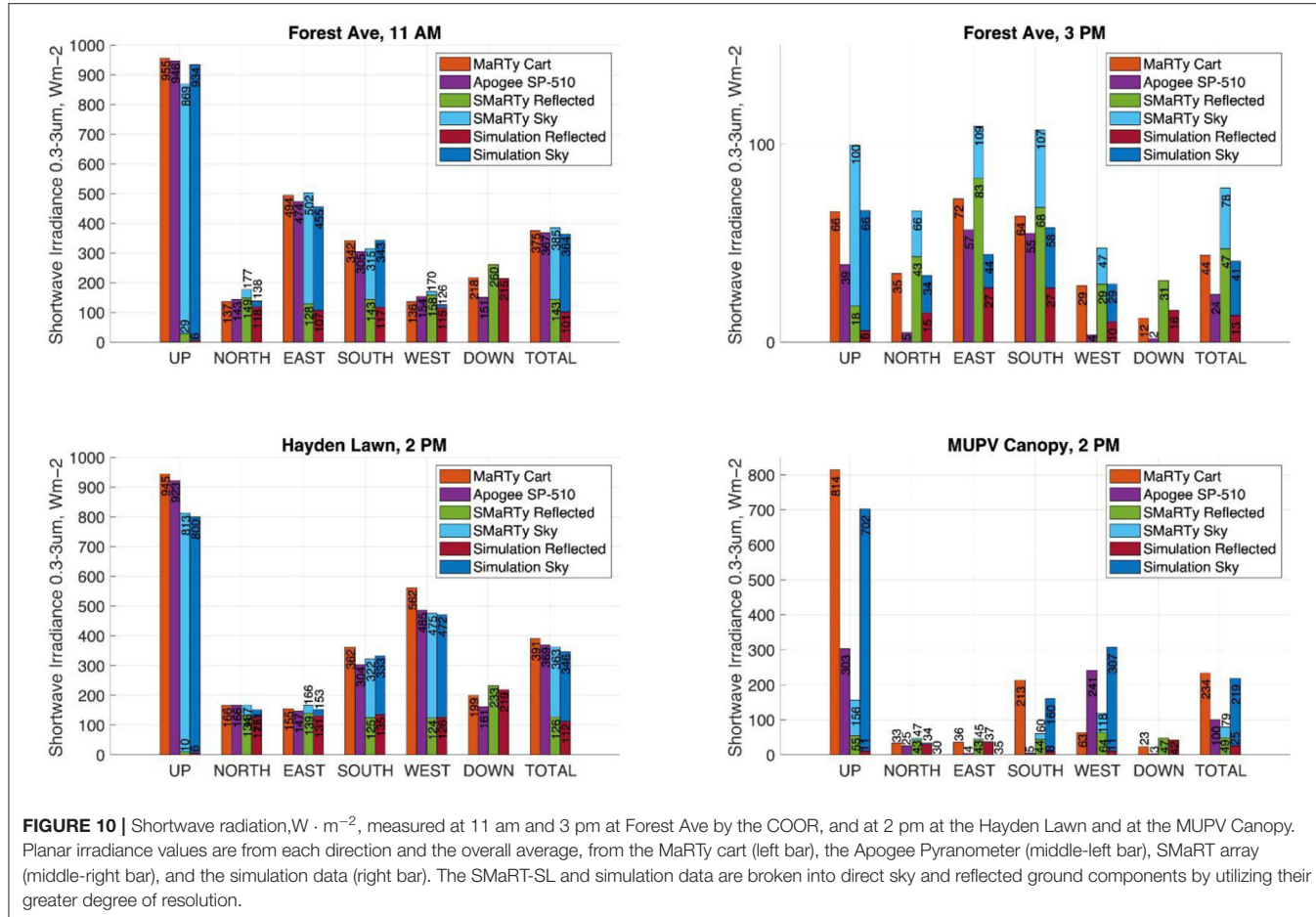


**FIGURE 10 |** Shortwave radiation,  $\text{W} \cdot \text{m}^{-2}$ , measured at 11 am and 3 pm at Forest Ave by the COOR, and at 2 pm at the Hayden Lawn and at the MUPV Canopy. Planar irradiance values are from each direction and the overall average, from the MaRTy cart (left bar), the Apogee Pyranometer (middle-left bar), SMArT array (middle-right bar), and the simulation data (right bar). The SMArT-SL and simulation data are broken into direct sky and reflected ground components by utilizing their greater degree of resolution.

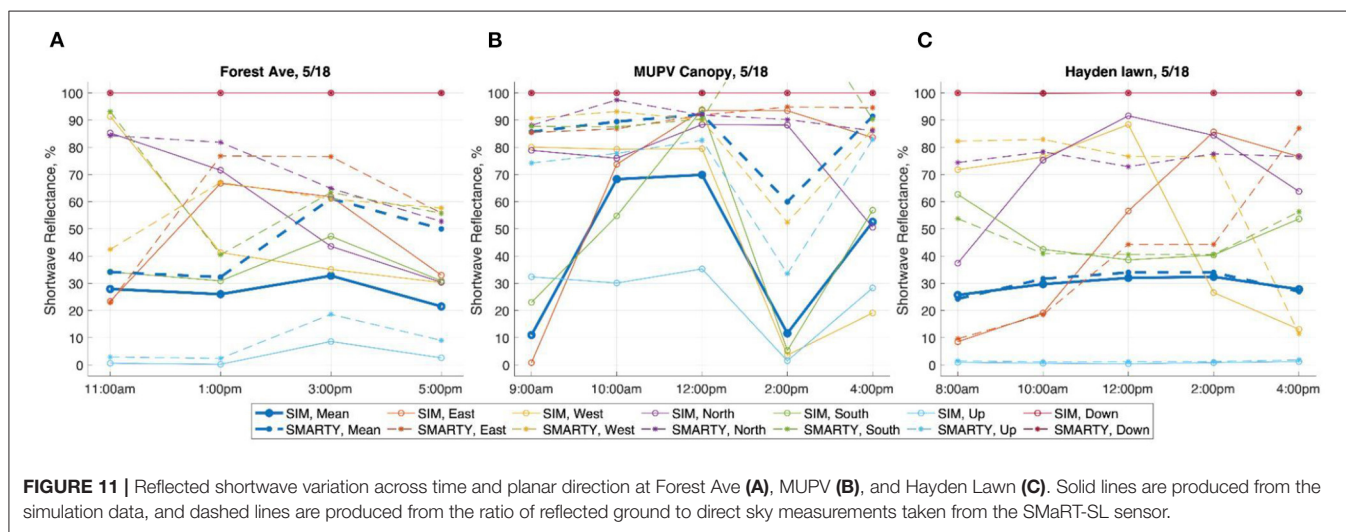


**FIGURE 11 |** Reflected shortwave variation across time and planar direction at Forest Ave (A), MUPV (B), and Hayden lawn (C). Solid lines are produced from the simulation data, and dashed lines are produced from the ratio of reflected ground to direct sky measurements taken from the SMArT-SL sensor.

( $797.6 \text{ W} \cdot \text{m}^{-2}$ ) without shade above. Because of the PV panels shading above with only some gaps between panels allowing direct sunlight, the shortwave irradiance received from every direction is lower than that in the open space such as the lawn. From the east direction the reflected percentage increases from 8 am and reaches the peak 87.6% ( $30.8 \text{ W} \cdot \text{m}^{-2}$ ) at 2 pm, when the

direct sun ray comes from the southwest direction and is reflected by the columns made of brick and semi-transparent glass and the pavement. From the west the reflected percentage is high in the morning and reaches the peak 91.9% ( $35.3 \text{ W} \cdot \text{m}^{-2}$ ) at 12 pm, and the irradiance from the north direction is relatively high and reaches the peak 94.2% ( $41.5 \text{ W} \cdot \text{m}^{-2}$ ) also at 12 pm, when the

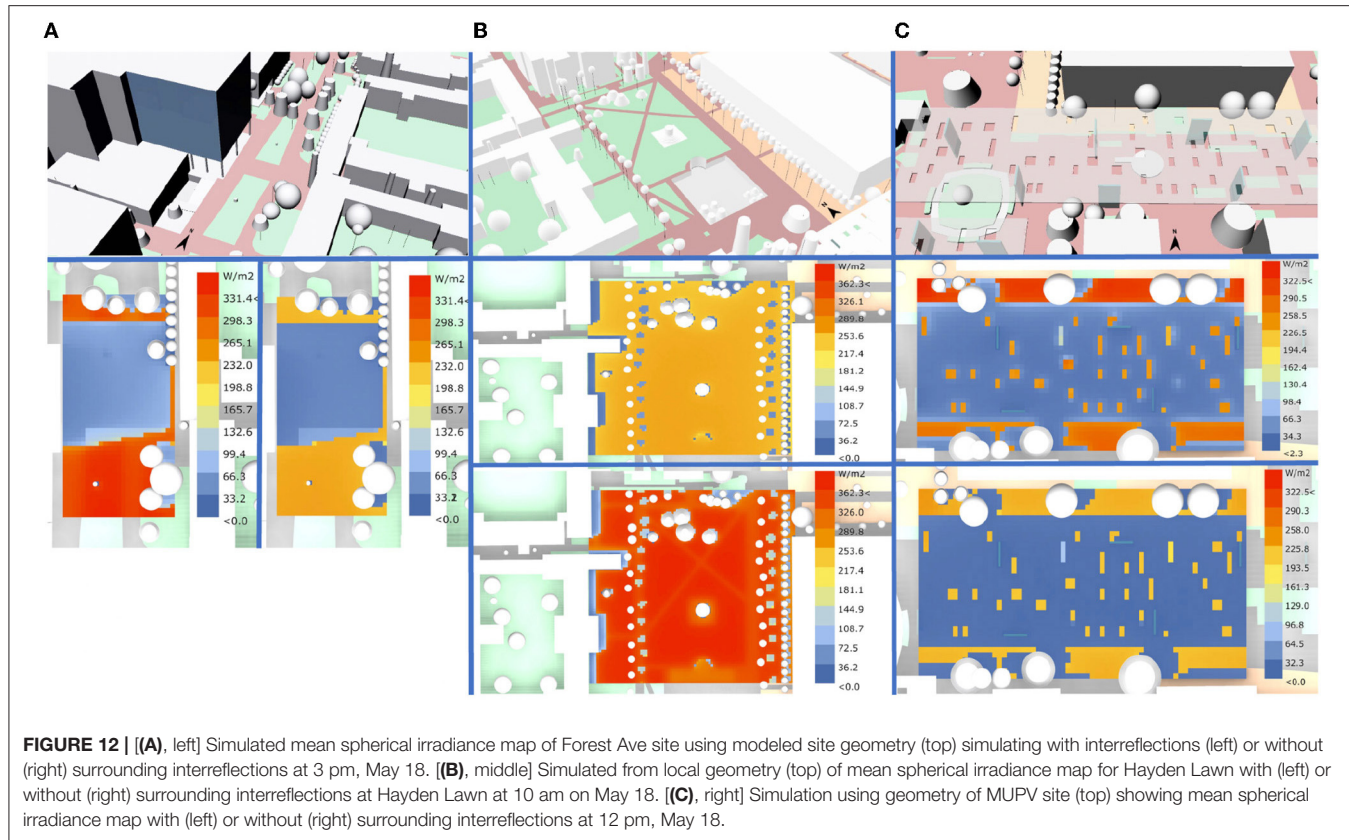


**FIGURE 12 |** [(A), left] Simulated mean spherical irradiance map of Forest Ave site using modeled site geometry (top) simulating with interreflections (left) or without (right) surrounding interreflections at 3 pm, May 18. [(B), middle] Simulated from local geometry (top) of mean spherical irradiance map for Hayden Lawn with (left) or without (right) surrounding interreflections at Hayden Lawn at 10 am on May 18. [(C), right] Simulation using geometry of MUPV site (top) showing mean spherical irradiance map with (left) or without (right) surrounding interreflections at 12 pm, May 18.

direct sun ray comes from the south direction and is reflected by the brick building, trees and the pavement on the north side. The canyon in the west-east direction has a larger height-to-width ratio, which results in higher reflection percentage for the north direction. The South reflection percentage decreases from 8 am and reaches the lowest at 12 pm, and increases after that. It is around 40–60% with more direct rays received and mainly reflected from the pavement.

For Figure 11C at Hayden Lawn the mean spherical irradiance reaches the highest at around 12 pm. The irradiance coming from the up direction makes the largest contribution. The second highest is from the south direction in compliance with the direct sunlight direction. The reflected portion reaches the highest as 33% at around 12–2 pm. For the east direction the reflected percentage increases from 8 am and reaches the peak 86.6% ( $107 \text{ W} \cdot \text{m}^{-2}$ ) at 2 pm, when the direct sun ray comes from the southwest direction and is reflected by the brick building, trees and grass on the east side. For the west direction it is high in the morning and reaches the peak 89.9% ( $119.8 \text{ W} \cdot \text{m}^{-2}$ ) at around 10am-12pm, when the direct sun ray comes from the southeast direction and is reflected by the brick building, grass on the west side. From the north it is high at 10 am - 2 pm with the peak over 90%, when the direct sun ray comes from the southeast/south/southwest direction and is reflected by the trees on the north side. From the south there are less obstacles for the direct sunlight from the south direction, the reflection percentage is around 40–60%, mainly reflected from the grass.

**TABLE 2 |** Height-to-width ratio.

H/W	Lawn	MUPV	Forest Avenue	COOR	Parking lot
East	0.19	/	0.23	/	0.07
West	0.1	/	1.1	/	0.04
North	/	0.38	/	0.8	0.1
South	/	0.39	/	0.4/2.1	0.5

## Simulation of Radiant Heat Variation Reflection Contribution

A further ability of the simulation method is to create 2D spatial heat maps of the total spherical Irradiance across a site as shown in Figure 12. These maps provide useful context for the reflected shortwave data points shown prior. One can see both the significant difference in intensity between just the direct incident radiation compared to a full accounting with reflections. The reflected portion can also be clearly seen as a strong driver of increased spatial variation in the overall Irradiance across the site.

## Reflection and Geometry Comparison Between All Sites

Table 2 provides an overview of the geometry of the site related to the height of surrounding infrastructure, terrain, or plants for all sites in the four horizontal directions. Table 3 gives the average reflected fraction of shortwave radiation for every site.

**TABLE 3 |** Average of reflection.

	<b>Lawn</b>	<b>MUPV</b>	<b>Forest avenue</b>	<b>COOR</b>	<b>Parking lot</b>
Mean Spherical	31.4%	<b>34.5%</b>	30.5%	25.9%	18.1%
East	59.2%	61.1%	61.3%	<b>63.7%</b>	57.4%
West	51.7%	<b>54.1%</b>	41.6%	39.4%	28.7%
North	79.8%	<b>83.1%</b>	70.0%	77.9%	56.4%
South	41.3%	<b>44.9%</b>	41.5%	39.7%	34.8%
Up	1.6%	<b>6.9%</b>	2.8%	4.0%	1.1%
Down	99.9%	100.0%	100.0%	100.0%	99.9%

The bold values indicate the highest reflected percentage for a given direction across the different sites.

A summary of the overall results of the reflections across all sites is as follows:

- Open spaces such as the Parking Lot have a relatively low percentage, while the Lawn has a high percentage because of reflected radiation, the grass.
- For the other three sites in urban canyons, the shading structure increases the reflection percentage of MUPV, while its H/W ratio is lower than that of Forest Avenue and COOR.
- Forest Avenue has a high average reflection percentage in the East direction, due to the concrete facade of the buildings on the east side next to the reflective ground.
- MUPV has the highest reflection percentage in general, however the mean spherical irradiance is the lowest during the day among all sites, which is attributed to the PV panels shading above with only some gaps between panels allowing direct sunlight.
- The reflection percentage of COOR is high especially in the East direction, because the concrete facade of the building on the north side contributes much to the reflection especially when the sun ray comes in from the South direction. Even though the average reflection percentage of COOR in each direction is not always the highest, its peak during the day is always higher than that of other sites. Since there is less surface facing East or West, the reflection percentage is not always high during the day, resulting in the not so high average.

## DISCUSSION AND FUTURE WORK

As compared to the recent work evaluating longwave (Vanossi et al., 2021), we have shown an alternative method to resolve longwave radiation with a thermopile array system using moderate cost sensors that are not sensitive to convection as with analog devices such as black globe thermometers. Comparing the recent work combining pyrometer data with sky imaging (Blum et al., 2022), we have shown an alternative method using a custom shortwave thermopile sensor that unlike a standard CMOS camera sensor provides an accurate and full spectrum measurement of the shortwave irradiance.

We have validated both the longwave and shortwave systems against simulation with results from a precise pyrometer and pyrometer net radiometer setup. Compared to a typical globe thermometer whose ISO 7726 standard even recognizes that convective flows around the analog device don't allow measurement better than  $\pm 2^{\circ}\text{C}$ , the systems we demonstrate can all produce radiant temperature values independent of convection with results within  $1^{\circ}\text{C}$  of each other across the platforms tested.

The principle set of results produced from the experiments is a set of data on the  $\text{W} \cdot \text{m}^{-2}$  of irradiance in both shortwave and longwave from two different sensor platforms and a simulation. In contrast to many studies on radiant heat, we do not focus on translating this into a proxy of Meat Radiant Temperature. While we recognize the importance of temperature proxy to interpret heat, the directional and geometric nature of radiant heat transfer is actually lost when using a temperature proxy that leads most to an association with air temperature. The  $\text{W} \cdot \text{m}^{-2}$  coming from each direction represent important drivers of sensation from radiant asymmetry, and the overall  $\text{W} \cdot \text{m}^{-2}$  has a more direct relationship to view factor and surface area, which are both aspects of radiant heat transfer that can be acted upon by urban designers for the case of surface sizes, and also something that urban dwellers can act upon by being either informed or guided by program to areas where the less direct sources of radiant heat like reflected shortwave and infrared longwave can be minimized.

One challenge of presenting radiant results as  $\text{W} \cdot \text{m}^{-2}$  is that since all surfaces are emitting, the positive values for surfaces like the sky or cooler plants are counterintuitive. They are emitting watts, but cooling because their emission is less than the temperature of the receiving human body. In our analysis we intentionally left out the temperature of the receiver. In the case of the human body, the temperature is in the range of  $30^{\circ}\text{C}$ , and thus it is itself emitting on the order of  $500 \text{ W} \cdot \text{m}^{-2}$ . It is the net negative exchange with cooler surfaces that makes them cold. But this analysis of net exchange can lead to a focus on the longwave exchanges and MRT analysis that are typically done for indoor thermal comfort in buildings. We argue that both indoors and outdoors an independent accounting of the spatially resolved shortwave and longwave radiant heat can provide more specific and actionable information about how the surrounding surfaces are imparting Watts of heat upon a location. For example, in the case of the PV canopy, the total spherical longwave Watts arriving at a point below the panels has about double the heat being delivered in the longwave emission from the hot PV panels above than what would be delivered by the cool and clear sky hidden behind them, but still only about half of what the unshaded direct sun in the shortwave would be. However, rather than diminishing the effect of the longwave heating of the panels, this further begs the question of whether the geometry of the shading structure could have had less random and more strategic placement of holes to both shade from the direct path of the sun path while exposing more clear sky to cool in the longwave. In future work, we hope to use these tools of analysis to make more informed

physical design and urban planning decisions based not just on average temperature proxies, but informed by a highly resolved understanding of radiant fluxes.

As we have mentioned, we neglect the temperature of the person, but that can be simply added in to estimate the net exchanges. What must also be recognized is the significance of the form of the person or other radiant receiver. The directional results are all for planar radiant fluxes, and our total results are for a spherical source receiving radiation from all directions. In other work indoors we have modeled the human body (Aviv et al., 2022), and we are working to better integrate the geometry of the human body as it is inserted into these complex radiant fields. With modern computing power it is possible to use the ray tracing techniques used to simulate reflections to include net interactions with more complex geometries of the actual person who may experience heat stress or significant discomfort due to localized heating of different body parts, and the higher resolution data provided by the SMaRT-SL is critical to the use these techniques which better account for the human form.

While our aim was to study the significance of shortwave reflections, we have also shown the significance of reflections in the longwave as well (Aviv et al., 2022). These become even more complex though because surface emissivity and reflectivity in the longwave can be even more difficult to evaluate. Still, reflections in the longwave offer yet another opportunity to engage with radiant heat.

Lastly, all of this analysis is inherently dependent on an understanding of the surface and sky properties. This includes shortwave reflectivities that were estimated, but also longwave emissivities. There are also some spectral effects that may not be accurately captured where black or greybody assumptions are made. We believe in future iterations of the SMaRT-SL we will be able to use the scanning of surfaces to not only capture radiant heat fluxes from resolved surfaces, but to also capture surface types and evaluate the emissivity and reflectivity of surfaces *in situ*. This would then feed forward to allow simulations to be done quickly to determine the radiant flux at any point in space while accurately accounting for all reflections with measured material properties.

## CONCLUSION

We have demonstrated a new method to improve how radiant heat transfer is resolved in both the shortwave and longwave spectral domains. It has long been recognized that the direct shortwave intense light from the sun causes significant heat, and that large warm surfaces can cause significant radiant heat in the longwave. In combination these present significant potential risk for outdoor heat stress and add to the thermal burden and energy demand of urban infrastructure.

The combination of novel tools illustrate how high precision net radiometry on a mobile platform can quickly evaluate

nuances of short and longwave radiant heat variation around the hot Tempe, Arizona ASU campus, and in concert with a scanning thermopile array detector we can further resolve the precise sources of short and longwave heat across the exact geometry of the site. The high resolution data has been validated through directional averaging against the net radiometer and also for the total spherical irradiance at the measurement location with good agreement with variation ranging from 10 to 20% for values  $>100 \text{ W} \cdot \text{m}^{-2}$ , and more significant relative difference at lower values where the internal device temperatures had a more significant impact on the relatively small measured values.

By resolving the shortwave radiation sources we can also differentiate the reflected sources from the ground vs the direct and diffuse sources from the sky. This was also validated using a simulation to consider how interreflections of shortwave contribute to the total radiant heat experienced at a location. We were able to show the sensor could accurately measure the reflected shortwave and also show that it was above 30% for three out of five sites when averaging the 4–5 measurements taken throughout the day.

In closing, we believe there is significant potential to better evaluate radiant heat fluxes as they affect urban dwellers in a variety of ways. In the future we hope these improved techniques can contribute to better characterization and ideally to exposing opportunities to better respond to the challenges presented in our ever warming urban climates.

## DATA AVAILABILITY STATEMENT

The datasets presented in this study can be found in online repositories. The names of the repository/repositories and accession number(s) can be found at: <https://github.com/chaos-laboratory/Resolving-Radiant-2022-Paper-Data>.

## AUTHOR CONTRIBUTIONS

CM, FM, MH, DA, FS, and AM planned the experiments and contributed to the interpretation of the results. FS and AM carried out the experiments and provided and operated their SMARTY cart sensor system. MH and DA planned and carried out the simulations and corresponding analysis. CM conceived and built the novel scanning array sensor SMART-LS and planned and carried out the novel analysis methods on the SMART-LS data. FM and CM took the lead in writing the manuscript, with MH providing contributions. All authors provided critical feedback and helped shape the research, analysis, and manuscript. All authors contributed to the article and approved the submitted version.

## FUNDING

This study was funded in part by the US National Science Foundation's Sustainability Research Network Cooperative Agreement # 1444758.

## REFERENCES

- Ali-Toudert, F. (2021). Exploration of the thermal behaviour and energy balance of urban canyons in relation to their geometrical and constructive properties. *Build. Environ.* 188, 107466. doi: 10.1016/j.buildenv.2020.107466
- Aviv, D., Gros, J., Alsaad, H., Teitelbaum, E., Voelker, C., Pantelic, J., et al. (2022). A data-driven ray tracing simulation for mean radiant temperature and spatial variations in the indoor radiant field with experimental validation. *Energy Buildings* 254, 111585. doi: 10.1016/j.enbuild.2021.111585
- Aviv, D., Guo, H., Middel, A., and Meggers, F. (2021). Evaluating radiant heat in an outdoor urban environment: Resolving spatial and temporal variations with two sensing platforms and data-driven simulation. *Urban Climate* 35, 100745. doi: 10.1016/j.ulclim.2020.100745
- Aviv, D. H. (2019). "Thermal reality capture. ACADIA 19:UBIQUITY AND AUTONOMY," in *Proceedings of the 39th Annual Conference of the Association for Computer Aided Design in Architecture (ACADIA)* (Austin, TC: The University of Texas at Austin School of Architecture), 338–345. Available online at: [http://papers.cumincad.org/cgi-bin/works/paper/acadia19\\_338](http://papers.cumincad.org/cgi-bin/works/paper/acadia19_338)
- Blum, N. B., Wilbert, S., Nouri, B., Lezaca, J., Huckebrink, D., Kazantzidis, A., et al. (2022). Measurement of diffuse and plane of array irradiance by a combination of a pyranometer and an all-sky imager. *Solar Energy* 232, 232–247. doi: 10.1016/j.solener.2021.11.064
- Chen, K. W., Teitelbaum, E., Meggers, F., Pantelic, J., and Rysanek, A. (2020). Exploring membrane-assisted radiant cooling for designing comfortable naturally ventilated spaces in the tropics. *Build. Res. Infrm.* 49, 483–495. doi: 10.1080/09613218.2020.1847025
- Chen, L., Yu, B., Yang, F., and Mayer, H. (2016). Intra-urban differences of mean radiant temperature in different urban settings in Shanghai and implications for heat stress under heat waves: a GIS-based approach. *Energy Build.* 130, 829–842. doi: 10.1016/j.enbuild.2016.09.014
- Doan, Q.-V., and Kusaka, H. (2019). Development of a multilayer urban canopy model combined with a ray tracing algorithm. *SOLA* 15, 37–40. doi: 10.2151/sola.2019-008
- Hoppe, H. (1992). A new procedure to determine the mean radiant temperature outdoors. *Wetter Unt Leben* 44, 147–151.
- Hou, M., Pantelic, J., and Aviv, D. (2021). Spatial analysis of the impact of UVGI technology in occupied rooms using ray-tracing simulation. *Indoor Air.* 31, 1625–1638.
- Houchois, N., Teitelbaum, E., Chen, K. W., Rucewicz, S., and Meggers, F. (2019). The SMART sensor: fully characterizing radiant heat transfer in the built environment. *J. Phys.s* 1343, 012073. doi: 10.1088/1742-6596/1343/1/012073
- IPCC. (2021). *Summary for Policymakers. Climate Change 2021: The Physical Science Basis. Contribution of Working Group I to the Sixth Assessment Report of the Intergovernmental Panel on Climate Change.* IPCC. Available online at: [https://www.ipcc.ch/report/ar6/wg1/downloads/report/IPCC\\_AR6\\_WGI\\_SPM\\_final.pdf](https://www.ipcc.ch/report/ar6/wg1/downloads/report/IPCC_AR6_WGI_SPM_final.pdf) (accessed May 30, 2022).
- Johansson, E., Thorsson, S., Emmanuel, R., and Krüger, E. (2014). Instruments and methods in outdoor thermal comfort studies – the need for standardization. *Urban Climate* 10, 346–366. doi: 10.1016/j.ulclim.2013.12.002
- Krayenhoff, E., Christen, A., Martilli, A., and Oke, T. (2013). A multi-layer radiation model for urban neighbourhoods with trees. *Urban Climate News* 151, 139–178. doi: 10.1007/s10546-013-9883-1
- Lindberg, F., and Grimmond, C. S. B. (2011). The influence of vegetation and building morphology on shadow patterns and mean radiant temperatures in urban areas: model development and evaluation. *Theor. Appl. Climatol.* 105, 311–323. doi: 10.1007/s00704-010-0382-8
- Lindberg, F., Holmer, B., and Thorsson, S. (2008). SOLWEIG 1.0 – modelling spatial variations of 3D radiant fluxes and mean radiant temperature in complex urban settings. *Int. J. Biometeorol.* 52, 697–713. doi: 10.1007/s00484-008-0162-7
- Lindberg, F., Onomura, S., and Grimmond, C. S. B. (2016). Influence of ground surface characteristics on the mean radiant temperature in urban areas. *Int. J. Biometeorol.* 60, 1439–1452. doi: 10.1007/s00484-016-1135-x
- Meggers, F., Aschwanden, G., Teitelbaum, E., Guo, H., Salazar, L., and Brueisauer, M. (2016). Urban cooling primary energy reduction potential: system losses caused by microclimates. *Sustai. Cities Soc.* 27, 315–323. doi: 10.1016/j.scs.2016.08.007
- Middel, A., Häb, K., Brazel, A. J., Martin, C. A., and Guhathakurta, S. (2014). Impact of urban form and design on mid-afternoon microclimate in Phoenix Local Climate Zones. *Landscape Urban Plan.* 110, 113–122. doi: 10.1016/j.landurbplan.2013.11.004
- Middel, A., and Krayenhoff, E. S. (2019). Micrometeorological determinants of pedestrian thermal exposure during record-breaking heat in Tempe, Arizona: introducing the MaRTy observational platform. *Sci. Total Environ.* 687, 137–151. doi: 10.1016/j.scitotenv.2019.06.085
- Oke, T. R. (1982). The energetic basis of the urban heat island. *Q. J. R. Meteorol. Soc.* 108, 1–24. doi: 10.1002/qj.49710845502
- Rizzo, G., Franzitta, G., and Cannistraro, G. (1991). Algorithms for the calculation of the mean projected area factors of seated and standing persons. *Energy Build.* 17, 221–230. doi: 10.1016/0378-7788(91)90109-G
- Rosado, P. J., Ban-Weiss, G., Mohegh, A., and Levinson, R. M. (2017). Influence of street setbacks on solar reflection and air cooling by reflective streets in urban canyons. *Solar Energy* 144, 144–157. doi: 10.1016/j.solener.2016.12.026
- Teitelbaum, E., Alsaad, H., Aviv, D., Kim, A., Voelker, C., Meggers, F., et al. (2022). Addressing a systematic error correcting for free and mixed convection when measuring mean radiant temperature with globe thermometers. *Sci. Rep.* 12, 6473. doi: 10.1038/s41598-022-10172-5
- Teitelbaum, E., Chen, K. W., Aviv, D., Bradford, K., Ruefenacht, L., Sheppard, D., et al. (2020). Membrane-assisted radiant cooling for expanding thermal comfort zones globally without air conditioning. *Proc. Nat. Acad. Sci. U.S.A.* 117:21162–21169. doi: 10.36227/techrxiv.12034971
- Teitelbaum, E., Guo, H., Read, J., and Meggers, F. (2017). "Mapping comfort with the SMART (Spherical Motion Average Radiant Temperature) sensor," in *Proceedings of the 15th IBPSA Conference*. Available online at: [http://www.ibpsa.org/proceedings/BS2017/BS2017\\_644.pdf](http://www.ibpsa.org/proceedings/BS2017/BS2017_644.pdf) (accessed May 30, 2022).
- Teitelbaum, E., Read, J., and Meggers, F. (2016). *Spherical Motion Average Radiant Temperature Sensor(SMART Sensor). Expanding Boundaries: Systems Thinking for the Built Environment.* (Zurich).
- Thorsson, S., Lindberg, F., Eliasson, I., and Holmer, B. (2007). Different methods for estimating the mean radiant temperature in an outdoor urban setting. *Int. J. Climatol.* 27, 1983–1993. doi: 10.1002/joc.1537
- Vallati, A., Mauri, L., and Colucci, C. (2018). Impact of shortwave multiple reflections in an urban street canyon on building thermal energy demands. *Energy Build.* 174, 77–84. doi: 10.1016/j.enbuild.2018.06.037
- Vanoss, J. K., Rykaczewski, K., Middel, A., Vecellio, D. J., Brown, R. D., and Gillespie, T. J. (2021). Improved methods for estimating mean radiant temperature in hot and sunny outdoor settings. *Int. J. Biometeorol.* 65, 967–983. doi: 10.1007/s00484-021-02131-y
- Ward, G. J. (1994). "The Radiance lighting simulation and rendering system," in *Proceedings of the 21st Annual Conference on Computer Graphics and Interactive Techniques*. (New York, NY). doi: 10.1145/192161.192286
- Yang, X., and Li, Y. (2015). The impact of building density and building height heterogeneity on average urban albedo and street surface temperature. *Build. Environ.* 90, 146–156. doi: 10.1016/j.buildenv.2015.03.037
- Conflict of Interest:** CM and FM are working to potentially commercialize technology based on and related to sensors developed as part of this work.
- The remaining authors declare that the research was conducted in the absence of any commercial or financial relationships that could be construed as a potential conflict of interest.
- Publisher's Note:** All claims expressed in this article are solely those of the authors and do not necessarily represent those of their affiliated organizations, or those of the publisher, the editors and the reviewers. Any product that may be evaluated in this article, or claim that may be made by its manufacturer, is not guaranteed or endorsed by the publisher.
- Copyright © 2022 Merchant, Meggers, Hou, Aviv, Schneider and Middel. This is an open-access article distributed under the terms of the Creative Commons Attribution License (CC BY). The use, distribution or reproduction in other forums is permitted, provided the original author(s) and the copyright owner(s) are credited and that the original publication in this journal is cited, in accordance with accepted academic practice. No use, distribution or reproduction is permitted which does not comply with these terms.**

# Frontiers in Environmental Science

Explores the anthropogenic impact on our natural world

An innovative journal that advances knowledge of the natural world and its intersections with human society. It supports the formulation of policies that lead to a more inhabitable and sustainable world.

## Discover the latest Research Topics

[See more →](#)

Frontiers

Avenue du Tribunal-Fédéral 34  
1005 Lausanne, Switzerland  
[frontiersin.org](http://frontiersin.org)

Contact us

+41 (0)21 510 17 00  
[frontiersin.org/about/contact](http://frontiersin.org/about/contact)



Frontiers in Environmental Science

